UNIVERSIDADE DE LISBOA

FACULDADE DE CIÊNCIAS

On the Nature of the Shallow Oxygen Minimum Zone of the Eastern Tropical North Atlantic

"Documento Definitivo"

Doutoramento em Ciências Geofísicas e da Geoinformação
Oceanografia

Cláudio Roberto Fernandes de Góis Cardoso

Tese orientada por:
Doutor Paulo H. R. Calil
Prof. Doutor Álvaro Peliz
Doutor Rui M. A. Caldeira

Documento especialmente elaborado para a obtenção do grau de doutor

2025

UNIVERSIDADE DE LISBOA

FACULDADE DE CIÊNCIAS

On the Nature of the Shallow Oxygen Minimum Zone of the Eastern Tropical North Atlantic

Doutoramento em Ciências Geofísicas e da Geoinformação

Oceanografia

Cláudio Roberto Fernandes de Góis Cardoso

Tese orientada por:

Doutor Paulo H. R. Calil

Prof. Doutor Álvaro Peliz

Doutor Rui M. A. Caldeira

Júri:
Presidente:

- Doutor Rui Pires de Matos Taborda, Professor Associado com Agregação e Membro do Conselho Científico da Faculdade de Ciências da Universidade de Lisboa

Vogais:

- Doutor Paulo Henrique Rezende Calil, *Research Scientist* do *Australian Institute of Marine* (orientador);
- Doutor Vincent Echevin, *Chargé de Recherche Classe Normale* do *Laboratoire d'Océanographie et du Climat: Expérimentations et Approches Numérique, Sorbonne Université*, Paris;
- Doutor Johannes Karstensen, *Scientist* do *GEOMAR Helmholtz-Zentrum für Ozeanforschung* Kiel;
- Doutora Ana Margarida Silva Pereira Teles Machado, Professora Auxiliar da Faculdade de Ciências da Universidade de Lisboa. .

Documento especialmente elaborado para a obtenção do grau de doutor

Financiado pela Fundação para a Ciência e a Tecnologia (SFRH/BD/143792/2019), com o apoio da Agência Regional para o Desenvolvimento da Investigação, Tecnologia e Inovação, e do Helmholtz-Zentrum Hereon

2025

Acknowledgements

Pursuing a PhD can often seem like a crazy decision. Yet the journey toward it begins long before we consciously realize it, quietly taking root in the back of our minds. Some might call it a calling–a kind of "spiritual" urge to uncover something that continues to fascinate and inspire us. In a way, it reflects a deep human desire to make sense of the natural world and our place within it. This path is not without its doubts, which tend to surface during the most difficult moments. But despite the challenges, this journey is also uniquely beautiful, especially when viewed from the vantage point of its conclusion. And like all meaningful endeavors, though it may feel solitary at times, it is never truly walked alone.

First, I would like to express my deepest gratitude to my exceptional supervisor, Paulo H. R. Calil, for your invaluable guidance, unwavering support, and scientific insight throughout this journey. Despite not being initially familiar with my work, you generously accepted the invitation to join this project and welcomed me at Hereon, hosting my research for an extended period. Beyond logistical support, you provided continuous mentorship and played a central role in shaping this thesis. In every sense, you took on the responsibilities of a main supervisor, and for your patience, availability, and generosity with your time and knowledge, I am profoundly grateful.

To my co-supervisor, Álvaro Peliz, thank you for accepting the invitation to be part of this project. Your insights and support–especially in handling logistical matters with the university, and during the hectic and intense final phase of writing–were invaluable and deeply appreciated.

To my co-supervisor, Rui M. A. Caldeira, I am sincerely thankful for the many opportunities you provided over the years, for believing in my work, and most importantly, for always supporting the directions I wished to pursue in my research. As a scientist, the freedom to explore and define one's own questions is among the most valuable things, and your respect for that has meant a great deal to me.

I would also like to thank Xavier Capet, Vincent Echevin, and Fehmi Dilmahamod for their generosity, valuable insights, and the stimulating discussions we shared. I am equally grateful to Birgit Quack and Thomas Browning for the opportunity to participate in the SO287 and M187 research campaigns, respectively–both of which were enriching and inspiring experiences.

I gratefully acknowledge the financial support provided by *Fundação para a Ciência e a Tecnologia* (FCT) through the PhD Grant SFRH/BD/143792/2019, as well as by *Agência Regional para o Desenvolvimento da Investigação, Tecnologia e Inovação* (ARDITI) through the Smart Islands Hub project (funded by the Regional Government of Madeira) and through the

Oceanic Observatory of Madeira (ORAM, Resolution No. 322/2022 of the Regional Government Council). I also wish to thank *Helmholtz-Zentrum Hereon* for providing essential research infrastructure and access to the HPC cluster ”Strand”, which was invaluable for the simulations and analyses carried out during this PhD.

To my colleagues and friends at Helmholtz Zentrum Hereon–Fernanda Telles, Hiram Meza, Carolina Gramcianinov, Nicolas Cevallos-Cueva, and Juanjo Tadeo–thank you for sharing this journey with me. Your companionship, advice, and humor during both the stressful and joyful moments made my time in Germany all the more meaningful. I also thank the entire “Physical-Biological Interactions” group at Hereon for their support and warm welcome.

To my colleagues and friends at ARDITI–Cátia Azevedo, Ricardo Faria, Jesus Reis, Carlos Lucas, Caroline Ferreira, Rui Vieira, Alexandra Rosa–and the rest of the team at the Oceanic Observatory of Madeira–thank you for your valuable feedback and, above all, for the laughter and camaraderie we shared over the years. These moments certainly made the work lighter and more enjoyable. I must also thank Élia Vieira, Beatriz Arraiol, Melina Teixeira and Leena Carvalho for their good humor (most of the time!) and for being such great lunchtime companions–your company always made the food a little tastier.

Quero também agradecer aos meus amigos Henrique Barros, Sara Melim, Élvio Escórcio e Laura Rodrigues, o meu muito obrigado pelos momentos de alegria, conversa e descontração. A vossa amizade foi fundamental para tornar esta fase mais leve e suportável.

Deixo também um agradecimento especial à minha família, e em especial à minha Mãe, pelo apoio incondicional desde sempre e em especial durante este percurso – desde a escrita do projeto até às últimas páginas desta tese. Ao meu Pai, que, embora já não esteja entre nós, continua presente na memória e no coração, dando-nos força para seguir em frente e dar sempre o melhor de nós. Ao meu irmão, Décio Cardoso, pelo teu apoio constante e pelo excelente trabalho como irmão mais velho – um agradecimento difícil de traduzir em palavras. Ao Miguel Ribeiro, um grande obrigado por estares presente no bons e maus momentos, e claro, pelo teu fantástico sentido de humor, sempre lá mesmo quando menos se espera.

To my German family, Sunje and Rüdiger Röttgers, I am deeply grateful for welcoming me into your home and making my stay in Germany so much warmer. A special thanks to Rüdiger–for your thoughtful comments on my work, for our many enriching conversations, and for sharing your wisdom about the life and calling of a scientist. I will carry those lessons with me throughout my life.

Finally, I want to express my deepest and most heartfelt gratitude to my partner in all aspects of life, Lucie Roettgers. Your support has been beyond words–steadfast, unwavering, and full of love. Thank you for always bringing out the best in me and for believing in me, even when I doubted myself. Your presence is a constant reminder that there is so much more to life than work. This very reminder also helps me reconnect with the purpose behind it all–the ideals and curiosity that inspired me to begin this journey in the first place. As Carl Sagan so simply and beautifully put it: ”We are a way for the universe to know itself.”

Abstract

The Eastern Tropical North Atlantic (ETNA) hosts a highly heterogeneous shallow Oxygen Minimum Zone (sOMZ), largely sustained by the remineralization of organic matter exported from productive surface waters. Despite its ecological importance, the spatial distribution, drivers, and evolution of hypoxic events remain poorly understood. This thesis investigates the physical and biogeochemical mechanisms forming the sOMZ in the ETNA using a high-resolution climatological simulation with CROCO-PISCES. A combined Eulerian-Lagrangian framework is employed to characterize the structure, dynamics, and water mass composition of hypoxic events. Persistent hypoxia is found along the continental margin, modulated by seasonal variability in the Poleward Undercurrent (PUC), while offshore hypoxia is more intermittent and associated with mesoscale eddies. Coastal hypoxia intensifies in summer, when a shoaling PUC reduces ventilation of upper central waters. Coastal-generated eddies play a key role in the recirculation and mixing of coastal waters through horizontal steering. Those formed in northern latitudes–where oxygen concentrations are lowest–often trap pre-existing hypoxic waters, intensifying them via internal remineralization and core isolation as they propagate westward. Anticyclonic Modewater Eddies (ACMEs) are the most susceptible to hypoxia, yet most hypoxic conditions develop independently due to their initial water mass composition delivered by the PUC. Mixed layer deepening appears to transform ACMEs into surface-intensified anticyclones, while simultaneously eroding their oxygen-poor, nutrient-rich cores–injecting nutrients into the euphotic zone and sustaining primary productivity. Cyclonic and anticyclonic eddies also contribute to offshore hypoxia via remineralization, driven by eddy-induced upwelling, and by the combined effects of nutrient trapping and eddy-induced Ekman pumping, respectively. Overall, sOMZ variability in the ETNA results from the interplay of coastal and offshore processes. Given the region's sensitivity to changes in ventilation and upwelling, climate-driven shifts are likely to increase the frequency and severity of hypoxic events, with significant implications for marine ecosystems and fisheries.

Keywords: Shallow Oxygen Minimum Zone, Eastern Tropical North Atlantic, Eddies, Poleward Undercurrent, Physical-biogeochemical modeling

Resumo Alargado

As Zonas de Oxigénio Mínimo (ZOM) são regiões oceânicas onde as concentrações de oxigénio (O_2) dissolvido são suficientemente baixas para impactar os ecossistemas marinhos e o ciclo biogeoquímico. No Atlântico Norte Tropical Oriental (ANTO), encontra-se uma das mais extensas ZOM do mundo, que se distingue pela presença de duas camadas hipóxicas: uma profunda, centrada a cerca de 400 m, associada à fraca ventilação, e outra pouco profunda (ZOMpp), com núcleo a $\approx$100 m, associada ao consumo de oxigénio decorrente da remineralização de matéria orgânica exportada pela elevada produtividade primária à superfície.

A ZOMpp do ANTO é particularmente dinâmica e heterogénea. Apesar da sua importância, os estudos sobre a sua formação são escassos. A investigação existente associa o seu desenvolvimento a vórtices oceânicos altamente produtivas mas com concentrações hipóxicas de oxigénio na sub-superficie ($O_2 < 40$ µmol L^{-1}). Contudo, a maioria destes estudos baseia-se num número limitado de vórtices, deixando lacunas significativas na compreensão da evolução espacial e temporal de eventos hipóxicos, especialmente no exterior dos vórtices. Por exemplo, embora seja provável que condições hipóxicas no interior dos vórtices persistam para além da sua dissipação, a evolução e impacto desses eventos permanece inexplorada.

Para além dos vórtices, foram observadas condições hipóxicas na plataforma e talude continental da Mauritânia e Senegal, atribuídas a uma combinação de elevada remineralização de matéria orgânica, fraca ventilação e variabilidade do afloramento costeiro. Dado que muitos vórtices são gerados perto da margem continental, levanta-se a hipótese de que possam aprisionar condições hipóxicas preexistentes. Contudo, permanece por investigar se os vórtices podem formar-se já com O_2 baixo ou se estas condições apenas se desenvolvem posteriormente.

Esta tese investiga os mecanismos físicos e biogeoquímicos que controlam a formação, manutenção e variabilidade de eventos hipóxicos que contribuem para a ZOMpp no ANTO. Para isso, recorre-se a uma simulação climatológica de cinco anos com um modelo físico-biogeoquímico de alta resolução ($\approx$3 km), acoplando o PISCES (”Pelagic Interactions Scheme for Carbon and Ecosystem Studies”) ao modelo CROCO (”Coastal and Regional Ocean COmmunity model”). Embora o domínio cubra todo o Atlântico Tropical – permitindo uma representação realista dos jatos zonais que desempenham um papel crucial na delimitação da ZOM – a análise centra-se no setor nordeste do domínio (10–22°N, 15–27°O), englobando o sistema de afloramento Mauritânia-Senegal e incluindo a região adjacente ao arquipélago de Cabo Verde. A metodologia combina análises Eulerianas com diagnósticos lagrangianos para rastrear eventos e massas de água hipóxicas no espaço e no tempo.

O Capítulo 3 identifica e classifica eventos hipóxicos lagrangianos com base nos processos físicos dominantes, permitindo uma caracterização inédita quanto à sua duração, intensidade, extensão e composição de massas de água. Verifica-se uma hipóxia quase permanente (>80%) entre os promontórios de Cap-Vert (Senegal) e Cap-Blanc (Mauritânia). O ciclo sazonal mostra intensificação costeira no verão, e eventos offshore mais intensos no inverno, devido à propagação de vórtices formados previamente na região costeira. Entre os tipos de vórtices, os Vórtices Anticiclónicos Modais (VAMs), com vorticidade intensificada na subsuperfície, são os que mais contribuem para a ZOMpp. A análise lagrangiana revela ainda que eventos de "fuga" e "dissipação" de hipóxia do interior de vórtices prolongam a presença de O_2 baixo para além da vida útil dos vórtices, promovendo a mistura regional de águas pobres em oxigénio.

Identificam-se dois regimes principais de massas de água hipóxicas: (1) Água Central do Atlântico Sul (ACAS) transformada localmente, de maior volume e particularmente dominante na região costeira – conhecida como ACAS de Cabo Verde (ACAScv); e (2) ACAS mais pura e relativamente ventilada, transportada pela Corrente Subsuperficial para o Pólo (conhecida como "Poleward Undercurrent", PUC), frequentemente aprisionada no interior de vórtices. Esta distinção indica que a hipóxia resulta tanto da mistura com águas regionais mais antigas e do prolongado tempo de residência da ACAScv, como da respiração acelerada associada à remineralização de matéria orgânica em vórtices altamente produtivos contendo ACAS pura. Uma fração significativa dos vórtices costeiros forma-se com águas hipóxicas, reforçando a hipotese de que vórtices hipóxicos podem de facto estar associados a condições pré-existentes. Muitos desses vórtices propagam-se em direção ao arquipélago de Cabo Verde e permanecem relativamente estacionários a leste das ilhas, expondo as costas orientadas a este a episódios intensos e duradouros de hipóxia, enquanto que as vertentes voltadas para o interior do arquipélago permanecem protegidas.

O Capítulo 4 analisa os controlos sazonais da hipóxia ao longo da zona costeira. Mostra-se que a ventilação subsuperficial promovida pela PUC desempenha um papel determinante: durante a fase de afloramento (inverno e primavera), a PUC transporta ACAS ventilada para a região costeira; já durante o verão, a corrente ascende para níveis mais superficiais, reduzindo o aporte de oxigénio às águas subsuperficiais, prolongando o tempo de residência e favorecendo o desenvolvimento de condições hipóxicas. Na transição entre as duas fases, este défice de O_2 é agravado pela intensificação da estratificação e pela manutenção da produtividade superficial, sustentada por nutrientes remanescentes previamente introduzidos na camada de mistura durante o afloramento. Mesmo quando a exportação de matéria orgânica diminui, devido ao esgotamento de nutrientes, a hipóxia persiste até que a PUC se reintensifique no outono, restabelecendo a ventilação da região.

As análises lagrangianas evidenciam que os vórtices costeiros desempenham um papel fundamental na troca de massas de água entre a margem continental e o oceano aberto. Um VAM persistente, localizado a norte de Cap-Vert, impede a ventilação direta da região costeira pela PUC durante a primavera, enquanto vórtices formados nas proximidades de 18°N favorecem a mistura entre águas costeiras e oceânicas durante o verão. Estima-se que pelo menos 65% da água hipóxica exportada do fundo da margem continental para o largo seja transportada no interior de vórtices. Apesar de ocuparem volumes relativamente reduzidos, estes resultados

sugerem que essas massas de água hipóxicas desempenham um papel significativo na formação e manutenção da ZOMpp offshore.

Por fim, o Capítulo 5 examina os mecanismos físicos responsáveis pela formação e evolução de vórtices hipóxicos gerados ao longo da costa Africana. Vórtices ciclónicos são geralmente formados por instabilidades baroclínicas associadas a gradientes de densidade, enquanto VAMs e anticiclones são principalmente gerados por instabilidades barotrópicas ligadas à interação da PUC com a batimetria. Contudo, muitos destes vórtices apresentam sinais de instabilidade baroclínica e mista, especialmente aqueles formados a sul de Cap-Vert. A maioria dos VAMs forma-se com ACAS pura e relativamente ventilada, mas rapidamente se tornam hipóxicos devido à remineralização de matéria orgânica e isolamento do núcleo, atingindo valores <20 $\mu mol\ L^{-1}$ em poucas semanas.

Inicialmente, a elevada produtividade nos VAMs decorre do aprisionamento de águas ricas em nutrientes durante a sua formação. À medida que os nutrientes são progressivamente consumidos, o fitoplâncton tende a concentrar-se na base da camada de mistura, onde nutrientes permanecem disponíveis devido ao levantamento das isopicnais superiores. Durante a propagação para oeste, o espessamento da camada de mistura pode transformar VAMs em anticiclones superficiais, promovendo a erosão do núcleo subsuperficial – tipicamente pobre em oxigénio mas rico em nutrientes. Esta erosão facilita a injeção de nutrientes para a camada de mistura, estimulando a produtividade primária, que sustenta a exportação de matéria orgânica e mantém o consumo de O_2 na subsuperfície. Vórtices ciclónicos, por sua vez, promovem a produtividade através de afloramento interno, enquanto os anticiclones dependem da retenção de nutrientes e do afloramento induzido pela interação vórtice-vento ("Ekman pumping"). Em todos os tipos de vórtices, o isolamento do núcleo subsuperficial permanece um fator determinante para o desenvolvimento e persistência da hipóxia.

Em síntese, os resultados desta tese evidenciam que a ZOMpp do ANTO é mantida por um conjunto complexo e interligado de processos físicos e biogeoquímicos que operam a múltiplas escalas. A formação de hipóxia costeira é regulada por alterações sazonais na ventilação, estratificação e exportação de matéria orgânica, enquanto a hipóxia offshore depende de vórtices costeiros que intensificam condições hipóxicas ao se propagarem para oeste. As interações entre circulação costeira, formação de vórtices e suas transformações internas são cruciais para a manutenção da ZOMpp.

Com as alterações climáticas, prevê-se que a redução da ventilação aliada a alterações na produtividade primária e à intensificação da atividade de vórtices, conduza a um aumento da frequência e intensidade de eventos hipóxicos na região. Tais alterações poderão ter impactos significativos sobre a biodiversidade, os recursos pesqueiros e os ciclos biogeoquímicos. Esta tese, portanto, oferece uma base robusta para a compreensão dos processos físicos e biogeoquímicos que sustentam a ZOMpp no ANTO, e representa um avanço metodológico relevante, com potencial aplicação na previsão e gestão da hipóxia em sistemas de afloramento de fronteiras orientais.

Palavras Chave: Zona de Oxigénio Mínimo pouco profunda, Atlântico Norte Tropical Oriental, Vórtices Ocêanicos, Corrente Subsuperficial para o Pólo, Modelação Física-Biogeoquímica

Contents

1 Introduction **1**

1.1 Oxygen Minimum Zones . . . 3

1.1.1 Impacts on marine ecosystems and biogeochemical cycles . . . 4

1.1.2 OMZs in the context of climate change . . . 6

1.2 Mesoscale dynamics of EBUSs . . . 7

1.2.1 Coastal upwelling . . . 8

1.2.2 Boundary currents . . . 9

1.2.3 Eddies . . . 11

1.3 The Eastern Tropical North Atlantic . . . 14

1.3.1 Mauritania-Senegal upwelling system . . . 14

1.3.2 Regional water masses and circulation . . . 16

1.3.3 The Oxygen Minimum Zone . . . 21

1.3.4 Low-oxygen eddies . . . 22

1.3.5 Hypoxic conditions at the coastal region . . . 24

1.4 Objectives and organization . . . 27

1.4.1 Approach . . . 27

1.4.2 Thesis structure . . . 28

2 Model and methods **31**

2.1 Model setup . . . 31

2.1.1 CROCO . . . 31

2.1.2 PISCES . . . 33

2.1.3 Model configuration . . . 35

2.2 Datasets for model validation . . . 37

2.2.1 Climatologies . . . 37

2.2.2 Satellite data . . . 39

2.2.3 Bottom observations . . . 39

2.3 Model evaluation . . . 40

2.3.1 Comparison with climatologies and satellite observations . . . 40

2.3.2 Bottom layer . . . 49

2.4 Methods . . . 51

2.4.1 Oxygen thresholds definition . . . 52

2.4.2 Season definition . . . 52

2.4.3 Water mass analysis . . . 52

2.4.4 Eddy detection and tracking . . . 53
2.4.4.1 Identification of Anticyclonic Mode-water eddies . . . 55
2.4.5 Lagrangian particle simulation . . . 56
2.4.6 Oxygen budget . . . 58

3 Characterization of the Shallow Oxygen Minimum Zone in the Eastern Tropical North Atlantic 61
3.1 Introduction . . . 61
3.2 Methods . . . 63
3.2.1 Identification and tracking of Lagrangian Hypoxic Events . . . 63
3.2.2 Metrics for the characterization of hypoxic events . . . 65
3.3 General characteristics of the sOMZ . . . 66
3.3.1 Spatial characterization . . . 67
3.3.2 Seasonal variability and distribution . . . 70
3.3.3 Hypoxic water mass composition . . . 71
3.4 A lagrangian perspective of hypoxic events . . . 73
3.4.1 Event dynamics . . . 74
3.4.2 Spatial distribution and characteristics . . . 75
3.4.3 Monthly distribution . . . 78
3.4.4 Temporal evolution and statistics of LHEs . . . 80
3.5 Discussion . . . 84
3.5.1 Relation between water masses and hypoxic events . . . 84
3.5.2 Eddies as vectors, intensifiers and suppliers of hypoxic conditions . . . 85
3.5.3 Origin of ”combined” and ”bottom” LHEs . . . 89
3.5.4 Potential impacts on ecosystems . . . 90
3.5.5 Method limitations and caveats . . . 91
3.6 Summary and conclusions . . . 92

4 Drivers of the shallow oxygen minimum zone off the northwestern African coast 95
4.1 Introduction . . . 95
4.2 Methods . . . 96
4.3 Overview of seasonal dynamics . . . 96
4.4 Coastal dynamics . . . 100
4.4.1 Meridional current variability . . . 100
4.4.2 Impact of meridional currents on tracers . . . 103
4.4.3 Time-series analysis of a ”virtual” mooring . . . 108
4.4.4 Bottom layer hypoxia . . . 112
4.5 Lagrangian assessment of hypoxic water masses . . . 114
4.5.1 Residence time . . . 114
4.5.2 Transport pathways . . . 116
4.5.3 Particle coastal import . . . 117
4.5.4 Export of hypoxic bottom waters . . . 119

4.6 Summary and conclusions . . . 120

5 Generation and evolution of low-oxygen eddies in the Eastern Tropical North Atlantic 123

5.1 Introduction . . . 123
5.2 Methods . . . 125
5.2.1 Composite analysis of eddy vertical structure . . . 125
5.2.2 Determination of eddy generation mechanisms . . . 125
5.3 Characteristics of coastal-generated eddies . . . 127
5.3.1 Trajectories and mean properties . . . 127
5.3.2 Vertical structure . . . 130
5.3.3 Spatial and seasonal patterns of eddy generation . . . 133
5.3.4 Eddy generation mechanisms . . . 135
5.3.4.1 Anticyclones and ACMEs . . . 136
5.3.4.2 Cyclones . . . 139
5.3.4.3 Relation between formation mechanisms and hypoxic conditions 141
5.4 Low-oxygen eddies . . . 142
5.4.1 Differences between hypoxic and non-hypoxic eddies . . . 142
5.4.2 Formation from pre-existing conditions . . . 145
5.4.3 En-route formation . . . 149
5.4.3.1 Cyclones . . . 149
5.4.3.2 Anticyclones . . . 152
5.4.3.3 ACMEs . . . 154
5.5 Summary and conclusions . . . 157

6 Synthesis and outlook 159

6.1 Major scientific findings . . . 159
6.2 Limitations and caveats . . . 164
6.3 Implications of our results . . . 169
6.4 Future perspectives . . . 172

Bibliography 175

A Supplementary material 223

A.1 Supplement to Chapter 3 . . . 223
A.2 Supplement to Chapter 4 . . . 230
A.3 Supplement to Chapter 5 . . . 235

List of Figures

1.1 Schematic representation of the physical and biogeochemical processes driving the formation and maintenance of Oxygen Minimum Zones 4
1.2 Global average distribution of surface Chlorophyll-*a* concentrations 8
1.3 Vertical density structure associated with three types of eddies in the process of formation/intensification 13
1.4 Seasonal frequency of occurrence of coastal wind jet along the Northwestern African coast 15
1.5 Mean monthly distribution of Sea Surface Temperature for the Eastern North Atlantic 16
1.6 Potential temperature–Salinity diagram from the CANOA08 cruise (November 2008, R/V Sarmiento de Gamboa) in the Canary Current Upwelling System . . 18
1.7 Mean proportion of South Atlantic Central Water relative to North Atlantic Central Water at 120 m depth in the Eastern Tropical North Atlantic, with representation of main currents 19
1.8 Minimum oxygen concentrations at the shallow and deep Oxygen Minimum Zones of the Eastern Tropical North Atlantic 22
1.9 Oxygen concentrations across a cross section through the center of a low-oxygen Anticyclonic Mode Water Eddy in the Eastern Tropical North Atlantic 24
1.10 Vertical distribution of oxygen concentrations along a longitudinal transect at approximately 18°N off the Mauritanian coast 25

2.1 Normalized Taylor diagrams for model-observation comparisons at selected depths 41
2.2 Normalized target diagrams for model-observation comparisons at selected depths 42
2.3 Comparison of yearly and seasonal mean oxygen concentrations at 100 m depth between model outputs and observations 43
2.4 Comparison of surface current speed and direction between model outputs and GDP drifters 44
2.5 Comparison of surface Mean Kinetic Energy between model outputs and altimetry observations 46
2.6 Comparison of surface Eddy Kinetic Energy between model outputs and altimetry observations 46
2.7 Comparison of Sea Surface Temperature between model outputs and satellite observations 48
2.8 Comparison of Chlorophyll-*a* concentrations between model outputs and satellite observations 49

2.9 Comparison between bottom model output and *in-situ* observations at seven stations along the continental shelf and slope off Mauritania 50
2.10 Proportion of South Atlantic Central Water relative to North Atlantic Central Water within the upper central water layer over Tropical Atlantic Ocean 54
2.11 Standard deviation of negative Okubo–Weiß values along a meridional section at 18.5°W 57

3.1 Schematic illustrating the detection and labeling of Lagrangian Hypoxic Events as clusters of hypoxic grid cells evolving in space and time 64
3.2 Snapshot of daily-averaged oxygen concentrations, taken on the 9th of July of year 1 67
3.3 Spatial projection of the main characteristics of hypoxic events 68
3.4 Seasonal variability of hypoxic conditions 70
3.5 Hydrographic characteristics of hypoxic water masses 72
3.6 Oxygen concentrations and Lagrangian Hypoxic Events on July 4th and 20th of year 1 73
3.7 Overview of the relations between Lagrangian Hypoxic Event categories 74
3.8 Spatial distribution of frequency of hypoxic conditions per Lagrangian Hypoxic Event category 76
3.9 Spatial distribution of median daily oxygen minimum/intensity maximum per Lagrangian Hypoxic Event category 77
3.10 Spatial distribution of hypoxic daily volume per Lagrangian Hypoxic Event category 77
3.11 Monthly cumulative distribution of key metrics per Lagrangian Hypoxic Event category 79
3.12 Temporal evolution of key metrics per Lagrangian Hypoxic Event category . . 81
3.13 Violin plot for key metrics per Lagrangian Hypoxic Event category 82
3.14 Oxygen consumption rate for eddy Lagrangian Hypoxic Events 86
3.15 Contribution of each Lagrangian Hypoxic Event category to the mean O_2 concentrations 88

4.1 Seasonal phytoplankton biomass concentration 97
4.2 Seasonal Export Production of Carbon at 100 m depth 99
4.3 Seasonal frequency of hypoxic conditions 100
4.4 Monthly-averaged meridional current velocities at four longitudinal sections . . 101
4.5 Hovmöller diagrams for the meridional and temporal variability of physical and biogeochemical tracers along the coast (part I) 104
4.6 Hovmöller diagrams for the meridional and temporal variability of physical and biogeochemical tracers along the coast (part II) 105
4.7 Meridional transport of oxygen along latitude 107
4.8 Daily hovmöller diagram of a point extraction at 18°N and ≈160 m depth . . . 109
4.9 Monthly-averaged oxygen biological budget terms of a point extraction at 18°N and ≈160 m depth 111

4.10 Monthly O_2 concentrations averaged over the two model bottom layers 112
4.11 Climatological daily variability of oxygen and physical parameters influencing vertical mixing at the bottom of the continental shelf and slope 114
4.12 Water residence time in the coastal region 115
4.13 Seasonal backward trajectories of coastal hypoxic water masses 116
4.14 Import of lagrangian particles released within the coastal region and crossing the respective boundary 118
4.15 Export of particles from the bottom of the continental margin 120

5.1 Trajectories of coastal-generated eddies 128
5.2 Mean vertical distribution of key physical parameters of coastal-generated eddies 130
5.3 Mean vertical distribution of key biogeochemical parameters within coastal-generated eddies 131
5.4 Monthly genesis of coastal-generated eddies along latitude 134
5.5 Spatial and temporal variability of anticyclonic and anticyclonic modewater eddy generation mechanisms along the Northwestern African coast 136
5.6 Spatial and temporal variability of cyclonic eddy generation mechanisms along the Northwestern African coast 140
5.7 Differences between vertical composites of hypoxic and non-hypoxic coastal-generated eddies 144
5.8 Moment of formation of low-oxygen eddies formed with pre-existing hypoxic conditions in their interior 146
5.9 Lagrangian perspective of the history of hypoxic water masses trapped within low-oxygen eddies at the moment of formation 147
5.10 Evolution of a hypoxic cyclonic eddy: Part I 150
5.11 Evolution of a hypoxic cyclonic eddy: Part II 151
5.12 Evolution of a hypoxic anticyclonic eddy 153
5.13 Evolution of a hypoxic Anticyclonic Modewater Eddy 155

A.1 Temporal evolution of complementary metrics per Lagrangian Hypoxic Event category 223
A.2 Potential temperature-Salinity histograms color-coded with volume-weighted average oxygen concentrations 224
A.3 Potential temperature-Salinity histograms color-coded with total volume 225
A.4 Spatial distribution of minimum daily oxygen minimum per Lagrangian Hypoxic Event category 226
A.5 Seasonal variability of minimum daily oxygen minimum within hypoxic events 227
A.6 Evolution of an Argo float trapped inside a cyclonic low-oxygen eddy 228
A.7 Glider observations from the M107 campaign off the Mauritanian coast 228
A.8 Hovmöller diagrams for the meridional and temporal variability of physical and biogeochemical tracers along the coast (WOA23 data) 230
A.9 Daily hovmöller diagram of a point extraction at 18°N and ≈160 m depth for complementary parameters 231

A.10 Snapshot of key parameters, taken on the 24th of July of year 2 232
A.11 Monthly oxygen supply to the bottom via vertical mixing 233
A.12 Monthly average particle residence time 233
A.13 Histogram indicating the proportion of coastal particles intersecting the coastal region boundaries per lifetime threshold 234
A.14 Import of lagrangian particles released within the coastal region and crossing the respective boundary, set at 1° distance from the shelf break 234
A.15 Monthly genesis of coastal-generated eddies (lifetime > 10 days) along latitude 235
A.16 Spatial and temporal variability of energy conversion terms to Eddy Kinetic Energy 236
A.17 Vertical and temporal variability of energy conversion terms to Eddy Kinetic Energy 236
A.18 Example of a snapshot with decomposition of Ertel Potential Vorticity terms at 100 m depth 237
A.19 Differences between vertical composites of hypoxic and non-hypoxic coastal-generated eddies, with no lifetime limit 238
A.20 Evolution of a second hypoxic cyclonic eddy 239
A.21 Evolution of a second hypoxic Anticyclonic Modewater Eddy 240
A.22 Evolution of a third hypoxic Anticyclonic Modewater Eddy 241
A.23 Evolution of a forth hypoxic Anticyclonic Modewater Eddy 242
A.24 Evolution of a fifth hypoxic Anticyclonic Modewater Eddy 243
A.25 Evolution of a sixth hypoxic Anticyclonic Modewater Eddy 244

List of Tables

1.1 Overview of research cruises conducted in the coastal region of the Eastern Tropical North Atlantic 26

3.1 Definition of metrics used to characterize hypoxic events 65

5.1 Mean properties of coastal-generated eddies 129
5.2 Summary of the proportion of anticyclones and Anticyclonic Modewater Eddies formed by different mechanisms within the respective major eddy generation hotspots 138
5.3 Summary of the proportion of cyclones formed by different mechanisms within the corresponding major eddy generation hotspots 141
5.4 Proportion of hypoxic eddies per mechanism of formation 142
5.5 Mean dynamical properties of hypoxic and non-hypoxic coastal-generated eddies 143

A.1 Summary statistics of Lagrangian Hypoxic Events for each category 229

Chapter 1

Introduction

The oxygenation of the ocean has undergone profound changes over geological timescales, tightly linked to atmospheric evolution and biological innovation (Canfield, 2005; Falkowski et al., 2005, 2011). Today, dissolved Oxygen (O_2) is not only a prerequisite for aerobic marine life, but also a key regulator of biogeochemical processes that sustain ocean productivity and climate feedbacks (Gruber, 2011; Helm et al., 2011). In particular, regions of the ocean where O_2 concentrations are persistently low–commonly referred to as Oxygen Minimum Zones (OMZs)–act as hotspots for nitrogen loss (Álvarez-Salgado et al., 2013; Sokoll et al., 2016; Gier et al., 2017), habitat compression (Stramma, Prince, et al., 2012; Köhn et al., 2022), and shifts in ecosystem structure (Gilly et al., 2013; Vedor et al., 2021). Although OMZs occupy only a small fraction of the ocean, their role in regulating elemental cycles and marine biodiversity is disproportionately large (Levin et al., 2009; Paulmier & Ruiz-Pino, 2009).

Anthropogenic climate change threatens to exacerbate oxygen loss in the ocean through warming-induced stratification, decreased ventilation, and altered circulation patterns (Falkowski et al., 2011; Oschlies et al., 2018; Mancini et al., 2024). Observational and modeling studies consistently report ongoing deoxygenation trends across the global ocean, including the vertical shoaling and lateral expansion of OMZs (Schmidtko et al., 2017; Breitburg et al., 2018; Stramma & Schmidtko, 2021). These changes have major ecological and socio-economic consequences, especially in coastal upwelling systems that sustain some of the world's most productive fisheries (Fréon, Barange, & Arístegui, 2009; Bakun et al., 2010; Pörtner et al., 2014). In these regions, the intersection of intense biological activity and sluggish circulation creates conditions conducive to O_2 depletion, with potential repercussions for marine food webs and local economies (reviewed by Levin et al., 2009).

The Eastern Tropical North Atlantic (ETNA) is one such region, hosting a layered OMZ structure that includes a particularly dynamic shallow OMZ (sOMZ) centered just beneath the thermocline (Karstensen et al., 2008; T. Fischer et al., 2013; Brandt et al., 2015). Unlike its deeper counterpart, the sOMZ is tightly coupled to seasonal upwelling variability, mesoscale eddies, coastal biogeochemical processes and boundary current dynamics (Karstensen et al., 2015; Schütte, Karstensen, et al., 2016; Klenz et al., 2018; Machu et al., 2019; Thomsen et al., 2019). Of growing interest are the so-called low-oxygen eddies–coherent mesoscale features that transport oxygen-deficient waters offshore–thought to play a central role in the formation and maintenance of the sOMZ (e.g., Löscher et al., 2015; Fiedler et al., 2016; Hauss et al., 2016; Grundle et al., 2017; Karstensen et al., 2017; Frenger et al., 2018).

Despite increased observational and modeling efforts, the spatial and temporal characteristics of hypoxic events contributing to the sOMZ remain poorly constrained. For instance, most studies have tracked and sampled only a limited number of eddies on multiple occasions (e.g., Karstensen et al., 2015; Karstensen et al., 2017), leaving substantial gaps in our understanding of how hypoxic conditions evolve, particularly in non-eddy environments. Additionally, while hypoxic conditions generated within eddies are likely to persist beyond their dissipation (Löscher et al., 2015), observational evidence on how such events evolve remains scarce.

Hypoxic conditions have also been observed on the continental shelf and slope of Mauritania and Senegal (e.g., Yücel et al., 2015; Thomsen et al., 2019; Dale et al., 2022). Given that low-oxygen eddies frequently form near the continental margin (Karstensen et al., 2015; Schütte, Karstensen, et al., 2016; Dilmahamod, 2023), it is surely possible that they trap pre-existing hypoxic conditions upon formation. However, despite recent evidence of extremely low O_2 concentrations within newly formed eddies off Mauritania (Ekau et al., 2016; Devresse et al., 2022), this hypothesis remains speculative (Schütte, Karstensen, et al., 2016).

A key challenge in understanding OMZ dynamics lies in the limited spatial and temporal resolution of both observations and global ocean models (Duteil et al., 2014; Schütte, Brandt, & Karstensen, 2016; Thomsen et al., 2019). Earth System Models, for instance, typically operate at horizontal resolutions too coarse to resolve mesoscale structures, relying instead on parameterizations that may misrepresent key transport and mixing processes (Oschlies et al., 2008; Frölicher & Laufkötter, 2018; Frölicher et al., 2018; Frölicher et al., 2020; Wong et al., 2024). In contrast, high-resolution eddy-resolving simulations can better capture the interplay between ocean circulation, productivity, and O_2 consumption that governs the OMZs at lower spatial scales (Lévy et al., 2012; Bianchi et al., 2018; Lévy et al., 2018). Recent studies suggest that explicitly resolving mesoscale features and basin-wide zonal jets improves the representation of the structure and intensity of OMZs (Calil, 2023), with potential consequences for biogeochemical fluxes and the global ocean oxygen inventory (Frenger et al., 2018; Lévy et al., 2022, 2024).

This thesis aims to improve the understanding of the occurrence, characteristics, and evolution of hypoxic events contributing to the formation of the sOMZ in the ETNA, here defined as the region between 10°–22°N and ≈15°–27°W. This investigation is conducted through the analysis of a high-resolution climatological physical-biogeochemical simulation covering the entire tropical Atlantic Ocean. A combined Eulerian-Lagrangian approach is employed, first by tracking the evolution of hypoxic events and subsequently reconstructing the origin and biogeochemical transformation of the water masses that become hypoxic. Particular emphasis is placed on the mesoscale features modulating the variability of physical and biogeochemical properties, with a particular focus on boundary currents and mesoscale eddies. Understanding these processes is essential for improving model projections of marine deoxygenation, assessing ecosystem resilience, and guiding policy decisions in the face of accelerating climate change (Gruber, 2011; Oschlies et al., 2018; Gruber et al., 2021).

1.1 Oxygen Minimum Zones

O_2 is a fundamental component of marine ecosystems and plays a key role in structuring biological communities and regulating key biogeochemical processes. Like other oceanic properties such as temperature, salinity, and nutrients, O_2 concentrations are not homogeneous but exhibit significant variability across spatial and temporal scales, particularly in the vertical dimension.

In the upper ocean, sunlight penetration warms the ocean and leads to thermal stratification. At the same time, sunlight drives photosynthesis by phytoplankton, sustaining primary production in the euphotic zone. Organic material produced in surface waters is subsequently exported to the ocean interior as sinking Particulate Organic Carbon (POC), a process known as export production (Eppley & Peterson, 1979). Below the euphotic layer, O_2 consumption is largely governed by heterotrophic microbial remineralization of this sinking organic matter (Karstensen et al., 2008), respiration by zooplankton grazing on sinking detritus (i.e., flux feeding; Fiedler et al., 2016), vertically migrating animals (Bianchi et al., 2013), and pelagic fishes (Bertrand et al., 2011; Stramma, Prince, et al., 2012; Clarke et al., 2022).

The balance between O_2 consumption via biological respiration and its replenishment through ocean circulation and mixing ultimately determines O_2 concentrations in subsurface waters. In regions where high surface productivity coincides with weak ventilation, O_2 levels decline and give rise to steady-state low-oxygen zones in the water column, known as OMZs (Wyrtki, 1962; Karstensen et al., 2008; Stramma et al., 2010).

Typically located along eastern oceanic boundaries, OMZs develop in unventilated shadow zones of the ocean, where sluggish circulation and weak water mass renewal contribute to prolonged residence times of old, oxygen-depleted waters (Figure 1.1; Luyten et al., 1983). Subsurface currents such as the Pacific and Atlantic Equatorial Undercurrents and Countercurrents play a crucial role in regulating O_2 levels in OMZs by modulating the import of oxygenated waters (Karstensen et al., 2008; Stramma et al., 2010; Brandt et al., 2015). Although to a lesser degree, stratification also limits vertical mixing, further restricting O_2 exchange between the surface and subsurface layers (Brandt et al., 2015; Pitcher et al., 2021).

Eastern boundary systems are also characterized by intense coastal upwelling, which fuels primary productivity (further discussed in Section 1.2.1) and enhances the export of organic matter to subsurface layers. As this material sinks, microbial decomposition consumes O_2, leading to pronounced depletion at intermediate depths (Figure 1.1). The intensity of O_2 loss is influenced by several factors, including the magnitude of export production, the efficiency of organic matter degradation, and microbial respiration rates (Engel et al., 2017; Oschlies et al., 2018; Engel et al., 2022).

Hence, unlike localized “dead zones” caused by eutrophication–such as those observed in the Gulf of Mexico (Rabalais et al., 2002), Chesapeake Bay (Sale & Skinner, 1917), the Baltic Sea (Carstensen et al., 2014), and the East China Sea (Z.-Y. Zhu et al., 2017)–OMZs are naturally occurring large-scale features primarily maintained by ocean circulation and primary productivity.

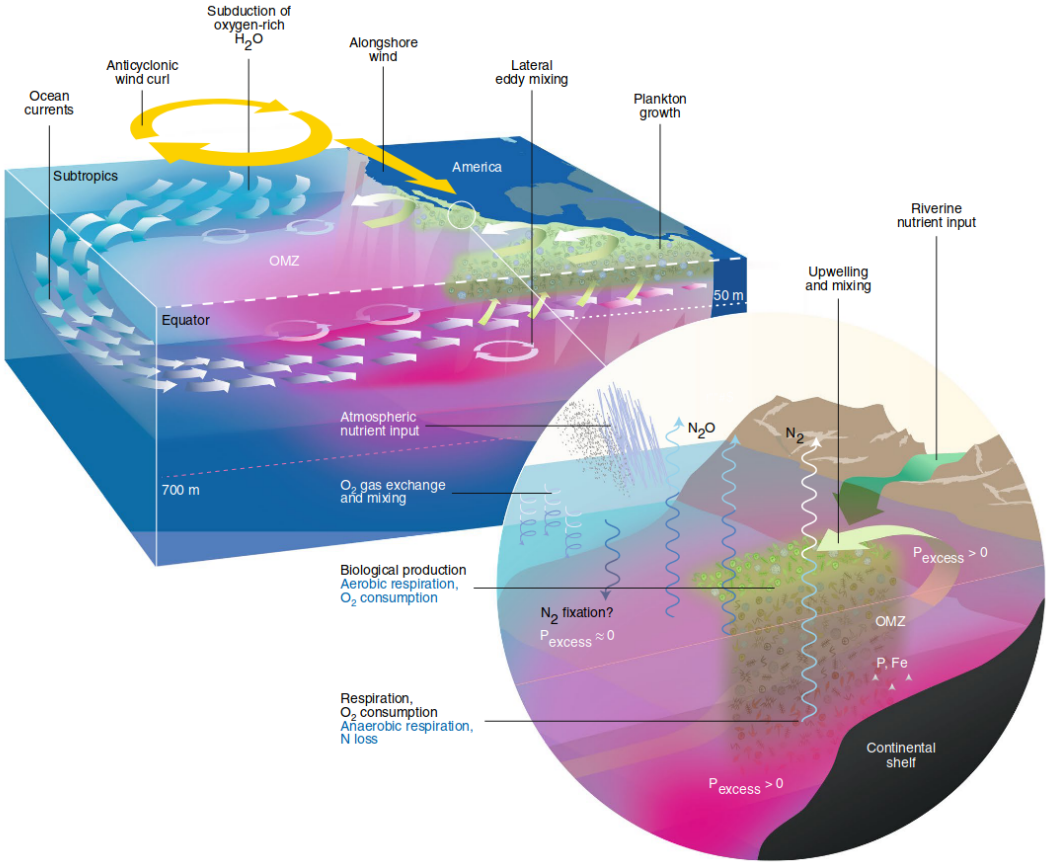


Figure 1.1: Schematic representation of the physical and biogeochemical processes driving the formation and maintenance of OMZs. Special focus is given to the eastern subtropical North Pacific, which is representative of mechanisms also active in the ETNA. The inset highlights key biogeochemical processes associated with eastern boundary OMZs: nitrogen loss via denitrification and anammox, which generates gaseous nitrogen and leaves behind excess phosphate (P_{excess}); potential compensation through nitrogen fixation; and the production of nitrous oxide (N_2O) and nitrogen gas (N_2). Under low-oxygen conditions, sediments may also release phosphate and iron into the water column. Retrieved from Oschlies et al. (2018).

1.1.1 Impacts on marine ecosystems and biogeochemical cycles

OMZs alter marine habitats by imposing oxygen constraints on aerobic organisms, primarily leading to avoidance behaviors and potential increases in mortality (Vaquer-Sunyer & Duarte, 2008; Ekau et al., 2010; Bertrand et al., 2011). Four distinct oxygen concentration thresholds are particularly relevant for understanding the biogeochemical and ecological impacts of low O_2 concentrations: (i) hypoxia, (ii) severe hypoxia, (iii) suboxia, and (iv) anoxia.

Hypoxia occurs when O_2 levels fall below the requirements for aerobic respiration in many fish and invertebrate species, causing physiological stress (e.g., Wilding, 1939) and leading to habitat compression, altered migration patterns, and shifts in species distributions (Gilly et al., 2013; Vedor et al., 2021). At O_2 between 20 and 6 µmol L^{-1}, conditions become severely hypoxic and pose lethal constraints for most large aerobic organisms (Diaz & Rosenberg, 2008). Organisms inhabiting these conditions exhibit specialized physiological and behavioral adaptations that increase their tolerance (Childress, 1995; Drazen & Seibel, 2007; Seibel, 2011).

At suboxic levels ($O_2 < 6$ µmol L^{-1}), microbial communities switch from aerobic to anaerobic respiration, using nitrate (NO_3^-) and other nitrogen compounds as terminal electron acceptors. This triggers denitrification and anaerobic ammonium oxidation (anammox) processes, resulting

in the loss of bioavailable nitrogen as dinitrogen (N_2) and nitrous oxide (N_2O, a potent green house gas; Gruber & Galloway, 2008), ultimately constraining primary productivity (Codispoti & Christensen, 1985; Kalvelage et al., 2011; Wright et al., 2012). Under anoxic conditions ($O_2 < 1$ µmol L^{-1}), only highly adapted microbial taxa persist, with sulfate (SO_4^{2-}) reduction replacing nitrate-based respiration as the dominant anaerobic pathway (Paulmier & Ruiz-Pino, 2009; Wright et al., 2012).

The hypoxic threshold is commonly used to define OMZ boundaries, but the exact O_2 threshold for physiological stress varies across species and regions. For example, in the Pacific Ocean, hypoxia is typically defined as $O_2 < 60$ µmol L^{-1}, but oxygen concentrations frequently drop below all the above thresholds. In contrast, a lower threshold of $O_2 < 40$ µmol L^{-1} has been proposed to define OMZs in the Atlantic Ocean, where O_2 concentrations rarely reach severe hypoxic levels (Karstensen et al., 2008; Stramma, Brandt, et al., 2008). To facilitate comparison with past studies conducted in the ETNA, it is this threshold that we use to define hypoxic conditions throughout this thesis.

The upper boundaries of OMZs serve as critical ecological zones, where large aggregations of micronekton seek refuge from visually-oriented predators during day. These aggregations, which form prominent acoustic scattering layers, are a key feature of mesopelagic ecosystems (Benoit-Bird & Au, 2001; Bertrand et al., 2010). They provide essential foraging grounds to a wide range of deep-diving pelagic predators, including swordfish and tuna (Carey & Robison, 1981; Abecassis et al., 2012; Stramma, Prince, et al., 2012; Fuller et al., 2015), sharks (Nakano et al., 2003; Coelho et al., 2015) and large marine mammals like elephant seals, beaked whales and sperm whales (Le Boeuf et al., 2000; Keates et al., 2022; Cox et al., 2023). At night, these organisms ascend to the surface to feed on plankton, facilitating vertical energy transfer across ocean layers and establishing dynamic trophic linkages between mesopelagic and epipelagic ecosystems (Hays, 2003; Robison, 2009; Klevjer et al., 2020).

OMZs also play a crucial role in structuring fisheries, particularly within the Eastern Boundary Upwelling Systems (EBUSs) of the Pacific and Atlantic Oceans. In the Pacific Ocean, two intense OMZs exist at different depths: one in the California Current and another in the Humboldt Current near Peru and Chile. Due to its shallower depth, the South Pacific OMZ compresses fish populations into a narrow surface layer, increasing their vulnerability to fishing and enhancing fishing efficiency (Chavez & Messié, 2009). This habitat compression effect is one of the key factors explaining why the Peru Current sustains significantly higher fish yields than the California Current, despite both systems exhibiting similar levels of primary production (Chavez et al., 2008; Brochier et al., 2011).

Beyond their ecological and fisheries impacts, OMZs function as biogeochemical hotspots, playing a critical role in the cycling of major elements such as carbon, nitrogen, phosphorus, and sulfur (reviewed in Levin, 2018). OMZs contribute substantially to oceanic nitrogen loss, as oxygen-deficient conditions promote anaerobic pathways like denitrification and anammox (Bianchi et al., 2012; Bograd et al., 2015). Additionally, OMZs regulate sulfur cycling, supporting microbial sulfate reduction and sulfur transformations that influence nutrient availability and redox balance in the water column (Schulz & Schulz, 2005; Brock & Schulz-Vogt, 2011). Besides

their role in regulating ocean ecology and chemistry, OMZs are also sensitive indicators of and contributors to global climate-driven changes.

1.1.2 OMZs in the context of climate change

In recent decades, OMZs have received increasing scientific attention due to their observed intensification, shoaling and expansion (e.g., Bograd et al., 2008; Diaz & Rosenberg, 2008; Stramma, Johnson, et al., 2008; Helm et al., 2011; Stramma & Schmidtko, 2021). These trends are closely linked to climate change. Ocean warming not only reduces the solubility of oxygen at the surface but also enhances upper-ocean stratification, thereby restricting the downward transport of oxygen into the thermocline (Sarmiento et al., 1998; Matear & Hirst, 2003; Keeling et al., 2010; Helm et al., 2011; Schmidtko et al., 2017; Bates & Johnson, 2020). Concurrent declines in the oxygen content of source waters that ventilate OMZs further contribute to their expansion and intensification (Gilly et al., 2013; Oschlies et al., 2018). Additionally, climate-driven shifts in large-scale circulation patterns can weaken interior ventilation, amplifying oxygen loss throughout the water column (Brandt et al., 2010; Keeling et al., 2010; Stramma, Oschlies, & Schmidtko, 2012; Hahn et al., 2014; Claret et al., 2018).

Regional case studies provide clear examples of these mechanisms. In the Southern California Bight, oxygen concentrations in the outer shelf have declined by an estimated 20–30% over the past three decades, a trend attributed to the intensification and shoaling of the poleward-flowing California Undercurrent, which transports low-oxygen tropical waters into the region (Bograd et al., 2015). Similarly, in Saint Lawrence Estuary, oxygen saturation has decreased from 37.7% in the 1930s to 20.7% in 2003 (Gilbert et al., 2005). This deoxygenation extends beyond the estuary into the entire Gulf of St. Lawrence (Claret et al., 2018) and has been linked to a diminished influx of well-oxygenated Labrador Current waters, coupled with an increased contribution of less-oxygenated waters from the North Atlantic. These observations suggest that a centennial-scale weakening or reorganization of the Labrador Current may be underway, underscoring the potential for large-scale ocean circulation changes to drive coastal deoxygenation in the coming century (Claret et al., 2018).

While physical mechanisms are the primary drivers of ocean deoxygenation (Gruber, 2011), biological processes–particularly surface primary production–also play an important role. Increased productivity leads to greater export of organic matter, enhancing microbial respiration at depth and accelerating O_2 consumption. However, trends in productivity vary across regions: some studies report increased productivity in upwelling zones overlying OMZs (Gregg et al., 2005; Behrenfeld et al., 2006; Chavez et al., 2011; Dai et al., 2023), while others find long-term global declines in phytoplankton biomass (Boyce et al., 2010). In upwelling systems, intensification of alongshore winds due to stronger land-sea temperature gradients has been linked to enhanced nutrient supply and surface productivity (Chavez et al., 2008; Bakun et al., 2010; Chavez et al., 2011; Doney et al., 2012; Ridder & England, 2014). However, climate projections predict a 10% weakening of the Mauritania-Senega upwelling system (Sylla et al., 2019). Although this is expected to reduce surface primary productivity and decrease oxygen

consumption at depth, it can also increase ocean stratification, therefore limiting the ventilation of the ocean's interior and counteracting the effects of reduced productivity.

Coupled physical-biogeochemical models predict a continued long-term oxygen loss under anthropogenic-driven global warming. Global O_2 concentrations are expected to decline by 1–7% by 2100 (Bopp et al., 2002; Keeling et al., 2010), with CMIP5 ensemble simulations under a "business-as-usual" (RCP8.5) scenario predicting a 1–2% decline in the oceanic oxygen inventory per decade relative to 1986–2005 (Henson et al., 2017). However, inter-model variability remains high, particularly in dynamic regions such as the EBUSs, where temperature and oxygen changes are projected to have the greatest biogeochemical impacts (Gruber, 2011).

Observational data corroborate these trends. By comparing historical (1960–1974) and modern (1990–2008) datasets, Stramma, Johnson, et al. (2008) found a net decrease in oxygen levels across the three major tropical OMZs, with a combined vertical and horizontal expansion of approximately 4.5 million km^2. Similarly, a global analysis of historical observations by Schmidtko et al. (2017) estimated a 2% decline in total oceanic oxygen content over the past 50 years, attributed to both solubility-related oxygen loss and reduced ventilation. In the ETNA, both the shallow and deep OMZs exhibit deoxygenation trends, with slightly stronger losses in the upper ocean (-0.49 ± 0.16 µmol L^{-1} yr^{-1}) compared to deeper layers (-0.38 ± 0.13 µmol L^{-1} yr^{-1}, Stramma et al., 2016).

The shoaling of OMZ upper boundaries has been consistently reported over recent decades in all major EBUSs (Whitney et al., 2007; Bograd et al., 2008; Stramma, Johnson, et al., 2008; Gilly et al., 2013; Pitcher et al., 2021). In the ETNA, the shoaling has led to a annual vertical habitat loss of approximately 1 m yr^{-1} for species such as the blue marlin–representing a cumulative habitat loss of 15% between 1960 and 2010 (Stramma, Prince, et al., 2012).

Not only is O_2 vulnerable to climate-driven changes, but oxygen itself can influence the climate system through feedbacks involving the carbon and nitrogen cycles. For instance, expansion of low-oxygen zones reduces the ocean's capacity to sequester carbon, potentially diminishing oceanic carbon uptake and amplifying greenhouse gas concentrations (Stramma et al., 2010). The production other green house gases (e.g., N_2O) may also increase in response to deoxygenation, reinforcing climate feedbacks (Bopp et al., 2002; Gruber & Galloway, 2008; Keeling et al., 2010; Arévalo-Martínez et al., 2015; Martinez-Rey et al., 2015). While many of these feedbacks remain uncertain and are the subject of ongoing research (e.g., Fu et al., 2018; Frölicher et al., 2020), their consequences for marine ecosystems and global biogeochemical cycles are significant (Stramma et al., 2010; Gilly et al., 2013; Vedor et al., 2021). These dynamics highlight the importance of advancing our understanding of the physical and biogeochemical governing OMZ variability to better predict future scenarios.

1.2 Mesoscale dynamics of EBUSs

EBUSs are among the most biologically productive regions in the global ocean. Despite covering less than 1% of the ocean surface, they contribute roughly 11% of global new primary production (Carr, 2001; Carr & Kearns, 2003) and support approximately 20% of the total marine fish catch

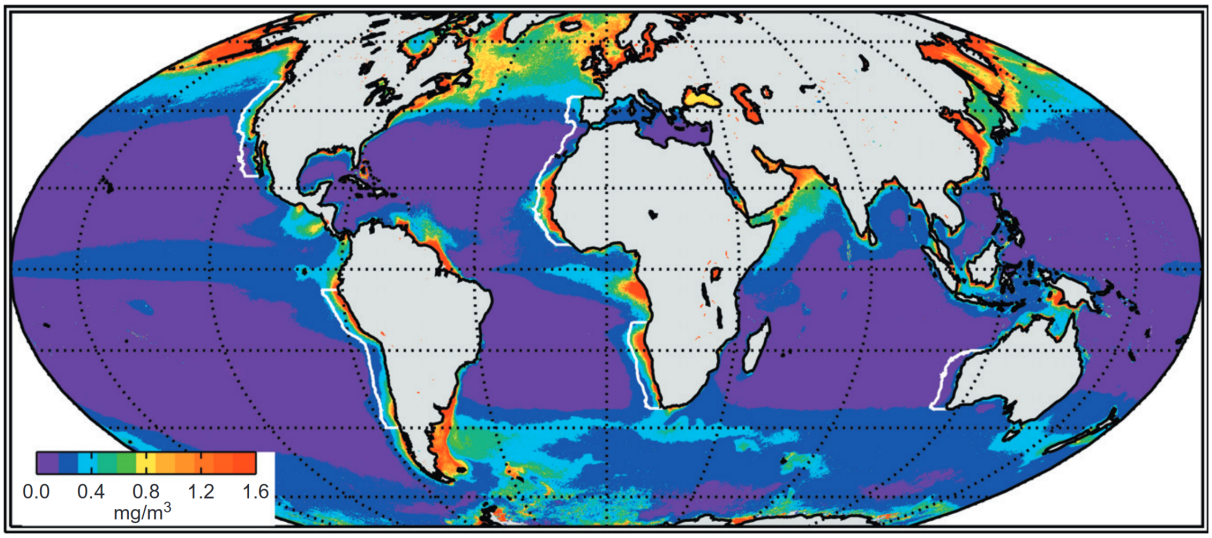


Figure 1.2: Global average distribution of surface Chlorophyll-*a* (Chl*a*) concentrations. Data derived from the SeaWiFS ocean color sensor, averaged over the period September 1997 to December 2010. The four major EBUSs are delineated in white. Adapted from Strub et al. (2013).

(Fréon, Barange, & Arístegui, 2009). This exceptional productivity (Figure 1.2) arises primarily from wind-driven coastal upwelling, which supplies nutrient-rich subsurface waters to the sunlit surface layer (Chavez & Messié, 2009; Messié et al., 2009) and forms the base of rich pelagic ecosystems (Fréon, Arístegui, et al., 2009). However, the structure and variability of EBUSs are not solely shaped by local upwelling dynamics. Mesoscale processes–including boundary currents, filaments and eddies–modulate the spatial distribution and intensity of upwelling, influence cross-shelf exchanges, and facilitate the lateral transport of heat, salt, oxygen, and nutrients (e.g., Gruber et al., 2011; Lovecchio et al., 2017, 2018). Understanding the interplay between upwelling, boundary currents, and eddies is thus essential to fully grasp the physical and biogeochemical functioning of EBUSs.

1.2.1 Coastal upwelling

Coastal upwelling is primarily driven by equatorward alongshore wind stress in combination with the Coriolis effect (Ekman, 1905). These winds induce offshore surface Ekman transport, which is balanced by onshore flow at depth, resulting in the upward transport of subsurface water. The source of the upwelled water is stratification-dependent and usually confined to the base of the surface mixed layer and the top of the thermocline (He & Mahadevan, 2021). Thus, coastal upwelling generally affects the upper 200–300 m of the water column and is associated with vertical velocities of approximately 5–10 m day^{-1} (Talley et al., 2011).

Coastal upwelling not only cools sea surface temperatures–affecting regional weather and air-sea interactions (Izumo et al., 2008)–but also enhances the near-surface nutrient inventory, stimulates phytoplankton blooms, and modifies carbon and oxygen fluxes at the ocean–atmosphere interface (Bakun & Nelson, 1991; Torres et al., 2002; Friederich et al., 2008; Bianucci & Denman, 2012; Send & Nam, 2012). The resulting sharp gradients in temperature, salinity, and nutrient concentrations establish strong coastal fronts that separate the productive shelf waters from

the typical oligotrophic ocean interior (Strub et al., 1991; Capet, McWilliams, et al., 2008). These fronts are subject to temporal and spatial modulation by wind variability and thermohaline intrusions (Brink & Cowles, 1991; Pelegrí et al., 2006; Capet, McWilliams, et al., 2008).

Although the main upwelling region is typically confined within a Rossby radius of the coast, its spatial extent can be substantially amplified by positive wind stress curl offshore. In regions where wind stress increases with distance from the coast, the divergence of Ekman transport leads to a broadening of the upwelling zone and deeper shoaling of isopycnals (Bakun, 1990; Bakun & Nelson, 1991; Pickett & Paduan, 2003; Koračin et al., 2004). Consequently, coastal upwelling may span tens to hundreds of kilometers offshore. In addition, upwelling responds rapidly to variations in wind forcing, with isopycnal uplift and sea surface cooling occurring within just a few days following the onset of favorable winds (Chereskin, 1995; Capet et al., 2017).

1.2.2 Boundary currents

Although continental slopes occupy a relatively small fraction of the ocean area, they play a key role in shaping upper ocean circulation, particularly along eastern boundaries. By interrupting the predominantly zonal flow of the upper thermocline, these steep topographic features deflect currents along isobaths, giving rise to narrow, topographically trapped boundary current systems with alternating directions along depth (e.g., Huthnance, 1984; Barton, 1989; Huthnance et al., 2020). These flows are modulated by wind forcing, mesoscale variability, and interactions with topographic features such as capes and canyons (Relvas et al., 2007; Connolly & Hickey, 2014; Gula et al., 2015, 2016).

Boundary currents are traditionally classified as western or eastern, each with distinct dynamical characteristics and climatological roles. Western boundary currents, such as the Gulf Stream and the Kuroshio, are fast, narrow, and deep-reaching flows that redistribute heat poleward and are central to large-scale climate regulation (Schmitz Jr., 1995; Johns et al., 2011). In contrast, eastern boundary currents are typically broader and slower, but are integral to some of the most biologically productive marine ecosystems in the world (Chavez et al., 2008; Chavez & Messié, 2009). Beyond their physical roles, boundary currents–irrespective of classification–strongly influence the distribution, foraging behavior, and life cycles of marine organisms (Boyle et al., 2009; Hood et al., 2017; Mansfield et al., 2017; Miyake et al., 2020).

In EBUSs, the upwelling-induced shoaling of isopycnals near the coast establishes cross-shelf pressure gradients that drive equatorward geostrophic surface currents (Allen, 1973). These surface currents are narrow (typically < 100 km), shallow (confined to the upper 100 m), and fast (up to 0.8 m s^{-1}), often exhibiting strong seasonality and meandering behavior (e.g., Huyer, 1983; Lázaro et al., 2005; Relvas et al., 2007; Chavez & Messié, 2009; Strub et al., 2013; Faye et al., 2015; Klenz et al., 2018).

Beneath the surface jet, a subsurface poleward current develops between approximately 100 and 500 m depth. This flow is ubiquitous in all major EBUSs and is responsible for the poleward advection of water masses with distinct thermohaline and biogeochemical properties (Barton, 1989; Gay & Chereskin, 2009; Todd et al., 2019). For instance, the California Undercurrent

transports oxygen-depleted and nutrient-rich waters from tropical to subtropical regions, with subsequent offshore export via mesoscale eddies and filaments (Garfield et al., 1999; Collins et al., 2013). Analogous structures exist in the Humboldt and Canary Current Systems. In the latter region, the Poleward Undercurrent (PUC) and the Iberian Slope Current play important roles in supplying nutrient-rich waters to coastal upwelling zones and shaping along-slope biogeochemical gradients (Relvas et al., 2007; Pastor et al., 2008; Peña-Izquierdo et al., 2012). For this reason, these subsurface currents are key in the ventilation (or intensification) of OMZs and deserve especial attention throughout this thesis.

The dynamics of subsurface poleward currents have been extensively studied and are known to exhibit significant regional variability due to the interplay of multiple mechanisms. A primary driver is the presence of alongshore density gradients, which can generate buoyancy-driven flows along continental slopes; although modulated by wind variability, these flows often maintain coherence due to persistent cross-shore pressure gradients (Peliz, Dubert, & Haidvogel, 2003). Wind stress curl is another key contributor: positive wind stress curl induces poleward Sverdrup transport in the ocean interior, reinforcing subsurface poleward flow along eastern boundaries (Mittelstaedt, 1983; Klenz et al., 2018). Remotely forced coastal trapped waves, particularly Kelvin waves, have also been shown to modulate the intensity and vertical structure of undercurrents in several EBUSs, including the Benguela (W. Fennel, 1999), Peru (Echevin et al., 2014), and Canary Current (Kounta et al., 2018) systems.

Additional processes may contribute to the generation and maintenance of these currents. One such mechanism is topographic stress, or form drag, which in barotropic frameworks has been shown to drive along-slope flows aligned with the direction of shelf wave propagation– that is, cyclonic with respect to the ocean basin (Holloway et al., 1989). More recently, this framework has been extended to baroclinic regimes through the concept of eddy rectification, whereby the interaction between eddies and sloping topography leads to the divergence of eddy form stress and the generation of mean poleward undercurrents. This process involves the stirring of Potential Vorticity (PV) gradients constrained by the bottom slope and enhanced by vertical frictional effects (Stewart et al., 2024). Closely related is the classical Joint Effect of Baroclinicity and Relief mechanism (also known as JEBAR), which attributes poleward flow to the joint effect of meridional density gradients and sloping bathymetry acting on the baroclinic pressure field (Huthnance, 1984; Peliz, Dubert, Haidvogel, & Le Cann, 2003). These mechanisms often act in combination, reinforcing one another in complex ways that make their individual contributions difficult to disentangle in realistic oceanic settings (Teles-Machado, Peliz, McWilliams, Couvelard, & Ambar, 2016; Malan et al., 2022).

Besides their role in advecting water masses and influencing upwelling source waters (Pastor et al., 2008; Peña-Izquierdo et al., 2012), boundary currents are highly susceptible to barotropic and baroclinic instabilities. These instabilities are particularly active at bathymetric irregularities, giving rise to eddies that mediate cross-shelf exchanges and drive the offshore transport of coastal waters (Relvas et al., 2007; Molemaker et al., 2015; Nagai et al., 2015a; Gula et al., 2016; Lovecchio et al., 2018).

1.2.3 Eddies

Nonlinear by definition and ubiquitous throughout the global ocean, mesoscale eddies are coherent rotating structures whose characteristic azimuthal speed U exceeds their translation speed c, such that $U/c > 1$ (Chelton et al., 2011). With horizontal scales on the order of tens to hundreds of kilometers and lifetimes ranging from weeks to several months, eddies constitute the principal reservoir of kinetic energy at the mesoscale in the ocean circulation system (Gill & Niller, 1973; McWilliams, 1985; Chelton et al., 2007; Ferrari & Wunsch, 2009; Chelton et al., 2011; Morrow & Le Traon, 2012). Their typical westward propagation is primarily governed by a combination of self-advection and the planetary vorticity gradient (i.e., the β-effect; Cushman-Roisin et al., 1990; Chelton et al., 2011). However, their trajectories, intensities, and lifespans are often modulated by interactions with large-scale currents, bathymetry, wind forcing, and other mesoscale or submesoscale features (e.g., Holland & Mitchum, 2001; Peliz, Dubert, Haidvogel, & Le Cann, 2003; Cenedese et al., 2005; Chaigneau et al., 2009; Sangrà et al., 2009; Chelton et al., 2011; Couvelard et al., 2012; Silva-Fernandes & Peliz, 2020).

Eddy generation is primarily driven by baroclinic instability, in which available potential energy associated with sloping isopycnals is converted into kinetic energy (Ferrari & Wunsch, 2009). In regions with strong horizontal shear, such as boundary systems where alongshore currents interact with topography, barotropic instability resulting from horizontal and vertical current shear also plays a key role (Molemaker et al., 2015; Gula et al., 2016). Additional generation mechanisms include topographic interactions with islands and seamounts (Pattiaratchi et al., 1987; Heywood et al., 1990), air-sea coupling (Wilson, 2016; Xu et al., 2016), and eddy-eddy interactions (Sangrà et al., 2009; Chelton et al., 2011). In EBUSs, eddies are commonly formed near the coast, where strong vertical and horizontal shears and density gradients coexist (Marchesiello et al., 2003; Capet, McWilliams, et al., 2008; Chelton et al., 2011; Liang et al., 2012). Eddies from the four major EBUSs share similar kinematic characteristics, with westward propagation speeds (0.05-0.1 m s^{-1}) and radii (50-150 km) directly linked to the Rossby radius of deformation, which is similar due to the similar latitudinal ranges theses systems are found (Morrow, 2004; Chaigneau et al., 2009; Pegliasco et al., 2015). Nevertheless, eddy generation, frequency and polarity differs slightly between these regions, indicating different forcing mechanisms (Chaigneau et al., 2009).

Eddies exert significant biogeochemical influence in the ocean, being either by self dynamical processes or by the trapping of water at formation. They can trap and transport water masses with distinct chemical signatures over long distances, even across strong frontal systems (Barton, 1987; Alpers et al., 2013; Gaube et al., 2014; Romero et al., 2016; Laxenaire et al., 2018). Eddies formed in EBUSs often enclose nutrient-rich waters, enabling enhanced productivity even in oligotrophic offshore regions (Löscher et al., 2015), and can facilitate larval transport and biological connectivity (Condie & Condie, 2016). Conversely, such cross-shore transport of nutrient-rich waters to offshore may result in a decrease of biological productivity in coastal regions (Gruber et al., 2011; Lachkar & Gruber, 2012; Nagai et al., 2015b). In EBUSs with low-oxygen waters, some eddies may even trap oxygen-depleted waters at formation, sustaining hypoxic environments over long distances into the open-ocean (Stramma et al., 2014).

Eddies are typically categorized as cyclonic or anticyclonic. However, the vertical position of their maximum azimuthal speed or vorticity core also determines whether they are surface or sub-surface intensified structures (McWilliams, 1985). In the classical view, surface-intensified cyclonic eddies induce surface divergence and uplift the thermocline, leading to higher nutrient concentrations in the euphotic zone and stimulating primary productivity (Figure 1.3a; Falkowski et al., 1991; McGillicuddy & Robinson, 1997; Siegel et al., 1999; Hasegawa et al., 2009; Alpers et al., 2013; Andrade et al., 2014; Romero et al., 2016; Chang et al., 2017). Conversely, anticyclonic eddies are associated with surface convergence and thermocline depression, suppressing vertical nutrient supply (Figure 1.3b). However, recent studies have shown that this classical paradigm is overly simplistic: wind forcing, submesoscale instabilities, ageostrophic secondary circulations and near-inertial waves can result in vertical transport of either sign within anticyclonic eddies (Martin & Richards, 2001; McGillicuddy et al., 2007; Gaube et al., 2015; Brannigan, 2016; Barceló-Llull et al., 2017; Karstensen et al., 2017; Pietri & Karstensen, 2018). Nevertheless, such vertical motions occur mostly in subsurface-intensified eddies.

Subsurface-intensified eddies–often referred to as Anticyclonic Modewater Eddies (ACMEs), Intrathermocline Eddies (ITEs; Dugan et al., 1982), or more generally as Submesoscale Coherent Vortices (McWilliams, 1985; Gula et al., 2019)–are typically centered between 200 and 1000 and are characterized by lenses of relatively well-mixed water embedded within the seasonal and permanent thermocline (Chaigneau et al., 2011; Colas et al., 2012). They exhibit a weakly stratified core, anticyclonic vorticity, and a distinct upward and downward doming of the upper and lower isopycnals, respectively, resulting in an anomalous vertical structure (Figure 1.3c; Kostianoy & Belkin, 1989). While most documented cases are anticyclonic, cyclonic variants of ITEs also exist, albeit less frequently (e.g., de Marez et al., 2020). Contrary to the ACMEs, cyclonic ITEs are characterized by the upward and downward displacement of the main and seasonal thermoclines, respectively, resulting in a thinning of the mode water layer–hence the term ”cyclonic thinny” (McGillicuddy, 2015). Although ITEs exhibit an opposite displacement of the seasonal thermocline relative to classical surface-intensified eddies, the displacement of the main thermocline dominates the geostrophic velocity field and sea level anomaly. As a result, both surface and subsurface-intensified anticyclonic and cyclonic eddies can be identified as positive sea level anomalies in satellite altimetry data (McGillicuddy et al., 2007; Chelton et al., 2011; Faghmous et al., 2015; Gaube et al., 2015; Schütte, Brandt, & Karstensen, 2016; Dilmahamod et al., 2018).

The defining characteristic of ACMEs is their low PV and low stratification core shielded from surrounding waters in the subsurface (McWilliams, 1985; D’Asaro, 1988; Thomsen et al., 2016; Pietri & Karstensen, 2018). Such low stratification within the eddy core is thought to result from preconditioning mechanisms such as deep convection (Oliver et al., 2008; Bosse et al., 2016), stratification of preexisting surface anticyclonic eddies due to seasonal surface heating (Hogan & Hurlburt, 2015; X. Wang et al., 2023), or diapycnal mixing near the surface (Thomas, 2008; McGillicuddy, 2015) or boundaries (D’Asaro, 1988; R. Zhu et al., 2024). Several studies have emphasized the importance of flow separation near topographic bends–commonly found along EBUSs–as favorable sites for the formation of ACMEs (D’Asaro, 1988; Peliz, Dubert, Haidvogel, & Le Cann, 2003; Molemaker et al., 2015; Gula et al., 2016; Teles-Machado, Peliz,

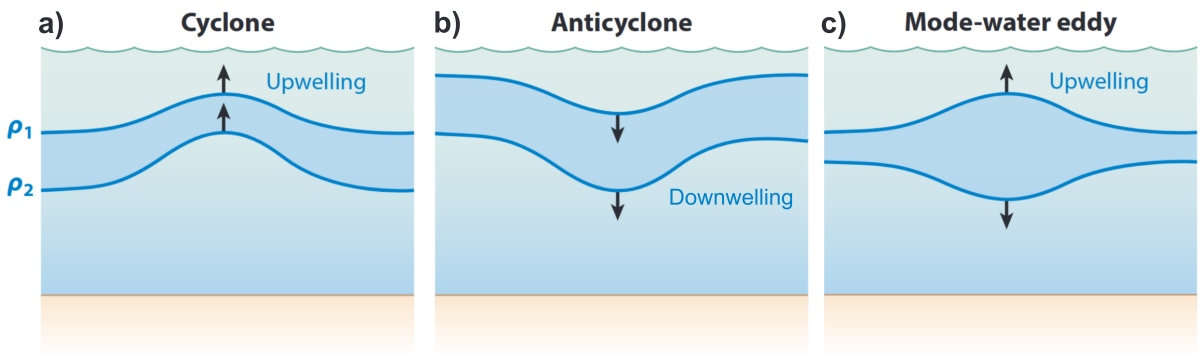


Figure 1.3: Vertical density structure associated with three types of eddies in the process of formation/intensification. Two density surfaces are depicted: the seasonal thermocline (ρ_1) and the main thermocline (ρ_2). Adapted from McGillicuddy (2015).

McWilliams, Dubert, & Cann, 2016; Thomsen et al., 2016; Contreras et al., 2019; Dilmahamod et al., 2022). The interaction between along-slope currents and steep topography along continental slopes is known to generate strong bottom friction and vertical shear, which are conducive of near zero or even negative PV formation.

The rapid rotation at their perimeters forms a dynamic barrier that hinders the lateral exchange between their core and surrounding waters (Armi et al., 1989; Fiedler et al., 2016; Karstensen et al., 2017). This, together with the shielding from atmospheric forcing (Dilmahamod et al., 2022), makes these eddies key features in the redistribution of thermohaline and biogeochemical properties in stratified regions of the ocean (Frenger et al., 2018; Auger et al., 2021).

Subsurface-intensified eddies have been documented in all global ocean basins. Mediterranean water eddies (Meddies) were the first of this kind to have been observed. Prominent features of the North Atlantic hydrology, these eddies are formed by the Mediterranean outflow through the Strait of Gibraltar and exhibit an anomalous core with a thickness of 500-1000 m centered at around 1000 m depth (Paillet et al., 2002). Although mostly found east of the Mid-Atlantic Ridge in the Iberian and Canary Basins (Armi & Zenk, 1984; P. L. Richardson et al., 1989, 1991), these eddies were first detected off the Bahamas (McDowell & Rossby, 1978), indicating their key role in the distribution of mediterranean water throughout the North Atlantic Ocean. Analogous to the Meddies, Persian water eddies (Peddies) are also found in the Indian Ocean as a result of the Persian Gulf outflow (Senjyu et al., 1998).

All the major EBUSs have been associated with the formation of subsurface-intensified eddies. In the California Current System, California Undercurrent Eddies (Cuddies) have been shown to transport nutrient-rich and oxygen-poor waters offshore, thereby influencing offshore productivity and biogeochemistry (Garfield et al., 1999; Lukas & Santiago-Mandujano, 2001; Collins et al., 2013). Similarly, in the Humboldt Current System, Poleward Undercurrent Eddies (Puddies) have been associated with the offshore transport of low-oxygen and nutrient-rich waters (Johnson & McTaggart, 2010; Chaigneau et al., 2011; Colas et al., 2012; Morales et al., 2012; Stramma et al., 2014; Frenger et al., 2018; Auger et al., 2021). Formed at the northern and western coasts of the Iberian Peninsula, Slope Water Oceanic eddies (SWOddies) are also important features of the northeast Atlantic and their formation has been mostly associated with instabilities generated by the poleward Iberian slope current at the main topographic features

(Pingree & Le Cann, 1992; Peliz, Dubert, Haidvogel, & Le Cann, 2003; Teles-Machado, Peliz, McWilliams, Dubert, & Cann, 2016).

In the ETNA, subsurface-intensified eddies are frequently generated along the Mauritanian and Senegalese coasts, where strong poleward subsurface currents and sharp topography provide favorable conditions for their formation (Schütte, Brandt, & Karstensen, 2016; Dilmahamod et al., 2022). These eddies have been shown to trap and transport oxygen-depleted or nutrient-rich water masses hundreds of kilometers offshore, making them important agents in the lateral extension of hypoxic conditions and coastal productivity into the ocean interior (Karstensen et al., 2015; Hauss et al., 2016; Schütte, Karstensen, et al., 2016; Grundle et al., 2017; Auger et al., 2021). Their role in shaping the shallow OMZ of the ETNA is a key focus of this thesis.

1.3 The Eastern Tropical North Atlantic

The EBUS of the North Atlantic is one of the four major upwelling systems in the world oceans (Chavez & Messié, 2009; Strub et al., 2013). It features a complex and dynamic circulation regime that drives pronounced subregional variability in both physical and biogeochemical properties, including water mass distribution, mesoscale activity, upwelling intensity, and biological productivity (Pelegrí et al., 2006; Pradhan et al., 2006; Pastor et al., 2008; Arístegui et al., 2009; Peña-Izquierdo et al., 2015; Schütte, Brandt, & Karstensen, 2016; Lovecchio et al., 2018). Occupying the southernmost extent of this system, the ETNA stands out as a region where mesoscale processes, coastal upwelling, and large-scale circulation interact to shape a highly variable oceanographic landscape.

1.3.1 Mauritania-Senegal upwelling system

A key component of the ETNA is the Mauritania-Senegal upwelling system, which is directly influenced by the large-scale atmospheric circulation over the North Atlantic. Northerly trade winds driven by the pressure gradient between the Azores High and the equatorial low-pressure system generate large-scale offshore Ekman transport along the northwest African coast (Mittelstaedt, 1983; Bakun & Nelson, 1991). This process leads to the development of the Canary Current Upwelling System (CCUS; Wooster et al., 1976), recognized as the second most productive upwelling region globally (Carr, 2001). The upwelling extends from approximately 9° to 33°N (Váldes & Déniz-González, 2015), with quasi-permanent activity between 20° and 25°N, where it peaks in summer and autumn in response to intensified trade winds (Figure 1.4; Mittelstaedt, 1991; Ould-Dedah et al., 1999).

South of 20°N, in the ETNA, upwelling becomes strongly seasonal, governed by the meridional migration of the InterTropical Convergence Zone (ITCZ; Van Camp et al., 1991; Nykjær & Van Camp, 1994; Lázaro et al., 2005). During winter and spring, the southward displacement of the ITCZ intensifies alongshore trade winds, extending the CCUS as far south as 15°N (Figure 1.5, left panel; Mittelstaedt, 1983; Bakun & Nelson, 1991; Van Camp et al., 1991; Nykjær & Van Camp, 1994; Tomczak & Godfrey, 1994; Pradhan et al., 2006; Lathuilière

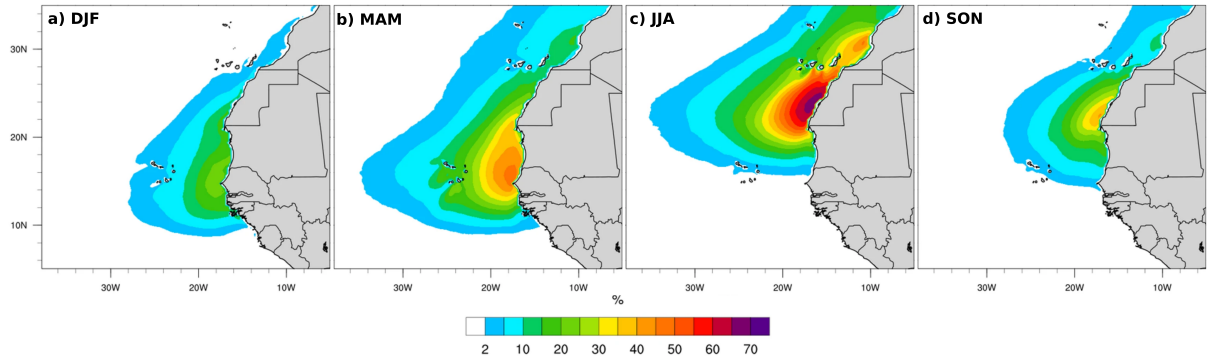


Figure 1.4: Seasonal frequency of occurrence of coastal wind jet along the Northwestern African coast. (a) Winter (DJF), (b) Spring (MAM), (c) Summer (JJA) and (d) Autumn (SON). Results from a hindcast model simulation with ≈25 km horizontal resolution. Adapted from Soares et al. (2019)

.

et al., 2008). During summer and autumn, the ITCZ shifts northward, weakening the alongshore winds and provoking a relaxation in coastal upwelling and a rapid increase in Sea Surface Temperature (SST; Figure 1.5, right panel; Mittelstaedt, 1983; Lathuilière et al., 2008). The variable width of the continental shelf, the presence of several headlands, and the local orientation of the coastline also contribute to the variable upwelling intensity across the region (Demarcq & Somoue, 2015). These pronounced latitudinal and seasonal fluctuations makes the Mauritania–Senegal upwelling region the most seasonally variable EBUS worldwide (Chavez & Messié, 2009; Faye et al., 2015).

As described in Section 1.2.1, alongshore trade winds generate offshore Ekman transport, resulting in the upwelling of cold, nutrient-rich waters that manifest as cooler SSTs (Figure 1.5) and enhanced primary productivity along the Mauritania–Senegal coast (Pradhan et al., 2006; Arístegui et al., 2009; Demarcq & Somoue, 2015). This persistent upwelling gives rise to a pronounced frontal system that separates the colder, nutrient-rich coastal waters from the warmer, oligotrophic offshore waters (Pelegrí et al., 2006; Chavez & Messié, 2009). As is characteristic of EBUSs, this frontal system can experience intense interleaving of contrasting water masses, which can in turn induce baroclinic instabilities and promote the generation of mesoscale eddies (Capet, McWilliams, et al., 2008).

The subsurface source waters in the southern CCUS are primarily of South Atlantic origin. These waters are richer in nutrients than those upwelled in the northern sectors (Carr & Kearns, 2003; Pelegrí et al., 2006; Pastor et al., 2013; Auger et al., 2016), making the southern subregion the most productive portion of the CCUS, despite experiencing weaker winds and greater seasonality (Demarcq & Somoue, 2015). Nevertheless, Ekman-driven nutrient supply alone does not fully explain the elevated productivity observed in the region (Pastor et al., 2013). Additional factors–such as favorable light and temperature conditions, coupled with long residence times–play a key role in supporting such high productivity levels (Lachkar & Gruber, 2012).

The high coastal productivity of the ETNA plays a key role in regional biogeochemical cycling, particularly through the offshore transport of nutrients and organic carbon mediated by mesoscale processes such as eddies and filaments (Pelegrí et al., 2006; Arístegui et al., 2009; Lovecchio et al., 2017, 2018). Mesoscale eddies can entrap coastal water masses at the

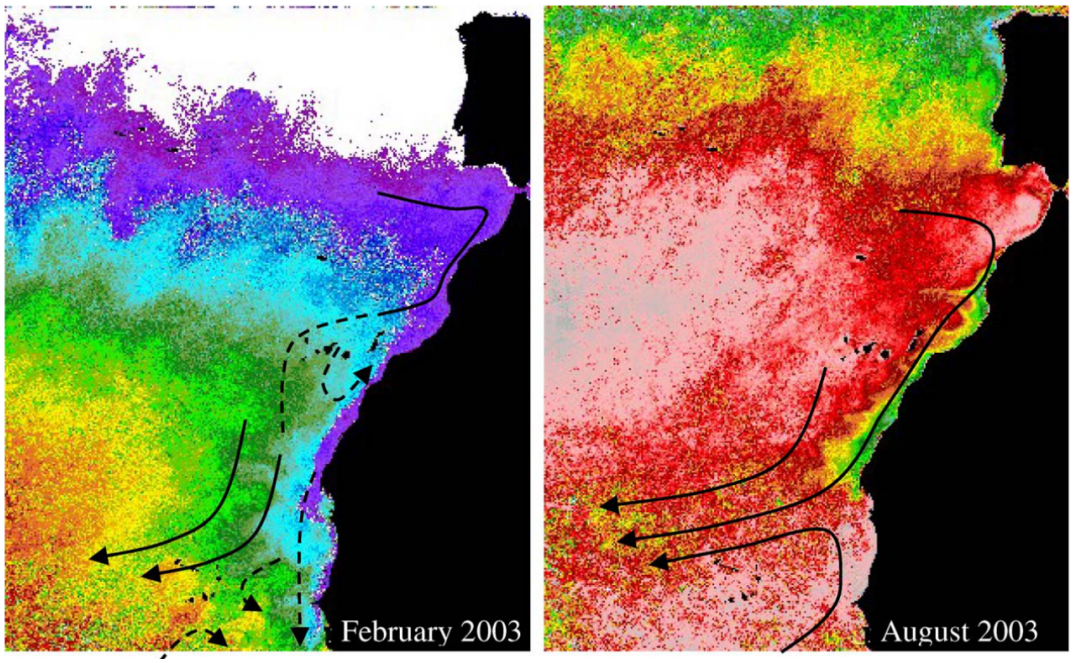


Figure 1.5: Mean monthly distribution of SST for the Eastern North Atlantic. (left) February and (right) August 2003. Overlaid are schematic representations of the mains currents. Solid lines indicate well-established pathways; dashed lines suggest inferred or possible connections. Retrieved from Pelegrí et al. (2006).

time of formation, preserving their distinct thermohaline and biogeochemical properties as they propagate westward into the subtropical gyre interior (Schütte, Brandt, & Karstensen, 2016). One particularly prominent feature is the persistent upwelling filament off Cap Blanc (near 22°N; Figure 1.5a), which is estimated to export up to 50% of the organic carbon produced in coastal waters, with its influence extending hundreds of kilometers offshore (Gabric et al., 1993; Ohde & Siegel, 2010). The spatial extent and intensity of this filament are modulated by seasonal variability in upwelling and boundary current dynamics (Van Camp et al., 1991).

1.3.2 Regional water masses and circulation

Understanding the regional circulation and water mass characteristics is essential to contextualizing the biogeochemical dynamics of the ETNA, including the development and maintenance of the sOMZ. The region hosts several distinct water masses distributed throughout the water column (Tomczak, 1981; Stramma et al., 2005). Focusing on the depth range relevant to the sOMZ, the upper ocean consists of Tropical Surface Water occupying the mixed layer, overlying the Subtropical Underwater (STUW, also known as Salinity Maximum Water), typically located at potential density (σ_θ) < 25.8 kg m^{-3}. The STUW forms through subduction of high-salinity waters in the central subtropical gyre, a process driven by large-scale wind convergence. Although its thermohaline characteristics vary both spatially and temporally, STUW generally exhibits elevated oxygen concentrations due to its recent origin and relatively short residence time (Stramma et al., 2005; Karstensen et al., 2008).

Beneath the permanent thermocline, the central water masses dominate the intermediate depths (100–700 m) of the ETNA. These water masses originate in the subtropical gyres of both

hemispheres, where they form through surface convergence associated with negative Ekman pumping (Sverdrup et al., 1942). Once subducted, they are advected equatorward by the North and South Equatorial Currents, contributing significantly to the ventilation of tropical thermocline waters. In the Potential temperature-Salinity (θ-S) space, these water masses exhibit near-linear relationships, reflecting their origin from well-mixed surface waters. Their biogeochemical characteristics are instrumental in setting the oxygen content and nutrient structure of the upper ocean, thereby exerting a strong influence on the formation, vertical extent, and persistence of OMZs (Tomczak, 1981).

Within the ETNA, two central water masses occupying the σ_θ range between 25.8 and 27.1 kg m^{-3} are particularly relevant: the North Atlantic Central Water (NACW) and the South Atlantic Central Water (SACW; Stramma et al., 2005). NACW forms through subduction in the subtropical gyre of the North Atlantic and is subsequently transported into the tropical thermocline via the North Equatorial Current (NEC; Tomczak, 1981; Poole & Tomczak, 1999). This subduction predominantly occurs during late winter and early spring, when Ekman pumping is strong enough to counteract the seasonal deepening of the mixed layer and allow surface waters to subduct into the permanent thermocline (Tsuchiya, 1986).

In contrast, SACW is a much older and more biogeochemically evolved water mass, formed through the mixing of central waters in the southeastern South Atlantic, particularly southwest of South Africa (R. G. Peterson & Stramma, 1991). Its thermohaline and biogeochemical properties partially reflect contributions from the Indian Ocean Subtropical Convergence, as SACW enters the Atlantic basin via Agulhas leakage (A. L. Gordon et al., 1992; Sprintall & Tomczak, 1993). It is subsequently advected northwestward by the South Equatorial Current into the western tropical South Atlantic and eventually reaches the ETNA through the eastward-flowing equatorial current system. When traced along isopycnals, SACW exhibits lower temperatures, reduced salinity, higher nutrient concentrations, and lower oxygen content compared to NACW (Tomczak, 1981; Karstensen & Tomczak, 1998; Poole & Tomczak, 1999; Peña-Izquierdo et al., 2012). These contrasting properties render the two water masses easily distinguishable in the θ-S space (Figure 1.6).

Due to the long transit pathway and mixing, the SACW found in the ETNA is no longer identical to its Southern Hemisphere source. Instead, it represents a diluted variety, resulting primarily from mixing with NACW in the region. This modified water mass has been referred to as the SACW of Cabo Verde (SACWcv; Figure 1.6; Pastor et al., 2008; Pastor et al., 2011; Peña-Izquierdo et al., 2012, 2015). This variety has lower O2 concentrations than the parent SACW, suggesting that it lost most of its oxygen content while also mixing slowly with saltier and oxygen-richer NACW (Peña-Izquierdo et al., 2012). In this context, the purer SACW variety represents a younger water mass that renovates the upper layers of the ETNA (Elmoussaoui et al., 2005; Peña-Izquierdo et al., 2015). As will be demonstrated throughout this thesis, distinguishing between SACW and SACWcv is crucial for understanding the formation and maintenance of the sOMZ.

The NACW and the regional diluted SACWcv meet at the basin-wide Cape Verde Frontal Zone (CVFZ) (Figure 1.7; Emery & Meincke, 1986; Zenk et al., 1991; Lozier et al., 1995), a density-compensated frontal system characterized by pronounced water mass interleaving

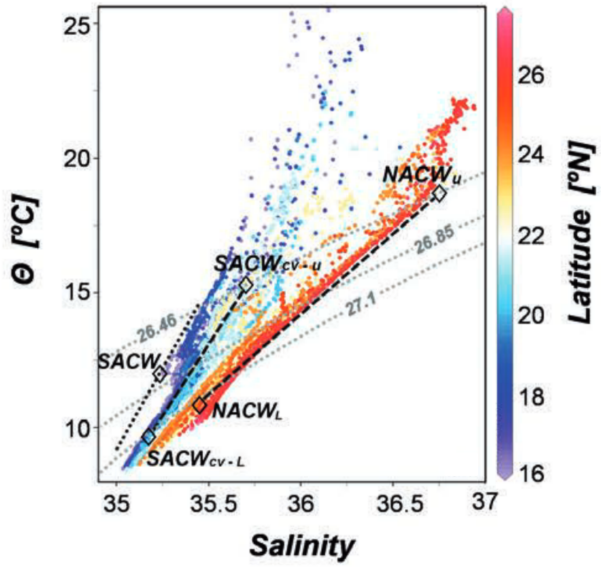


Figure 1.6: θ-S diagram from the CANOA08 cruise (November 2008, R/V Sarmiento de Gamboa) in the CCUS. Colored dots represent observed TS values, while void diamonds mark the upper and lower end-members of the three water masses identified. Adapted from Peña-Izquierdo et al. (2012).

(Tomczak, 1981; Stramma et al., 2005; Martínez-Marrero et al., 2008; Pastor et al., 2011; Burgoa et al., 2021; Valiente et al., 2021). Despite its weak signature in the density field, the CVFZ exhibits sharp thermohaline contrasts (D. Zhang et al., 2003) and even stronger gradients in inorganic nutrients and dissolved oxygen concentrations (Barton, 1987; Pelegrí & Peña-Izquierdo, 2015). Nevertheless, intense lateral exchange occurs across it, primarily driven by double diffusion (Zenk et al., 1991; Pastor et al., 2008).

A distinct separation between upper and lower central waters is observed at σ_θ = 26.8 kg m^{-3}, where a thermohaline transition serves as a useful boundary for analyzing thermocline circulation patterns (Stramma et al., 2005; Kirchner et al., 2009; Peña-Izquierdo et al., 2012). Given the depth range and processes involved in formation of the sOMZ (Voituriez & Chuchla, 1978; Stramma et al., 2005), the upper central waters are of particular interest throughout this thesis.

Besides the interplay of distinct water masses, the ETNA is shaped by a complex and seasonally varying large-scale circulation, strongly influenced by the meridional migration of the ITCZ (Stramma & Schott, 1999). To the north, the region is bounded by the North Equatorial Current (NEC) (Figure 1.7), a permanent southwestward extension of the Canary Current (CC). The NEC exhibits mean velocities ranging from 0.1 to 0.15 m s^{-1} (Mittelstaedt, 1983, 1991; Tomczak & Godfrey, 1994; Stramma et al., 2005), with maximum strength observed during summer and seasonal weakening in winter (Arnault, 1987; Stramma & Siedler, 1988; D. Zhang et al., 2003).

To the south, the North Equatorial Counter Current (NECC) and the North Equatorial Undercurrent (NEUC) link the western and eastern tropical Atlantic. The NECC is a surface-intensified (0–100 m), eastward-flowing current centered between 5° and 10°N, with mean velocities around 0.42 m s^{-1} (Stramma & Schott, 1999; Fratantoni, 2001). Its strength increases during summer and early autumn, coinciding with the northward migration of the ITCZ and a relaxation of easterly wind stress (Arnault, 1987; Mittelstaedt, 1991; Lázaro et al., 2005), while it weakens in winter as the ITCZ shifts southward (Rosell-Fieschi et al., 2015; Hahn et al., 2017).

Below the surface, the NEUC and the northern deeper branch of the NECC (nNECC) form prominent eastward jets located near 5°N and 9°N, reaching depths of approximately 300 m and 800 m, respectively (Stramma et al., 2005). These subsurface currents play a central role in ventilating the ETNA's OMZ by advecting relatively pure SACW from the western tropical Atlantic into the region (Karstensen et al., 2008; Stramma, Brandt, et al., 2008; Brandt et al., 2010, 2012; Hahn et al., 2017).

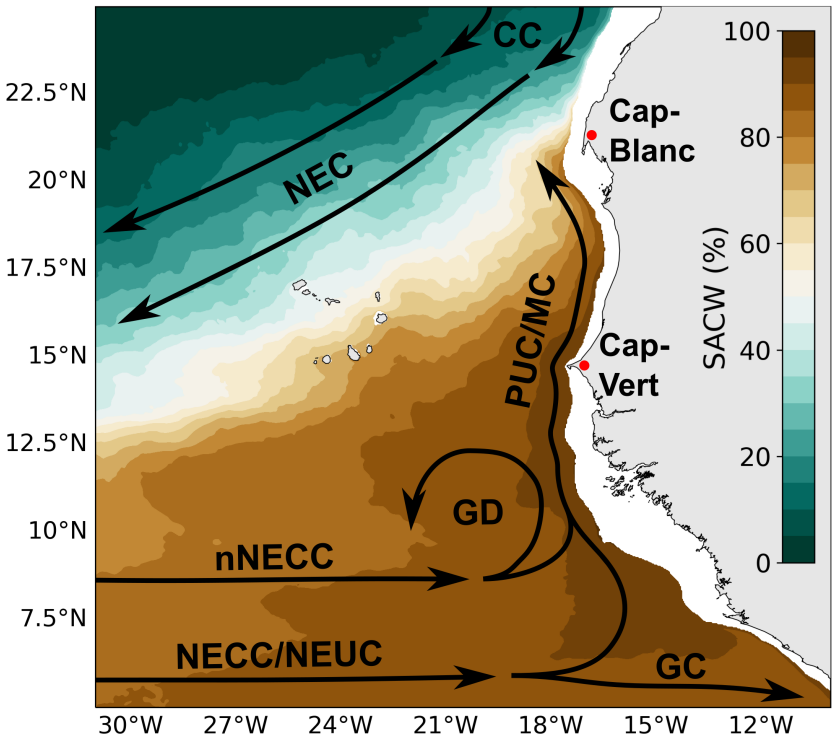


Figure 1.7: Mean proportion of SACW relative to NACW at 120 m depth in the ETNA, with representation of main currents. Data was derived from our model simulation. Arrows indicate the mean current field (adapted from Brandt et al., 2015; Peña-Izquierdo et al., 2015): Canary Current (CC), North Equatorial Current (NEC), North Equatorial Countercurrent (NECC), northern branch of the NECC (nNECC), North Equatorial Undercurrent (NEUC), Poleward Undercurrent (PUC)/Mauritania Current (MC), Guinea Current (GC) and Guinea Dome (GD). Location of Cap-Vert and Cap-Blanc headlands are indicated. Note the mean position of the CVFZ, depicted by the 50% SACW values.

Southeast of the ETNA at approximately 10°N and 22°W lies the Guinea Dome (GD)–a quasi-permanent geostrophic cyclonic feature associated with the NECC and NEUC (Siedler et al., 1992). Formed by divergent wind stress curl and intensified Ekman pumping, the GD is characterized by an uplifted isotherm structure (cold dome) and low hydrostatic pressure (P. L. Richardson, 1983; Siedler et al., 1992; Faye et al., 2015). Given that the GD is mostly forced by the wind field, it follows the seasonal migration of the ITCZ and moves southeast from summer to winter (Nykjær & Van Camp, 1994), ultimately influencing the dynamics of the boundary currents along the African coast (Mittelstaedt, 1976, 1991; Lázaro et al., 2005).

A portion of the SACW transported eastward by the equatorial current system recirculates poleward along the eastern boundary (Peña-Izquierdo et al., 2012, 2015). This circulation forms part of a complex alongshore current system characterized by vertically alternating flow structures (Kirichek, 1971; Barton, 1989; Mittelstaedt, 1991; Lázaro et al., 2005). During the upwelling season, the system is dominated in the surface by a narrow equatorward coastal jet that extends the Canary Upwelling Current (CUC) southward to approximately 15°N (Pelegrí et al., 2006).

This coastal jet results from geostrophic adjustment to cross-shore density gradients between cold, upwelled waters near the coast and warmer offshore waters (Allen, 1973; Pelegrí et al., 2006).

In the subsurface, circulation within the central water density range exhibits a vertically structured pattern. The upper central water is dominated by the PUC, which flows poleward along the continental slope, while the lower central water is characterized by an equatorward current. This vertical alternation in flow direction likely plays a key role in shaping the distribution of water masses, contributing to the contrasting proportions of SACW and NACW observed in the upper and lower central water layers, respectively (Pastor et al., 2008; Pastor et al., 2011; Peña-Izquierdo et al., 2012, 2015).

Centered between 100 and 300 m depth but occasionally reaching down to ≈1000 m along the continental slope, the PUC is a narrow (30–60 km wide) yet dynamically significant feature of the eastern boundary circulation (Mittelstaedt, 1983; Barton, 1989). It is thought to originate from the Gulf of Guinea (Mittelstaedt, 1976) and is driven by a combination of factors: Sverdrup transport induced by positive wind curl (Mittelstaedt, 1976), a large-scale alongshore pressure gradient set by equatorward winds (Barton, 1989; Tomczak & Godfrey, 1994), and remote forcing by coastal trapped waves and Rossby wave dynamics (Kounta et al., 2018).

During the relaxation season, the poleward Mauritania Current (MC) dominates the surface flow, while a weaker equatorward flow occupies the subsurface to ≈500 m (Klenz et al., 2018). The MC reaches ≈14°N during winter and early spring, but extends to ≈20°N in summer/autumn due to the relaxation of the trade winds and the intensification of the NECC, being partly responsible for the suppression of coastal upwelling and rapid increase in SST (Mittelstaedt, 1991).

Although the PUC and MC exhibit distinct seasonal patterns, observations (Peña-Izquierdo et al., 2012; Klenz et al., 2018) and model simulations (Elmoussaoui et al., 2005; Kounta et al., 2018) suggest that they are dynamically linked and represent seasonal phases of the same current. However, some discrepancies remain. For instance, using shipboard data along 18°N, Klenz et al. (2018) reported weak poleward flow at the subsurface during January–April (upwelling season), and strong poleward flow at the surface in May–July (relaxation). In contrast, model simulations by Kounta et al. (2018) found maximum poleward velocities in spring and autumn, when the PUC is dominant and the MC is absent. These differences likely stem from limited observational coverage, given that available data reported by Klenz et al. (2018) correspond to only five cruises during the upwelling season and four during the relaxation season.

With data collected during a November 2008 cruise, Peña-Izquierdo et al. (2012) identified a coherent poleward current extending from surface to intermediate depths along the continental slope. This current exhibited peak velocities exceeding 0.25 m s^{-1} and transported up to 2.8 Sv–substantially greater than earlier estimates of approximately 1 Sv for the PUC during the upwelling season (Mittelstaedt, 1991; Schafstall et al., 2010). North of Cap Blanc, where the PUC encounters the opposing southward-flowing CC, the undercurrent typically weakens and deepens (Barton, 1989). Despite this, Peña-Izquierdo et al. (2012) reported that the PUC remained traceable as far north as 24°N, retaining nearly 50% of its transport compared to the 18°N section.

The PUC represents a key conduit for the transport of SACW into the upwelling system, supported by its upstream connections to the eastward-flowing equatorial currents (NEUC, NECC, and nNECC) and the North Brazil Current (Glessmer et al., 2009; Peña-Izquierdo et al., 2015). As these relatively pure SACWs enter the ETNA, they mix with NACW, producing the modified, oxygen-depleted SACWcv variety (Pastor et al., 2011; Peña-Izquierdo et al., 2012; Klenz et al., 2018). As a result, the PUC emerges as a localized oxygen maximum along the continental slope and constitutes a crucial ventilation pathway for the region's upper central waters (Peña-Izquierdo et al., 2012; Brandt et al., 2015). In addition, the PUC has been implicated in the generation of mesoscale eddies along the Northwest African margin (Schütte, Brandt, & Karstensen, 2016; Dilmahamod et al., 2022), which play a pivotal role in the offshore maintenance of the sOMZ (Karstensen et al., 2015; Fiedler et al., 2016; Schütte, Karstensen, et al., 2016).

1.3.3 The Oxygen Minimum Zone

The OMZ of the ETNA was first identified with hydrographic data collected during the German Meteor expedition between 1925 and 1927 (Wattenberg, 1938). These early observations revealed low oxygen concentrations between 300 and 700 m depth in both the northern and southern hemispheres of the eastern tropical Atlantic. Building on these findings, a conceptual framework began to emerge, attributing OMZ formation to organic matter remineralization and weak oxygen renewal at depth (Redfield, 1942; Wyrtki, 1962). Subsequent studies have since established that the ETNA hosts a distinct OMZ which, unlike the more intense suboxic or anoxic OMZs of the Pacific and Indian Oceans, exhibits a vertically layered structure composed of two discrete cores (Karstensen et al., 2008; T. Fischer et al., 2013; Brandt et al., 2015).

These two layers are separated by an intermediate oxygen maximum located around 300–400 m depth, which is thought to result from the eastward advection of oxygen-rich waters by a system of narrow zonal jets (Brandt et al., 2015). However, this structure remains difficult to reproduce in eddy-resolving models–even at resolutions of 0.1°–likely due to the poor representation of these intermediate zonal jets (Matear & Hirst, 2003; Duteil et al., 2014; Frenger et al., 2018). These jets are critical to the oxygen dynamics of the ETNA, as decadal to multidecadal variations in their strength may exert substantial control over long-term OMZ trends (Brandt et al., 2010).

The intensity and shape of these alternating zonal jets have been studied both empirically (Maximenko et al., 2005; Ollitrault et al., 2006; Brandt et al., 2010) and theoretically (Berloff et al., 2009; Ascani et al., 2010; Qiu et al., 2013). However, their accurate representation is often lacking in basin-scale and global ocean circulation models (Duteil et al., 2014; Frenger et al., 2018). Recent high-resolution simulations by Calil (2023) demonstrated that resolving zonal jets at horizontal scales near 3 km is essential for accurately representing the horizontal extent of OMZs, as it significantly improves their capacity to transport oxygen from the ventilated western boundary eastward. According to the author, these jets exhibit marked asymmetry: while westward flows are broader and associated with homogenized PV, eastward jets are sharper and follow PV gradients, ultimately constraining the westward expansion of the OMZ by ventilating its western edge.

The two OMZ cores in the ETNA are shaped by distinct physical and biogeochemical mechanisms (Brandt et al., 2015). The dOMZ, characterized by mean O_2 concentrations of approximately 40 µmol L^{-1} centered near 450 m depth, is primarily influenced by sluggish isopycnal ventilation within the so-called "shadow zones" of the ocean interior (Wyrtki, 1962; Luyten et al., 1983). Minimum oxygen concentrations in this layer are typically observed at approximately 10°N and 20°W, near the GD (Figure 1.8a; Brandt et al., 2015).

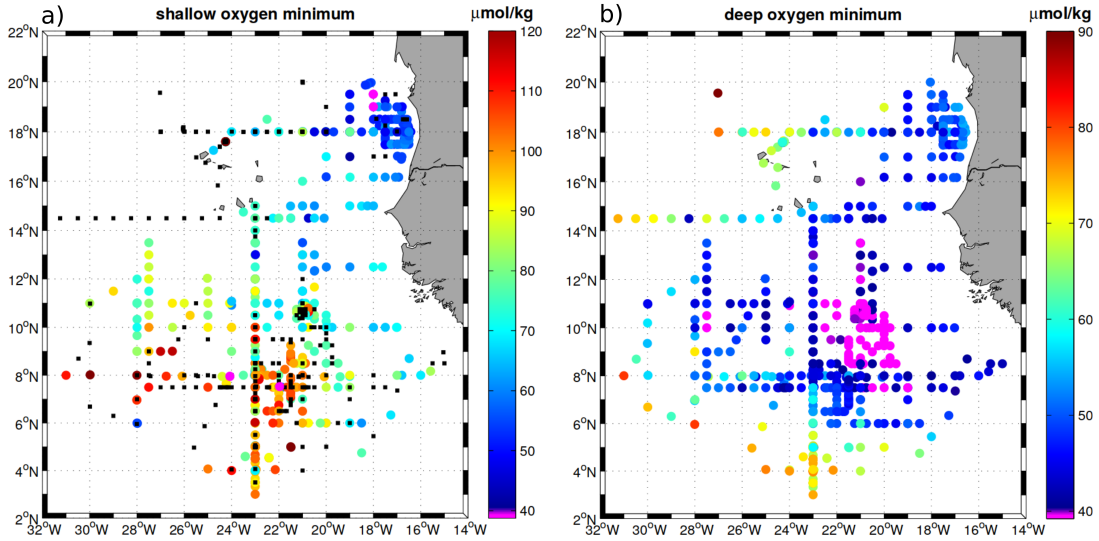


Figure 1.8: Minimum O_2 concentrations at the shallow and deep OMZs of the ETNA. (a) Shallow and (b) deep OMZs are divided at 200 m depth. Data obtained from CTD station data taken during the period 2006–2013. O_2 concentrations < 40 µmol L^{-1} are highlighted by purple colors. Adapted from Brandt et al. (2015).

In contrast, the sOMZ is typically centered between 50–150 m depth and intensifies toward the north, where minimum O2 concentrations of 35–40 µmol L^{-1} have been observed along the African shelf near 20°N (Figure 1.8b; Brandt et al., 2015). Its maintenance is attributed to a combination of physical circulation and enhanced biological activity (Brandt et al., 2015). High primary production driven by upwelling and eddy activity leads to elevated organic matter export and subsequent oxygen consumption in the thermocline (Karstensen et al., 2008). As a result, the sOMZ exhibits stronger temporal and spatial variability than its deeper counterpart (Brandt et al., 2015; Klenz et al., 2018; Thomsen et al., 2019). However, due to the scarcity of systematic *in-situ* observations, the role of seasonal processes in modulating the sOMZ remains poorly understood.

1.3.4 Low-oxygen eddies

The ETNA is characterized by weak mean circulation but strong mesoscale variability (Mittelstaedt, 1991; Stammer & Wunsch, 1999; Lázaro et al., 2005), making mesoscale eddies key features in shaping regional O_2 distributions and biogeochemical tracers (Schütte, Brandt, & Karstensen, 2016). In a comprehensive study combining Argo floats, shipboard and glider observations, Schütte, Karstensen, et al. (2016) found that 96% of all vertical profiles with O_2 < 40 µmol L^{-1} in the upper 200 m were associated with 27 independent eddies (17 ACMEs and 10 cyclonic). However, these hypoxic conditions were primarily detected offshore, often by Argo

floats with typical drifting depths of ≈1000 m, potentially underrepresenting coastal dynamics. In addition, only three of the eleven ship-based campaigns included in the study were conducted during the upwelling relaxation season, which suggests a potential seasonal bias in existing datasets.

Most low-oxygen eddies detected in the ETNA are ACMEs, characterized by low PV and high SACW content (Schütte, Brandt, & Karstensen, 2016; Karstensen et al., 2017; Pietri & Karstensen, 2018). Similar to processes reported in other EBUSs (e.g., Molemaker et al., 2015; Contreras et al., 2019), these eddies are typically generated through interactions between the PUC and steep continental slope (Dilmahamod et al., 2022). Once formed, ACMEs efficiently trap and transport distinct water masses in their interior, which can be rich in nutrients, particulate and dissolved organic matter, and microbial and plankton communities, isolating them from mixing over timescales of weeks to months (Hauss et al., 2016; Schütte, Karstensen, et al., 2016; Christiansen et al., 2018).

The biogeochemical impact of ACMEs extends beyond their ability to isolate and transport distinct water masses offshore. Several studies conducted in the ETNA have shown that their surface layers often exhibit enhanced primary productivity (Löscher et al., 2015; Fiedler et al., 2016; Hauss et al., 2016), driven by vertical nutrient fluxes sustained by submesoscale dynamics at the base of the mixed layer and at their peripheries (Karstensen et al., 2017; Pietri & Karstensen, 2018). Increased surface productivity enhances export fluxes, and remineralization within the isolated cores further reduces O_2 (G. Fischer et al., 2016; Christiansen et al., 2018). Observed respiration rates within ACMEs, reported to reaching 0.26 µmol L^{-1} d^{-1} (Fiedler et al., 2016), significantly exceed typical thermocline values of about 0.03 µmol L^{-1} d^{-1} (Karstensen et al., 2008), leading to hypoxic (and occasionally anoxic, Figure 1.9) conditions which ultimately influence microbial community composition (Löscher et al., 2015), biogeochemical cycling (Fiedler et al., 2016), and zooplankton and pelagic fish behavior (Hauss et al., 2016). Furthermore, strong vertical gradients in carbon and nitrogen cycling within ACMEs have been reported, including evidence of denitrification and shifts in dissolved organic matter composition (G. Fischer et al., 2016; Grundle et al., 2017; G. Fischer et al., 2021; Devresse et al., 2022).

Although low-oxygen eddies have been predominantly associated with ACMEs, some studies have demonstrated that cyclonic eddies can also foster hypoxic conditions (e.g., Schütte, Karstensen, et al., 2016; Devresse et al., 2022). Karstensen et al. (2015) described a cyclonic eddy tracked with an Argo float from the Mauritanian shelf into the open ocean for several months, where minimum O2 concentrations as low as 14 µmol L^{-1} were systematically detected just below the mixed layer. The observed oxygen utilization rates (>0.15 µmol L^{-1} day^{-1}) were roughly three to five times greater than typical thermocline values (Karstensen et al., 2008), suggesting significant remineralization of organic matter at depth. Still, such intense oxygen utilization rates could not have been achieved without a coherent hydrographic structure and limited lateral exchange at depth. Although ACMEs generally display stronger and more persistent hypoxia due to their higher coherence and shallower mixed layers (Karstensen et al., 2017; Pietri & Karstensen, 2018), cyclonic eddies also have the potential to develop hypoxic conditions, given sufficient biological productivity and limited ventilation.

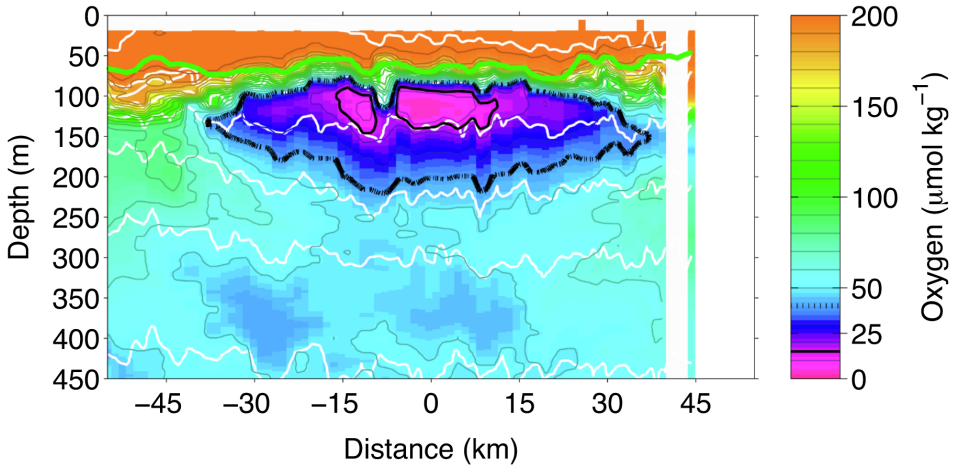


Figure 1.9: Oxygen concentrations across a cross section through the center of a low-oxygen ACME in the ETNA. Data were collected by a glider. The ACME had been active for at least seven months when sampled north of the Cabo Verde Islands. The horizontal axis denotes distance relative to the eddy center. White contours indicate selected isopycnals (density anomaly intervals of $\Delta\sigma_\theta = 0.2\text{kg m}^{-3}$), and the green contour marks the base of the mixed layer. Adapted from Karstensen et al. (2017).

Low-oxygen eddies in the ETNA have been termed "open-ocean dead zones" due to their ability to sustain hypoxic and often near-anoxic conditions far from coastal regions (Karstensen et al., 2015; Hauss et al., 2016; Karstensen et al., 2017). Yet, paradoxically, they may also act as biological "oases," supporting elevated surface productivity–which favors predatory species–and microbial niche diversification (Hauss et al., 2016). The persistence of these eddies and their impact on oxygen distributions suggest they are not only integral to the formation and maintenance of the sOMZ, but may also serve as analogs for future ocean deoxygenation scenarios (Löscher et al., 2015; Fiedler et al., 2016).

1.3.5 Hypoxic conditions at the coastal region

While low-oxygen eddies are considered important drivers of the sOMZ offshore (Schütte, Karstensen, et al., 2016), recent studies have also documented hypoxic conditions along the ETNA continental shelves and slopes (e.g., Yücel et al., 2015; Thomsen et al., 2019; Dale et al., 2022). Klenz et al. (2018) analyzed CTD profiles from nine research cruises off the Mauritania coast, at ≈18°N, and detected hypoxic waters attached to the shelf break (around 100 m depth) in two summer cruises conducted shortly after the upwelling season. The authors proposed that enhanced stratification restricts diapycnal oxygen transport from the surface, which when coupled coupled with high respiration rates results in an oxygen deficit, driving O_2 concentrations to their minimum levels. Similarly to observations from Peña-Izquierdo et al. (2012), their results also highlighted a general oxygen decline downstream of the main flow–hence poleward in the upper central waters–presumably due to the degradation of the organic matter over the shelf.

By examining observational data from one of the latter cruises (M107, conducted in June 2014), Thomsen et al. (2019) provided evidence of hypoxic waters extending from the continental shelf towards offshore, suggesting these hypoxic conditions originated near the seabed (Figure 1.10). They highlighted a complex interplay of local biogeochemical processes, driven by rapid

oxygen respiration associated with remineralization of organic matter from the seabed, and remote physical forcing via the advection of old, oxygen-depleted waters (Peña-Izquierdo et al., 2012; Klenz et al., 2018). These findings highlight the difficulty of isolating individual mechanisms using traditional ship-based observations alone and emphasize the need for enhanced observational coverage combined with high-resolution numerical simulations to disentangle the relative contributions of local and remote processes.

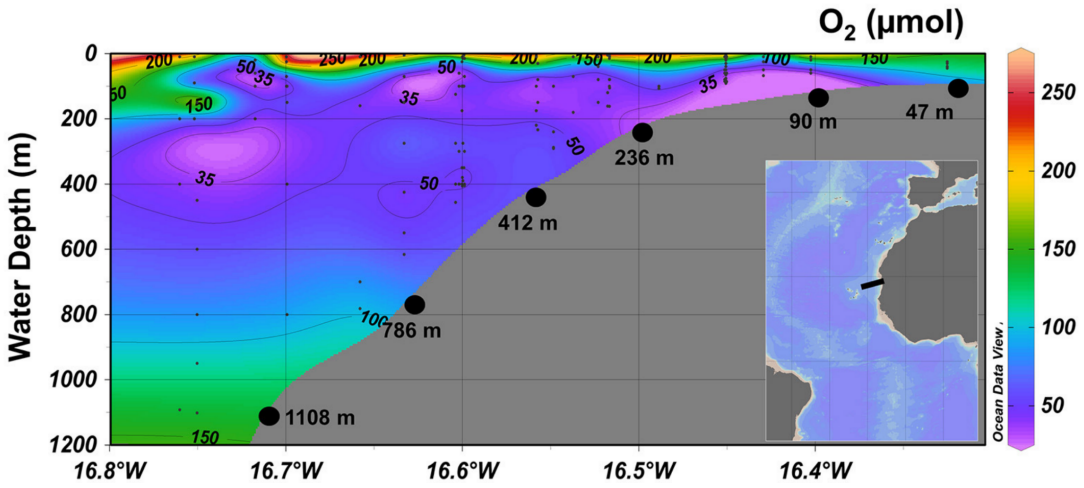


Figure 1.10: Vertical distribution of oxygen concentrations along a longitudinal transect at approximately 18°N off the Mauritanian coast. Data were obtained from CTD profiles and spatially interpolated. Black dots indicate the locations of benthic lander deployments along the continental shelf and slope. The inset provides the geographic context of the sampling area (marked by the black rectangle). Retrieved from Gier et al. (2017).

Additional support for these processes was provided by Gier et al. (2017), who during the same cruise identified peak dinitrogen (N_2) fixation rates on the shelf's bottom at 90 m depth, where O2 concentrations reached minimum values of 30 µmol L^{-1}. A complementary 30-hour time series at a shallower site (53 m depth) also revealed a concurrent decline in O_2 and rise in nitrate (NO_3) concentrations (Yücel et al., 2015). Similar to hypoxic events observed in the northern Californian shelf (J. O. Peterson et al., 2013), these patterns were attributed to cross-shelf intrusions of deeper, nutrient-rich, and oxygen-poor waters.

Similar findings emerged from a 19-month time series conducted by Tall et al. (2021) at 30 m depth on the Senegalese shelf, where minimum O2 concentrations occurred during the peak upwelling season due to intrusion of deeper, oxygen-poorer water masses. According to previous studies, these upwelled waters are more likely to originate the upper thermocline waters (Capet et al., 2017; Ndoye et al., 2017), given that only 1% of surface water are thought to originate from the dOMZ (Glessmer et al., 2009). Also in the same location, Machu et al. (2019) described a severe anoxic event driven by the degradation of a diatom bloom in highly stratified waters. The authors argued that before degradation occurred, this bloom was fueled by the availability of nutrients and by stable conditions promoted by the relaxation of coastal upwelling, suggesting that these events are recurrent in the region.

The wide and shallow continental shelf off southern Senegal is characterized by long water residence times which, when combined with high productivity, favor the development of hypoxic conditions (Ndoye et al., 2017). Yet, the first confirmed evidence of anoxic conditions was only recently reported (Machu et al., 2019). Such events have previously been proposed as a possible

explanation for sporadic, unexplained mass mortality events of demersal fish (Caverivière & Touré, 1990), although many of these occurrences remain poorly documented and insufficiently understood (Machu et al., 2019).

Table 1.1 shows an compilation of research cruises conducted in the coastal region of the ETNA (from 2006 to present date) with publicly available data, cruise reports or scientific publications. In this table, we highlight minimum O2 concentrations detected in the upper 200 m and outside the direct influence of eddies. Most hypoxic conditions were detected in summer cruises, especially at northern latitudes. These observations align with the known susceptibility of shelf OMZs in EBUSs to seasonal cycles in upwelling dynamics (as it also occurs in the northerrn Californian and Namibian shelf; Monteiro et al., 2011; J. O. Peterson et al., 2013; K. Fennel & Testa, 2019).

Table 1.1: Overview of research cruises conducted in the coastal region of the ETNA. Minimum O_2 values (µmol L^{-1}) only comprise those detected or reported between the surface and 200 m depth in the coastal region and outside the influence of eddies. Minimum O_2 values marked with * were measured in the bottom of the continental shelf or slope. Rows in bold highlight the cruises where minimum O_2 < 40 µmol L^{-1}.

Campaign	Season	Year	Min. O_2	Lat. (°N)	Source	References
POS346	**Winter**	**2006**	**<40**	**≈19.7**	**Report**	**Westphal, 2007**
POS347	**Winter**	**2007**	**32.96**	**18**	**Data**	**Dengler et al., 2008**
POS348	Winter	2007	52.1	19	Data	Bange, 2008
ATA03	Winter	2008	49.7	17.67	Data	Körtzinger, 2012
POS531	Winter	2019	?	?	Report	Iversen et al., 2019
POS320/1	Spring	2005	41.13	17.5	Data	Ruhland, 2005
MSM11/2	Spring	2009	>65	?	Report	Bickert et al., 2011
MSM17/4	Spring	2011	42*	≈18	Report	Pfannkuche, 2014
POS399	Spring / Summer	2010	41.49	19.5	Data	Bange, 2011
M97	Spring / Summer	2013	57.61	≈14.5	Data	Tanhua, 2014
M107	**Summer**	**2014**	**25***	**16.45**	**Data**	**Sommer et al., 2015**
M68/3	Summer	2006	44	18.20	Data	Koschinsky et al., 2009 Tanhua and Liu, 2015
M129	**Summer**	**2016**	**<40**	**≈18.8**	**Report**	**Ekau et al., 2016**
Fluxes I	**Summer**	**2017**	**<40**	**≈20**	**Paper**	**Burgoa et al., 2021**
M156	**Summer**	**2019**	**25.77**	**18.58**	**Data**	**Krahmann, 2022**
M83/1	Autumn	2010	58.31	15.02	Data	Visbeck, 2013
CANOA08	Autumn	2008	≈50	21.25	Paper	Peña-Izquierdo et al., 2012
MSM16/3	Autumn	2010	≈48	?	Report	Westphal et al., 2014
MSM104	**Autumn Winter**	**2021**	**<40**	**20**	**Report**	Zonneveld et al., 2021

In summary, hypoxic conditions off the coast of Mauritania and Senegal appear to be driven by a combination of local biogeochemical processes and remote drivers, hence distinct from eddy-driven processes. Such hypoxic conditions have the potential to influence sOMZ dynamics, either by directly contributing to regional oxygen concentrations through the export of bottom waters rich in organic matter (Thomsen et al., 2019), or by becoming entrained and subsequently intensified within coastal-generated eddies. Together, these findings raise critical questions about

the interplay between coastal biogeochemistry, boundary currents and eddy dynamics in shaping the sOMZ–questions that this thesis aims to address.

1.4 Objectives and organization

To date, most studies have concentrated on the dOMZ, with relatively few focused investigations into the formation, variability, and spatial extent of the sOMZ. While recent research has begun to shed light on the dynamics of hypoxic conditions shaping the sOMZ–many of which have presented important and novel findings with regional and global implications (Karstensen et al., 2015; Löscher et al., 2015; Fiedler et al., 2016; Hauss et al., 2016; Grundle et al., 2017; Machu et al., 2019)–significant knowledge gaps remain. These are largely driven by the scarcity of long-term and high-resolution observations, especially during the relaxation season, which paradoxically corresponds to the highest incidence of coastal hypoxia (Klenz et al., 2018).

Building on the complexities and gaps outlined in the preceding sections, the overarching goal of this thesis is to **provide a comprehensive understanding of the characteristics, processes, and drivers of hypoxic events that contribute to the formation of the sOMZ in the ETNA**, with a focus not only on low-oxygen eddies but also on the physical and biogeochemical dynamics occurring along the northwestern African coast. To achieve this, this thesis addresses the following key scientific questions:

Q1: What are the spatial and temporal patterns of hypoxic conditions in the ETNA, and how are they linked to different regional water masses?

Q2: Which large-scale physical processes control the formation and distribution of hypoxia across the ETNA?

Q3: What physical and biogeochemical mechanisms sustain hypoxic conditions in the coastal region during different seasons?

Q4: How do hypoxic conditions at the bottom of the continental shelf and slope contribute to the regional formation of the sOMZ?

Q5: Which physical processes drive the formation and evolution of low-oxygen eddies, and what are the main biogeochemical consequences within them?

1.4.1 Approach

Given the inherent limitations of observational datasets–particularly in terms of spatial and temporal coverage–this study relies on a high-resolution ($\approx$3 km) coupled physical-biogeochemical climatological model simulation encompassing the entire tropical Atlantic Ocean. The use of a basin-scale configuration at such fine resolution enables the realistic representation of both remote and local processes that are critical for accurately simulating the drivers of the sOMZ (Thomsen et al., 2019). This configuration also resolves the basin-wide zonal jets that are essential for

reproducing the vertical and horizontal structures of both shallow and deep OMZs (Brandt et al., 2015; Calil, 2023). Given the study's focus on the ETNA, the analysis is confined to a subdomain spanning 10-22°N and 15-27°W, consistent with the spatial extent used in previous investigations (e.g., Arístegui et al., 2009; Pegliasco et al., 2015; Schütte, Brandt, & Karstensen, 2016).

The analyses presented throughout the thesis employ a combined Eulerian-Lagrangian framework. Eulerian methods are used to characterize the spatial and temporal patterns of hypoxic events, including their seasonality. Complementarily, Lagrangian methods are employed in two stages: first, to identify and track individual hypoxic features through space and time; second, to perform particle tracking that reconstructs the trajectories and biogeochemical history of water parcels evolving into hypoxic conditions within the ETNA.

1.4.2 Thesis structure

This thesis is organized into six chapters and an appendix. Excluding the Introduction, Methods and Conclusion, the main findings are addressed in three main chapters, each addressing a specific aspect of the sOMZ.

Chapter 2: Model and methods
This chapter provides a detailed description of the model configuration, including the setup of the physical-biogeochemical simulation and its initial and boundary conditions. The model is validated against climatological datasets at a regional scale, and against *in-situ* observations at the bottom of the continental shelf and slope. The chapter also outlines the analytical framework employed throughout the thesis, including the water mass analysis and the backward-in-time Lagrangian particle tracking analysis.

Chapter 3: Characterization of the Shallow Oxygen Minimum Zone OMZ in the Eastern Tropical North Atlantic (Q1 and Q2)
This chapter examines the spatial and temporal variability of hypoxic events forming the sOMZ, focusing on their seasonality, intensity, duration, and spatial extent. Special attention is also given to the role of water mass composition. Lastly, coherent clusters of hypoxic conditions are tracked in space and time, and their characteristics are quantified to offer a comprehensive view of their variability across the ETNA.

Chapter 4: Drivers of the Shallow Oxygen Minimum Zone off the Northwestern African Coast (Q3 and Q4)
This chapter investigates the processes contributing to the development and persistence of hypoxia along the Mauritania-Senegal coastal region. The seasonality of these hypoxic conditions and their connection to upwelling and boundary current dynamics is also assessed. The analysis also explores the drivers and seasonality of bottom-layer hypoxia along the continental shelf and slope, examining its contribution to the sOMZ offshore.

Chapter 5: Generation and evolution of low-oxygen eddies in the Eastern Tropical North Atlantic (Q4 and Q5)
This chapter investigates the physical conditions that govern the generation and evolution of low-oxygen eddies, as well as their biogeochemical consequences within them. It explores how different formation mechanisms and dynamical properties influence the development of hypoxic conditions within eddy cores. Additionally, it identifies and characterizes long-lived eddies with oxygen-deficient interiors and examines their subsequent evolution over time.

Chapter 6: Synthesis and outlook
This final chapter summarizes the key findings of the thesis and discusses their broader implications in relation to past studies. It also outlines the main limitations of the study and suggests directions for future research, emphasizing the need for sustained observational efforts and high-resolution modeling to improve understanding of the physical-biogeochemical mechanisms that shape the sOMZ in the ETNA.

Chapter 2

Model and methods

2.1 Numerical framework

The core of this thesis, and the foundation of the results presented in Chapters 3, 4, and 5, is a coupled physical-biogeochemical simulation of the entire Tropical Atlantic Ocean. The simulation was performed using version 1.1 of the ”Coastal and Regional Ocean Community Model” (CROCO; available at http://www.croco-ocean.org), coupled with the version 1 of the biogeochemical module ”Pelagic Interactions Scheme for Carbon and Ecosystem Studies” (PISCES-v1; Aumont & Bopp, 2006). The following subsections provide a detailed description of each component of the coupled model system, along with its configuration, forcing datasets, and boundary conditions.

2.1.1 CROCO

CROCO is a state-of-the-art ocean model designed for high-resolution applications in coastal and regional domains. It has been applied extensively across diverse regions (Capet, McWilliams, et al., 2008; Renault et al., 2019; Combes et al., 2021; Echevin et al., 2021; Thomsen et al., 2021), including the northwestern African coast (Marchesiello & Estrade, 2009; Lachkar & Gruber, 2012; Auger et al., 2015; Auger et al., 2016; Ndoye et al., 2017; Hailegeorgis et al., 2020; Tall et al., 2025). The model builds on the primitive-equation, hydrostatic, free-surface Regional Oceanic Modeling System (ROMS) kernel (Shchepetkin & McWilliams, 2005), while also incorporating a nonhydrostatic and non-Boussinesq solver (Auclair et al., 2018), thereby extending its applicability to the simulation of small-scale processes (Fox-Kemper et al., 2019; Hilt et al., 2020). CROCO features adaptive grid refinement through the AGRIF nesting tool (Debreu et al., 2012), allowing high-resolution child domains to be embedded within coarser parent domains. Together with advanced numerical schemes for spatial and temporal discretization (Shchepetkin & McWilliams, 2005), this provides high computational efficiency and accuracy.

CROCO solves the hydrostatic primitive equations of motion, which are expressed as follows (with variables defined below the set of equations). The horizontal momentum equations (zonal and meridional) are given by Equations (2.1) and (2.2); the temporal evolution (advection–diffusion) of a conservative tracer (e.g., temperature or salinity) is described by Equation (2.3); and the nonlinear equation of state for seawater is represented by Equation (2.4) (Shchepetkin &

McWilliams, 2005). In our configuration, we apply both the hydrostatic and Boussinesq approximations (Shchepetkin & McWilliams, 2003, 2005). The hydrostatic approximation balances the vertical pressure gradient with the buoyancy force, while the Boussinesq approximation neglects density variations in the inertial terms due to their small magnitude, except where they affect buoyancy, as shown in Equation (2.5). Assuming the fluid is incompressible, the continuity equation enforces mass conservation and is given in Equation (2.6).

$$\frac{\partial u}{\partial t} + \vec{v} \cdot \nabla u - fv = -\frac{\partial \phi}{\partial x} + F_u + D_u \tag{2.1}$$

$$\frac{\partial v}{\partial t} + \vec{v} \cdot \nabla v + fu = -\frac{\partial \phi}{\partial y} + F_v + D_v \tag{2.2}$$

$$\frac{\partial C}{\partial t} + \vec{v} \cdot \nabla C = F_C + D_C \tag{2.3}$$

$$\rho = \rho(T, S, P) \tag{2.4}$$

$$\frac{\partial \phi}{\partial z} = -\frac{\rho g}{\rho_0} \tag{2.5}$$

$$\nabla \cdot \vec{v} = \frac{\partial u}{\partial x} + \frac{\partial v}{\partial y} + \frac{\partial w}{\partial z} = 0 \tag{2.6}$$

In the above equations, D_u, D_v, and D_C represent diffusive terms; F_u, F_v, and F_C represent external forcing terms; the Coriolis parameter is defined as $f(x, y) = 2\Omega \sin\theta$, where Ω is the Earth's angular velocity and θ is latitude (in radians); g is the acceleration due to gravity; ϕ denotes the dynamic pressure; and (u, v, w) are the zonal, meridional and vertical (x, y, z) components of the velocity vector $\vec{v}$.

For time integration, CROCO uses a split-explicit time-stepping scheme to solve the primitive equations, distinguishing between the fast barotropic and slower baroclinic modes (Shchepetkin & McWilliams, 2005). Governing surface elevation and depth-integrated momentum, the barotropic mode is computed using short time steps nested within larger baroclinic steps, which resolve temperature, salinity, and internal momentum. A two-way time-averaging procedure ensures consistency between modes and reduces aliasing errors arising from frequency mismatches. For the baroclinic mode, a third-order Leapfrog predictor combined with an Adams–Moulton corrector enables stable integration with relatively large time steps.

For horizontal and vertical spatial integration, CROCO employs a staggered Arakawa-C grid (Arakawa & Lamb, 1977). On this grid, tracer variables such as salinity and temperature are defined at the center of each grid cell, while the horizontal velocity components u, v and w are located at the center of the eastern, northern and bottom cell faces, respectively. In the vertical, CROCO uses a stretched, terrain-following σ-coordinate system, which is particularly advantageous in modeling studies with complex bathymetry because it guarantees a higher vertical resolution in shallow ocean regions (Song & Haidvogel, 1994). The vertical levels are non-linearly distributed throughout the water column and can be stretched to concentrate resolution near the surface or bottom. While this vertical discretization offers great flexibility, it can introduce pressure gradient errors over steep topography (Haney, 1991). To minimize

these errors, CROCO uses the energy-conserving pressure gradient formulation developed by Shchepetkin and McWilliams (2003, 2005, 2009), which significantly improves accuracy in regions of complex bathymetry.

To parameterize subgrid-scale vertical mixing, we use the non-local K-Profile Parameterization (KPP) turbulence closure scheme (Large et al., 1994). Vertical mixing is represented separately for the surface and bottom boundary layers, as well as for the ocean interior. The depth of the surface boundary layer is diagnosed based on surface forcing, buoyancy, and vertical shear, by equating a bulk Richardson number to a critical threshold. A non-local transport term is included to represent convective processes in the surface boundary layer. Below this layer, interior mixing is represented through a combination of vertical shear instability and convective adjustment. Although double-diffusive mixing can be parameterized, it is not considered in our configuration. At the bottom boundary, vertical mixing follows the same conceptual framework as at the surface but is driven by bottom stress and local stratification near the seabed. This parameterization framework has been shown to reproduce key boundary layer processes, including surface boundary layer deepening, diurnal cycling, storm-driven mixing, and enhanced bottom mixing over sloping or rough topography (Large et al., 1994).

In terms of horizontal mixing, tracers in CROCO are advected using the RSUP3 scheme (Marchesiello et al., 2009), a rotated third-order upwind method designed to follow isopycnal surfaces and minimize numerical diapycnal mixing. This scheme is effective in reducing spurious diapycnal tracer mixing in σ-coordinate models, ensuring accurate conservation of water mass properties without the need for explicit horizontal diffusivity. This makes it particularly suitable for regional studies where the integrity of tracer pathways is essential. In this configuration, the tracer mixing coefficient is formulated as a function of the absolute value of the local velocity and the horizontal grid spacing, and is expressed as

$$B = \frac{1}{12} |U| (\Delta x)^3 \tag{2.7}$$

where U represents the magnitude of the velocity field and Δx is the grid size. As a result, the finer horizontal resolution leads to smaller diffusivity coefficients, enhancing the emergence of zonal jets at depth (Calil, 2023). As discussed in Chapter 1, this is of critical importance for investigating remote forcing mechanisms that influence the sOMZ in the ETNA (Brandt et al., 2010; Brandt et al., 2015; Peña-Izquierdo et al., 2015; Thomsen et al., 2019).

2.1.2 PISCES

One of the main advantages of CROCO is its highly modular structure, which facilitates coupling with various physical and biogeochemical components, including PISCES. Designed to simulate ocean productivity and the associated biogeochemical cycles of carbon and nutrients, PISCES was originally developed by Aumont and Bopp (2006) and derived from the fifth version of the ”HAMburg Ocean Carbon Cycle” model (HAMOCC; Aumont et al., 2003).

PISCES comprises 24 compartments, including four living components: two phytoplankton size classes–nanophytoplankton (2–20 nm) and diatoms (20–200 µm)–and two zooplankton size classes–microzooplankton (20–200 µm) and mesozooplankton (200 µm–2 mm). Phytoplankton growth is limited by five nutrient pools: Nitrate (NO_3), Ammonium (NH_4), Phosphate (PO_4), silicate, and iron. Dissolved and particulate organic matter are also key components of the model. Within the particulate organic matter compartment there are two particle classes–small and large. The sinking speed of the large particles varies between 50 m d^{-1} and 200 m d^{-1}, while for small particles is set at about 3 m d^{-1}.

Phytoplankton growth in PISCES is governed by bottom-up factors, including light availability, temperature, and nutrient concentrations, such that the growth rate μ^P reads as follows:

$$\mu^P = \mu_P \left(1 - \exp\left(-\frac{\alpha^P \left(\frac{Chl}{C}\right) \mathrm{PAR}}{\mu_P L^P_{\mathrm{lim}}}\right)\right) L^P_{\mathrm{lim}}, \tag{2.8}$$

where μ_P is the maximum growth rate as a function of temperature, computed as $\mu_P = ab^{(cT)}$, with a, b, and c being constants representing the growth rate at 0°C, the temperature sensitivity of growth, and the temperature dependence, respectively. α^P is the initial slope of the photosynthesis-irradiance curve, Chl/C is the Chlorophyll-to-Carbon ratio, and PAR is the Photosynthetically Available Radiation. L^P_{lim} represents the nutrient limitation term. Assuming constant Redfield stoichiometry, Monod kinetics are applied to compute L^P_{lim} for nitrogen, phosphorus, and silicate (Monod, 1942). For iron, a quota-based formulation is used, allowing the Fe:C ratio to vary according to external availability. Diatoms differ from nanophytoplankton by requiring silicate and exhibiting higher iron demands (Sunda & Huntsman, 1997) and larger half-saturation constants due to their cell size.

In addition to bottom-up regulation, phytoplankton biomass is subject to top-down controls including zooplankton grazing, mortality, and aggregation-induced sinking. The prognostic equation governing the evolution of phytoplankton biomass is:

$$\frac{\partial P}{\partial t} = (1 - \delta^P)\mu^P P - m^P \frac{P}{K_P + P} P - \omega_p^P P^2 - g^Z(P)Z - g^M(P)M, \tag{2.9}$$

where P is the phytoplankton biomass, δ^P is the fraction of production lost to respiration, m^P is the mortality rate, K_P is the half-saturation constant for mortality, and ω_p^P is the aggregation coefficient. The terms $g^Z(P)$ and $g^M(P)$ represent grazing by microzooplankton (Z) and mesozooplankton (M), respectively (Aumont & Bopp, 2006).

In terms of external nutrient input, PISCES-v1 includes parameterizations for multiple sources, including river discharge, atmospheric dust deposition and sediment mobilization. River inputs of inorganic and organic nutrients are computed based on elemental ratios relative to dissolved carbon. Atmospheric dust deposition contributes to the particulate iron pool, which becomes available for phytoplankton uptake at a specific rate of solubility. This is important, considering that over the northwest African margin, high atmospheric iron deposition from Saharan dust typically prevents iron limitation in surface waters (Messié & Chavez, 2015). Lastly, sediment

mobilization provides an additional source of iron to the water column (Aumont & Bopp, 2006; Tagliabue et al., 2009).

In PISCES-v1, nitrogen fixation is not explicitly represented. Instead, the nitrogen cycle is closed through external inputs (as described above) and internal transformations. As such, in oligotrophic regions where nitrogen fixation is ecologically significant, PISCES-v1 may underestimate primary production due to the absence of a mechanism for converting atmospheric nitrogen into bioavailable nitrogen (Aumont & Bopp, 2006). Despite this limitation, the model's robust representation of plankton dynamics and nutrient cycling has supported numerous studies at global (Aumont et al., 2003; Aumont & Bopp, 2006), basin (Gorgues et al., 2010; Dilmahamod et al., 2016), and regional (Echevin et al., 2008; Dilmahamod et al., 2020) scales, including in our study domain (Auger et al., 2015; Auger et al., 2016; Tall et al., 2025).

An important aspect to consider throughout this thesis is the model's ability to represent benthic oxygen consumption along continental shelves and slopes. In PISCES-v1, which does not include an explicit sediment module as in version 2 (Aumont et al., 2015), benthic remineralization is parameterized using a simplified empirical approach. The flux of POC reaching the seafloor, F_{OC}, is partially lost via a burial efficiency E_{burial} (Dunne et al., 2007), while the remaining fraction is remineralized through oxic and suboxic (denitrifying) pathways. The partitioning between these pathways is computed using the metamodel of Middelburg et al. (1996), which relates the proportion of degradation occurring via denitrification, P_{denit}, to the local flux of POC, bottom water oxygen and nitrate concentrations, and depth. To avoid unrealistic results, minimum thresholds are imposed on bottom water nitrate and oxygen concentrations (1 and 10 µmol L^{-1}, respectively). The resulting sediment fluxes of nitrate (due to denitrification, $F_{\mathrm{NO_3}}^{\mathrm{denit}}$) and oxygen (due to remineralization, $F_{\mathrm{O_2}}^{\mathrm{oxic}}$) are given by:

$$F_{\mathrm{NO_3}}^{\mathrm{denit}} = R_{\mathrm{NO_3}} \cdot P_{\mathrm{denit}} \cdot F_{\mathrm{OC}} \tag{2.10}$$

$$F_{\mathrm{O_2}}^{\mathrm{oxic}} = O_2^{\mathrm{ut}} \cdot (1 - P_{\mathrm{denit}}) \cdot F_{\mathrm{OC}} \tag{2.11}$$

where $R_{\mathrm{NO_3}}$ and O_2^{ut} are stoichiometric coefficients representing nitrate and oxygen demand, respectively, for organic matter remineralization. The associated nutrient release is represented as NH_4 input to bottom waters, derived from both oxic and suboxic degradation processes. The accuracy of the model in simulating benthic oxygen and nitrate concentrations is tested against *in-situ* observations in Section 2.3.2.

2.1.3 Model configuration

To achieve a realistic representation of the oxygen distribution within the OMZ of the North Atlantic Ocean, which is extremely sensitive to the large-scale circulation of the systems of equatorial currents and zonal jets, the simulation used throughout this thesis is the same as the one used in Calil (2023). The model domain covers the whole Tropical Atlantic Ocean, from 19°S–31°N, with an horizontal resolution of 1/30° (≈3 km) thus it doesn't require any grid nesting. Given our focus on the ETNA, we analyze a subdomain of the model consistent with

past studies (e.g., Arístegui et al., 2009; Pegliasco et al., 2015; Schütte, Brandt, & Karstensen, 2016), spanning from 10–22°N and 15–27°W.

The simulation covers a 14-year period, with the first 9 years dedicated to model spin-up and the final 5 years of daily-averaged outputs used for analysis. Yearly, seasonal and monthly averages are also used throughout the thesis.

CROCO

The bathymetry used in this configuration was derived from the 1-arcminute global relief model ETOPO1, developed by the American National Oceanic and Atmospheric Administration (NOAA; Amante & Eakins, 2009). To minimize horizontal pressure gradient errors, the topography was smoothed such that the bathymetric slope parameter r remained below 0.2, following the criterion proposed by Beckmann and Haidvogel (1993). The vertical resolution, implemented in σ-coordinates, consists of 50 levels, with surface, bottom, and minimum depth-stretching parameters set to $\theta_s = 7$, $\theta_b = 2$, and $h_c = 300$ m, respectively.

To represent the climatological mean state of the tropical Atlantic, the physical component of the model was initialized on 1 January 2003 using temperature, salinity, Sea Surface Height (SSH), and horizontal velocity fields from the Simple Ocean Data Assimilation reanalysis product (SODA; Carton et al., 2018). Lateral boundary conditions for the same variables were prescribed every 5 days for the same year using the same dataset[1]. We should note that although the model domain encompasses part of the Pacific Ocean with an open boundary in the west, the Tropical Atlantic Ocean only takes two open boundaries (in the north and south), making the representation of basin-wide features such as the zonal jets better constrained.

SODA is a widely used ocean reanalysis that provides dynamically consistent estimates of the ocean state by assimilating historical observational data into a global ocean general circulation model. The specific version employed in this study, SODA 3.3.1, spans the period 1980–2015 and assimilates observations from multiple sources, including satellite-derived SSH, *in-situ* temperature and salinity profiles (e.g., Argo, XBTs, CTDs), and SST data. It is based on the Modular Ocean Model version 5 (MOM5), with a horizontal resolution of 0.5° and 50 vertical levels, and is forced by surface fluxes from the NOAA/CIRES 20th Century Reanalysis, version 2c (20CRv2c). This configuration ensures a realistic and observation-constrained representation of the evolving ocean state, making it well suited for basin-scale model initialization and boundary forcing.

The year 2003 was selected for initialization and forcing because it corresponds to a neutral phase of both the North Atlantic Oscillation and the Atlantic Meridional Mode (Chassignet & Xu, 2017), thus minimizing the influence of large-scale climate anomalies and favoring a representation of the mean-state circulation.

Although river runoff is deactivated in our configuration, its regional influence on salinity is implicitly represented through the initial and boundary conditions derived from the SODA reanalysis. These fields reflect observed salinity distributions influenced by freshwater input from major rivers, as SODA assimilates *in-situ* salinity observations and is constrained by surface

[1]Accessed via the Asia-Pacific Data Research Center: http://apdrc.soest.hawaii.edu:80/dods/public_data/SODA/soda_3.3.1/

freshwater fluxes, including rain which can be significant during the monsoon seasons in the tropics.

At the surface, the model is forced with monthly climatological wind stress and heat fluxes from the International Comprehensive Ocean-Atmosphere Data Set (ICOADS version 2.1; Worley et al., 2005). ICOADS is the most comprehensive archive of marine meteorological observations, compiled from ships, buoys, and other platforms. It provides monthly climatological fields based on observations from 1854 to 1992, with a spatial resolution of $\delta x = 0.5^{\circ}$. These fields offer a realistic representation of the mean seasonal cycle of atmospheric conditions, making them particularly appropriate for climatological simulations targeting the mean oceanic state.

PISCES

The biogeochemical initial and boundary conditions are derived from a climatological simulation using the PISCES model (Aumont & Bopp, 2006), with tracer fields updated at every baroclinic time step. All biogeochemical parameters are set to their default values. External sources of iron from both the atmosphere and sediments are included. Oxygen and nitrate fluxes at the seafloor are computed using the sediment metamodel of Middelburg et al. (1996), which provides an empirical representation of benthic remineralization processes. To maintain consistency with the physical configuration, riverine nutrient inputs and atmospheric nitrogen deposition are deactivated. Atmospheric dust deposition is prescribed from monthly climatological fields based on the global dust transport model of Tegen and Fung (1995), assuming a dust sinking speed of 2 m d^{-1}, an iron content of 1% and a solubility of 1.4%.

2.2 Datasets for model validation

In order to evaluate the model's ability to reproduce key physical and biogeochemical properties of the tropical Atlantic Ocean, we used a combination of climatological, satellite-based and *in-situ* datasets. These include global and regional products describing temperature, salinity, O_2, NO_3, PO_4, SSH, Chl*a* concentration, and SST. Below, we describe the main characteristics of each dataset used for validation.

2.2.1 Climatologies

World Ocean Atlas

The 2023 version of the World Ocean Atlas (WOA23; Reagan et al., 2023) was produced by NOAA. WOA23 provides objectively analyzed climatological fields of the main physical (temperature, salinity) and biogeochemical (O_2, NO_3, PO_4) parameters at standard depth levels, based on all available quality-controlled *in-situ* measurements from 1955 to 2023. It is distributed with a annual, seasonal or monthly temporal resolution with an horizontal resolution of 1/4° and 1° for physical and biogeochemical variables, respectively. It is particularly useful for the computation of anomalies (Dufois et al., 2016; Schütte, Brandt, & Karstensen, 2016; Baudena

et al., 2023) and for validating hydrographic structure and large-scale distributions of water masses in model (Chavez & Messié, 2009; Grégoire et al., 2021). In addition to its crucial role in model evaluation, WOA23 is employed in Chapter 4 to perform a comparative analysis of seasonal dynamics along the coastal region, contrasting model outputs with observational data.

CSIRO Atlas of Regional Seas

The 2009 version of the Commonwealth Scientific and Industrial Research Organisation (CSIRO) Atlas of Regional Seas (CARS09; Ridgway et al., 2002) provides monthly-averaged gridded fields of physical and biogeochemical parameters on a 1/2° global grid. It is constructed from a quality-controlled archive of historical subsurface measurements, including research vessel profiles, Argo floats, and data from the Hydrographic Programme of the international World Ocean Circulation Experiment (WOCE). The temperature and salinity fields in CARS09 are based on the World Ocean Database 2005 (updated in 2008; Boyer & Levitus, 2006), Argo profiles through May 2009, and additional hydrographic datasets. CARS applies enhanced in-house quality control and an adaptive local regression mapping technique (also referred to as LOESS) that varies with data density, along with a barrier-aware interpolation scheme that accounts for topographic constraints. These features allow CARS09 to preserve oceanic structures and improve the accuracy of point estimates, particularly in regions with complex topography or strong gradients such as boundary currents and upwelling regions.

GOBAI-O_2

GOBAI-O_2 (Gridded Ocean Biogeochemistry from Artificial Intelligence - Oxygen; Sharp et al., 2023) is a global, four-dimensional monthly dataset of dissolved oxygen covering the year from 2004 to 2022. It extends from the surface to 2000 dbar and has an horizontal resolution of 1°. It is derived from a machine learning ensemble–comprising feed-forward neural networks and random forest regressions–trained on quality-controlled dissolved oxygen measurements from Argo floats and GLODAPv2.2022 shipboard profiles (Lauvset et al., 2022). Predictor variables include gridded temperature and salinity from the RG09 Argo Climatology (Roemmich & Gilson, 2009) and spatiotemporal features such as pressure, density, latitude, and time of year. GOBAI-O_2 effectively captures the seasonal and decadal variability of ocean oxygen and provides realistic climatological fields across the upper 2 km of the ocean, including in regions with sparse direct observations such as the ETNA.

Surface drifters

To validate surface circulation patterns, we used the near-surface velocity climatology derived from the Global Drifter Program (GDP; Laurindo et al., 2017). This dataset combines current velocity fields from both drogued and undrogued drifters, with slip corrections applied to the latter to account for wind-induced biases. The climatology represents surface currents at approximately 15 m depth and is constructed using a Gauss-Markov estimation framework that decomposes the drifter velocities into mean, seasonal, and eddy components while minimizing the spatial smoothing typical of traditional bin-averaging methods. The resulting pseudo-Eulerian fields are mapped onto a 0.25° grid and resolve mesoscale structures with greater fidelity than previous

GDP-based climatologies (Lumpkin & Johnson, 2013). This dataset provides an observational benchmark for assessing the model's ability to reproduce the structure and intensity of the mean and eddy surface currents in ETNA.

2.2.2 Satellite data

Altimetry

To assess the model accuracy in reproducing the mean mesoscale variability and surface circulation patterns, we use the Global Ocean Gridded Level 4 product (CMEMS, 2017), processed by the DUACS multi-mission altimeter data system and provided by the Copernicus Marine Environment Monitoring Service (CMEMS). Data is derived through optimal interpolation of Level 3 along-track measurements from multiple satellite altimeter missions onto a global grid with 1/8° resolution. Anomalies are computed relative to a 20-year mean climatology (1993-2012). The dataset provides sea level anomaly, absolute dynamic topography and geostrophic surface currents. For model validation, we computed monthly averages with daily data from 1993 to 2023.

OSTIA

The Operational Sea Surface Temperature and Sea Ice Analysis (OSTIA; Good et al., 2020) system is a global, high-resolution daily product developed by the UK Met Office and distributed by CMEMS. OSTIA combines satellite observations from multiple sensors with *in-situ* measurements from drifting and moored buoys using the NEMOVAR data assimilation system. The assimilation framework enables the generation of gap-free SST fields by optimally interpolating sparse or cloud-obstructed observations in space and time. This dataset also estimates the foundation SST–the temperature at the base of the diurnal warm layer–by filtering out daytime diurnal warming effects. SST analyses are produced on a $1/20°$ grid and are bias-corrected using a reference dataset composed of *in-situ* and nighttime satellite observations. For comparison with model results, we use monthly climatologies calculated with daily data from 2007 to 2023.

GlobColour

For validation of surface primary productivity, we use monthly climatologies derived from daily, gap-free satellite observations of surface Chl*a* concentration are provided by the CMEMS-GlobColour dataset (CMEMS, 2016), developed by ACRI-ST (France). The dataset spans 1997 to 2023 and merges observations from multiple ocean color sensors, including SeaWiFS, MODIS, MERIS, VIIRS (SNPP and JPSS1), and OLCI (Sentinel-3A and -3B). The multi-sensor merging and spatio-temporal interpolation approach enables the generation of cloud-free maps with a nominal spatial resolution of 4 km and 300 m (for OLCI products only).

2.2.3 Bottom observations

To validate the model's representation of bottom biogeochemical parameters along the continental shelf and slope off Mauritania and Senegal, we use *in-situ* observations from two research

cruises: MSM17/4 (Pfannkuche, 2014) and M107 (Sommer et al., 2015). Both campaigns were conducted under the framework of the SFB 754 project "Climate-Biogeochemistry Interactions in the Tropical Ocean" (Krahmann et al., 2021) and deployed benthic landers (Biogeochemical Observatories, also known as BIGOs) at roughly the same locations across a cross-shelf section centered at ≈18°N during contrasting seasonal conditions: MSM17/4 during the peak upwelling season (March–April 2011), and M107 during the transition toward the upwelling relaxation season (May-July 2014). These autonomous landers were equipped with sensors inside and outsite benthic chambers, enabling direct measurement of solute concentrations and fluxes across the sediment–water interface (e.g., O_2, NO_3, PO_4 and NH_4). Together, these datasets[2] provide a unique seasonal perspective on benthic-pelagic coupling and nutrient cycling under variable oxygen conditions (Dale et al., 2014a, 2022). They serve as essential benchmarks for assessing model performance in simulating benthic biogeochemical concentrations and sediment-water fluxes at the continental shelf and slope off Mauritania.

2.3 Model evaluation

A model evaluation of the main physical and biogeochemical variables was performed by Calil (2023), who demonstrated the model's ability to capture the large-scale structure of the Atlantic OMZs and the Equatorial current system. The authors calculated the model drift over the full domain with seven years of monthly-averaged outputs (following spin-up). They found that the model exhibited minimal drift across key variables, with domain-averaged rates of 4.0×10^{-3} °C yr^{-1} for temperature and 4.8×10^{-4} PSU yr^{-1} for salinity. Oxygen showed a small negative trend of -0.01 μmol L^{-1} yr^{-1}, while nitrate drift was estimated at 2×10^{-2} μmol L^{-1}. These low values indicate that the simulation remains relatively stable over the analysis period and is suitable for examining the regional-scale biogeochemical dynamics of the Tropical Atlantic Ocean. Despite this comprehensive validation, a detailed model evaluation focused specifically on the ETNA follows.

2.3.1 Comparison with climatologies and satellite observations

To ensure a comprehensive and robust evaluation of model performance, we validate the simulation against multiple climatological datasets, namely the WOA23, CARS and GOBAI-O_2. Each of these products is based on distinct data sources, quality control procedures, and mapping techniques, offering complementary perspectives on the ocean's mean state. By comparing the model outputs to all three products, we reduce the risk of dataset-specific biases and improve the reliability of our validation metrics.

The statistics required for the Taylor and target diagrams (Figures 2.1 and 2.2), as well as the spatial comparisons between the model and climatologies (Figures 2.3, 2.4, 2.5, 2.6, 2.7 and 2.8), are derived from regridded model averages adjusted to match the resolution of the climatologies. Due to the relatively coarse resolution and time-averaged nature of the climatologies, these

[2]Datasets are publicly available at PANGEA under Dale et al. (2014b) and Sommer and Dale (2021), respectively

metrics evaluate the model's ability to replicate large-scale, climatological patterns of the tracers. However, one should note that this approach does not allow for assessing the model's performance in simulating extreme events, such as hypoxic conditions.

Normalized Taylor and target diagrams for oxygen, nitrate, phosphate, temperature, and salinity at four depths within the sOMZ (70, 100, 150, and 200 m) indicate generally good agreement between the model and climatological datasets (Figures 2.1 and 2.2). For all variables and depths, correlation coefficients exceed 0.9, except for oxygen at 70 m, which shows a lower agreement (Figure 2.1a). Root Mean Square Error (RMSE) is typically below 0.6 for all variables. Modeled O_2 concentrations exhibit minimal bias at 100, 150, and 200 m, but are underestimated at 70 m (Figure 2.2a). In contrast, nitrate and phosphate exhibit the opposite behavior, with overestimation most pronounced at 70 m (Figures 2.2b and c). This pattern suggests a shallower mixed layer base in the model compared to the climatologies, likely reflecting weaker wind-driven mixing due to the use of low-resolution, climatological wind forcing that lacks synoptic-scale variability and underestimates wind stress. Temperature and salinity both exhibit a systematic cold and fresh bias that diminishes with depth, approaching zero at 200 m (Figures 2.2d and e).

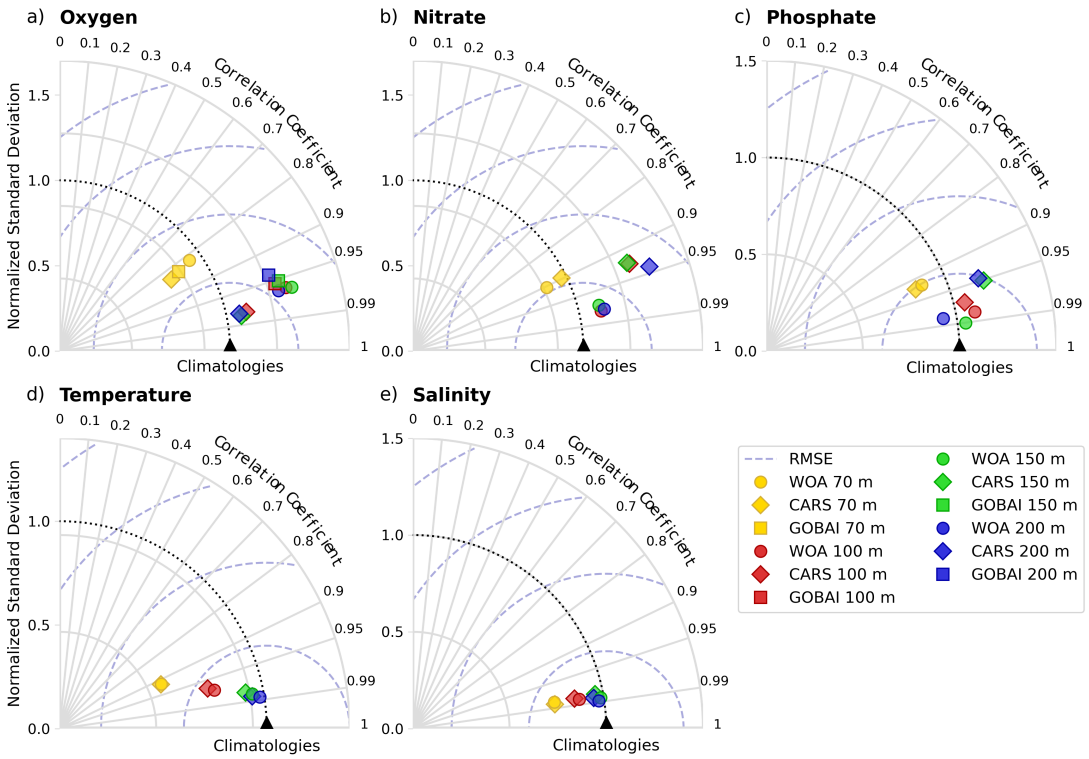


Figure 2.1: Normalized Taylor diagrams for model-observation comparisons at selected depths. Normalized Taylor diagrams for yearly mean oxygen, nitrate, phosphate, temperature and salinity variables compared against WOA, CARS, and GOBAI-O_2 at 70, 100, 150, and 200 m depths. Purple contours represent the RMSE with an interval of 0.4.

Further insight is gained by comparing model skill against individual climatologies. Oxygen concentrations show notably higher accuracy when compared to the CARS climatology at all depths except at 70 m (Figures 2.1a). For nitrate, WOA23 exhibits the best agreement, while phosphate does not show a clear optimal reference, although WOA23 yields exceptionally high correlation coefficients nearing 0.99 (Figures 2.1b,c). For temperature and salinity, depth emerges

as the dominant factor influencing model performance (Figures 2.1d,e), with the bias and variance metrics improving substantially from the surface to deeper levels (Figures 2.2d,e).

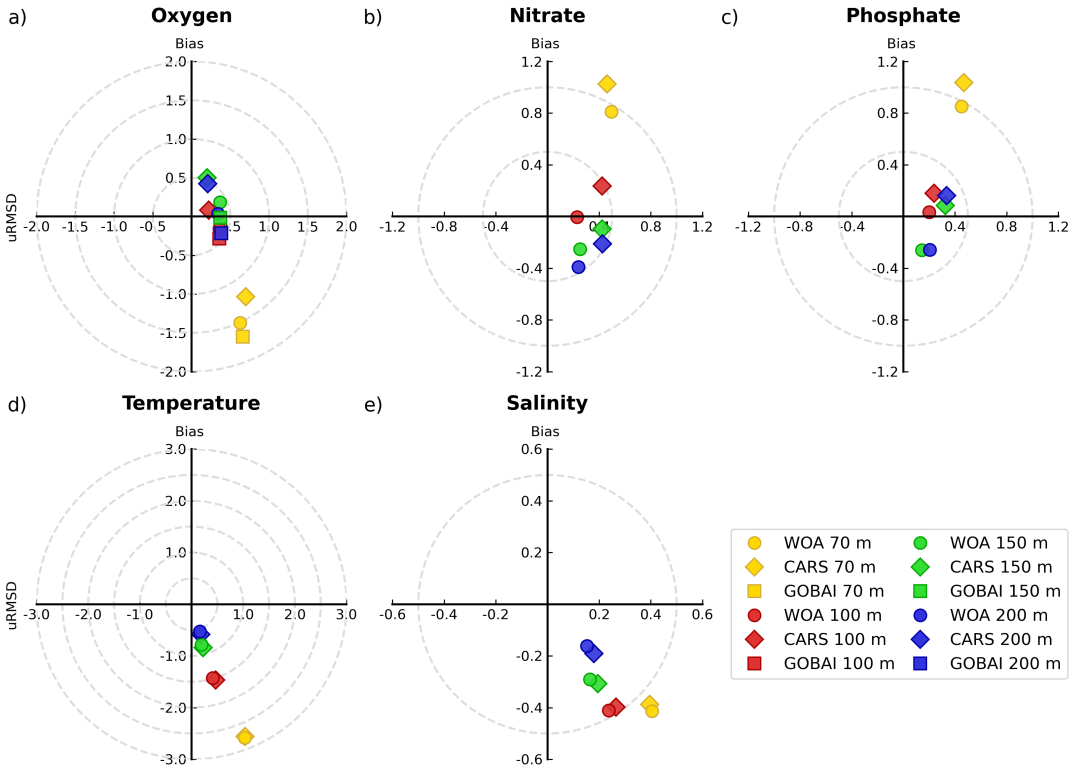


Figure 2.2: Normalized target diagrams for model-observation comparisons at selected depths. Normalized target diagrams for modeled yearly mean oxygen, nitrate, phosphate, temperature and salinity variables compared against WOA, CARS, and GOBAI-O_2 at 70, 100, 150, and 200 m depths. uRMSD in the horizontal axis stands for unbiased Root Mean Square Difference.

Taking into account the significant seasonal variability on the ETNA (Lázaro et al., 2005; Chavez & Messié, 2009), the 5-year and seasonal mean O_2 concentrations at a depth of 100 m are compared against three reference climatologies: WOA23, GOBAI-O_2, and CARS09 (Figure 2.3). The CROCO-PISCES simulation exhibits good overall agreement with these datasets, with Spearman's correlation coefficient (r_s) typically exceeding 0.9 and Mean Absolute Error (MAE) below 20 µmol L^{-1}. Among the climatologies, CARS09 shows the best agreement across all seasons, with the highest r_s and lowest MAEs (Figure 2.3p–t).

Seasonally, the model captures the broad patterns of oxygen distribution, including the intensification of low-oxygen waters along the coastal region during spring and summer, likely associated with intensified upwelling and subsequent transition to the relaxation season (Klenz et al., 2018). However, it consistently simulates lower O_2 concentrations than those found in the climatologies, particularly along the continental margin, resulting in a more extensive 60 µmol L^{-1} isoline throughout the seasonal cycle (panels a–e). This discrepancy may be a result of a shallower mixed-layer depth or enhanced biological oxygen demand in the simulation.

It is also important to note the uncertainties inherent in the climatological datasets, which arise from the interpolation of sparse and unevenly distributed observations in space and time. In the ETNA, although the region contains a relatively high number of high-quality O_2 Argo float profiles compared to other regions (Stoer et al., 2023), the absolute number of profiles

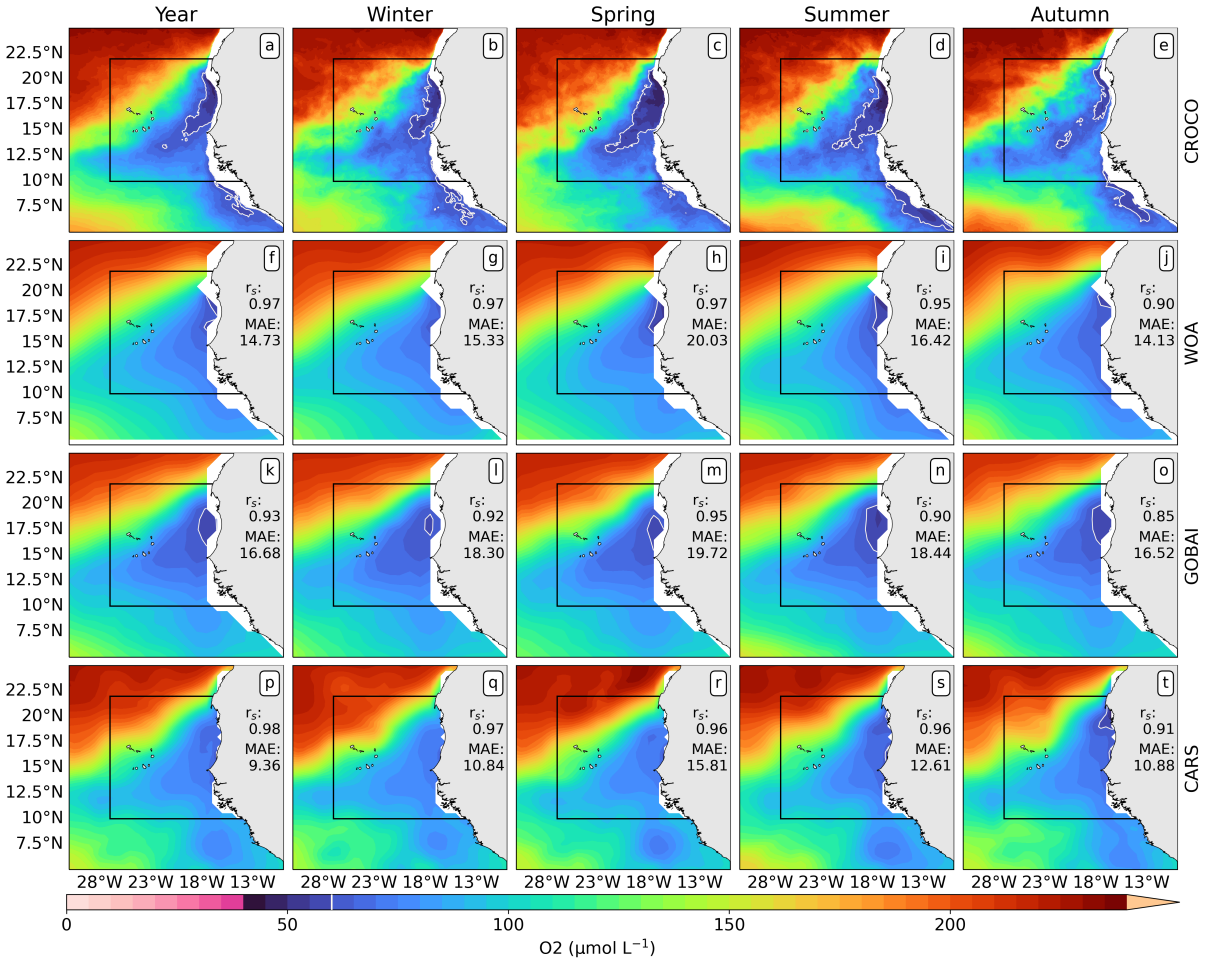


Figure 2.3: Comparison of yearly and seasonal mean oxygen concentrations at 100 m depth between model outputs and observations. r_s and MAE are computed within the study area, outlined by black solid lines. The white contour represents the 60 µmol L^{-1} mean O_2 concentration.

remains limited and insufficient to fully resolve the seasonal variability of oxygen, especially near the continental margin (Chen et al., 2021). Ship-based observations are more spatially concentrated along the Mauritanian and Senegalese coasts and likely compensate for this gap, but these are mainly conducted during the upwelling season (Schütte, Brandt, & Karstensen, 2016). As a result, climatological fields are likely to be more accurate during the upwelling season than during the relaxation season. These observational limitations must be considered when evaluating model-data mismatches in oxygen distributions across the region.

To evaluate the model's performance in simulating surface circulation, Figure 2.4 presents a comparison between model-derived velocities and climatological currents from GDP drifters (Laurindo et al., 2017). Overall, the model captures the large-scale structure of the regional circulation reasonably well, including the eastward-flowing NECC south of the study domain–an important pathway for oxygen transport into the ETNA (Brandt et al., 2010; Brandt et al., 2015). Within the study region, it also reproduces the expected seasonal dynamics associated with coastal upwelling, namely the offshore Ekman transport during winter and spring (Figure 2.4b,c) and the development of the northward MC during summer and autumn (Figure 2.4d,e).

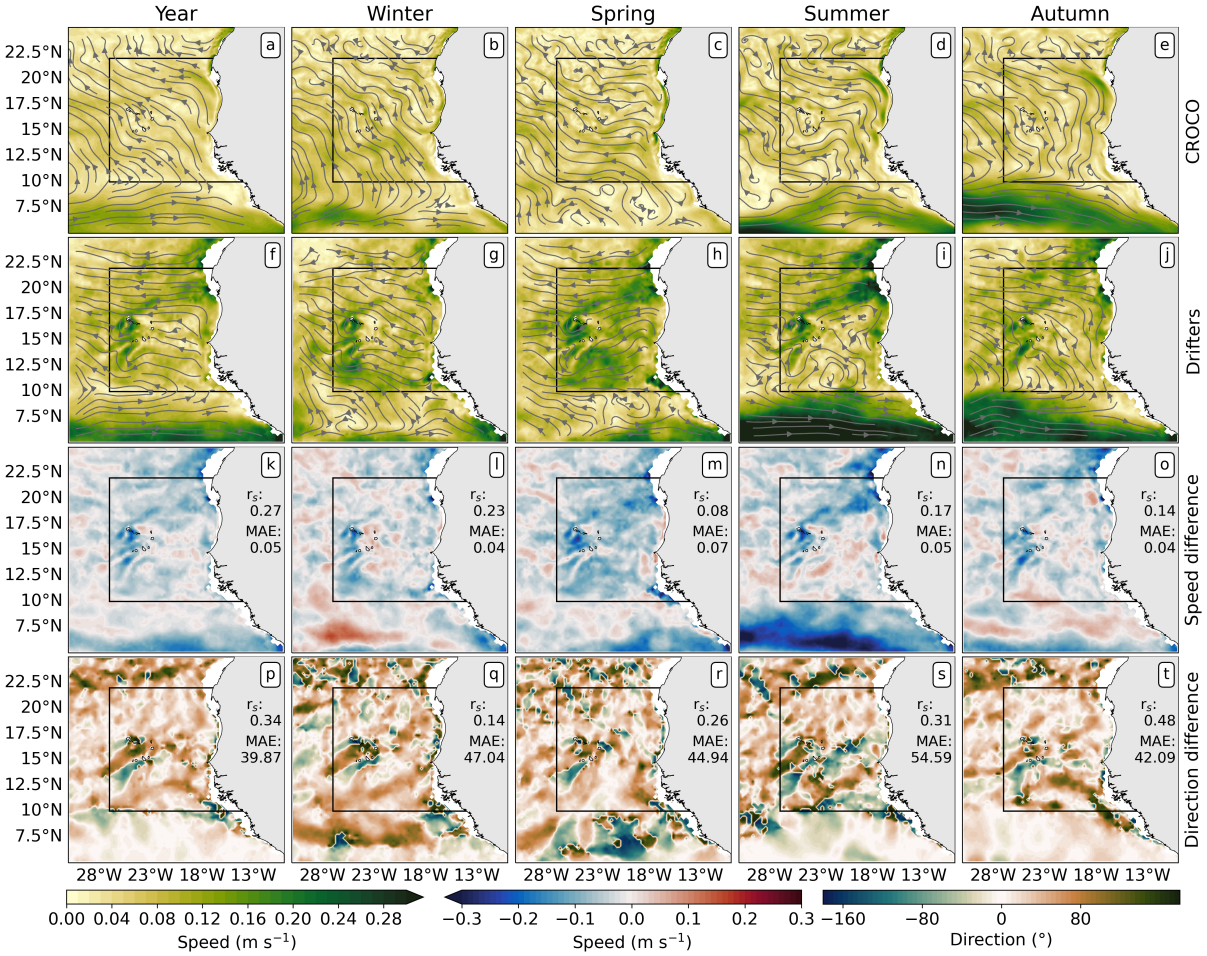


Figure 2.4: Comparison of surface current speed and direction between model outputs and GDP drifters. Differences between model and drifters are shown in (k-o) and (p-t), along with the respective r_s and MAE – computed within the study area, delimited by black square.

Despite this general agreement, several discrepancies are evident. The model systematically underestimates current speeds–most notably near the CVFZ during spring and summer (Figure 2.4m,n)–and exhibits directional biases, with MAE values exceeding 40° across all seasons (Figure 2.4q–t). These discrepancies are accompanied by low r_s for both speed and direction. However, the largest mismatches are concentrated in the wake of the Cabo Verde Islands. This discrepancy is likely due to the use of low-resolution, climatological wind forcing, which cannot resolve the alternating bands of wind-stress curl generated by flow-topography interaction over the high-altitude islands (Chavanne et al., 2002; Cardoso et al., 2020). While the agreement in current speed and direction improves along the African coast, the modeled MC appears weaker and more zonally extensive than observed, particularly during summer. Nonetheless, the model successfully reproduces the spatial structure and seasonal evolution of the main circulation features in the region, especially along the Mauritania and Senegal coasts.

To assess the model's accuracy in representing both the mean and eddy components of the surface circulation, we computed the Mean Kinetic Energy (MKE) and Eddy Kinetic Energy (EKE) using model and altimetry-derived geostrophic surface velocities (CMEMS, 2017). Geostrophic

velocities were first calculated from the SSH as follows:

$$u_g = -\frac{g}{f}\frac{\partial \eta}{\partial y}, \tag{2.12}$$

$$v_g = \frac{g}{f}\frac{\partial \eta}{\partial x}, \tag{2.13}$$

where u_g and v_g are the zonal and meridional geostrophic velocity components, respectively, η is the SSH, g is the gravitational acceleration, and f is the Coriolis parameter. Subsequently, MKE and EKE were computed as:

$$\text{MKE} = \frac{1}{2}\left(\overline{u_g}^2 + \overline{v_g}^2\right), \tag{2.14}$$

$$\text{EKE} = \frac{1}{2}\left(u_g'^2 + v_g'^2\right), \tag{2.15}$$

where the overbar denotes the temporal mean and the primes indicate deviations from that mean, i.e., $u_g' = u_g - \overline{u_g}$ and $v_g' = v_g - \overline{v_g}$. Depending on the analysis, the temporal mean may refer to the total or seasonal average.

In comparison with altimetry-derived MKE, the model shows good spatial agreement, particularly in the coastal region during summer when the poleward MC is most intense. However, correlation coefficients are relatively low across all seasons, with values not exceeding 0.35 in autumn (Figure 2.5). Consistent to the comparison with drifter-derived current velocities (Figure 2.4), the model systematically underestimates MKE in the lee of the Cabo Verde Islands, where bands of elevated kinetic energy are observed in the altimetry product but absent in the model. In contrast, higher modeled MKE values over the continental shelf during winter and spring likely reflect the model's higher spatial resolution and the known limitations of altimetric observations near the coast (Figure 2.5b,c; Amores et al., 2018).

Compared to altimetry-derived EKE, the model tends to overestimate EKE, particularly in the vicinity of the CVFZ (Figure 2.6). This overestimation is likely attributable to the model's higher spatial resolution, which allows the simulation of submesoscale processes that are not captured by satellite altimetry. Altimetric geostrophic velocities are derived from nadir altimeter tracks with a native resolution of 1 Hz (approximately 5–8 km along-track), but with cross-track distances ranging from 76 to 230 km depending on the satellite constellation and latitude (Carret et al., 2023). Although the gridded altimetry product provides a nominal horizontal resolution of 0.125° (roughly 13 km at these latitudes) through interpolation, it remains primarily sensitive to mesoscale variability and underrepresents smaller-scale and high-frequency motions (Y. Wang et al., 2022). Another aspect to consider is the relatively short duration of the simulation, which may influence EKE estimates by limiting the robustness of temporal anomaly calculations, potentially amplifying discrepancies.

The absence of elevated model EKE in the wake of the Cabo Verde Islands–particularly evident during winter and spring (Figure 2.6l,m)–further highlights the importance of realistic wind forcing for accurately representing eddy generation in this region (Cardoso et al., 2020). This signal is likely suppressed in the model due to the use of low-resolution climatological wind

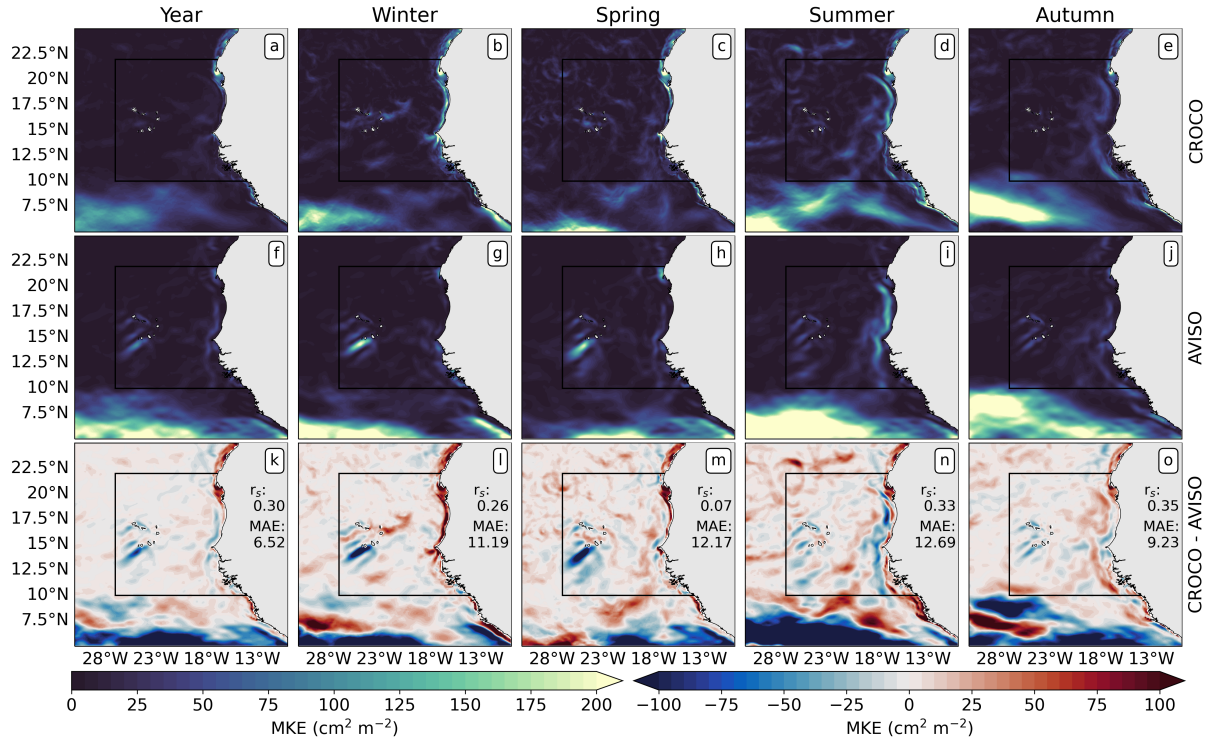


Figure 2.5: Comparison of surface MKE between model outputs and altimetry observations. Differences between the model and altimetry are shown in the bottom panels (k-o), along with the respective r_s and MAE – computed within the study area, delimited by black square.

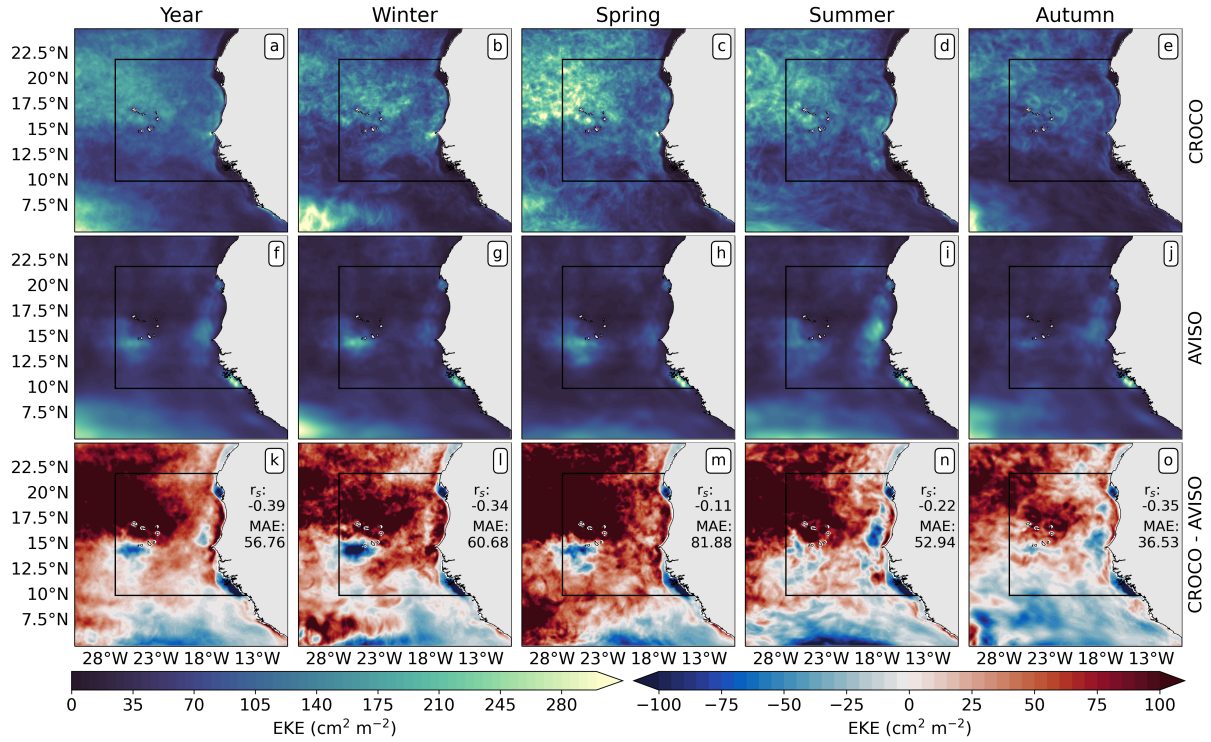


Figure 2.6: Comparison of surface EKE between model outputs and altimetry observations. Differences between the model and altimetry are shown in the bottom panels (k-o), along with the respective r_s and MAE – computed within the study area, delimited by black square.

fields, which lack the synoptic variability and orographic effects necessary to generate wind-stress curl and the associated mesoscale activity. Nonetheless, we consider this limitation to have a

relatively minor impact on the simulation of mesoscale dynamics relevant to the sOMZ, which are predominantly driven by coastal processes (Karstensen et al., 2015; Schütte, Karstensen, et al., 2016). In this context, the model reasonably captures the seasonal enhancement of EKE associated with the intensification of the MC during summer (Figure 2.6d,i). However, a localized increase in modeled EKE near the Cap-Vert headland during winter and spring is not reproduced in the altimetry-derived product. This discrepancy likely reflects the submesoscale nature of wind-generated, surface-intensified eddies in that region (Alpers et al., 2013), which remained below the effective spatial resolution of satellite altimetry products available up to 2023, despite the recent advances enabled by the SWOT mission (Du & Jing, 2024; Z. Zhang et al., 2024; Archer et al., 2025).

To evaluate the model's ability to simulate the seasonal variability of coastal upwelling, Figure 2.7 shows a comparison between model and satellite-derived SST from OSTIA (Good et al., 2020). The correlation coefficients exceed 0.9 across all seasons and for the annual mean, with a MAE not exceeding 1.3°C. The model successfully captures the seasonal variation between the coastal upwelling season (winter and spring) and the relaxation season (summer and autumn). However, satellite observations indicate a steeper SST gradient from the coast to offshore during the upwelling season, with coastal SST values approximately 1–2°C lower than those simulated by the model. Again, this discrepancy is likely due to the use of climatological wind forcing in the model, which lacks the synoptic variability required to reproduce strong wind-driven upwelling events (Capet et al., 2017). Additionally, the model tends to produce slightly cooler SST in the offshore region, in part because surface heat fluxes are prescribed from the COADS climatology for the year 2003. These fluxes do not reflect the long-term warming trend associated with climate change (Gruber, 2011), which are likely contributing to the offset between observed and simulated SST.

Considering the strong coupling between primary productivity and oxygen consumption through the remineralization of sinking organic matter at depth (Redfield, 1942; Karstensen et al., 2008), accurately simulating surface productivity is essential for a realistic representation of the sOMZ. As such, Figure 2.8 compares modeled surface Chl*a* concentrations with satellite-derived observations. Because satellite sensors capture signals from only the uppermost layer of the ocean–often referred to as the "first optical depth" (H. R. Gordon & McCluney, 1975)–whose thickness varies depending on phytoplankton biomass and water clarity (Morel, 1988), we averaged modeled Chl*a* over the upper 30 m to improve comparability.

The model generally underestimates Chl*a* concentrations within the study region, particularly along the northwestern African coast, suggesting weaker simulated surface productivity relative to satellite observations. Nevertheless, the seasonal variability associated with coastal upwelling is well captured, with peak concentrations and spatial extent occurring in spring, while lowest concentrations and extent occur in autumn (Figure 2.8c,h and e,j, respectively). This agreement is supported by the seasonal and annual correlation coefficients, which remain above 0.74 in all seasons–lowest in spring–and by the low MAE, which does not exceed 0.79 mg m^{-3}. The model also reflects the influence of the MC in suppressing coastal productivity during summer, although the offshore extent of the Cap-Blanc filament appears more confined in the simulation than in the satellite-derived product (Figure 2.8d,i).

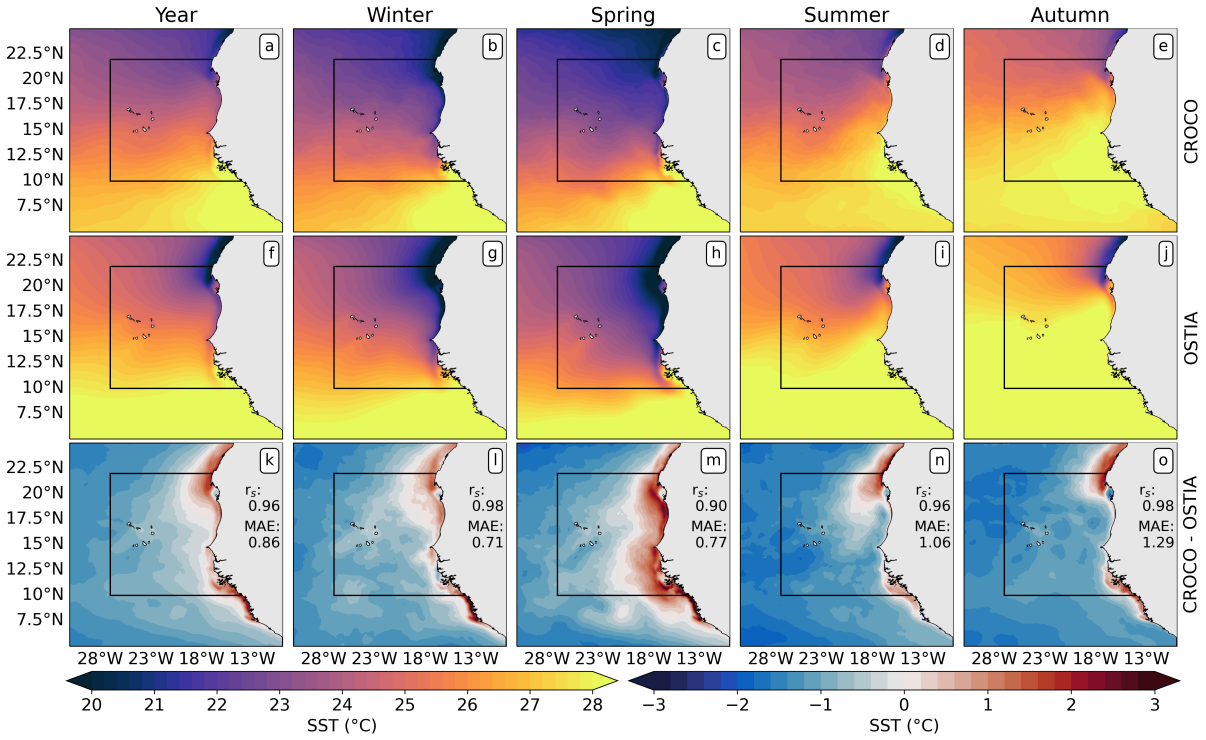


Figure 2.7: Comparison of Sea Surface Temperature (SST) between model outputs and satellite observations. Differences between the model and satellite observations are shown in the bottom panels (k-o), along with the respective r_s and MAE – computed within the study area, delimited by black square.

It is important to note that nutrient supply in the ETNA is not solely regulated by coastal upwelling, but also influenced by Saharan dust deposition (Kaufman et al., 2005; Pradhan et al., 2006; Messié & Chavez, 2015; Ohde et al., 2015; G. Fischer et al., 2019). By analyzing 57 desert storms between 2000 and 2008, Ohde and Siegel (2010) showed that atmospheric dust events can episodically enhance surface Chl*a* concentrations independently of upwelling. In particular, six strong dust storms were associated with Chl*a* increases of up to 2.4 mg m^{-3}. Although dust-driven events explained a smaller fraction of the Chl*a* variability than coastal upwelling (5% and 24%, respectively), their contribution for primary productivity can still be important, especially in offshore oligotrophic regions. Thus, the lower Chl*a* concentrations observed in model outputs are likely partly linked to the use of climatological dust fields (Tegen & Fung, 1995), which are unable to capture the episodic and intense nature of Saharan dust deposition (Chiapello et al., 2005).

It is also important to note that elevated satellite-derived Chl*a* values may be affected by non-biological optical interference, including aerosols, atmospheric dust, and re-suspended sediments. These factors introduce uncertainties in ocean color retrievals and can lead to overestimations of Chl*a* (Helmke et al., 2005; Tilstone et al., 2011). Despite these observational and modeling limitations, we assume that the simulation captures the seasonal variability and large-scale spatial distribution of surface Chl*a* with reasonable accuracy.

In summary, model evaluations shows that the model reproduces the main seasonal and spatial patterns of physical and biogeochemical variables in the ETNA with reasonable accuracy, particularly those most relevant to the dynamics of the sOMZ. It successfully captures the dominant features of coastal upwelling, surface circulation, and tracer distributions, with generally

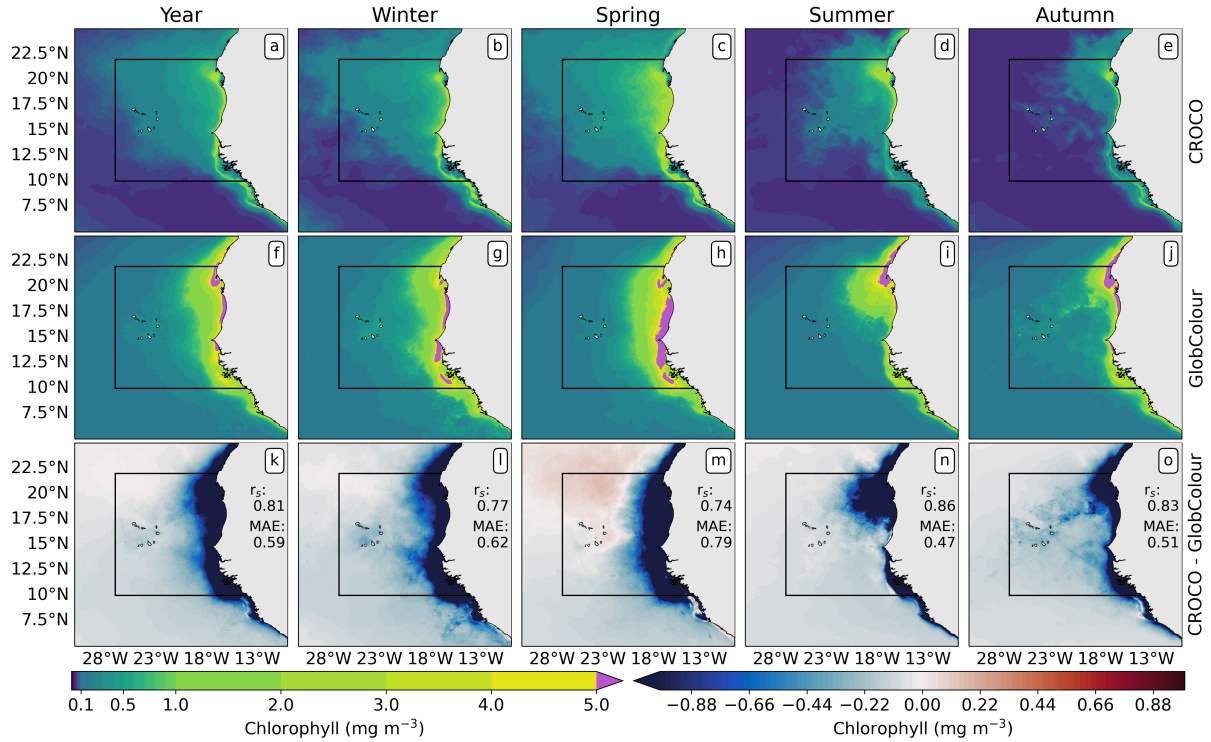


Figure 2.8: Comparison of Chl*a* concentrations between model outputs and satellite observations. Model outputs are averaged over the top 30 m. Differences between the model and satellite observations are shown in the bottom panels (k-o), along with the respective r_s and MAE – computed within the study area, delimited by black square.

high correlations and low errors across multiple climatological references. Some biases persist–especially near the Cabo Verde Archipelago and along the continental margin–likely due to the use of climatological forcing and the limited representation of synoptic variability. These limitations, along with their potential implications for the interpretation of our results, are discussed in greater detail in Chapter 6.

2.3.2 Bottom layer

Given the potential role of near-bottom hypoxic O_2 concentrations in contributing to the formation of the sOMZ in the ETNA (Brandt et al., 2015), we conducted a targeted validation of the model's bottom water output. This validation focuses on comparing modeled concentrations of O_2, NH_4, and NO_3, as well as O_2 sediment fluxes, against available *in-situ* observations collected at seven stations along the Mauritanian shelf and slope in two separate campaigns (Figure 2.9). Observational NO_3 and NH_4 concentrations were obtained from publicly accessible datasets, while O2 concentrations and O_2 sediment fluxes were retrieved from the studies of Dale et al. (2014a) and Dale et al. (2022) for the campaigns MSM17/4 (March) and M107 (June), respectively.

Model outputs used for this comparison are limited to the final two simulation years, during which monthly-averaged diagnostic variables required for the calculation of O_2 sediment fluxes were stored (further discussed in Section 2.4.6). Furthermore, while observational O_2 concentrations are available as a single time-instant measurements, NO_3 and NH_4 observations are

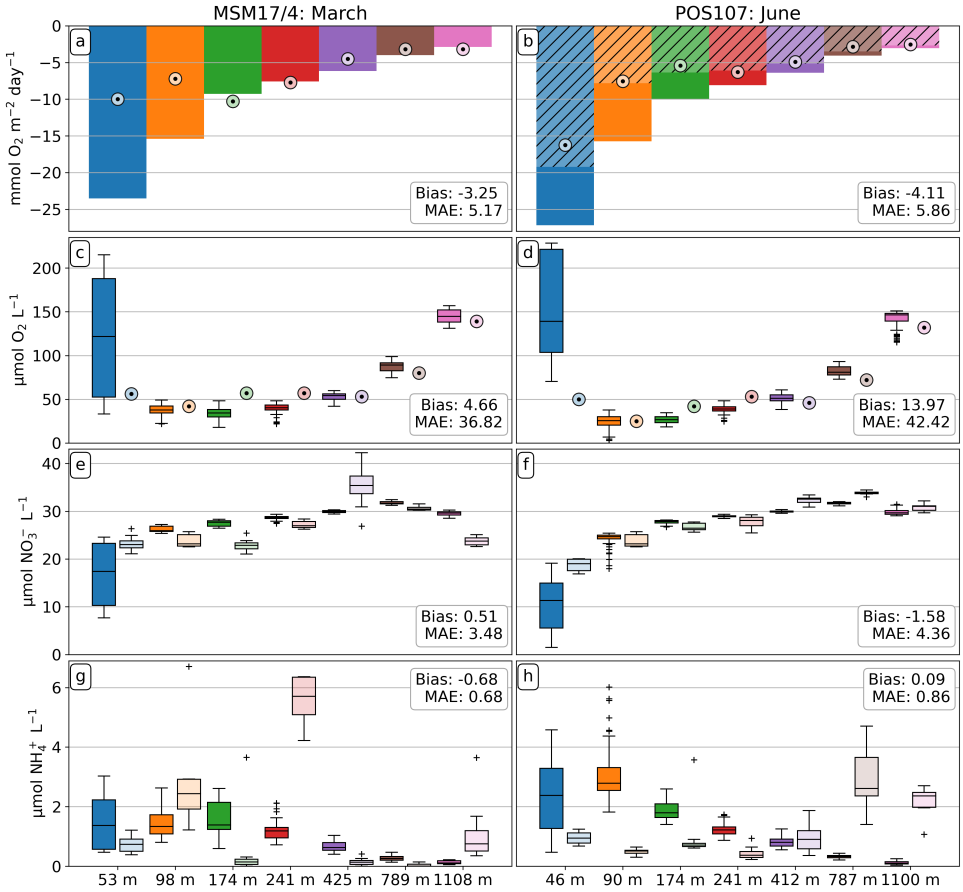


Figure 2.9: Comparison between bottom model output and *in-situ* observations at seven stations along the continental shelf and slope off Mauritania. *In-situ* measurements were acquired during the MSM17/4 (March, left panels) and POS107 (June, right panels) oceanographic campaigns at ≈18°N. Model data are limited to the final two simulation years, corresponding to the period for which diagnostic variables for the oxygen budget are available. Panels (a-b) show monthly mean O_2 sediment fluxes from the model (colored bars) and observed values (lighter-colored circles), with hatched bars in (b) indicating model means for July as reference. Panels (c-d), (e-f), and (g-h) present comparisons for bottom water O_2, NO_3, and NH_4 concentrations, respectively. For O_2 (c-d), boxplots represent daily model values, while observed values–available only as single time-instant measurements (Dale et al., 2014a, 2022)–are plotted as circles. For NO_3 and NH_4 (e–h), both model and observational data are shown as boxplots, with observed values representing a approximately 36-hour time series. Darker and lighter elements correspond to model and observations, respectively. Text boxes in each panel report the overall bias and MAE between model and observations, aggregated across all stations.

composed of timeseries extending up to 36 hours. Given these constraints, this validation aims to assess how well the model's climatological state for March and June aligns with conditions observed during the respective field campaigns, acknowledging the intrinsic limitations and shortcomings of the available datasets.

Modeled O_2 sediment fluxes at the two shallowest stations are overestimated relative to observations, whereas values at depths greater than 174 m show much better agreement (Figure 2.9a-b). The overall bias and MAE across all stations do not exceed -4.11 and 5.86 mmol m^{-2} day^{-1}, respectively, indicating that the model's errors are within a reasonable margin. Interestingly, the monthly-averaged model values for July show closer agreement with observations than those from June (Figure 2.9b), suggesting a potential time lag in the model's representation of benthic oxygen dynamics. However, this interpretation should be made with caution due to fundamental differences in the methods used to derive these fluxes. Whereas model estimates represent monthly averages, the observational fluxes are derived from short-term deployments

and reflect instantaneous conditions. Specifically, observational O_2 fluxes are calculated based on the decline of O_2 concentrations within benthic chambers sealed from ambient water at the time of deployment (Sommer et al., 2008). As a result, the measured fluxes reflect the properties of the water mass enclosed within the chamber at the time of deployment and may not capture the broader temporal variability expected over the course of a month.

Despite slight mismatches in O_2 sediment fluxes, modeled bottom O_2 concentrations agree more closely with observations, with a bias and MAE not exceeding 13.97 and 42.42 µmol L^{-1}, respectively (Figure 2.9c-d). The poorest agreement is observed at the shallowest station (≈50 m) in both months, which also exhibits the highest variability in the model, suggesting strong environmental fluctuations on the shelf. This variability likely contributes to the mismatch between model and observations, especially if we consider the brief observational window available for comparison. Observed bottom O_2 concentrations also reveal seasonal variability. During the MSM17/4 cruise in March, minimum concentrations of 42 µmol L^{-1} were recorded at 98 m depth near the shelf break, while the POS107 campaign in June registered lower values of 25 µmol L^{-1} at the same location. This seasonal decline is well captured by the model, providing us confidence to its ability to reproduce seasonal O2 bottom dynamics.

For nitrate, modeled and observed concentrations exhibit similar depth-dependent patterns in both months, with bias and MAE not exceeding -1.58 and 4.36 µmol L^{-1}, respectively (Figure 2.9e-f). As with O_2, the shallowest station (≈50 m) displays the highest variability in the model, likely driven by episodic cross-shelf intrusions of nutrient-rich, oxygen-depleted upwelled waters (Yücel et al., 2015). In contrast, NH_4 shows greater discrepancies between model and observations (Figure2.9g-h), particularly in June. While variability is more pronounced for this species, the overall concentration range remains within reasonable bounds, with the largest bias and MAE reaching -0.68 and 0.86 µmol L^{-1}, respectively. The elevated observed NH_4 values in June are likely attributable to enhanced remineralization of organic matter at the sediment-water interface– a process that is inherently variable, difficult to constrain with short-term measurements (Jahnke, 1996), and not explicitly resolved in the PISCES-v1 model formulation (Aumont & Bopp, 2006).

Overall, the comparison between modeled and observed bottom biogeochemical conditions shows reasonable agreement. Despite the simplicity of the sediment flux parameterization employed in the model (Middelburg et al., 1996), the dynamics of oxygen, nitrogen species, and benthic fluxes are captured with sufficient accuracy to support confidence in the model's representation of bottom water processes.

2.4 Methods

To avoid repetition in the presentation of methods used throughout this thesis, the following sections describe the core methods that are applied across multiple chapters. For clarity, the chapters in which each method is used are indicated as superscripts in the corresponding section headings. Chapter-specific methods that are not shared across multiple analyses are presented separately within the respective chapters where they are applied.

2.4.1 Oxygen thresholds definition[3,4,5]

A key aspect to consider throughout this thesis is the definition of thresholds used to characterize low-oxygen environments. As introduced in Chapter 1, the most commonly applied threshold in the study of OMZs is that which defines hypoxia. While the upper limit of hypoxic conditions is often set at 60 µmol L^{-1} (e.g., Gruber et al., 2021; Köhn et al., 2022), this value can vary depending on regional differences in the tolerance of marine organisms to low-oxygen conditions. To facilitate direct comparison with previous studies conducted in the ETNA (e.g., Brandt et al., 2015; Karstensen et al., 2015; Schütte, Karstensen, et al., 2016; Klenz et al., 2018), hypoxia in this thesis is defined as O_2 concentrations below 40 µmol L^{-1}. Additional thresholds are applied at 6 µmol L^{-1} and 1 µmol L^{-1} to identify suboxic and anoxic conditions, respectively. The suboxic threshold is particularly relevant for the PISCES biogeochemical model, as it represents the critical point where microbial respiration shifts from aerobic to anaerobic pathways (Aumont et al., 2003; Aumont & Bopp, 2006). Below this threshold, NO_3 rather than O_2 is used in the remineralization of organic matter–a process known as denitrification (e.g., Karstensen et al., 2015; Grundle et al., 2017).

2.4.2 Season definition[3,4,5]

Given the strong seasonal variability in the study region (Lázaro et al., 2005; Chavez & Messié, 2009), accurately defining upwelling and relaxation seasons is essential for model evaluation and interpreting seasonal dynamics. While Klenz et al. (2018) defined the upwelling season as December to April and relaxation as May to July, this leaves August to November unclassified–despite its importance for boundary current activity and associated O_2 variability. Alternatively, Lathuilière et al. (2008) studied seasonal dynamics of primary productivity in the region and extended the upwelling season from October to May. This lack of consensus for season delimitation is a consequence of the meridional variations observed along the coast, where the upwelling season ends earlier at southern latitudes, while northern latitudes experience shorter relaxation periods. For the purposes of this thesis, we adopt a four-season division: winter (December, January and February) and spring (March, April and May) represent the upwelling season, while summer (June, July and August) and autumn (September, October and November) represent the relaxation period.

2.4.3 Water mass analysis[3,4,5]

To estimate the proportion of SACW relative to NACW (%SACW), we employed a simplified isopycnal formulation of the Optimum MultiParameter Analyses (OMPA; Mackas et al., 1987; Tomczak & Large, 1989; Poole & Tomczak, 1999), following the approach of Peña-Izquierdo et al. (2015). This method assumes that water masses mix linearly in θ-S space and aims to solve for the fractional contributions of two predefined end-members: SACW and NACW. Unlike the extended OMPA which incorporates multiple chemical and physical tracers and requires the usage of tracer-specific weighting factors and Redfield ratios (i.e., Karstensen & Tomczak,

1998), this simplified implementation relies solely on conservative hydrographic properties–potential temperature and salinity–which are interpolated onto isopycnal surfaces. To ensure equal weighting, the two variables were normalized to have zero mean and unit variance across the entire domain:

$$\theta_{\text{norm}} = \frac{\theta - \bar{\theta}}{\text{SD}_\theta}, \quad S_{\text{norm}} = \frac{S - \bar{S}}{\text{SD}_S}, \tag{2.16}$$

where $\bar{\theta}$ and $\bar{S}$ denote the mean potential temperature and salinity, and SD_θ and SD_S represent their respective standard deviations. These normalized variables were then used to solve a system of linear equations that determine the contribution of each end-member, constrained by mass conservation. The least squares solution was obtained via a non-negative least squares approach, with mass conservation enforced by assigning a weight of $w_{\text{mass}} = 10$ to the mass constraint, and equal weights ($w_\theta = w_S = 1$) to the tracer equations, following the recommendations of Glover et al. (2011). This weighting scheme prioritizes the enforcement of mass conservation while ensuring balanced contributions from θ and salinity in the optimization procedure.

End-member characteristics for SACW and NACW were derived from θ and salinity profiles interpolated onto isopycnal surfaces, using an interval of $\Delta\sigma_\theta = 0.02$ kg m^{-3}. These profiles were selected from two distinct regions known to represent the core properties of each water mass (Peña-Izquierdo et al., 2015): SACW profiles were extracted from the South Atlantic (18.83–13.22°S, 45°W–15°E), and NACW profiles from the North Atlantic (26.01–31.62°N, 60–15°W). For reference, we also computed the characteristic θ-S profile of the diluted SACWcv variety, based on profiles within the ETNA (10–22°N, 27–15°W). For each water mass, end-member properties were defined as the mean of the 10% lowest (SACW and SACWcv) or highest (NACW) θ-S values, following the methodology of Johns et al. (2003). All profiles were sampled at a spatial interval of approximately 0.07° and a temporal interval of 2 days to ensure adequate resolution and coverage.

This analysis was restricted to the central water layer. While there is no universal agreement on the exact bounds of central waters (e.g., Kirchner et al., 2009; Peña-Izquierdo et al., 2015; Liu & Tanhua, 2021), we adopt σ_θ values of 25.8 and 27.1 kg m^{-3} as the upper and lower limits, respectively, in accordance with previous studies conducted in the ETNA (Johns et al., 2003; Stramma et al., 2005; Stramma, Brandt, et al., 2008; T. Fischer et al., 2013; Hahn et al., 2017; Klenz et al., 2018; Dilmahamod et al., 2022).

To illustrate the characteristic spatial variability of the modeled water masses, Figure 2.10 presents a representative selection of θ-S profiles from spatially distributed sampling boxes. These profiles are overlaid with the corresponding characteristic end-member curves for SACW, SACWcv, and NACW. The figure also includes the average distribution of %SACW computed within the upper central water stratum, which is separated from the lower central waters at σ_θ 26.8 kg m^{-3} (Stramma et al., 2005; Klenz et al., 2018).

2.4.4 Eddy detection and tracking[3,4,5]

Given the importance of mesoscale eddies in shaping the dynamics of the sOMZ in the ETNA (e.g., Karstensen et al., 2015; Schütte, Karstensen, et al., 2016; Karstensen et al., 2017), their

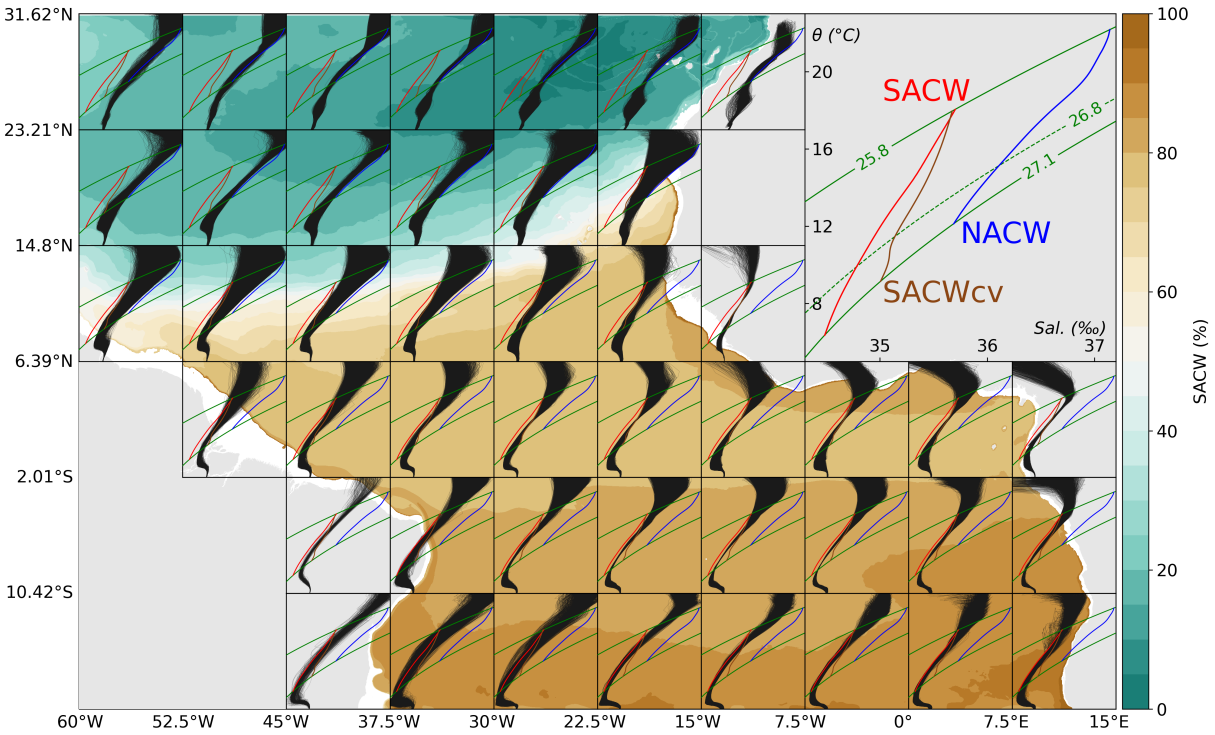


Figure 2.10: Proportion of SACW relative to NACW within the upper central water layer over Tropical Atlantic Ocean. θ-S diagrams for profiles sampled within spatially delimited boxes regularly spaced across the model domain (zonal and meridional intervals of 7.50° and 8.41°, respectively) are shown. Within each box, profiles were selected at a time interval of 30 days and a zonal and meridional spatial resolution of 1° and 0.5°, respectively. Solid green lines denote the upper and lower boundaries of the central water layer (σ_θ = 25.8 and 27.1 kg m^{-3}), while the dashed green line marks the division between upper and lower central waters at σ_θ = 26.8 kg m^{-3}. Red, brown, and blue lines represent the characteristic end-member profiles for SACW, SACWcv, and NACW, respectively.

identification and tracking in the model outputs is a key component of this study. For this purpose, we applied the Angular Momentum Eddy Detection and tracking Algorithm (AMEDA; Le Vu et al., 2018), a robust and widely used tool that has been employed in both observational (Ioannou et al., 2017; Garreau et al., 2018; Moschos et al., 2021; Stegner et al., 2021; Barboni et al., 2023) and numerical studies (Akpınar et al., 2020; de Marez et al., 2020; Ioannou, Stegner, Dubos, et al., 2020; Ioannou, Stegner, Dumas, & Le Vu, 2020), including in the ETNA (Cardoso et al., 2020; Devresse et al., 2022; Dilmahamod et al., 2022; Katzenmeier et al., 2024).

AMEDA combines both dynamical and geometrical criteria to identify eddy cores and contours. Eddy centers are first located using the Local Normalized Angular Momentum (LNAM), a dimensionless parameter computed from the horizontal velocity field that quantifies the local rotational tendency of the flow (Mkhinini et al., 2014). LNAM reaches extreme values of $+1$ or -1 at the centers of cyclonic and anticyclonic eddies, respectively. To eliminate spurious detections, LNAM maxima are filtered by the local Okubo-Weiß parameter, which is calculated over the same local domain. The Okubo-Weiß parameter is defined as:

$$\mathrm{OW} = s_n^2 + s_s^2 - \zeta^2, \tag{2.17}$$

where $s_n = \partial u/\partial x - \partial v/\partial y$ is the normal strain, $s_s = \partial v/\partial x + \partial u/\partial y$ is the shear strain, and $\zeta = \partial v/\partial x - \partial u/\partial y$ is the relative vorticity. Eddy centers are only retained if the local Okubo-Weiß value is negative, indicating a vorticity-dominated flow regime (Okubo, 1970).

To ensure that identified centers correspond to coherent, materially bounded eddies, a geometrical criterion is applied: the eddy core must be enclosed by at least one closed streamline. The outermost closed streamline at which the azimuthal velocity reaches a maximum defines the eddy's characteristic radius. From this contour, AMEDA computes various dynamical properties, including eddy radius, maximum and mean azimuthal velocity, Rossby number, and EKE. The tracking of eddies over space and time is performed using a nearest-neighbor algorithm, associating eddies of the same polarity across time steps within a search radius based on the maximum observed propagation speed in the region (in our case defined at 6.5 km d^{-1}; Schütte, Brandt, & Karstensen, 2016; Cardoso et al., 2020).

Although AMEDA was originally designed for use with satellite altimetry data (Ioannou et al., 2017; Garreau et al., 2018; Cardoso et al., 2020), it has been shown to perform reliably across a range of data types and resolutions (Le Vu et al., 2018; Dilmahamod et al., 2022). Its minimal number of tunable parameters and the ability to capture both the geometry and full dynamical evolution of eddies–including splitting and merging events–make it particularly suited for application to regional model outputs, such as those used in this thesis (Cardoso et al., 2020).

Given the subsurface-intensified nature of ACMEs and their known influence on the sOMZ (Karstensen et al., 2015; Fiedler et al., 2016; Schütte, Karstensen, et al., 2016; Karstensen et al., 2017), eddy detection was performed using modeled horizontal velocities at 100 m depth, corresponding approximately to the typical core depth of ACMEs (Schütte, Brandt, & Karstensen, 2016). Only eddies with lifetimes greater than 10 days and radii larger than 5 km are retained. To evaluate the sensitivity of the detection depth, a complementary analysis was conducted at 30 m depth. While cyclonic eddy patterns remained largely consistent, the number of anticyclonic eddies increased and the number of ACMEs decreased–highlighting the importance of choosing a depth that aligns with the scientific focus of the study.

2.4.4.1 Identification of Anticyclonic Mode-water eddies

Because AMEDA can only distinguish between cyclonic- and anticyclonic-rotating eddies, a more specific classification was required to identify ACMEs, given their distinct vertical structure and biogeochemical impact on the sOMZ. For this purpose, we implemented a multi-criteria approach inspired by Frenger et al. (2018) and Dilmahamod et al. (2022), integrating dynamical, thermohaline, and geometric properties to distinguish ACMEs from surface-intensified anticyclones.

Step 1: Potential Vorticity threshold

We began by computing Ertel PV, a dynamical metric sensitive to the combined effects of stratification and vorticity. PV was calculated as:

$$PV = (\zeta + f\mathbf{z}) \cdot \nabla b, \tag{2.18}$$

where **z** the vertical unit vector and $b = -g\rho/\rho_0$ is buoyancy, with $\rho_0 = 1025$ kg m^{-3}. In line with previous studies (Contreras et al., 2019; Dilmahamod et al., 2022), anticyclonic eddies with PV values below 5×10^{-10} s^{-3} were flagged as candidate ACMEs. However, we found that this dynamical criterion alone was not sufficient. Some eddies with vertical structures typical of ACMEs (e.g., subsurface vorticity minima or upward doming of the upper isopycnals) did not meet the PV threshold. Conversely, anticyclonic eddies with a normal vertical structure were often detected above the continental shelf, where PV lower than the threshold is often found at the bottom boundary layer due to instabilities provoked by the interaction of boundary currents with bottom topography (e.g., Molemaker et al., 2015; Gula et al., 2016). This highlighted the need for additional constraints.

Step 2: Thermohaline signature
To further discriminate ACMEs, we evaluated their thermohaline properties by examining the %SACW, following the water mass analysis described in Section 2.4.3. Given that ACMEs typically form along the African continental slope where SACW is most prevalent (Schütte, Brandt, & Karstensen, 2016; Dilmahamod et al., 2022), anticyclones with high SACW content were flagged as candidates for ACMEs. We note, however, that some ACMEs formed offshore near CVFZ exhibited higher proportions of NACW, likely originating from different mechanisms such as down-front wind forcing (Thomas, 2005).

Step 3: Thickness anomaly method
Finally, we applied a geometric criterion based on the vertical structure of ACMEs. Following Frenger et al. (2018), we identified eddies with positive anomalies in isopycnal layer thickness–indicative of the presence of a subsurface, lens-like structure with the upward and downward dooming of the isopyacnals. Rather than use fixed isopycnal bounds, we first analyzed the meridional distribution of eddy signatures using the standard deviation of negative OW values along a transect at 18.5°W (Figure 2.11). Based on the latitude-dependent distribution of OW variability, we defined three isopycnal layers for anomaly detection, all with a fixed lower bound at $\sigma_\theta = 26.8$ kg m^{-3} and upper bounds set at: $\sigma_\theta = 25.4$ kg m^{-3} for latitudes < 14.2°N; $\sigma_\theta = 25.8$ kg m^{-3} for 14.2–20.8°N; and $\sigma_\theta = 26.0$ kg m^{-3} for latitudes > 20.8°N.

2.4.5 Lagrangian particle simulation[4,5]

To investigate the origin and pathways of shallow water masses that eventually become hypoxic, we conducted offline Lagrangian simulations using TRACMASS v7.0 (Döös et al., 2013; Aldama-Campino et al., 2020). TRACMASS is a mass-conserving Lagrangian trajectory model originally developed for ocean circulation studies (Döös, 1995; Blanke & Raynaud, 1997) and later extended to atmospheric flows (Kjellsson & Döös, 2012). Its main distinguishing feature lies in its analytical integration scheme: rather than using iterative time-stepping methods such as Euler or Runge-Kutta schemes–which integrate particle positions incrementally with small time steps (Butcher, 2008)–TRACMASS integrates the trajectories of water parcels by solving a differential equation which depends on the velocity fields in each grid-cell face, so that it can calculate the volume

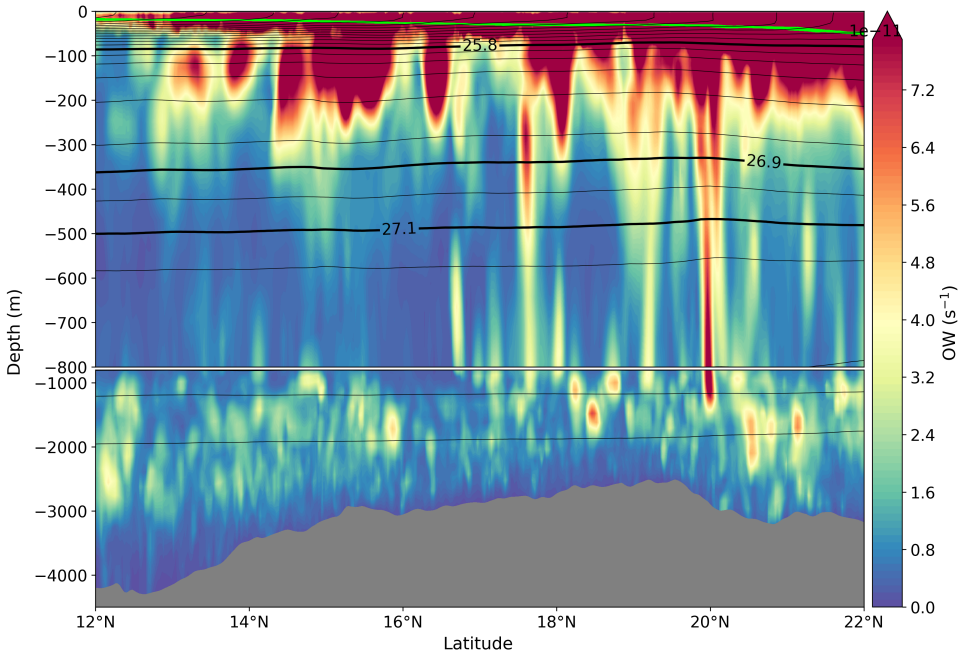


Figure 2.11: Standard deviation of negative Okubo–Weiß values along a meridional section at 18.5°W. Black contours show mean σ_θ at 0.2 kg m^{-3} intervals. The green contour denotes the mean mixed layer depth, defined as the depth where σ_θ differs from the surface value by 0.03 kg m^{-3}.

transport across the grid-cells. This cell-by-cell analytical solution avoids cumulative numerical errors and ensures volume conservation along particle paths, which is particularly important for analyzing tracer evolution and water mass transformations (e.g., Berglund et al., 2017, 2021).

Another key advantage of TRACMASS is its ability to operate on the native Arakawa C-grid and terrain-following σ-coordinates used by CROCO, allowing for impermeable boundary conditions and precise resolution of topographic features. This is especially important in our study, given the role of narrow boundary currents and continental shelf topography in shaping the oxygen distributions in the ETNA (Peña-Izquierdo et al., 2012; Klenz et al., 2018), as well as in the generation of ACMEs (Dilmahamod et al., 2022).

Particles were released every 5 days in hypoxic grid cells, within the depth range of 50–200 m and at a horizontal resolution of 0.125°, covering the region between 33°–15°W and 10°–22°N. Due to computational constraints, it was not feasible to release particles in all hypoxic cells. However, the chosen temporal and spatial resolution ensured a representative sampling of the hypoxic water masses that contribute to the formation of the sOMZ.

Each particle was then traced backward in time for as long as it remained within the model domain, sampling along its trajectory a suite of physical and biogeochemical properties, including temperature, salinity, O_2, NO_3, NH_4, and PV. Particle trajectories were computed under purely advective conditions–that is, without explicitly including horizontal or vertical diffusion during the integration. The only diffusivity present in the trajectories reflects the sub-grid motions already accounted for in the parent CROCO simulation.

To prevent particles from erroneously exiting the ocean through the surface or bottom boundaries–an issue that can arise when using daily-averaged velocity fields–we implemented a high-resolution time-stepping scheme with 120 intermediate substeps per day. Out of approx-

imately 2.4 million particles released, only about 80,000 (≈3.35%) exited the model domain, either through the northern or southern open boundaries, or by intersecting the surface or seafloor.

2.4.6 Oxygen budget[2,4]

To evaluate the leading sources and sinks of O_2 in the ETNA, we analyze the full oxygen budget from the CROCO-PISCES simulation following Resplandy et al. (2012). In the model, changes in O_2 concentrations result from physical transport, biological production and consumption, benthic fluxes and air-sea gas exchange:

$$\frac{\partial \mathrm{O}_2}{\partial t} = \underbrace{\left(\frac{\partial \mathrm{O}_2}{\partial t}\right)_{\mathrm{dyn}}}_{\text{dynamical transport}} + \underbrace{\left(\frac{\partial \mathrm{O}_2}{\partial t}\right)_{\mathrm{bio}}}_{\text{biological sources and sinks}} - \underbrace{\left(\frac{\partial \mathrm{O}_2}{\partial t}\right)_{\mathrm{sed}}}_{\text{sediment flux}} + J_{\mathrm{flux}} \tag{2.19}$$

The air-sea flux term J_{flux}, while prognostically calculated, is of minor importance below the mixed layer and thus not further discussed here. The physical contribution to O_2 changes is governed by horizontal and vertical advection and vertical mixing:

$$\left(\frac{\partial \mathrm{O}_2}{\partial t}\right)_{\mathrm{dyn}} = - \underbrace{u_h \cdot \nabla_h \mathrm{O}_2}_{\text{horizontal advection}} - \underbrace{w \frac{\partial \mathrm{O}_2}{\partial z}}_{\text{vertical advection}} + \underbrace{\frac{\partial}{\partial z}\left(K_z \frac{\partial \mathrm{O}_2}{\partial z}\right)}_{\text{vertical mixing}}, \tag{2.20}$$

where u_h and w are the horizontal and vertical velocities, respectively, and K_z is the vertical diffusivity. For the biological terms, O2 sources and sinks are linked to five processes:

$$\begin{aligned}\left(\frac{\partial O_2}{\partial t}\right)_{\mathrm{bio}} = & \underbrace{(R^1_{o:c} + R^2_{o:c})\left(\mu^P_{NO_3} P + \mu^D_{NO_3} D\right)}_{\text{new production}} + \underbrace{R^1_{o:c}\left(\mu^P_{NH_4} P + \mu^D_{NH_4} D\right)}_{\text{regenerated production}} \\ & - \underbrace{\lambda^*_{DOC} f(O_2) DOC}_{\text{remineralization}} - \underbrace{G^Z Z + G^M M}_{\text{respiration}} - \underbrace{R^2_{o:c}\mathrm{Nitrif.}}_{\text{nitrification}}\end{aligned} \tag{2.21}$$

Oxygen sources arise from both new production, driven by NO_3 uptake, and regenerated production, which occurs through NH_4 uptake by diatoms (D) and nanophytoplankton (P). Oxygen consumption, on the other hand, is associated with the breakdown of Dissolved Organic Carbon (DOC), respiration by small (Z) and large (M) zooplankton, and the nitrification processes (Nitrif), which represents the conversion of NH_4 into NO_3. The parameter λ^*_{DOC} denotes the remineralization rate of DOC. Because the remineralization of DOC is sensitive to O_2 concentrations and can proceed through oxic or anoxic pathways, the model uses the function $f(O_2)$ to modulate the proportion of remineralization that occurs aerobically. This function smoothly transitions between 1 and 0 as O_2 concentrations decrease, and is defined as:

$$f(O_2) = 1 - \min\left[1,\, 0.4 \frac{\max(0,\, 6 - O_2)}{1 + O_2}\right], \tag{2.22}$$

When $O_2 > 6$ µmol L^{-1}, $f(O_2) = 1$, and all remineralization occurs under oxic conditions. Below this threshold, an increasing fraction of remineralization is attributed to denitrification, whereby NO_3 is consumed instead of oxygen. The oxygen-to-carbon stoichiometric ratios are set to 140:122 for NH_4 assimilation into organic matter ($R^1_{o:c}$) and 32:122 for the nitrification process ($R^2_{o:c}$). The terms G^Z and G^M describe the grazing activity of small and mesozooplankton.

With the exception of benthic fluxes, all budget terms are available as prognostic outputs from CROCO-PISCES (Aumont et al., 2015). However, the benthic oxygen sink–representing oxygen consumption at the sediment-water interface due to the remineralization of POC reaching the seafloor (see Section 2.1.2)–is not available as a diagnostic output. This term was therefore inferred as the residual needed to close the local oxygen budget:

$$\left(\frac{\partial \mathrm{O}_2}{\partial t}\right)_{\mathrm{sed}} = \frac{\partial \mathrm{O}_2}{\partial t} - \left[\left(\frac{\partial \mathrm{O}_2}{\partial t}\right)_{\mathrm{dyn}} + \left(\frac{\partial \mathrm{O}_2}{\partial t}\right)_{\mathrm{bio}}\right], \tag{2.23}$$

and is non-zero only in the bottom model layer. It is important to note that because the model diagnostics were saved only as monthly means for the final two years of simulation, this analysis is constrained by its coarse temporal resolution, which prevents its usage for the investigation of transient or short-term hypoxic events.

Chapter 3

Characterization of the Shallow Oxygen Minimum Zone in the Eastern Tropical North Atlantic

3.1 Introduction

In recent decades, OMZs have experienced significant changes, including intensification, expansion, and shoaling (Bograd et al., 2008; Stramma, Johnson, et al., 2008; Helm et al., 2011; Stramma & Schmidtko, 2021, e.g.,). These changes are closely tied to climate change, particularly ocean warming, which reduces oxygen solubility and increases stratification (Keeling et al., 2010; Helm et al., 2011; Schmidtko et al., 2017; Bates & Johnson, 2020). While the feedback mechanisms governing these changes remain uncertain (Fu et al., 2018; Frölicher et al., 2020, e.g.,), the ecological and biogeochemical consequences are significant, with the potential to disrupt nutrient cycling (Grundle et al., 2017, e.g.,), compress marine habitats (Stramma et al., 2010; Gilly et al., 2013), and drive shifts in species distributions across ocean ecosystems (Vedor et al., 2021).

Understanding the impact of low-oxygen environments requires an analytical framework that accounts for the spatial and temporal variability of these conditions. For example, the compression of marine habitats due to the shoaling of low-oxygen environments can be studied from a Eulerian perspective, that is, in a fixed, grid-point-wise manner (e.g., Köhn et al., 2022; Wong et al., 2024). However, low-oxygen events are often dynamic, moving with currents and eddies across hundreds or even thousands of kilometers (e.g., Stramma et al., 2014; Frenger et al., 2018; Atkins et al., 2022). The impact of these conditions on marine organisms is mostly determined by the intensity and exposure timescales (Gruber et al., 2021). As such, a Eulerian framework is particularly effective for assessing the impacts on sessile organisms or fixed ecosystems (i.e., benthos), while a Lagrangian approach offers better insights into the impacts on free-drifting organisms, such as those trapped within eddies (Löscher et al., 2015; Hauss et al., 2016).

The ETNA hosts a highly heterogeneous OMZ at shallow depths, strongly influenced by the seasonal dynamics of the coastal upwelling system, mesoscale eddies and boundary current dynamics (Schütte, Karstensen, et al., 2016; Klenz et al., 2018; Machu et al., 2019; Thomsen et al., 2019; Tall et al., 2021). The hypoxic conditions that form the sOMZ have been mainly linked to westward-propagating eddies (Schütte, Karstensen, et al., 2016), which transport and

intensify low-oxygen waters in their interior through local remineralization and strong isolation from surrounding waters (Karstensen et al., 2015; Fiedler et al., 2016; Karstensen et al., 2017), with important implications for biogeochemical cycling (Löscher et al., 2015; Grundle et al., 2017) and ecosystem dynamics (Hauss et al., 2016). Nonetheless, most studies tracked and sampled only a few eddies more than once (e.g., Karstensen et al., 2015; Karstensen et al., 2017), leaving significant gaps in understanding the spatial and temporal evolution of hypoxic events, particularly outside of eddies. While these hypoxic conditions are likely to persist after eddies dissipate (Löscher et al., 2015), there is, to the best of our knowledge, no observational evidence describing how such events evolve.

While low-oxygen eddies are major contributors to offshore hypoxia, hypoxic conditions have also been recently observed along the continental shelf and slope off Mauritania and Senegal (e.g., Yücel et al., 2015; Machu et al., 2019; Dale et al., 2022). Some of these events have been linked to enhanced oxygen consumption and limited ventilation (Machu et al., 2019), while others were attributed to seasonal upwelling variability (Yücel et al., 2015; Tall et al., 2021) and stratification (Klenz et al., 2018; Dale et al., 2022). Given that low-oxygen eddies are frequently formed near the continental margin (Karstensen et al., 2015; Schütte, Karstensen, et al., 2016; Dilmahamod, 2023), it is possible that eddies trap pre-existing hypoxic conditions in their interior at formation. However, despite recent evidence of extremely low O_2 levels within two newly formed eddies off Mauritania (Ekau et al., 2016; Devresse et al., 2022), this possibility remains speculative (Schütte, Karstensen, et al., 2016).

The purpose of this chapter is to investigate how hypoxic events shape the sOMZ in the ETNA, by analyzing their intensity, spatial extent and temporal evolution within the upper 300 m. Reports of hypoxic events at the continental margin (e.g., Dale et al., 2014a; Thomsen et al., 2019; Tall et al., 2021) and in the open ocean (e.g., Karstensen et al., 2015; Fiedler et al., 2016; Schütte, Karstensen, et al., 2016) highlight the need for a combined Eulerian-Lagrangian framework to comprehensively characterize these events and evaluate their potential impacts on marine ecosystems in the ETNA. Here, we define a Lagrangian Hypoxic Event (LHE) as a coherent cluster of grid points that meet hypoxic conditions and evolve in space and time. By tracking and categorizing LHEs according to the processes influencing them throughout their lifetime, this approach provides a detailed understanding of the physical and biogeochemical processes shaping their evolution and distribution, from the moment they are formed to the moment they dissipate.

This chapter is structured as follows: Section 3.3 presents the general characteristics of the sOMZ, focusing on the distribution, seasonality, and water masses associated with hypoxic events from an Eulerian perspective. Section 3.4 shifts to a Lagrangian perspective, examining the spatial distribution, temporal evolution, and statistical properties of LHEs. In Section 3.5, we contextualize our findings within the broader literature and discuss model limitations and caveats. Finally, we summarize the key findings and present our conclusions in Section 3.6.

3.2 Methods

This Chapter builds upon several methodologies previously detailed in Chapter 2, used across multiple chapters. Some of the methods employed include water mass analysis (Section 2.4.3) and eddy detection and tracking (Section 2.4.4). To avoid redundancy, these common methods are not repeated here but are referenced as needed throughout the text.

3.2.1 Identification and tracking of Lagrangian Hypoxic Events

Extreme events occur when conditions deviate significantly from the norm (Hauri et al., 2013; Hobday et al., 2018). They can be classified using absolute thresholds (Hauri et al., 2013)–based on species-specific physiological and metabolic requirements (Vaquer-Sunyer & Duarte, 2008; Ekau et al., 2010; Giomi et al., 2023)–or in relative terms, defined as a percentile value within the cumulative distribution (Gruber et al., 2021; Köhn et al., 2024; Wong et al., 2024). Given that metabolic oxygen requirements are generally species-specific and fixed (Wilding, 1939; Hofmann et al., 2011), we adopt an absolute threshold to define hypoxic events. Most heterotrophic organisms experience stress below 60 µmol L^{-1} (Ekau et al., 2010). However, we use a more restrictive threshold of 40 µmol L^{-1} to ensure consistency with previous studies in the ETNA (Karstensen et al., 2015; Schütte, Karstensen, et al., 2016).

LHEs are defined as coherent clusters of hypoxic grid cells that evolve in space and time (Figure 3.1). Within these clusters, each grid cell is no more than two grid points away from another, allowing the inclusion of both directly adjacent cells and those separated by up to two grid points in any direction (horizontal or vertical; e.g., t_0 in Figure 3.1). This clustering approach minimizes fragmentation and ensures that hypoxic cells belonging to the same event–though not directly neighboring–are identified as part of a single event. LHEs can also merge with other events, adopting the label of the event with the largest volume (Figure 3.1 scenario a).

To avoid premature termination due to temporary merging, LHEs that merge and split within a short time retain their identity and are treated as individual clusters, even when temporarily sharing adjacent hypoxic grid cells at their boundaries (Figure 3.1 scenario b). New LHEs can emerge independently or originate from a pre-existing event through splitting. Those that split and merge with another LHE–or even with the parent–within two days immediately adopt the label of the merged cluster (Figure 3.1 scenarios c and d). Otherwise, they are assigned a new label (Figure 3.1 scenario e). The identification of individual LHEs is also limited by a minimum volume of five grid cells (Figure 3.1 scenario f). This approach differs from past studies, which define events based on a minimum duration of five days (e.g., Desmet et al., 2022; Köhn et al., 2022; Köhn, 2023). We believe this adjustment is better suited for our study, as it accounts for scenarios where clusters were part of a pre-existing event but active for a short period of time (e.g., eddy leakage). If a discarded LHE later expands beyond the size threshold, it gets reassigned its original label (Figure 3.1 scenario g).

LHEs are classified based on the prevailing process affecting them. These processes are ACMEs, Cyclonic eddies, Anticyclonic eddies, ”eddy leakage”, ”eddy dissipation”, bottom

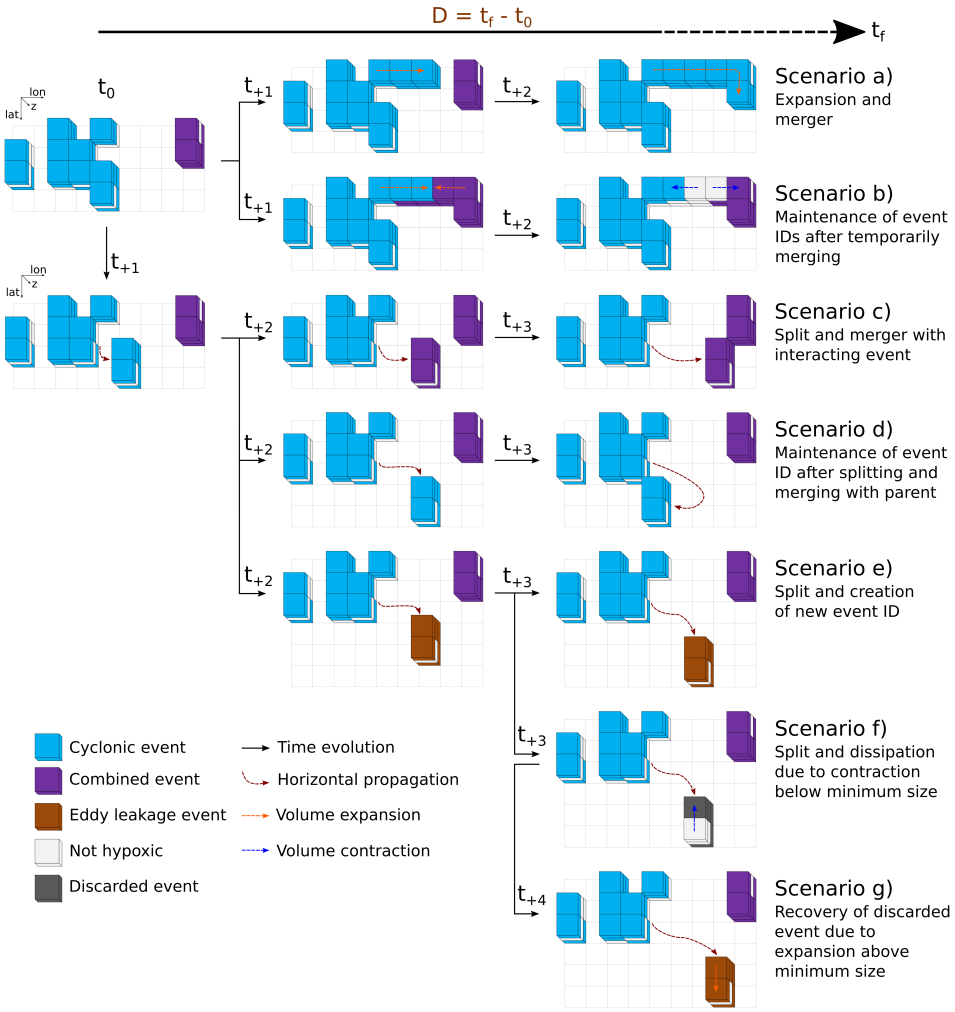


Figure 3.1: Schematic illustrating the detection and labeling of LHEs as clusters of hypoxic grid cells evolving in space and time. Main scenarios and respective descriptions are indicated. Each square symbolizes a grid cell, with colors indicating individual LHEs. D represents the total duration of an event, where t_0 and t_f denote the initial and final timesteps, respectively.

processes (hereafter referred to ”bottom” LHEs), other processes (such as eddy stirring or bottom export; hereafter referred to ”other” LHEs), and combined processes (occurring when LHEs are influenced by more than one process; hereafter referred to ”combined” LHEs). Since LHEs can be associated with processes different from those that initiated them, this categorization was performed manually, by visually analyzing the evolution of each individual LHE and correlating them with the eddy shapes detected with AMEDA. Besides enabling us to identify relationships between LHEs, this methodology ensures that each LHE is categorized according to the process influencing it at different times. Additionally, some LHEs associated with eddies cannot be distinguished from others due to shared neighboring cells. In such cases, hypoxic grid cells detected within eddy perimeters for more than 10 days are separated from the main clusters and assigned a new label. Examples of these procedures are given in Section 3.4.

3.2.2 Metrics for the characterization of hypoxic events

To evaluate the characteristics of hypoxic events, we apply a range of metrics to quantify aspects such as temporal dynamics, structural features, intensity, propagation patterns and biogeochemical properties (Table 3.1).

For temporal metrics (Table 3.1a), the Duration (D) of a LHE refers to its lifespan, whereas Local Duration (D_L) measures the longest period of uninterrupted hypoxic conditions at a specific location. Recurrence interval (R_i), which is critical for understanding the resilience of marine organisms to low-oxygen conditions (Gruber et al., 2021), represents the time interval between uninterrupted hypoxic events. We also introduce the Frequency of hypoxic events (F_h), defined as the proportion of hypoxic days relative to the total simulation days. Considering that hypoxic events in the sOMZ occur within a specific depth range and are seldom decoupled along depth, D_L, R_i and F_h are only calculated in the horizontal dimension and on a grid-cell basis, that is, from an Eulerian perspective.

Table 3.1: Definition of metrics used to characterize hypoxic events. Overview of the metrics used to quantify the temporal, structural, intensity, propagation, and biogeochemical properties of hypoxic events. Definitions are provided alongside corresponding units. Metrics marked with an asterisk (*) are computed using an Eulerian framework (i.e., grid-cell based).

	Name	Definition	Unit
a)	**Temporal metrics**		
	Duration (D)	Lifetime of a hypoxic event	days
	Local duration* (D_L)	Maximum uninterrupted duration of a hypoxic event in a given horizontal grid-cell	days
	Recurrence interval* (R_i)	Time interval between uninterrupted hypoxic events in a given horizontal grid-cell	days
	Frequency of hypoxic events* (F_h)	Percentage of hypoxic days (relative to the total number of days) in each horizontal grid-cell	%
b)	**Structural metrics**		
	Daily volume (V_d)	Total volume divided by total number of days	$km^3\ d^{-1}$
	Vertical extent (h)	Vertical thickness	m
	Average depth (Z)	Volume-weighted center of gravity	m
	Top depth (Z_t)	Mean depth of the top of a LHE	m
c)	**Intensity metrics**		
	Intensity index (I_i)	Daily volume weighted intensity index: $I_i = \int [(T - O_{2(t,x,y,z)})/T] dv/V$, with T= 40 µmol L^{-1}	unitless
	Heterogeneity (H)	Daily mean standard deviation of I_i	unitless
d)	**Propagation metrics**		
	Horizontal prop. (HP)	Cumulative distance of Z between time steps	km
	Vertical prop. (VP)	Vertical displacement of Z between first and final time steps	m
	Horizontal speed (HS)	$HS = HP/D$	$km\ d^{-1}$
e)	**Biogeochemical characteristics**		
	VAR	Daily volume-weighted average parameter p: $VAR = \int p_{(t,x,y,z)} dv/V$	p unit

Structural metrics were calculated on a daily basis (Table 3.1b). The three-dimensional extent of an LHE is characterized by its mean Daily volume (V_d) and Vertical extent (h). We also calculated the average depth of the volume-weighted center of gravity Z and, most importantly, the Top depth (Z_t), representing the mean shallowest depth of the clusters. While Z is used to calculate metrics related to the propagation of LHEs, Z_t is used to assess their influence along the water column due to its impact on ecosystem dynamics (e.g., Hauss et al., 2016; Köhn et al., 2022).

The intensity of an event quantifies how far O_2 concentrations fall below a defined threshold. In this study, we use an intensity index (I_i, hereafter referred to as intensity for simplicity), which normalizes the difference between O_2 concentrations and the threshold (e.g., Wong et al., 2024). This means that values range from 0 to 1, with values closer to 1 indicating O_2 near 0 µmol L^{-1} (Table 3.1c). We also calculate Heterogeneity (H), which quantifies fluctuations in intensity within individual events (Gruber et al., 2021). This metric is particularly relevant for non-mobile organisms unable to escape unfavorable conditions (e.g., Adjeroud et al., 2018; Samuel et al., 2019) and is computed as the daily standard deviation of I_i within each event.

To analyze spatial characteristics (Table 3.1d), we calculate Horizontal and Vertical Propagation distances (HP and VP) to track the spatial displacement of LHEs throughout their lifetime. HP represents the cumulative horizontal distance of Z between time steps, while VP measures the vertical displacement of Z between the first and final time steps. Mean Horizontal Speed (HS) is derived by dividing HP by D. These metrics are not computed for ”bottom” and ”combined” LHEs due to their complex shapes, which prevent realistic estimates of Z.

Lastly, the mean values of several physical and biogeochemical parameters, such as %SACW and NO_3, were computed within the LHEs (Table 3.1e). Like I_i, these calculations accounted for the varying volume of each grid cell in the sigma (terrain-following) vertical coordinate system.

3.3 General characteristics of the sOMZ

In order to have a broad understanding of the spatial and temporal distribution of the hypoxic conditions that contribute to the formation of sOMZ, we first assess the spatial, seasonal and hydrographic characteristics of these conditions from an Eulerian perspective, that is, for each horizontal grid cell, without discerning individual events.

To have a first overview of the general horizontal and vertical distribution of O_2 concentrations in the ETNA, Figure 3.2 shows a daily snapshot captured in summer of year 1, illustrating modeled O_2 concentrations at 100 m depth and at three longitudinal cross sections. Two distinct regions can be easily depicted. The coastal region is predominantly characterized by hypoxic O_2 concentrations, particularly between Cap-Vert and Cap-Blanc (≈15–21°N). These hypoxic conditions exhibit a vertical structure extending from ≈60 to 140 m depth, spanning from the base of the continental slope to offshore waters (Figure 3.2b–d). Interestingly, this pattern closely resembles observations reported during an oceanographic survey conducted in June 2014 (M107; Schroller-Lomnitz et al., 2019; Thomsen et al., 2019). Adjacent to this coastal region, the offshore area is delineated to the west by the CVFZ, which is marked by a sharp gradient in O_2

concentrations extending from southwest to northeast. This offshore region exhibits a broad range of O_2 values, where hypoxic water masses are observed in close proximity to well-ventilated waters with O_2 concentrations exceeding 150 µmol kg^{-1}.

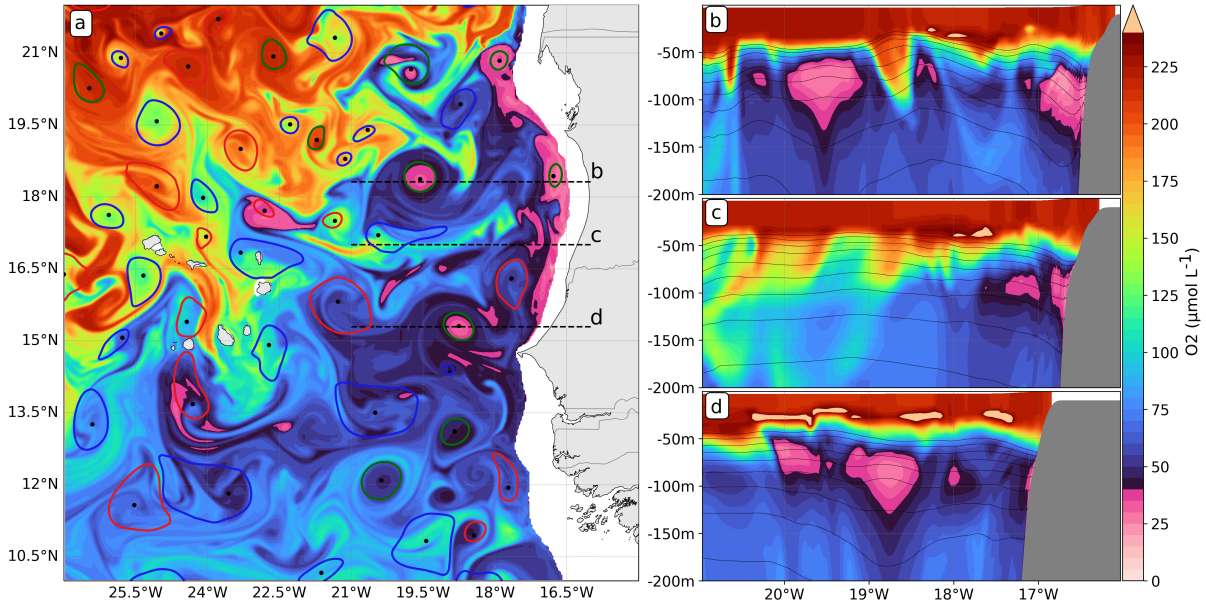


Figure 3.2: Snapshot of daily-averaged O_2 concentrations, taken on the 9th of July of year 1. (a) O_2 concentrations at 100 m depth, with eddy centers and perimeters represented by black points blue (cyclonic), red (anticyclonic) and green (ACMEs) contours. (b–d) O_2 concentrations at the three longitudinal cross sections identified in (a) by horizontal black dashed lines, with potential density surfaces represented by black contours (from σ_θ 25 to 27 kg m^{-3} with a 0.2 kg m^{-3} interval). Note that hypoxic concentrations are highlighted by purple color gradient.

Common to both regions, several eddies are observed with hypoxic waters in their interior. In the offshore region, two low-oxygen ACMEs exhibit a distinctive ”wineglass” vertical structure (Figure 3.2b and d), likely indicative of enhanced vertical export (Waite et al., 2016) and subsequent O_2 consumption due to the remineralization of organic matter (Karstensen et al., 2017). Interestingly, the eastward intrusions of well-ventilated NACW through the CVFZ at ≈16.7 (Figure 3.2C) and 19°N appear to be associated with the horizontal stirring induced by a westward-propagating cyclonic eddy and an ACME, respectively. Low-oxygen eddies also seem to contribute to the leakage and subsequent dispersion of hypoxic waters in the offshore region, as depicted by two elongated anticyclonic eddies south and north of the Archipelago of Cabo Verde (Figure 3.2a).

In the coastal region, two young ACMEs (≈1 month) with hypoxic O_2 concentrations are observed close to the continental margin (Figure 3.2a). Interestingly, hypoxic conditions inside one of the eddies appear to be attached to the continental slope (Figure 3.2b), suggesting that coastal-generated eddies can be formed with pre-existing hypoxic O_2 concentrations in their interior.

3.3.1 Spatial characterization

In the following, we evaluate the spatial characteristics of hypoxic events shaping the sOMZ at the level of individual horizontal grid cells, independently of LHEs. For context, we also

briefly compare these results with those obtained using a Lagrangian approach. Here, an Eulerian hypoxic event is defined as a continuous period during which O_2 concentrations remain below the hypoxic threshold within a given grid cell (e.g., Hauri et al., 2013; Köhn et al., 2022; Wong et al., 2024). This method detects substantially more hypoxic events than the Lagrangian approach (Figure 3.3a and b, respectively), with a maximum of approximately 90 events along the continental margin. In contrast, the Lagrangian method identifies significantly fewer events, with maximum values of 34 events per grid cell, primarily concentrated at northern latitudes between 18–19.5°W. It also reveals a weaker gradient between the continental margin and the offshore region, particularly between 16.5–22°N. These differences suggest that LHEs generally have longer lifetimes than Eulerian hypoxic events and may revisit the same locations during their lifetime. Nevertheless, despite methodological differences, both approaches consistently highlight a high frequency of hypoxic events between Cap-Vert and Cap-Blanc, as well as the absence of hypoxic conditions in the wake of the Cabo Verde Islands.

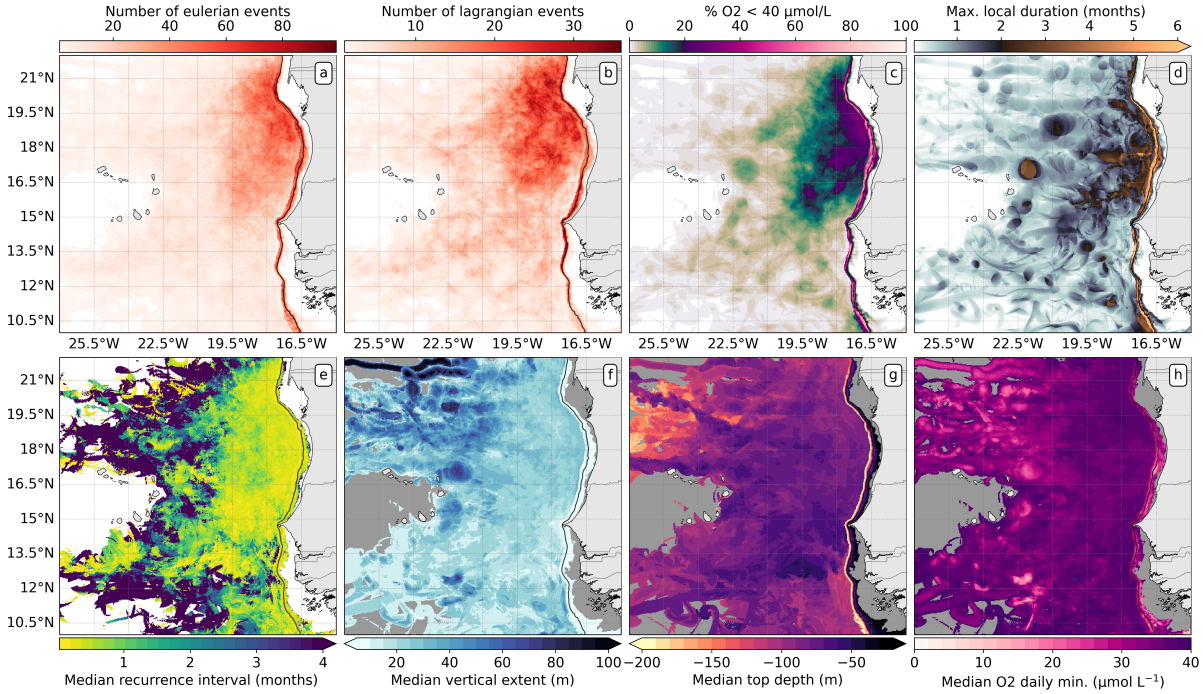


Figure 3.3: Spatial projection of the main characteristics of hypoxic events. Spatial histograms were computed with the native horizontal resolution of the model grid. Black contour parallel to the coast represents the continental shelf break, defined at 100 m depth. (a) Eulerian and (b) Lagrangian number of events detected in each grid cell, respectively. (c) Frequency of hypoxic conditions. (d) Maximum local uninterrupted duration. (e) Median vertical extent. (f) Median time interval between hypoxic conditions. (g) Median top depth. (h) Median O_2 daily minimum along depth. Except for (b), all parameters were computed from an Eulerian perspective.

In terms of hypoxia frequency, Figure 3.3c shows that the coastal region–hereafter defined as the area east of 19.5°W–is the most affected, with hypoxic conditions occurring approximately 25% of the time. Within this region, the continental margin–which includes both the continental shelf and slope–exhibits maximum hypoxic frequencies reaching up to 80%, indicating a near-permanent presence of low-oxygen conditions.

This high frequency along the continental margin is also reflected in the maximum local duration, with some hypoxic events persisting for more than six months within individual grid cells (Figure 3.3d). In contrast, the offshore region is characterized by swirling patterns and round-

shaped features, indicative of the influence of westward-propagating eddies transporting hypoxic waters offshore (e.g., Karstensen et al., 2015; Karstensen et al., 2017). Although these eddies propagate at an average speed of approximately 3.2 km d^{-1} (Schütte, Brandt, & Karstensen, 2016; Cardoso et al., 2020), the occasional local duration of 1–2 months observed offshore suggests variability in their propagation speeds. The easternmost islands appear to retain some of these eddies, forming a distinct circular pattern where maximum local duration exceed three months. Consequently, this area experiences the longest uninterrupted hypoxic events in the offshore domain, while the sheltered region behind the islands remains well-ventilated throughout the simulation.

Similarly to hypoxic frequency and maximum local duration, the median recurrence interval between uninterrupted hypoxic events displays a clear gradient from the continental margin to offshore waters (Figure 3.3e). East of 19.5°W, median recurrence intervals are generally shorter than 15 days, whereas offshore regions exhibit greater variability, with intervals exceeding four months. It should be noted, however, that a shorter recurrence interval does not necessarily imply a higher frequency of hypoxic events. This is particularly evident south of the Cabo Verde Islands, where low recurrence intervals coexist with relatively low hypoxic frequencies (Figure 3.3c).

In terms of median vertical extent, Figure 3.3f reveals a clear offshore-increasing gradient. Along the continental margin, hypoxic conditions exhibit a minimum vertical extent of approximately 10 m, whereas in the broader coastal region, values typically range between 20 and 50 m. Further offshore, west of approximately 20°W, the median vertical extent increases markedly, reaching up to 60 m. The influence of eddies is particularly evident north of Cabo Verde, where swirling patterns with median vertical extents of up to 100 m are clearly observed. South of Cabo Verde, although eddies also contribute to hypoxic conditions, the median vertical extent remains significantly lower, with maximum values not exceeding 60 m.

Median top depths of hypoxic conditions are generally consistent across the domain, ranging from 50 to 100 m (Figure 3.3g). However, notable deviations from this pattern occur. Near the coast, hypoxic conditions are detected as shallow as 30 m depth, with a rapid deepening offshore to maximum depths exceeding 200 m along the continental slope. This sharp vertical transition over a short horizontal distance, combined with the significantly reduced vertical extent observed in the same region (Figure 3.3f), suggests that hypoxic waters closely follow the sloping bathymetry, occurring primarily near the seabed along the continental shelf and slope. Although less abrupt, a gradual deepening of median top depths is also observed north of Cabo Verde, decreasing from approximately 100 m near the coast to more than 150 m offshore (Figure 3.3g). In contrast to the patterns observed along the continental margin, this offshore deepening is likely associated with the subduction of westward-propagating eddies (Dilmahamod et al., 2022), a process that appears to intensify as eddies cross the CVFZ.

Lastly, Figure 3.3h illustrates the median O_2 minimum concentrations detected within hypoxic events throughout the water column. The lowest concentrations are observed along the continental margin, where minimum values approach 10 µmol L^{-1}. These extremely low O_2 levels, combined with the high frequency and short recurrence intervals of hypoxic events (Figures 3.3c and e), indicate a persistent recurrence of intense hypoxic conditions in this region. In the broader

coastal domain, O_2 minimum concentrations are relatively higher, generally nearing the hypoxic threshold of 40µmol L^{-1}. Further offshore, swirling patterns–particularly north of Cabo Verde–exhibit significantly more intense hypoxic conditions, with O_2 minimum concentrations again reaching values as low as 10 µmol L^{-1}. These offshore low-oxygen features are likely associated with the en-route consumption of O_2 within highly productive eddies, which progressively intensify hypoxia as they propagate westward (Karstensen et al., 2015; Karstensen et al., 2017).

3.3.2 Seasonal variability and distribution

To elucidate on the seasonal variability and spatial distribution of the intensity and daily volume of hypoxic conditions, Figure 3.4 presents the median daily O_2 minimum (or intensity maximum; top panels) and the corresponding hypoxic volume (bottom panels), integrated along depth as well as zonal and meridional dimensions for each season.

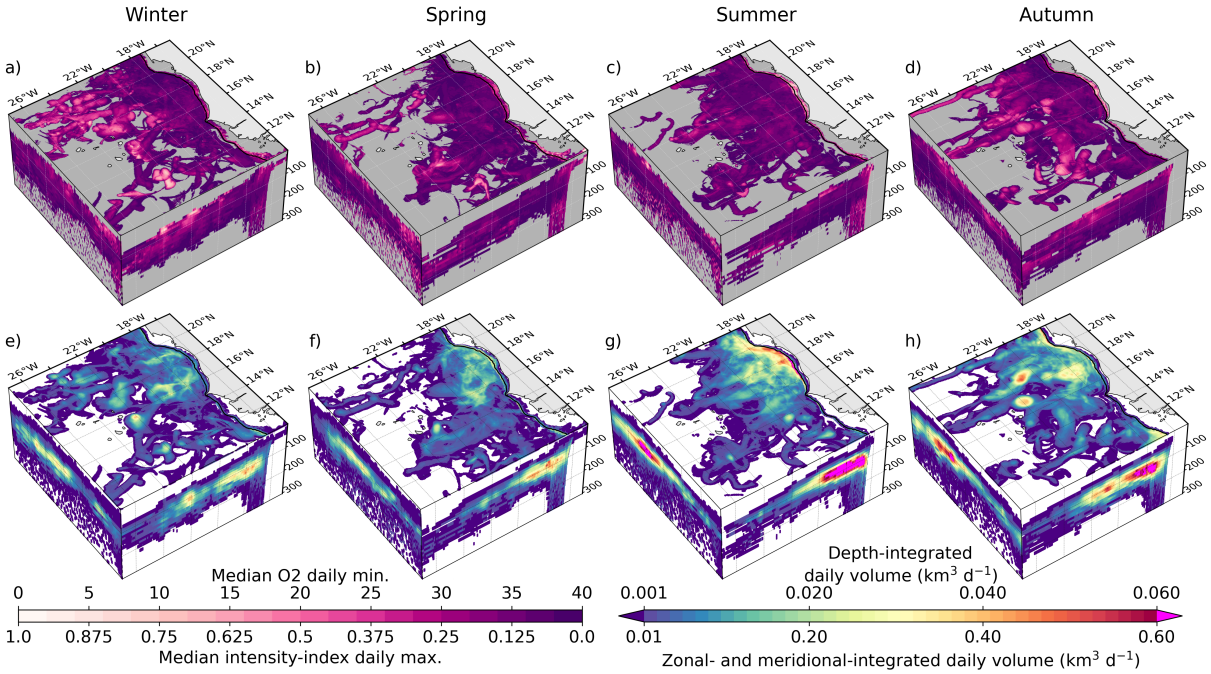


Figure 3.4: Seasonal variability of hypoxic conditions. (a-d) Median daily O_2 minimum / intensity-index maximum along depth (horizontal plane), zonal (meridional plane) and meridional (zonal plane) dimensions. (e-h) Daily hypoxic volume integrated across depth, zonal and meridional dimensions. Different scales in color bars are used to illustrate relation between O_2 concentrations and intensity-index (a-d), and different magnitude between depth- and zonal/meridional-integrated daily volumes (e-h). Black contour parallel to the coast represents the continental shelf break.

During winter, hypoxic waters reach their greatest offshore extent, particularly west of 22°W (Figure 3.4a). Swirling patterns with median minimum O_2 concentrations of approximately 15 µmol L^{-1} are observed, indicative of the influence of westward-propagating eddies. These features are centered around 100 m depth and account for the majority of the offshore hypoxic volume (Figure 3.4e). Nevertheless, the total hypoxic volume during winter remains relatively modest and evenly distributed across the region, with higher concentrations occurring north of 14°N and between Cabo Verde and the African coast.

In spring, hypoxic conditions are generally less intense across the domain (Figure 3.4b). The daily hypoxic volume reaches its minimum during this season, although a slight increase

is observed along the coastal region between the Cap-Vert and Cap-Blanc headlands (Figure 3.4f). Similar to winter, the shoaling of hypoxic waters toward the coastline is evident between Cap-Vert and Cap-Blanc, likely associated with cross-shelf intrusions driven by coastal upwelling (Yücel et al., 2015).

During summer, hypoxic conditions reach their lowest intensity and volume in the offshore region (Figures 3.4c and g, respectively). In contrast, the coastal region experiences an increase in both intensity and volume, particularly along the continental shelf, where median maximum intensity reaches its highest values among all seasons. Most of the hypoxic volume is concentrated between 16–20°N and east of 20°W, especially near the continental shelf break (100 m isobath). This pattern suggests the influence of processes associated with the relaxation of upwelling conditions (Klenz et al., 2018).

In autumn, hypoxic intensity increases across the domain (Figure 3.4d), particularly in the offshore region. Swirling patterns observed offshore are likely associated with eddies formed near the coast in late spring to early summer, subsequently propagating westward (e.g., Karstensen et al., 2015; Schütte, Karstensen, et al., 2016). Despite the offshore intensification, the coastal region experiences a decrease in hypoxic volume compared to summer (Figure 3.4h), suggesting a dissipation of nearshore hypoxic conditions. Similar to winter, eddy-like patterns are most prominent north of the Cabo Verde Islands, highlighting the persistent role of eddies in modulating offshore hypoxia in this region.

Together, these results reveal strong seasonal and spatial variability in hypoxic conditions, both in terms of intensity and volume. The coastal region exhibits the highest hypoxic volumes during summer and autumn, with moderate intensity throughout the year except on the continental shelf, where intensity peaks during these seasons. In contrast, offshore areas are primarily influenced by eddies during autumn and winter, when hypoxic intensity reaches its maximum.

3.3.3 Hypoxic water mass composition

In the following, we explore the relationship between hypoxic conditions and water masses by analyzing θ-S histograms alongside the spatial distribution of three water mass groups (Figure 3.5). Hypoxic waters are primarily confined to the density range of 25.8–26.3kgm^{-3}, with mean O_2 concentrations between 30 and 40 µmol L^{-1} and depths ranging from 60 to 140 m (Figures 3.5a–c). Interestingly, hypoxic conditions also occur above the upper density limit of central waters ($\sigma_\theta < 25.8$ kg m^{-3}; Stramma et al., 2005), concentrated along the Mauritanian continental shelf, the coastal region between 12–19.5°N, and in two eddy-related areas east of the Cabo Verde Islands (Figure 3.5d). These lighter hypoxic waters are most prominent during summer and autumn (not shown), suggesting an influence of upwelling relaxation and increased stratification (Brandt et al., 2015; Klenz et al., 2018).

Hypoxic waters in the upper 200 m are primarily associated with the diluted SACWcv variety, characterized by salinity values ranging between the SACWcv and 60% SACW σ_θ profiles (Figure 3.5a). However, a distinct hypoxic SACW variety, with salinity values lower than the SACWcv σ_θ profile, is also evident. The separation between these two volume maxima highlights a clear distinction between hypoxic water masses dominated by SACW and those dominated

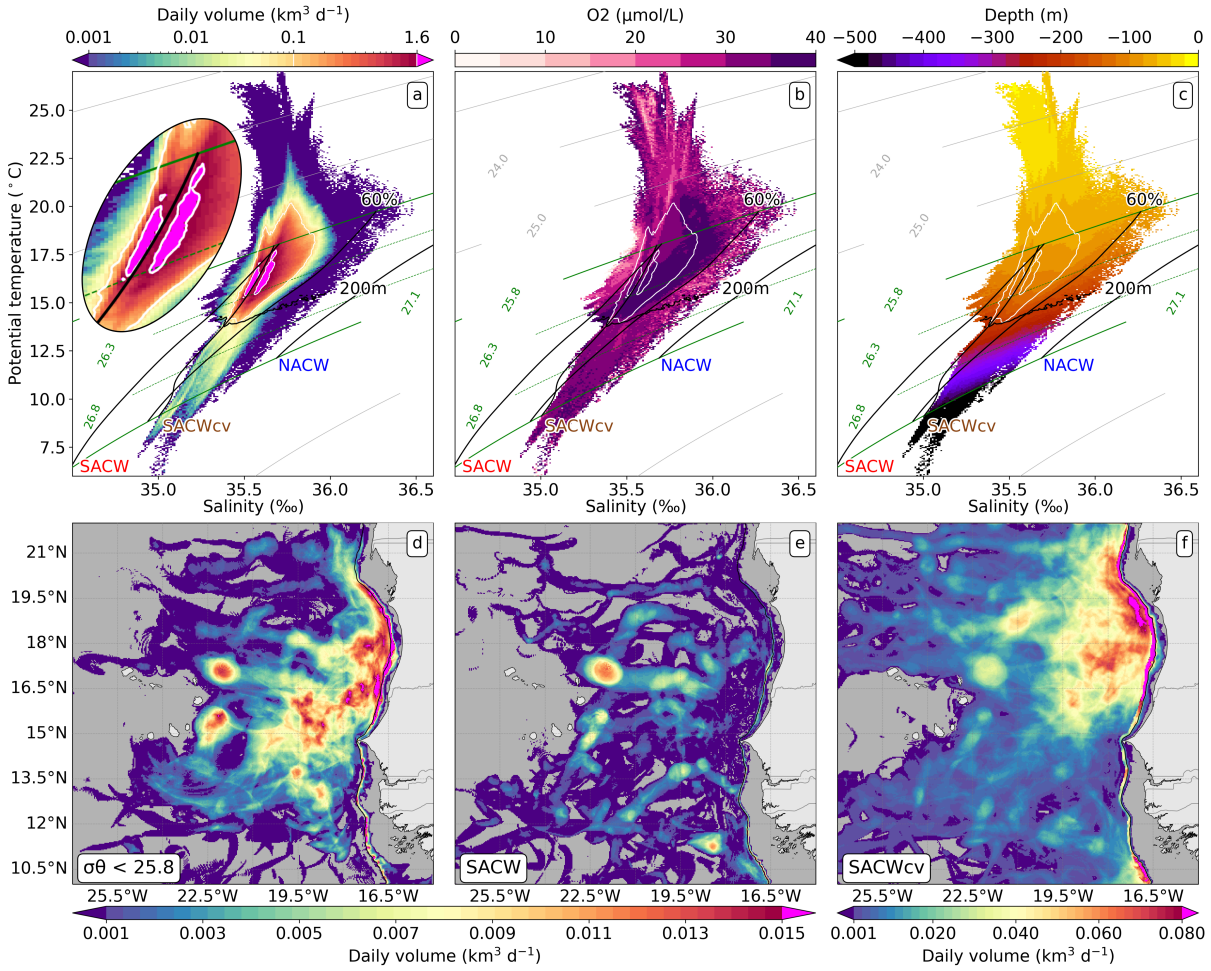


Figure 3.5: Hydrographic characteristics of hypoxic water masses. (a–c) θ-S histograms accounting for all hypoxic grid cells: (a) daily volume; (b) volume-weighted average O_2 concentrations; and (c) volume-weighted average depth. An enlarged view of the two volume maximums is shown in (a). Characteristic profiles for SACW, SACWcv and NACW are represented by black lines, together with 60% SACW. (d-f) Spatial distribution of grid cells accounting for: (d) $\sigma_\theta < 25.8$ kg m^{-3}; (e) salinity $<$ SACWcv; and (f) salinity $>$ SACWcv. Black contour parallel to the coastline represents the shelf break. Water masses deeper than -300 m are accounted in the θ-S diagrams but excluded from the maps.

by SACWcv varieties. Exhibiting lower mean O_2 concentrations than the diluted SACWcv, the purer SACW variety is primarily concentrated within swirling patterns and circular features, particularly offshore (Figure 3.5e). The limited connectivity of these SACW waters to the coastal region suggests that hypoxic conditions in SACW-dominated waters likely develop en route within westward-propagating eddies.

In contrast, hypoxic conditions associated with SACWcv are less intense and predominantly concentrated in the coastal region, particularly north of 16°N (Figure 3.5f). Round-shaped features and trails connecting coastal and offshore regions suggest that eddies carrying SACWcv waters can form with pre-existing hypoxic or near-hypoxic waters in their interiors. This observation implies that hypoxic SACWcv waters exist prior to eddy formation, with eddies acting as transport pathway to offshore. The dispersed distribution of SACWcv waters also suggest that both SACW- and SACWcv-rich eddies contribute to the offshore redistribution of hypoxic waters through processes such as horizontal stirring, leakage, and dissipation.

3.4 A lagrangian perspective of hypoxic events

Here, we focus on analyzing the characteristics and dynamics of hypoxic events from a Lagrangian perspective – that is, by tracking coherent clusters of hypoxic grid cells through space and time, and identifying them based on the processes influencing them throughout their lifetime. As a demonstration of our method, Figure 3.6 shows daily mean O_2 concentrations for July 4th of year 1, alongside the corresponding LHEs and their evolution 20 days later.

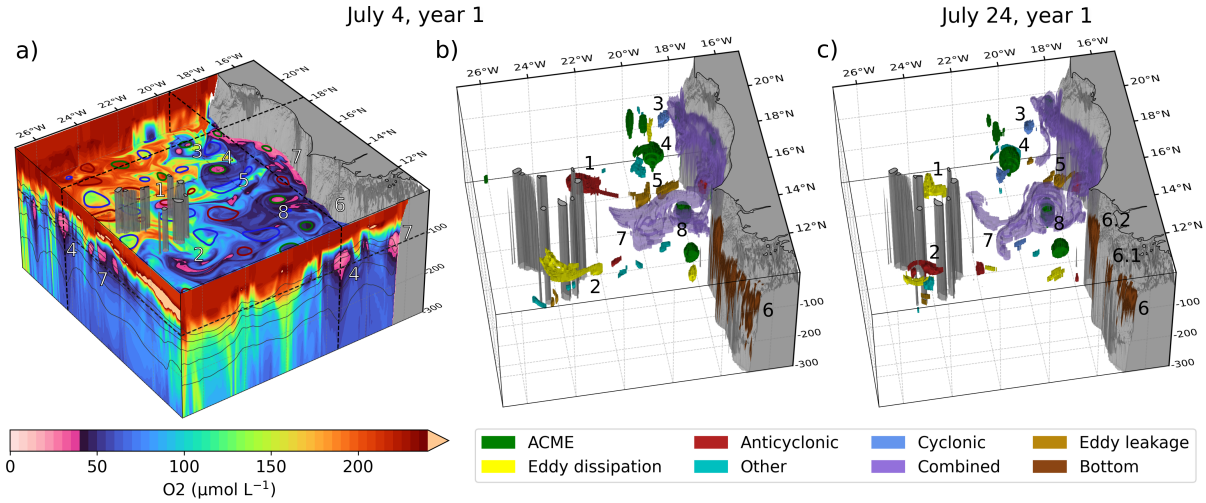


Figure 3.6: O_2 concentrations and LHEs on July 4th and 20th of year 1. (a) Snapshot of O_2 concentrations at 100 m depth. Zonal and meridional vertical sections at 18.4°N and 19.4°W, identified by dashed black lines, are represented at the southern and western faces of the cube, respectively. Thin gray lines are representative of isopycnals from σ_θ 25.8 to 26.6 kg m^{-3} ($\delta\sigma_\theta$ = 0.2 kg m^{-3}). Green, blue and red lines in horizontal slice represent the perimeter of ACMEs, cyclonic and anticyclonic eddies, respectively. Hypoxic O_2 concentrations are color-coded in purple. (b) Three-dimensional representation of the LHEs identified on the same time step as (a), with colors indicating different categories. (c) Same as (b), 20 days later.

Given its large spatial extent and interaction with multiple mesoscale features, LHE 7 is classified as a ”combined” event. When considering only a horizontal slice at 100 m depth, the event appears confined to the coastal region between Cap-Vert and Cap-Blanc (Figure 3.6a). However, a 3D analysis reveals its true structure as a single, coherent structure spanning offshore toward Cabo Verde (Figure 3.6b,c).

Surrounded by this ”combined” event, several eddy LHEs are identified between Cap-Vert and Cap-Blanc (Figure 3.6a–c). Among them is LHE 8 – an ACME LHE initially classified as an independent event, which later merged with LHE 7 two months after its formation. The two remained connected for over three months before separating and persisting independently for an additional five months. Without this separation procedure based on the eddy perimeter, this 10-month-long event would have been incorrectly classified as two shorter ACME LHEs. Similar cases, involving an anticyclone and two other ACMEs between Cap-Vert and Cap-Blanc, further highlight the method’s robustness and the importance of distinguishing such events (Figure 3.6a).

Additional examples illustrate the reclassification of LHEs based on the processes influencing them. LHE 1 was initially detected within an anticyclonic eddy north of Cabo Verde on July 4th (Figure 3.6b) but was later reclassified as an ”eddy dissipation” event following the eddy’s termination (Figure 3.6c). Similarly, LHE 2, initially classified as an ”eddy dissipation” event

(Figure 3.6b), was reclassified after becoming trapped in an anticyclonic eddy (Figure 3.6c). Other LHEs underwent changes in position and structure, such as the ”bottom” LHE 6, which split into three smaller related but independent clusters.

3.4.1 Event dynamics

Over the 5-year simulation period, we identified a total of 1,181 individual LHEs, averaging approximately 236 LHE yr^{-1} (Figure 3.7a). The ”other” category accounts for the largest proportion (47%), followed by eddy LHEs (19%), which include Cyclonic, Anticyclonic, and ACME LHEs. Cyclonic LHEs are the most frequent within this group, while ”bottom”, ”eddy leakage” and ”eddy dissipation” LHEs make up smaller portions of the total population.

a)

	ACME	Anticyc.	Cyclonic	Eddy leak.	Eddy diss.	Other	Combined	Bottom
Events	75 6%	54 5%	95 8%	156 13%	46 4%	551 47%	12 1%	192 16%
Independent	57%	30%	31%	0%	0%	35%	17%	38%
Origin. from	43%	70%	69%	100%	100%	65%	83%	62%
Exported	77%	31%	61%	46%	74%	22%	1683%	75%
Transformed	44%	30%	28%	5%	11%	4%	42%	0%
Merged with	17%	22%	16%	17%	26%	20%	8%	54%

b)

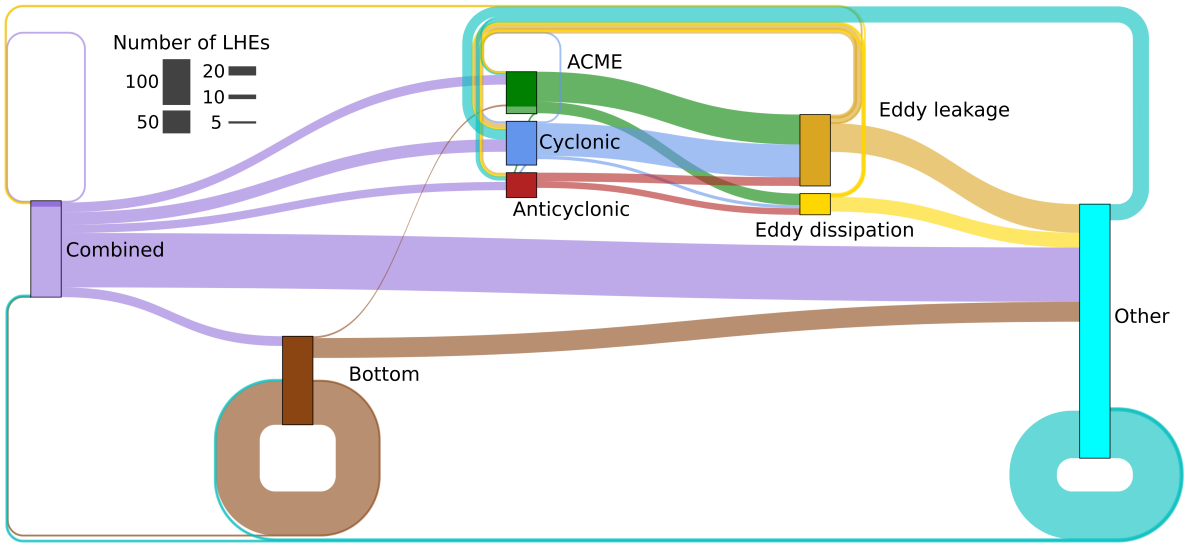


Figure 3.7: Overview of the relations between LHEs categories. (a) Number of LHEs and corresponding proportion per category (in respect to the total number of events), along with category-specific proportions of LHEs that were independently initiated, originated from a pre-existing clusters, exported/split to another category, transformed into a different category, and merged with existing LHEs. Small color bars represent the proportion of each event category within each metric. (b) Sankey diagram illustrating the transitions and relationships between LHEs across different categories. Links between nodes represent the flow of LHEs, with transitions moving from the right side of the source node to the left side of the sink node. Note that the outflow from source nodes represents both ”exported” and ”transformed” proportions in (a). Lighter colors in nodes ”combined” and ”ACME” represent the surplus of LHEs that were exported.

The transitions between LHE categories reveal important processes governing their dynamics (Figure 3.7b). For example, ”eddy dissipation” LHEs (46) are significantly fewer in number compared to eddy LHEs (224; Figure 3.7a). Detailed analysis revealed that 27% of ACME, 44% of Anticyclonic and 53% of Cyclonic LHEs terminate before their respective eddies, indicating that the dissipation of hypoxic conditions within eddies often precede the physical dissipation of the eddies themselves. Moreover, while Cyclonic LHEs are the main contributors to ”eddy

leakage" LHEs, ACMEs are the main contributors to "eddy dissipation" LHEs, indicating a contrasting behavior in terms of coherence.

ACME LHEs have the highest proportion of independently initiated events, standing out as the only category where over half of the events (57%) are formed without external influence (Figure 3.7a). In contrast, Anticyclonic (70%) and Cyclonic (69%) LHEs have the majority events linked to pre-existing conditions, highlighting their tendency to trap and retain hypoxic conditions during or even after their formation. "Bottom" LHEs exhibit the highest proportion of self-generated events (49%) and mainly merge with events of the same category, reflecting their self-contained, localized nature.

Despite comprising only 1% of the total population, "combined" LHEs play a key role in generating new LHEs (Figure 3.7a). Detailed examination revealed that a significant proportion of these exported events (69%) are linked to the horizontal stirring of nearby eddies. Similarly, ACME LHEs serve as significant net sources, contributing to new events through export and transformation into "eddy leakage" and "eddy dissipation" LHEs.

Interestingly, Cyclonic LHEs are frequently transformed into "eddy leakage" events (Figure 3.7a). Although counter intuitive, this transformation occurs when the entire hypoxic cluster leaks from an eddy while the eddy itself remains active, a process most commonly observed when their shape becomes more elongated and loses coherence, transitioning toward dissipation (e.g., Cetina-Heredia et al., 2019; Malan et al., 2022).

The "other" category functions primarily as a terminal sink, with most of its exported events remaining within the same category and only a small fraction transforming into different categories (Figure 3.7b). By contrast, "eddy leakage" and "eddy dissipation" LHEs contribute significantly to new eddy LHEs, with 21% of their exported and transformed events being recycled into new eddy LHEs. This highlights the dynamic nature of eddy-related LHEs, where hypoxic waters can persist even as their parent eddies lose coherence and dissipate.

3.4.2 Spatial distribution and characteristics

The spatial distribution of LHEs reveals a clear distinction between categories more commonly detected in coastal versus offshore regions. Offshore hypoxia is primarily associated with eddy LHEs, particularly west of 21°W (Figures 3.8a–c), while coastal hypoxia is mainly linked to "other," "combined," and "bottom" LHEs (Figures 3.8d–h). "Eddy dissipation" and "eddy leakage" LHEs are more evenly distributed across the ETNA but show a stronger offshore presence at southern latitudes (below 15°N; Figures 3.8e,f).

Eddy LHEs exhibit consistent westward propagation patterns and the longest trajectories, particularly in the case of ACME LHEs (Figure 3.8a). Although less frequent than "combined" LHEs, ACME LHEs cover the largest spatial extent, effectively connecting the coastal and offshore regions. Initiation hotspots near the shelf break at approximately 18°N and 20°N suggest that ACMEs can either form under hypoxic conditions or rapidly develop hypoxia after formation. Nevertheless, many ACME LHE trajectories initiate further offshore, indicating that hypoxic conditions can also develop en-route.

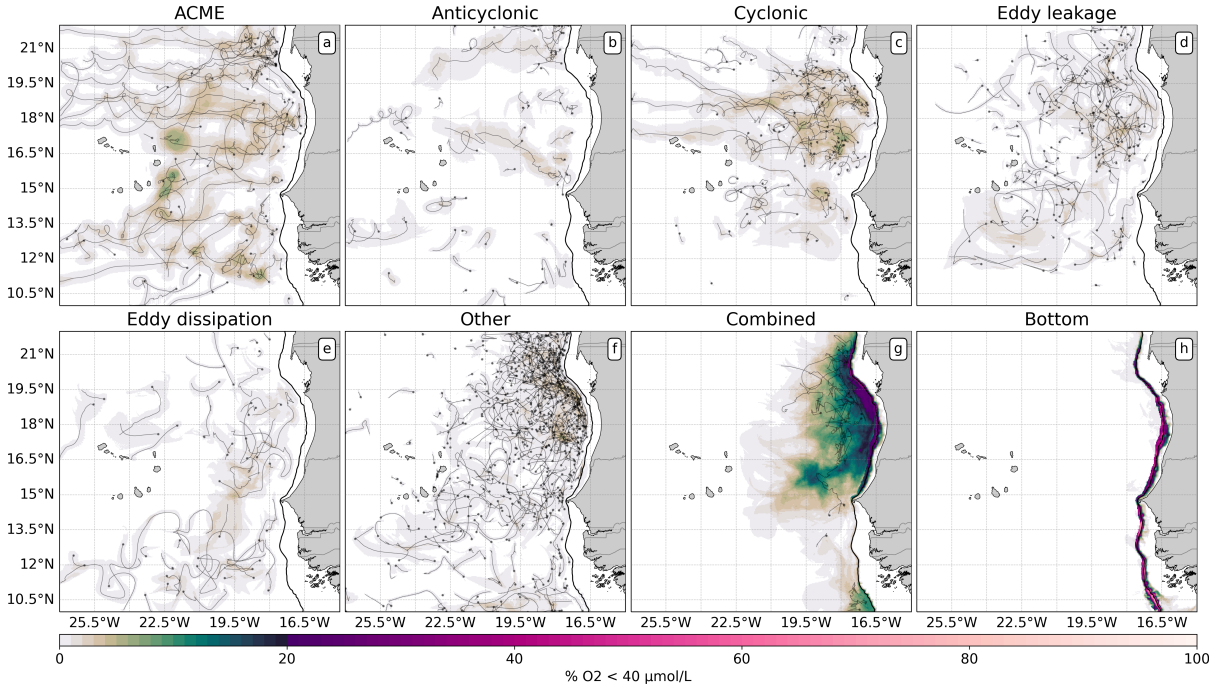


Figure 3.8: Spatial distribution of frequency of hypoxic conditions per LHE category. Horizontal trajectory of the clusters' center of gravity is represented by thin black lines, except in (h). Small black dotes represent the LHEs initial location. Trajectories of "combined" LHEs are represented only to demonstrate the impracticality of calculating trajectories for this type of event. Black thick line parallel to the coastline represents the shelf break.

Hypoxic intensity within ACMEs generally increases westward, peaking further offshore (Figure 3.9a). Notably, ACME LHEs exhibit the highest cumulative volume and the greatest vertical extent among eddy LHEs, spanning depths from approximately 50 to 200 meters (Figure 3.10a). However, this vertical range is confined to latitudes north of 16°N. Two distinct, round-shaped areas of high daily volume are observed east of the Cabo Verde Islands (Figure 3.10a). Trajectories reveal that these features result from ACMEs becoming relatively stationary upon interacting with the islands (Figure 3.8a), making this region the most impacted area in the offshore domain.

With the exception of a few events initiated near the coast, Anticyclonic LHEs generally display shorter trajectories and a higher proportion of offshore initiations (Figure 3.8b). Since most Anticyclonic LHEs originate from pre-existing events (Figure 3.7a), those forming offshore likely result from the trapping of hypoxic waters, although similar processes may also occur in the coastal region. Characterized by generally low intensity (Figure 3.9), Anticyclonic LHEs exhibit the lowest cumulative volume among eddy LHEs (4%) and the shallowest vertical extent (Figure 3.10b).

Cyclonic LHEs are primarily concentrated between 16° and 20°N (Figure 3.8c). Although a considerable number of trajectories initiate near the Mauritanian coast, most originate west of 18°W. This distribution aligns with the high rates of cyclonic eddy formation reported between 18° and 19°W (Schütte, Brandt, & Karstensen, 2016; Dilmahamod et al., 2022), explaining the high proportion of Cyclonic LHEs forming from pre-existing conditions (Figure 3.7a).

Cyclonic LHEs extend beyond 22.5°W only when propagating north of Cabo Verde, where they reach maximum median hypoxic intensities (Figure 3.9c) and minimum O_2 concentrations

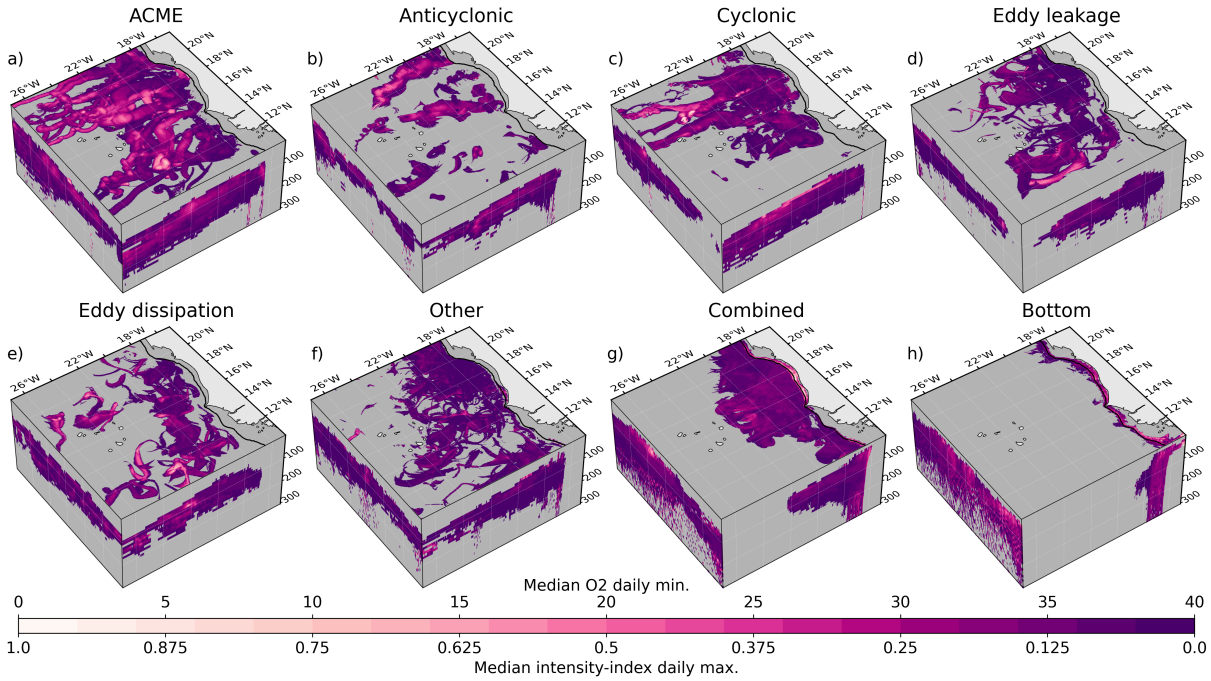


Figure 3.9: Spatial distribution of median daily O_2 minimum/intensity maximum per LHE category. Computation is made along depth (horizontal plane), zonal (meridional plane) and meridional (zonal plane) dimensions. Black think line parallel to the coastline represents the shelf break. Different color scales are used to illustrate relation between O_2 concentrations and intensity-index values.

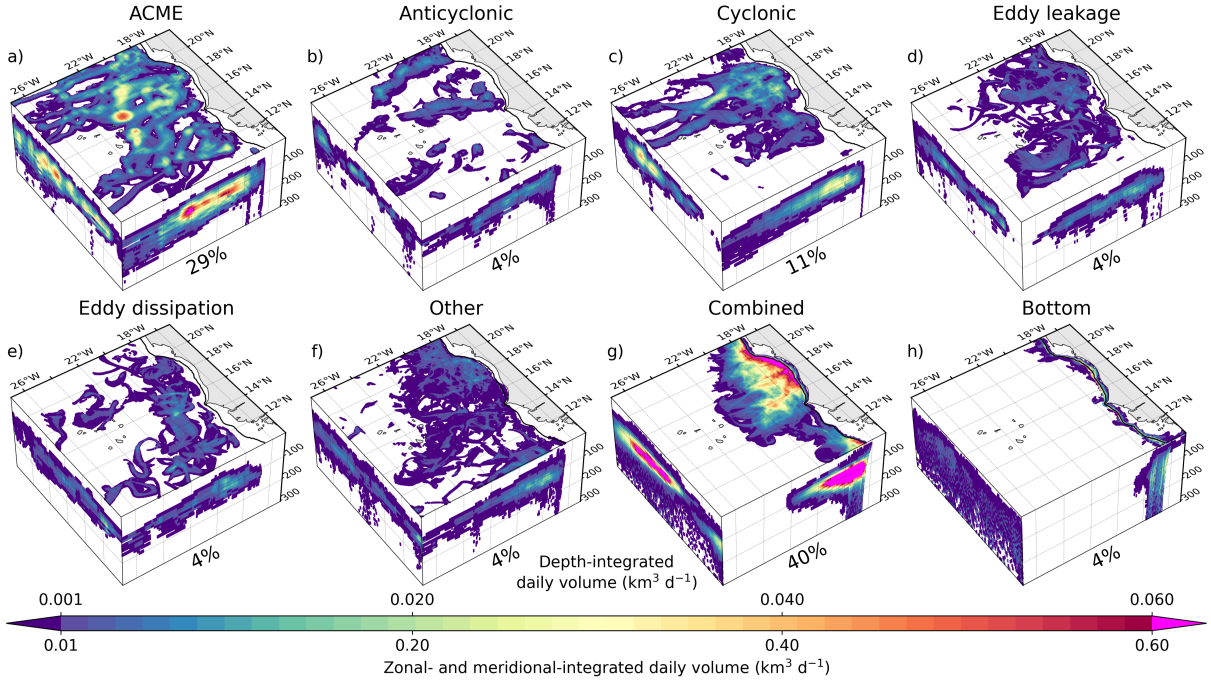


Figure 3.10: Spatial distribution of hypoxic daily volume per LHE category. Daily volume is integrated along depth (horizontal plane), zonal (meridional plane) and meridional (zonal plane) dimensions. Black think line parallel to the coastline represents the shelf break. Proportion of cumulative volume relative to the total is indicated for each category. Different color scales are used to illustrate different magnitude between depth- and zonal/meridional-integrated daily volumes.

below 2 µmol L^{-1} (Figure A.4c). As for ACME LHEs, this pattern indicates that Cyclonic LHEs intensify as they propagate westward, consistent with past observations of low-oxygen cyclones

exhibiting similar O_2 concentrations and propagation characteristics (Karstensen et al., 2015; Fiedler et al., 2016; Karstensen et al., 2017).

In contrast, ”eddy dissipation” and ”eddy leakage” LHEs exhibit irregular trajectories, occasionally moving eastward and resupplying hypoxic waters to the coastal region (Figure 3.8d,e). Although their daily volume and intensity are generally low, their intensity can reach higher values offshore (Figures 3.10e,f and 3.9e,f). This elevated offshore intensity is expected, given that eddy LHEs typically exhibit lower O_2 concentrations in the offshore domain.

A similarly irregular pattern is observed in the trajectories of LHEs categorized as ”other” (Figure 3.8f). These LHEs are predominantly concentrated north of 18°N and east of 19.5°W. Although representing the highest number of trajectories, they are generally short, indicating low coherence and duration. Their corresponding daily volume and intensity values are also the lowest among all categories (Figures 3.10d and 3.9d). Notably, most of these LHEs occur south and east of the CVFZ, a region dominated by SACWcv (Figure 2.10).

”Combined” LHEs exhibit the greatest horizontal extension, with hypoxic conditions present for at least 10% of the simulation time, reaching up to 20% along the continental margin between Cap-Vert and Cap-Blanc (Figure 3.8g). Their high frequency is accompanied by the largest daily volume among all categories (Figure 3.10g), making them the most significant category in terms of size. However, their median intensity is generally low, except on the continental shelf where they merge with ”bottom” LHEs (Figure 3.9g).

Although displaying the lowest horizontal extension, ”bottom” LHEs have the highest frequency (Figure 3.8h) but are confined to the continental margin. Their quasi-permanent nature contrasts with their low cumulative volume, reflecting a limited impact on the water column (Figure 3.10h). Interestingly, their intensity is lower than that of ”combined” LHEs at the continental margin, suggesting a seasonal coupling during peak hypoxic conditions in summer and autumn (Figures 3.9c,d).

3.4.3 Monthly distribution

To evaluate the monthly distribution of each LHE category and corresponding characteristics in terms of shape and intensity, Figure 3.11 shows the cumulative monthly distribution of events initiated in each month, their duration (representative of the proportion of active events), volume, and median volume-weighted daily intensity.

In general, eddy LHEs tend to thrive during the relaxation season, as indicated by relatively higher proportions of initiation rates, active events, and volume (Figure 3.11a–$c_{1\text{-}3}$). Among these, ACME LHEs exhibit the most pronounced seasonality (Figure 3.11$a_{1\text{-}4}$). While initiation rates remain relatively steady throughout the year, over 20% of events initiate in June, with half of these forming independently (Figure 3.11a_1). This finding aligns with Dilmahamod et al. (2022), who identified June as the peak month for ACME formation. Event duration gradually increases from April to July, then follows a decreasing trend until March (Figure 3.11a_2), a period corresponding to peak coastal upwelling (e.g., Pradhan et al., 2006). Volume peaks later, rising from June to November (Figure 3.11a_3), with intensity following a similar trend, increasing from June to January (Figure 3.11a_4). These patterns suggest that although the number of active

ACME LHEs decreases from June to March, those that persist tend to increase in volume and intensity, particularly during the relaxation season.

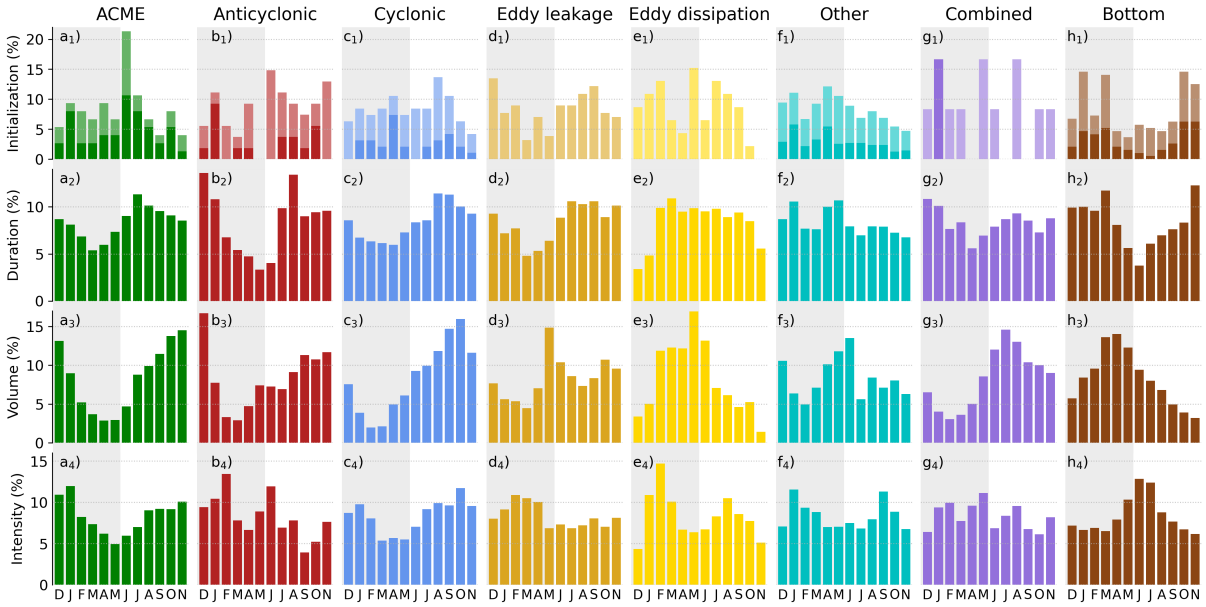


Figure 3.11: Monthly cumulative distribution of key metrics per LHE category. (a-h_1) Day of initialization; (a-h_2) duration, which is representative of the proportion of active events; (a-h_3) volume; and (a-h_4) median volume-weighted daily intensity. Lighter colors in (a-h_1) represent proportion of LHEs associated with pre-existing events. Values are expressed as percentage relative to the total of each LHE category. Shaded area from December to May represents the upwelling season, while non-shaded area from June to November represents the relaxation season.

Anticyclonic LHEs share some seasonal patterns with ACMEs. Event initiation peaks in June, but all of these originate from pre-existing conditions (Figure 3.11b_1). Although with a delay of one to two months, their duration follows a similar pattern, peaking in August and December. Volume peaks concurrently with duration in December (Figure 3.11b_3). However, intensity displays a less consistent pattern, peaking in winter like ACMEs but fluctuating erratically throughout the year (Figure 3.11b_4).

For Cyclonic LHEs, all key characteristics peak between August and October (Figure 3.11$c_{1\text{-}4}$). Initiation rates are evenly distributed across the year, although a clearer pattern emerges when considering independently initiated events, which peak in April (Figure 3.11c_1). Event duration peaks in August, while volume and intensity peak two months later, in October, indicating concurrent growth and intensification.

”Eddy leakage” and ”eddy dissipation” LHEs exhibit random initiation patterns but more defined trends in duration and volume (Figures 3.11d–$e_{1\text{-}3}$). ”Eddy leakage” LHEs maintain high duration from June to December–when most eddy LHEs are active–while their volume peaks sharply in May. In contrast, ”eddy dissipation” LHEs maintain high duration from February to October, with peak volume occurring from February to May. Intensity values for both categories peak in February, aligning with those of ACMEs and Anticyclonic LHEs (Figures 3.11d–e_4), their main contributors (Figure 3.7a).

In contrast to all other categories, ”other” LHEs are primarily initiated during the upwelling season (Figure 3.11f_1). These events show the least pronounced seasonal variation in duration (Figure 3.11f_2), but their volume increases steadily over the four months preceding its peak in

June (Figure 3.11f$_3$). Their intensity remains relatively stable, with minor peaks in January and September (Figure 3.11f$_4$).

"Combined" LHEs display a highly irregular initiation pattern, reflecting their smaller number (Figure 3.11g$_1$). Nevertheless, their duration shows a subtle seasonal variation, peaking in winter and late summer (Figure 3.11g$_2$). Volume follows a distinct Gaussian distribution, reaching maximum values in July and remaining high throughout the relaxation season (Figure 3.11g$_3$). In contrast, intensity values remain evenly distributed throughout the year (Figure 3.11g$_4$).

"Bottom" LHEs are primarily initiated in January, March, October, and November (Figure 3.11h1). Interestingly, most events formed between April and September are linked to pre-existing "bottom" events (Figure 3.7a), suggesting significant fragmentation during these months. Duration peaks in March and November, while volume rises and reaches its highest during the upwelling season (Figure 3.11h2-3). In contrast, intensity peaks in June and July (Figure 3.11h$_4$), clearly diverging from initiation and duration patterns.

3.4.4 Temporal evolution and statistics of LHEs

Previous analyses suggest that LHEs can experience significant changes in shape and intensity over time. To better understand the dynamics of these changes, we herein analyze the temporal evolution of key characteristics (Figure 3.12). This analysis is complemented by the statistical distribution of these characteristics, shown in Figure 3.13. For reference, a summary of the median metrics for each category is provided as supplementary material (Table A.1).

"Combined" LHEs are the most persistent among all categories, with 25% of events lasting up to nine months (Figure 3.12a3) and a median lifespan of four months (Figure 3.13a). ACME LHEs are the second longest-lived, with a median lifespan of almost two months. "Eddy dissipation" LHEs follow, with a median lifespan of 41.5 days and 25% of events persisting for nearly three months. Interestingly, "eddy dissipation" events often outlive Cyclonic and Anticyclonic LHEs, highlighting an important pathway for the redistribution of hypoxic conditions across the region. Other categories, such as "eddy leakage," "bottom," and "other" LHEs, tend to transform or dissipate quickly, with fewer than 20% persisting more than two months (Figure 3.12a2-3).

"Combined" LHEs also dominate in terms of volume, with a median daily volume four times greater than ACME LHEs (Figure 3.13b) and 25% of their population exceeding 1,500 km^3 ten months after initialization (Figure 3.12b$_3$). Eddy LHEs initiate with much smaller volumes but grow steadily over time, with ACME LHEs increasing to ≈280 km^3 within the initial seven months, while Cyclonic LHEs stabilize at around 100 km^3 two months after initiation. Anticyclonic LHEs exhibit slower initial growth but experience a significant volume increase when accounting for the 10% of events that remain active for at least six months. In contrast, dissipative categories like "eddy leakage" and "eddy dissipation" LHEs maintain relatively low volumes throughout their lifetimes, though "eddy leakage" LHEs experience a slight growth during the two initial months (Figure 3.12b$_2$). "Other" LHEs display the lowest and most stable volumes among all categories, while "bottom" follows a similar pattern but experiences a small growth during the five initial months (Figure 3.12b$_3$).

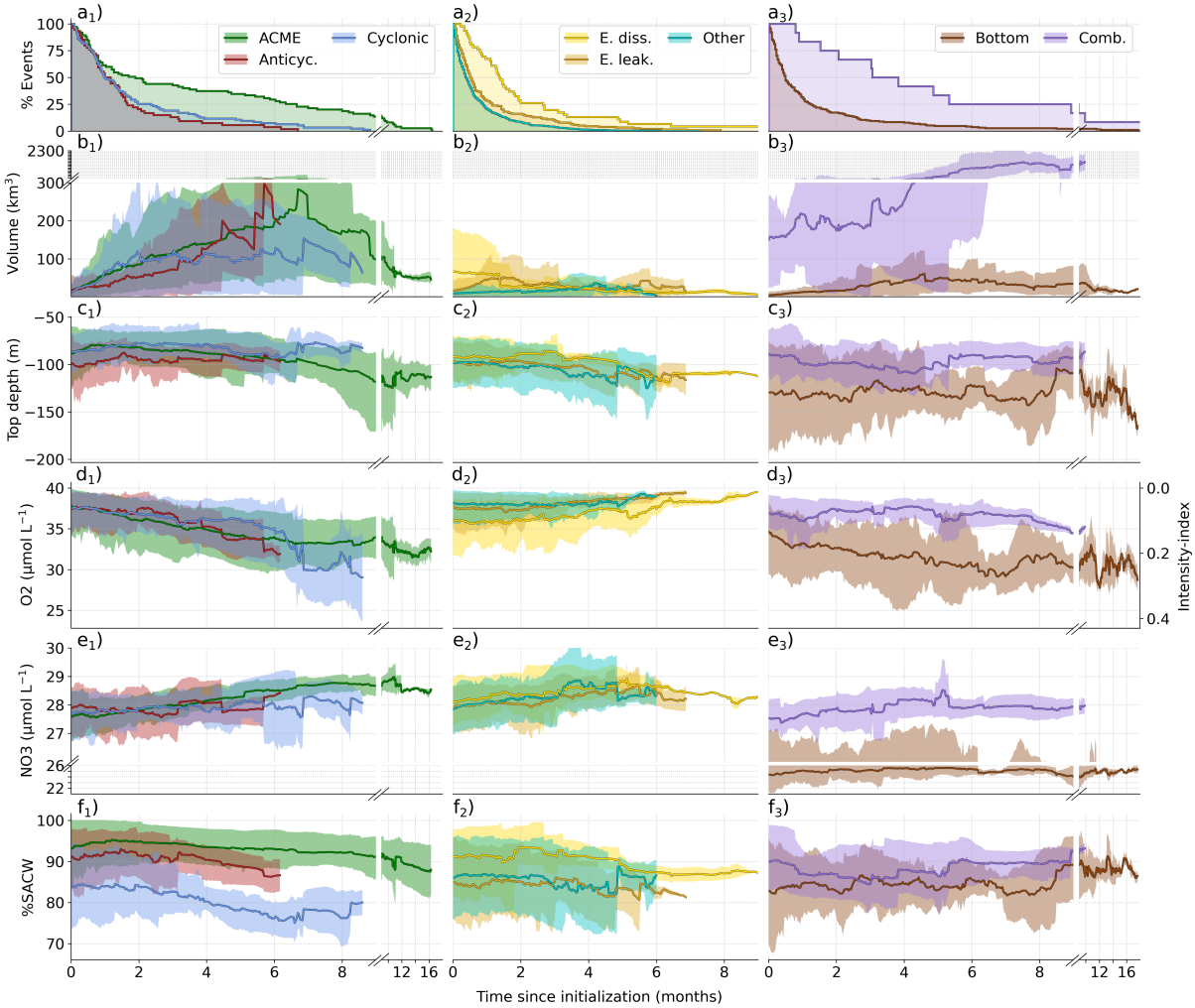


Figure 3.12: Temporal evolution of key metrics per LHE category. Evolution is computed relative to the initiation date of each LHE. Except for ($a_{1\text{-}3}$), which represent the cumulative distribution of events in respect to age, solid lines and shaded areas from ($b_{1\text{-}3}$) to ($f_{1\text{-}3}$) represent the mean and the interquartile range between the 10th and 90th percentiles, respectively. Panels ($d_{1\text{-}3}$-$f_{1\text{-}3}$) refer to volume-weighted daily means. The horizontal axis is divided into two segments, with greater emphasis on the initial 9 months. Vertical axis is also split into two sections in ($b_{1\text{-}3}$) and ($f_{1\text{-}3}$) to enhance clarity. Note the second y-axis used in ($e_{1\text{-}3}$) to illustrate the corresponding mean intensity-index.

Patterns in the evolution of mean vertical extent closely resemble those observed for volume, except for ”combined” LHEs, which maintain a relatively stable vertical extent throughout their lifetime (Figure A.1a). This stability suggests that horizontal expansion, rather than vertical growth, primarily drives their volume, whereas the opposite is true for eddy LHEs. ACME LHEs display the highest median vertical extent (35.6 m), with maximum values exceeding 80 m (Figure 3.13c). ”Combined” LHEs follow with a median of 24 m, though their maximum vertical extent remains below 40 m. Anticyclonic, Cyclonic, ”eddy leakage” and ”eddy dissipation” LHEs exhibit similar median values of ≈18 m and maximum values reaching 70 m. ”Bottom” LHEs stand out as the less expressive, reinforcing their limited impact in the water column.

Except for ”bottom” LHEs, most categories exhibit a mean top depth between ≈80 and 120 (Figure 3.12c). ACME and Cyclonic LHEs typically subduct over time, with ACME LHEs reaching a mean top depth of -120 m one year after initialization. In contrast, Anticyclonic LHEs exhibit more stable and consistently deeper top depths throughout their lifetimes, suggesting distinct dynamics between these types of eddies (Figure 3.12c_2). ”Eddy leakage”, ”eddy dissi-

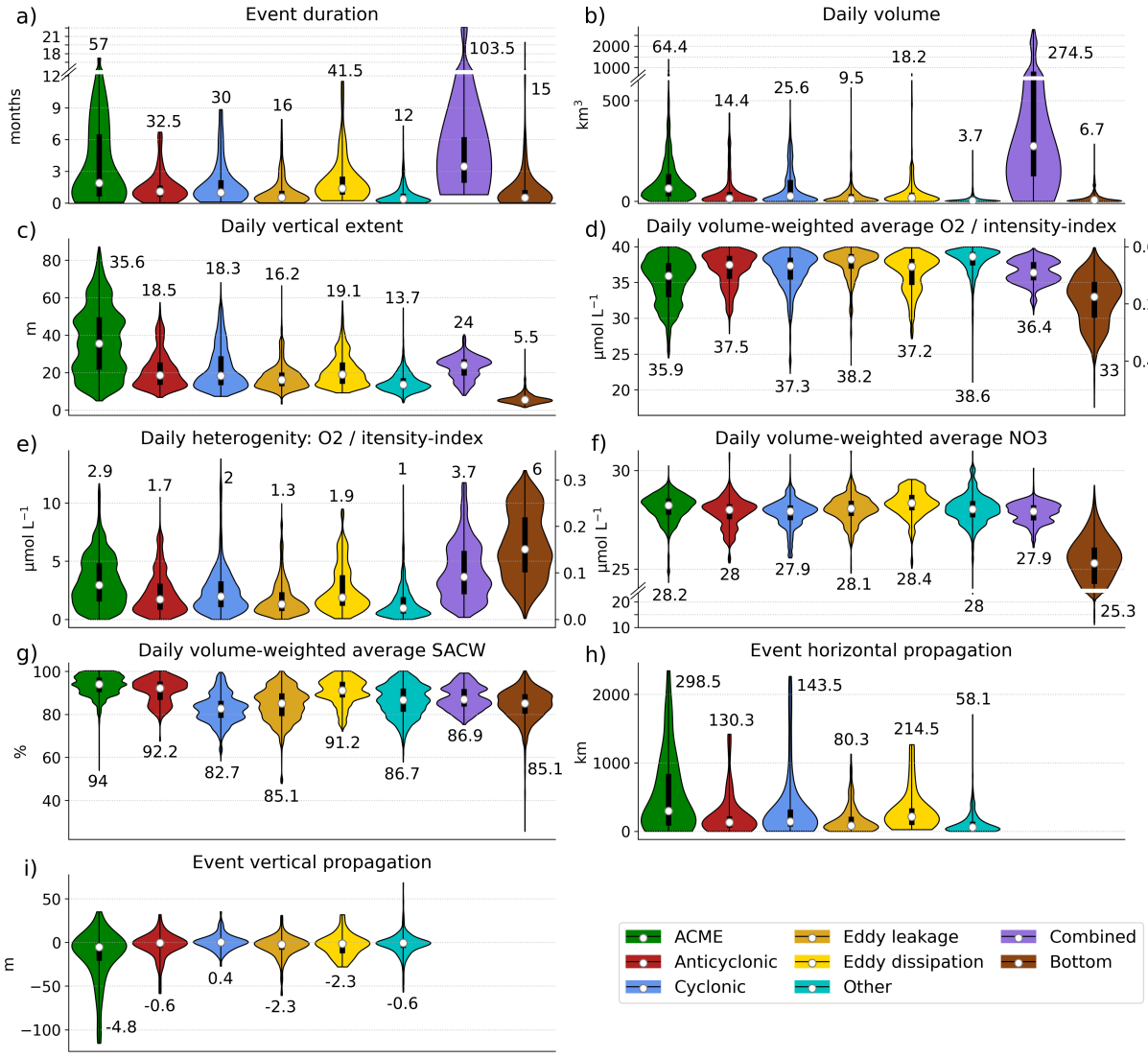


Figure 3.13: Violin plot for key metrics per LHE category. Medians are represented by white circles, with values indicated near each category. Black bars indicate the interquartile range from the 25th to the 75th percentile. In panel (a), median values are expressed in days. In panels (d) and (e), the median values refer to O_2 concentrations. Note that vertical axis in (g) is inverted.

pation" and "other" LHEs also show a general deepening trend, though "other" LHEs display a broader daily mean variability (Figure 3.12c$_2$). While "combined" LHEs maintain relatively shallow depths, "bottom" LHEs are significantly deeper (Figure 3.12c$_3$, which is likely due to their limited vertical extent and confinement to the sloping bathymetry.

Regarding the volume-weighted O_2 concentrations, "bottom" LHEs exhibit the lowest median values and daily means (Figures 3.13d and 3.12d$_3$). Nevertheless, eddy LHEs show the most pronounced declining rates (Figure 3.12d$_1$). These LHEs show similar initial O_2 levels but diverge after 1.7 months, with ACME LHEs experiencing a steady decline up to eight months, Anticyclonic LHEs showing sharper drops after four months, and Cyclonic LHEs reaching the lowest O_2 levels among eddy LHEs after seven months. In contrast, "eddy dissipation", "eddy leakage" and "other" LHEs maintain higher and more stable O_2 concentrations. Notably, "eddy dissipation" events initiate with much lower O_2 levels but maintain a similar positive O_2 rate as "eddy leakage" and "other" LHEs, explaining their longer life expectancy (Figure 3.13a).

Events within these three categories tend to terminate with mean O_2 concentrations near the hypoxic threshold, which also explains the very low percentage of transformed events (Figure 3.7a). ”Combined” LHEs sustain relatively high and stable O_2 concentrations throughout their lifetimes, whereas ”bottom” LHEs exhibit a general decreasing trend during the first six months, marked by the highest variability (Figure 3.12d_3).

Although these patterns reflect the mean daily evolution of O_2 within LHEs, they differ from true O_2 respiration rates because of their possible expansion, which recruits less hypoxic waters and dilutes mean O_2 concentrations. Such dilution is reflected in the daily mean heterogeneity, which show a similar but inversely increasing rate (Figure A.1b). ”Bottom” LHEs exhibit the highest daily median heterogeneity values, while ”other” LHEs display the lowest (Figure 3.13e).

In terms of NO_3 concentrations, ACME LHEs exhibit the most significant increase, reaching maximum values 10 months after initialization (Figure 3.12e_1). Cyclonic LHEs exhibit a similar initial trend but stabilize after four months. Concurrent increasing and decreasing trends are also observed for PO_4 and POC, respectively (Figure 3.12e_1 and c_1), suggesting enhanced remineralization of organic matter within ACME and Cyclonic LHEs. In contrast, Anticyclonic LHEs maintain relatively stable NO_3 concentrations over time, with variations likely related to the decline of active events (Figure 3.12a_1).

”Eddy leakage”, ”eddy dissipation” and ”other” LHEs show slight NO_3 increases early on, followed by stabilization and eventual declines as they mix with surrounding waters near termination (Figure 3.12e_2). In contrast, ”combined” LHEs display modest increases in NO_3 early in their lifetimes, whereas ”bottom” LHEs exhibit the lowest NO_3 concentrations. Elevated NH_4 levels in ”bottom” LHEs (Figure A.1e_3) strongly suggest that concurrent low NO_3 concentrations are linked to denitrification. These results align with previous studies that reported high dinitrogen fixation under hypoxic conditions on the continental shelf of Mauritania (Gier et al., 2017), and NO_3 loss under anoxic conditions ($O_2 < 1$ µmol L^{-1}) on the shelf of Senegal (Machu et al., 2019).

Most LHE categories show a general decline in daily volume-weighted %SACW over time (Figure 3.12f), likely due to mixing or incorporation of a more diluted SACWcv variety. ACME LHEs maintain the highest %SACW, decreasing from 95% to 91% over 10 months (Figure 3.12f_1). Anticyclonic LHEs follow a similar pattern with lower values and a steeper decline after two months. Cyclonic LHEs have the lowest %SACW, initiating at 82.7% and dropping to ≈76% within six months. ”Eddy dissipation” LHEs have higher %SACW than ”eddy leakage” and ”other” LHEs (Figure 3.12f_2), reflecting their primary origin from ACME LHEs (Figure 3.7a). ”Bottom” and ”combined” LHEs exhibit more erratic %SACW trends (Figure 3.12f_3), with ”bottom” LHEs showing the lowest values detected in hypoxic waters (SACW < 30%; Figure 3.13g).

As previously noted in Figure 3.8a, ACME LHEs demonstrate the greatest horizontal propagation, with a median distance of 298.5 km and a maximum of 2346 km, followed by ”eddy dissipation” LHEs with a median of 214 km (Figure 3.13h). Cyclonic LHEs have a lower median (143.5 km) but show comparable maximum propagation (2264 km). Anticyclonic LHEs rank next, followed by ”eddy leakage” and ”other” LHEs.

Vertically, ACME LHEs exhibit the most pronounced displacement, with a median and maximum subduction of 4.8 m and 116 m, respectively (Figure 3.13i). ”Eddy leakage” and ”eddy

dissipation" LHEs show similar median subduction values (2.3 m), although subduction of "eddy leakage" LHEs occasionally exceed 50 m. Anticyclonic and "other" LHEs have median vertical propagation of -0.6 m, though "other" LHEs exhibit a broader range (-57 m to 69 m). Cyclonic LHEs show slight uplift (median of 0.4 m) with minimal variation compared to other categories.

3.5 Discussion

Our results show that hypoxic events forming the sOMZ are associated with a range of processes. The Lagrangian analysis of these events provide a synoptic perspective that differs significantly from previous studies, which were largely based on sparse *in-situ* observations. In this context, we aim to discuss and compare our results with past studies, highlighting the added insights from our approach.

3.5.1 Relation between water masses and hypoxic events

Given that ETNA's central water masses primarily consist of NACW and SACW (Tomczak, 1981; Stramma et al., 2005; Pastor et al., 2008), it is unsurprising that most hypoxic waters detected in the upper 200 m are associated with the diluted SACWcv variety. However, the detection of a distinct, fresher, and colder hypoxic volume maximum indicates the presence of a purer SACW variety (Figure 3.5a), which is typically linked to higher O_2 concentrations (Peña-Izquierdo et al., 2012). Such low salinity at this density range is also observed near the northeastern Brazilian coast (Figure 2.10), aligning with past studies that highlight the role of eastward-flowing equatorial currents in ventilating upper central water masses in the ETNA (Elmoussaoui et al., 2005; Stramma et al., 2005; Karstensen et al., 2008; Brandt et al., 2010; Peña-Izquierdo et al., 2012; Duteil et al., 2014; Hahn et al., 2014; Hahn et al., 2017).

Such hypoxic SACW masses are largely concentrated in swirling patterns offshore (Figure 3.5e), which are mainly associated with ACMEs (Figure A.2d). Their presence along the continental shelf and slope, where the PUC transports SACW-rich waters (Peña-Izquierdo et al., 2012; Klenz et al., 2018), also suggest strong modification of typical O_2 concentrations near the bottom (Thomsen et al., 2019). As the PUC interacts with slopping bathymetry and generates ACMEs (Dilmahamod et al., 2022), these waters become trapped within these eddies, which further intensify hypoxic conditions as they propagate westward (Fiedler et al., 2016).

These findings are consistent with previous observations of low-oxygen ACMEs characterized by distinct low-salinity and low-temperature cores (e.g., Karstensen et al., 2015; Fiedler et al., 2016; Karstensen et al., 2017; Pietri & Karstensen, 2018). Although these eddies generally maintain their hydrographic properties over time (Karstensen et al., 2015; Fiedler et al., 2016), minor increases in salinity suggest some mixing (Karstensen et al., 2017). Our results also show a general decrease in %SACW across all eddy types, though this is likely enhanced by the recruitment of more diluted waters as eddy LHEs expand (Figure 3.12f_1). Notably, hypoxic SACW masses tend to dissipate near the CVFZ (Figure 3.5f), though ACME trajectories persist beyond this point (Figure 3.8a). Similarly, Schütte, Brandt, and Karstensen (2016) found that

anticyclones experience the highest dilution of SACW when passing through the CVFZ (30%), followed by cyclones (17%) and ACMEs (6%), thus suggesting a varying degree of coherence between eddy types.

Although ACMEs have been more frequently studied in the ETNA, two low-oxygen cyclonic eddies were also sampled shortly after formation (Karstensen et al., 2015; Devresse et al., 2022). Despite sharing similar SACWcv characteristics (see Figure A.6 for water mass characteristics within one of them), they exhibited contrasting higher (Karstensen et al., 2015) and lower (Devresse et al., 2022) temperature and salinity values compared to surrounding waters. Minimum O_2 concentrations of 8.23 µmol L^{-1} were found within one of them (Krahmann, 2022), suggesting the trapping and subsequent intensification of pre-existing hypoxic conditions upon formation near the continental shelf break, where similar temperature and salinity values were observed. Indeed, cyclonic eddies formed in upwelling regions often trap waters rich in nutrients and organic carbon (Chenillat, Blanke, et al., 2015; Lovecchio et al., 2022), playing an important role in fertilizing the open ocean (Chenillat, Blanke, et al., 2015; Lovecchio et al., 2018). Given the seasonal variability of boundary currents and water mass characteristics in the ETNA (Klenz et al., 2018), cyclonic eddies are likely to contain varying proportions of SACW.

Indeed, Cyclonic LHEs show the greatest variation in %SACW among all eddy types (Figure 3.13g). They also exhibit the lowest mean values (Figures 3.12f_1), even when considering both hypoxic and ventilated eddies (Figure A.3b). In contrast, Schütte, Brandt, and Karstensen (2016) reported higher SACW content in cyclonic eddies than in anticyclones. This discrepancy likely stems from methodological differences: While we account for all eddies detected by the AMEDA algorithm, the earlier study could only account for the vertical profiles available from observations (i.e., Argo floats, ship-based CTDs and gliders), which can lead to a sampling bias.

Surprisingly, ”bottom” LHEs have relatively low %SACW (Figure 3.12f_3), despite their exposure to pure SACW transported by the PUC (Figure 1.7). These events, which follow the sloping bathymetry to depths exceeding 200 m, are likely influenced by opposing currents transporting NACW-rich waters equatorward (Peña-Izquierdo et al., 2012, 2015; Klenz et al., 2018). Although more ventilated than SACW, these waters experience increased oxygen consumption due to the remineralization of organic matter accumulating on the seabed (Brandt et al., 2015; Machu et al., 2019; Thomsen et al., 2019; Tall et al., 2021), explaining the highest dispersion of %SACW mean values (Figure 3.13h).

3.5.2 Eddies as vectors, intensifiers and suppliers of hypoxic conditions

Collectively, eddy-related LHEs are the primary contributors to hypoxic conditions (Figures 3.9a-e), accounting for 52% of the total hypoxic volume (Figure 3.10a-e). Eddy LHEs are most intense in autumn and winter, particularly in the offshore region north of Cabo Verde, where near-anoxic conditions are associated with ACME and Cyclonic LHEs (Figure A.5). It is also in this region that maximum vertical extents are observed, with median values easily exceeding 80 m (Figure 3.3f). These results align with past studies, who reported $O_2 < 3$ µmol L^{-1} and maximum thickness exceeding 150 m depth in two ACMEs transiting through the same region in winter (Karstensen et al., 2015; Karstensen et al., 2017).

While most ACME LHEs form independently, Anticyclonic and Cyclonic LHEs form mostly from pre-existing conditions (Figure 3.7). Regardless of their origin, O_2 concentrations tend to decrease over time (Figure 3.12d_1). When accounting for eddy LHEs active for at least 30 days and for periods in which minimum O_2 concentrations generally decline, ACME and Cyclonic LHEs are characterized by mean and maximum O_2 consumption rates of 0.11 and 0.32 µmol L^{-1} d^{-1}, respectively, while Anticyclonic LHEs have lower rates of 0.08 and 0.13 µmol L^{-1} d^{-1} (Figure 3.14). These values align remarkably well with past studies: Karstensen et al. (2015) reported maximum respiration rates exceeding 0.15 µmol L^{-1} d^{-1} during the first 8 months of a cyclonic eddy, while Fiedler et al. (2016) observed a mean rate of 0.26 µmol L^{-1} d^{-1} in an ACME aged 1–8 months. Conversely, Karstensen et al. (2017) documented a slower consumption rate of 0.08 µmol L^{-1} d^{-1} in an ACME sampled between 4.8 and 6.9 months. As also observed in our estimates, these differences emphasize that O_2 consumption rates vary even within eddies of the same type, depending on their age at the time of observation. Ultimately, such variations in O_2 consumption are linked to fluctuations in upwelling intensity (Sweeney et al., 2003; Mouriño-Carballido & McGillicuddy, 2006; McGillicuddy, 2016), which drive variability in export production and the subsequent remineralization of organic matter within the eddy interior.

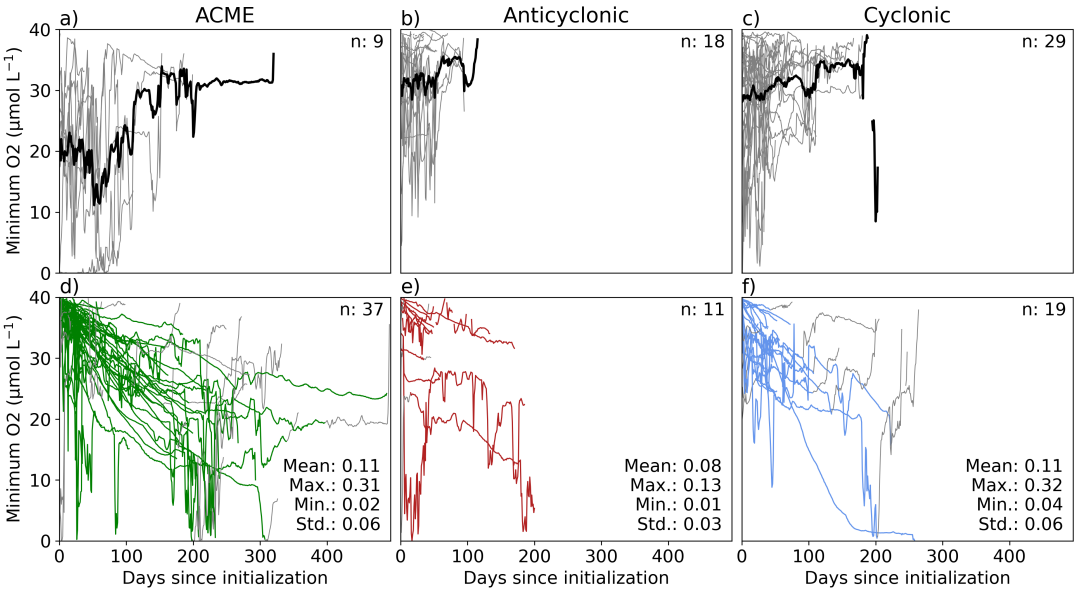


Figure 3.14: O_2 consumption rates for eddy LHEs. Calculation is based on the daily evolution of minimum O_2 concentrations within LHEs with lifetime > 30 days. Following Karstensen et al. (2015), only those in which minimum O_2 concentrations generally decline are accounted for (bottom panels), while the others are discarded (upper panels). Colored lines in bottom panels indicate the period used for the calculation.

By compiling vertical profiles taken within 17 ACMEs and 10 cyclonic low-oxygen eddies, Schütte, Karstensen, et al. (2016) estimated a similar mean consumption rate for cyclones (≈0.10 ± 0.12 µmol L^{-1} d^{-1}), but a slightly higher rate for ACMEs (0.19 ± 0.08 µmol L^{-1} d^{-1}). Despite this, their maximum rates remain consistent with our estimates. Several factors may account for these differences: (i) the use of distinct methodologies across studies; (ii) our focus on hypoxic events, which may exclude early phases when eddies are not yet hypoxic but potentially more productive (McGillicuddy, 2016); and (iii) observational bias, specifically the tendency to target

the sampling of intense low-oxygen eddies during oceanographic campaigns (Frenger et al., 2018).

Although anticyclonic eddies in the ETNA are typically associated with positive oxygen anomalies (Schütte, Karstensen, et al., 2016), 5% of the LHEs detected in our study were linked to these features. These events are typically short lived (Figures 3.12a$_1$) and have low propagation distances, intensity and volume (Figures, 3.8b, 3.9b and 3.10b), suggesting an opportunistic nature, where pre-existing hypoxic waters are trapped and rarely intensify as they evolve (Figure 3.14b,e).

Similarly to some of the anticyclonic eddies detected in our study, Kolodziejczyk et al. (2018) observed low-intensity hypoxic conditions in the form of a thin, shallow layer just below the mixed layer in an anticyclonic eddy. The surface-intensified nature of the eddy, coupled with the typical upwelling conditions at the place and time of formation (e.g., Pradhan et al., 2006; Lathuilière et al., 2008; Pastor et al., 2008), suggest that high surface productivity detected within the eddy (Brandt & Krahmann, 2020) likely resulted from the trapping (Moore et al., 2007; Gaube et al., 2014) and transport of nutrient-rich waters in the eddy's interior (Abernathey & Haller, 2018; Denes et al., 2022; Jones-Kellett & Follows, 2024), resulting in the consumption of O_2 due to the remineralization of sinking organic matter below the mixed layer (Fiedler et al., 2016; G. Fischer et al., 2016). Indeed, Lovecchio et al. (2018) showed that anticyclones formed in the region effectively transport waters rich in organic carbon offshore. However, recent reports of anoxic conditions near the eddy formation site (Machu et al., 2019; Tall et al., 2021) suggest that hypoxic waters may also have been trapped during the eddy's formation.

Our results also show that eddy LHEs not only intensify but also subduct as they propagate westward (Figure 3.12c$_1$). For those that remain active for at least 30 days, ACMEs, Anticyclonic and Cyclonic LHEs exhibit average subduction rates of 0.10, 0.05, and 0.04 m d^{-1}, respectively, with maximum subduction rates reaching 0.98, 0.64, and 0.83 m d^{-1}. However, eddy LHEs propagating south of Cabo Verde do not to experience such a pronounced deepening pattern as those moving north of the archipelago (Figure 3.3g). Given that the CVFZ is located further offshore in the southern region (Figure 3.5), this disparity suggests that eddies subduct as they cross the front.

Indeed, past studies have shown that eddy subduction along isopycnals is a recurrent phenomenon (e.g., Laxenaire et al., 2018; Ioannou et al., 2022), with important implications to the distribution of biogeochemical tracers in the ocean's interior (Frenger et al., 2018). In the ETNA, this has been especially evident when following tracers such as PV (Dilmahamod et al., 2022) or O_2. One cyclone and one ACME exhibited a deepening of the shallowest hypoxic O_2 concentrations from approximately 57 to 83 meters over two months (0.41 m d^{-1}; Karstensen et al., 2015), and from approximately 30 to 72 meters over the first six months (0.23md^{-1}; Karstensen et al., 2017), respectively. In one of the eddies, the subduction was only evident when it approached the typical location of the CVFZ, further suggesting that the front can influence the behavior of transiting eddies.

To assess the overall impact of eddy-related LHEs on mean O_2 concentrations and compare them with the other categories, we calculated the contributions of each LHE category to the mean O_2 concentrations both spatially and along depth (Figure 3.15). Here, eddy-related LHEs are

grouped into one category. Maximum values of around -7 µmol L^{-1} are observed at the continental margin (Figure 3.15b), mainly due to the combined influence of "combined" and "bottom" LHEs (Figure 3.15e, g). However, the overall impact of LHEs on mean O_2 concentrations does not exceed -2.4 µmol L^{-1} (Figure 3.15h). As expected, eddy-related events have the most significant impact (Figure 3.15h), particularly in the offshore region where maximum reductions of ≈-5 µmol L^{-1} are observed near Cabo Verde (Figure 3.15c). "Combined" LHEs dominate the coastal region, whereas "other" LHEs have an negligible impact and "bottom" LHEs are limited to the continental margin (Figure 3.15). Despite this, the combined contribution of LHEs to mean O_2 concentrations in the ETNA is minimal (Figure 3.15d). However, it is important to note that these findings are constrained by our methods, i.e., the usage of a fixed threshold of 40 µmol L^{-1}. For example, eddies not deemed as hypoxic can still contribute negatively to the mean O_2 concentrations, as long as O_2 concentrations are lower than the mean. Naturally, increasing this threshold to 60 µmol L^{-1} (Köhn et al., 2022) would result in a greater contribution to the overall O_2 concentrations.

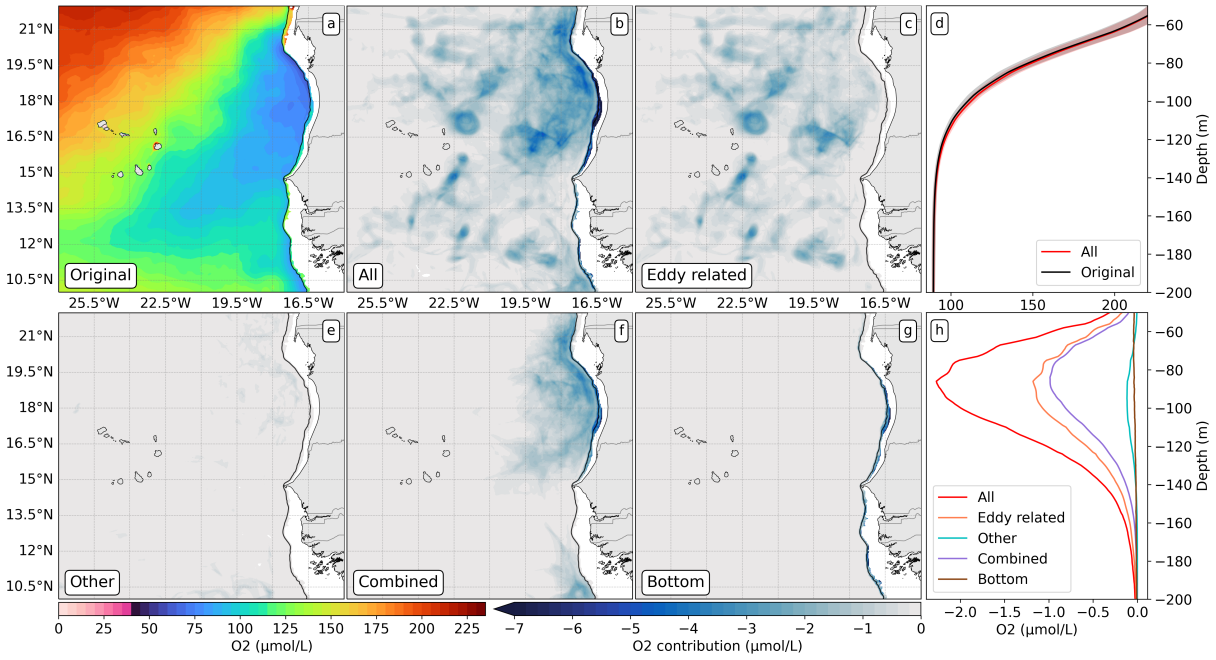


Figure 3.15: Contribution of each LHE category to the mean O_2 concentrations. (a) Mean O_2 concentrations between 50 and 150 m depth. (b) Difference between the original mean O_2 and the mean calculated by masking hypoxic grid cells. Individual contributions of (c) eddy-related, (e) "other", (f) "combined" and (g) "bottom" LHEs to the mean O_2 anomaly. (d) Mean O_2 concentrations along depth. (e) Individual contributions of each LHE category to the mean O_2 concentrations along depth.

Using a box model approach, Schütte, Karstensen, et al. (2016) estimated that ACMEs and cyclonic eddies contribute to a mean O_2 decline of 7 µmol L^{-1} between 50–150 m, with a peak decrease of 16 µmol L^{-1} at 100 m depth. Although their estimate is significantly higher than ours, the authors noted that their values may still be conservative, as they detected only 2 low-oxygen ACMEs per year propagating from the upwelling region to offshore and dissipating there. Given the methodological differences between the two studies, these comparisons should therefore be approached with caution.

One of the most relevant findings in our study is the frequent occurrence of "eddy-leakage" and "eddy-dissipation" events, which although speculated in the past (Löscher et al., 2015), have,

to our knowledge, not yet been reported. While a limited proportion of these events evolve into new LHEs, their dissipative nature often leads to further splitting (Figures 3.7a) as they decay and mix with surrounding waters (Figure 3.12d_2). In doing so, they further contribute to the dilution of SACW and to the formation of the regional SACWcv variety, as evidenced by the higher concentration of seemingly chaotic trajectories in the SACWcv-dominated region (Figure 3.8d,e). This highlights their role as transitional stages in the life cycle of low-oxygen eddies, acting as pathways for O_2 exchange and water mass transformation in the ETNA.

3.5.3 Origin of ”combined” and ”bottom” LHEs

Unlike other events, which are primarily shaped by a single dominant process, ”combined” events are defined by their complex nature, involving multiple processes that share adjacent cells with each other. This complexity results in the absence of a distinct center of mass and well-defined propagation patterns (e.g., Figure 3.6b,c). Instead, their dynamics are marked by alternating periods of expansion–as they are advected by currents and merge with other events–and contraction or fragmentation–driven by eddy trapping and stirring. These events are both long-lived and spatially extensive, covering a mean area of 12,175 km^2 (Table A.1) and accounting for 40% of the total hypoxic volume (Figure 3.10g). Although ”combined” LHEs occasionally extend offshore, they are mostly constrained to the coastal region (Figure 3.8g) and reach highest volume during the relaxation season (Figure 3.11g_3).

It is also in the relaxation season that hypoxic conditions are most intense at the bottom of the continental margin (Figures 3.4c,d and 3.11h_4). This bottom intensification aligns with previous studies reporting the lowest O_2 concentrations at the continental margin during summer (Dale et al., 2022), even as O_2 consumption rates remain similar to those observed in spring (Dale et al., 2014a). Also in summer, observations of hypoxic waters extending tens of kilometers offshore have been attributed to the re-suspension of oxygen-depleted, particle-rich bottom waters (Gier et al., 2017; Thomsen et al., 2019). Glider observations revealed that these hypoxic waters were not constrained to a specific location; instead, they covered a broad meridional extension along the coast (Figure A.7), sharing similar characteristics as those observed for ”combined” LHEs.

The absence of upwelling-favorable conditions in summer and autumn increases stratification, at the same time that the PUC shoals and likely reduces the ventilation of central water masses along the coast (Klenz et al., 2018). Given their close proximity and tendency to merge, ”combined” and ”bottom” events are likely to be influenced by such seasonal stratification and surfacing of the PUC. This is particularly evident in ”combined” LHEs, where stable O_2 concentrations and reduced SACW content (Figure 3.12d_3 and f_3) highlight the predominance of physical (remote) drivers (Thomsen et al., 2019). Conversely, persistently low O_2 and NO_3 levels in ”bottom” LHEs (Figure 3.12e_3) suggest stronger decoupling between water mass properties and local biochemical processes.

Given their spatial extent and duration, it might be expected that ”combined” LHEs would have been observed in the past. However, a limited number of campaigns conducted in the ETNA took place during the relaxation season (Schütte, Karstensen, et al., 2016), when these events are larger (Figure 3.11g_3). The tendency to target low-oxygen eddies during these campaigns

also introduces a sampling bias, potentially under-representing other types of hypoxic events. Untargeted glider deployments, for instance, have revealed previously undocumented hypoxic features–capturing a low-oxygen anticyclonic eddy for the first time (Kolodziejczyk et al., 2018) and detecting hypoxic O_2 concentrations extending offshore from the continental margin (Figure A.7).

3.5.4 Potential impacts on ecosystems

Hypoxic conditions impact marine life and biogeochemistry in various ways, depending on event characteristics, geography, and ecosystems involved (Gruber et al., 2021). For example, plankton trapped in low-oxygen eddies concentrate in surface layers, becoming more vulnerable to predators that thrive on increased biomass (Stramma, Prince, et al., 2012; Hauss et al., 2016). Conversely, some zooplankton and microbial species benefit from these low-oxygen environments, which act as offshore-moving niches for hypoxia-tolerant organisms (Löscher et al., 2015; Grundle et al., 2017; Christiansen et al., 2018). For benthic and sessile communities, exposure to hypoxic eddies can last days to weeks, with recurrence intervals influenced by regional dynamics. Episodic increases in O_2 respiration and limited ventilation (Chan et al., 2008; Machu et al., 2019), or advection of low-oxygen waters (Hernández-Miranda et al., 2010) can trigger abrupt events, sometimes causing mass mortality even among mobile species (Cockcroft, 2001; Grantham et al., 2004; Hernández-Miranda et al., 2010). Alternatively, seasonal hypoxia may persist for months (Siedlecki et al., 2015; Low et al., 2021; Tall et al., 2021; Kekuewa et al., 2022), though organisms facing such conditions often develop metabolic or physiological adaptations to endure low-oxygen environments (Levin et al., 2009; Gruber et al., 2021).

In the ETNA, the continental shelf and slope experience the highest frequency of hypoxic conditions, the longest local duration, and the shortest recurrence intervals (Figure 3.3c,d,e). While mass mortality of demersal fish has been observed in the region (Caverivière & Touré, 1990), these events remain largely undocumented (Machu et al., 2019) and no comprehensive study has yet explored their full extent. Similarly, impacts on biogeochemical processes are limited to a few studies suggesting potential effects on the marine nitrogen cycle (Dale et al., 2014a; Yücel et al., 2015; Sokoll et al., 2016; Gier et al., 2017; Dale et al., 2022). Given the ongoing deoxygenation trends in the region (Stramma, Johnson, et al., 2008; Stramma, Prince, et al., 2012; Brandt et al., 2015), our results highlight the need for further research to better understand and predict their ecological and biogeochemical consequences.

Offshore areas experience hypoxic conditions less frequently and with longer recurrence intervals (Figure 3.3c,e). However, eddies often transport and intensify hypoxic conditions as they move offshore (Figure 3.9a-c), leading to events with greater vertical extent and intensity (Figure 3.3f,h). At the same time, the trapping and transport of pre-existing hypoxic waters by eddies facilitates the import of oxygenated waters to the coastal region through stirring and eastward filaments (e.g., Frenger et al., 2018). This process was likely observed by Devresse et al. (2022), who reported an intense low-oxygen cyclone surrounded by oxygenated NACW close to the Mauritania coast. Although mean O_2 concentrations in the ETNA are generally

higher than in other OMZs (Karstensen et al., 2008), these dynamics make O_2 concentrations highly heterogeneous, varying abruptly both spatially and temporally (Figure 3.2).

Positioned at the interface between oxygen-rich NACW and oxygen-poorer SACWcv (Zenk et al., 1991; Schütte, Brandt, & Karstensen, 2016), the Cabo Verde Archipelago is significantly exposed to such O_2 fluctuations. In addition, its west-facing horseshoe layout acts as a natural barrier to westward-moving low-oxygen eddies, which often become stationary when intersecting the easternmost islands (Figure 3.8a-c), resulting in prolonged hypoxic events (Figure 3.3d). Indeed, Cardoso et al. (2020) demonstrated that these islands effectively block the westward propagation of eddies, causing deflection, merging, splitting, and even termination. Low-oxygen eddies have also been observed transiting less than 100 km north of the archipelago (Fiedler et al., 2016; Karstensen et al., 2017; Pietri & Karstensen, 2018), with undocumented mass mortality events possibly linked to their interaction with the islands (Karstensen et al., 2015). While the outer-facing coasts are particularly vulnerable to these events, the islands' shielding effect protects the inner-facing coasts where hypoxic conditions are rarely detected (Figure 3.3c). As a result, the vulnerability of ecosystems varies significantly between the two sides, potentially contributing to different species abundance on each side of the islands (Entrambasaguas et al., 2008).

3.5.5 Method limitations and caveats

To ensure that our findings are properly contextualized, it is important to address the limitations of the method employed for the identification and tracking of LHEs, as it carries inherent constraints that may influence the results. While the usage of a restrictive threshold facilitates comparison with previous studies in the ETNA (e.g., Karstensen et al., 2015; Schütte, Karstensen, et al., 2016), it may underestimate the duration, frequency and extent of hypoxic events relative to studies using a higher threshold (e.g., Gruber et al., 2021; Köhn et al., 2022). The categorization of LHEs also introduces some subjectivity, as it is not based on environmental parameters (e.g., Okubo-Weiss, Köhn et al., 2024) or event characteristics (Desmet et al., 2022). Nevertheless, our approach enables more precise associations with processes affecting LHEs throughout their lifetime, and facilitates the identification of relationships between events (Figure 3.7), albeit at the expense of reduced automation and reproducibility.

Another important aspect to consider is that by identifying and tracking hypoxic events based on a fixed threshold, the conservation of mass or the material coherence of the tracked features is not ensured. In this sense, LHEs are not necessarily constrained to follow water parcels, but rather to follow a biogeochemical condition (i.e., $O_2 < 40$ µmol L^{-1}). As such, the evolution of an LHE does not imply that the same water mass is being tracked over time. Instead, it reflects the spatial and temporal persistence of the hypoxic condition itself. While this approach offers a valuable ecosystem-oriented diagnostic, it lacks a dynamical perspective in terms of mass conservation. In contrast, a fully Lagrangian framework–such as the backward tracking of hypoxic water masses or the tracking of coherent eddies–would ensure a material perspective, more suitable for dynamical analyses. Such framework is explored in Chapters 4 and 5. Therefore, the current methodology provides an effective means of analyzing the spatial and temporal variability of

hypoxic conditions, but should not be interpreted as representing the evolution of a conserved water mass.

3.6 Summary and conclusions

Our results reveal that hypoxic events forming the sOMZ in the ETNA are characterized by a strong spatial and seasonal variability. The coastal region is primarily affected by ”combined”, ”other” and ”bottom” LHEs, while offshore regions are more susceptible to eddy LHEs. Although eddy LHEs mostly originate near the coast, they tend to intensify as they propagate westward, resulting in intense hypoxic conditions and greater vertical extent in the offshore region. Despite this, ”bottom” LHEs exhibit the most intense conditions, though they are confined to the continental margin and have limited impact on the water column. The only region not affected by hypoxic conditions is located in the wake Cabo Verde Islands. These islands act as an effective shield to the propagation of westward-propagating, low-oxygen eddies, which leads the most exposed islands and coasts to be vulnerable to long uninterrupted hypoxic events, while the inner-facing coasts remain largely unaffected.

Seasonally, the occurrence and intensity of hypoxic events vary, with offshore regions being more affected during autumn and winter due to the propagation of eddies. The coastal region experience higher intensity and volume in summer and autumn, particularly at northern latitudes. We hypothesize that this seasonal variability in coastal areas is linked to the combined effect of increased stratification and migration of the PUC to surface layers (Klenz et al., 2018). The specific mechanisms driving these hypoxic conditions are investigated in detail Chapter 4.

In terms of water masses, hypoxic conditions are primarily associated with SACWcv, which although spread across the entire domain, exhibit highest concentration near the Mauritania coast. In contrast, hypoxic SACW masses are mostly constrained to swirling patterns associated with ACMEs. Generally formed with more-oxygenated waters, ACMEs trap and transport these SACW waters offshore, leading to a gradual decrease of O_2 concentrations and ultimately reaching hypoxic concentrations en-route. Because of this, ACMEs are the only LHEs in which most events are formed independently.

While eddies have the largest impact on O_2 concentrations, non-eddy events also contribute to the sOMZ, having the potential to influence the formation of eddy LHEs by seeding them with pre-existing conditions. This is particularly evident for Anticyclonic and Cyclonic LHEs, though a considerable proportion of ACMEs also showed links to pre-existing conditions. Formed by the interaction of the PUC with slopping bathymetry, ACMEs are characterized by a low PV core originating from the bottom boundary layer (Dilmahamod et al., 2022). Since this bottom boundary layer is often hypoxic, such conditions likely shape initial O_2 concentrations within ACMEs, supporting earlier speculations that this mechanism can influence the formation of low-oxygen ACMEs (Schütte, Karstensen, et al., 2016). Mechanisms of low-oxygen ACME formation and their relation with bottom hypoxia are explored in detail in Chapter 5.

The lagrangian identification and tracking of hypoxic events in the ETNA provides a new perspective on their characteristics and distribution, which have been largely based on sparse

in-situ observations. These events pose serious risks to marine ecosystems, especially when compounded with stressors such as ocean acidification and marine heatwaves (Gruber et al., 2021). With climate change expected to amplify these stressors (Gruber, 2011), the knowledge of the mean state of the system is crucial to understand how hypoxic events may evolve in the region and thus better anticipate their ecological and biogeochemical impacts.

Chapter 4

Drivers of the shallow oxygen minimum zone off the northwestern African coast

4.1 Introduction

As demonstrated in the previous Chapter 3, the sOMZ exhibits a pronounced seasonal variability along the coastal region, closely following the dynamics of the Mauritanian-Senegalese upwelling system. This seasonal upwelling variability has long been recognized as a key modulator of regional hydrography, primarily by influencing boundary current dynamics (Elmoussaoui et al., 2005; Lázaro et al., 2005; Klenz et al., 2018), stimulating coastal primary productivity (Mittelstaedt, 1983; Pradhan et al., 2006; Lathuilière et al., 2008), and driving the offshore export and fertilization of the oligotrophic open-ocean (Pelegrí et al., 2006; Lovecchio et al., 2018).

In the ETNA, the upwelling season typically spans from winter to early summer, though its timing varies along latitude (Lázaro et al., 2005; Pradhan et al., 2006; Lathuilière et al., 2008). During this period, the coastal circulation features an equatorward surface jet and the subsurface PUC beneath the mixed layer (Barton, 1989; Klenz et al., 2018). In contrast, during the relaxation season, weakening of upwelling-favorable winds causes the PUC to migrate upward, ultimately manifesting as the so-called MC in surface layers (Mittelstaedt, 1991; Lázaro et al., 2005).

The PUC constitutes the primary pathway for the transport of SACW into the region (see Figure 1.7a; Voituriez & Chuchla, 1978; Barton, 1989; Elmoussaoui et al., 2005; Brandt et al., 2015; Peña-Izquierdo et al., 2015; Klenz et al., 2018). SACW is characterized by lower O_2 concentrations compared to the younger NACW found further north (Tomczak, 1981; Stramma et al., 2005). Nevertheless, as SACW is younger and more oxygenated than the older, regionally modified SACWcv variety (Pastor et al., 2008; Peña-Izquierdo et al., 2012), the PUC serves as an important ventilation pathway into the ETNA. Consequently, SACW influx via the PUC plays a critical role in shaping the hydrographic properties of the Mauritanian-Senegalese upwelling system, modulating both nutrient supply and subsurface oxygen concentrations (Pastor et al., 2011; Peña-Izquierdo et al., 2012).

Interactions between the PUC and steep bathymetry can generate subsurface-intensified anticyclonic eddies (Molemaker et al., 2015; Contreras et al., 2019). These eddies, commonly referred to as submesoscale coherent vortices (McWilliams, 1985; Gula et al., 2019), intrathermocline eddies (Dugan et al., 1982), or more specifically as ACMEs in the ETNA (Karstensen et al., 2015; Schütte, Brandt, & Karstensen, 2016; Dilmahamod et al., 2022), facilitate lateral transport of water masses and further influence the spatial distribution of nutrients and O_2. Understanding

the dynamics of the PUC is thus essential for characterizing the physical and biogeochemical processes that affect the coastal waters of the ETNA.

Recent studies have also highlighted additional processes that contribute significantly to coastal O_2 variability (see Section 1.3.5). Among these are bottom-intensified hypoxic and anoxic events on the southern Senegal shelf (Machu et al., 2019; Tall et al., 2021), and along the Mauritanian shelf and slope (Dale et al., 2022). Besides their implications for local biogeochemical cycling (Yücel et al., 2015; Gier et al., 2017; Schroller-Lomnitz et al., 2019), these benthic hypoxic events have also been associated with offshore export of turbid, low-oxygen waters (Thomsen et al., 2019). Although these events may impact both benthic and pelagic ecosystem structure (Ekau et al., 2010; Bertrand et al., 2011), the specific mechanisms sustaining these conditions remain unclear.

Given the intricate coupling between physical circulation and biogeochemical processes, this chapter aims to provide a comprehensive analysis of the drivers of hypoxic conditions along the northwestern African coast. We examine the seasonal variability of boundary current dynamics, oxygen fluxes, and water mass characteristics to elucidate on the mechanisms controlling low-oxygen events. To this end, we employ a coupled Eulerian-Lagrangian framework that integrates outputs from a physical-biogeochemical model with particle-tracking simulations. This approach enables a detailed investigation of the pathways and transformations of hypoxic water masses across seasonal timescales.

This chapter is structured as follows: in Section 4.3, we provide an overview of regional and seasonal variability in primary productivity and hypoxic conditions. Section 4.4 focuses on the coastal region, presenting an Eulerian perspective of seasonal and meridional patterns associated with hypoxia. Section 4.5 examines the Lagrangian dynamics of water masses before they become hypoxic within the coastal region. Finally, Section 4.6 summarizes the key findings of the study.

4.2 Methods

This Chapter builds upon several methodologies previously detailed in Chapter 2, which are employed in multiple chapters and include the water mass analysis (Section 2.4.3), eddy detection and tracking (Section 2.4.4), oxygen budget (Section 2.4.6) and Lagrangian particle simulation (Section 2.4.5). For the sake of brevity, the description of these methods are not repeated here but are referenced as needed throughout the text.

4.3 Overview of seasonal dynamics

Given the intricate link between primary productivity and OMZ dynamics (see Chapter 1), characterizing the seasonal variability of phytoplankton biomass is essential for understanding the main drivers of hypoxic conditions in the ETNA. Figure 4.1 presents the seasonal distribution of phytoplankton biomass both horizontally and vertically, with values averaged over two distinct

vertical ranges: within the mixed layer (panels a–d, with mixed layer depth indicated by red contours in panels i–x) and from the surface to the upper boundary of central water masses (panels e–h), defined here by the σ_θ = 25.8 kg m^{-3} isopycnal (blue contours in panels i–x; Stramma et al.). Additionally, longitudinal sections at four selected latitudes are shown in the lower panels.

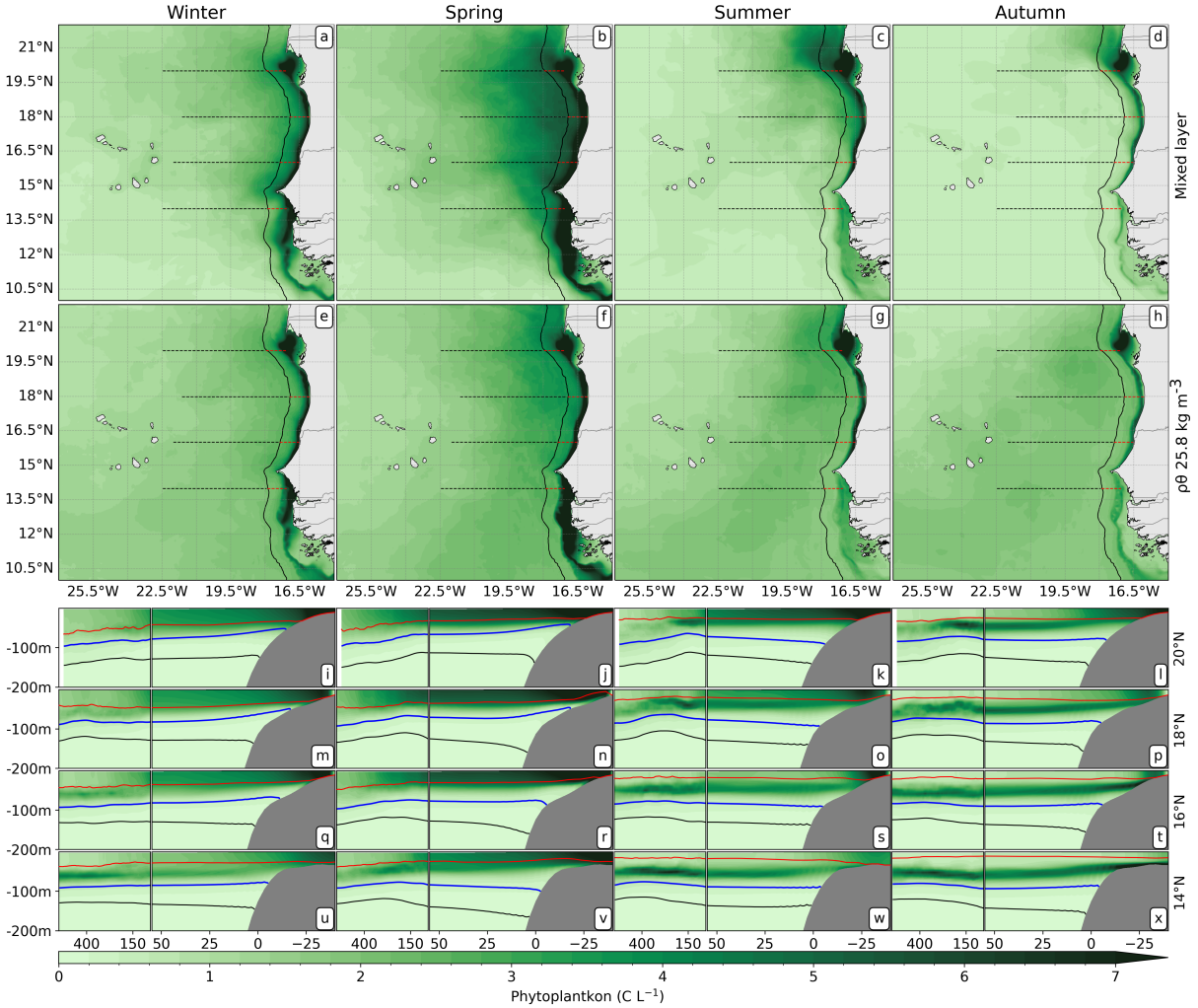


Figure 4.1: Seasonal phytoplankton biomass concentration. (a–d) Averaged within the mixed layer and (e–h) averaged from the surface to the upper central water limit (σ_θ 25.8 kg m^{-3}). Vertical sections at 20°, 18°, 16°, and 14°N are shown in panels (i–x). The black solid contour parallel to the coast in the upper panels represents the 0.5° (≈55 km) distance from the shelf break, defined at 100 m depth. In the vertical sections, the horizontal axis indicates the distance (km) from the shelf break. The sections are split into two regions with different horizontal scales: the offshore region (450 to 55 km) and the coastal region (55 to -30 km), delineated by dashed black and red lines in the upper panels, respectively. Red, blue, and black contours in the vertical sections represent the mixed layer depth (calculated as the depth where difference between σ_θ and surface σ_θ = 0.05 kg m^{-3}) and the σ_θ 25.8 and 26.3 kg m^{-3} isopycnals, respectively.

The seasonal variability associated with coastal upwelling is evident in the phytoplankton biomass averaged within the mixed layer (Figure 4.1a–d), with significantly higher values observed during winter and spring, followed by a notable decline in summer and autumn. This seasonal pattern aligns well with past observations of satellite-derived Chl*a* concentration (e.g., Pradhan et al., 2006; Lathuilière et al., 2008), only representative of the first optical depth (H. R. Gordon & McCluney, 1975). When averaged from the surface to the upper central water limit, this seasonal variability persists but is less pronounced, with only a moderate decrease from the upwelling to the relaxation season (Figure 4.1e–h). In this study, phytoplankton biomass

is analysed instead of Chl*a* to avoid the confounding effects of photoacclimation (Falkowski & LaRoche, 1991). In PISCES, Chl*a* concentrations are not only controlled by phytoplankton carbon biomass but also modulated by dynamic chlorophyll-to-carbon ratios that respond to changes in light availability, nutrient limitation, and temperature (Geider et al., 1996; Aumont et al., 2015). Although ecologically relevant, this physiological adjustment can obscure the interpretation of biomass-driven variability, especially in regions with strong seasonal fluctuations in mixed layer depth and irradiance (Cornec, Claustre, et al., 2021; Masuda et al., 2021).

Vertical sections indicate that this reduced decline is associated with the formation of a Deep Biomass Maximum (DBM) just below the mixed layer during the relaxation season. Such DBM is known to occur during periods of increased stratification (Estrada et al., 1993), which limits nutrient supply to the surface and results in the shifting of phytoplankton production to subsurface layers, where nutrient availability and light intersect optimally (Beckmann & Hense, 2007; Cornec, Claustre, et al., 2021; Masuda et al., 2021). These findings suggest that export production, that is, the sinking of particulate organic carbon produced by phytoplankton in surface layers (Eppley & Peterson, 1979), is expected to vary between the upwelling and relaxation seasons, though not as dramatically as might be inferred when considering only primary productivity averaged over the mixed layer.

Indeed, Figure 4.2 shows that Export Production of Carbon at 100 m depth (EPC100) reaches its maximum in spring and its minimum in autumn, particularly within the coastal region. Nonetheless, EPC100 remains relatively elevated during summer compared to winter and autumn, with especially high values observed at northern latitudes near Cap-Blanc. The influence of the seasonal formation of a DBM during summer and autumn is particularly evident around the Cabo Verde Islands, where EPC100 is markedly lower than in adjacent waters. This reduction likely reflects the limited ability of phytoplankton to migrate vertically within the island shelf, where shallow bathymetry constrains access to deeper, nutrient-rich layers of the nutricline.

To have a better perspective on the horizontal and vertical structure of the sOMZ, Figure 4.3 shows the seasonal frequency of hypoxic conditions on the top 300 m (upper panels) and at four longitudinal sections along the coast (lower panels). For the computation of hypoxic frequency in the upper 300 m, the vertical dimension is collapsed, meaning that occurrences are counted as long as at least one hypoxic value is detected at any depth within this range. These occurrences are then normalized by the number of days in each season.

As detailed in Chapter 3, a clear distinction emerges between coastal and offshore regions. In the offshore domain, hypoxic conditions display a broader spatial extent during winter, despite this season exhibiting the lowest overall frequency of hypoxia. Westward-propagating, low-oxygen eddies are evident as swirling trails with frequencies approaching 25%. These eddies occasionally intersect the Cabo Verde Islands and, when sufficiently persistent, appear as quasi-stationary circular patterns with frequencies reaching up to 20% during winter and autumn (Figure 4.3a,d).

In contrast, the coastal region exhibits a higher frequency of hypoxic conditions during summer and autumn, with filament-like structures extending offshore from the continental margin, where the highest values are observed (Figures 4.3c–d). Notably, this seasonal pattern diverges from that of phytoplankton biomass (Figures 4.1a–h), indicating that coastal hypoxia is not solely driven by the remineralization of organic matter.

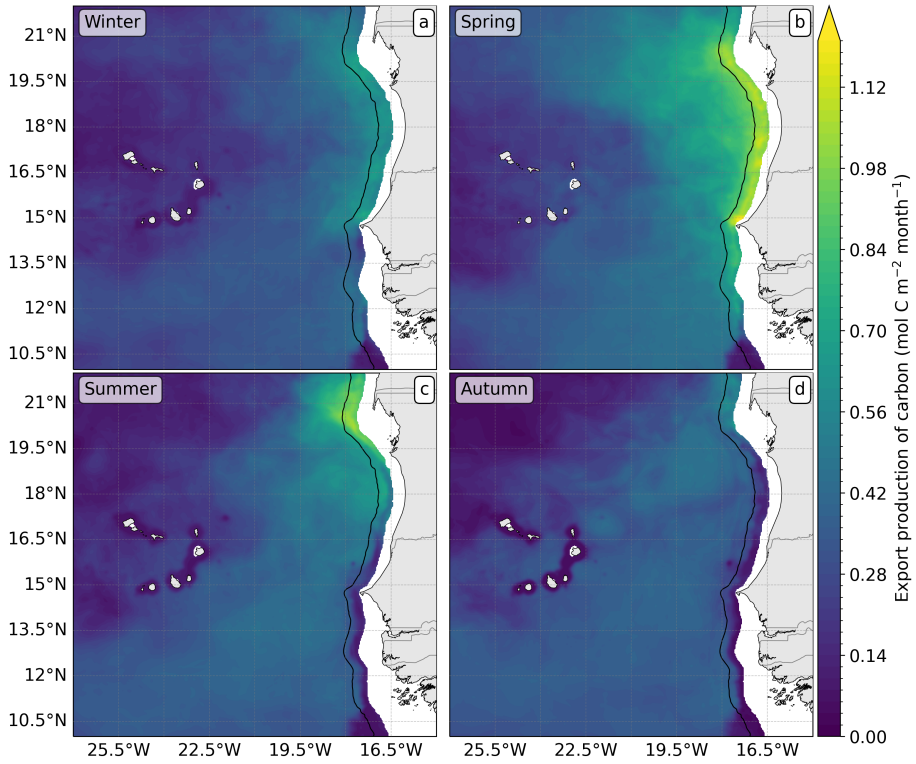


Figure 4.2: Seasonal Export Production of Carbon at 100 m depth. Averages were calculated for the 4th and 5th year of simulation. The black solid contour parallel to the coast in the upper panels represents the 0.5° (≈55 km) distance from the shelf break, defined at 100 m depth.

In terms of vertical distribution, a progressive intensification of hypoxic conditions from winter to summer is observed across all coastal latitudes (Figure 4.3e–t), with the lowest and highest frequencies detected at 14°N in winter and at 18°N in summer, respectively. Although hypoxic conditions are mostly detected between the 25.8 and 26.3 kg m^{-3} isopycnals, a vertical shoaling from spring to summer is apparent at all latitudes, particularly evident at 16°N. This upward displacement of hypoxia toward lighter densities likely results from increased stratification driven by the seasonal warming of surface waters (Mittelstaedt, 1983; Ould-Dedah et al., 1999), which reduces mixed layer depth and elevates the oxycline toward the surface (Klenz et al., 2018).

Along the continental margin, hypoxia is a persistent feature year-round, with frequencies always exceeding 25% and reaching 100% in summer between Cap-Vert and Cap-Blanc (Figure 4.3b,c). Vertical sections indicate that these elevated frequencies correspond to hypoxic conditions occurring near the bottom of the continental shelf and slope (Figure 4.3e–t). In spring, these bottom-intensified conditions extend to shallower depths along the shelf, particularly at 18°N, where they nearly reach the coastline (Figure 4.3b,j). This shoaling is likely driven by cross-shelf intrusions of deeper, oxygen-depleted waters associated with upwelling dynamics (e.g., Yücel et al., 2015). A more detailed analysis of the seasonal variability and mechanisms driving bottom hypoxia is provided in Section 4.4.4.

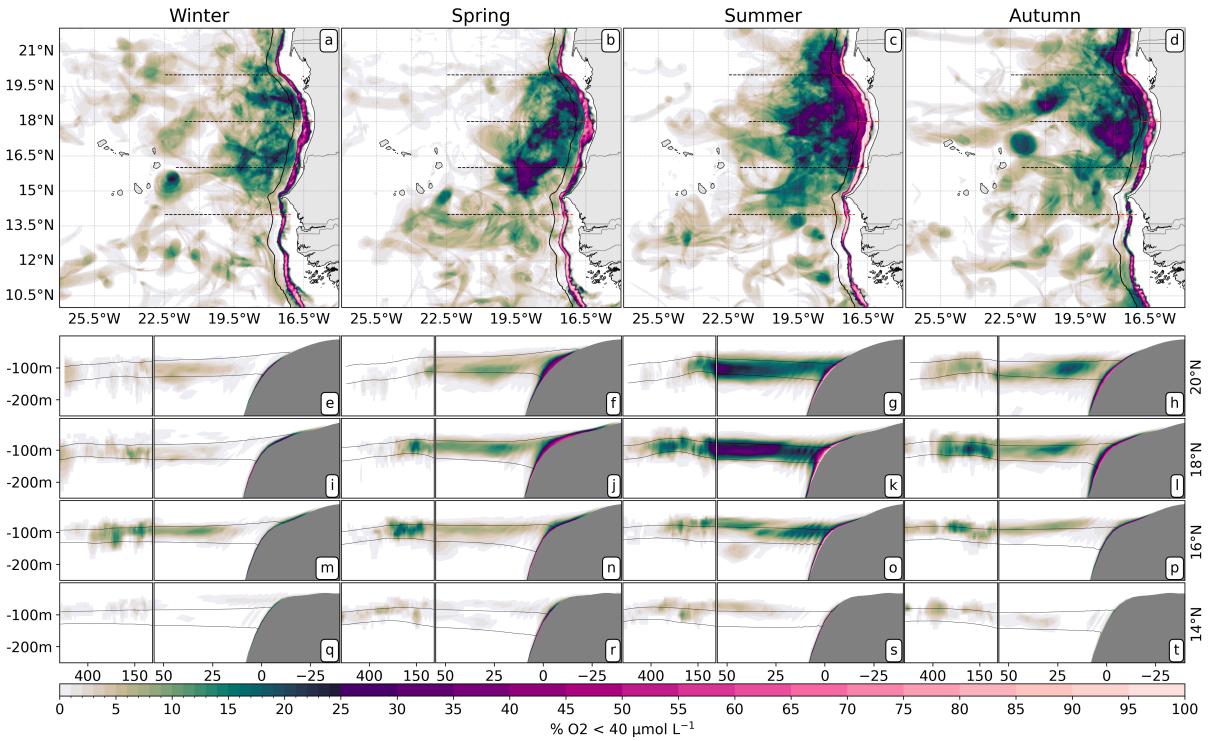


Figure 4.3: Seasonal frequency of hypoxic conditions. (a–d) Percentage of occurrences from the surface to 300 m depth, and (e–t) corresponding vertical sections at 20°, 18°, 16°, and 14°N. The black solid contour parallel to the coast in the upper panels represents the 55 km distance from the shelf break, defined at 100 m depth. In the vertical sections, the horizontal axis indicates the distance (km) from the shelf break. The sections are split into two regions with different horizontal scales: the offshore region (450 to 55 km) and the coastal region (55 to -30 km), delineated by dashed black and red lines in the upper panels, respectively. Thin black contours in the lower panels represent potential density surfaces σ_θ 25.8 and 26.3 kg m^{-3}.

4.4 Coastal dynamics

In the following sections, our analysis focuses specifically on the coastal region, which is defined as the area extending from the coastline to a western boundary located at a distance of 0.5° (≈55 km) from the continental shelf break (100 m depth). This distance is chosen to effectively isolate the boundary current circulation, which has a typical extension between 30 and 60 km (Mittelstaedt, 1983; Peña-Izquierdo et al., 2012). By adopting this boundary, we aim to minimize the direct influence of mesoscale eddies, which are more likely to dominate ocean circulation farther offshore (Klenz et al., 2018).

4.4.1 Meridional current variability

Although the PUC and the MC are often considered manifestations of the same forcing mechanisms and should be treated as a single current (Klenz et al., 2018; Kounta et al., 2018), its vertical positioning likely exerts a significant influence on the ventilation of northwestern African coastal waters (Peña-Izquierdo et al., 2012, 2015; Klenz et al., 2018). To investigate these dynamics, we analyze the monthly variability of Meridional current velocities (V) at four longitudinal sections within the coastal region.

For clarity, V is decomposed into three components: the (negative) equatorward flow and the (positive) poleward surface and subsurface flows, corresponding to the MC and PUC, respectively (Figure 4.4). The distinction between the MC and PUC is based on the vertical position of the poleward velocity maximum, with the MC occurring above 40 m depth and the PUC located below this threshold. Additionally, the volume transport associated with each of these currents is computed for all sections (Figure 4.4, right panels). To accurately delineate the PUC, only poleward velocities that are enclosed within closed contours and exhibit a monotonic decrease towards offshore are considered.

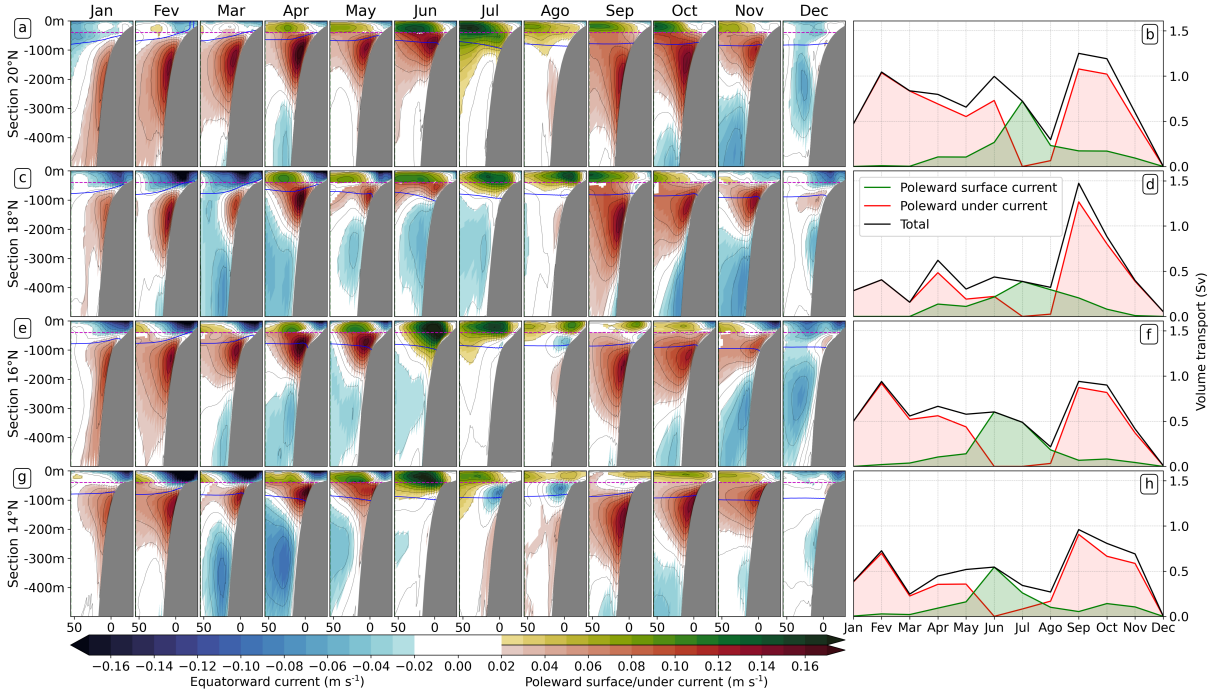


Figure 4.4: Monthly-averaged meridional current velocities at four longitudinal sections. Left panels (a,c,e,g): Vertical sections at 20°, 18°, 16° and 14°N (indicated by red dashed lines in Fig. 4.3 upper panels). Positive values indicate poleward current velocities, while negative values represent equatorward velocities. Poleward currents are further distinguished into surface (green) and subsurface (red) currents. The horizontal axis represents the distance from the shelf break (in km), defined at 100 m depth. Current velocities with magnitudes less than 0.02 m s^{-1} are masked. Purple dashed line marks the 40 m depth, while the blue contour corresponds to the σ_θ 25.8 kg m^{-3} isopycnal. Thin solid and dashed contours represent positive and negative current velocities, respectively, with a 0.2 m s^{-1} interval. Right Panels (b,d,f,h): Monthly volume transport calculated for poleward surface (green) and subsurface (red) currents, along with their combined total (black).

The seasonal vertical displacement of the PUC is clearly evident across all latitudes (Figure 4.4, left panels). During the upwelling season, the PUC remains closely attached to the continental slope, with its core gradually migrating from deeper depths (approximately 200 m) toward shallower layers from January to May. The maximum intensity of the PUC is observed in April, with velocities exceeding 0.18 m s^{-1} between 16° and 20°N.

Consistent with previous studies (Lázaro et al., 2005; Klenz et al., 2018), the upwelling season is also characterized by the presence of an intense equatorward coastal jet above the PUC, with peak velocities reaching approximately 0.6 m s^{-1} at 14°N. As in other EBUSs, these equatorward baroclinic coastal jets arise due to the geostrophic adjustment to surface density gradient between cold, upwelled coastal waters and warmer waters present offshore (Allen, 1973). For this reason, the strength of these coastal jets is directly related to the strength of the wind stress and wind stress curl, especially near the coast (e.g., Capet et al., 2004).

The full transition of the PUC to surface layers occurs progressively, first at lower latitudes (14° and 16°N) in June, followed by higher latitudes (18° and 20°N) in July. From July to August, the poleward current is mainly confined to surface layers, although weaker subsurface expressions persist below 100 m depth. This separation between surface and subsurface poleward velocities results from the emergence of a weak equatorward flow centered around 100 m depth, which remains largely undetectable at higher latitudes due to its low magnitude ($|V| < 0.02$ m s^{-1}).

This seasonal weakening and reversal of V from poleward to equatorward flow at 100 m depth in July and August is consistent with previous observational and model-based studies (Klenz et al., 2018; Kounta et al., 2018), reinforcing the accuracy of our model in simulating seasonal boundary current dynamics. Interestingly, mean velocities below the σ_θ 25.8 kg m^{-3} isopycnal remain consistently low ($|V| < 0.02$ m s^{-1}), suggesting a potential increase in water residence time within the upper central water density range during these months. This prolonged residence time, combined with reduced ventilation due to the surface intensification of the PUC, may contribute to oxygen depletion. Even under conditions of reduced primary productivity, an average apparent Oxygen Utilization Rate (aOUR) of just 0.03 µmol L^{-1} d^{-1} in the region (Karstensen et al., 2008) could be sufficient to drive the development of hypoxic conditions.

From September to November, a gradual weakening of the poleward surface current is observed, coinciding with a sharp intensification of the PUC (Figure 4.4, right panels). Interestingly, the simultaneous presence of two distinct poleward velocity maxima–one at the surface and another below 40 m depth–is evident across all latitudes during this period. This dual-core structure is particularly pronounced at 16°N in September and October (Figure 4.4e). These findings are remarkably consistent with the observations of Peña-Izquierdo et al. (2012), who analyzed ocean current data collected along the northwestern African coast in November 2008 and concluded that the MC and PUC were indistinguishable during this time.

The seasonal evolution of both the surface and subsurface poleward currents revealed in this study also mirrors the patterns documented by Klenz et al. (2018) at 18°N (Figure 4.4c). Specifically, three key phases are observed: (i) February and March, when the core of the poleward current is closely attached to the continental slope; (ii) June, characterized by the emergence of separate poleward maxima in the surface and subsurface layers, situated above and below the mixed layer, respectively; and (iii) July and August, when a single, strong poleward current core is confined to the surface.

Although less relevant to the present study, equatorward current velocities are in general predominant throughout the year at depths below 200 m (Figure 4.4left panels). These currents are particularly evident from March to June and from October to December, with maximum $|V|$ not exceeding 0.1 m s^{-1}. These findings are again in good agreement with the observations from Klenz et al. (2018), who reported similar equatorward current intensities between 250 and 500 m from May to July at 18°N. Considering that these depths are composed of lower central water masses (i.e., $26.8 < \sigma_\theta < 27.1$ kg m^{-3}), our results are consistent with Peña-Izquierdo et al. (2015), who suggested that the equatorward transport of oxygen-rich NACW within the lower central water contributes to the separation between the shallow and deep OMZs.

The seasonal variability of the poleward surface and undercurrents is clearly reflected in the volume transport calculated for each section (Figure 4.4, right panels). During the upwelling

season, poleward transport reaches its peak in February, despite the highest velocities occurring in April. This apparent discrepancy arises from the greater vertical extent of the PUC in February when compared to April.

Transport by the MC increases steadily from approximately 0.2 Sv in May to a peak of around 0.7 Sv in July. Concurrently, transport by the PUC decreases to nearly 0 Sv, indicating a marked reduction in the inflow of SACW and, consequently, a potential decline in the advective supply of oxygen to the region. As the MC transport decreases from July to September, the PUC experiences a sudden re-intensification, reflected in a sharp increase in transport during September which reaches maximum values of approximately 1.3 Sv at 18°N (Figure 4.4d). Following this peak, poleward transport both at surface and subsurface layers gradually declines, reaching near-zero values in December.

The peaks in PUC transport observed in February and September in our simulation exhibit a slight temporal offset compared to the findings of Kounta et al. (2018), who reported maximum transport in May and November at 14°N. Nevertheless, the average poleward current velocities are in good agreement, with peak values around 0.15 m s^{-1} occurring between February–April and September–November, indicating consistent seasonal patterns of poleward flow.

This discrepancy in timing is likely attributable to methodological differences. Kounta et al. (2018) estimated transport by integrating positive velocities over a broader domain extending 3° offshore, thereby capturing the influence of westward-propagating Rossby waves. This wider spatial extent likely accounts for both the two-month lag between peak velocity and peak transport, and the higher transport magnitudes (2.0–2.5 Sv) reported in their study. In contrast, our analysis is restricted to a narrower coastal region extending 0.5° offshore, which is more appropriate for isolating the local influence of the PUC within the boundary current system.

4.4.2 Impact of meridional currents on tracers

Building on the analysis presented in the previous section, it is reasonable to expect that the seasonal variability V exerts a significant influence on region's water mass characteristics, particularly in terms of nutrients and oxygen supply. To evaluate this hypothesis, this section provides a detailed analysis of the seasonal and meridional variability of O_2 concentrations and other relevant tracers.

Figure 4.5 presents a Hovmöller diagram showing the isopycnal, zonally averaged daily climatology for V, %SACW, O_2 concentrations and frequency of hypoxic conditions[1] within the coastal region. To complement this analysis, Figure 4.6 presents a similar Hovmöller diagram, but with buoyancy frequency squared (N^2), phytoplankton biomass, NH_4 and NO_3 concentrations. Given the central water upper isopycnal boundary and the highest frequency of hypoxic conditions between the 25.8 and 26.3 kg m^{-3} isopycnals (Figure 4.3, lower panels), data is averaged within this density range, except for N^2 and phytoplankton biomass, which are averaged from the surface down to the depth of the 25.8 kg m^{-3} isopycnal.

[1]The mean frequency of hypoxic conditions was calculated by first identifying all horizontal grid cells with at least one hypoxic vertical cell. The number of hypoxic cells along the zonal axis was then normalized by the maximum number of zonal grid cells containing isopycnal-interpolated data (red-shaded area in Figure 4.5a). Finally, daily climatological means were computed from these normalized values.

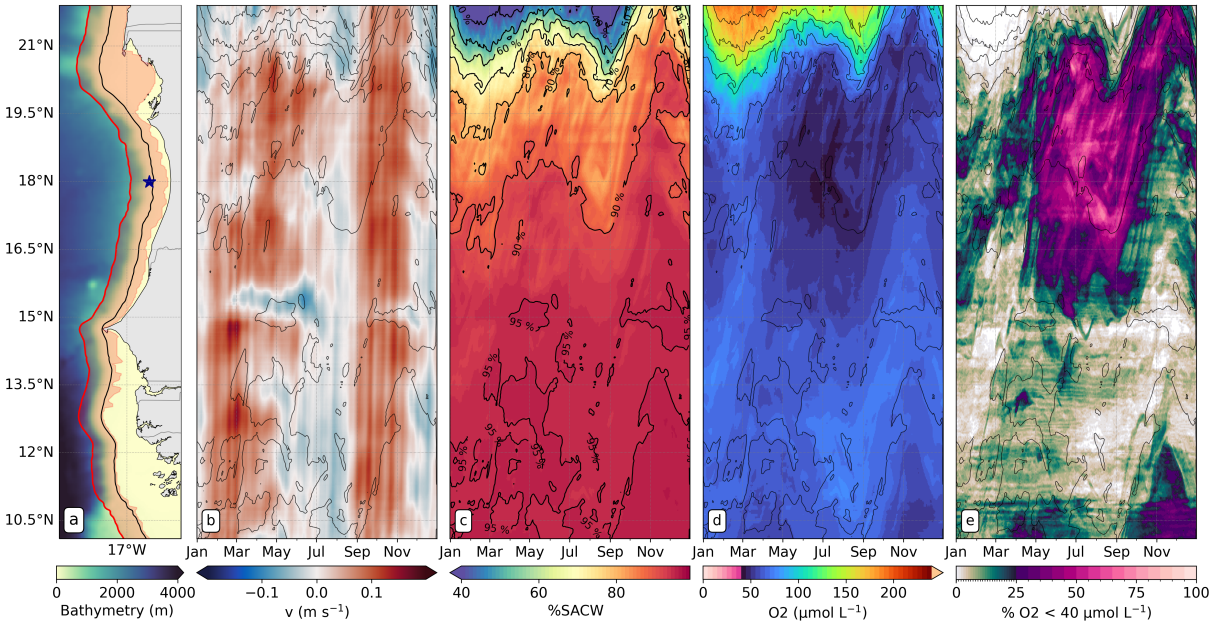


Figure 4.5: Hovmöller diagrams for the meridional and temporal variability of physical and biogeochemical tracers along the coast (part I). Daily climatologies were computed along latitude, with data averaged between σ_θ 25.8 and 26.3 kg m^{-3} and within the coastal region. (a) Bathymetry map with the zonal extent of the interpolated data indicated by the red shaded patch along the coast. The 100 m isobath is represented by a solid black contour, and the blue star marks the location of the data used for Figure 4.8. (b) Average V. (c) Average proportion (%) of SACW relative to NACW. (d) Average O_2 concentration. (e) Average frequency of hypoxic conditions, considering the maximum zonal extent of the interpolated data.

The dominant poleward V is evident along the coast at all latitudes (Figure 4.5b), with a few notable exceptions. These include: (i) north of the Cap-Vert headland (around 15°N) from February to July, where an opposing equatorward flow likely associated with an anticyclonic eddy disrupts the normal flow of the PUC; and (ii) at latitudes greater than 20°N during December–April and July–September. Seasonal variability in V is also evident in the transition from poleward to equatorward flow between May and September, starting at lower latitudes in May and progressively shifting northward, reaching approximately 18.5°N by August.

Regardless of the time of the year, mean %SACW generally decreases from south to north, with maximum and minimum values spanning from 96% to 38%, respectively (Figure 4.5c). The spatial extent of high %SACW values appears to be strongly influenced by the seasonal dynamics of V, particularly during periods when the PUC is most intense (March–June and September–November). During these periods, the 95% SACW contour line extends as far north as Cap-Vert, but retreats to approximately 11°N when V decreases and reverses direction. The re-intensification of the PUC in September is also evident in the northward displacement of the 90% SACW contour line, which reaches its northernmost extent at 20°N in December.

Seasonal shifts in V also facilitate the equatorward transport of NACW at higher latitudes. SACW values below 50% are observed north of 20°N during December–April and July–September, coinciding with periods of predominantly negative V that indicate equatorward transport of NACW along the coast. These patterns suggest that the seasonal variability of V plays an important role in positioning the CVFZ near the coast.

Average O_2 concentrations exhibit a pattern similar to %SACW, generally decreasing from south to north (Figure 4.5d). Nevertheless, exceptions to this pattern are observed at both the

southern and northern edges of the coastal region. At latitudes below 12°N, low O_2 concentrations are associated with high %SACW. In contrast, at latitudes greater than 20°N, O_2 concentrations increase sharply from approximately 50 to 120 µmol L^{-1}, while %SACW decreases from 70% to 50% within a distance of less than 50 km. Considering that pure SACW is typically associated with higher O_2 concentrations when compared to the regional SACWcv variety (Peña-Izquierdo et al., 2012), low O_2 concentrations observed at lower latitudes are likely the result of increased local O_2 consumption. At higher latitudes, however, the observed increase in O_2 concentrations is associated with the equatorward transport of NACW, which brings significantly O_2-rich waters to the region.

Between 12°N and 20°N, the prevailing poleward V and the gradual decline in %SACW suggest that the general decrease in O_2 concentrations is partly due to the downstream dilution of SACW along the PUC (Figure 4.5b–d). However, oxygen consumption associated with the remineralization of organic matter likely plays a significant additional role (Klenz et al., 2018). This is supported by the observed increase in NH_4 concentrations from south to north (Figure 4.6d), indicative of cumulative remineralization processes along the coast.

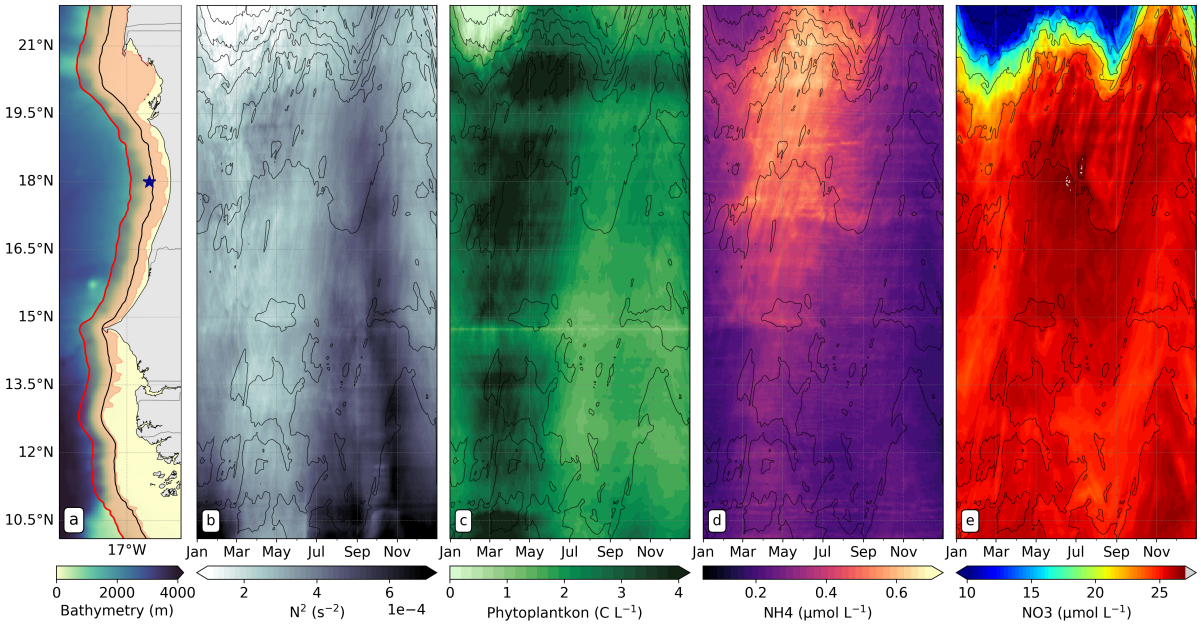


Figure 4.6: Hovmöller diagrams for the meridional and temporal variability of physical and biogeochemical tracers along the coast (part II). Same as Figure 4.5, but for different variables. Panel (b) and (c) present the N^2 and Phytoplankton biomass, respectively, averaged within $\sigma_\theta < 25.8$ kg m^{-3}. Panel (d) and (e) present concentrations of NH_4 and NO_3, respectively, averaged between σ_θ 25.8 and 26.3 kg m^{-3}. Contours in panels (b–e) represent the average percentage of SACW, with respective values detailed in panel 4.6c.

Naturally, the occurrence of hypoxic conditions follows an inverse relation to O_2 concentrations (Figure 4.5e), with a clear increase to maximum values of ≈70 % observed at latitudes between 15 and 20°N from May–September. Although most hypoxic conditions are detected in water masses with 80–90% SACW, a significant amount of hypoxic conditions are also associated with SACW exceeding 90%, particularly between 15° and 18°N from May–July. This pattern coincides with elevated NO_3 concentrations, indicating that these water masses have been more exposed to organic matter remineralization (Figure 4.6e).

From September to December, the impact of the PUC on O_2 concentrations and hypoxic conditions becomes evident at latitudes greater than 15°N (Figure 4.5b,d,e). During this time, the re-intensification of the PUC supplies the coastal region with SACW and drives the northward transport of hypoxic waters, ultimately contributing to the ventilation of the Mauritanian coastal region.

These O_2 dynamics align with the observations of Peña-Izquierdo et al. (2012). The authors documented a south-to-north decline in O_2 concentrations, attributing it to the degradation of sinking organic matter from the upwelling season and the northward advection driven by the PUC. Their findings revealed O_2 concentrations typical of SACW associated with the PUC extending as far as 24°N, well beyond the typical position of the CVFZ at approximately 22°N. Together with our results, this highlights the critical role of the PUC in transporting oxygen-rich SACW along the continental margin.

Closely following the seasonal cycle of upwelling and relaxation along the coast, N^2 values are lowest during the upwelling season and highest during the relaxation season, with peak stratification observed at southern latitudes (Figure 4.6b). Notably, the highest N^2 values at latitudes with the lowest mean O_2 concentrations occur 1–2 months after minimum O_2 concentrations are reached. This temporal offset suggests that stratification likely plays a secondary role in the seasonal intensification of hypoxia.

Naturally, phytoplankton biomass above central waters also reflects the upwelling-relaxation dynamics, peaking during the upwelling season and reaching its lowest levels late in the relaxation season (Figure 4.6c). The meridional variability of the upwelling dynamics is clearly evident, with southern latitudes experiencing shorter periods of high productivity compared to northern latitudes. The impact of primary productivity on NH_4 concentrations is also apparent, as a similar meridional increase in NH_4 from south to north (Figure 4.6d) indicates a close relationship with the remineralization of organic matter resulting from increased export production.

Similarly, NO_3 concentrations generally increase from south to north (Figure 4.6g), with the highest concentrations aligning with the lowest O_2 concentrations near 18°N. This pattern highlights the cumulative effect of oxygen consumption via nitrification. Interestingly, patches of elevated NO_3 are also associated with %SACW exceeding 95% at southern latitudes. Given that the northward transport of NO_3 is an important term in the regional NO_3 budget Auger et al., 2016, such elevated NO_3 in combination with %SACW > 95% likely results from the direct transport of NO_3-rich SACW by the PUC (Poole & Tomczak, 1999). In contrast, elevated NO_3 concentrations associated with the diluted SACWcv variety suggest the transport of older water masses, regionally exposed to nitrification (e.g., Thomsen et al., 2019).

Comparison with the WOA23 climatology reveals overall good agreement with the model (Figure A.8). Key features–such as the seasonal northward extension of SACW-rich waters and the southward intrusions of NACW at northern latitudes–are well represented. Notably, the timing and extent of low O_2 concentrations align with the model's summer peak in hypoxia, as does the seasonal increase in NO_3 levels. Minor discrepancies remain, particularly regarding the timing of the autumn PUC re-intensification and the consistently lower observed NO_3 concentrations. However, given the limited number of observations available in the region, especially during the relaxation season, such discrepancies should be addressed with caution.

To better evaluate the contribution of boundary currents to the ventilation of the coastal region, Figure 4.7 shows the meridional O_2 transport across a series of longitudinal sections spaced at 0.5° intervals along latitude. As the focus is on total O_2 transport, the Hovmöller diagram (panel b) displays absolute values, without distinguishing between poleward and equatorward directions. For additional context, the non-absolute transport time series for each section are provided separately in panel (c).

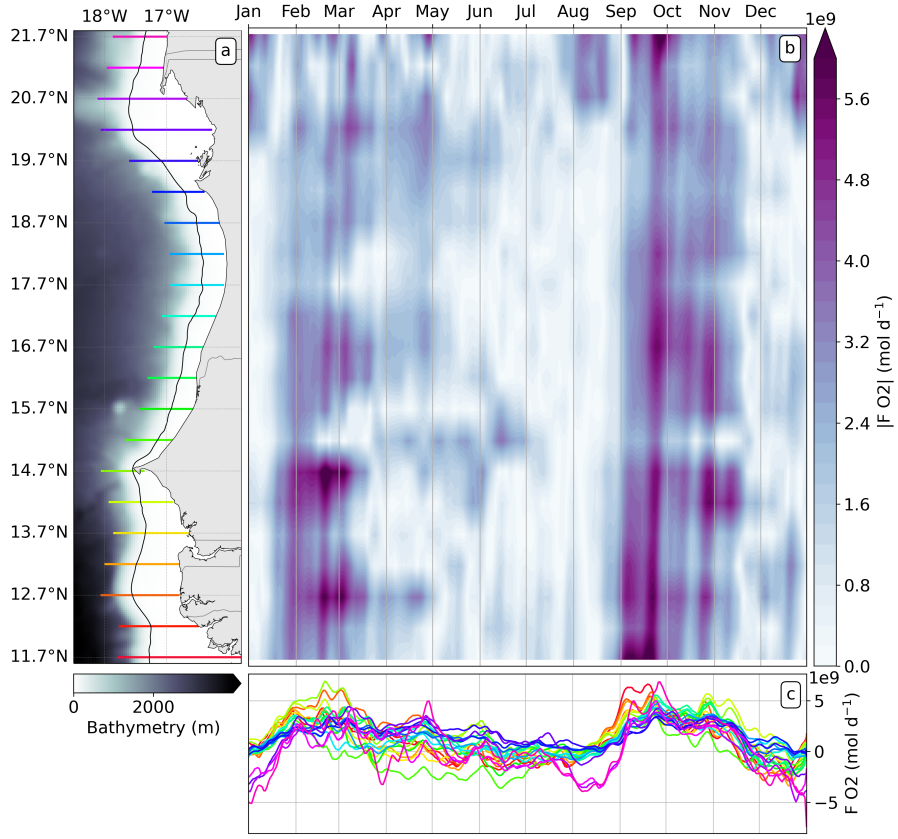


Figure 4.7: Meridional transport of O_2 along latitude. (a) Bathymetry map with the representation of the longitudinal cross sections used for the calculation, each identified with a unique color. The shelf break, defined at 100 m depth, is represented by a black contour parallel to the coastline. (b) Hovmöller diagram showing the daily absolute transport of O_2 by the meridional currents passing through each longitudinal cross section, integrated over depths ranging from 70 to 250 m. Panel (c) displays the corresponding O_2 transport at each section, differentiated by the colors indicated in panel (a).

Following the seasonal pattern of the PUC, the meridional transport of O_2 is significantly higher from February to April and from September to December (Figure 4.7b). A clear disruption of this transport pattern occurs in the wake of the Cap-Vert headland, where the direction of mean flow reverses to equatorward in the section immediately north of the headland (Figure 4.7c). Compared to sections south of the headland (i.e., < 14.7°N), the magnitude of O_2 transport is substantially reduced in the northern sections during this period, suggesting that this circulation anomaly likely impedes the direct supply of O_2 by the PUC.

From April to August, O_2 transport declines across most latitudes (Figure 4.7c), except north of 20.7°N, where southward intrusions of NACW are evident (Figure 4.5c). Between 16.7° and 19.7°N, near-zero transport from June to September indicates a significant reduction in oxygen supply, coinciding with the strongest decrease in O_2 concentrations (Figure 4.5d). Given that the potentially increased cross-shore transport during this period is likely dominated by

the oxygen-poorer, regionally diluted SACWcv variety, these results strongly suggest that the seasonal shoaling of the PUC leads to a pronounced deficit in O_2 supply, contributing to the seasonal intensification of hypoxia within the coastal region.

4.4.3 Time-series analysis of a ”virtual” mooring

While spatial and temporal averaging is useful for identifying seasonal patterns, it hinders the analysis of short-term variability critical for understanding the physical-biogeochemical interactions that drive hypoxic conditions. To overcome this limitation, we analyze a five-year daily time series from a ”virtual” mooring located at 18°N and 160 m depth on the continental slope (blue star in Figures 4.5a and 4.6a). This site was selected due to the high frequency of hypoxic events (Figures 4.3k and 4.5d) and its repeated sampling in previous studies (e.g., Dale et al., 2014a; Klenz et al., 2018; Dale et al., 2022). For clarity, only the most relevant parameters are presented here, while additional variables are included in Figure A.9.

The seasonal decline in O_2 concentrations during summer is consistently observed across all years in the time series (Figure 4.8a). As discussed in the previous section, a key consequence of the seasonal shoaling of the PUC during the relaxation period (Figure A.9a) is a simultaneous decrease in SACW content and an increase in NO_3 concentrations (Figure 4.8b,d), suggesting the intrusion of an older, more diluted SACWcv variety.

Although hypoxic conditions persistently occur below the σ_θ = 25.8 kg m^{-3} isopycnal and are typically associated the diluted SACWcv variety, exceptions do occur, such as the prolonged period of low O_2 concentrations from May to August of year 1. During this period, hypoxic conditions coincide with relatively fresher, SACW-rich water masses, with elevated concentrations of NH_4 and NO_3 further suggesting significant alterations in the typical water mass characteristics (Thomsen et al., 2019). A closer analysis reveals that this event is associated with a coastal-generated ACME (Figure 3.2). While this ACME was present, the mixed layer exhibited anomalously elevated phytoplankton and zooplankton biomass (Figure A.9e and 4.8f, respectively), supported by unusual elevated NO_3 concentrations likely driven by eddy-induced upwelling (e.g., McGillicuddy, 2016; Karstensen et al., 2017).

Relatively high O_2 concentrations (≈80 µmol L^{-1}) are occasionally observed bellow σ_θ 25.8 kg m^{-3}. These can be related to two ventilation pathways. The first, more prominent pathway occurs in spring and autumn and involves the transport of a purer (fresher) and more oxygenated SACW variety by the PUC (Figure 4.8b). The second, less frequent mechanism is related to high-salinity and low-%SACW waters (e.g., August of year 2), associated with the eastward intrusion of NACW through the CVFZ (Figure A.10). Although direct observations of such events are limited, a similar event may have been reported by Devresse et al. (2022), who documented a low-oxygen cyclone encircled by oxygenated NACW off the Mauritanian coast.

Lowest O_2 levels are typically found near the bottom, frequently reaching suboxic concentrations (O_2 < 6 µmol L^{-1}). Interestingly, bottom hypoxia is associated with both high and low %SACW, though suboxic conditions tend to coincide with lower %SACW values (Figure 4.8b). Similarly to the findings of Thomsen et al. (2019) in the same location, such low O2

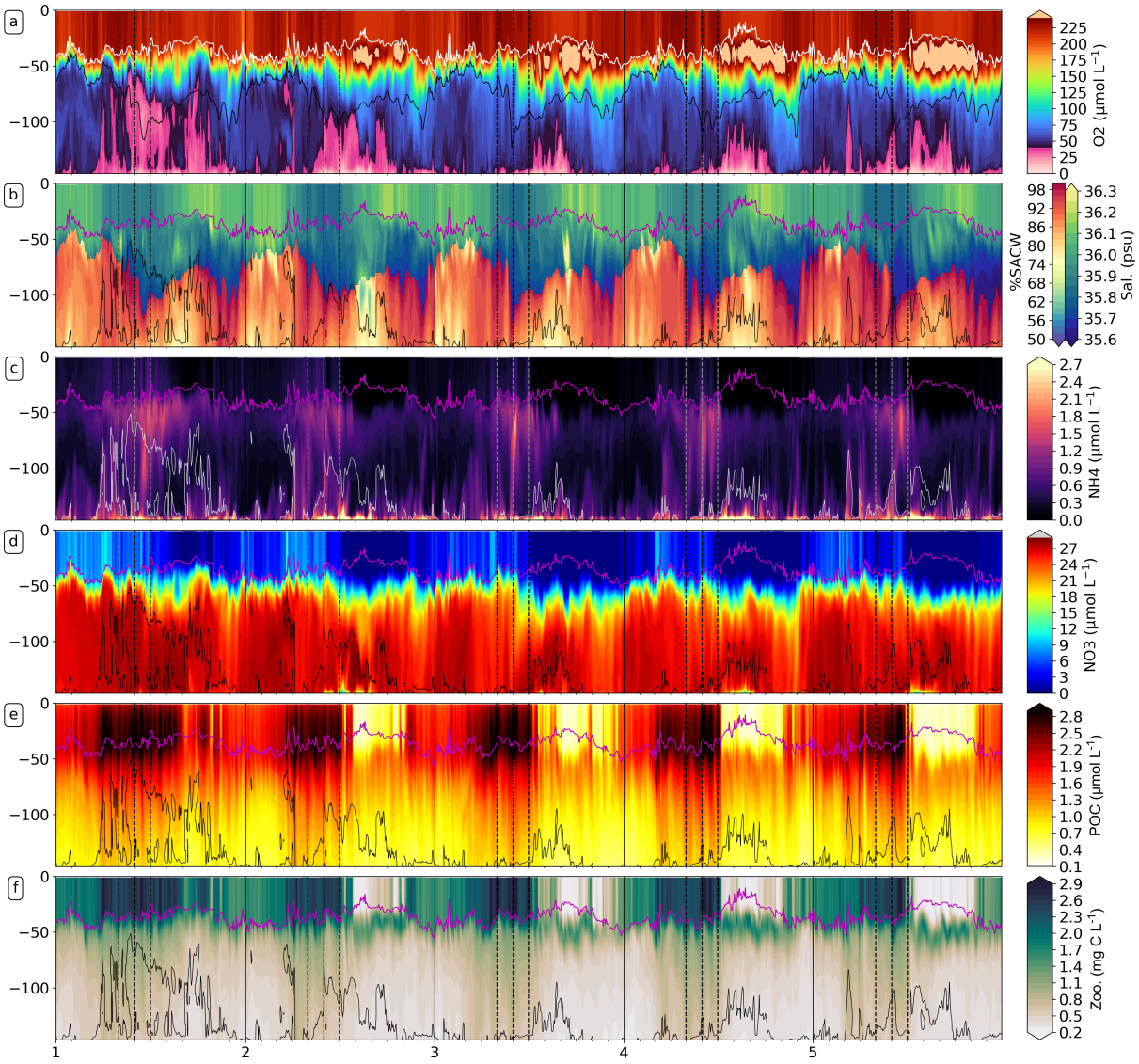


Figure 4.8: Daily hovmöller diagram of a point extraction at 18°N and ≈160 m depth. (a) O_2 concentrations, (b) %SACW and salinity, (c) NH_4, (d) NO_3, (e) POC, and (f) zooplankton biomass. Mixed layer depth (calculated as the depth where the difference between σ_θ and surface σ_θ = 0.05 kg m^{-3}) is represented by white (a) and purple (b–f) lines. O_2 = 40 µmol L^{-1} is represented by black (b,c,e,f) and white (d) contours. Black contour in (a) represents σ_θ 25.8 kg m^{-3}. Months of May, June and July are identified by black dashed lines. Location of point extraction is represented by blue star in Figure 4.5a.

concentrations in SACW-rich waters suggests substantial modification of typical water mass characteristics due to enhanced respiration driven by benthic biogeochemical processes.

Seasonal bottom hypoxia consistently co-occurs with elevated NH_4 concentrations across all years (Figure 4.8c), while low NO_3 levels are also observed–except during the first simulation year (Figure 4.8d). In PISCES-v1, bottom O_2 loss due to organic matter degradation is directly proportional to the flux of POC reaching the seafloor (see Section 2.1.2; Aumont et al., 2015). Under suboxic conditions, remineralization of POC proceeds via denitrification, using NO_3 as the terminal electron acceptor and producing NH_4 as a byproduct of organic nitrogen breakdown. However, PISCES assumes that this NH_4 is fully oxidized by NO_3 at a rate equivalent to nitrification, preventing its accumulation in bottom waters.

This mechanistic framework aligns with observations by Dale et al. (2014a), who reported simultaneous declines in O_2 and NO_3, along with elevated NH_4 concentrations, consistent with active benthic denitrification. Notably, they found that the fraction of POC remineralized via denitrification (≈24%) was significantly higher than the global average (< 10%) (Middelburg et al., 1996), attributing such amplification to the underlying O_2-deficient waters. Together, their findings and our results underscore the critical role of benthic processes in modulating bottom-layer O_2 and NO_3 dynamics in the region.

The highest concentrations of NH_4 in the water column (excluding bottom layers) are observed approximately two months before the onset of hypoxic conditions, particularly between the base of the mixed layer and the σ_θ 25.8 kg m^{-3} isopycnal (Figure 4.8c). These elevated levels indicate that O_2 consumption via nitrification is likely a major O_2 sink during this pre-hypoxic period.

Examination of the monthly-averaged O_2 biological budget terms confirms that nitrification is indeed the dominant O_2 sink in the months preceding the development of hypoxic conditions (Figure 4.9i and f, respectively). This is followed by zooplankton respiration and, subsequently, by the remineralization of organic matter[2] (Figure 4.9g and h, respectively). The contribution of zooplankton respiration further supported by the presence of zooplankton biomass below the mixed layer during periods of elevated NH_4 concentrations (Figure 4.8c). This zooplankton biomass is mainly composed of mesozooplankton at these depths (not shown), which, combined with the relatively high POC levels (Figure 4.8e), suggests that flux feeding by zooplankton (Kiørboe, 2011) plays a key role at this site. This grazing activity contributes to increased NH_4 concentrations, thereby further enhancing nitrification rates and amplifying O_2 consumption.

Iversen et al. (2010) provided important insights into the vertical export of POC off Cap-Blanc, emphasizing the dominant role of zooplankton flux feeding in degrading POC within the upper 150 m of the water column. Given the persistently high primary productivity in this region–sustained by year-round coastal upwelling (Mittelstaedt, 1983; Pradhan et al., 2006; Lathuilière et al., 2008) and the presence of an extensive upwelling filament (Van Camp et al., 1991; Gabric et al., 1993)–it is reasonable to expect higher concentrations of sinking detritus and, consequently, a more significant role for zooplankton respiration in the O2 budget than in southern latitudes.

At 18°N, the upwelling season is active from December to May, while the relaxation season occurs from June to November (Lathuilière et al., 2008). However, our analysis reveals that the effects of upwelling on primary productivity can last up to two months after upwelling relaxation. The declining intensity of upwelling in May is marked by a deepening of the σ_θ 25.8 kg m^{-3} isopycnal from around 70 m to 120 m depth (Figure 4.8a), coinciding with the progressive warming of surface waters (Figure A.9b). The intensification of the surface poleward current velocities in June (Figure A.9a) further contributes to the rapid warming of the mixed layer due to the transport of warmer waters from the south (Lázaro et al., 2005; Lathuilière et al., 2008). This warming leads to increased stratification, particularly between the base of the mixed layer and the deepened σ_θ 25.8 kg m^{-3}, with stratification peaking in September (Figure A.9c).

[2]Although nitrification is a key component of the organic matter remineralization process, O_2 consumption associated with nitrification and remineralization are computed separately in PISCES.

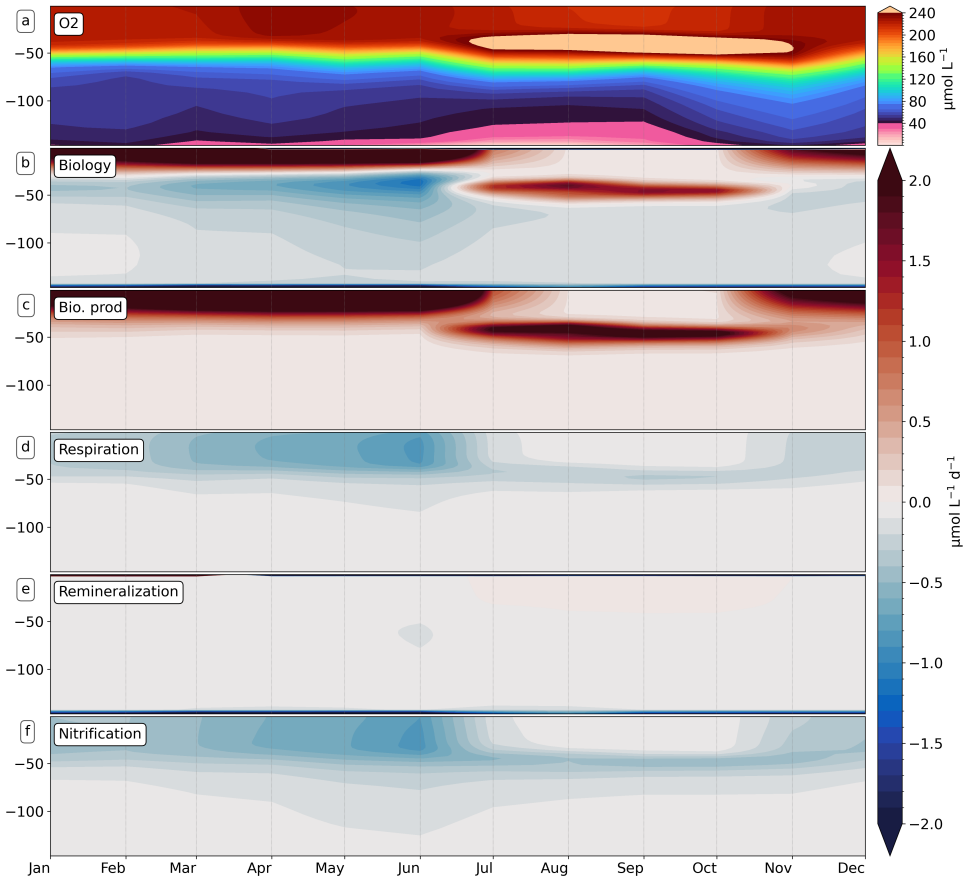


Figure 4.9: Monthly-averaged O_2 biological budget terms of a point extraction at 18°N and ≈160 m depth. (a) Average O_2 concentrations; (b) biological O_2 terms, which are composed by processes related with (c) O_2 production by phytoplankton, (d) respiration by zooplankton, (e) remineralization of organic matter by bacteria, and (f) nitrification. Only data from the 4th and 5th years of simulation are considered.

Despite upwelling relaxation, NO_3 concentrations in the mixed layer remain relatively high until the end of June (Figure 4.8d), with elevated zooplankton and phytoplankton biomass persisting until mid July (Figure 4.8f and A.9e, respectively). Indeed, such time lag between the warming of surface waters and the decrease of primary productivity is in good agreement with the satellite observations reported by Lathuilière et al. (2008) for this latitude.

This transition period, referred in the past as the ”wake of the upwelling season” (Klenz et al., 2018), is marked by a gradual decline in O_2 concentrations, culminating in hypoxic conditions in July. We hypothesize that this decline is driven by a combination of biological and physical factors. Residual NO_3 injected to the mixed layer during the upwelling season continues to fuel surface primary productivity into July, sustaining elevated export production and subsequent degradation of POC below the mixed layer. This degradation, which is dominated by bacterial nitrification and zooplankton flux feeding, drives significant O_2 consumption. Although these processes occur more intensely during the upwelling season, what sets this period apart is the intensification of stratification (Figure A.9d), which limits vertical mixing, and, more importantly, the slowdown of the PUC below the mixed layer (Figure A.9a), which reduces lateral ventilation and increases water residence times. Together, these changes create an O_2 deficit that ultimately drives the development of hypoxic conditions in the region.

4.4.4 Bottom layer hypoxia

To further elucidate on the seasonal and spatial dynamics of bottom hypoxia, we examine monthly mean bottom O_2 concentrations along the continental margin (Figure 4.10). These values are derived from the average of the model's two bottom layers, which range in thickness from 5.5 m at 100 m depth to 20 m at 300 m.

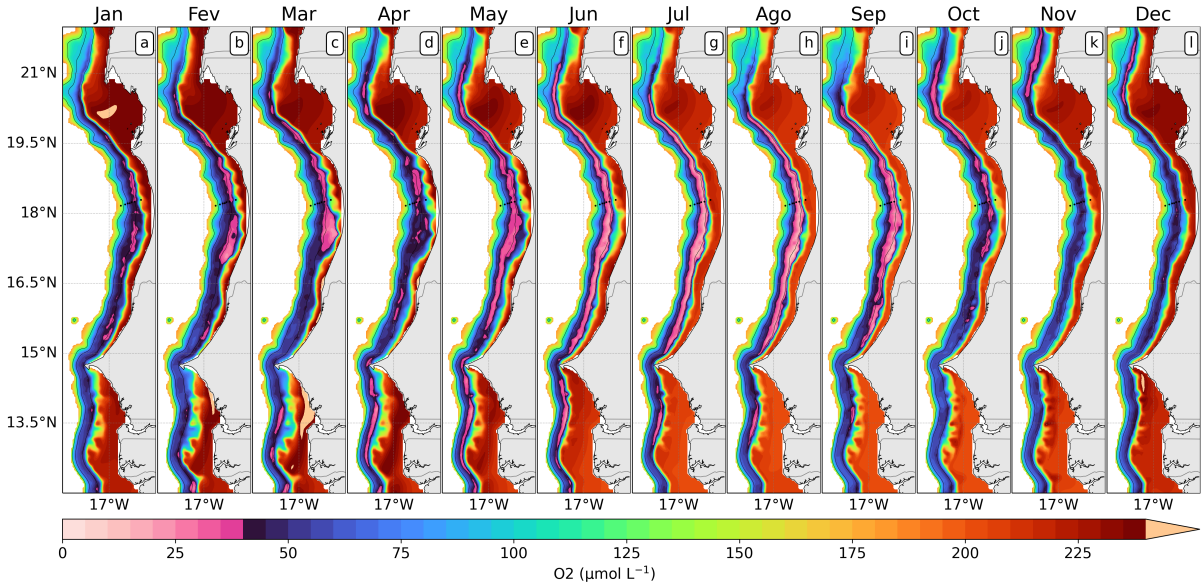


Figure 4.10: Monthly O_2 concentrations averaged over the two bottom model layers. Only depths between 0 and 1500 m are shown. Solid black contours indicate bathymetric depths of 100, 500, and 1000 m. Black dots at 18°N mark the positions of bottom stations sampled during the MSM17/4 and M107 campaigns, whose data are used for model validation (Section 2.3.2).

As expected, a clear seasonal decline in bottom O_2 concentrations is observed across all latitudes from the upwelling to the relaxation season, with the most pronounced decreases occurring between Cap-Vert and Cap-Blanc (Figure 4.10). From January to May, low O_2 levels extend across the continental shelf, with the greatest zonal extent observed over the Senegalese shelf in February–March and off Mauritania between 17°–18°N from February to May. These patterns are consistent with recent observations (Yücel et al., 2015; Tall et al., 2021) and model results (Tall et al., 2025), which link bottom low-O_2 and high-NO_3 conditions to cross-shelf intrusions of oxygen-poor waters driven by coastal upwelling. During the relaxation season, the zonal extent of hypoxic waters contracts, but their intensity increases, with average O_2 concentrations reaching as low as ≈10 µmol L^{-1} along the Mauritanian shelf break and upper slope between June and August.

Field observations support this seasonal trend. In March 2011 (MSM17/4), bottom O_2 concentrations of 42 µmol L^{-1} were measured at the shelf break (Dale et al., 2014a), while in June 2014 (M107), values at the same location dropped to 26 µmol L^{-1} (Dale et al., 2022). Despite this difference, benthic oxygen consumption remained largely unchanged, estimated at ≈7 mmol m^{-2} d^{-1}. Although higher than observations (≈15 mmol m^{-2} d^{-1}), model estimates also exhibit no variation in O_2 sediment fluxes between these two months at this site (Figure 2.9a). However, when all months are considered, a seasonal cycle emerges, reaching maximum and minimum

values in May and in August, respectively (Figure 4.8e), which is consistent with the seasonal variability in EPC100 (Figure 4.2c).

Diapycnal O_2 fluxes during the upwelling season have been estimated at ≈73 mmol m^{-2} d^{-1}, exceeding benthic uptake by a factor of seven (Schafstall et al., 2010; Brandt et al., 2015). However, these fluxes declines exponentially with depth, dropping to less than 10 mmol m^{-2} d^{-1} at 60 m below the mixed layer. This corresponds to a depth of ≈100 m during upwelling and ≈80 m during the relaxation season, given average mixed layer depth of 40 m and 20 m, respectively (Figure 4.8a). Thus, while diapycnal mixing may satisfy upper-layer O_2 demands, it appears insufficient to ventilate deeper shelf and slope waters under increased stratification.

Consistent with these *in-situ* observations, our model indicates that O_2 supply due to vertical mixing at 100 m declines from ≈15 to ≈11 mmol m^{-2} d^{-1} between March and June (Figure A.11a). Given that benthic O_2 demand remains relatively stable between these two months, this reduction in vertical supply is likely to contribute to the onset of bottom hypoxia during the transition from upwelling to relaxation.

Beyond seasonal stratification, seasonal variations in boundary current dynamics can also influence O_2 vertical supply to the bottom. Specifically, turbulence generated by the interaction of the PUC with bathymetry may enhance vertical mixing (e.g., Gula et al., 2016), thereby influencing the transport of O_2 from the water column to the bottom boundary layer. To explore this further, Figure 4.11 illustrates the climatological daily variability of bottom O_2, V, and PV at the four longitudinal sections analyzed in Sections 4.3 and 4.4.1.

Seasonal cross-shelf intrusions of low-oxygen waters onto the shelf are evident during the upwelling season at 16° and 18°N (Figures 4.11b,c). During this period, the poleward flow is concentrated near the shelf break, and PV is mostly negative due to instabilities generated by the interaction of the PUC with bathymetry (Figures 4.11e–h and i–l). These interactions intensify vertical shear and modify vertical density gradients, reducing stability and enhancing mixing, which in reduces PV (Todd et al., 2016). Additionally, the flow over sloping bathymetry induces vertical stretching and tilting of vorticity, leading to negative relative vorticity ($\zeta < 0$). Such dynamics are common along eastern boundary continental slopes, where poleward undercurrents interacting with complex bathymetry generate strong vertical and horizontal shear (e.g., Molemaker et al., 2015; Gula et al., 2016; Contreras et al., 2019; Dilmahamod et al., 2022).

As the PUC shoals along the continental slope, negative PV is progressively replaced by positive PV, indicating reduced turbulence from bottom shear and a more stable bottom boundary layer. This transition is accompanied by a decline in O_2 concentrations across all latitudes, likely driven by reduced ventilation–both by vertical mixing and horizontal advection–and longer residence times. Under these conditions, O_2 consumption processes become dominant, despite their overall reduction relative to earlier months (Figure 4.9e).

When the PUC re-intensifies and returns to deeper layers along the continental slope, negative PV re-emerge due to elevated bottom shear stress and O_2 concentrations increase. This increase is likely driven by the advection of more oxygenated waters and enhanced vertical mixing. These results highlight the sensitive interplay between horizontal oxygen supply, vertical stratification, and turbulence generated by the bottom shear stress–factors that collectively govern bottom oxygen variability along the continental margin.

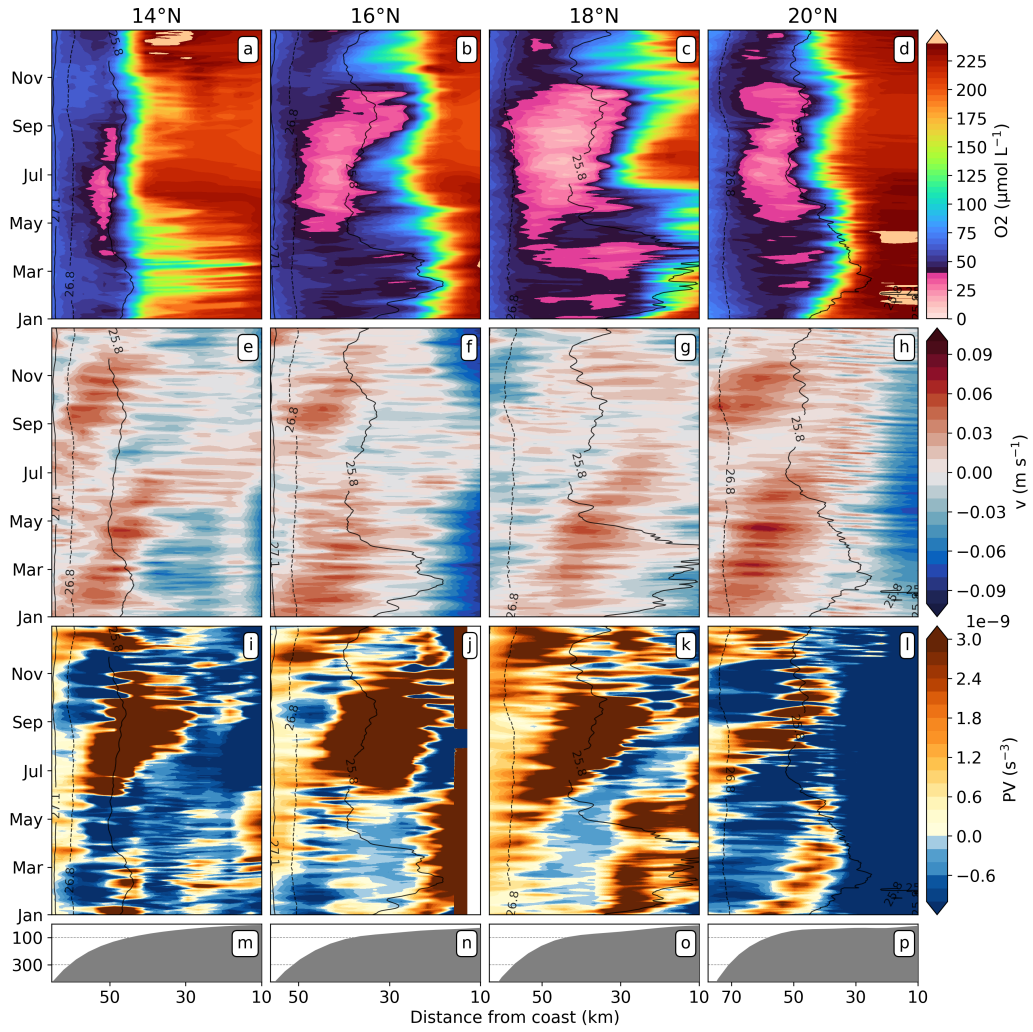


Figure 4.11: Climatological daily variability of O_2 and physical parameters influencing vertical mixing at the bottom of the continental shelf and slope. Daily climatologies were computed with data averaged from the two bottom layers at four longitudinal sections. (a–d) O_2 concentrations; (e–h) V; (i–l) PV. Solid and dashed black contours represent relevant σ_θ isopycnals (kg m^{-3}). (m–p) Bathymetry profiles for each longitudinal section.

4.5 Lagrangian assessment of hypoxic water masses

To gain a deeper understanding of the origins and evolution of water masses that become hypoxic in the coastal region, we employ a Lagrangian framework based on the analysis of particle trajectories released in hypoxic grid cells and tracked bakward in time. This approach enables a detailed assessment of residence times, transport pathways, and the import–export dynamics governing the distribution and persistence of coastal hypoxic waters.

4.5.1 Residence time

The seasonal shoaling of the PUC during the relaxation season, along with the consequent reduction in meridional current velocities below the mixed layer, is expected to increase water residence time along the coast, likely contributing to declining O_2 concentrations (e.g., Pitcher et al., 2021, and references within). To assess these dynamics, Figure 4.12 presents the total

and monthly averaged residence time of particles detected within each 0.1° bin along latitude, considering only those at depths greater than 40 m. For a broader perspective on the spatial variations in particle retention, Figure A.12 is provided in supplementary material.

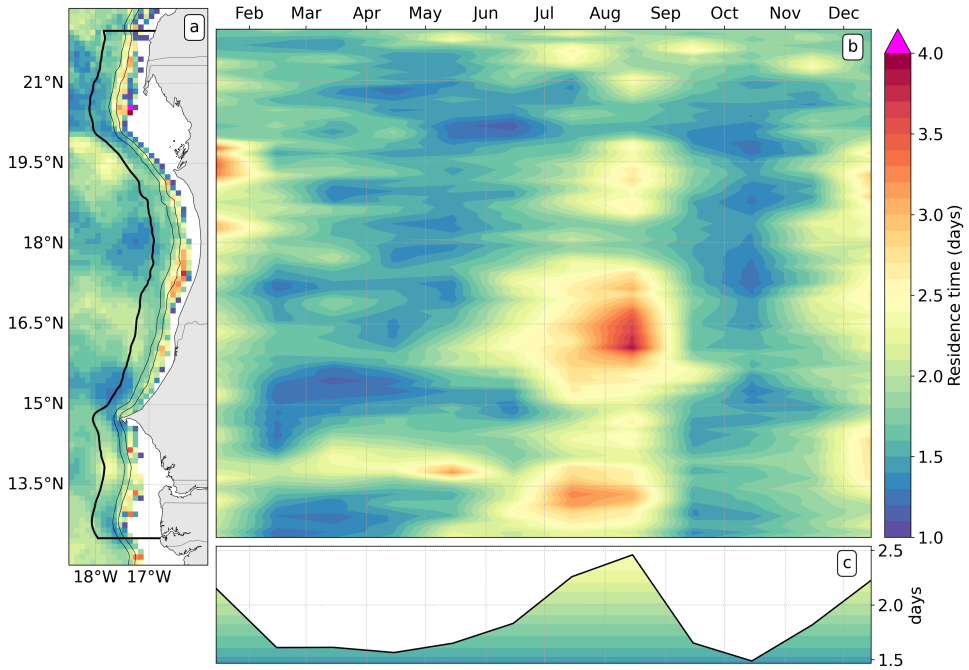


Figure 4.12: Water residence time in the coastal region. (a) Time-averaged residence time of particles for each 0.1° bin. Thick black contour represents the coastal region boundary, while thin black contours indicate the 100 m and 300 m isobaths. (b) Hovmöller diagram of monthly averaged residence time along latitude, calculated only within the coastal region. (c) Monthly average residence time integrated across all latitudes.

The shortest residence times are observed immediately downstream of major topographic features, particularly near the Cap-Vert and Cap-Blanc headlands (Figure 4.12a). Another area of low residence time is detected around 18°N, though it lies mostly outside the defined coastal region. These low-residence zones become more pronounced from March to June and from October to November (Figure 4.12b), coinciding with periods of peak PUC intensity (Figure 4.4). The presence and timing of these dispersal zones suggests that the interaction of the PUC with the complex bathymetry facilitates the rapid offshore export of water masses. During these periods, a sharp contrast in residence times emerges between the coastal and offshore regions (Figures A.12d–e, i–j), reinforcing the effectiveness of the coastal region's 0.5° delimitation in capturing the PUC's influence on local dynamics.

In contrast, the longest residence times are observed between June and September–especially between 15° and 18°N–and again from December to January (Figures 4.12b–c). Both these periods coincide with reduced PUC transport across all latitudes (Figure 4.4, right panels), further highlighting the role of reduced poleward transport in prolonging water retention and promoting hypoxic conditions.

4.5.2 Transport pathways

To investigate the transport pathways of hypoxic water masses in the coastal region, Figure 4.13 shows the seasonal distribution of passive particles released in hypoxic grid cells and detected within each 0.1° bin, along with a representative subset of randomly selected trajectories originating from each 0.2° bin. This analysis focuses on the first 60 days of particle lifetime; thus, although particles are released in a given season, their trajectories reflect advective pathways over the preceding two months and may extend into the prior season. Particles are grouped into two categories: bottom particles, released within the model's two lowest layers, and water column particles. Of the 103,234 particles released in the coastal region, 78.52% originated from the water column, while 21.47% were released from bottom layers.

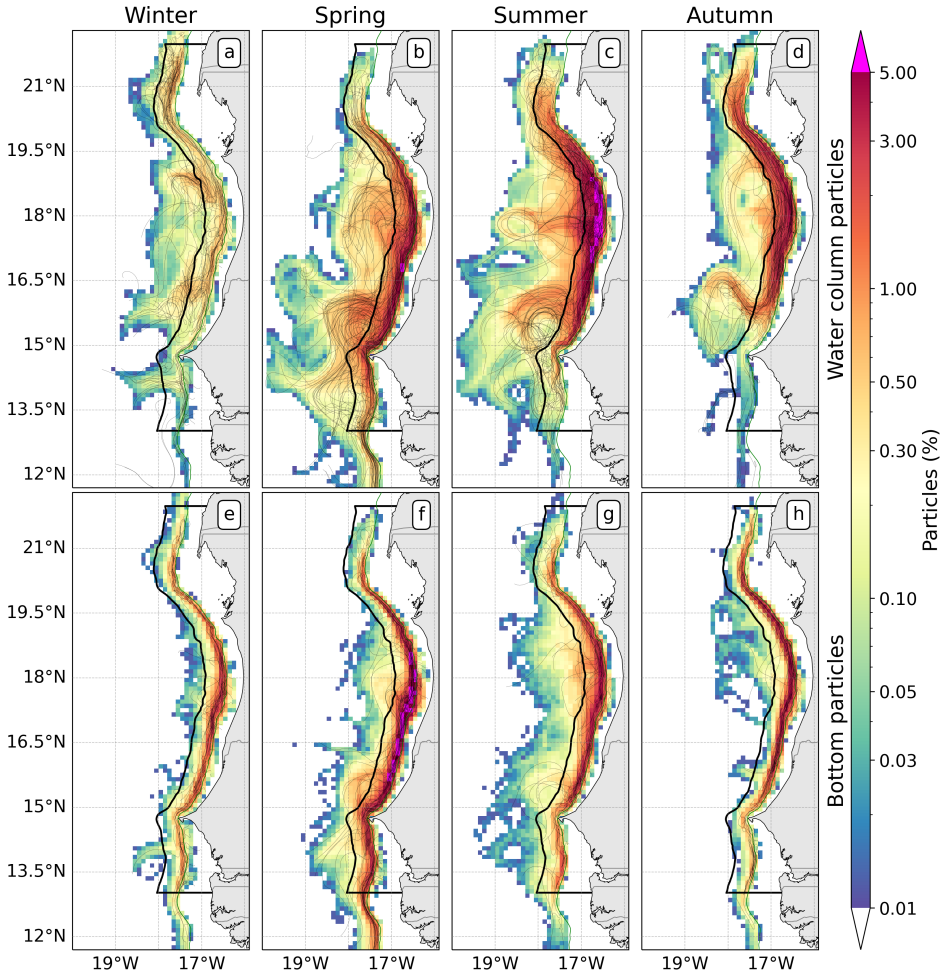


Figure 4.13: Seasonal backward trajectories of coastal hypoxic water masses. (a–d) Water column particles, and (e–h) bottom particles, released within the two last model layers. Only the initial 60 days of particle trajectories are considered. Thin black lines represent randomly selected particle trajectories (one per 0.2° bin). Thick black lines outline the coastal region. Thin green contours parallel to the coast represent the 100 m isobath.

Across all seasons, most particle trajectories exhibit a predominant meridional orientation along the coast, highlighting the key role of the PUC in shaping coastal dynamics. This pattern is especially pronounced for bottom particles, which remain largely confined to the continental margin and show minimal cross-shore exchange (Figures 4.13e–h). Water column particles exhibit greater variability, particularly during spring and summer, when a significant fraction

is traced back to the offshore region via two preferential pathways. One pathway is located north of Cap-Vert, where trajectories form a distinct clockwise-rotating pattern indicative of an anticyclonic eddy in the headland's wake (Figures 4.13b–d). This feature is consistent with the disruption of poleward currents previously identified in the same region (Figure 4.5b). As it will be shown in Chapter 5, this anticyclonic eddy is actually a recurrent ACME formed by the interaction of the PUC with the headland. A second area of cross-shelf exchange appears near 18°N, also during spring and summer. Here, particle trajectories are more irregular, suggesting the influence of transient or spatially variable eddy activity rather than a persistent, coherent structure.

Although bottom particles generally show limited connectivity with offshore waters, those released in summer extend farther offshore compared to other seasons (Figures 4.13g), supporting the hypothesis that the shoaling of the PUC enhances cross-shelf exchange. Some bottom particles released in spring and summer also appear to be partially influenced by the ACME north of Cap-Vert. However, their trajectories suggest localized recirculation of waters coming from the south, rather than direct import of offshore waters from the west.

4.5.3 Particle coastal import

To better understand the dynamics and characteristics of hypoxic water masses detected within the coastal region, we analyze particle intersections with the southern, western, and northern boundaries of the coastal region (Figure 4.14). For each intersection, parameters such as the day of the year, particle lifetime, O_2 concentration, depth, and %SACW were recorded. Given that particles may cross the boundaries multiple times before reaching their final destination, only the first intersection following their release is considered. Additionally, only particles that crossed the boundaries within a maximum of 180 days (6 months) after their release are considered, corresponding to ≈95% of the total coastal particles (Figure A.13).

Most particles (90.98%) enter through the western boundary, with a slightly lower proportion for bottom particles (83.32%) compared to water column particles (93.08%). The southern boundary accounts for 8.28% of the particles. However, it serves as a much more significant entry point for bottom particles (16.05%) than for water column particles (6.43%), emphasizing the role of the PUC in bottom water transport. As expected, particle import through the northern boundary is residual (0.63% for bottom and 0.60% for water column particles), being primarily associated to short-term re-circulation events.

Three major entry points are identified along the coastal boundary, with particle intersection depths concentrated mostly between 50 and 150 m (Figures 4.14b, d). The southern boundary entry point is active from February–May and September–November. Particles crossing here exhibit high O_2 concentrations (≈80 µmol L^{-1}), long transit times (60–90 days), and high SACW proportions (>96%), indicating well-ventilated SACW transported by the PUC.

To reach hypoxic conditions within the coastal region, these particles likely experience at least one of two possible scenarios: (i) prolonged residence times, allowing for gradual oxygen depletion, or (ii) exposure to elevated respiration rates. Both scenarios are possible within the bottom boundary layer, where slower current speeds (Figure 4.11e–h) and the accumulation of

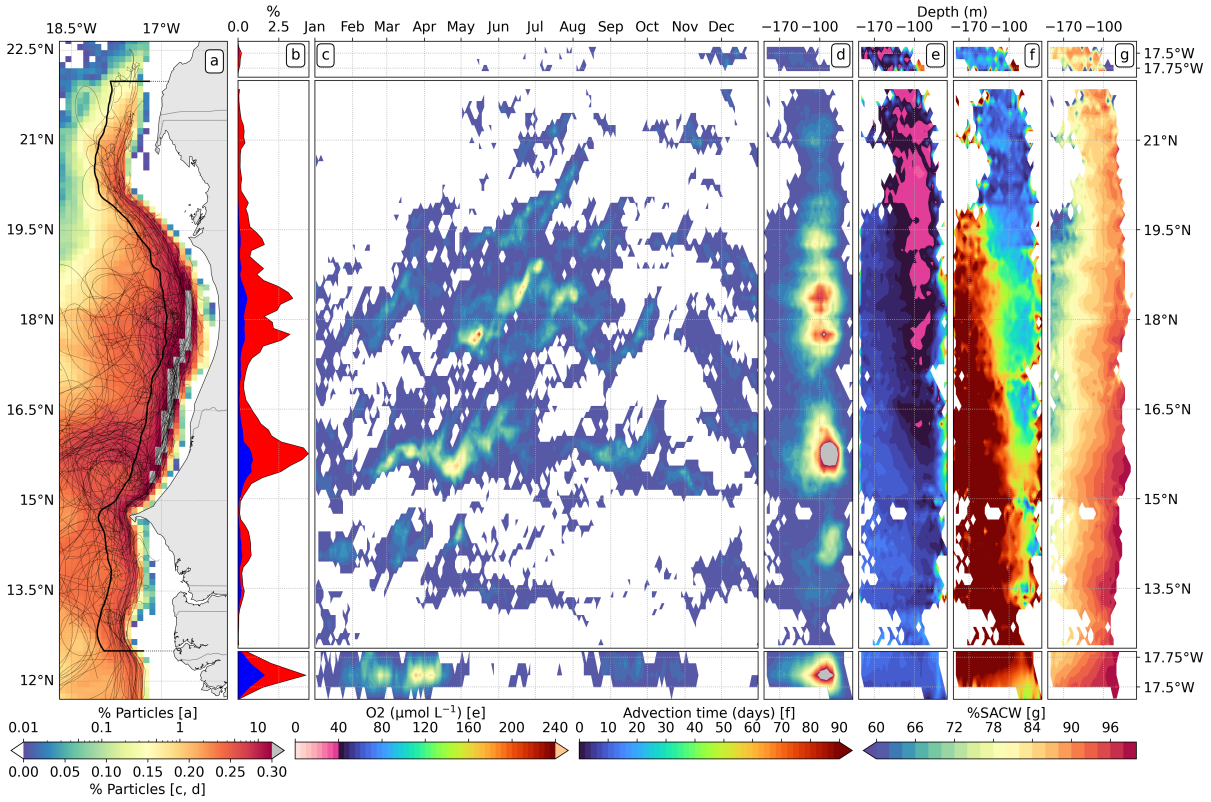


Figure 4.14: Import of lagrangian particles released within the coastal region and crossing the respective boundary. Coastal region is defined at 0.5° distance from the shelf break (100 m depth). Only particles intersecting the boundaries within 180 days after being released are accounted for. (a) Proportion of particles crossing each 0.1° bin. Thin black lines represent a subset of randomly selected trajectories of particles released in each 0.2° bin. Solid thick black line represents coastal boundary. (b) Total proportion of particles intersecting the coastal boundary along latitude and longitude. Following the same procedure as in Figure 4.13, blue and red areas represent the proportion of bottom and water column particles, respectively. (c) Hovmöller diagram with the proportion of particles intersecting the boundaries, with latitude and day of the year represented in the vertical and horizontal axis, respectively. (d–g) Vertical sections (with depth in the horizontal axis) for the proportion of intersecting particles, and average particle O_2 concentrations, advection time (from release to intersection with the boundary) and %SACW, respectively. Note the separation between upper, central and lower sub-panels from (b–g), representative of the northern, western and southern boundaries, respectively.

sinking POC create ideal conditions for increased respiration. These dynamics likely explain the higher proportion of bottom particles transiting through the southern boundary compared to water column particles.

The most important entry point is located north of Cap-Vert headland (15°–16.5°N, Figure 4.14b), accounting for 32% of the hypoxic water masses detected in the coastal region. These particles intersect the boundary primarily from March–May (Figure 4.14c), coinciding with periods of strong alternating positive and negative meridional velocities upstream and downstream of the headland, respectively (Figure 4.5). As suggested in the previous section, swirling particle trajectories reveal the influence of a recurrent anticyclonic eddy, which seems to facilitate the onshore transport of offshore waters (Figure 4.14a). These waters have average O_2 concentrations between 40–50 µmol L^{-1} and take 30–60 days to reach hypoxic conditions (Figure 4.14e and f, respectively), indicating that hypoxic conditions develop during northward transport within the coastal region.

The second most important entry point is depicted between 17.3° and 18.7°N (Figure 4.14b), accounting for 31% of the total coastal particles. This entry point is mostly active between May

and August (Figure 4.14c), aligning with the surfacing of the PUC and the seasonal decline in O_2 concentrations at these latitudes (Figures 4.4c and 4.5d, respectively). With mean O_2 levels of $\approx$40 µmol L^{-1}, shorter transit times (< 30 days), and lower SACW proportions (< 90%), particles entering here have characteristics closely resembling their final form. Such seasonality and water mass characteristics suggest that the surfacing of the PUC facilitates the cross-shore transport of older, oxygen-poorer SACWcv into the coastal region (as shown in Figures 4.5c and 4.8b), contributing to the seasonal formation of hypoxic conditions.

To further validate these findings, particle intersections are also analyzed at a boundary located farther offshore (1° from the shelf break, Figure A.14). The proportion of particles imported near 18°N shows a substantial reduction, whereas those imported further south become significantly more dominant, with the Cap-Vert pathway increasing from 32% to 44%. This difference indicates that many of the intersections observed at 18°N result from particle re-circulation within the coastal region. The existence of two peaks adjacent to each other (Figure 4.14b), combined with a more dispersed trajectory pattern at these latitudes (Figure 4.14a) suggest that eddy horizontal stirring is likely to play na important role in the re-circulation and mixing of SACW from May to August.

4.5.4 Export of hypoxic bottom waters

Given the potential contribution of bottom waters to the sOMZ (Brandt et al., 2015; Thomsen et al., 2019), this section examines the export of hypoxic Lagrangian particles from the continental margin to both coastal and offshore regions. The analysis focuses on particles released in the coastal and offshore domains that can be traced back to the continental margin within 120 days and exhibit hypoxic O_2 concentrations upon crossing the respective boundary. The continental margin is defined here as the area shallower than 300 m depth, east of the easternmost green contour shown in Figure 4.15. As in the previous sections, bottom particles refer to those whose past trajectories originate from the model's two lowermost layers. To assess the influence of eddies, particles are further classified based on whether they are detected inside or outside the perimeter of coastal-generated eddies.

Of the 45,724 particles detected within the coastal region after export from the continental margin, approximately 9% originated from bottom layers. While this fraction may appear small, it is consistent with the relatively limited volume represented by the bottom layers compared to the entire coastal water column (Brandt et al., 2015). Notably, around 65% of these bottom particles were detected within coastal-generated eddies, underscoring the important role of eddies in facilitating the export of hypoxic bottom waters. It is important to note, however, that eddy perimeters were identified based on modeled current velocities at 100 m depth (Section 2.4.4). Given that eddy structures can vary significantly with depth (e.g., Haller et al., 2016; Oke et al., 2019), some bottom particles may have been influenced by eddies without being classified as inside an eddy perimeter. Indeed, swirling particle trajectories evident in Figure 4.15a suggest that eddy-driven export may be somewhat underestimated by this method.

Approximately 48% of the exported bottom particles detected within the coastal region reached offshore waters, with 84% of these associated with eddy structures. The prominent

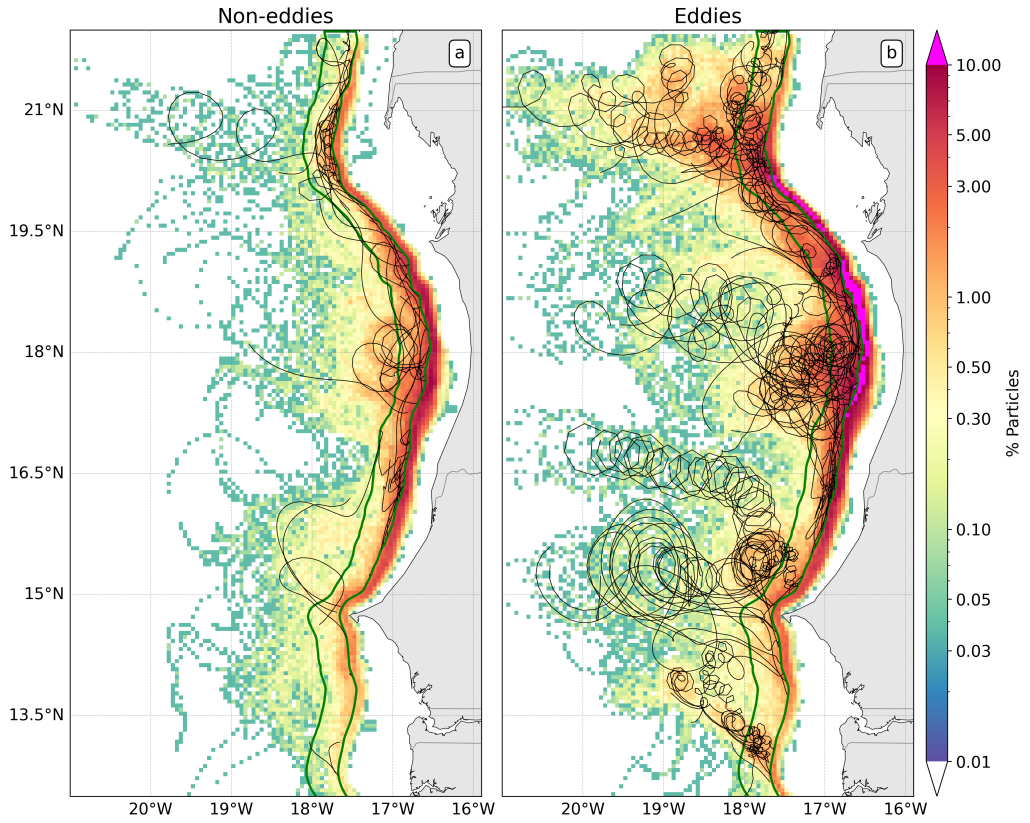


Figure 4.15: Export of particles from the bottom of the continental margin. Particles are categorized into those detected outside (a) and inside (b) the perimeter of eddies. Here, the coastal area is bounded by two green contours parallel to the coast, whereas the continental margin is defined as the area with bathymetry shallower than 300 m (east of the easternmost green contour). Thin black lines represent randomly selected particle trajectories detected in each 0.1° latitude within the continental margin. Spatial histogram has an horizontal resolution of 0.1°.

role of coastal-generated eddies in promoting offshore transport is further illustrated in Figure 4.15b, where anticyclonic-rotating particle trajectories extend westward as far as 20°W. Given the 120-day maximum particle lifetime considered here–and the larger westward extensions of eddy LHEs documented in Chapter 3–this offshore reach is also likely underestimated.

Interestingly, the main regions of bottom particle export coincide with previously identified hotspots for ACME generation (Schütte, Brandt, & Karstensen, 2016; Dilmahamod et al., 2022), supporting earlier findings that ACMEs effectively trap low-PV waters from the bottom boundary layer within their cores (e.g., Molemaker et al., 2015; Contreras et al., 2019; Gula, 2020). Given that these low-PV bottom waters are often hypoxic (Figure 4.11a–d), out results strongly suggest that ACMEs play a key role in redistributing hypoxic waters from the continental margin to the open ocean. These eddy-driven dynamics are explored in greater detail in the next chapter.

4.6 Summary and conclusions

This chapter provides a comprehensive analysis of the mechanisms driving the formation and transport of hypoxic waters along the northwestern African coast. By integrating an Eulerian-Lagrangian approach, we examined the seasonal variability of oxygen concentrations and bound-

ary current dynamics, revealing the interplay between physical and biogeochemical processes that drive the seasonal development of hypoxic conditions within the coastal region of the ETNA.

The seasonal variability of the PUC is the primary driver regulating the onset and intensity of coastal hypoxia along the northwestern African margin. During the upwelling season (December–May), the PUC advects relatively oxygenated SACW at subsurface depths (90–100% SACW), ventilating upper central water masses and maintaining O_2 concentrations above 60 μmol L^{-1}. As upwelling-favorable winds weaken, the PUC progressively shoals and weakens at depth, particularly from May to July, reducing the influx of oxygenated waters while increasing water residence times by up to 130%. Simultaneously, cross-shelf mixing with older, oxygen-poorer SACWcv waters intensifies, leading to a rapid decline in O_2 concentrations, particularly between 15° and 20°N, where summer hypoxic frequencies reach up to 70%.

The transition from upwelling to relaxation season (May–July) marks the critical period for hypoxia formation. Despite a gradual decrease in upwelling intensity after May, residual NO_3 sustains elevated primary productivity in the mixed layer, driving export production and fueling oxygen consumption through nitrification and zooplankton respiration at subsurface depths. Concurrently, the relaxation of upwelling dynamics leads to the surfacing of the PUC–which cuts off subsurface oxygen supply–and increases stratification by up to 30%, further isolating subsurface waters. This combination of persistent biological consumption and diminished physical ventilation, either by horizontal advection and vertical mixing, results in a mean O_2 deficit of up to $\approx$3 μmol L^{-1} $month^{-1}$ between June and July, which, although apparently insignificant, is sufficient for the onset of hypoxia. Hypoxic conditions are maintained until the re-intensification of the PUC in September–October restores ventilation with pure SACW, flushing the region and resetting oxygen levels.

In bottom layers, hypoxia is primarily driven by physical rather than biogeochemical processes. Although O_2 sediment fluxes decrease during the relaxation season by up to 60%–reflecting reduced POC export to the seafloor–bottom hypoxic conditions intensify during this period. This is mainly because the seasonal weakening of the PUC reduces the advection of oxygen-rich SACW into the region, while diminished turbulence from bottom shear stress further limits vertical O_2 supply through vertical mixing. Combined with enhanced stratification in the upper ocean, these processes create favorable conditions for the development and persistence of hypoxic bottom waters. Hypoxia prevails until the PUC re-intensifies in autumn, restoring oxygen supply via renewed ventilation and enhanced vertical mixing.

Beyond seasonal variability in boundary current dynamics, mesoscale eddies play a crucial role in shaping regional O_2 dynamics. A recurrent ACME generated downstream of the Cap-Vert headland disrupts direct oxygen supply to northern latitudes while facilitating the onshore transport of an older, oxygen-poorer SACWcv variety. Our Lagrangian analysis reveals that 32% of the waters that become hypoxic within the coastal region originate from this entry point, a value that increases significantly to 44% when considering a more conservative offshore boundary (at a distance of 1° from the shelf break). This suggests that the Cap-Vert ACME plays a key role in transporting diluted, oxygen-poorer SACWcv into the coastal region, which, although not hypoxic at the time of import, contributes to the development of hypoxic conditions within the region.

Eddy activity also appears to play an important role in cross-boundary exchanges near 18°N during summer, when the PUC is manifested at the surface as the MC. However, a more conservative analysis revealed that these particle trajectories results from the re-circulation of particles entering the region further south. This means that the surfacing of the PUC opens a window for the mixing of SACW with the regional SACWcv variety, further contributing to the dilution of O_2 concentrations.

The export of bottom hypoxic waters is another important process contributing to the formation of the sOMZ. Eddies, likely generated by the interaction of the PUC with bathymetry (Dilmahamod et al., 2022), are responsible for trapping and redistributing at least 65% of the exported bottom hypoxic waters. These structures serve as key transport pathways, extending hypoxic conditions into the open ocean as far west as 20°W. Given that ACMEs are most likely the main features responsible for this offshore transport, our results highlight their major role in redistributing low-oxygen waters from the continental margin to the open ocean.

Taken together, our findings highlight the complex interplay between boundary current dynamics, biogeochemical processes and coastal-generated eddies in shaping the sOMZ along the coastal region of the ETNA, with important consequences to its maintenance further offshore. The seasonal displacement of the PUC emerges as the most important direct and indirect driver of hypoxic conditions, regulating O_2 supply, water residence time, and onshore and offshore transports through eddy horizontal stirring. Although this chapter focused primarily on coastal dynamics, the role of coastal-generated eddies could not be neglected.

These insights improve our understanding of O_2 dynamics in EBUSs and emphasize the need for further investigations into the long-term impacts of climate variability on hypoxia. Given the uncertainty in climate projections for the Mauritania-Senegal upwelling system (Sylla et al., 2019; Vázquez et al., 2023; Du et al., 2024), future changes in circulation patterns, export production, and eddy activity will likely shape the evolution of low-oxygen conditions in the region, with profound implications for biogeochemical cycling, marine ecosystems, and regional fisheries.

Chapter 5

Generation and evolution of low-oxygen eddies in the Eastern Tropical North Atlantic

5.1 Introduction

The ETNA is characterized by the frequent occurrence of mesoscale features that have a profound effect on the regional oceanography. Prominent among these features are coastal filaments, which extend hundreds of kilometers offshore from the northwestern African coast (Van Camp et al., 1991; Gabric et al., 1993; Kostianoy & Zatsepin, 1996; Lange et al., 1998), and mesoscale eddies, predominantly formed along the continental margin. These eddies often exhibit high biological productivity and are frequently associated with low-oxygen conditions in their interior (e.g., Karstensen et al., 2015; Fiedler et al., 2016; Schütte, Karstensen, et al., 2016). Owing to their ability to trap and transport distinct water masses over long distances into the open ocean (e.g., Schütte, Brandt, & Karstensen, 2016; Cardoso et al., 2020), they can sustain unique biogeochemical characteristics (Grundle et al., 2017) and distinct bacterial communities (Löscher et al., 2015). These eddies can simultaneously act as subsurface dead zones, while promoting the formation of open-ocean oases by concentrating biomass in surface layers, thus benefiting pelagic predator species (Hauss et al., 2016).

The formation of hypoxic conditions within eddies in the ETNA has traditionally been attributed to en-route oxygen consumption, primarily driven by the remineralization of sinking organic matter below the mixed layer (e.g., Karstensen et al., 2015; Schütte, Karstensen, et al., 2016; Karstensen et al., 2017). Sustaining such elevated export production requires enhanced primary productivity, which in turn depends on increased nutrient availability. In cyclonic eddies, the mechanisms driving nutrient injection are well established and are commonly linked to surface divergence and the upward displacement of isopycnals, a process known as eddy pumping (Falkowski et al., 1991; Siegel et al., 1999; McGillicuddy, 2016). In contrast, the processes that support nutrient injection in ACMEs are more diverse. These include eddy-wind interactions (McGillicuddy et al., 2007; Gaube et al., 2015), submesoscale instabilities (Mahadevan et al., 2008), ageostrophic secondary circulations (Barceló-Llull et al., 2017; Estrada-Allis et al., 2019), and the generation of Near-Inertial Waves (NIWs; Karstensen et al., 2017; Pietri & Karstensen, 2018), the latter of which have received particular attention in the ETNA.

Low-oxygen ACMEs in this region are characterized by a vertically coherent subsurface core, flanked by local maxima in buoyancy frequency. Observational studies have revealed vertical layering in hydrographic profiles and direct velocity measurements consistent with the

downward propagation of NIWs along the eddy flanks (Karstensen et al., 2017). Since the phase speed of NIWs can match the background flow, the formation of a critical layer is likely, potentially enhancing vertical mixing near the base of the mixed layer (Pietri & Karstensen, 2018). According to Karstensen et al. (2017), this mechanism may explain the apparent coexistence of upward nutrient fluxes and the persistence of an isolated, weakly ventilated core (Fiedler et al., 2016; Schütte, Karstensen, et al., 2016). Although the horizontal and vertical resolution of our model hinders the explicit representation of such small-scale processes, low-oxygen ACMEs are still well represented in our simulations (Chapter 3). This suggests that additional larger-scale mechanisms–potentially overlooked in past observational studies–may play an important role in the development of hypoxia within these eddies.

Besides the en-route formation and intensification of hypoxic conditions inside eddies, results presented in Chapters 3 and 4 suggest that a substantial proportion of eddies forming along the northwestern African coast originate in already hypoxic environments. This phenomenon appears particularly pronounced during the transition from the upwelling to the relaxation season between June and July, and again in early autumn, prior to the re-intensificatio of the PUC.

Previous studies have shown that the generation of ACMEs in EBUSs is closely related to the interaction of poleward subsurface currents with sharp bathymetric bends. This interaction promotes current separation and the generation of submesoscale instabilities with anticyclonic vorticity, which eventually coalesce into coherent, subsurface-intensified structures (Molemaker et al., 2015; Thomsen et al., 2016; Contreras et al., 2019). Numerical simulations by Dilmahamod et al. (2022) have demonstrated that ACMEs generated along the Mauritanian and Senegalese margins efficiently trap low-PV waters in their cores. Although this low-PV signature has been attributed to the interaction of the PUC with sloping bathymetry, a link between these water masses and low-oxygen conditions inside eddies has not yet been established.

Given the widespread hypoxic conditions along the continental shelf and slope indicated by our biogeochemical model, it is plausible that low-PV waters generated at the continental margin are also characterized by low oxygen concentrations, even though oxygen concentrations tend to be lower under conditions of reduced bottom shear stress and positive PV (Figure 4.11). Consequently, ACMEs could already trap hypoxic waters upon formation, particularly at northern latitudes where hypoxia is more likely to develop. This hypothesis is further supported by the high number of ACME LHEs initiating near Cap-Blanc (Figure 3.8), and by the significant proportion of bottom particles being exported by eddies on that region (Figure 4.15).

Building on these findings, the main objective of this chapter is to investigate the mechanisms responsible for the formation of hypoxic conditions within coastal-generated eddies in the ETNA. Specifically, we assess whether the physical processes involved in eddy generation influence the development of hypoxia. We also examine the role of primary productivity, core isolation, and the initial properties of the source water masses (e.g., oxygen concentration and composition) in shaping these low-oxygen features. Beyond formation, we explore the processes that sustain hypoxic conditions over time and evaluate how these mechanisms differ among eddy types.

This chapter is organized as follows: Section 5.2 presents the methods specifically applied for this chapter. In Section 5.3, we describe the general characteristics of the eddy trajectories, vertical structures, generation hotspots, and primary formation mechanisms. Section 5.4 ex-

amines differences between hypoxic and non-hypoxic coastal-generated eddies and presents representative case studies of eddies formed with pre-existing low-oxygen conditions as well as those that develop hypoxia during their evolution. Finally, Section 5.5 summarizes and discusses the key findings of the study.

5.2 Methods

Similarly to the previous Chapter 3 and 4, this Chapter builds upon methodologies previously detailed in Chapter 2. Specifically, the methods employed include the water mass analysis (Section 2.4.3), eddy detection and tracking (Section 2.4.4), and Lagrangian particle simulation (Section 2.4.5). As these methods are common across chapters, their descriptions are not repeated here but referenced where appropriate.

5.2.1 Composite analysis of eddy vertical structure

To assess the mean vertical structure of the different types of eddies generated along the northwestern African coast, we conducted a comprehensive composite analysis comprising all timesteps of coastal-generated eddies with a minimum lifetime of 30 days. Following a methodology similar to that of Chenillat et al. (2018), we extracted longitudinal cross-sections through the eddy center, extending from -2.5R (west) to +2.5R (east), where R represents the eddy radius. To ensure consistency across all eddies, the horizontal coordinates were normalized by R, and relevant physical and biogeochemical parameters were interpolated and averaged along this axis.

Given the ability of eddies to transport anomalous water masses within their cores (Chenillat, Franks, et al., 2015; Condie & Condie, 2016; Schütte, Brandt, & Karstensen, 2016; Lovecchio et al., 2018), cross-section anomalies were computed relative to monthly climatological averages to account for seasonal variability. This approach differs from previous methods that relied on vertical profiles located just outside the eddy periphery as a reference (Schütte, Brandt, & Karstensen, 2016; Dilmahamod et al., 2022), but offers a more robust assessment of eddy-induced deviations from background conditions (Chaigneau et al., 2011). The use of climatologies is particularly appropriate in the ETNA, where the distribution of biogeochemical tracers is highly heterogeneous and eddy-induced horizontal advection can transport distinct water masses along the eddy periphery (Figure A.10). Such effects likely explain the discrepancies reported by Schütte, Brandt, and Karstensen (2016) between anomalies computed using the ”next profile outside” method and those based on climatological fields.

5.2.2 Determination of eddy generation mechanisms

To elucidate on the main eddy generation mechanisms, an analysis on the dynamical instabilities along the Northwestern African coast is conducted to determine the sources of EKE. For that, the energy conversion from MKE to EKE is divided into two components: the Horizontal Shear

Production (HSP) and the Vertical Shear Production (VSP). The conversion from Eddy Potential Energy (EPE) to EKE is also determined by computing Buoyancy Production (BP):

$$EKE = \frac{1}{2}u'^2 + v'^2 \tag{5.1a}$$

$$HSP = -\overline{u'^2}\frac{\partial \overline{u}}{\partial x} - \overline{u'v'}\frac{\partial \overline{u}}{\partial y} - \overline{v'^2}\frac{\partial \overline{v}}{\partial y} - \overline{u'v'}\frac{\partial \overline{v}}{\partial x} \tag{5.1b}$$

$$VSP = \overline{u'w'}\frac{\partial \overline{u}}{\partial z} - \overline{v'w'}\frac{\partial \overline{v}}{\partial z} \tag{5.1c}$$

$$BP = \overline{w'b'} \tag{5.1d}$$

Here, all variables are decomposed into their mean (overbar) and fluctuating (prime) components. The velocity components u, v, and w denote the zonal, meridional, and vertical flow, respectively, and buoyancy is defined as $b = -g\rho/\rho_0$, where g is gravitational acceleration, ρ is density, and $\rho_0 = 1025\,\mathrm{kg\,m^{-3}}$ is the reference density. This analysis enables the identification of the dominant dynamical instability responsible for eddy formation (e.g., Thomas et al., 2013; Gula et al., 2015; Contreras et al., 2019; Calil et al., 2021). Barotropic instabilities are driven by horizontal shear in the flow and arise when HSP > 0. Vertical shear instabilities (Kelvin-Helmholtz type) are driven by vertical shear in the flow and arise when VSP > 0. Lastly, baroclinic instabilities are driven by vertical eddy buoyancy flux and arise when BP > 0.

In addition, several overturning instabilities can arise when Ertel PV (q) takes the opposite sign of the Coriolis parameter and becomes negative in the northern hemisphere:

$$q = (\zeta + f\hat{k}) \cdot \nabla b \tag{5.2}$$

where $\zeta = \nabla \times \mathbf{u}$ is the relative vorticity, $\hat{k}$ is the vertical unit vector, $\mathbf{u} = (u, v)$ is the horizontal velocity vector with components in zonal and meridional axes and f is the Coriolis force. From here, PV can be decomposed into two terms: one associated with the vertical component of the absolute vorticity and stratification:

$$q_{vert} = \zeta N^2 \tag{5.3}$$

and the other associated with the horizontal components of vorticity and buoyancy gradient:

$$q_{bc} = \left(\frac{\partial u}{\partial z} - \frac{\partial w}{\partial x}\right)\frac{\partial b}{\partial y} + \left(\frac{\partial w}{\partial y} - \frac{\partial v}{\partial z}\right)\frac{\partial b}{\partial x} \tag{5.4}$$

Assuming that the flows are in geostrophic balance, q_{bc} is derived through the thermal wind relation:

$$q_{bc}^{g} = -f\left|\frac{\partial \mathbf{u}_g}{\partial z}\right|^2 = -\frac{1}{f}\left|\nabla_h b\right|^2 \tag{5.5}$$

where $\mathbf{u}_g$ is the geostrophic current velocity. When $q_{vert} < 0$ and $N^2 > 0$, inertial instabilities arise. Inertial instabilities that extract the energy of the mean current through horizontal shear,

that is, from barotropic instabilities (i.e., HSP > 0), are called centrifugal instabilities (e.g., Thomas et al., 2013). Gravitational instability occur when $N^2 < 0$; and symmetric instability when $|q_{bc}| > q_{vert}$ and $q_{vert} > 0$.

5.3 Characteristics of coastal-generated eddies

The key characteristics of coastal-generated eddies are assessed in this section. By doing so, we aim to gain a comprehensive understanding of their distribution, kinematic characteristics and behavior. This analysis also allows us to compare our findings with those of previous studies (e.g., Schütte, Brandt, & Karstensen, 2016; Dilmahamod et al., 2022) and thus help validate our model results. For the purposes of this study, coastal-generated eddies are defined as those formed within an area extending 1.5° from the continental shelf break, defined at 100 m depth. This extended definition accounts for the fact that while many eddies are expected to originate from the interaction of the PUC with bathymetry (e.g., Dilmahamod et al., 2022), their centers may be sometimes located beyond the immediate influence of the PUC (i.e., ≈55 km from the shelf break; see Chapter 4). Unless stated otherwise, our analyses include only eddies with a minimum lifetime of 30 days.

5.3.1 Trajectories and mean properties

The general eddy trajectory patterns exhibit predominantly westward propagation, with limited meridional deviations along the way (Figure 5.1a). The most pronounced deflections are primarily caused by interactions with the Cabo Verde Islands, which act as physical obstacles, redirecting or in some cases terminating the eddy trajectories (Schütte, Brandt, & Karstensen, 2016; Cardoso et al., 2020). Although some altimetry-derived eddies have been observed to squeeze between the islands or generate new eddies via splitting events (Cardoso et al., 2020), such processes are not captured in this study due to the use of ocean currents at 100 m depth for eddy tracking.

The distribution of eddy origins shows distinct spatial patterns in the formation of cyclones, anticyclones and ACMEs (Figure 5.1b). While ACMEs appear to originate predominantly along the continental slope, a substantial number of cyclonic and anticyclonic eddies is formed between the shelf break and the coastal boundary. This spatial differentiation suggests that different mechanisms may drive the formation of each eddy type. Specifically, ACMEs may primarily result from the separation of the PUC from the continental slope (Molemaker et al., 2015; Contreras et al., 2019), while cyclonic and anticyclonic eddies may emerge from other processes, such as large-scale circulation instabilities or interactions between boundary currents and pre-existing mesoscale features (Dilmahamod et al., 2022).

Cyclonic and anticyclonic-rotating eddy trajectories (including ACMEs) show slight meridional preferences, with cyclonic eddies tending to deflect northward and anticyclonic eddies southward. This pattern is consistent with global (Chelton et al., 2011) and regional altimetry-derived observations (Schütte, Brandt, & Karstensen, 2016; Cardoso et al., 2020), and aligns

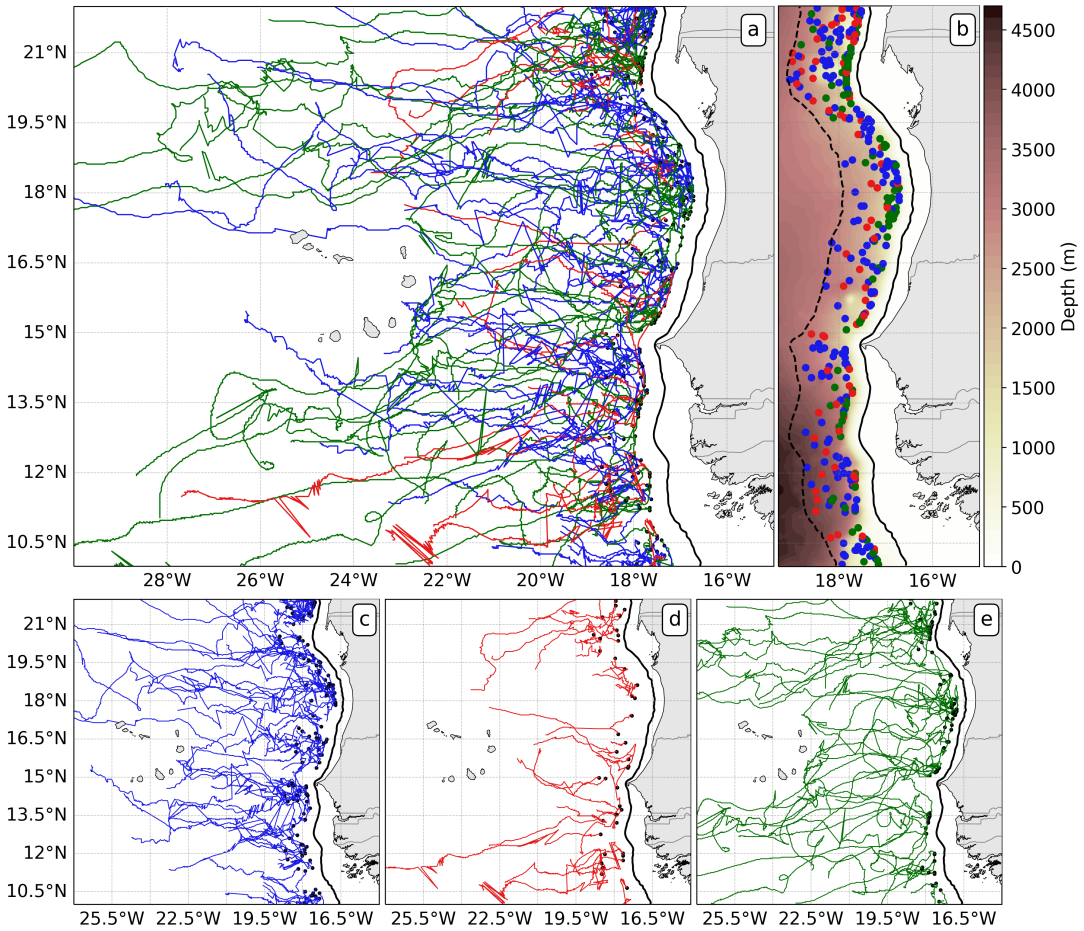


Figure 5.1: Trajectories of coastal-generated eddies. (a) Eddy trajectories and respective (b) origins, with bathymetry represented in the background. Blue, red and green colors indicate cyclones, anticyclones and ACMEs. Panels (c), (d), and (e) show the trajectories for cyclonic, anticyclonic, and ACME eddies, respectively. The dashed black line in (b) represents the boundary of the coastal area, while the solid black line in all panels represents the shelf break at 100 m depth.

with theoretical predictions of westward eddy propagation influenced by the meridional gradient of the Coriolis parameter (the β-effect; Cushman-Roisin et al., 1990).

A comparison of mean properties between eddy types reveals differences in their lifetime, propagation distance, and structural characteristics (Table 5.1). Cyclonic eddies, which account for 49% of all coastal-generated eddies, are on average bigger than anticyclones and ACMEs, with an average radius of 43 km. They also have an average lifetime of 108 days and a mean propagation distance of 422 km. Their trajectories are predominantly confined east of 22.5°W (Figure 5.1c), indicating that these eddies generally do not propagate as far offshore as ACMEs. Nevertheless, there are some exceptions to this, particularly those that propagate through the north of Cabo Verde.

Anticyclonic eddies, which represent 18% of the total, exhibit the lowest mean lifetime and average propagation distance. Their trajectories (Figure 5.1d) display significant variability, with most eddies remaining near the coastal region and only one propagating beyond the Cabo Verde Archipelago. This relatively short lifetime and limited trajectory extent suggest that anticyclonic eddies are substantially less coherent than cyclones and ACMEs, potentially reflecting distinct formation mechanisms.

Table 5.1: Mean properties of coastal-generated eddies. Number, annual frequency, mean and standard deviation (Std.) of lifetime, radius, rotation velocity, and propagation distance are shown for cyclones, anticyclones and ACMEs.

		Cyclonic	Anticyclonic	ACME
Number		122 | 49% 24 yr^{-1}	42 | 17% 8 yr^{-1}	85 | 34% 17 yr^{-1}
Lifetime (days)	Mean	108.20	92.19	183.35
	Std.	93.37	59.84	158.28
Radius (km)	Mean	43.26	40.01	32.34
	Std.	20.12	18.60	14.28
Rotation velocity (m s^{-1})	Mean	0.08	0.09	0.16
	Std.	0.04	0.04	0.05
Propagation distance (km)	Mean	269.84	250.95	434.43
	Std.	269.31	207.03	468.83

ACMEs account for 34% of coastal-generated eddies and represent the longest-lived and farthest-propagating eddy type, with an average lifetime of 183 days and a mean displacement of 434 km, frequently extending beyond the Cabo Verde Islands (Figure 5.1e). Their extended propagation suggests that ACMEs are more resilient than surface-intensified cyclonic and anticyclonic eddies, as indicated by their higher mean rotation velocity[1] of 0.16 m s^{-1}, compared to 0.09 and 0.10 m s^{-1} for cyclonic and anticyclonic eddies, respectively. Similar findings have been reported for ACMEs formed by topographically induced instabilities of the California Undercurrent, which significantly outlive cyclones (Kurian et al., 2011). It has also been hypothesized that the subsurface-intensified structure of ACMEs insulates them from atmospheric forcing, thereby enhancing their longevity in the open ocean (Dilmahamod et al., 2022). However, it is important to note that the rotation velocities reported in this study are derived from currents at 100 m depth, potentially underestimating the rotation velocity of surface-intensified cyclonic and anticyclonic eddies (Combes et al., 2015; McGillicuddy, 2016).

Our results show some differences compared to the observational findings of Schütte, Brandt, and Karstensen (2016). In particular, eddies identified in our study exhibit longer lifetimes but smaller average sizes. These discrepancies likely stem from the intrinsic limitations of altimetry-based eddy detection, which, at the time of their study, was constrained by a horizontal resolution of 0.25° and relied heavily on interpolated nadir, along-track measurements (Amores et al., 2018). Furthermore, the Schütte, Brandt, and Karstensen dataset included eddies with lifetimes as short as seven days, which lowers the reported mean lifetime. Despite this, their total number of detected eddies is lower than ours, which is unexpected given their less restrictive lifetime threshold. This difference is especially pronounced for ACMEs, of which only ≈13 were detected per year. Such limited number of ACMEs in their study is likely attributable to the challenges of detecting subsurface-intensified eddies using surface-derived altimetric fields (Assassi et al., 2016; C. Li et al., 2017).

[1] Defined as the mean azimuthal velocity along the outermost closed contour that defines the eddy perimeter (Le Vu et al., 2018).

5.3.2 Vertical structure

To characterize the mean vertical structure of coastal-generated eddies, we present composite sections of their physical and biogeochemical properties. Figure 5.2 displays the average physical structure, while Figure 5.3 shows the corresponding biogeochemical fields. These composites were derived from longitudinal cross-sections through the eddy center. Given the near-radial symmetry of the eddy fields, these sections are considered representative of the overall eddy structure (Chenillat et al., 2018).

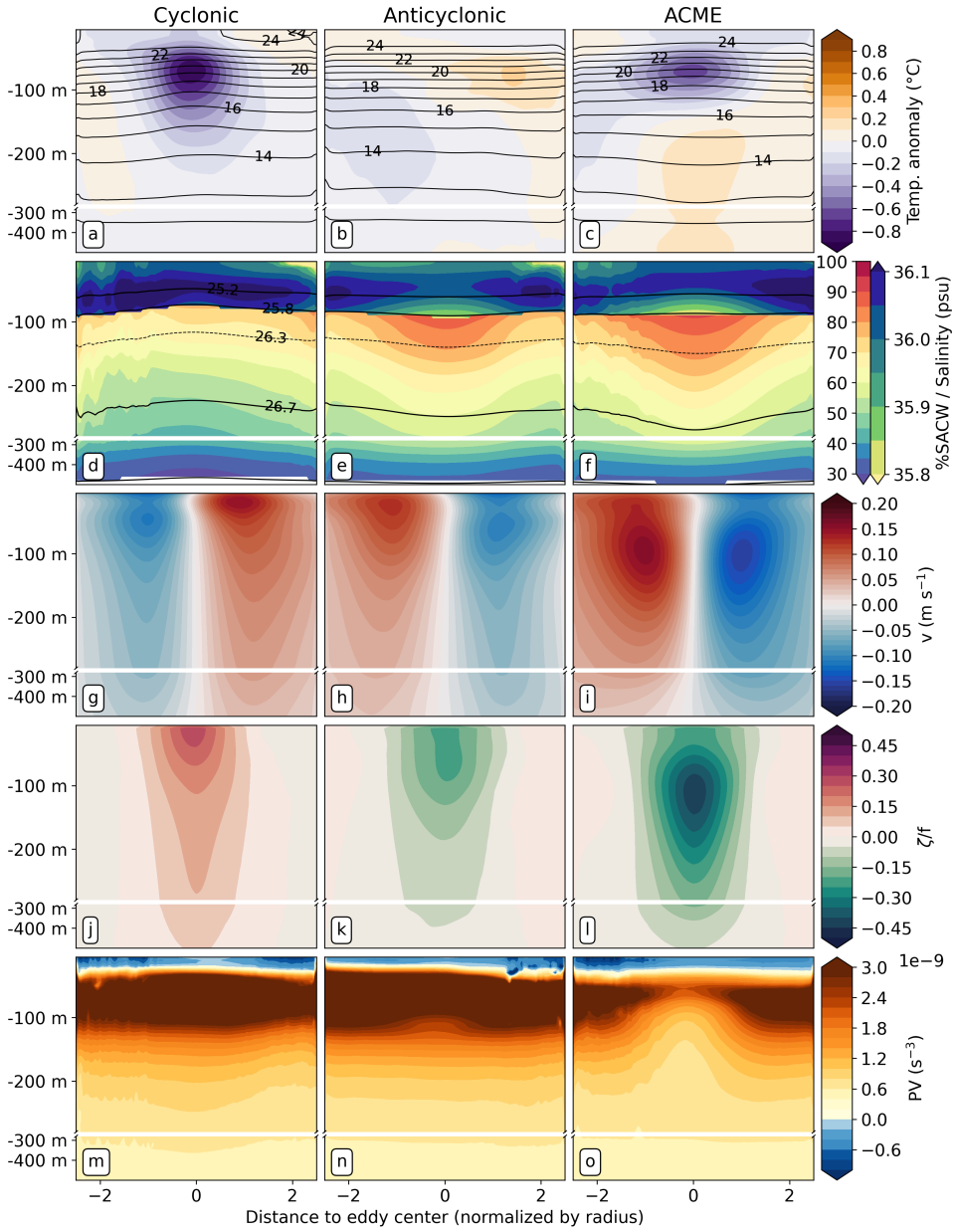


Figure 5.2: Mean vertical distribution of key physical parameters of coastal-generated eddies. Distinction is made between cyclones, anticyclones and ACMEs. (a–c) Temperature anomaly, with temperature distribution represented by solid contours. (d–f) %SACW, together with salinity for $\sigma_\theta < 25.8$ kg m^{-3}. Relevant σ_θ isopycnals are represented by black solid and dahsed contours. (g–i) Average meridional current velocities (v). (j–l) Average relative vorticity normalized f. (m–o) Average of the 10% lowest values per eddy for Ertel PV,

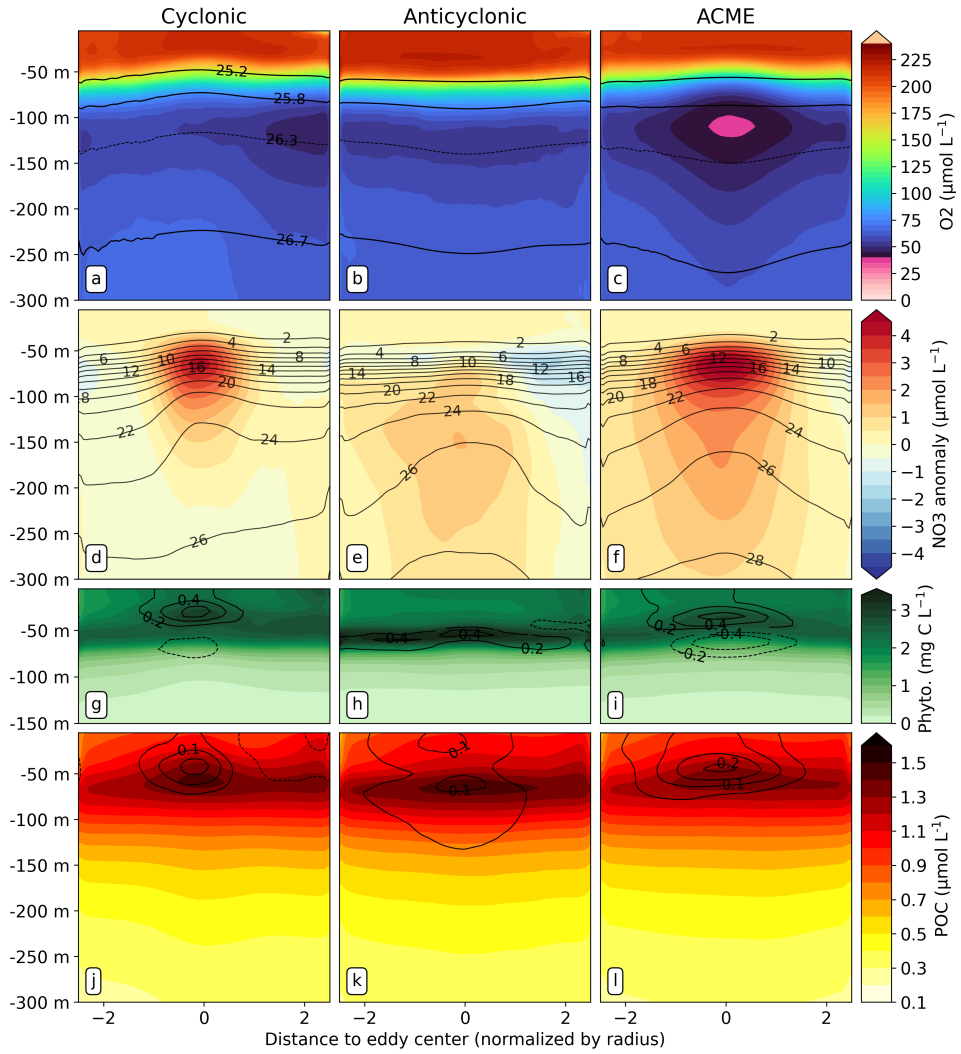


Figure 5.3: Mean vertical distribution of key biogeochemical parameters within coastal-generated eddies. (a–c) Average of the 10% lowest O_2 concentrations, with the representation of σ_θ isopycnal surfaces. (d–f) NO_3 anomalies, with NO_3 average concentrations represented by solid contours. (g–i) Average phytoplankton biomass, with positive and negative anomalies represented by solid and dashed black contours, respectively. (j–l) Average POC, with anomalies represented by vertical contours.

Cyclonic eddies are characterized by a cold-core structure, with negative temperature anomalies at the center reaching -0.8°C relative to the monthly mean (Figure 5.2a). This anomaly is associated with the shoaling of the upper isopycnals toward the surface (Figure 5.2d), induced by the divergence of surface waters and resulting eddy-pumping (Falkowski et al., 1991). As observed in Chapter 3, these eddies contain a significantly lower proportion of SACW compared to anticyclones and ACMEs (Figure 5.2, panels d–f).

In contrast, anticyclonic eddies generally exhibit slightly positive temperature anomalies (Figure 5.2b), consistent with a density structure characterized by a modestly deepened thermocline that suppresses the vertical transport of colder waters to the surface (Figure 5.2e). Similar to cyclonic eddies, ACMEs display a distinct but less intense subsurface cold anomaly, again associated with the upward displacement of upper isopycnals (Figure 5.2c). Both anticyclones and ACMEs contain a high proportion of fresher, SACW-rich waters at the subsurface, suggesting similar source waters and possibly related formation mechanisms. Nevertheless, the primary feature distinguishing ACMEs from anticyclones is the more pronounced upward bending of

upper isopycnals, indicative of a weakly stratified, subsurface mode water core (e.g., Schütte, Brandt, & Karstensen, 2016; Karstensen et al., 2017).

The mean hydrographic properties of coastal-generated cyclones and anticyclones analyzed in here differ from those reported in past studies of the region. Schütte, Brandt, and Karstensen (2016) found that anticyclones were primarily composed of NACW-rich waters, whereas cyclones were associated with SACW-rich waters. However, their composite analysis was based on a limited number of vertical profiles sampled within eddies and included eddies formed both near the coast and offshore. With results from a numerical model simulation, Dilmahamod et al. (2022) examined a single representative eddy of each type. They found that the anticyclonic eddy exhibited warmer and more saline waters than the cyclonic eddy, which shared similar hydrographic characteristics with an ACME. However, the cyclonic eddy analyzed displayed a vertical density structure typical of an intrathermocline eddy (also referred to as a "thinny"; McGillicuddy, 2015), characterized by a subsurface positive vorticity core squeezed by downward- and upward-bending upper and lower isopycnals, respectively. This atypical structure suggests that the selected cyclonic eddy is not representative of the surface-intensified cyclones typically generated along the northwestern African coast and warrants caution when comparing results across studies that employ different methods for the same purpose.

As expected, the meridional velocity (V) structure exhibits opposite flow directions for cyclonic and anticyclonic eddies, while maintaining a surface-intensified character (Figure 5.2g,h). This surface intensification is also evident in the relative vorticity normalized by the Coriolis parameter (ζ/f, also referred to as the Rossby number), which reaches its maximum near the surface and decreases with depth. A secondary subsurface maximum in V intensity is also observed in both cyclonic and anticyclonic eddies, particularly in the equatorward (negative) component.

As noted in Table 5.1, ACMEs exhibit the strongest rotational velocities among all eddy types, with peak intensity centered around 100 m depth (Figure 5.2i; Table 5.1). This leads to a well-defined anticyclonic ζ/f core, further highlighting their subsurface-intensified nature (Figure 5.2l). Notably, average ζ/f intensity in ACMEs is significantly greater than in cyclonic and anticyclonic eddies, which likely contributes to their longer lifetimes (McWilliams, 1985; Early et al., 2011). Additionaly, PV distributions reveal strong stratification in both cyclonic and anticyclonic eddies, while ACMEs exhibit much lower PV at their core. This pattern reinforces their modewater characteristics and underscores their capacity to retain low-PV waters, likely originated from the bottom boundary layer (e.g., D'Asaro, 1988; Molemaker et al., 2015; Thomsen et al., 2016; Contreras et al., 2019).

The vertical biogeochemical structure of the eddies reveals distinct characteristics across eddy types. Anticyclones exhibit the highest mean O_2 concentrations (based on the 10% lowest values), while cyclones show slightly lower values (Figure 5.3a–b). As expected, ACMEs present the lowest O_2 concentrations, forming a well defined hypoxic core between isopycnals 25.8 and 26.3 kg m^{-3} (Figure 5.3c). The close correlation between the hypoxic and ζ/f cores strongly suggests that core isolation, driven by enhanced rotational velocities, plays a key role in limiting exchange with surrounding waters and promoting O_2 depletion (Karstensen et al., 2017; Pietri & Karstensen, 2018).

The upward displacement of upper isopycnals leads to elevated nitrate concentrations at shallower depths in cyclones and ACMEs compared to anticyclones (Figure 5.3d–f), supporting higher primary productivity in surface layers (Figure 5.3g–i; McGillicuddy & Robinson, 1997). Nevertheless, anticyclones and ACMEs exhibit slightly higher nitrate concentrations at deeper depths than cyclones, likely due to a greater presence of SACW, which is typically richer in nitrate (Tomczak, 1981; Pastor et al., 2008). In contrast, anticyclones display a distinct DBM near the base of the mixed layer, which may compensate for their lower surface phytoplankton biomass and result in POC concentrations comparable to those of cyclones and ACMEs (Figure 5.3j–l).

5.3.3 Spatial and seasonal patterns of eddy generation

Figure 5.4 presents the spatial and monthly distribution of eddy generation along the coast, binned at 1° latitudinal intervals. When analyzing the total number of eddies (Figure 5.4a), the highest number of eddy formation is observed near Cap Blanc (20°–22°N), with a total of 61 eddies generated over the five-year simulation (≈12 yr^{-1}). Most of these eddies are formed between January and May, aligning with the upwelling season. South of this latitude, eddy formation remains relatively uniform until 13°, with the majority of eddies also generated during the upwelling season.

Distinct spatial patterns emerge when differentiating between eddy types, particularly between cyclones and ACMEs (Figure 5.4b,d), which exhibit alternating formation hotspots along the coast. This spatial segregation points to the action of distinct yet consistent formation mechanisms for each eddy type and suggests the potential formation of eddy dipoles (Dilmahamod et al., 2022), whose dynamic interplay may facilitate the exchange of water masses between the coastal and offshore regions (e.g., Lovecchio et al., 2018; Cetina-Heredia et al., 2019; Malan et al., 2020, 2022, 2023).

Cyclonic eddies are mostly formed intermittently at approximately 1° intervals between 14 and 21°N, with highest numbers being detected north of Cap-Blanc and south of Cap-Vert (Figure 5.4b). These cyclonic eddy generation patterns align with altymetry-derived observations, particularly near Cap-Timris (16°N) and Cap-Vert (Schütte, Brandt, & Karstensen, 2016). Their formation peaks in January, coinciding with the intensification of the upwelling season and the strengthening of the equatorward baroclinic coastal jet (Lázaro et al., 2005; Pelegrí et al., 2006; Pastor et al., 2008). Conversely, the lowest number of cyclonic eddies is observed in October, a period marked by the intensification of the PUC. This seasonality in cyclones formation aligns with model results from Dilmahamod et al. (2022), but contrasts with altimetry observations from Schütte, Brandt, and Karstensen (2016). A possible reason might be related to the limited reliability of satellite products close to the coast (Amores et al., 2018).

Anticyclonic eddies, in contrast, exhibit a more diffuse spatial distribution, with preferred generation sites near Cap-Blanc, 11°N, and 13°N (Figure 5.4c). Their formation does not follow a well-defined seasonal pattern. However, when considering eddies with a minimum lifetime of 10 days, a distinct peak emerges in July (Figure A.15), coinciding with the surface manifestation of the PUC as the MC. The total number of anticyclones increases substantially when accounting

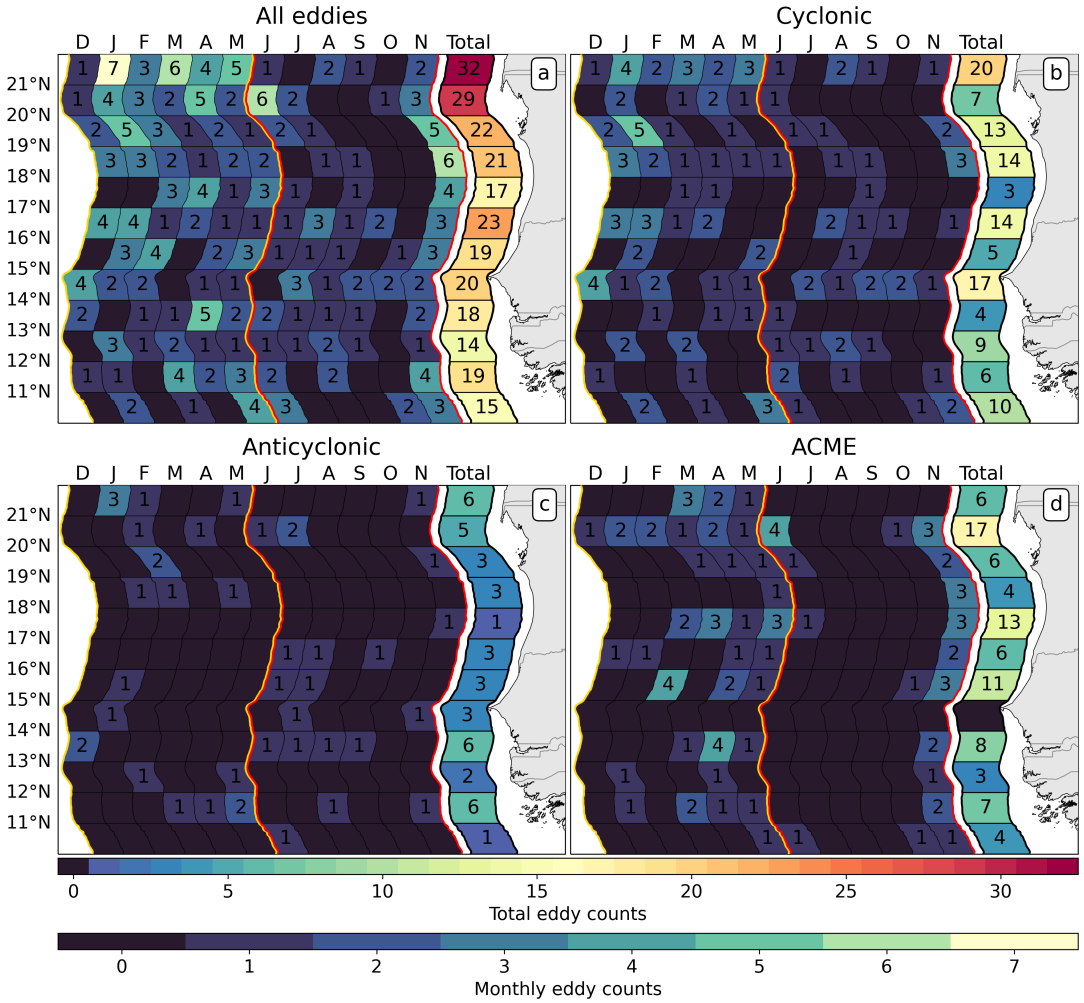


Figure 5.4: Monthly genesis of coastal-generated eddies along latitude. Only eddies formed within a 1.5° distance from the shelf break are accounted for. Latitudinal sections are spaced at a 1° interval. (a) Total number of eddies, with distinction between (b) cyclones, (c) anticyclones and (d) ACMEs. The yellow and red lines indicate the boundaries of the upwelling and relaxation seasons, respectively.

for these shorter-lived eddies, rising from 46 to 79. This suggests that a significant portion of coastal-generated anticyclonic eddies terminate or merge with other eddies within the first 30-day period.

The generation of ACMEs exhibits a well-defined spatial pattern, with hotspots identified north of Cap-Vert (15°N), at 17°N and 20°N (Figure 5.4d). All of these regions are characterized by sharp topographic bends located downstream of a poleward undercurrent, suggesting that interactions between the PUC and the bathymetry play an important role in ACME formation (e.g., Molemaker et al., 2015; Thomsen et al., 2016; Contreras et al., 2019). ACMEs also display the most pronounced seasonal cycle among eddy types, with a marked decline in generation during the relaxation season. Notably, no ACMEs are formed between July and September, likely due to the vertical shoaling of the PUC toward the surface layers (see Chapter 4). This seasonal pattern aligns with the altimetry-derived observations of Schütte, Brandt, and Karstensen (2016), who reported peak ACME generation in April and May. However, this contrasts with the numerical simulations of Dilmahamod et al. (2022), which showed a peak in June, likely associated with stronger subsurface poleward currents between May and August. Additional

discrepancies arise when compared to Karstensen et al. (2015), who reported exceptionally low O_2 concentrations in two ACMEs formed near the Mauritanian coast in July–a month where no ACME is generated in our simulation. However, these low-oxygen ACMEs were tracked with altimetry data, which has known limitations near the coast (Amores et al., 2018) and, at the time, had a horizontal resolution of only 0.25°. It is therefore plausible that the low-oxygen ACMEs described by Karstensen et al. (2015) were formed earlier than their first detection in the altimetry SSH maps.

Interestingly, the ACME generation hotspot at 20°N exhibits a notable peak in June, contrasting with southern latitudes where almost no ACMEs is generated. This outlier aligns with the continued presence of the PUC, whereas at lower latitudes, the PUC has already migrated to the surface by this time (Figure 4.4). Given the susceptibility of this region to hypoxic conditions during this time (Figure 4.5c), ACMEs formed here have a high probability of trapping pre-existing hypoxic conditions in their interior when formed.

The wake of the Cap-Vert headland also constitutes a significant ACME generation hotspot, with peak activity observed in February and November (Figure 5.4d). However, this region produces fewer ACMEs compared to the hotspots further north. The persistent negative meridional current velocities during the upwelling season (Figure 4.5b), together with the significant import of lagrangian particles during the same period (Figure 4.14), suggest that ACMEs formed here experience longer residence times. This extended residence time may reduce the overall formation rate, as existing eddies inhibit the generation of new ones.

5.3.4 Eddy generation mechanisms

In EBUSs, eddy generation is primarily driven by barotropic and baroclinic instabilities, which convert energy from the mean flow and from the density field into mesoscale turbulence (Capet, Colas, et al., 2008). These instabilities are often associated with upwelling fronts (Leth & Shaffer, 2001; Marchesiello et al., 2003; Capet, McWilliams, et al., 2008; Chaigneau et al., 2008), lateral shear in nearshore currents (e.g., Peliz, Dubert, Haidvogel, & Le Cann, 2003; Kurczyn et al., 2012; Pantoja et al., 2012; Combes et al., 2015), the passage of poleward coastal trapped waves (Zamudio et al., 2007), wind-induced perturbations (Pares-Sierra et al., 1993; Liang et al., 2012), or interactions between boundary currents and complex bottom topography (Leth & Shaffer, 2001; Kurian et al., 2011; Alpers et al., 2013; Thomsen et al., 2016; Contreras et al., 2019; Dilmahamod et al., 2022).

To elucidate the dominant eddy generation mechanisms along the northwestern African coast, we diagnose the energy conversion pathways associated with key dynamical instabilities. By decomposing the energy pathways associated with barotropic (through HSP and VSP) and baroclinic instabilities (through BP), we aim to quantify their relative contributions to eddy formation (e.g., Gula et al., 2015; Molemaker et al., 2015; Gula et al., 2016; Calil et al., 2021; J. Li & Roughan, 2023). In addition, we examine potential vorticity (PV) dynamics to assess the occurrence of centrifugal/inertial, gravitational, and symmetric instabilities, which may further modulate eddy formation (Thomas, 2008; Contreras et al., 2019; Napolitano et al., 2021).

5.3.4.1 Anticyclones and ACMEs

Figure 5.5 presents the mean spatial distribution of EKE, HSP, and BP integrated from 50 to 300 m depth (left panels), along with box-averaged timeseries for each of these parameters and meridional current velocities at five ACME eddy generation hotspots. In order to determine which instabilities are associated with the generation of each eddy, we identify their generation dates within the EKE time series, considering eddies with a minimum lifetime of 10 days. VSP is excluded from this analysis as its magnitude is an order of magnitude lower than HSP and BP (Figure A.16). The 50–300 m integration depth is chosen to capture instabilities driving ACMEs while minimizing contamination from dominant mixed-layer baroclinic instabilities (Figure A.17; Boccaletti et al., 2007; Sasaki et al., 2014).

Anticyclones are included here primarily for comparison, as they often share generation hotspots with ACMEs and may exhibit partially overlapping formation mechanisms. The spatial averaging boxes used for the time series analysis are not perfectly aligned with the eddy generation hotspots defined earlier (Figure 5.4; indicated here by dotted lines) because instabilities tend to develop upstream of the locations where eddies are first detected (e.g., Contreras et al., 2019).

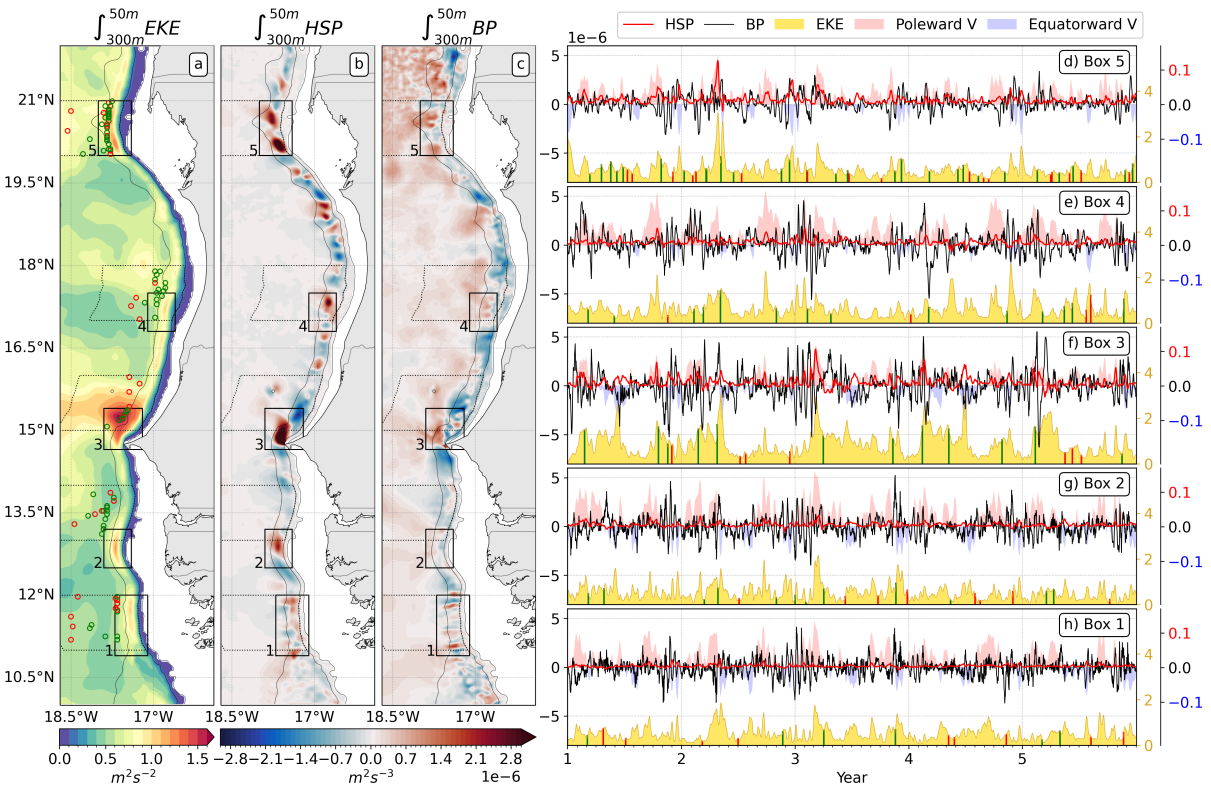


Figure 5.5: Spatial and temporal variability of anticyclonic and ACME generation mechanisms along the Northwestern African coast. (a) Time-averaged EKE integrated from 50 to 300 m depth. Green and red circles indicate the formation locations of ACMEs and anticyclonic eddies, respectively. Only eddies with lifetimes greater than 10 days are included. (b) Barotropic (HSP-dominated) and (c) Baroclinic (BP-dominated) instabilities, both integrated over the same depth range. In panels (a–c), thin coastal-parallel contours mark the 50, 100, and 1000 m isobaths, and dashed polygons indicate the ACME generation hotspots defined in Figure 5.4d. (d–h) Box-averaged time series of depth-integrated (50–300 m) HSP (red), BP (black), EKE (yellow shading), and meridional velocity components: poleward (pink) and equatorward (blue). Boxes 1–5 correspond to the solid-line regions in (a–c). Vertical green and red lines within the EKE time series mark the initiation dates of ACMEs and anticyclones, respectively, formed within each dashed polygon. Units: HSP and BP in $m^2\ s^{-3}$ (black axis), EKE in $m^2\ s^{-2}$ (yellow axis), and V in $m\ s^{-1}$ (red, black, and blue axes).

The spatial distribution of depth-integrated EKE (Figure 5.5a) highlights regions of intense eddy activity, particularly along sharp topographic bends where ACMEs and anticyclones preferentially form. These regions exhibit an elongated meridional band of high EKE values closely aligned with the continental slope. Most ACMEs and anticyclones are initially detected near the continental slope, with the exception of Boxes 1 and 2, where a considerable fraction of eddies are first detected farther offshore. The highest EKE values are found downstream of the Cap-Vert headland, supporting the hypothesis that eddies generated in this region are highly energetic and remain in their formation region for longer before propagating westward–consistent with the elevated nonlinearity[2] reported for in this region (Cardoso et al., 2020).

The time-averaged distributions of HSP and BP (Figure 5.5b–c) indicate that barotropic instability is the dominant mechanism of eddy generation, as evidenced by the widespread occurrence of positive HSP. This signal is particularly large in Boxes 3 and 5, where topographic curvature is more pronounced. Similar to other continental boundaries, this enhanced HSP likely results from the interaction of the PUC with the continental slope. In these regions, the combination of sharp topographic curvature and inertial effects causes the PUC to intensify near the slope and detach downstream, driven by form drag and bottom pressure torque, ultimately generating strong horizontal shear that fuels barotropic instability (Gula et al., 2015; Molemaker et al., 2015; Contreras et al., 2019).

Although time-averaged fields indicate that barotropic instability dominate energy conversion to EKE, the box-averaged time series reveal that baroclinic instability frequently exhibit higher-amplitude fluctuations (Figure 5.5d–h). This apparent discrepancy arises from the temporal variability of BP, which alternates between positive and negative values. Positive BP reflects energy conversion from EPE to EKE, while negative values indicate conversion from EKE to EPE (Gula et al., 2015). These frequent sign reversals in BP may reflect the influence of vertical motions associated with coastal upwelling and downwelling. As described by Marchesiello et al. (2003), the exchange of energy from kinetic to potential forms is often associated with the upwelling of colder subsurface water and the subduction of warmer surface water. This mechanism may also explain why the most intense BP variability is observed during the upwelling season. As a result, the frequent occurrence of negative BP values may obscure the contribution of episodic baroclinic instabilities to energy conversion, leading to an underestimation of their importance in time-averaged diagnostics.

The link between eddy formation and alongshore current variability is also evident in the time series. Peaks in EKE frequently coincide with intensified poleward flow, suggesting that eddy generation is strongly modulated by the strength of the PUC. However, these peaks do not always align with the initial detection of eddies. This temporal offset reflects adjustment timescales associated with the ocean's response to perturbations in the mean current, which can vary depending on the growth rate and spatial scale of the underlying instability (Feng et al., 2021).

Table 5.2 summarizes the proportion of eddies associated with each type of instability. As expected, persistent stand-alone HSP peaks indicate that most eddies formed in Boxes 3 and 5 are

[2]The nonlinearity parameter is the ratio between eddy rotational speed and propagation speed and is used to assess the efficiency of an eddy in trapping water in its interior (Chelton et al., 2007).

Table 5.2: Summary of the proportion of Anticyclones and ACMEs formed by different mechanisms within the respective major eddy generation hotspots. Boxes 1–5 refer to those identified in Figure 5.5. Columns indicate the total number of eddies identified in each category, as well as the percentage of eddies primarily generated by barotropic instability (HSP-dominated), baroclinic instability (BP-dominated), or a combination of both (mixed instability). The dominant instability mechanism for each box and eddy category is highlighted in bold.

Box	Type	N°	Barotropic (%)	Baroclinic (%)	Mixed (%)
5	ACME	29	**55.17**	0.00	44.83
	Anticyclones	17	23.53	**47.06**	29.41
4	ACME	14	21.43	35.71	**42.86**
	Anticyclones	4	**50.00**	25.00	25.00
3	ACME	12	**66.67**	16.67	16.67
	Anticyclones	8	25.00	37.50	37.50
2	ACME	13	7.69	**53.85**	38.46
	Anticyclones	8	12.50	**62.50**	25.00
1	ACME	7	0	**57.14**	42.86
	Anticyclones	9	33.33	22.22	**44.44**

linked to barotropic instability, likely driven by the separation of the PUC at sharp bathymetric bends. However, BP peaks frequently coincide with HSP peaks, suggesting that mixed instability events are common and, in fact, dominate ACME and anticyclone formation in Boxes 4 and 1, respectively. Stand-alone baroclinic instability represents the dominant mechanism in Box 2 for both eddy types, in Box 5 for surface-intensified anticyclones, and in Box 1 for ACMEs. These findings indicate that distinct instability regimes characterize regions to the north and south of Cap-Vert.

Consistent with previous studies, subsurface barotropic instability at the subsurface appear to be a defining feature of EBUSs, particularly in regions where a poleward undercurrent interacts with sharp bathymetric features along the continental slope (Molemaker et al., 2015; Contreras et al., 2019). In contrast, baroclinic instability is typically dominant in surface layers and along the upwelling front, where strong vertical density gradients prevail (Leth & Shaffer, 2001; Marchesiello et al., 2003; Capet, McWilliams, et al., 2008).

The dominance of barotropic instability in our simulations contrasts with the findings of Dilmahamod et al. (2022), who, using a nested-domain model configuration to study eddy generation mechanisms in the ETNA, identified baroclinic instability as the primary driver. This discrepancy may stem from differences in the representation of boundary current dynamics. While Dilmahamod et al. (2022) reported peak poleward velocities near 100 m depth during the summer months–when the PUC is known to shoal toward the surface (Lázaro et al., 2005; Klenz et al., 2018; Kounta et al., 2018)–our results show maximum subsurface flow between February-May and September-November (Figure 4.5b). It is therefore possible that differences in the seasonal positioning and intensity of the PUC between studies contributed to contrasting HSP values.

Contreras et al. (2019) found that ACMEs forming along the Chilean coast were characterized by negative or near-zero PV within their cores. Given their distance from the bottom boundary layer–which imply inertial instabilities as the main source of negative PV (Hoskins, 1974)–and their co-occurrence with barotropic instabilities (HSP > 0), the authors suggested that such low PV values were indicative of centrifugal instabilities (Thomas et al., 2013). However, these

instabilities were only captured in high-resolution simulations (0.3 km), whereas lower-resolution simulations (3 km) continued to show barotropic instabilities but lacked low-PV signatures.

In our study, the PV decomposition confirms that near-zero or even negative PV detected within ACMEs are consistently associated with inertial instability (e.g., Figure A.18), and in most cases, with centrifugal instability, as indicated by positive HSP. Additionally, N^2 remains strictly positive throughout, ruling out gravitational instability. Moreover, the symmetric instability term ($|q_{bc}|$) is consistently an order of magnitude smaller than the inertial instability term (q_{vert}), further reinforcing the dominance of centrifugal instability in these features (Thomas, 2008).

These findings suggest that barotropic and baroclinic instabilities play distinct yet often complementary roles in the formation of ACMEs and anticyclones along the northwestern African coast. While barotropic instability dominates the time average, baroclinic instability contributes significantly during episodic events, highlighting the need to consider short-term variability. The spatial heterogeneity in eddy generation mechanisms is also evident: regions north of Cap-Vert are primarily influenced by barotropic instability, whereas southern regions exhibit a stronger contribution from baroclinic instability. Although the simultaneous occurrence of both kind of instabilities is common, it tends to be less dominant than cases where one mechanism clearly prevails.

5.3.4.2 Cyclones

To further elucidate on the instabilities leading to the generation of cyclonic eddies along the Northwestern African coast, we conduct a similar analysis as the one previously conducted for ACMEs and anticyclones. However, here we focus on the top 50 m depth because of the surface-intensified nature of cyclonic eddies (Figure 5.2). To associate the dominant instabilities with the formation of cyclonic eddies, their formation dates are also marked within the EKE time series, considering eddies with a minimum lifetime of 10 days.

The spatial distribution of EKE (Figure 5.6a) reveals elevated eddy activity near the continental margin. However, unlike the deeper layers, high EKE values in the surface layer are more zonally extensive. As a result, most cyclones tend to form farther offshore, particularly in Boxes 1, 4, and 5, whereas formation closer to the shelf is more common in Boxes 2 and 3. This spatial contrast suggests that cyclones may arise from distinct formation mechanisms depending on their location relative to the slope.

The spatial distribution of HSP and BP (Figure 5.6b,c) indicates that barotropic instability plays a relatively minor role in cyclonic eddy formation, which is instead dominated by baroclinic processes along the coast. This pattern is particularly evident in Box 5, the most prominent cyclonic eddy generation hotspot (Figure 5.4b). Regions with the highest BP values are often characterized by sharp buoyancy gradients and strong density fronts, consistent with conditions that promote baroclinic instability (Capet, McWilliams, et al., 2008). At northern latitudes near Cap-Blanc, the persistence of equatorward currents suggests that coastal upwelling is active throughout most of the year (Figure 5.6d; Pelegrí et al., 2006; Pradhan et al., 2006; Lathuilière et al., 2008). This, in combination with the recurrent development of a large upwelling filament (Gabric et al., 1993; Kostianoy & Zatsepin, 1996), creates favorable conditions for the

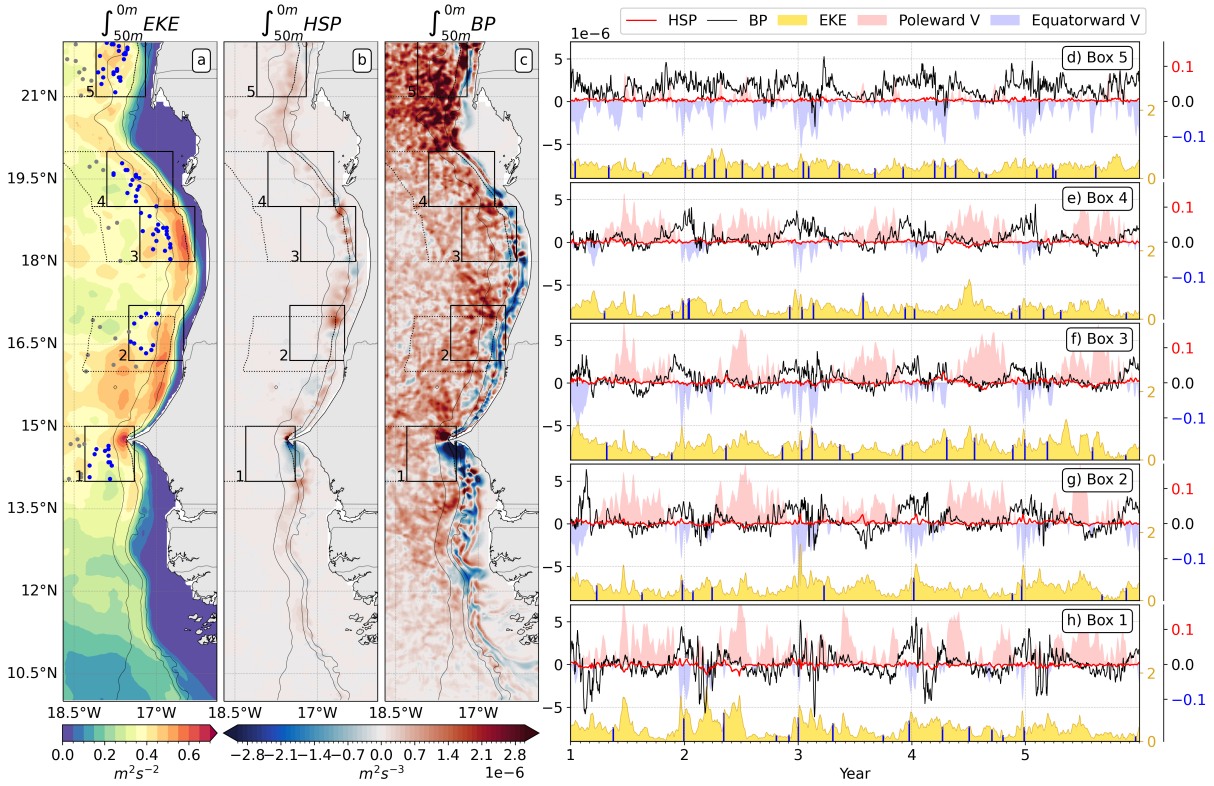


Figure 5.6: Spatial and temporal variability of cyclonic eddy generation mechanisms along the Northwestern African coast. (a) Time-averaged EKE integrated over the top 50 m. Blue circles indicate the formation locations of cyclonic eddies generated within the five defined boxes, while gray circles mark those formed outside these boxes but within the dashed regions. Only eddies with lifetimes greater than 10 days are included. (b) Barotropic (HSP-dominated) and (c) Baroclinic (BP-dominated) instabilities, both integrated over the same depth range. In panels (a–c), thin coastal-parallel contours mark the 50, 100, and 1000 m isobaths, and dashed polygons indicate the cyclonic eddy generation hotspots defined in Figure 5.4b. (d–h) Box-averaged time series of depth-integrated (0–100 m) HSP (red), BP (black), EKE (yellow shading), and meridional velocity components: poleward (pink) and equatorward (blue). Boxes 1–5 correspond to the solid-line regions in (a–c). Vertical blue lines within the EKE time series mark the initiation dates of cyclonic eddies formed within each dashed polygon. Units: HSP and BP in $m^2\ s^{-3}$ (black axis), EKE in $m^2\ s^{-2}$ (yellow axis), and V in $m\ s^{-1}$ (red, black, and blue axes).

development of frontal instabilities, thus likely explaining the increased BP signal observed in this region (Marchesiello et al., 2003; Meunier et al., 2012).

Examination of the time series reveals that BP-driven events are both more frequent and more intense than those driven by HSP (Figure 5.6d–h), further supporting the dominant role of baroclinic instability in cyclonic eddy formation. Notably, most cyclones are formed during periods of equatorward flow, which follows a marked seasonal cycle closely associated with coastal upwelling dynamics. Maximum BP values also coincide with these periods, suggesting that baroclinic instability is more likely to occur when the upwelling-induced density front is strongest (Chaigneau et al., 2011).

Nevertheless, interactions between the equatorward coastal jet and topography may contribute to cyclone formation near the continental slope. This is particularly evident in Boxes 2 and 3, where barotropic instabilities (HSP > 0) are more common (Figure 5.6f). Such mechanisms may also explain the relatively low SACW content observed within these cyclones compared to anticyclones and ACMEs (Figure 5.2d–f). In addition, instabilities in coastal currents induced by the presence of pre-existing anticyclones or ACMEs may also play a role in cyclonic eddy

Table 5.3: Summary of the proportion of cyclones formed by different mechanisms within the corresponding major eddy generation hotspots. Boxes 1–5 refer to those identified in Figure 5.6. Columns indicate the total number of eddies identified in each category, as well as the percentage of eddies primarily generated by barotropic instability (HSP-dominated), baroclinic instability (BP-dominated), or a combination of both (mixed instability). The dominant instability mechanism for each box and edd category is highlighted in bold.

Box	Eddies	Barotropic (%)	Baroclinic (%)	Mixed (%)
5	25	0.00	**78.57**	21.43
4	16	0.00	**70.59**	29.41
3	17	0.00	50.00	50.00
2	11	0.00	27.27	**72.73**
1	15	20.00	**53.33**	26.67

formation, particularly during periods of poleward surface flow (Peliz, Dubert, Haidvogel, & Le Cann, 2003; Dilmahamod et al., 2022).

Table 5.3 provides a quantitative summary of the proportion of cyclones associated with each type of instability. In most regions, baroclinic instability dominates, accounting for nearly 80% of cyclonic eddies in Box 5. In contrast, Boxes 2 and 3 show a higher prevalence of mixed instability events, suggesting that horizontal shear–likely induced by the interaction of the equatorward coastal jet with local topographic features–acts in combination with density gradients to drive cyclone formation. Interestingly, Box 1 is the only region where stand-alone barotropic instabilities are linked to cyclonic eddy formation (20%). All eddies in this box form south of the Cap-Vert headland predominantly during periods of equatorward flow, implying that current-topography interactions play a key role in eddy generation at this latitude. This interpretation is consistent with observations by Alpers et al. (2013), who documented the formation of a small-scale cyclonic eddy downstream of Cap-Vert following a sudden intensification of trade winds. Their analysis indicates that the separation of a strong wind-driven coastal jet at the headland was the primary mechanism behind eddy formation, highlighting flow separation as a key process governing eddy generation in this region.

Overall, these findings underscore the dominant role of baroclinic instability in cyclonic eddy formation along the northwestern African coast. The prevalence of BP over HSP, and its alignment with the equatorward coastal jet, highlights the importance of vertical density gradients in driving cyclone generation. Nevertheless, the occurrence of mixed instabilities in certain regions suggests that horizontal shear can can also play a role through interactions with coastal topography, although it rarely acts as the primary driver on its own.

5.3.4.3 Relation between formation mechanisms and hypoxic conditions

To assess potential differences in formation mechanisms between hypoxic and non-hypoxic eddies, Table 5.4 presents the proportion of hypoxic eddies associated with each instability type. This analysis includes only eddies formed within the regions previously examined in Figures 5.5 and 5.6 that persist for at least 30 days.

The vast majority of eddies formed in these region either originate as hypoxic or eventually develop hypoxic conditions. Cyclonic and anticyclonic eddies formed by mixed barotropic and baroclinic instabilities exhibit the highest probability of having hypoxic conditions in their

Table 5.4: Proportion of hypoxic eddies per mechanism of formation. Only eddies identified in Figures 5.5 and 5.6 with minimum lifetime of 30 days are accounted for. Columns indicate the number of eddies, the percentage of those that become hypoxic, and the percentage of eddies–classified by dominant formation mechanism (barotropic, baroclinic, or mixed instabilities)–that develop hypoxic conditions. Note that the instability-specific percentages reflect the fraction of eddies within each mechanism that become hypoxic.

Type	Nr.	Hyp. eddies (%)	Barotropic (%)	Baroclinic (%)	Mixed (%)
Cyclonic	83	72.29	66.67	63.64	83.33
Anticyclonic	33	72.73	75.00	66.67	76.92
ACME	96	83.33	86.49	80.00	82.35

interior. For ACMEs, those formed by barotropic instabilities have a higher probability of developing hypoxia. Despite these patterns, however, the differences in hypoxic versus non-hypoxic proportions across formation mechanisms are not statistically significant, suggesting that the main instability responsible for eddy formation plays a minor role in determining whether an eddy develops low-oxygen conditions.

5.4 Low-oxygen eddies

In this section, we examine the physical and biogeochemical processes underlying hypoxia in coastal-generated eddies. We first compare hypoxic and non-hypoxic eddies to identify structural features linked to oxygen depletion, and then analyze representative cases to distinguish between eddies that form with hypoxic waters and those that develop hypoxia en route.

5.4.1 Differences between hypoxic and non-hypoxic eddies

To distinguish between hypoxic and non-hypoxic eddies, we first categorize them into those containing hypoxic conditions at any point during their lifetime and those that remain oxygenated. Among the 249 coastal-generated eddies with a minimum lifetime of 30 days, 56% exhibit hypoxic conditions at some stage. Of these, 50% already contain hypoxic waters within their interior during the first five days. Notably, ACMEs have the highest proportion of hypoxic eddies (66%), yet they account for the lowest fraction of eddies that initially form with hypoxic conditions (34%). In contrast, 52% of the cyclonic eddies are hypoxic, with the majority (57%) originating with pre-existing conditions. Anticyclones exhibit an equal split between hypoxic and non-hypoxic eddies (50%), though the vast majority of the hypoxic ones have hypoxic conditions when formed (71%).

Table 5.5 provides a comparative summary of the mean key properties for hypoxic and non-hypoxic eddies. Hypoxic eddies have longer lifetimes, with hypoxic ACMEs persisting for an average of 236 days–nearly three times the duration of their non-hypoxic counterparts. Given the close relationship between eddy age and propagation distance, hypoxic eddies also travel farther than non-hypoxic ones. Interestingly, the average lifetime of non-hypoxic eddies remains consistent across all eddy types ($\approx$81 days), suggesting that eddy age is a critical factor in the development of hypoxic conditions. Except for anticyclones, hypoxic eddies also tend to have larger radii, indicating a potential link between oxygen depletion and eddy spatial extent.

Table 5.5: Mean dynamical properties of hypoxic and non-hypoxic coastal-generated eddies. Columns labeled "Hyp." and "Non-hyp." refer to hypoxic and non-hypoxic eddies, respectively. Reported values include the proportion of eddies in each category, mean lifetime, propagation distance, eddy radius, rotation velocity, nonlinearity, and kinetic energy.

	Cyclonic		Anticyclonic		ACME	
	Hyp.	Non-hyp.	Hyp.	Non-hyp.	Hyp.	Non-hyp.
Proportion	52%	48%	50%	50%	66%	34%
Lifetime (days)	133.37	81.34	103	81.38	236.23	81.24
Prop. distance (km)	669.51	382.71	504.25	505.39	996.84	294.08
Radius (km)	45.52	39.31	39.85	40.22	33.33	26.75
Rotation vel. ($m\ s^{-1}$)	0.08	0.08	0.09	0.08	0.16	0.14
Prop. speed ($km\ d^{-1}$)	5.03	4.73	4.69	5.81	4.1	3.52
Nonlinearity	1.38	1.43	1.72	1.23	3.3	3.51
Kinetic energy ($m^2\ s^{-2}$)	2.17	1.26	1.69	1.41	3.6	1.9

Differences in eddy characteristics are particularly evident in their kinetic energy[3] and rotation velocity. Hypoxic ACMEs exhibit the highest mean rotational velocities (0.16 $m\ s^{-1}$), which likely contribute to enhanced core isolation from surrounding waters (Karstensen et al., 2015). ACMEs also display the highest mean nonlinearity, followed by anticyclonic and cyclonic eddies. Interestingly, non-hypoxic cyclones and ACMEs exhibit slightly higher nonlinearity values than their hypoxic counterparts. This difference primarily reflects their higher propagation speeds rather than lower rotation velocities. These results may suggest that hypoxic cyclones and ACMEs are more prone to lateral exchange and potential leakage than their non-hypoxic counterparts. Nonetheless, the significantly higher mean kinetic energy observed in hypoxic eddies relative to non-hypoxic ones indicates that elevated energy levels may facilitate the development or maintenance of hypoxic conditions.

To assess differences in the vertical structure between hypoxic and non-hypoxic eddies, Figure 5.7 shows the mean anomaly fields obtained by subtracting non-hypoxic eddy composites from those of hypoxic eddies. The analysis is limited to the first 120 days of each eddy's lifetime, as older eddies typically weaken and become less productive, while simultaneously being more likely to exhibit hypoxic conditions developed earlier but maintained due to core isolation. Including these older eddies could bias the comparison–particularly for ACMEs–by highlighting structural differences that are not directly related to the mechanisms responsible for hypoxia formation (see Figure A.19).

Hypoxic cyclones are generally colder than their non-hypoxic counterparts, particularly near the base of the mixed layer, suggesting enhanced upwelling (Figure 5.7a). This interpretation is supported by a more pronounced upward displacement of upper isopycnals in hypoxic cyclones compared to non-hypoxic ones (Figure 5.7d). In contrast, hypoxic anticyclones and ACMEs exhibit slight surface warming and subsurface cooling (Figure 5.7b,c). Interestingly, hypoxic cyclones show no significant difference in %SACW relative to non-hypoxic cyclones (Figure 5.7d). In anticyclones, however, hypoxic cases are associated with a marked increase in %SACW, indicating that water mass composition in their formation region plays a significant role in their susceptibility to hypoxic conditions (Figure 5.7e). Although hypoxic ACMEs also exhibit a slight

[3] Calculated as the sum of horizontal kinetic energy within the eddy perimeter (Le Vu et al., 2018).

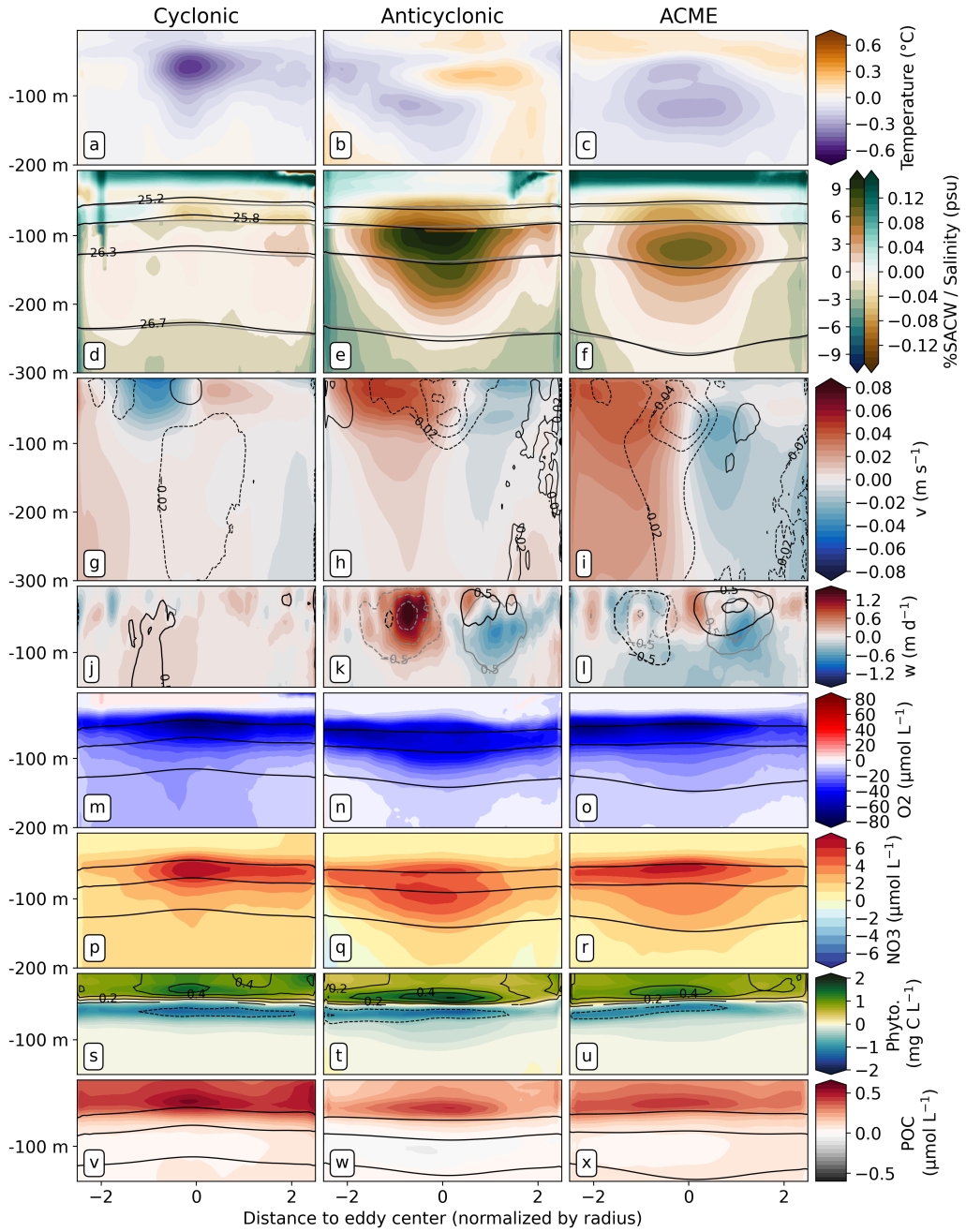


Figure 5.7: Differences between vertical composites of hypoxic and non-hypoxic coastal-generated eddies. Each eddy type is represented separately. Only eddies with lifetime exceeding 30 days are considered, accounting for the initial 120 days. (a–c) Temperature anomaly (with respect to the monthly climatology); (d–f) %SACW, with salinity differences for σ_θ < 25.8 kg m^{-3}. Black and gray contours represent average σ_θ isopycnal surfaces of hypoxic and non-hypoxic eddies, respectively. Differences in (g–i) meridional current velocities (v), with differences in ζ/f represented by dashed (negative) and solid (positive) contours; (j–l) vertical velocities (w), with average w for hypoxic and non-hypoxic eddies represented by black and gray contours respectively (upward and downward velocities are represented by solid and dashed lines, respectively); (m–o) O_2 concentrations; (p–r) NO_3 concentrations; (s–u) phytoplankton biomass, with differences in zooplankton biomass represented by solid (positive) and dashed (negative) contours; and (v–x) POC concentrations. Black contours in (m–p) and (v–x) represent isopycnals of hypoxic eddies at σ_θ 25.2, 25.8 and 26.3 kg m^{-3}.

increase in %SACW, the difference appears too small to be a dominant factor in the development of low-oxygen conditions (Figure 5.7f).

Regardless of eddy type, hypoxic eddies exhibit stronger meridional velocity components than non-hypoxic ones (Figure 5.7g–i), with increased ζ/f intensity indicating greater core isolation. Vertical velocity differences reveal a net positive (upward) anomaly in hypoxic cyclones

and anticyclones, suggesting either enhanced upwelling or reduced downwelling compared to non-hypoxic eddies (Figure 5.7j–l). This pattern is most pronounced in anticyclones, where non-hypoxic eddies exhibit stronger downward velocities, resulting in a positive vertical velocity difference on the eastern flank. Although ACMEs exhibit a net positive vertical transport, differences between hypoxic and non-hypoxic eddies are minimal, suggesting that such differences play a minor role in the development of hypoxic conditions.

As expected, O_2 concentrations are significantly lower in hypoxic eddies, with maximum differences reaching -80 µmol L^{-1} for both cyclones and ACMEs (Figure 5.7m–o). In contrast, NO_3 concentrations are elevated throughout the water column in hypoxic eddies, particularly between 50 and 150 m depth (Figure 5.7p–r). While the positive nitrate anomalies observed in cyclones and ACMEs are likely driven by enhanced remineralization, the differences in anticyclones appear to be primarily linked to the significantly higher %SACW content (Tomczak, 1981; Pastor et al., 2008). Increased nitrate availability in the mixed layer supports elevated phytoplankton growth and enhanced primary productivity in hypoxic eddies. This is reflected in the higher concentrations of phytoplankton and zooplankton biomass in the mixed layer, contrasting with the negative differences at the depth of the DBM, a typical feature of non-hypoxic eddies (Figure 5.7s–u). The resulting increase in POC–particularly in cyclones and ACMEs (Figure 5.7v–x)–suggests enhanced export production and subsequent remineralization of sinking organic matter in the subsurface, playing a central role in the development and maintenance of hypoxic conditions (Schütte, Karstensen, et al., 2016).

5.4.2 Formation from pre-existing conditions

To assess how eddies form with pre-existing hypoxic conditions in their interior, Figure 5.8 shows the formation of a cyclone, an anticyclone, and an ACME along the northwestern African coast. For each case, horizontal O_2 concentrations at 100 m depth are shown, along with vertical cross-sections of key physical and biogeochemical parameters centered on the eddy at the time of formation ($\pm$5 days). All three eddies form at relatively high latitudes (Figure 5.8a,g,m), where O_2 concentrations are typically lower (see Chapter 4). While the cyclone forms in winter, the anticyclone and ACME form during summer, coinciding with the seasonal minimum in coastal O_2 levels.

Hypoxic conditions in the anticyclone and ACME are substantially more intense than those observed in the cyclone (Figure 5.8b,h,n). In addition to the timing of formation, the influence of poleward surface and subsurface currents appears to play a key role in the development of hypoxia in the anticyclone and ACME, respectively. This vertical distinction is further reflected in the distribution of relative vorticity: the anticyclone exhibits maximum anticyclonic vorticity in the mixed layer, while the ACME shows a more pronounced subsurface vorticity core, with a secondary minimum also present near the surface (Figure 5.8i,o). The ACME is also characterized by a subsurface low-PV core, likely originating from the continental slope, where strong anticyclonic vorticity and low PV values coexist. Previous modeling studies in the ETNA (Dilmahamod et al., 2022) and other EBUSs (Peru–Chile and California; Molemaker et al., 2015; Contreras et al., 2019) have shown that such anticyclonic (negative) vorticity in

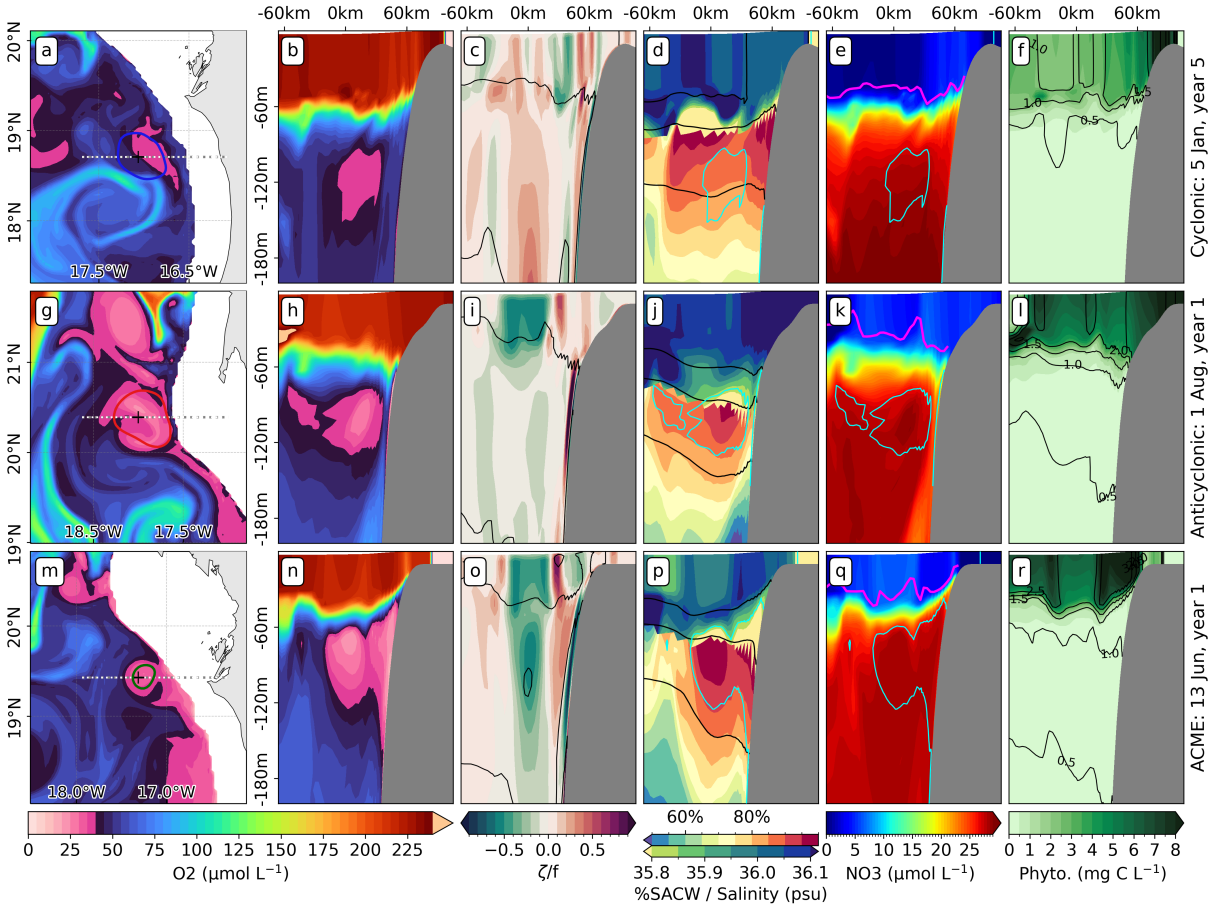


Figure 5.8: Moment of formation of low-oxygen eddies formed with pre-existing hypoxic conditions in their interior. (a,g,m) Horizontal slices of O_2 concentrations at 100 m depth for a cyclone, anticyclone, and ACME, with their respective perimeters outlined in blue, red, and green contours. The black crosses mark the eddy centers, while the white/black dashed lines indicate the zonal extent of the vertical cross-sections shown in the right panels. Vertical sections display (b,h,n) O_2 concentrations; (c,i,o) ζ/f, with black contour lines representing potential vorticity values of 1.4×10^{-9}; (d,j,p) %SACW, overlaid with salinity values for $\sigma_\theta < 25.8$ kg m^{-3} and isopycnal surfaces at σ_θ 25.2, 25.8 and 26.3 kg m^{-3} represented by black contours; (e,k,q) NO_3 concentrations, with base of the mixed layer represented by magenta line; and (f,l,r) phytoplankton biomass, with zooplankton biomass represented by black contours. Cyan contours in (d,j,p) and (e,k,q) indicate $O_2 = 40$ µmol L^{-1}.

the bottom boundary layer is generated by the drag induced by the interaction of the PUC with the sloping bathymetry, which leads to strong horizontal ($\partial \mathbf{V}/\partial x$) and vertical shear ($\partial \mathbf{V}/\partial z$). The apparent connection between the ACME's hypoxic core and the continental slope further supports the hypothesis that bottom waters are exported and trapped within the eddy following PUC separation (e.g., Molemaker et al., 2015; Contreras et al., 2019), contributing to the early development of hypoxic conditions.

Unlike the anticyclone and ACME, the cyclone exhibits a less coherent vortical structure, making its formation mechanism unclear (Figure 5.8c). It also differs in SACW composition (Figure 5.8d,j,p). Although waters near $\sigma_\theta = 25.8$ kg m^{-3} within the cyclone approach 100% SACW, the hypoxic core itself contains a more diluted variety (80–90% SACW). In contrast, the hypoxic core of the anticyclone contain highly variable portions (85–100%), while the ACME contain purer SACW (95–100%), resembling waters found in the continental slope boundary layer. This suggests that substantial oxygen depletion occurred prior to the ACME formation, likely driven by remineralization of organic matter accumulating near the bottom of the slope (Thomsen et al., 2019).

The potential density structure indicates that both the cyclone and the ACME formed under active upwelling conditions, while the anticyclone developed during a relaxation phase (Figure 5.8d,j,p). Despite these differences, NO_3 concentrations in the mixed layer are relatively high across all cases (Figure 5.8e,k,q). This is particularly unexpected for the anticyclone, but it likely reflects the influence of upwelling preceding the eddy's formation, considering that upwelling dynamics at these northern latitudes typically weaken later in the year (see Chapter 4; Pradhan et al., 2006; Lathuilière et al., 2008). Elevated nitrate availability in the mixed layer supports enhanced primary productivity (Figure 5.8f,l,r), which in turn promotes increased export production and subsequent subsurface O_2 consumption–establishing favorable conditions for the further intensification of hypoxia.

To elucidate on the history of the water masses trapped within these eddies, we analyze the trajectories and evolution of Lagrangian particles released within them at formation and tracked backward in time for up to 70 days, sampling key parameters along the way (Figure 5.9).

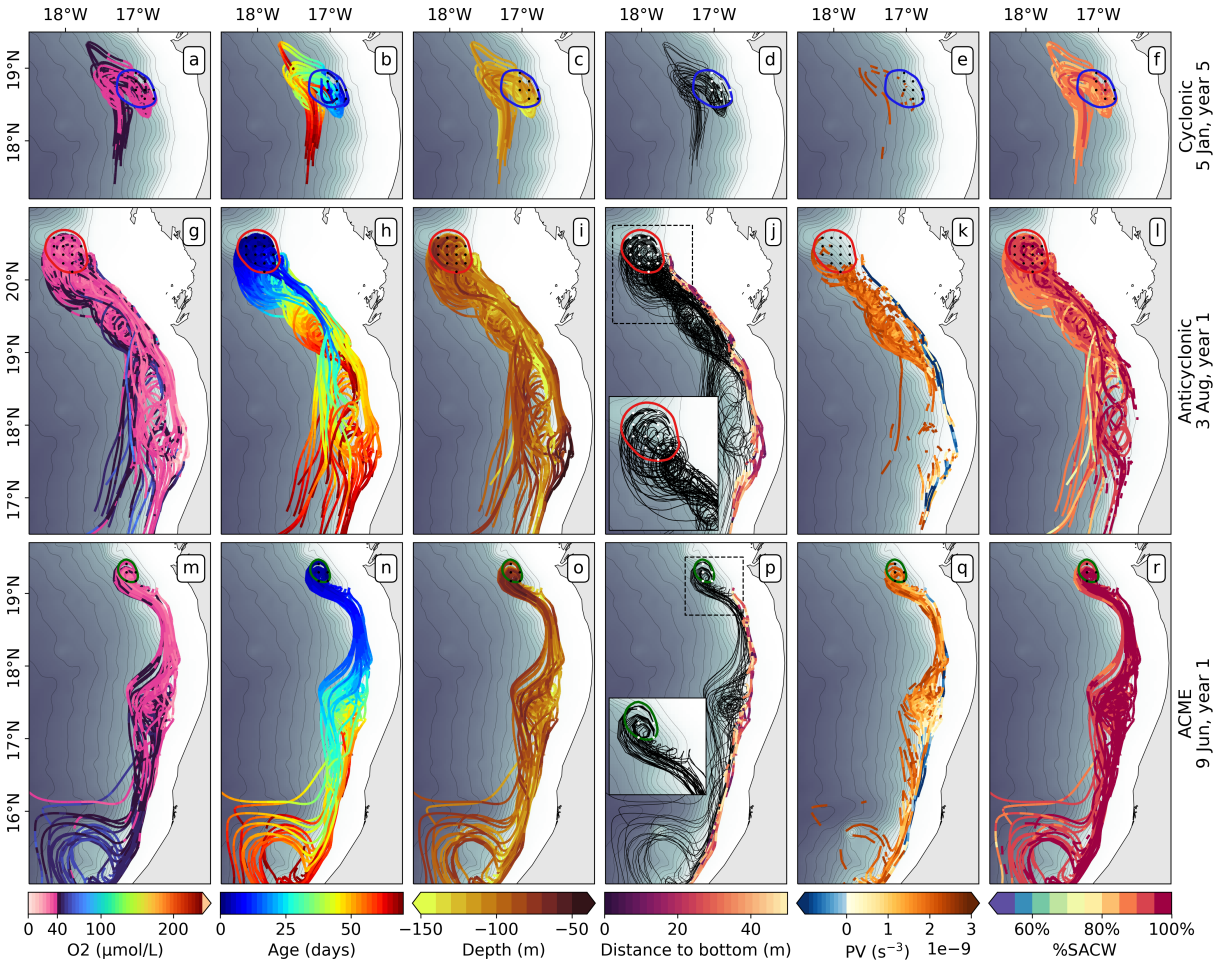


Figure 5.9: Lagrangian perspective of the history of hypoxic water masses trapped within low-oxygen eddies at the moment of formation. Eddies are the same (a–f) cyclone, (g–l) anticyclone, and (m–r) ACME shown in Figure 5.8, with blue, red and green contours representing the respective perimeters. Only the first 70 days following Lagrangian particle release are considered. (a,g,m) O_2 concentrations; (b,h,n) particle age, counting backward from the moment of release; (c,i,o) particle depth; (d,j,p) distance from the bottom (up to 50 m), with particle trajectories represented by thin black lines. For the anticyclone and ACME, an enlarged view of the formation region is shown (only half of the trajectories are represented), with the target area outlined by a dashed black box. Additional panels display (e,k,q) Ertel PV (only for values $< 2.5 \times 10^{-9}$); and (f,l,r) %SACW, calculated only for $\sigma_\theta > 25.8$ kg m^{-3}. Black and white points represent the release location of Lagrangian particles. Gray color gradient in the background represents bathymetry, with thin black contours indicating depths with a 200 m interval.

The past evolution of O_2 concentrations reveals that hypoxic conditions were established well before the eddies formed (Figure 5.9a,g,m). However, their transport pathways and timescales differ significantly–especially between the cyclone and the two anticyclonic eddies–suggesting distinct processes leading to hypoxia (Figure 5.9b,h,n). In the cyclone, water masses exhibit a gradual decline in O_2 due to slow advection and prolonged residence time prior to eddy formation, which is expected during this time of the year (Figure 4.12). In contrast, water parcels forming the anticyclone and ACME experience O_2 depletion during northward transport by the alongshore current, reaching hypoxic levels during the transition from the upwelling to the relaxation season. Interestingly, some of the ACME's water masses are influenced by recirculation associated with the recurrent Cap-Vert ACME. This further suggests that the presence of such a persistent feature may partially inhibit direct ventilation of the Mauritanian coastal region by the PUC (see Chapter 4).

Water masses forming the anticyclonic eddy exhibit two distinct phases of transport (Figure 5.9h): an earlier phase characterized by swirling motions along the continental slope, and a later phase in which particles follow a more direct trajectory toward the eddy core. This pattern suggests that older particles are advected by the PUC, while younger ones are transported by the surface-intensified MC. During the PUC-dominated phase, water parcels experience strong perturbations as they interact with the slope, leading to flow separation and the generation of anticyclonic oscillations. However, these instabilities alone appear insufficient to immediately generate a coherent eddy, as approximately 60 days are required for the anticyclone to fully develop further downstream during the MC-dominated phase. A similar, though less pronounced, sequence is observed in the ACME's formation (Figure 5.9n). In this case, instabilities are only observed near 17.5°N–coincident with the first perturbations experienced by water parcels forming the anticyclone–and are short-lived, with particles following a more linear trajectory thereafter.

Differences in the evolution of these instabilities may be linked to the seasonal variability in PUC intensity, which is stronger in April–May than in June–July, when waters forming the ACME and the anticyclone, respectively, experience these instabilities. A weaker PUC during the latter period may promote a more chaotic and fragmented flow, whereas a stronger PUC likely produces a more coherent and linear jet, facilitating its reorganization following submesoscale perturbations.

Particle depth variations indicate that, in general, water masses maintain relatively stable depths during transport (Figure 5.9c,i,o). However, exceptions do occur for water parcels forming the anticyclone and the ACME. Some of these parcels are advected near the seafloor along the continental shelf and slope, at times approaching within 2 m of the bottom (Figure 5.9j,p). These near-bottom trajectories often follow the bathymetric contours northward, with particles subducting from approximately 50 m to 100 m depth (Figure 5.9i,o), leading to the development of negative PV values (Figure 5.9k,q). Instabilities arising from PUC-bathymetry interactions are particularly evident in the low-PV water masses forming the ACME, which display small-scale anticyclonic oscillations immediately after separating from the continental slope at 19°N (Figure 5.9p–q). This behavior is strongly indicative of centrifugal instability (Molemaker et al., 2015;

Gula et al., 2016; Contreras et al., 2019), which later coalesces into a coherent eddy structure that grows and entrains surrounding water masses into its interior.

Finally, the past evolution of water mass composition reveals that the ACME is primarily composed of pure SACW transported by the PUC, whereas the cyclone contains a more diluted SACW variety, and the anticyclone consists of a mixture of both (Figure 5.9f,l,r). Although the anticyclone also forms from poleward-advected waters, its composition reflects two distinct phases: an early influence from the PUC, delivering pure SACW, and a later contribution from the surface-intensified MC, which transports a more diluted mixture. These findings suggest that, while the anticyclone and ACME share similar formation mechanisms, their primary difference lies in their timing relative to the PUC. The ACME forms while the PUC remains active at depth, continuously supplying SACW to its core. In contrast, the anticyclone–although partially shaped by instabilities in the PUC at an earlier phase–fully develops after the PUC transitions into its surface-intensified phase.

5.4.3 En-route formation

Given that eddies can develop and intensify hypoxic conditions as they propagate westward (see Chapter 3; e.g., Karstensen et al., 2015; Fiedler et al., 2016; Karstensen et al., 2017), we now focus on the mechanisms driving such conditions by examining one representative example from each eddy type.

5.4.3.1 Cyclones

Figure 5.10 shows the evolution of a cyclonic eddy formed close to the continental slope during the upwelling season. At the time of formation, O_2 concentrations within the eddy are relatively low but not yet hypoxic (≈50 µmol L^{-1}; Figure 5.10a,b). The initial trapping of upwelled waters in the mixed layer (defined as water masses where σ_θ difference from 5 m depth < 0.03 kg m^{-3}; de Boyer Montégut et al., 2004) results in elevated nutrients concentrations and phytoplankton biomass (Figure 5.10e–g, column A; d'Ovidio et al., 2013), setting the necessary conditions for increased export production and consequent O_2 respiration due to the remineralization of sinking POC below the mixed layer.

As the eddy evolves and propagates westward, O_2 concentrations decrease significantly, reaching a minimum of ≈4 µmol L^{-1} six months after formation (Figure 5.10b, column E). This decline corresponds to an average O_2 consumption rate of ≈0.25 µmol L^{-1} d^{-1}, consistent with values reported for a similar cyclonic eddy in the region by Karstensen et al. (2015). From timestep E onward, the cyclonic eddy transits through the CVFZ into a NACW-dominated region, as indicated by increasing O_2 concentrations and a decline in SACW content surrounding the eddy (Figure 5.10b,d). The interaction with these distinct water masses likely facilitates their intrusion, leading to the gradual erosion of the eddy's core, particularly at depth where the eddy's vortical structure is less intense (Figure 5.10c; Karstensen et al., 2015).

Values of %SACW between the 25.8 and 26.3 kg m^{-3} isopycnals are initially low but increase over time, reaching nearly 100% in the final months (Figure 5.10d). Despite the westward intru-

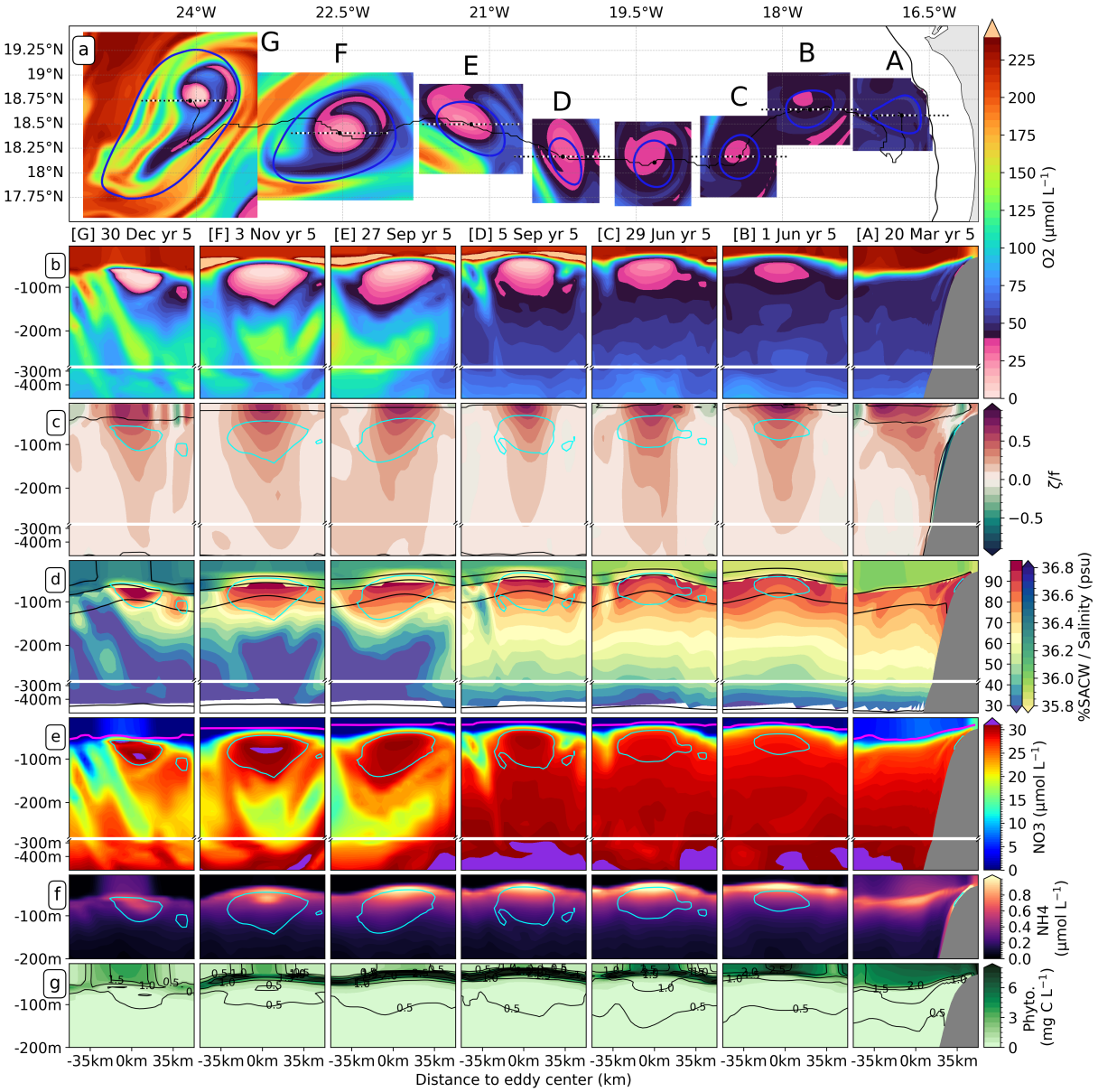


Figure 5.10: Evolution of a hypoxic cyclonic eddy: Part I. (a) Selected timesteps of O_2 concentrations at 100 m depth around the perimeter of the eddy. The blue contours outline the eddy perimeter, the black dot marks the eddy center, the black thin line represents the eddy trajectory, and the dashed black/white line indicates the location of the vertical cross-sections shown in below panels. Vertical cross-sections taken at timesteps A–G of (b) O_2 concentrations; (c) relative vorticity (ζ/f), with black contours representing the 0.5×10^{-9} PV values; (d) water mass composition, showing %SACW at $\sigma_\theta > 25.8$ kg m^{-3}, and salinity at $\sigma_\theta < 25.8$ kg m^{-3}, with isopycnal surfaces at σ_θ 25.2, 25.8, 26.3 and 26.7 kg m^{-3} represented by contour lines; (e) NO_3 concentrations, with magenta line representing the base of the mixed layer; (f) NH_4 concentrations; and (g) Phytoplankton biomass, with contours representing zooplankton biomass (in mg C L^{-1}). Vertical sections are ordered from left to right to reflect the eddy's westward propagation. Cyan contours in (c–f) indicate O_2 = 40 µmol L^{-1}.

sion of NACW, salinity within the eddy core decreases from timestep E to G, while temperature remains largely unchanged (Figure 5.11a–b). This behavior is unexpected, as mixing with saltier NACW would typically result in increased salinity and a reduction in %SACW.

We hypothesize that the observed decrease in salinity results from the upward displacement of fresher water parcels, driven by internal eddy dynamics (e.g., Cetina-Heredia et al., 2019). At approximately 150 m depth, waters are initially colder but also fresher than their surroundings, maintaining density equilibrium due to compensating temperature and salinity effects (Figure

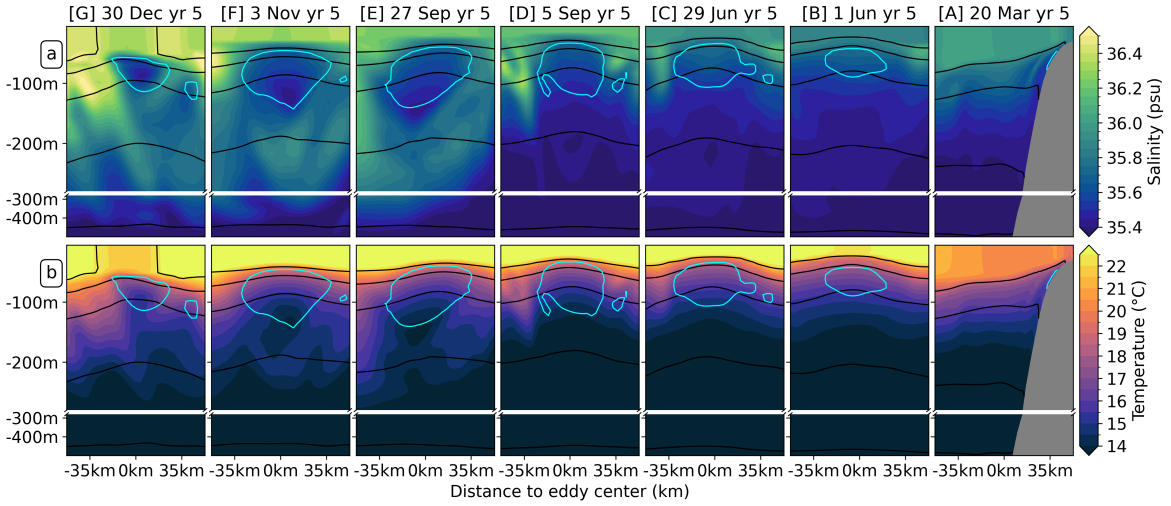


Figure 5.11: Evolution of a hypoxic cyclonic eddy: Part II. Panels show (a) salinity and (b) potential temperature. Black contour lines in all panels represent isopycnal surfaces at σ_θ 25.2, 25.8, 26.3, 26.7 and 27.1 kg m^{-3}. Cyan contours in (c–f) indicate O_2 = 40 µmol L^{-1}. Vertical sections are ordered from left to right to reflect the eddy's westward propagation.

5.11a–b, timestep E). As they ascend, molecular diffusion modifies temperature more rapidly than salinity, reducing salinity and ultimately increasing %SACW at the eddy's hypoxic core. However, we should note that such increase in %SACW is not a universal feature among hypoxic cyclones; in most cases, %SACW declines over time due to mixing with surrounding NACW (e.g., Figure A.20d).

This cyclone maintains a strong and coherent vortical structure throughout its lifetime, with maximum ζ/f near the surface gradually decreasing with depth (Figure 5.10c). This persistent positive vorticity likely contributes to the eddy's longevity (McWilliams, 1985; Early et al., 2011) and to the isolation of the core, inhibiting mixing and intensifying hypoxic conditions (Karstensen et al., 2017). Such strong vorticity also leads to the upward displacement of the isopycnals at the eddy's interior (Figure 5.10d), compensating for the divergence of surface waters (Gaube et al., 2014; McGillicuddy, 2016). This also coincides with seasonal shoaling of the mixed layer between timesteps B and D (Figure 5.10e), bringing the nutricline closer to the surface. As NO_3 in the mixed layer becomes depleted, phytoplankton biomass migrates toward the base of the mixed layer from timestep D to F, where its growth benefits from the optimal availability of light and nutrients (Figure 5.10e; Beckmann & Hense, 2007; Cornec, Claustre, et al., 2021; Cornec, Laxenaire, et al., 2021). This increased primary production enhances organic matter remineralization due to sinking detritus, as indicated by rising NH_4 concentrations (Figure 5.10g).

The cumulative effect of organic matter remineralization is also reflected in the progressive increase of NO_3 within the subsurface eddy core (Figure 5.10e). Seven months after eddy formation, NO_3 levels close to 32 µmol L^{-1} coincide with elevated NH_4 concentrations and suboxic O_2 conditions (Figure 5.10e,f,b, timesteps F–G), indicating the onset of denitrification. When O_2 concentrations fall below 6 µmol L^{-1}, microbial communities shift to anaerobic respiration, using NO_3 as an alternative electron acceptor and producing NH_4 as a byproduct (e.g., Aumont & Bopp, 2006; Kalvelage et al., 2011; Wright et al., 2012). In the final timestep–marking the end of the simulation but not of the eddy itself–a re-intensification of vorticity triggers upwelling,

causing the σ_θ 25.2 kg m^{-3} isopycnal to outcrop at the surface, supplying nitrate-rich waters to the mixed layer and stimulating phytoplankton growth.

These findings indicate that the formation and intensification of hypoxia in this cyclonic eddy are primarily driven by enhanced primary productivity and the associated microbial O_2 consumption linked to the remineralization of sinking organic matter. Although ventilated NACW intrusions occur during the eddy's evolution, the persistent and coherent vortical structure effectively isolates the core from surrounding waters, thereby sustaining and amplifying the hypoxic conditions.

5.4.3.2 Anticyclones

Figure 5.12 shows the evolution of an anticyclonic eddy formed north of the Cap-Vert headland during the upwelling season. Contrary to the previously analyzed cyclonic eddy, hypoxic waters in this anticyclone develop as a vertically confined, elongated layer that persists in this form as it propagates westward, even as minimum O_2 concentrations decline to $\approx$22 µmol L^{-1} six months after formation (Figure 5.12b). Interestingly, this vertical structure closely resembles that of the only documented hypoxic anticyclone in the same region (Kolodziejczyk et al., 2018). At the time of formation, the vorticity field displays a double-core pattern (Figure 5.12c); however, the subsurface vorticity gradually weakens, resulting in a predominantly surface-intensified structure.

This anticyclone is primarily composed of a diluted variety of SACW in subsurface layers (Figure 5.12d). The water mass composition remains relatively stable until just before eddy dissipation (timestep E), indicating limited exchange with surrounding waters. The potential density structure suggests a weakly stratified system, with isopycnals largely aligned with the sea surface throughout most of its lifetime. However, during the initial two months, a more pronounced downward doming of isopycnals is evident, indicating a more intense state shortly after formation (McGillicuddy, 2016).

As the deepening of isopycnals displaces nutrient-rich waters below the well-illuminated surface layer, the initially high NO_3 concentrations within the mixed layer (Figure 5.12e) suggest efficient trapping of nutrient-rich waters during eddy formation. However, positive vertical velocities on the eddy's western half–extending from the surface to just below the mixed layer–indicate that vertical injection of nutrients also contributed to the increase in NO_3 from timestep A to B (Figure 5.12f). This process is further supported by a slight decrease in O_2 concentrations in the mixed layer, which could have only been driven by the mixing of upwelled, low-oxygen waters with surface waters.

Given that the model's vertical and horizontal resolution may limit the representation of submesoscale processes at the eddy periphery (Mahadevan et al., 2008), as well as symmetric instabilities (Brannigan, 2016) and NIWs (Karstensen et al., 2017; Pietri & Karstensen, 2018) at the base of the mixed layer, the observed vertical velocities are most likely associated with eddy-induced Ekman pumping (McGillicuddy et al., 2007; Calil & Richards, 2010; McGillicuddy, 2016; Estrada-Allis et al., 2019). This mechanism arises from the interaction between wind stress and eddy surface currents, which generates a wind stress curl due to differential air-sea

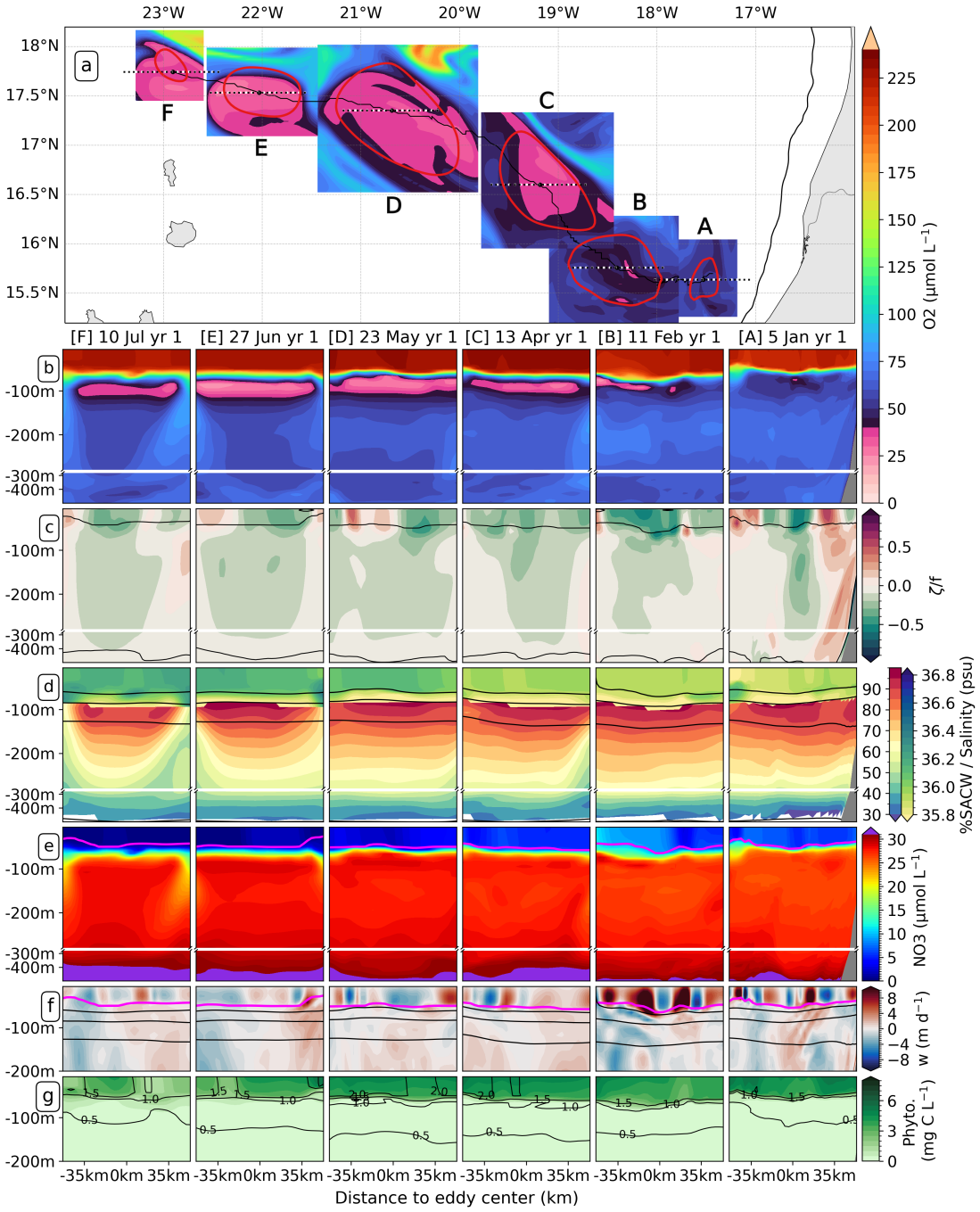


Figure 5.12: Evolution of a hypoxic anticyclonic eddy. (a) Selected timesteps of O_2 concentrations at 100 m depth around the perimeter of the eddy. The red contours outline the eddy perimeter, the black dot marks the eddy center, the black thin line represents the eddy trajectory, and the dashed black/white line indicates the location of the vertical cross-sections shown in below panels. Vertical cross-sections taken at timesteps A–F of (b) O_2 concentrations; (c) relative vorticity (ζ/f), with black contours representing the 0.5×10^{-9} PV values; (d) water mass composition, showing %SACW at $\sigma_\theta > 25.8$ kg m^{-3}, and salinity at $\sigma_\theta < 25.8$ kg m^{-3}; (e) NO_3 concentrations; vertical velocities (with positive and negative values indicating upward and downward transport, respectively); and (g) phytoplankton biomass, with contours representing zooplankton biomass (in mg C L^{-1}). Black contours in (d,f) represent isopycnal surfaces at 25.2, 25.8, 26.3 and 26.7 kg m^{-3}, while magenta line in (e,f) represent the base of the mixed layer. Vertical sections are ordered from left to right to reflect the eddy's westward propagation.

velocity–stronger where winds oppose the eddy surface flow and weaker where they align (Dewar & Flierl, 1987; Martin & Richards, 2001; Gaube et al., 2013). In radially symmetric anticyclones subjected to uniform northerly wind stress, this produces a dipole of upwelling and downwelling on the western and eastern flanks of the eddy, respectively (Gaube et al., 2015; Estrada-Allis

et al., 2019). The timing of this event, coinciding with strong and persistent northwesterly trade winds in the region (Mittelstaedt, 1983; Soares et al., 2019; Cardoso et al., 2020), together with the dominant positive velocities in the western flank of the eddy, further supports the hypothesis that eddy-wind interactions enhance vertical nutrient fluxes into the mixed layer.

The presence of nutrient-rich waters in the mixed layer sustains phytoplankton growth throughout the eddy's lifetime (Figure 5.12g), supporting persistent export production and associated O_2 consumption below the mixed layer through the remineralization of sinking organic matter. In this particular case, the eddy's biogeochemical evolution appears to be driven by a combination of two specific conditions: the efficient trapping of nutrient-rich surface waters at formation, and the short-lived but intense enhancement of vertical nutrient fluxes via wind-driven Ekman pumping. This synergistic interaction creates optimal conditions for elevated primary productivity and export productions, with subsequent O_2 depletion in the subsurface. Although vertical nutrient injection is limited to the initial two months, the trapping of productive water masses has been shown to strongly influence eddy biogeochemistry (Moore et al., 2007; Gaube et al., 2014; Chenillat, Franks, et al., 2015), enabling the long-range transport of anomalous tracers (Chelton et al., 2011; Atkins et al., 2022; Ioannou et al., 2022) and sustaining surface productivity over extended periods (d'Ovidio et al., 2013; Condie & Condie, 2016; McGillicuddy, 2016; Romero et al., 2016). This case thus exemplifies how even structurally weaker eddies that lack strong subsurface isolation can play a disproportionately large role in shaping regional biogeochemical dynamics.

5.4.3.3 ACMEs

Figure 5.13 shows the evolution of an ACME generated off the Mauritanian coast near the end of the upwelling season. At formation, the eddy exhibits relatively high O_2 concentrations (>55 µmol L^{-1}; Figure 5.13b), associated with the presence of pure SACW in its core (Figure 5.13e). Over the following eight months, O_2 concentrations steadily decline to a minimum of ≈18 µmol L^{-1} (timestep D), reflecting an average consumption rate of ≈0.15 µmol L^{-1} d^{-1}, consistent with previous observations in the region (Fiedler et al., 2016; Schütte, Karstensen, et al., 2016; Karstensen et al., 2017). As the eddy crosses the CVFZ, it transitions from oxygen-poor, SACW-dominated waters to oxygen-rich, NACW-dominated conditions (Figure 5.13b,e), while its hypoxic core progressively deepens in parallel with the mixed layer depth, which increases from ≈20 m near the coast to 120 m offshore (Figure 5.13f; Karstensen et al., 2015).

In contrast to the subduction of the hypoxic core, the eddy's vorticity structure shifts upward (Figure 5.13c). Initially, maximum anticyclonic vorticity is centered near 120 m depth, co-located with a low-PV core indicative of flow instabilities driven by the interaction with sloping bathymetry (Molemaker et al., 2015; Contreras et al., 2019). As the eddy matures, subsurface vorticity weakens and shifts toward the surface, becoming confined to the mixed layer. By timestep F–shortly after crossing the CVFZ–the ACME is fully transformed into a surface-intensified anticyclone.

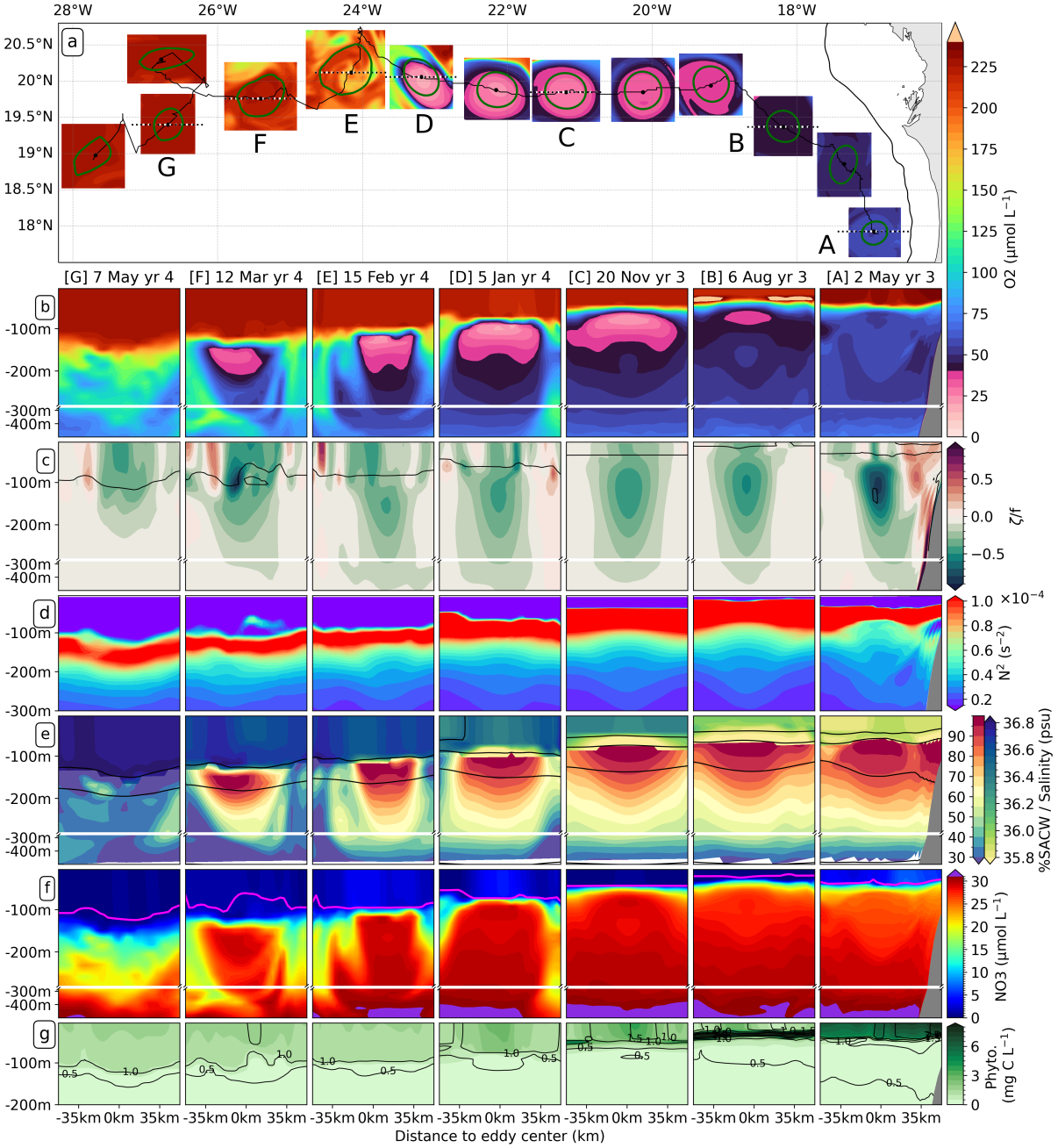


Figure 5.13: Evolution of a hypoxic ACME. (a) Selected timesteps of O_2 concentrations at 100 m depth around the perimeter of the eddy. The green contours outline the eddy perimeter, the black dot marks the eddy center, the black thin line represents the eddy trajectory, and the dashed black/white line indicates the location of the vertical cross-sections shown in below panels. Vertical cross-sections taken at timesteps A–G of (b) O_2 concentrations; (c) relative vorticity (ζ/f), with black contours representing the 0.5×10^{-9} PV values; (d) N^2; (e) water mass composition, showing %SACW at $\sigma_\theta > 25.8$ kg m^{-3}, and salinity at $\sigma_\theta < 25.8$ kg m^{-3}, with isopycnal surfaces at 25.2, 25.8, 26.3 and 26.7 kg m^{-3} represented by contour lines; (f) NO_3 concentrations; and (g) Phytoplankton biomass, with contours representing zooplankton biomass (in mg C L^{-1}). Vertical sections are ordered from left to right to reflect the eddy's westward propagation.

This structural transition is further evidenced by changes in N^2 and water mass composition (Figure 5.13d–e). The initial biconvex lens (Karstensen et al., 2015), characterized by low stratification and pure SACW, evolves into a plano-convex form as the upper core erodes (timestep A–C). This transition is fully consolidated when the initially upward-domed σ_θ 25.8 kg m^{-3} isopycnal inverts into a downward-bent isopycnal (timestep F), as it is typical of surface-intensified anticyclones (McGillicuddy, 2016). Erosion and outcropping of the 25.2 kg m^{-3} isopycnal subse-

quently inject fresher, nitrate-rich waters into the surface layer (Figure 5.13e–f), promoting a redistribution of phytoplankton biomass through the euphotic zone (Figure 5.13g).

Similar transitions are observed in other ACMEs formed at approximately the same location and time of year (Figures A.21, A.22), suggesting this is not an isolated case. Although crossing the CVFZ appears to promote the upward migration of the vorticity core, similar transformations occur in ACMEs that do not cross this front (e.g., Figure A.23), indicating additional drivers–such as seasonal changes in stratification or wind forcing. Nonetheless, some ACMEs maintain their subsurface structure until dissipation (Figures A.24, A.25), suggesting that this transformation is not a universal feature in ACMEs.

To the best of our knowledge, the transition from an ACME to a surface-intensified anticyclone has not been described in the literature. However, the inverse process has been documented in several regions. For instance, A. L. Gordon et al. (2017) reported the conversion of a surface-intensified eddy into an ACME following a tropical cyclone in the Bay of Bengal. Simulations by McGillicuddy (2015) showed that wind-driven upwelling can produce subsurface lenses in anticyclones. Similarly, in the northern South China Sea, X. Wang et al. (2023) found that winter surface cooling combined with Kuroshio intrusion produced a cold, saline core that evolved into a subsurface-intensified structure through geostrophic adjustment. As seasonal warming resumed, the lens-shaped structure was capped by the seasonal thermocline, which sheltered the subsurface core from atmospheric forcing. In our case, we hypothesize that the deepening of the mixed layer–either by intensified wind stress or the eddy's transit across the CVFZ–erodes the upper subsurface core, facilitating the upward shift in vorticity. Nonetheless, the exact mechanisms remain uncertain and require further investigation.

Although this structural transformation appears to modulate primary productivity and the maintenance of hypoxia at later stages, it is not a necessary condition for the onset of hypoxia. In this case, hypoxia results mainly from favorable biogeochemical conditions at formation and internal eddy dynamics–specifically the shoaling of the nutricline and subsurface core isolation. The eddy forms under upwelling conditions, trapping nitrate- and phytoplankton-rich waters within the mixed layer (Figure 5.13f–g, timestep A), which fuel export production and remineralization of organic matter in the isolated core. This leads to declining O_2 and elevated NO_3 as a byproduct (timestep B). As nutrients get depleted at the surface, phytoplankton biomass concentrates near the shoaling nutricline at the base of the thinning mixed layer, forming a distinct DBM (timestep B) and maintaining elevated POC fluxes. Later, the deepening of the mixed layer subducts the nutricline and erodes the upper core, releasing fresh, nutrient-rich waters into the surface, which supports moderate productivity and continued subsurface O_2 consumption (timesteps D–F). Similar cases (e.g., Figures A.23, A.24, A.25) demonstrate that even when surface productivity declines and a DBM is formed, the persistence of core isolation is critical for maintaining hypoxic conditions.

Similar DBMs have been documented in oxygen-depleted ACMEs near the Cabo Verde Archipelago (Pietri & Karstensen, 2018), in the Sargasso Sea (McGillicuddy et al., 2007), and in the eastern Pacific Ocean (Stramma et al., 2014). Although previous studies have emphasized the roles of NIWs (Karstensen et al., 2017; Pietri & Karstensen, 2018) and submesoscale instabilities (Mahadevan et al., 2008; Eden & Dietze, 2009; Brannigan, 2016; Barceló-Llull et al.,

2017) in promoting vertical nutrient fluxes, our simulations show that elevated productivity and nutrient concentrations within ACMEs can also emerge under relatively coarse resolution (∼3 km horizontal; 5–20 m vertical in the upper 200 m). This suggests a complementary mechanism may be at play: namely, the uplift of the nutricline associated with the mode-water structure (McGillicuddy et al., 2007; Stramma et al., 2014), combined with the gradual erosion of the upper subsurface core driven by mixed-layer deepening. Together with efficient core isolation, these processes appear sufficient to sustain primary productivity and support the development of hypoxia in the eddy interior. Nevertheless, further work is required to evaluate the relative contribution of these mechanisms–particularly in the absence of a systematic observational record tracking the offshore evolution of ACMEs (e.g., Karstensen et al., 2017). In this context, the modeled erosion of the upper core due to mixed-layer deepening should be interpreted with caution until supported by targeted *in-situ* observations.

5.5 Summary and conclusions

This chapter investigated the formation, characteristics, and evolution of low-oxygen eddies along the northwestern African coast. Through composite analyses of eddy trajectories, vertical structure, and energy conversion diagnostics, we provide novel insights into the physical mechanisms governing eddy generation and the biogeochemical processes responsible for the onset and persistence of hypoxia. Particular attention was given to the development and intensification of hypoxic conditions, drawing from detailed case studies of individual cyclonic, anticyclonic, and ACMEs.

Our results demonstrate that distinct dynamical pathways govern the formation of each eddy type. Cyclonic eddies are primarily generated by baroclinic instabilities likely associated with the equatorward coastal jet and upwelling front. In contrast, ACMEs and anticyclonic eddies are mainly produced by barotropic instabilities linked to the interaction of the PUC with sloping bathymetry, especially at northern latitudes. Mixed instability regimes were also common among these eddies, particularly in the southern latitudes, underscoring the spatial variability and complexity of eddy generation mechanisms.

Despite these distinct formation processes, the type of dynamical instability was not a reliable predictor of whether an eddy would become hypoxic. Instead, the development of hypoxia was closely linked to eddy lifespan, size, and internal properties. Hypoxic eddies–comprising 56% of all coastal-generated eddies–were consistently longer-lived, more energetic, and larger in radius than their oxygenated counterparts. ACMEs were particularly prone to hypoxia, with 66% exhibiting low-oxygen conditions at some stage. The longer lifespans and stronger core vorticity of hypoxic eddies suggest that effective isolation from surrounding waters is a key determinant of sustained oxygen depletion.

Two dominant pathways for hypoxia development were identified: (i) trapping of pre-existing hypoxic waters at formation and (ii) progressive oxygen consumption during offshore propagation. Eddies forming at higher latitudes were more likely to trap hypoxic waters, reflecting the meridional gradient in background O_2. In contrast, en-route hypoxia was primarily driven

by enhanced biological productivity and subsequent remineralization of sinking organic matter, often under conditions of strong core isolation and shoaling nutriclines.

Contrary to the hypothesis proposed by Dilmahamod et al. (2022), our findings do not support the idea that onshore Ekman transport is the main mechanism supplying SACW into newly-formed ACMEs. Lagrangian particle analyses indicate that the PUC is the dominant source of pure SACW and also drives ACME formation through instabilities induced by flow separation at rough topographic bends. This dual role of the PUC–in both eddy generation and biogeochemical preconditioning–provides a more consistent explanation for the observed vertical structure and water mass characteristics of ACMEs, which ultimately influence their susceptibility to hypoxia. In contrast, anticyclonic eddies tend to form when poleward currents are manifested at the surface, giving rise to surface-intensified vortical structures that weaken with depth. As a result, these eddies do not exhibit the upward doming of upper-layer isopycnals and possess less isolated cores, making them less conducive to the development and maintenance of hypoxic conditions.

The mechanisms promoting primary productivity were found to vary between eddy types. In cyclones, enhanced productivity was primarily driven by internal upwelling. Anticyclones relied on the trapping of nutrient-rich waters during formation, occasionally supplemented by vertical nutrient fluxes induced by eddy-wind interactions. ACMEs benefited from both mechanisms: they formed under upwelling conditions that preconditioned the surface layer with nutrients and phytoplankton, while also sustaining productivity via the shoaling of the nutricline and the formation of a pronounced DBM. The erosion of the subsurface, oxygen-poor but nutrient-rich core during offshore propagation further modulated productivity patterns and biogeochemical structure at a later phase, when hypoxic conditions were already set.

Importantly, our simulations reproduce the characteristic oxygen, nutrient, and biomass distributions observed in low-oxygen ACMEs, despite the absence of explicitly resolved submesoscale processes and instabilities. This suggests that large-scale mechanisms–such as modewater-induced uplift of the nutricline, core isolation, and erosion of the core due to mixed-layer deepening–may be sufficient to drive hypoxia in these features. Nonetheless, the relative contribution of unresolved processes remains uncertain and warrants further investigation.

In summary, mesoscale eddies–particularly ACMEs–play a critical role in shaping oxygen distribution and biogeochemical variability in the ETNA. Their ability to trap, isolate, and transform water masses makes them key agents in the lateral transport of low-oxygen conditions. A mechanistic understanding of their generation and evolution is therefore essential for assessing their ecological impacts and improving model projections under future climate scenarios.

Chapter 6

Synthesis and outlook

This thesis aimed at providing a comprehensive understanding of the characteristics, processes, and drivers of hypoxic conditions contributing to the sOMZ in the ETNA. Recognizing significant gaps in existing knowledge, this work employed a high-resolution coupled physical-biogeochemical model complemented by Eulerian-Lagrangian analyses to investigate the complex interplay between coastal dynamics, boundary currents, and mesoscale eddies.

The analysis began with a detailed characterization of hypoxic events, identifying their spatial extent, seasonal variability, and relationship with regional water masses from both Eulerian and Lagrangian perspectives (Chapter 3). Subsequent analyses examined coastal hypoxic dynamics, highlighting the influence of seasonal variability in coastal upwelling and boundary current dynamics, giving special attention to the role of the PUC in modulating oxygen fluxes and maintaining bottom hypoxia on the continental shelf and slope (Chapter 4). Finally, the mechanisms of generation and evolution of low-oxygen eddies were examined, revealing the processes responsible for their formation, as well as their evolution as they propagate offshore (Chapter 5).

Integrating these insights, this concluding chapter synthesizes the main findings, assesses their implications within the current literature, and provides perspectives on future research necessary to improve our understanding of the ETNA's sOMZ.

6.1 Major scientific findings

This thesis addressed five distinct, yet interrelated, scientific questions. This section summarizes the main findings corresponding to each question, highlighting how these results contribute to an improved understanding of the physical and biogeochemical processes that govern the emergence and maintenance of the sOMZ.

Q1: What are the spatial and temporal patterns of hypoxic conditions in the ETNA, and how are they linked to different regional water masses?
Chapter 3 provides a comprehensive characterization of hypoxic events forming the sOMZ using an integrated Eulerian-Lagrangian approach. Our results reveal pronounced spatial and temporal variability, largely shaped by coastal dynamics, boundary current variability, and eddy activity. Eulerian diagnostics indicate persistent hypoxic conditions along the continental shelf and slope, where hypoxia is recurrent and long-lived, with local occurrence frequencies reaching up to 80%

in the Mauritania shelf. Offshore, hypoxic conditions form distinct swirling patterns associated with westward-propagating eddies, which transport and intensify these conditions toward the open ocean. Although mobile, these structures can persist for up to three months near the Archipelago of Cabo Verde, where topographic steering inhibits further westward propagation.

Seasonal variability also plays a key role in shaping the distribution of hypoxic events. In spring, hypoxic volumes and intensities are generally low in both coastal and offshore regions. During summer, hypoxia intensifies along the Mauritanian shelf, reaching peak values, while remaining relatively modest offshore. Autumn and winter are marked by a widespread expansion and intensification of offshore hypoxia, primarily associated with westward-propagating coastal-generated eddies formed in earlier seasons.

The relationship between hypoxia and regional water mass composition is complex. Most hypoxic conditions occur within the 25.8–26.3 kg m^{-3} density range, at depths between 60 and 140 m, and exhibit mean oxygen concentrations of 30–40 µmol L^{-1}. These events are primarily associated with the regionally-diluted variety of SACWcv, widely distributed across the ETNA but particularly prevalent in the northern coastal region. However, a distinct, colder and fresher hypoxic volume maximum–clearly separated from SACWcv–indicates the presence of hypoxic conditions within the purer SACW variety. Contrary to the widespread hypoxic SACWcv, hypoxic SACW is mostly detected within eddy-related swirling patterns with limited connectivity to the coast, peaking in volume further offshore.

As it was later discussed in Chapter 5, ACMEs contain a substantial fraction of pure SACW due to their intrinsic relation with the PUC–identified in Chapter 4 as the primary pathway for SACW into the region. Because these waters are relatively well-ventilated compared to the older and oxygen-depleted SACWcv, ACMEs are typically not hypoxic at the time of formation. However, as they propagate westward, oxygen concentrations in their core progressively decline due to the combined effects of remineralization of sinking organic matter and the eddy's effecting isolation from mixing with surrounding waters. Aside from localized hypoxic events along the continental shelf and slope–where intense oxygen consumption occurs due to POC deposition and benthic respiration–ACMEs represent the only mechanism by which hypoxia develops within the pure SACW variety.

Q2: Which large-scale physical processes control the formation and distribution of hypoxia across the ETNA?

Partly linked to the previous Q1, this question is also addressed in Chapter 3, and was mainly motivated by the fact that most of what is known about hypoxic conditions in the ETNA stems from sparse observations that associate such conditions with low-oxygen eddies (Karstensen et al., 2015; Schütte, Karstensen, et al., 2016) and sporadic events detected at the bottom of the continental shelf and slope (Machu et al., 2019; Thomsen et al., 2019; Tall et al., 2021; Dale et al., 2022). To address this, we employed a Lagrangian approach to identify and track coherent clusters of hypoxic grid cells–defined as Lagrangian Hypoxic Events (LHEs). These events were then classified based on the dominant physical processes governing their formation and evolution, revealing a diverse range of drivers across the ETNA. These included ACMEs, Cyclonic and

Anticyclonic eddies, ”eddy leakage,” ”eddy dissipation,” ”bottom” processes, ”other” processes (e.g., eddy stirring or bottom export), and ”combined” processes.

Among these, eddy-related events emerged as the most extensive and impactful category, accounting for over half of the total hypoxic volume detected in the ETNA. ACMEs and Cyclonic eddies were particularly dominant, with the most intense cases occurring in the offshore region north of the Cabo Verde Archipelago. In this region, near-anoxic conditions and vertical extents exceeding 80 m were frequently observed, consistent with previous in-situ measurements (e.g., Karstensen et al., 2015; Fiedler et al., 2016). ACME-related LHEs typically formed independently due to the higher proportion of pure SACW within their core. On the other hand, cyclonic and anticyclonic LHEs tended to originate from pre-existing hypoxic conditions, supporting earlier hypotheses that low-oxygen eddies can indeed originate from the trapping of low-oxygen waters at formation (Brandt et al., 2015; Schütte, Karstensen, et al., 2016).

In the coastal region, “combined” and “bottom” LHEs were the most prevalent. “Bottom” LHEs were confined to the continental margin and associated with the most intense hypoxic conditions, though their vertical extent remained limited. In contrast, “combined” LHEs were spatially extensive, long-lived, and were mostly associated with the older, regionally-diluted SACWcv variety. Their frequency peaked in summer, which–as shown in Chapter 4–coincides with the shoaling of the PUC. This seasonal shift reduces the ventilation and increases the residence time of upper central waters, thereby contributing to the widespread decrease of O_2 concentrations along the coast. For this reason, no specific process could be linked to these events

In the offshore region, eddy LHEs were most frequent and intense, especially in north of the Cabo Verde Islands. Eddy leakage and dissipation events–especially those originating from ACMEs–emerged as key transitional processes that contribute to the regional dilution of low-oxygen waters and the transformation of pure SACW into its more oxygen-depleted, regionally modified SACWcv variety. Notably, the region west of Cabo Verde Islands remained largely unaffected by hypoxia due to the physical blocking of westward-propagating eddies. This sheltering effect results in prolonged exposure to hypoxic conditions on the outer-facing coasts of the archipelago, while inner-facing coasts remain relatively insulated. We hypothesize that such spatial differences in hypoxic exposure may contribute to variations in species composition and biodiversity between outward- and inward-facing coastal zones of the archipelago.

Q3: What physical and biogeochemical mechanisms sustain hypoxic conditions in the coastal region during different seasons?

This question is addressed in Chapter 4. The analysis identified the seasonal variability of the PUC as the dominant physical driver regulating coastal oxygen dynamics. During the upwelling season, the PUC transports relatively oxygenated SACW at intermediate depths, ventilating upper central water masses along the coast. However, as upwelling-favorable winds weaken, the PUC shoals and transitions into the surface-intensified MC. This transition, typically occurring between May and July, reduces the inflow of oxygen-rich SACW and increases residence time of upper central water masses, setting the stage for the onset of coastal hypoxia.

During the transition from the upwelling to the relaxation season, persistent primary productivity in the mixed layer–sustained by nutrients supplied earlier by upwelling–continues to drive organic matter export and oxygen consumption at depth, primarily through nitrification and zooplankton respiration. Concurrently, the shoaling of the PUC reduces subsurface ventilation, creating an oxygen deficit that favors the development of hypoxic conditions. Although primary productivity and export production decline as nutrient concentrations are depleted, the established oxygen deficit persists into late summer due to limited oxygen replenishment. Hypoxic conditions are only relieved once the PUC re-intensifies in autumn, flushing the region with oxygenated SACW and restoring oxygen concentrations.

At the bottom of the continental shelf and slope, hypoxic conditions are governed primarily by physical rather than biological processes. Although benthic oxygen consumption remains relatively constant throughout the year–as supported by previous studies (Dale et al., 2014a, 2022)–the seasonal decline in POC fluxes during the relaxation season reduces biological oxygen demand. However, this reduction is offset by physical constraints: increased stratification, the absence of the PUC, and the decrease in turbulent mixing within the bottom boundary layer collectively limit oxygen supply. These conditions create a persistent oxygen deficit near the seafloor, favoring the development and maintenance of bottom hypoxia until the PUC resumes in autumn and re-establishes ventilation.

In addition to its direct impact on oxygen supply, the PUC also plays an important but indirect role on coastal hypoxia through the generation of mesoscale eddies. A quasi-permanent ACME formed downstream of the Cap-Vert headland acts as a barrier to the direct northward advection of oxygen-rich SACW, while simultaneously facilitating the onshore transport of older, oxygen-poorer SACWcv. Lagrangian analyses reveal that up to 32% of hypoxic water parcels in the coastal region originate from offshore via eddy-induced horizontal stirring–a proportion that increases to 44% when considering an extended coastal boundary. During the relaxation season, longer residence times and eddy activity promote cross-shelf exchanges off the Mauritania coast, which dilute pure SACW with SACWcv and further contributes to the decrease of oxygen concentrations along the coast.

In summary, the seasonal dynamics of the PUC emerge as the primary driver of coastal hypoxia in the ETNA. These dynamics influence oxygen variability both directly, by regulating the supply of ventilated SACW, and indirectly, by generating eddies that modulate cross-shore transports. The interaction between these physical processes and biogeochemical oxygen sinks ultimately governs the timing, intensity, and spatial distribution of hypoxic conditions along the northwestern African coast.

Q4: How do hypoxic conditions at the bottom of the continental shelf and slope contribute to the regional formation of the sOMZ?

This question is addressed in Chapters 4 and 5. Using a Lagrangian particle-tracking experiment, we found that bottom-origin particles accounted for 9% of all coastal hypoxic particles. Although this proportion may appear small, it becomes significant when considering the limited vertical extent and volume of bottom layers relative to the full coastal water column (Brandt et al., 2015).

Approximately 65% of these bottom-origin particles were transported offshore inside coastal-generated eddies. This estimate is likely conservative, given the difficulty in accurately defining eddy perimeters at depth due to the vertical variability of the eddy structure (e.g., Haller et al., 2016; Oke et al., 2019). Most of the eddies responsible for bottom export were ACMEs, formed by instabilities triggered by the interaction of the PUC with sloping bathymetry. Once generated, these eddies trap low-PV, often hypoxic waters from the bottom boundary layer. Their strong rotation and core isolation restrict exchange with surrounding waters, enabling the long-range transport and intensification of hypoxic conditions.

A latitudinal gradient in oxygen concentration along the continental margin, decreasing from south to north, further suggests that ACMEs formed in northern regions are particularly effective in exporting hypoxic bottom waters offshore. This is supported by the greater horizontal extent of particle trajectories originating near Cap-Blanc (Figure 4.15), which coincides with a major hotspot of ACME formation (Figure 5.4).

Altogether, these results indicate that the continental shelf and slope are key contributors of low-oxygen waters to the broader offshore sOMZ. The export of hypoxic bottom waters–primarily via ACMEs–demonstrates a strong physical-biogeochemical coupling between coastal and offshore regions, emphasizing the critical role of boundary layer processes and eddy-driven transport in regulating regional oxygen dynamics.

Q5: Which physical processes drive the formation and evolution of low-oxygen eddies, and what are the main biogeochemical consequences within them?

This question is comprehensively addressed in Chapter 5, with supporting insights from Chapters 3 and 4. The formation of low-oxygen eddies along the northwestern African coast is primarily driven by interactions between boundary currents and bathymetry, which give rise to barotropic and baroclinic instabilities that generate coherent mesoscale structures. Barotropic instability dominates in northern latitudes, contributing to both surface- and subsurface-intensified anticyclones, while eddies formed further south are more influenced by baroclinic and mixed instabilities. In contrast, cyclonic eddies are typically generated via baroclinic instability, likely linked to upwelling fronts and interactions with adjacent anticyclones.

Two main pathways for hypoxia development within eddies were identified: (i) the trapping of pre-existing hypoxic waters at formation, especially in northern coastal regions where background O_2 is lowest; and (ii) en-route hypoxia development during westward propagation, driven by core isolation and internal oxygen consumption from remineralization of exported organic matter.

The characteristics of low-oxygen eddies vary with eddy type. ACMEs are the most likely to develop hypoxia (≈66%), typically through en-route processes due to their initial ventilation with pure SACW. Their strong subsurface vorticity, elevated rotation, and low potential vorticity promote core isolation, limiting lateral exchange and enabling sustained hypoxia. In contrast, surface-intensified cyclonic and anticyclonic eddies exhibit weaker isolation and are more dependent on surface productivity and export production to generate subsurface oxygen deficits.

Primary productivity mechanisms also differ by eddy type. In ACMEs, productivity is initially elevated due to nutrient trapping at formation, especially during the upwelling season. As surface nutrients decline, phytoplankton accumulate near the base of the mixed layer, where

upward-bent isopycnals deliver nutrients into the euphotic zone. In later stages, mixed-layer deepening erodes the nutrient-rich, oxygen-poor core, injecting nutrients into the surface layer, sustaining productivity, and reinforcing subsurface oxygen consumption. Cyclonic eddies enhance productivity primarily via internal upwelling from eddy pumping. Anticyclones rely on nutrient trapping during formation, and in some cases, also benefit from eddy-induced Ekman pumping through eddy-wind interaction.

Chapter 3 also quantified O_2 consumption rates in eddies. Low-oxygen ACMEs and cyclones showed similar maximum and mean rates of ≈0.32 and 0.11 µmol L^{-1} d^{-1}, consistent with previous observations (Karstensen et al., 2015; Fiedler et al., 2016; Schütte, Karstensen, et al., 2016). Hypoxic anticyclones had lower maximum rates (<0.13 µmol L^{-1} d^{-1}) and represented only ≈5% of detected LHEs. These events were typically short-lived and low in intensity, resulting mostly from the trapping of hypoxic waters or enhanced productivity at formation.

Another notable result from Chapter 3 was the apparent westward subduction of eddy LHEs during propagation, with ACMEs showing the highest average subduction rate (0.10 m d^{-1}). This pattern was particularly evident north of the Cabo Verde Archipelago, where the influence of the CVFZ is strongest. However, Chapter 5 clarified that this deepening is not due to vertical displacement of the eddy core, but rather to mixed-layer deepening and erosion of the upper hypoxic layers. This contributes to the transformation of ACMEs into surface-intensified anticyclones, as subsurface vorticity is transferred toward the surface. As a result, the core becomes less coherent, facilitating gradual mixing and lateral leakage of hypoxic waters into the surrounding environment before dissipation.

Together, these findings demonstrate that the generation of low-oxygen eddies is governed by a complex interplay between barotropic and baroclinic instabilities, whose relative importance varies with latitude. Their subsequent evolution is primarily shaped by internal processes–most notably, the processes regulating nutrient supply to the euphotic zone and the degree of subsurface core isolation. External environmental factors also exert a significant influence, particularly the water mass composition at the time and place of formation, and the deepening of the mixed layer, which appears to modulate vertical nutrient fluxes during later stages. Among all eddy types, ACMEs play a particularly critical role in trapping, isolating, and transporting hypoxic waters over long distances, reinforcing their central role in shaping both the spatial extent and intensity of the sOMZ.

6.2 Limitations and caveats

The numerical simulation employed in this thesis offers valuable insights into the physical and biogeochemical processes shaping the formation and variability of the sOMZ. However, several limitations and caveats must be acknowledged to appropriately contextualize the results. These arise from simplifications in the model configuration, the use of climatological forcing, the absence of certain physical processes, and uncertainties associated with parameterizations. Each of these factors can influence the representation and accuracy of simulated oxygen concentrations.

In the following, we outline these limitations and discuss their potential implications for the interpretation of our findings.

Climatological forcing

Our model configuration was designed to reproduce the climatological state of the ETNA, and as such, it effectively captures the mean hydrographic structure and seasonal variability of the region (see Section 2.3). However, the use of climatological forcing inherently excludes synoptic wind variability, which can significantly influence coastal upwelling dynamics, stratification, and oxygen ventilation (Capet, McWilliams, et al., 2008; Capet et al., 2017; Machu et al., 2019; Tall et al., 2025). Transient but intense upwelling-favorable wind events can enhance vertical mixing and promote oxygen ventilation of subsurface layers (Ndoye et al., 2014; Duteil, 2019). Conversely, wind relaxation following strong upwelling events can increase stratification and reduce vertical mixing, promoting oxygen depletion due to the accumulation and remineralization of sinking particulate organic matter. Such dynamics have been associated with anoxic conditions along the Senegalese shelf (Machu et al., 2019) and are now increasingly recognized as key drivers of low-frequency oxygen variability in the region (Brandt et al., 2015; Tall et al., 2025).

By relying on climatological wind fields with low temporal and spatial resolution, the model likely underrepresents short-term variability in oxygen concentrations. This limitation may bias the simulation toward emphasizing seasonal trends while neglecting the occurrence and impact of abrupt events, such as short-lived anoxic episodes (Machu et al., 2019) or transient oxygenation pulses (Tall et al., 2021). Although these events are brief, they can exert disproportionate ecological impacts, especially in shallow, productive environments where oxygen levels are already close to hypoxic conditions.

Moreover, the use of climatological forcing in our simulation prevents the representation of interannual to decadal variability associated with large-scale climate modes such as the North Atlantic Oscillation, the Atlantic Meridional Mode, and the Atlantic Multidecadal Oscillation. These modes are known to influence key drivers of oxygen variability, including upwelling intensity (Cropper et al., 2014; Bonino et al., 2019), thermocline depth (Buckley & Marshall, 2016), and the strength and positioning of boundary currents (Lozier, 2010; McCarthy et al., 2015) and equatorial zonal jets (Dommenget & Latif, 2000; Brandt et al., 2010). In particular, variability in the equatorial jet system has been shown to modulate ventilation pathways and oxygen distributions in the ETNA on both seasonal and interannual timescales (Brandt et al., 2010; Monteiro et al., 2011; Duteil et al., 2014; Hahn et al., 2014; Burmeister et al., 2019). As such, our model may underestimate the amplitude and frequency of low-oxygen events and fail to capture compound events that develop under favorable large-scale conditions (Gruber et al., 2021; Wong et al., 2024).

Tidal forcing and coastal trapped waves

Another important limitation to consider is the absence of tidal forcing and internal waves, which can significantly influence coastal and bottom water dynamics, particularly along the continental shelf. Internal tides and waves enhance vertical mixing and turbulence, facilitating the ventilation of bottom waters and the upward flux of nutrients (Colosi et al., 2001; Schafstall et al., 2010;

Mohrholz et al., 2014). By excluding these processes, the model may overestimate stratification and underestimate oxygen supply to the bottom layers, especially in shelf regions where tidal currents play an important role in vertical mixing. Furthermore, in areas where internal wave activity contributes to the resuspension of organic-rich sediments (e.g., Bogucki et al., 1997; Klymak & Moum, 2003; Carter et al., 2005), the absence of this mechanism may result in an underestimation of benthic oxygen demand (Almroth et al., 2009; Moriarty et al., 2018) and, consequently, an overestimation of near-bottom O_2 concentrations.

Tidal forcing is also essential for the generation of Coastal Trapped Waves (CTWs), which can arise from the interaction of tides with bathymetry and are known to influence short-term variability in shelf biogeochemistry (Schafstall et al., 2010; Yücel et al., 2015; Espinoza-Morriberón et al., 2019). CTWs can drive the offshore export of oxygen-depleted, particle-rich bottom waters (Thomsen et al., 2019) and have been linked to fluctuations in nitrate concentrations and bottom oxygen levels (Echevin et al., 2014). Moreover, remotely forced CTWs may modulate the strength of the PUC (Polo et al., 2008; Kounta et al., 2018), which supplies oxygenated SACW to the coastal region (Peña-Izquierdo et al., 2012; Brandt et al., 2015; Klenz et al., 2018). The omission of these dynamics may therefore contribute to biases in the simulation of coastal oxygen variability, especially in shelf regions where internal wave breaking and CTW activity are important contributors to vertical and lateral exchanges of biogeochemical tracers (Schafstall et al., 2010; Echevin et al., 2014; Lauton et al., 2021).

River runoff

Another limitation of our model setup is the absence of explicit river runoff. Although the model captures the influence of the West African monsoon on surface salinity through the use of boundary conditions derived from the SODA reanalysis, it does not account for the input of nutrients delivered by rivers. This omission may lead to an underestimation of coastal primary productivity, particularly during the relaxation season when river discharge typically peaks (Thouvenin-Masson et al., 2024) and hypoxic conditions are most intense (see Chapter 4).

In addition to its role in supplying nutrients, river runoff contributes to freshwater input that alters salinity, density stratification, and coastal circulation. Recent studies demonstrate that river plumes modify SSH gradients, generating geostrophic currents that redistribute heat and nutrients along coastlines (Awo et al., 2022; Aroucha et al., 2025). While Thouvenin-Masson et al. (2024) argue that precipitation dominates seasonal mixed-layer salinity changes in the ETNA, river discharge remains critical for modulating local density gradients. The exclusion of riverine input thus represents a potential source of bias in simulated coastal dynamics and nutrients input, particularly in regions influenced by major river plumes such as Senegal and Gambia.

Parameterization of Biogeochemical Processes and Oxygen Consumption

The biogeochemical module PISCES employs parameterized formulations to represent key processes influencing oxygen dynamics, including the remineralization of organic matter, nitrification, and zooplankton respiration (Aumont & Bopp, 2006; Aumont et al., 2015). Although these formulations are based on empirical relationships and observations, they rely on globally

tuned constants and simplified assumptions that may not adequately capture the spatial and temporal heterogeneity of biogeochemical processes (Henson et al., 2022). For instance, oxygen consumption is primarily governed by depth-dependent remineralization length scales, which are fixed and do not explicitly account for variations in microbial community composition (Löscher et al., 2015), lability of dissolved organic matter (Thomsen et al., 2019; Devresse et al., 2022, 2024), ambient oxygen levels (with the exception of nitrification; Cavan et al., 2017; Bianchi et al., 2018), or metabolic sensitivity to temperature (Laufkötter et al., 2017). This can result in inaccuracies in simulated oxygen demand, particularly in regions with sharp biogeochmical gradients.

Bottom boundary layer and sediment dynamics

A key limitation of the model–particularly relevant to the results presented in Chapter 4–is the absence of an explicit sediment compartment, which prevents the full representation of benthic biogeochemical processes. Oxygen consumption at the sediment-water interface is strongly influenced by benthic respiration, organic matter degradation, and denitrification (e.g., Monteiro et al., 2008; Siedlecki et al., 2015; Yücel et al., 2015; Schmidt & Eggert, 2016; Sokoll et al., 2016; Gier et al., 2017; K. Fennel & Testa, 2019). Without a dynamic sediment layer, the model may underestimate bottom oxygen demand, especially in the productive continental margins of Senegal and Mauritania, where high rates of POC deposition stimulate intense benthic respiration (Dale et al., 2014a, 2022).

In PISCES-v1, bottom boundary conditions for oxygen and nitrate are prescribed using a simplified empirical formulation based on the metamodel developed by Middelburg et al. (1996). By relating POC flux at the seafloor to depth-dependent degradation processes, this approach estimates the proportion of O_2 and NO_3 consumed via oxic and suboxic degradation of POC, along with the release of NH_4 as a byproduct of remineralization. Although this method does not explicitly resolve sediment dynamics or benthic-pelagic feedbacks, it provides a computationally efficient means of estimating bottom fluxes of key nutrients and oxidants. As shown in Chapter 2, the resulting oxygen and nitrate fluxes align reasonably well with available observations conducted along the Mauritanian shelf and slope.

In addition, the hydrodynamic model used here does not explicitly resolve sediment transport processes. Although CROCO includes bottom boundary layer parameterizations capable of representing sediment resuspension via drag-coefficient or wave-current interaction formulations (Blaas et al., 2007), this study relies on the KPP vertical mixing scheme. While KPP represents vertical mixing near the seabed and implicitly responds to shear, it does not compute bottom shear stress explicitly or simulate sediment dynamics. Consequently, the model cannot represent the resuspension of organic-rich particles, a process known to trigger rapid oxygen depletion and hypoxia in coastal waters off Mauritania (Thomsen et al., 2019). This limitation likely results in an underestimation of both benthic oxygen consumption and the offshore export of low-oxygen waters, thereby reducing the simulated contribution of bottom hypoxia to the formation and maintenance of the sOMZ.

Submesoscale dynamics

Although the model simulation used throughout this thesis has a relatively high horizontal resolution of approximately 3 km and allows partial representation of submesoscale dynamics, it remains insufficient to fully resolve submesoscale instabilities that emerge along the continental margin and within mesoscale eddies. Recent studies have shown that fine-scale dynamical instabilities–such as inertial and centrifugal instabilities–play a critical role in the formation of ACMEs (Gula et al., 2016), particularly in EBUSs (Molemaker et al., 2015; Contreras et al., 2019). Using two realistic numerical simulations of the Peruvian upwelling system with contrasting horizontal resolutions (0.3 km vs. 3 km), Contreras et al. (2019) found that the ACME formed in the high-resolution run exhibited more intense negative PV anomalies at its core, which were associated with the coalescence of centrifugal instabilities during formation. In contrast, the low-resolution simulation was unable to resolve such instabilities, and eddy generation was instead associated with the barotropic conversion of MKE to EKE. Given the similarities between the Peruvian and Mauritanian upwelling systems, it is thus likely that the role of fine-scale instabilities in ACME formation is underestimated in our simulation.

In addition to the generation mechanisms, the model's representation of the vertical structure and internal dynamics of ACMEs may be limited by both horizontal and vertical resolution. Numerous studies have shown that vertical transport of tracers within ACMEs is mediated by short-lived but intense submesoscale upwelling and downwelling events associated with ageostrophic circulations, frontal instabilities at the eddy periphery, and symmetric instabilities at the base of the mixed layer (McGillicuddy, 2015; Brannigan, 2016; Barceló-Llull et al., 2017). In the ETNA, glider observations have shown that Near-Inertial Waves (NIWs) can interact with the eddy field, producing submesoscale ($\approx$1 km) vertical motions concentrated along the eddy flanks (Karstensen et al., 2017; Pietri & Karstensen, 2018). These motions have been linked to enhanced nutrient supply into the euphotic zone, promoting elevated primary productivity in the mixed layer (Karstensen et al., 2015). In the case of low-oxygen ACMEs, a distinct, vertically coherent core has been observed beneath the mixed layer, bordered by local maxima in buoyancy frequency, while vertical layering in hydrographic profiles and direct velocity measurements have revealed the downward propagation of NIWs along the eddy flanks (Karstensen et al., 2017). Because the phase speed of these NIWs often matches the background flow, the potential formation of a critical layer may enhance vertical mixing near the base of the mixed layer. Such processes may explain the coexistence of upward nutrient fluxes and a weakly ventilated, isolated eddy core (Fiedler et al., 2016; Schütte, Karstensen, et al., 2016). Although both the upward nutrient supply and the isolation of hypoxic subsurface cores appear to be reasonably well represented in our model, the absence of NIWs and submesoscale instabilities likely results in an underestimation of vertical exchange within eddies, potentially leading to the development of weaker hypoxic conditions offshore.

6.3 Implications of our results

Despite the limitations discussed above, the findings presented in this thesis provide valuable new insights into the characteristics of the hypoxic events contributing to the sOMZ in the ETNA, as well as the physical and biogeochemical processes that govern their formation, maintenance, and offshore evolution. In the following, we discuss the broader implications of these results and situate them within the context of existing literature, highlighting how they contribute to ongoing efforts to understand regional oxygen dynamics the potential impacts of climate change on the ETNA.

Expanding the paradigm of hypoxia formation

Findings from Chapter 3 challenge the prevailing notion that hypoxic conditions in the ETNA are primarily restricted to mesoscale eddies (Schütte, Karstensen, et al., 2016). Our results provide strong evidence that hypoxia can also develop independently in the coastal region off Mauritania, particularly during the relaxation season, when the PUC shoals and manifests near the surface as the MC. These nearshore hypoxic waters may act as a source for the formation of low-oxygen eddies, especially in autumn when ambient oxygen concentrations reach seasonal minima and the re-intensification of the PUC promotes current instabilities and subsequent formation of eddies along the coast.

Although anticyclonic eddies are typically associated with positive oxygen anomalies (Schütte, Karstensen, et al., 2016), our results reveal that a small but non-negligible fraction of these eddies can exhibit hypoxic cores. We hypothesize that these events are more frequent than previously recognized but remain under-detected due to the limited availability of *in-situ* observations. The incidental detection of low-intensity hypoxic conditions in an anticyclonic eddy during untargeted glider surveys off the Senegalese coast further supports this hypothesis (Kolodziejczyk et al., 2018), highlighting the need for similar observational efforts in the future.

Beyond the direct role of eddies in shaping the extent and intensity of the sOMZ in the ETNA, our Lagrangian analysis from Chapter 3 reveals that hypoxic conditions initially trapped within eddies can persist long after the eddy itself dissipates–sometimes for up to one year. Once released from coherent eddy structures, these LHEs follow less organized trajectories but continue to interact with other features in the region. They may contribute to the formation of new hypoxic events through processes such as merging with LHEs or fragmentation into smaller LHEs. While the potential for low-oxygen eddy leakage and dissipation had been hypothesized in earlier studies (Karstensen et al., 2015; Löscher et al., 2015), our results represent the first quantitative characterization of these events. This finding opens new perspectives on their role in sustaining and distributing low-oxygen conditions, influencing regional biogeochemical cycling and contributing to water mass transformation in the ETNA.

The central role of the PUC

Results from Chapter 4 underscore the dual role of the PUC in shaping oxygen variability along the coastal region of the ETNA. While its role in ventilating the upper central water masses has

been well established in previous studies (Voituriez & Chuchla, 1978; Elmoussaoui et al., 2005; Pastor et al., 2008; Peña-Izquierdo et al., 2012; Brandt et al., 2015; Peña-Izquierdo et al., 2015; Klenz et al., 2018), our results reveal a less recognized indirect effect: during the transition from the upwelling to the relaxation season, the PUC shoals and transforms into the near-surface MC, significantly reducing subsurface ventilation. This shift contributes to the general decrease of O_2 concentrations and consequent development of hypoxic conditions, despite the fact that export production and associated oxygen consumption remains relatively low during the relaxation season.

We suggest that this previously neglected mechanism has remained largely overlooked due to the limited availability of year-round, systematic observations in the region. For example, Klenz et al. (2018) reported relatively weak poleward flow during the upwelling season and observed the highest SACW proportions associated with the lowest O_2 concentrations off Mauritania in summer. These findings contrast with our results, which show enhanced subsurface poleward transport during the upwelling season and a minimum in the proportion of SACW during summer–precisely when the PUC shoals and water residence time increases within the upper central water density stratum. Important to note, however, is that the Klenz et al. study was based on nine oceanographic campaigns–five during the upwelling season and four during the relaxation season. Given this limited sampling, it is plausible that these cruises did not fully capture the seasonal dynamics of boundary currents and water mass distributions. Our analysis of the WOA23 climatology provides additional support for our interpretation, showing that the proportion of SACW peaks at the end of the upwelling season in late spring (see Figure A.8). These findings point to a seasonally modulated ventilation mechanism along the ETNA margin, with important implications for the timing and severity of hypoxic events.

Susceptibility of bottom waters to remote forcing

As observed in other EBUSs, such as those off Oregon (Grantham et al., 2004; Siedlecki et al., 2015) and Namibia (Monteiro et al., 2006, 2008; Schmidt & Eggert, 2016), the delivery of oxygen-poor source waters via subsurface boundary currents can have a significant influence on the formation of hypoxic conditions on continental shelves. In the ETNA, the transport of such waters to the Senegalese and Mauritanian shelves occurs through the PUC, which carries ventilated waters from the equatorial Atlantic. Variability in the equatorial system of zonal jets has been shown to strongly modulate oxygen supply to the region, with significant implications to regional O_2 variability (Brandt et al., 2010; Hahn et al., 2014; Burmeister et al., 2019). Projected long-term declines in the oxygen content of source waters carried by these currents, as suggested by both observations and Earth system models (Gruber, 2011; Gilly et al., 2013; Oschlies et al., 2018), are therefore expected to further increase the risk of coastal hypoxia. Compounding this, the shoaling of the dOMZ by approximately 22 ± 17 m over the past decade (Hahn et al., 2017) could lead to increased exposure of the upper slope and shelf to lower oxygen concentrations. Although only a small fraction of upwelling source waters are reported to originate from these depths (Glessmer et al., 2009), even modest vertical shifts in OMZ structure could influence the oxygen properties of waters reaching the coastal margin (Grantham et al., 2004). Additional stressors include the observed warming of surface waters (Vélez□Belchí et al., 2015; Gómez-

Letona et al., 2017) and the projected reduction in wind stress in the ETNA (Sylla et al., 2019), both of which are expected to enhance water column stratification. Increased stratification can limit diapycnal mixing and oxygen renewal near the bottom (T. Fischer et al., 2013; Brandt et al., 2015), thereby intensifying the vulnerability of coastal bottom waters to hypoxia.

From an ecological point of view, these processes raise serious concerns about the increased likelihood of low-oxygen events and associated mass mortality events (Caverivière & Touré, 1990; Machu et al., 2019). However, the implications extend beyond the shelf: as shown in Chapter 5, many low-oxygen eddies–particularly ACMEs–form in the coastal region and partly incorporate bottom waters from the continental slope in their interior. As these bottom waters become increasingly hypoxic, both the frequency and intensity of low-oxygen eddies are expected to rise. Moreover, if eddies form with more intense hypoxic conditions, the en-route oxygen consumption within them will further intensify these conditions, leading to more severe offshore hypoxia and contributing to the overall expansion and intensification of the sOMZ offshore.

Implications of coastal-generated eddies for oxygen variability

In addition to supplying relatively oxygenated, pure SACW to the ETNA, findings from Chapters 4 and 5 indicate that the PUC plays a central role in the generation of ACMEs via instabilities triggered by its interaction with coastal bathymetry. These coastal-generated eddies can substantially affect regional oxygen dynamics by facilitating the onshore transport of offshore waters and promoting the mixing between purer SACW and the more oxygen-depleted, regionally diluted SACWcv variety. Such eddy-induced horizontal stirring modifies the oxygen content of coastal waters and contributes to the spatial and temporal variability of hypoxic conditions along the continental margin.

A particularly illustrative example is the formation of a quasi-permanent, relatively stationary ACME in the wake of the Cap-Vert headland. Although this region was previously identified as an eddy generation hotspot during winter, and eddies formed there have been shown to be highly nonlinear (Cardoso et al., 2020), the mechanisms driving their formation–primarily linked to barotropic instabilities–have been elucidated here for the first time. Given the significant role these features may play in modulating coastal oxygen dynamics, either by onshore transport of offshore waters of through the trapping and transport of pre-existing hypoxic conditions, our findings underscore the need for targeted observational campaigns to further investigate the formation of these eddies (e.g., Thomsen et al., 2019).

Formation mechanisms of ACMEs

A key aspect of this thesis concerns the mechanisms underlying the formation of ACMEs in the ETNA. Dilmahamod et al. (2022) proposed that baroclinic instabilities are primarily responsible for ACME generation, with the high SACW content in their cores attributed to onshore Ekman transport of SACW-rich waters from the open ocean. In their view, this distinguishes ACMEs from surface-intensified anticyclones, as the denser SACW core remains isolated from direct surface forcing.

Our results point to a different formation pathway. While baroclinic instability may play a secondary role, we find–consistent with findings from the Chile upwelling system (Contreras

et al., 2019)–that centrifugal and barotropic instabilities arising from the interaction of the PUC with sloping bathymetry are the dominant drivers of ACME formation. Furthermore, offshore waters exhibit a lower SACW signature than those transported by the PUC. Given that most ACMEs in our simulation form during periods of intensified PUC flow, we conclude that the PUC not only initiates ACME formation but also delivers the purer SACW that characterizes their low-PV cores.

In contrast, surface-intensified anticyclonic eddies tend to form under weaker PUC conditions, when it shoals and transitions into the surface-dominated MC. These eddies typically exhibit weaker core isolation and a higher proportion of the more diluted SACWcv variety. Although the presence of pure SACW may influence the vertical structure of ACMEs, we argue that their defining dynamical features–namely, low PV and a subsurface-intensified vorticity core–are primarily shaped by their formation dynamics, rather than by water mass composition.

Internal dynamics in low-oxygen ACMEs

Although our simulation does not explicitly resolve submesoscale dynamics within ACMEs, our results show that these eddies can nevertheless sustain elevated surface primary productivity and persistent hypoxic conditions at depth. This suggests that, in addition to the influence of submesoscale processes such as nutrient injection into the euphotic layer via NIWs (Karstensen et al., 2015; Karstensen et al., 2017; Pietri & Karstensen, 2018), larger-scale processes may also play a central role in shaping the primary productivity and internal oxygen structure of ACMEs.

As demonstrated in Chapter 5, one key mechanism–largely overlooked in previous studies–is the deepening of the mixed layer as these eddies propagate westward. This process can erode the upper boundary of the nutrient-rich, oxygen-depleted eddy core, injecting nutrients into the surface layer and fueling phytoplankton growth. The resulting export of organic matter enhances subsurface oxygen consumption via remineralization, which contributes to the maintenance or intensification of hypoxia within the eddy interior. Additionally, the upward doming of isopycnals within ACMEs elevates the nutricline toward the euphotic zone, promoting the formation of a pronounced DBM (McGillicuddy, 2015). Even in the absence of strong surface productivity, our results suggest that the existence of a pronounced DBM may be sufficient to sustain high export production and subsequent depletion of O_2 in an isolated subsurface core.

6.4 Future perspectives

The results presented in this thesis also raise important unresolved questions. As with any modeling study, limitations in both the numerical framework and the availability of observational data leave room for uncertainty. Although the model employed in this study captures the large-scale spatial and seasonal patterns of oxygen distribution in the ETNA, it does not resolve the full spectrum of physical and biogeochemical processes operating on short temporal and spatial scales–especially in the highly dynamic coastal region. Addressing these limitations in future modeling efforts could involve several key improvements:

- Employing high-resolution atmospheric forcing with finer spatial and temporal scales to better represent synoptic wind variability and its influence on upwelling dynamics;
- Running simulations in hindcast mode with interannually varying atmospheric datasets to capture low-frequency climate variability and its impact on oxygen dynamics;
- Including tidal forcing to improve representation of bottom boundary layer mixing and the generation of coastal trapped waves to better estimate near-bottom oxygen levels;
- Coupling with a sediment model to explicitly resolve sediment-water oxygen fluxes, benthic remineralization, and the resuspension and offshore export of low-oxygen bottom waters.

Implementing these refinements would significantly improve the model's ability to simulate key physical and biogeochemical processes and lead to a more accurate and comprehensive representation of oxygen variability and hypoxia formation in the ETNA.

Our results also highlight the need for improved observational strategies. Schütte, Brandt, and Karstensen (2016) were the first to systematically characterize the regional eddy field using satellite altimetry and SST data, identifying roughly 13 ACMEs per year–representing 9% of all eddies–compared to the 34% identified in this study. In contrast to our findings, however, their results did not identify the region adjacent to the Cap-Vert headland as a significant ACME formation hotspot. These discrepancies likely reflect methodological differences and limitations in the resolution of altimetry datasets, especially near the coast (Amores et al., 2018). Frequent cloud cover further hampers the detection of cold-core ACMEs from SST. Given the strong seasonality in eddy generation near Cap-Vert, future observational campaigns should prioritize targeted sampling in this region in February, when the PUC is most intense (Figure 4.4) and ACME formation is most likely (Figure 5.4). Similar efforts in the Peruvian upwelling system have already proven successful in capturing the formation of ACMEs (Thomsen et al., 2016).

Due to the complexity and uncertainty associated with many of the processes described in this thesis, validation using *in-situ* observations remains limited. Improved observational coverage is therefore essential to refine our understanding of oxygen dynamics and validate model results. Systematic, untargeted deployments of autonomous platforms, such as gliders and biogeochemical Argo floats, would enhance coverage and allow for the detection of understudied processes, which include low-oxygen eddy dissipation and leakage events, as well as the formation of low-oxygen eddies with pre-existing hypoxic conditions in their interior. These efforts are especially relevant in the context of ongoing climate change, which is projected to alter regional oxygen budgets (Keeling et al., 2010; Pitcher et al., 2021).

The upcoming FUTURO project ("FUture of Tropical Upwelling Regions in the Atlantic Ocean")[1] is a multi-scale, multidisciplinary observational campaign scheduled for 2027-2029 and represents an opportunity to test many of the hypotheses presented in this study. With its focus on the ETNA, FUTURO in expected to provide the high-resolution temporal and spatial data necessary to validate model results and further improve our understanding of oxygen dynamics in the region. As argued through Chapters 3, 4 and 5, the year-round temporal coverage of the

[1] https://futuro-campaign.org

campaign is especially relevant for assessing the nature of the sOMZ, as it would provide new insights into the dynamics of the system during the relaxation season–a period marked by a lack of observations and by the seasonal decrease of O_2 concentrations along the Mauritanian coast.

In conclusion, this thesis highlights the need to consider both local and remote forcing mechanisms when assessing oxygen variability in the ETNA. Seasonal shifts in boundary current dynamics, variability in upwelling intensity, and changes in the oxygen content of source waters all interact to shape the regional oxygen budget. As climate change continues to modify these processes, a deeper understanding of their interplay is therefore essential for anticipating the future evolution of the ETNA's sOMZ.

Bibliography

Abecassis, M., Dewar, H., Hawn, D., & Polovina, J. (2012). Modeling swordfish daytime vertical habitat in the North Pacific Ocean from pop-up archival tags. *Marine Ecology Progress Series*, *452*, 219–236. https://doi.org/10.3354/meps09583

Abernathey, R., & Haller, G. (2018). Transport by Lagrangian Vortices in the Eastern Pacific. *Journal of Physical Oceanography*, *48*(3), 667–685. https://doi.org/10.1175/JPO-D-17-0102.1

Adjeroud, M., Kayal, M., Iborra-Cantonnet, C., Vercelloni, J., Bosserelle, P., Liao, V., Chancerelle, Y., Claudet, J., & Penin, L. (2018). Recovery of coral assemblages despite acute and recurrent disturbances on a South Central Pacific reef. *Scientific Reports*, *8*(1), 9680. https://doi.org/10.1038/s41598-018-27891-3

Akpınar, A., Charria, G., Theetten, S., & Vandermeirsch, F. (2020). Cross-shelf exchanges in the northern Bay of Biscay. *Journal of Marine Systems*, *205*, 103314. https://doi.org/10.1016/j.jmarsys.2020.103314

Aldama-Campino, A., Döös, K., Kjellsson, J., & Jönsson, B. (2020, December). TRACMASS: Formal release of version 7.0. https://doi.org/10.5281/zenodo.4337926

Allen, J. S. (1973). Upwelling and Coastal Jets in a Continuously Stratified Ocean. *Journal of Physical Oceanography*, *3*(3), 245–257. https://doi.org/10.1175/1520-0485(1973)003<0245:UACJIA>2.0.CO;2

Almroth, E., Tengberg, A., Andersson, J. H., Pakhomova, S., & Hall, P. O. J. (2009). Effects of resuspension on benthic fluxes of oxygen, nutrients, dissolved inorganic carbon, iron and manganese in the Gulf of Finland, Baltic Sea. *Continental Shelf Research*, *29*(5), 807–818. https://doi.org/10.1016/j.csr.2008.12.011

Alpers, W., Brandt, P., Lazar, A., Dagorne, D., Sow, B., Faye, S., Hansen, M. W., Rubino, A., Poulain, P.-M., & Brehmer, P. (2013). A small-scale oceanic eddy off the coast of West Africa studied by multi-sensor satellite and surface drifter data. *Remote Sensing of Environment*, *129*, 132–143. https://doi.org/10.1016/j.rse.2012.10.032

Álvarez-Salgado, X. A., Nieto-Cid, M., Álvarez, M., Pérez, F. F., Morin, P., & Mercier, H. (2013). New insights on the mineralization of dissolved organic matter in central, intermediate, and deep water masses of the northeast North Atlantic. *Limnology and Oceanography*, *58*(2), 681–696. https://doi.org/10.4319/lo.2013.58.2.0681

Amante, C., & Eakins, B. W. (2009). *ETOPO1 1 arc-minute global relief model: Procedures, data sources and analysis* (NOAA Technical Memorandum NESDIS NGDC-24) (Accessed: 19 September 2019). NOAA National Geophysical Data Center, NESDIS. https://doi.org/10.7289/V5C8276M

Amores, A., Jordà, G., Arsouze, T., & Le Sommer, J. (2018). Up to What Extent Can We Characterize Ocean Eddies Using Present-Day Gridded Altimetric Products? *Journal of Geophysical Research: Oceans*, 1–17. https://doi.org/10.1029/2018JC014140

Andrade, I., Sangrà, P., Hormazabal, S., & Correa-Ramirez, M. (2014). Island mass effect in the Juan Fernández Archipelago (33°S), Southeastern Pacific. *Deep Sea Research Part I: Oceanographic Research Papers*, *84*, 86–99. https://doi.org/10.1016/j.dsr.2013.10.009

Arakawa, A., & Lamb, V. R. (1977, January). Computational Design of the Basic Dynamical Processes of the UCLA General Circulation Model. In J. Chang (Ed.), *Methods in Computational Physics: Advances in Research and Applications* (pp. 173–265, Vol. 17). Elsevier. https://doi.org/10.1016/B978-0-12-460817-7.50009-4

Archer, M., Wang, J., Klein, P., Dibarboure, G., & Fu, L.-L. (2025). Wide-swath satellite altimetry unveils global submesoscale ocean dynamics. *Nature*, *640*(8059), 691–696. https://doi.org/10.1038/s41586-025-08722-8

Arévalo-Martínez, D. L., Kock, A., Löscher, C. R., Schmitz, R. A., & Bange, H. W. (2015). Massive nitrous oxide emissions from the tropical South Pacific Ocean. *Nature Geoscience*, *8*(7), 530–533. https://doi.org/10.1038/ngeo2469

Arístegui, J., Barton, E. D., Álvarez-Salgado, X. A., Santos, A. M. P., Figueiras, F. G., Kifani, S., Hernández-León, S., Mason, E., Machú, E., & Demarcq, H. (2009). Sub-regional ecosystem variability in the Canary Current upwelling. *Progress in Oceanography*, *83*(1-4), 33–48. https://doi.org/10.1016/j.pocean.2009.07.031

Armi, L., Hebert, D., Oakey, N., Price, J. F., Richardson, P. L., Rossby, H. T., & Ruddick, B. (1989). Two Years in the Life of a Mediterranean Salt Lens.

Armi, L., & Zenk, W. (1984). Large Lenses of Highly Saline Mediterranean Water.

Arnault, S. (1987). Tropical Atlantic geostrophic currents and ship drifts. *Journal of Geophysical Research*, *92*(C5), 5076. https://doi.org/10.1029/JC092iC05p05076

Aroucha, L. C., Lübbecke, J. F., Brandt, P., Schwarzkopf, F. U., & Biastoch, A. (2025). River discharge impacts coastal southeastern tropical Atlantic sea surface temperature and circulation: A model-based analysis. *Ocean Science*, *21*(2), 661–678. https://doi.org/10.5194/os-21-661-2025

Ascani, F., Firing, E., Dutrieux, P., McCreary, J. P., & Ishida, A. (2010). Deep Equatorial Ocean Circulation Induced by a Forced–Dissipated Yanai Beam. https://doi.org/10.1175/2010JPO4356.1

Assassi, C., Morel, Y., Vandermeirsch, F., Chaigneau, A., Pegliasco, C., Morrow, R., Colas, F., Fleury, S., Carton, X., Klein, P., & Cambra, R. (2016). An index to distinguish surface- and subsurface-intensified vortices from surface observations. *Journal of Physical Oceanography*, *46*(8), 2529–2552. https://doi.org/10.1175/JPO-D-15-0122.1

Atkins, J., Andrews, O., & Frenger, I. (2022). Quantifying the Contribution of Ocean Mesoscale Eddies to Low Oxygen Extreme Events. *Geophysical Research Letters*, *49*(15), e2022GL098672. https://doi.org/10.1029/2022GL098672

Auclair, F., Bordois, L., Dossmann, Y., Duhaut, T., Paci, A., Ulses, C., & Nguyen, C. (2018). A non-hydrostatic non-Boussinesq algorithm for free-surface ocean modelling. *Ocean Modelling*, *132*, 12–29. https://doi.org/10.1016/j.ocemod.2018.07.011

Auger, P. A., Bento, J. P., Hormazabal, S., Morales, C. E., & Bustamante, A. (2021). Mesoscale Variability in the Boundaries of the Oxygen Minimum Zone in the Eastern South Pacific: Influence of Intrathermocline Eddies. *Journal of Geophysical Research: Oceans*, *126*(2), 1–21. https://doi.org/10.1029/2019JC015272

Auger, P. A., Machu, E., Gorgues, T., Grima, N., & Waeles, M. (2015). Comparative study of potential transfer of natural and anthropogenic cadmium to plankton communities in the North-West African upwelling. *Science of the Total Environment*, *505*, 870–888. https://doi.org/10.1016/j.scitotenv.2014.10.045

Auger, P. A., Gorgues, T., Machu, E., Aumont, O., & Brehmer, P. (2016). What drives the spatial variability of primary productivity and matter fluxes in the north-west African upwelling system? A modelling approach. *Biogeosciences*, *13*(23), 6419–6440. https://doi.org/10.5194/bg-13-6419-2016

Aumont, O., & Bopp, L. (2006). Globalizing results from ocean in situ iron fertilization studies. *Global Biogeochemical Cycles*, *20*(2). https://doi.org/10.1029/2005GB002591

Aumont, O., Ethé, C., Tagliabue, A., Bopp, L., & Gehlen, M. (2015). PISCES-v2: An ocean biogeochemical model for carbon and ecosystem studies. *Geoscientific Model Development*, *8*(8), 2465–2513. https://doi.org/10.5194/gmd-8-2465-2015

Aumont, O., Maier-Reimer, E., Blain, S., & Monfray, P. (2003). An ecosystem model of the global ocean including Fe, Si, P colimitations: AN ECOSYSTEM MODEL OF THE WORLD OCEAN. *Global Biogeochemical Cycles*, *17*(2), n/a–n/a. https://doi.org/10.1029/2001GB001745

Awo, F. M., Rouault, M., Ostrowski, M., Tomety, F. S., Da-Allada, C. Y., & Jouanno, J. (2022). Seasonal Cycle of Sea Surface Salinity in the Angola Upwelling System. *Journal of Geophysical Research: Oceans*, *127*(7), e2022JC018518. https://doi.org/10.1029/2022JC018518

Bakun, A. (1990). Global Climate Change and Intensification of Coastal Ocean Upwelling. *Science*, *247*(4939), 198–201. https://doi.org/10.1126/science.247.4939.198

Bakun, A., Field, D. B., Redondo-Rodriguez, A., & Weeks, S. J. (2010). Greenhouse gas, upwelling-favorable winds, and the future of coastal ocean upwelling ecosystems. *Global Change Biology*, *16*(4), 1213–1228. https://doi.org/10.1111/j.1365-2486.2009.02094.x

Bakun, A., & Nelson, C. S. (1991). The seasonal cycle of wind-stress curl in subtropical eastern boundary current regions. *Journal of Physical Oceanography*, *21*(12), 1815–1834. https://doi.org/10.1175/1520-0485(1991)021<1815:TSCOWS>2.0.CO;2

Bange, H. (Ed.). (2008). Fs poseidon fahrtbericht = cruise report p 348 [pos348]: Sopran ; mauritanian upwelling study 2007, las palmas - las palmas, 08.02. - 26.02.2007. https://doi.org/10.3289/ifm-geomar_rep_18_2008

Bange, H. (Ed.). (2011). Fs poseidon fahrtbericht/cruise report p399 - 2&3 : Eastern tropical north atlantic ; p399-2: 31.04.2010-17.06.2010 las palmas - las palmas (canary islands), p399-3: 18.-24.06.2010 las palmas (canary islands) - vigo (spain) ; drive (diurnal and regional variability of halogen emmissions), sopran. https://doi.org/10.3289/ifm-geomar_rep_48_2011

Barboni, A., Coadou-Chaventon, S., Stegner, A., Le Vu, B., & Dumas, F. (2023). How subsurface and double-core anticyclones intensify the winter mixed-layer deepening in the Mediterranean Sea. *Ocean Science*, *19*(2), 229–250. https://doi.org/10.5194/os-19-229-2023

Barceló-Llull, B., Pallàs-Sanz, E., Sangrà, P., Martínez-Marrero, A., Estrada-Allis, S. N., & Arístegui, J. (2017). Ageostrophic Secondary Circulation in a Subtropical Intrathermocline Eddy. *Journal of Physical Oceanography*, *47*(5), 1107–1123. https://doi.org/10.1175/JPO-D-16-0235.1

Barton, E. D. (1987). Meanders, eddies and intrusions in the thermohaline front off Northwest Africa. *Oceanologica acta.Paris*, *10*(3), 267–283.

Barton, E. D. (1989). The Poleward Undercurrent on the Eastern Boundary of the Subtropical North Atlantic. In S. J. Neshyba, C. N. K. Mooers, R. L. Smith, & R. T. Barber (Eds.), *Poleward Flows Along Eastern Ocean Boundaries* (pp. 82–95). Springer. https://doi.org/10.1007/978-1-4613-8963-7_8

Bates, N. R., & Johnson, R. J. (2020). Acceleration of ocean warming, salinification, deoxygenation and acidification in the surface subtropical North Atlantic Ocean. *Communications Earth & Environment*, *1*(1), 1–12. https://doi.org/10.1038/s43247-020-00030-5

Baudena, A., Laxenaire, R., Catalano, C., Claustre, H., Ioannou, A., Leymarie, E., Picheral, M., Poteau, A., Speich, S., Stemmann, L., & Kiko, R. (2023, June). A Lagrangian perspective on the carbon and oxygen budget of an oceanic eddy. https://doi.org/10.21203/rs.3.rs-3014931/v1

Beckmann, A., & Haidvogel, D. B. (1993). Numerical Simulation of Flow around a Tall Isolated Seamount. Part I: Problem Formulation and Model Accuracy.

Beckmann, A., & Hense, I. (2007). Beneath the surface: Characteristics of oceanic ecosystems under weak mixing conditions – A theoretical investigation. *Progress in Oceanography*, *75*(4), 771–796. https://doi.org/10.1016/j.pocean.2007.09.002

Behrenfeld, M. J., O'Malley, R. T., Siegel, D. A., McClain, C. R., Sarmiento, J. L., Feldman, G. C., Milligan, A. J., Falkowski, P. G., Letelier, R. M., & Boss, E. S. (2006). Climate-driven trends in contemporary ocean productivity. *Nature*, *444*(7120), 752–755. https://doi.org/10.1038/nature05317

Benoit-Bird, K. J., & Au, W. W. L. (2001). Target strength measurements of Hawaiian mesopelagic boundary community animals. *The Journal of the Acoustical Society of America*, *110*(2), 812–819. https://doi.org/10.1121/1.1382620

Berglund, S., Döös, K., Campino, A. A., & Nycander, J. (2021). The Water Mass Transformation in the Upper Limb of the Overturning Circulation in the Southern Hemisphere. *Journal*

of Geophysical Research: Oceans, *126*(8), e2021JC017330. https://doi.org/10.1029/2021JC017330

Berglund, S., Döös, K., & Nycander, J. (2017). Lagrangian tracing of the water–mass transformations in the Atlantic Ocean. *Tellus A: Dynamic Meteorology and Oceanography*, *69*(1), 1306311. https://doi.org/10.1080/16000870.2017.1306311

Berloff, P., Kamenkovich, I., & Pedlosky, J. (2009). A Model of Multiple Zonal Jets in the Oceans: Dynamical and Kinematical Analysis. https://doi.org/10.1175/2009JPO4093.1

Bertrand, A., Ballón, M., & Chaigneau, A. (2010). Acoustic Observation of Living Organisms Reveals the Upper Limit of the Oxygen Minimum Zone. *PLOS ONE*, *5*(4), e10330. https://doi.org/10.1371/journal.pone.0010330

Bertrand, A., Chaigneau, A., Peraltilla, S., Ledesma, J., Graco, M., Monetti, F., & Chavez, F. P. (2011). Oxygen: A Fundamental Property Regulating Pelagic Ecosystem Structure in the Coastal Southeastern Tropical Pacific. *PLOS ONE*, *6*(12), e29558. https://doi.org/10.1371/journal.pone.0029558

Bianchi, D., Dunne, J. P., Sarmiento, J. L., & Galbraith, E. D. (2012). Data-based estimates of suboxia, denitrification, and N2O production in the ocean and their sensitivities to dissolved O2. *Global Biogeochemical Cycles*, *26*(2). https://doi.org/10.1029/2011GB004209

Bianchi, D., Galbraith, E. D., Carozza, D. A., Mislan, K. a. S., & Stock, C. A. (2013). Intensification of open-ocean oxygen depletion by vertically migrating animals. *Nature Geoscience*, *6*(7), 545–548. https://doi.org/10.1038/ngeo1837

Bianchi, D., Weber, T. S., Kiko, R., & Deutsch, C. (2018). Global niche of marine anaerobic metabolisms expanded by particle microenvironments. *Nature Geoscience*, *11*(4), 263–268. https://doi.org/10.1038/s41561-018-0081-0

Bianucci, L., & Denman, K. L. (2012). Carbon and oxygen cycles: Sensitivity to changes in environmental forcing in a coastal upwelling system. *Journal of Geophysical Research: Biogeosciences*, *117*(G1). https://doi.org/10.1029/2011JG001849

Bickert, T., Braun, S., Fricke, S., Hermann, B., Just, J., Keil, H., Klann, M., Krastel, S., Kurschat, S., Mai, A., Meyer, I., Meyer, M., Mollenhauer, G., Nowald, N., Ruhland, G., Schilling, S., Schwab, A., Schwenk, T., Stuut, J.-B., & Vega, D. (2011). Pre-site survey for an iodp cruise neogene paleoclimate and sediment transport at the continental margin of nw africa - cruise no. msm11/2 - march 14 - april 09, 2009 - dakar $Senegal$ - las palmas $CanaryIslands$, $Spain$, maria s. merian-berichte. https://doi.org/10.2312/cr_msm11_2

Blaas, M., Dong, C., Marchesiello, P., McWilliams, J. C., & Stolzenbach, K. D. (2007). Sediment-transport modeling on Southern Californian shelves: A ROMS case study. *Continental Shelf Research*, *27*(6), 832–853. https://doi.org/10.1016/j.csr.2006.12.003

Blanke, B., & Raynaud, S. (1997). Kinematics of the Pacific Equatorial Undercurrent: An Eulerian and Lagrangian Approach from GCM Results.

Boccaletti, G., Ferrari, R., & Fox-Kemper, B. (2007). Mixed Layer Instabilities and Restratification. https://doi.org/10.1175/JPO3101.1

Bograd, S. J., Buil, M. P., Lorenzo, E. D., Castro, C. G., Schroeder, I. D., Goericke, R., Anderson, C. R., Benitez-Nelson, C., & Whitney, F. A. (2015). Changes in source waters to the Southern California Bight. *Deep Sea Research Part II: Topical Studies in Oceanography*, *112*, 42–52. https://doi.org/10.1016/j.dsr2.2014.04.009

Bograd, S. J., Castro, C. G., Di Lorenzo, E., Palacios, D. M., Bailey, H., Gilly, W., & Chavez, F. P. (2008). Oxygen declines and the shoaling of the hypoxic boundary in the California Current. *Geophysical Research Letters*, *35*(12), 2008GL034185. https://doi.org/10.1029/2008GL034185

Bogucki, D., Dickey, T., & Redekopp, L. G. (1997). Sediment Resuspension and Mixing by Resonantly Generated Internal Solitary Waves.

Bonino, G., Di Lorenzo, E., Masina, S., & Iovino, D. (2019). Interannual to decadal variability within and across the major Eastern Boundary Upwelling Systems. *Scientific Reports*, *9*(1), 19949. https://doi.org/10.1038/s41598-019-56514-8

Bopp, L., Le Quéré, C., Heimann, M., Manning, A. C., & Monfray, P. (2002). Climate-induced oceanic oxygen fluxes: Implications for the contemporary carbon budget. *Global Biogeochemical Cycles*, *16*(2), 6-1-6–13. https://doi.org/10.1029/2001GB001445

Bosse, A., Testor, P., Houpert, L., Damien, P., Prieur, L., Hayes, D., Taillandier, V., Durrieu de Madron, X., d'Ortenzio, F., Coppola, L., Karstensen, J., & Mortier, L. (2016). Scales and dynamics of Submesoscale Coherent Vortices formed by deep convection in the northwestern Mediterranean Sea. *Journal of Geophysical Research: Oceans*, *121*(10), 7716–7742. https://doi.org/10.1002/2016JC012144

Boyce, D. G., Lewis, M. R., & Worm, B. (2010). Global phytoplankton decline over the past century. *Nature*, *466*(7306), 591–596. https://doi.org/10.1038/nature09268

Boyer, T. P., & Levitus, S. (2006). *World ocean database 2005* (NOAA Atlas NESDIS 60). National Oceanographic Data Center, Ocean Climate Laboratory, National Environmental Satellite, Data, and Information Service. https://repository.library.noaa.gov/view/noaa/1131

Boyle, M., FitzSimmons, N., Limpus, C., Kelez, S., Velez-Zuazo, X., & Waycott, M. (2009). Evidence for transoceanic migrations by loggerhead sea turtles in the southern Pacific Ocean. *Proceedings of the Royal Society B: Biological Sciences*, *276*(1664), 1993–1999. https://doi.org/10.1098/rspb.2008.1931

Brandt, P., Bange, H. W., Banyte, D., Dengler, M., Didwischus, S. H., Fischer, T., Greatbatch, R. J., Hahn, J., Kanzow, T., Karstensen, J., Körtzinger, A., Krahmann, G., Schmidtko, S., Stramma, L., Tanhua, T., & Visbeck, M. (2015). On the role of circulation and mixing in the ventilation of oxygen minimum zones with a focus on the eastern tropical North Atlantic. *Biogeosciences*, *12*(2), 489–512. https://doi.org/10.5194/bg-12-489-2015

Brandt, P., Greatbatch, R. J., Claus, M., Didwischus, S. H., Hormann, V., Funk, A., Hahn, J., Krahmann, G., Fischer, J., & Krtzinger, A. (2012). Ventilation of the equatorial Atlantic by the equatorial deep jets. *Journal of Geophysical Research: Oceans*, *117*(12), 1–15. https://doi.org/10.1029/2012JC008118

Brandt, P., Hormann, V., Körtzinger, A., Visbeck, M., Krahmann, G., Stramma, L., Lumpkin, R., & Schmid, C. (2010). Changes in the Ventilation of the Oxygen Minimum Zone of the Tropical North Atlantic. *Journal of Physical Oceanography*, *40*(8), 1784–1801. https://doi.org/10.1175/2010JPO4301.1

Brandt, P., & Krahmann, G. (2020). Physical oceanography from glider mission IFM02_depl21. https://doi.org/10.1594/PANGAEA.920589

Brannigan, L. (2016). Intense submesoscale upwelling in anticyclonic eddies. *Geophysical Research Letters*, *43*(7), 3360–3369. https://doi.org/10.1002/2016GL067926

Breitburg, D., Levin, L. A., Oschlies, A., Grégoire, M., Chavez, F. P., Conley, D. J., Garçon, V., Gilbert, D., Gutiérrez, D., Isensee, K., Jacinto, G. S., Limburg, K. E., Montes, I., Naqvi, S. W. A., Pitcher, G. C., Rabalais, N. N., Roman, M. R., Rose, K. A., Seibel, B. A., … Zhang, J. (2018). Declining oxygen in the global ocean and coastal waters. *Science*, *359*(6371), eaam7240. https://doi.org/10.1126/science.aam7240

Brink, K. H., & Cowles, T. J. (1991). The Coastal Transition Zone program. *Journal of Geophysical Research: Oceans*, *96*(C8), 14637–14647. https://doi.org/10.1029/91JC01206

Brochier, T., Lett, C., & Fréon, P. (2011). Investigating the 'northern Humboldt paradox' from model comparisons of small pelagic fish reproductive strategies in eastern boundary upwelling ecosystems. *Fish and Fisheries*, *12*(1), 94–109. https://doi.org/10.1111/j.1467-2979.2010.00385.x

Brock, J., & Schulz-Vogt, H. N. (2011). Sulfide induces phosphate release from polyphosphate in cultures of a marine Beggiatoa strain. *The ISME Journal*, *5*(3), 497–506. https://doi.org/10.1038/ismej.2010.135

Buckley, M. W., & Marshall, J. (2016). Observations, inferences, and mechanisms of the Atlantic Meridional Overturning Circulation: A review. *Reviews of Geophysics*, *54*(1), 5–63. https://doi.org/10.1002/2015RG000493

Burgoa, N., Machín, F., Rodríguez-Santana, Á., Marrero-Diáz, Á., Álvarez-Salgado, X. A., Fernández-Castro, B., Gelado-Caballero, M. D., & Arístegui, J. (2021). Cape Verde Frontal Zone in summer 2017: Lateral transports of mass, dissolved oxygen and inorganic nutrients. *Ocean Science*, *17*(3), 769–788. https://doi.org/10.5194/os-17-769-2021

Burmeister, K., Lübbecke, J. F., Brandt, P., & Duteil, O. (2019). Interannual Variability of the Atlantic North Equatorial Undercurrent and Its Impact on Oxygen. *Journal of Geophysical Research: Oceans*, *124*(4), 2348–2373. https://doi.org/10.1029/2018JC014760

Butcher, J. C. (2008, March). *Numerical Methods for Ordinary Differential Equations* (1st ed.). Wiley. https://doi.org/10.1002/9780470753767

Calil, P. H., & Richards, K. J. (2010). Transient upwelling hot spots in the oligotrophic North Pacific. *Journal of Geophysical Research: Oceans*, *115*(2), 1–20. https://doi.org/10.1029/2009JC005360

Calil, P. H. (2023). High-Resolution, Basin-Scale Simulations Reveal the Impact of Intermediate Zonal Jets on the Atlantic Oxygen Minimum Zones. *Journal of Advances in Modeling Earth Systems*, *15*(2), e2022MS003158. https://doi.org/10.1029/2022MS003158

Calil, P. H., Suzuki, N., Baschek, B., & da Silveira, I. C. (2021). Filaments, fronts and eddies in the cabo frio coastal upwelling system, Brazil. *Fluids*, *6*(2), 1–31. https://doi.org/10.3390/fluids6020054

Canfield, D. E. (2005). THE EARLY HISTORY OF ATMOSPHERIC OXYGEN: Homage to Robert M. Garrels. *Annual Review of Earth and Planetary Sciences*, *33*(Volume 33, 2005), 1–36. https://doi.org/10.1146/annurev.earth.33.092203.122711

Capet, X., Colas, F., Mcwilliams, J. C., Penven, P., & Marchesiello, P. (2008). Eddies in Eastern Boundary Subtropical Upwelling Systems. In *Ocean Modeling in an Eddying Regime* (pp. 131–147). American Geophysical Union (AGU). https://doi.org/10.1029/177GM10

Capet, X., Marchesiello, P., & McWilliams, J. C. (2004). Upwelling response to coastal wind profiles. *Geophysical Research Letters*, *31*(13). https://doi.org/10.1029/2004GL020123

Capet, X., McWilliams, J. C., Molemaker, M. J., & Shchepetkin, A. F. (2008). Mesoscale to Submesoscale Transition in the California Current System. Part I: Flow Structure, Eddy Flux, and Observational Tests. https://doi.org/10.1175/2007JPO3671.1

Capet, X., Estrade, P., Machu, E., Ndoye, S., Grelet, J., Lazar, A., Marié, L., Dausse, D., & Brehmer, P. (2017). On the dynamics of the southern senegal upwelling center: Observed variability from Synoptic to superinertial scales. *Journal of Physical Oceanography*, *47*(1), 155–180. https://doi.org/10.1175/JPO-D-15-0247.1

Cardoso, C., Caldeira, R. M., Relvas, P., & Stegner, A. (2020). Islands as eddy transformation and generation hotspots: Cabo Verde case study. *Progress in Oceanography*, *184*, 102271. https://doi.org/10.1016/j.pocean.2020.102271

Carey, F. G., & Robison, B. H. (1981). Daily patterns in the activities of swordfish, Xiphias gladius, observed by acoustic telemetry. *Fishery Bulletin*, *79*, 277–292.

Carr, M.-E. (2001). Estimation of potential productivity in Eastern Boundary Currents using remote sensing. *Deep Sea Research Part II: Topical Studies in Oceanography*, *49*(1), 59–80. https://doi.org/10.1016/S0967-0645(01)00094-7

Carr, M.-E., & Kearns, E. J. (2003). Production regimes in four Eastern Boundary Current systems. *Deep Sea Research Part II: Topical Studies in Oceanography*, *50*(22-26), 3199–3221. https://doi.org/10.1016/j.dsr2.2003.07.015

Carret, A., Birol, F., Estournel, C., & Zakardjian, B. (2023). Assessing the capability of three different altimetry satellite missions to observe the Northern Current by using a high-resolution model. *Ocean Science*, *19*(3), 903–921. https://doi.org/10.5194/os-19-903-2023

Carstensen, J., Andersen, J. H., Gustafsson, B. G., & Conley, D. J. (2014). Deoxygenation of the Baltic Sea during the last century. *Proceedings of the National Academy of Sciences*, *111*(15), 5628–5633. https://doi.org/10.1073/pnas.1323156111

Carter, G. S., Gregg, M. C., & Lien, R.-C. (2005). Internal waves, solitary-like waves, and mixing on the Monterey Bay shelf. *Continental Shelf Research*, *25*(12), 1499–1520. https://doi.org/10.1016/j.csr.2005.04.011

Carton, J. A., Chepurin, G. A., & Chen, L. (2018). SODA3: A New Ocean Climate Reanalysis. *Journal of Climate*, *31*(17), 6967–6983. https://doi.org/10.1175/JCLI-D-18-0149.1

Cavan, E. L., Trimmer, M., Shelley, F., & Sanders, R. (2017). Remineralization of particulate organic carbon in an ocean oxygen minimum zone. *Nature Communications*, *8*(1), 14847. https://doi.org/10.1038/ncomms14847

Caverivière, A., & Touré, D. (1990). Note sur les mortalités de mérou (serranidae) observées en fin de saison chaude devant les côtes du sénégal, particulièrement en 1987. *Dakar Thiaroye: CRODT*, *116*, 43–63.

Cenedese, C., Adduce, C., & M. Fratantoni, D. (2005). Laboratory experiments on mesoscale vortices interacting with two islands. *Journal of Geophysical Research*, *110*(C9), C09023. https://doi.org/10.1029/2004JC002734

Cetina-Heredia, P., Roughan, M., van Sebille, E., Keating, S., & Brassington, G. B. (2019). Retention and Leakage of Water by Mesoscale Eddies in the East Australian Current System. *Journal of Geophysical Research: Oceans*, *124*(4), 2485–2500. https://doi.org/10.1029/2018JC014482

Chaigneau, A., Eldin, G., & Dewitte, B. (2009). Eddy activity in the four major upwelling systems from satellite altimetry (1992–2007). *Progress in Oceanography*, *83*(1-4), 117–123. https://doi.org/10.1016/j.pocean.2009.07.012

Chaigneau, A., Gizolme, A., & Grados, C. (2008). Mesoscale eddies off Peru in altimeter records: Identification algorithms and eddy spatio-temporal patterns. *Progress in Oceanography*, *79*(2-4), 106–119. https://doi.org/10.1016/j.pocean.2008.10.013

Chaigneau, A., Le Texier, M., Eldin, G., Grados, C., & Pizarro, O. (2011). Vertical structure of mesoscale eddies in the eastern South Pacific Ocean: A composite analysis from altimetry and Argo profiling floats. *Journal of Geophysical Research: Oceans*, *116*(11), 1–16. https://doi.org/10.1029/2011JC007134

Chan, F., Barth, J. A., Lubchenco, J., Kirincich, A., Weeks, H., Peterson, W. T., & Menge, B. A. (2008). Emergence of Anoxia in the California Current Large Marine Ecosystem. *Science*, *319*(5865), 920–920. https://doi.org/10.1126/science.1149016

Chang, Y.-L., Miyazawa, Y., Oey, L.-Y., Kodaira, T., & Huang, S. (2017). The formation processes of phytoplankton growth and decline in mesoscale eddies in the western North Pacific Ocean. *Journal of Geophysical Research: Oceans*, *122*(5), 4444–4455. https://doi.org/10.1002/2017JC012722

Chassignet, E. P., & Xu, X. (2017). Impact of Horizontal Resolution (1/12° to 1/50°) on Gulf Stream Separation, Penetration, and Variability. *Journal of Physical Oceanography*, *47*(8), 1999–2021. https://doi.org/10.1175/JPO-D-17-0031.1

Chavanne, C., Flament, P., Lumpkin, R., Dousset, B., & Bentamy, A. (2002). Scatterometer observations of wind variations induced by oceanic islands: Implications for wind-driven ocean circulation. *Canadian Journal of Remote Sensing*, *28*(3), 466–474. https://doi.org/10.5589/m02-047

Chavez, F. P., Bertrand, A., Guevara-Carrasco, R., Soler, P., & Csirke, J. (2008). The northern Humboldt Current System: Brief history, present status and a view towards the future. *Progress in Oceanography*, *79*(2), 95–105. https://doi.org/10.1016/j.pocean.2008.10.012

Chavez, F. P., & Messié, M. (2009). A comparison of Eastern Boundary Upwelling Ecosystems. *Progress in Oceanography*, *83*(1), 80–96. https://doi.org/10.1016/j.pocean.2009.07.032

Chavez, F. P., Messié, M., & Pennington, J. T. (2011). Marine Primary Production in Relation to Climate Variability and Change. *Annual Review of Marine Science*, *3*(Volume 3, 2011), 227–260. https://doi.org/10.1146/annurev.marine.010908.163917

Chelton, D. B., Schlax, M. G., & Samelson, R. M. (2011). Global observations of nonlinear mesoscale eddies. *Progress in Oceanography*, *91*(2), 167–216. https://doi.org/10.1016/j.pocean.2011.01.002

Chelton, D. B., Schlax, M. G., Samelson, R. M., & de Szoeke, R. A. (2007). Global observations of large oceanic eddies. *Geophysical Research Letters*, *34*(15), 1–5. https://doi.org/10.1029/2007GL030812

Chen, X., Chen, G., Ge, L., Huang, B., & Cao, C. (2021). Global Oceanic Eddy Identification: A Deep Learning Method From Argo Profiles and Altimetry Data. *Frontiers in Marine Science*, *8*. https://doi.org/10.3389/fmars.2021.646926

Chenillat, F., Blanke, B., Grima, N., Franks, P. J. S., Capet, X., & Rivière, P. (2015). Quantifying tracer dynamics in moving fluids: A combined Eulerian-Lagrangian approach. *Frontiers in Environmental Science*, *3*.

Chenillat, F., Franks, P. J. S., Capet, X., Rivière, P., Grima, N., Blanke, B., & Combes, V. (2018). Eddy properties in the Southern California Current System. *Ocean Dynamics*, *68*(7), 761–777. https://doi.org/10.1007/s10236-018-1158-4

Chenillat, F., Franks, P. J. S., Rivière, P., Capet, X., Grima, N., & Blanke, B. (2015). Plankton dynamics in a cyclonic eddy in the Southern California Current System. *Journal of Geophysical Research: Oceans*, *120*(8), 5566–5588. https://doi.org/10.1002/2015JC010826

Chereskin, T. K. (1995). Direct evidence for an Ekman balance in the California Current. *Journal of Geophysical Research: Oceans*, *100*(C9), 18261–18269. https://doi.org/10.1029/95JC02182

Chiapello, I., Moulin, C., & Prospero, J. M. (2005). Understanding the long-term variability of African dust transport across the Atlantic as recorded in both Barbados surface concentrations and large-scale Total Ozone Mapping Spectrometer (TOMS) optical thickness. *Journal of Geophysical Research: Atmospheres*, *110*(D18). https://doi.org/10.1029/2004JD005132

Childress, J. J. (1995). Are there physiological and biochemical adaptations of metabolism in deep-sea animals? *Trends in Ecology & Evolution*, *10*(1), 30–36. https://doi.org/10.1016/S0169-5347(00)88957-0

Christiansen, S., Hoving, H.-J., Schütte, F., Hauss, H., Karstensen, J., Körtzinger, A., Schröder, S.-M., Stemmann, L., Christiansen, B., Picheral, M., Brandt, P., Robison, B., Koch, R., & Kiko, R. (2018). Particulate matter flux interception in oceanic mesoscale eddies by

the polychaete Poeobius sp. *Limnology and Oceanography*, *63*(5), 2093–2109. https://doi.org/10.1002/lno.10926

Claret, M., Galbraith, E. D., Palter, J. B., Bianchi, D., Fennel, K., Gilbert, D., & Dunne, J. P. (2018). Rapid coastal deoxygenation due to ocean circulation shift in the northwest Atlantic. *Nature Climate Change*, *8*(10), 868–872. https://doi.org/10.1038/s41558-018-0263-1

Clarke, T. M., Wabnitz, C. C. C., Frölicher, T. L., Reygondeau, G., Pauly, D., & Cheung, W. W. L. (2022). Linking observed changes in pelagic catches to temperature and oxygen in the Eastern Tropical Pacific. *Fish and Fisheries*, *23*(6), 1371–1382. https://doi.org/10.1111/faf.12694

CMEMS. (2016). *Global ocean colour (copernicus-globcolour), bio-geo-chemical, l4 (monthly and interpolated) from satellite observations (1997-ongoing)* [Accessed on 29 Nov 2024]. https://doi.org/10.48670/moi-00281

CMEMS. (2017). *Global ocean gridded l4 sea surface heights and derived variables reprocessed (1993 - ongoing)* [Accessed on 29 Nov 2024]. https://doi.org/10.48670/moi-00148

Cockcroft, A. C. (2001). Jasus lalandii 'walkouts' or mass strandings in South Africa during the 1990s: An overview. *Marine and Freshwater Research*, *52*(8), 1085. https://doi.org/10.1071/MF01100

Codispoti, L. A., & Christensen, J. P. (1985). Nitrification, denitrification and nitrous oxide cycling in the eastern tropical South Pacific ocean. *Marine Chemistry*, *16*(4), 277–300. https://doi.org/10.1016/0304-4203(85)90051-9

Coelho, R., Fernandez-Carvalho, J., & Santos, M. N. (2015). Habitat use and diel vertical migration of bigeye thresher shark: Overlap with pelagic longline fishing gear. *Marine Environmental Research*, *112*, 91–99. https://doi.org/10.1016/j.marenvres.2015.10.009

Colas, F., McWilliams, J. C., Capet, X., & Kurian, J. (2012). Heat balance and eddies in the Peru-Chile current system. *Climate Dynamics*, *39*(1), 509–529. https://doi.org/10.1007/s00382-011-1170-6

Collins, C. A., Margolina, T., Rago, T. A., & Ivanov, L. (2013). Looping RAFOS floats in the California Current System. *Deep Sea Research Part II: Topical Studies in Oceanography*, *85*, 42–61. https://doi.org/10.1016/j.dsr2.2012.07.027

Colosi, J. A., Beardsley, R. C., Lynch, J. F., Gawarkiewicz, G., Chiu, C.-S., & Scotti, A. (2001). Observations of nonlinear internal waves on the outer New England continental shelf during the summer Shelfbreak Primer study. *Journal of Geophysical Research: Oceans*, *106*(C5), 9587–9601. https://doi.org/10.1029/2000JC900124

Combes, V., Hormazabal, S., & Di Lorenzo, E. (2015). Interannual variability of the subsurface eddy field in the Southeast Pacific. *Journal of Geophysical Research: Oceans*, *120*(7), 4907–4924. https://doi.org/10.1002/2014JC010265

Combes, V., Matano, R. P., & Palma, E. D. (2021). Circulation and Cross-Shelf Exchanges in the Northern Shelf Region of the Southwestern Atlantic: Kinematics. *Journal of Geophysical Research: Oceans*, *126*(4), e2020JC016959. https://doi.org/10.1029/2020JC016959

Condie, S., & Condie, R. (2016). Retention of plankton within ocean eddies. *Global Ecology and Biogeography*, *25*(10), 1264–1277. https://doi.org/10.1111/geb.12485

Connolly, T. P., & Hickey, B. M. (2014). Regional impact of submarine canyons during seasonal upwelling. *Journal of Geophysical Research: Oceans*, *119*(2), 953–975. https://doi.org/10.1002/2013JC009452

Contreras, M., Pizarro, O., Dewitte, B., Sepulveda, H. H., & Renault, L. (2019). Subsurface Mesoscale Eddy Generation in the Ocean off Central Chile. *Journal of Geophysical Research: Oceans*, *124*(8), 5700–5722. https://doi.org/10.1029/2018JC014723

Cornec, M., Claustre, H., Mignot, A., Guidi, L., Lacour, L., Poteau, A., D'Ortenzio, F., Gentili, B., & Schmechtig, C. (2021). Deep Chlorophyll Maxima in the Global Ocean: Occurrences, Drivers and Characteristics. *Global Biogeochemical Cycles*, *35*(4), e2020GB006759. https://doi.org/10.1029/2020GB006759

Cornec, M., Laxenaire, R., Speich, S., & Claustre, H. (2021). Impact of Mesoscale Eddies on Deep Chlorophyll Maxima. *Geophysical Research Letters*, *48*(15). https://doi.org/10.1029/2021GL093470

Couvelard, X., Caldeira, R. M. A., Araújo, I. B., & Tomé, R. (2012). Wind mediated vorticity-generation and eddy-confinement, leeward of the Madeira Island: 2008 numerical case study. *Dynamics of Atmospheres and Oceans*, *58*, 128–149. https://doi.org/10.1016/j.dynatmoce.2012.09.005

Cox, T. M., Ragen, T. J., Read, A. J., Vos, E., Baird, R. W., Balcomb, K., Barlow, J., Caldwell, J., Cranford, T., Crum, L., D'Amico, A., D'Spain, G., Fernandez, A., Finneran, J., Gentry, R., Gerth, W., Gulland, F., Hildebrand, J., Houser, D., … Benner, L. (2023). Understanding the impacts of anthropogenic sound on beaked whales. *J. Cetacean Res. Manage.*, *7*(3), 177–187. https://doi.org/10.47536/jcrm.v7i3.729

Cropper, T. E., Hanna, E., & Bigg, G. R. (2014). Spatial and temporal seasonal trends in coastal upwelling off Northwest Africa, 1981–2012. *Deep Sea Research Part I: Oceanographic Research Papers*, *86*, 94–111. https://doi.org/10.1016/j.dsr.2014.01.007

Cushman-Roisin, B., Tang, B., & Chassignet, E. P. (1990). Westward Motion of Mesoscale Eddies. *Journal of Physical Oceanography*, *20*(5), 758–768. https://doi.org/10.1175/1520-0485(1990)020<0758:WMOME>2.0.CO;2

Dai, Y., Yang, S., Zhao, D., Hu, C., Xu, W., Anderson, D. M., Li, Y., Song, X.-P., Boyce, D. G., Gibson, L., Zheng, C., & Feng, L. (2023). Coastal phytoplankton blooms expand and intensify in the 21st century. *Nature*, *615*(7951), 280–284. https://doi.org/10.1038/s41586-023-05760-y

Dale, A. W., Clemens, D., Dähnke, K., Korth, F., Wankel, S. D., Schroller-Lomnitz, U., Wallmann, K., & Sommer, S. (2022). Nitrogen cycling in sediments on the NW African margin inferred from N and O isotopes in benthic chambers. *Frontiers in Marine Science*, *9*.

Dale, A. W., Sommer, S., Ryabenko, E., Noffke, A., Bohlen, L., Wallmann, K., Stolpovsky, K., Greinert, J., & Pfannkuche, O. (2014a). Benthic nitrogen fluxes and fractionation of nitrate

in the Mauritanian oxygen minimum zone (Eastern Tropical North Atlantic). *Geochimica et Cosmochimica Acta*, *134*, 234–256. https://doi.org/10.1016/j.gca.2014.02.026

Dale, A. W., Sommer, S., Ryabenko, E., Noffke, A., Bohlen, L., Wallmann, K., Stolpovsky, K., Greinert, J., & Pfannkuche, O. (2014b). Porewater and particulate geochemistry during Maria S. Merian cruise MSM17/4 [Supplement to: Dale, AW et al. (2014): Benthic nitrogen fluxes and fractionation of nitrate in the Mauritanian oxygen minimum zone (Eastern Tropical North Atlantic). Geochimica et Cosmochimica Acta, 134, 234-256, https://doi.org/10.1016/j.gca.2014.02.026]. https://doi.org/10.1594/PANGAEA.835700

D'Asaro, E. A. (1988). Generation of submesoscale vortices: A new mechanism. *Journal of Geophysical Research: Oceans*, *93*(C6), 6685–6693. https://doi.org/10.1029/JC093iC06p06685

de Boyer Montégut, C., Madec, G., Fischer, A. S., Lazar, A., & Iudicone, D. (2004). Mixed layer depth over the global ocean: An examination of profile data and a profile-based climatology. *Journal of Geophysical Research: Oceans*, *109*(C12). https://doi.org/10.1029/2004JC002378

de Marez, C., Carton, X., L'Hégaret, P., Meunier, T., Stegner, A., Le Vu, B., & Morvan, M. (2020). Oceanic vortex mergers are not isolated but influenced by the β-effect and surrounding eddies. *Scientific Reports*, *10*(1), 1–10. https://doi.org/10.1038/s41598-020-59800-y

Debreu, L., Marchesiello, P., Penven, P., & Cambon, G. (2012). Two-way nesting in split-explicit ocean models: Algorithms, implementation and validation. *Ocean Modelling*, *49–50*, 1–21. https://doi.org/10.1016/j.ocemod.2012.03.003

Demarcq, H., & Somoue, L. (2015). Phytoplankton and primary productivity off Northwest Africa. In L. Valdés & Déniz-González (Eds.), *Oceanographic and biological features in the Canary Current Large Marine Ecosystem* (pp. 161–171, Vol. 115). IOC-UNESCO.

Denes, M. C., Froyland, G., & Keating, S. R. (2022). Persistence and material coherence of a mesoscale ocean eddy. *Physical Review Fluids*, *7*(3), 034501. https://doi.org/10.1103/PhysRevFluids.7.034501

Dengler, M., Schafstall, J., Tanhua, T., Fiedler, B., Krahmann, G., & Löptin, U. (Eds.). (2008). Fs poseidon fahrtbericht / cruise report p347 [pos347]: Mauritanian upwelling and mixing process study. https://doi.org/10.3289/ifm-geomar_rep_16_2008

Desmet, F., Gruber, N., Köhn, E. E., Münnich, M., & Vogt, M. (2022). Tracking the Space-Time Evolution of Ocean Acidification Extremes in the California Current System and Northeast Pacific. *Journal of Geophysical Research: Oceans*, *127*(5), e2021JC018159. https://doi.org/10.1029/2021JC018159

Devresse, Q., Becker, K. W., Bendinger, A., Hahn, J., & Engel, A. (2022). Eddy-enhanced primary production sustains heterotrophic microbial activities in the Eastern Tropical North Atlantic. *Biogeosciences*, *19*(22), 5199–5219. https://doi.org/10.5194/bg-19-5199-2022

Devresse, Q., Becker, K. W., & Engel, A. (2024). Distribution of polysaccharidic and proteinaceous gel-like particles in three cyclonic eddies in the Eastern Tropical North Atlantic. *Frontiers in Marine Science*, *11*, 1357646. https://doi.org/10.3389/fmars.2024.1357646

Dewar, W. K., & Flierl, G. R. (1987). Some Effects of the Wind on Rings.

Diaz, R. J., & Rosenberg, R. (2008). Spreading Dead Zones and Consequences for Marine Ecosystems. *Science*, *321*(5891), 926–929. https://doi.org/10.1126/science.1156401

Dilmahamod, A. F., Aguiar-González, B., Penven, P., Reason, C. J., De Ruijter, W. P., Malan, N., & Hermes, J. C. (2018). SIDDIES Corridor: A Major East-West Pathway of Long-Lived Surface and Subsurface Eddies Crossing the Subtropical South Indian Ocean. *Journal of Geophysical Research: Oceans*, *123*(8), 5406–5425. https://doi.org/10.1029/2018JC013828

Dilmahamod, A. F., Hermes, J. C., & Reason, C. J. C. (2016). Chlorophyll-*a* variability in the Seychelles–Chagos Thermocline Ridge: Analysis of a coupled biophysical model. *Journal of Marine Systems*, *154*, 220–232. https://doi.org/10.1016/j.jmarsys.2015.10.011

Dilmahamod, A. F., Penven, P., Aguiar-González, B., Reason, C. J. C., & Hermes, J. C. (2020). A Model Investigation of the Influences of the South-East Madagascar Current on the South-East Madagascar Bloom. *Journal of Geophysical Research: Oceans*, *125*(6), e2019JC015761. https://doi.org/10.1029/2019JC015761

Dilmahamod, A. F. (2023). Apparent oxygen utilization and relative percentage of South Atlantic Central Water (SACW) during METEOR cruise M156. https://doi.org/10.1594/PANGAEA.959741

Dilmahamod, A. F., Karstensen, J., Dietze, H., Löptien, U., & Fennel, K. (2022). Generation Mechanisms of Mesoscale Eddies in the Mauritanian Upwelling Region. *Journal of Physical Oceanography*, *52*(1), 161–182. https://doi.org/10.1175/JPO-D-21-0092.1

Dommenget, D., & Latif, M. (2000). Interannual to Decadal Variability in the Tropical Atlantic.

Doney, S. C., Ruckelshaus, M., Duffy, J. E., Barry, J. P., Chan, F., English, C. A., Galindo, H. M., Grebmeier, J. M., Hollowed, A. B., Knowlton, N., Polovina, J., Rabalais, N. N., Sydeman, W. J., & Talley, L. D. (2012). Climate Change Impacts on Marine Ecosystems. *Annual Review of Marine Science*, *4*(Volume 4, 2012), 11–37. https://doi.org/10.1146/annurev-marine-041911-111611

Döös, K. (1995). Interocean exchange of water masses. *Journal of Geophysical Research: Oceans*, *100*(C7), 13499–13514. https://doi.org/10.1029/95JC00337

Döös, K., Kjellsson, J., & Jönsson, B. (2013). TRACMASS—A Lagrangian Trajectory Model. In T. Soomere & E. Quak (Eds.), *Preventive Methods for Coastal Protection* (pp. 225–249). Springer International Publishing. https://doi.org/10.1007/978-3-319-00440-2_7

d'Ovidio, F., De Monte, S., Penna, A. D., Cotté, C., & Guinet, C. (2013). Ecological implications of eddy retention in the open ocean: A Lagrangian approach. *Journal of Physics A: Mathematical and Theoretical*, *46*(25), 254023. https://doi.org/10.1088/1751-8113/46/25/254023

Drazen, J. C., & Seibel, B. A. (2007). Depth-related trends in metabolism of benthic and benthopelagic deep-sea fishes. *Limnology and Oceanography*, *52*(5), 2306–2316. https://doi.org/10.4319/lo.2007.52.5.2306

Du, T., & Jing, Z. (2024). Fine-Scale Eddies Detected by SWOT in the Kuroshio Extension. *Remote Sensing*, *16*(18), 3488. https://doi.org/10.3390/rs16183488

Du, T., Wang, S., Jing, Z., Wu, L., Zhang, C., & Zhang, B. (2024). Future changes in coastal upwelling and biological production in eastern boundary upwelling systems. *Nature Communications*, *15*(1), 6238. https://doi.org/10.1038/s41467-024-50570-z

Dufois, F., Hardman-Mountford, N. J., Greenwood, J., Richardson, A. J., Feng, M., & Matear, R. J. (2016). Anticyclonic eddies are more productive than cyclonic eddies in subtropical gyres because of winter mixing. *Science Advances*, *2*(5), e1600282–e1600282. https://doi.org/10.1126/sciadv.1600282

Dugan, J. P., Mied, R., Mignerey, P., & Schuetz, A. (1982). Compact, intrathermocline eddies in the Sargasso Sea. *J. Geophysical Res.*, *87*(C1), 385–393. https://doi.org/10.1029/JC087iC01p00385

Dunne, J. P., Sarmiento, J. L., & Gnanadesikan, A. (2007). A synthesis of global particle export from the surface ocean and cycling through the ocean interior and on the seafloor. *Global Biogeochemical Cycles*, *21*(4). https://doi.org/10.1029/2006GB002907

Duteil, O. (2019). Wind Synoptic Activity Increases Oxygen Levels in the Tropical Pacific Ocean. *Geophysical Research Letters*, *46*(5), 2715–2725. https://doi.org/10.1029/2018GL081041

Duteil, O., Schwarzkopf, F. U., Böning, C. W., & Oschlies, A. (2014). Major role of the equatorial current system in setting oxygen levels in the eastern tropical Atlantic Ocean: A high-resolution model study. *Geophysical Research Letters*, *41*(6), 2033–2040. https://doi.org/10.1002/2013GL058888

Early, J. J., Samelson, R. M., & Chelton, D. B. (2011). The Evolution and Propagation of Quasigeostrophic Ocean Eddies*. *Journal of Physical Oceanography*, *41*(8), 1535–1555. https://doi.org/10.1175/2011JPO4601.1

Echevin, V., Aumont, O., Ledesma, J., & Flores, G. (2008). The seasonal cycle of surface chlorophyll in the Peruvian upwelling system: A modelling study. *Progress in Oceanography*, *79*(2), 167–176. https://doi.org/10.1016/j.pocean.2008.10.026

Echevin, V., Hauschildt, J., Colas, F., Thomsen, S., & Aumont, O. (2021). Impact of Chlorophyll Shading on the Peruvian Upwelling System. *Geophysical Research Letters*, *48*(19), 1–10. https://doi.org/10.1029/2021GL094429

Echevin, V., Albert, A., Lévy, M., Graco, M., Aumont, O., Piétri, A., & Garric, G. (2014). Intraseasonal variability of nearshore productivity in the Northern Humboldt Current System: The role of coastal trapped waves. *Continental Shelf Research*, *73*, 14–30. https://doi.org/10.1016/j.csr.2013.11.015

Eden, C., & Dietze, H. (2009). Effects of mesoscale eddy/wind interactions on biological new production and eddy kinetic energy. *Journal of Geophysical Research: Oceans*, *114*(5), 1–13. https://doi.org/10.1029/2008JC005129

Ekau, W., Auel, H., Pörtner, H.-O., & Gilbert, D. (2010). Impacts of hypoxia on the structure and processes in pelagic communities (zooplankton, macro-invertebrates and fish). *Biogeosciences*, *7*(5), 1669–1699. https://doi.org/10.5194/bg-7-1669-2010

Ekau, W., Bachmann, J., Bahlmann, E., Balde, B., Börner, G., Bröhl, S., Heimbach, T., Hornidge, A.-K., Howes, C., Klenz, T., Martens, W., Mawick, J., Müller, C., Müller, P., Ndiaye, M., Otto, K., Reymond, C. E., Rixen, T., Sinner, A., … Wischnewski, F. (2016). *The role of the Banc d'Arguin and Sine Saloum as sink for matter fluxes and source for productivity of the southern Canary Current system - BASS, Cruise No. M129, 30 July - 25 August 2016, Ponta Delgada, Portugal - Mindelo, Cape Verde* (tech. rep.). Bonn. https://doi.org/10.2312/cr_m129

Ekman, V. W. (1905). On the influence of the earth's rotation on ocean-currents. *Arkiv for Matematik, Astronomi och Fysik*, *2*, 1–52.

Elmoussaoui, A., Arhan, M., & Treguier, A. M. (2005). Model-inferred upper ocean circulation in the eastern tropics of the North Atlantic. *Deep Sea Research Part I: Oceanographic Research Papers*, *52*(7), 1093–1120. https://doi.org/10.1016/j.dsr.2005.01.010

Emery, W. J., & Meincke, J. (1986). Global water masses: Summary and review. *Oceanologica Acta*, *9*(4), 383–391.

Engel, A., Kiko, R., & Dengler, M. (2022). Organic Matter Supply and Utilization in Oxygen Minimum Zones. *Annual Review of Marine Science*, *14*(1), 1–24. https://doi.org/10.1146/annurev-marine-041921-090849

Engel, A., Wagner, H., Le Moigne, F. A., & Wilson, S. T. (2017). Particle export fluxes to the oxygen minimum zone of the eastern tropical North Atlantic. *Biogeosciences*, *14*(7), 1825–1838. https://doi.org/10.5194/bg-14-1825-2017

Entrambasaguas, L., Pérez-Ruzafa, Á., García-Charton, J. A., Stobart, B., & Bacallado, J. J. (2008). Abundance, spatial distribution and habitat relationships of echinoderms in the Cabo Verde Archipelago (eastern Atlantic). *Marine and Freshwater Research*, *59*(6), 477. https://doi.org/10.1071/MF07109

Eppley, R. W., & Peterson, B. J. (1979). Particulate organic matter flux and planktonic new production in the deep ocean. *Nature*, *282*(5740), 677–680. https://doi.org/10.1038/282677a0

Espinoza-Morriberón, D., Echevin, V., Colas, F., Tam, J., Gutierrez, D., Graco, M., Ledesma, J., & Quispe-Ccalluari, C. (2019). Oxygen Variability During ENSO in the Tropical South Eastern Pacific. *Frontiers in Marine Science*, *5*(JAN), 1–20. https://doi.org/10.3389/fmars.2018.00526

Estrada, M., Marrasé, C., Latasa, M., Berdalet, E., Delgado, M., & Riera, T. (1993). Variability of deep chlorophyll maximum characteristics in the Northwestern Mediterranean. *Marine Ecology Progress Series*, *92*, 289–300. https://doi.org/10.3354/meps092289

Estrada-Allis, S. N., Barceló-Llull, B., Pallàs-Sanz, E., Rodríguez-Santana, A., Souza, J. M., Mason, E., Mcwilliams, J. C., & Sangrà, P. (2019). Vertical velocity dynamics and mixing

in an anticyclone near the Canary Islands. *Journal of Physical Oceanography*, *49*(2), 431–451. https://doi.org/10.1175/JPO-D-17-0156.1

Faghmous, J. H., Frenger, I., Yao, Y., Warmka, R., Lindell, A., & Kumar, V. (2015). A daily global mesoscale ocean eddy dataset from satellite altimetry. *Scientific Data*, *2*, 150028. https://doi.org/10.1038/sdata.2015.28

Falkowski, P. G., Algeo, T., Codispoti, L., Deutsch, C., Emerson, S., Hales, B., Huey, R. B., Jenkins, W. J., Kump, L. R., Levin, L. A., Lyons, T. W., Nelson, N. B., Schofield, O. S., Summons, R., Talley, L. D., Thomas, E., Whitney, F., & Pilcher, C. B. (2011). Ocean deoxygenation: Past, present, and future. *Eos, Transactions American Geophysical Union*, *92*(46), 409–410. https://doi.org/10.1029/2011EO460001

Falkowski, P. G., Katz, M. E., Milligan, A. J., Fennel, K., Cramer, B. S., Aubry, M. P., Berner, R. A., Novacek, M. J., & Zapol, W. M. (2005). The Rise of Oxygen over the Past 205 Million Years and the Evolution of Large Placental Mammals. *Science*, *309*(5744), 2202–2204. https://doi.org/10.1126/science.1116047

Falkowski, P. G., & LaRoche, J. (1991). Acclimation to Spectral Irradiance in Algae. *Journal of Phycology*, *27*(1), 8–14. https://doi.org/10.1111/j.0022-3646.1991.00008.x

Falkowski, P. G., Ziemann, D., Kolber, Z., & Bienfang, P. K. (1991). Role of eddy pumping in enhancing primary production in the ocean. *Nature*, *352*(6330), 55–58. https://doi.org/10.1038/352055a0

Faye, S., Lazar, A., Sow, B. A., & Gaye, A. T. (2015). A model study of the seasonality of sea surface temperature and circulation in the Atlantic North-eastern Tropical Upwelling System. *Frontiers in Physics*, *3*(September), 1–20. https://doi.org/10.3389/fphy.2015.00076

Feng, L., Liu, C., Köhl, A., Stammer, D., & Wang, F. (2021). Four Types of Baroclinic Instability Waves in the Global Oceans and the Implications for the Vertical Structure of Mesoscale Eddies. *Journal of Geophysical Research: Oceans*, *126*(3), e2020JC016966. https://doi.org/10.1029/2020JC016966

Fennel, K., & Testa, J. M. (2019). Biogeochemical Controls on Coastal Hypoxia. *Annual Review of Marine Science*, *11*(Volume 11, 2019), 105–130. https://doi.org/10.1146/annurev-marine-010318-095138

Fennel, W. (1999). Theory of the Benguela Upwelling System. *Journal of Physical Oceanography*, *29*(2), 177–190. https://doi.org/10.1175/1520-0485(1999)029<0177:TOTBUS>2.0.CO;2

Ferrari, R., & Wunsch, C. (2009). Ocean Circulation Kinetic Energy: Reservoirs, Sources, and Sinks. *Annual Review of Fluid Mechanics*, *41*(Volume 41, 2009), 253–282. https://doi.org/10.1146/annurev.fluid.40.111406.102139

Fiedler, B., Grundle, D. S., Schütte, F., Karstensen, J., Löscher, C. R., Hauss, H., Wagner, H., Loginova, A., Kiko, R., Silva, P., Tanhua, T., & Körtzinger, A. (2016). Oxygen utilization and downward carbon flux in an oxygen-depleted eddy in the eastern tropical North Atlantic. *Biogeosciences*, *13*(19), 5633–5647. https://doi.org/10.5194/bg-13-5633-2016

Fischer, G., Romero, O., Toby, E., Iversen, M., Donner, B., Mollenhauer, G., Nowald, N., Ruhland, G., Klann, M., Hamady, B., & Wefer, G. (2019). Changes in the Dust-Influenced Biological Carbon Pump in the Canary Current System: Implications From a Coastal and an Offshore Sediment Trap Record Off Cape Blanc, Mauritania. *Global Biogeochemical Cycles*, *33*(8), 1100–1128. https://doi.org/10.1029/2019GB006194

Fischer, G., Karstensen, J., Romero, O., Baumann, K.-H., Donner, B., Hefter, J., Mollenhauer, G., Iversen, M., Fiedler, B., Monteiro, I., & Körtzinger, A. (2016). Bathypelagic particle flux signatures from a suboxic eddy in the oligotrophic tropical North Atlantic: Production, sedimentation and preservation. *Biogeosciences*, *13*(11), 3203–3223. https://doi.org/10.5194/bg-13-3203-2016

Fischer, G., Romero, O. E., Karstensen, J., Baumann, K.-H., Moradi, N., Iversen, M., Ruhland, G., Klann, M., & Körtzinger, A. (2021). Seasonal flux patterns and carbon transport from low-oxygen eddies at the Cape Verde Ocean Observatory: Lessons learned from a time series sediment trap study (2009–2016). *Biogeosciences*, *18*(24), 6479–6500. https://doi.org/10.5194/bg-18-6479-2021

Fischer, T., Banyte, D., Brandt, P., Dengler, M., Krahmann, G., Tanhua, T., & Visbeck, M. (2013). Diapycnal oxygen supply to the tropical North Atlantic oxygen minimum zone. *Biogeosciences*, *10*(7), 5079–5093. https://doi.org/10.5194/bg-10-5079-2013

Fox-Kemper, B., Adcroft, A., Böning, C. W., Chassignet, E. P., Curchitser, E., Danabasoglu, G., Eden, C., England, M. H., Gerdes, R., Greatbatch, R. J., Griffies, S. M., Hallberg, R. W., Hanert, E., Heimbach, P., Hewitt, H. T., Hill, C. N., Komuro, Y., Legg, S., Le Sommer, J., … Yeager, S. G. (2019). Challenges and Prospects in Ocean Circulation Models. *Frontiers in Marine Science*, *6*. https://doi.org/10.3389/fmars.2019.00065

Fratantoni, D. M. (2001). North Atlantic surface circulation during the 1990's observed with satellite-tracked drifters. *Journal of Geophysical Research: Oceans*, *106*(C10), 22067–22093. https://doi.org/10.1029/2000JC000730

Frenger, I., Bianchi, D., Stührenberg, C., Oschlies, A., Dunne, J., Deutsch, C., Galbraith, E., & Schütte, F. (2018). Biogeochemical Role of Subsurface Coherent Eddies in the Ocean: Tracer Cannonballs, Hypoxic Storms, and Microbial Stewpots? *Global Biogeochemical Cycles*, *32*(2), 226–249. https://doi.org/10.1002/2017GB005743

Fréon, P., Arístegui, J., Bertrand, A., Crawford, R. J. M., Field, J. C., Gibbons, M. J., Tam, J., Hutchings, L., Masski, H., Mullon, C., Ramdani, M., Seret, B., & Simier, M. (2009). Functional group biodiversity in Eastern Boundary Upwelling Ecosystems questions the wasp-waist trophic structure. *Progress in Oceanography*, *83*(1), 97–106. https://doi.org/10.1016/j.pocean.2009.07.034

Fréon, P., Barange, M., & Arístegui, J. (2009). Eastern Boundary Upwelling Ecosystems: Integrative and comparative approaches. *Progress in Oceanography*, *83*(1-4), 1–14. https://doi.org/10.1016/j.pocean.2009.08.001

Friederich, G. E., Ledesma, J., Ulloa, O., & Chavez, F. P. (2008). Air–sea carbon dioxide fluxes in the coastal southeastern tropical Pacific. *Progress in Oceanography*, *79*(2), 156–166. https://doi.org/10.1016/j.pocean.2008.10.001

Frölicher, T. L., Aschwanden, M. T., Gruber, N., Jaccard, S. L., Dunne, J. P., & Paynter, D. (2020). Contrasting Upper and Deep Ocean Oxygen Response to Protracted Global Warming. *Global Biogeochemical Cycles*, *34*(8), e2020GB006601. https://doi.org/10.1029/2020GB006601

Frölicher, T. L., Fischer, E. M., & Gruber, N. (2018). Marine heatwaves under global warming. *Nature*, *560*(7718), 360–364. https://doi.org/10.1038/s41586-018-0383-9

Frölicher, T. L., & Laufkötter, C. (2018). Emerging risks from marine heat waves. *Nature Communications*, *9*(1), 650. https://doi.org/10.1038/s41467-018-03163-6

Fu, W., Primeau, F., Keith Moore, J., Lindsay, K., & Randerson, J. T. (2018). Reversal of Increasing Tropical Ocean Hypoxia Trends With Sustained Climate Warming. *Global Biogeochemical Cycles*, *32*(4), 551–564. https://doi.org/10.1002/2017GB005788

Fuller, D. W., Schaefer, K. M., Hampton, J., Caillot, S., Leroy, B. M., & Itano, D. G. (2015). Vertical movements, behavior, and habitat of bigeye tuna (*Thunnus obesus*) in the equatorial central Pacific Ocean. *Fisheries Research*, *172*, 57–70. https://doi.org/10.1016/j.fishres.2015.06.024

Gabric, A. J., Garcia, L., Van Camp, L., Nykjaer, L., Eifler, W., & Schrimpf, W. (1993). Offshore export of shelf production in the Cape Blanc (Mauritania) giant filament as derived from coastal zone color scanner imagery. *Journal of Geophysical Research: Oceans*, *98*(C3), 4697–4712. https://doi.org/10.1029/92JC01714

Garfield, N., Collins, C. A., Paquette, R. G., & Carter, E. (1999). Lagrangian Exploration of the California Undercurrent, 1992–95. *Journal of Physical Oceanography*, *29*(4), 560–583. https://doi.org/10.1175/1520-0485(1999)029<0560:LEOTCU>2.0.CO;2

Garreau, P., Dumas, F., Louazel, S., Stegner, A., & Le Vu, B. (2018). High-Resolution Observations and Tracking of a Dual-Core Anticyclonic Eddy in the Algerian Basin. *Journal of Geophysical Research: Oceans*, *123*(12), 9320–9339. https://doi.org/10.1029/2017JC013667

Gaube, P., Chelton, D. B., Strutton, P. G., & Behrenfeld, M. J. (2013). Satellite observations of chlorophyll, phytoplankton biomass, and Ekman pumping in nonlinear mesoscale eddies. *Journal of Geophysical Research: Oceans*, *118*(12), 6349–6370. https://doi.org/10.1002/2013JC009027

Gaube, P., Chelton, D. B., Samelson, R. M., Schlax, M. G., & O'Neill, L. W. (2015). Satellite Observations of Mesoscale Eddy-Induced Ekman Pumping. *Journal of Physical Oceanography*, *45*(1), 104–132. https://doi.org/10.1175/JPO-D-14-0032.1

Gaube, P., McGillicuddy, D. J., Chelton, D. B., Behrenfeld, M. J., & Strutton, P. G. (2014). Regional variations in the influence of mesoscale eddies on near-surface chlorophyll. *Journal of Geophysical Research: Oceans*, *119*(12), 8195–8220. https://doi.org/10.1002/2014JC010111

Gay, P. S., & Chereskin, T. K. (2009). Mean structure and seasonal variability of the poleward undercurrent off southern California. *Journal of Geophysical Research: Oceans*, *114*(C2). https://doi.org/10.1029/2008JC004886

Geider, R. J., MacIntyre, H. L., & Kana, T. M. (1996). A dynamic model of photoadaptation in phytoplankton. *Limnology and Oceanography*, *41*(1), 1–15. https://doi.org/10.4319/lo.1996.41.1.0001

Gier, J., Löscher, C. R., Dale, A. W., Sommer, S., Lomnitz, U., & Treude, T. (2017). Benthic Dinitrogen Fixation Traversing the Oxygen Minimum Zone Off Mauritania (NW Africa). *Frontiers in Marine Science*, *4*.

Gilbert, D., Sundby, B., Gobeil, C., Mucci, A., & Tremblay, G.-H. (2005). A seventy-two-year record of diminishing deep-water oxygen in the St. Lawrence estuary: The northwest Atlantic connection. *Limnology and Oceanography*, *50*(5), 1654–1666. https://doi.org/10.4319/lo.2005.50.5.1654

Gill, A., & Niller, P. (1973). The theory of the seasonal variability in the ocean. *Deep Sea Research and Oceanographic Abstracts*, *20*(2), 141–177. https://doi.org/10.1016/0011-7471(73)90049-1

Gilly, W. F., Beman, J. M., Litvin, S. Y., & Robison, B. H. (2013). Oceanographic and Biological Effects of Shoaling of the Oxygen Minimum Zone. *Annual Review of Marine Science*, *5*(Volume 5, 2013), 393–420. https://doi.org/10.1146/annurev-marine-120710-100849

Giomi, F., Barausse, A., Steckbauer, A., Daffonchio, D., Duarte, C. M., & Fusi, M. (2023). Oxygen dynamics in marine productive ecosystems at ecologically relevant scales. *Nature Geoscience*, *16*(7), 560–566. https://doi.org/10.1038/s41561-023-01217-z

Glessmer, M. S., Eden, C., & Oschlies, A. (2009). Contribution of oxygen minimum zone waters to the coastal upwelling off Mauritania. *Progress in Oceanography*, *83*(1-4), 143–150. https://doi.org/10.1016/j.pocean.2009.07.015

Glover, D. M., Jenkins, W. J., & Doney, S. C. (2011, June). *Modeling Methods for Marine Science* (1st ed.). Cambridge University Press. https://doi.org/10.1017/CBO9780511975721

Gómez-Letona, M., Ramos, A. G., Coca, J., & Arístegui, J. (2017). Trends in Primary Production in the Canary Current Upwelling System—A Regional Perspective Comparing Remote Sensing Models. *Frontiers in Marine Science*, *4*. https://doi.org/10.3389/fmars.2017.00370

Good, S., Fiedler, E., Mao, C., Martin, M. J., Maycock, A., Reid, R., Roberts-Jones, J., Searle, T., Waters, J., While, J., & Worsfold, M. (2020). The current configuration of the OSTIA system for operational production of foundation sea surface temperature and ice concentration analyses. *Remote Sensing*, *12*(4), 1–20. https://doi.org/10.3390/rs12040720

Gordon, A. L., Shroyer, E., & Murty, V. S. N. (2017). An Intrathermocline Eddy and a tropical cyclone in the Bay of Bengal. *Scientific Reports*, *7*(1), 46218. https://doi.org/10.1038/srep46218

Gordon, A. L., Weiss, R. F., Smethie, W. M., & Warner, M. J. (1992). Thermocline and intermediate water communication between the south Atlantic and Indian oceans. *Journal of Geophysical Research: Oceans*, *97*(C5), 7223–7240. https://doi.org/10.1029/92JC00485

Gordon, H. R., & McCluney, W. R. (1975). Estimation of the Depth of Sunlight Penetration in the Sea for Remote Sensing. *Applied Optics*, *14*(2), 413. https://doi.org/10.1364/AO.14.000413

Gorgues, T., Menkes, C., Slemons, L., Aumont, O., Dandonneau, Y., Radenac, M. .-., Alvain, S., & Moulin, C. (2010). Revisiting the La Niña 1998 phytoplankton blooms in the equatorial Pacific. *Deep Sea Research Part I: Oceanographic Research Papers*, *57*(4), 567–576. https://doi.org/10.1016/j.dsr.2009.12.008

Grantham, B. A., Chan, F., Nielsen, K. J., Fox, D. S., Barth, J. A., Huyer, A., Lubchenco, J., & Menge, B. A. (2004). Upwelling-driven nearshore hypoxia signals ecosystem and oceanographic changes in the northeast Pacific. *Nature*, *429*(6993), 749–754. https://doi.org/10.1038/nature02605

Gregg, W. W., Casey, N. W., & McClain, C. R. (2005). Recent trends in global ocean chlorophyll. *Geophysical Research Letters*, *32*(3). https://doi.org/10.1029/2004GL021808

Grégoire, M., Garçon, V., Garcia, H., Breitburg, D., Isensee, K., Oschlies, A., Telszewski, M., Barth, A., Bittig, H. C., Carstensen, J., Carval, T., Chai, F., Chavez, F., Conley, D., Coppola, L., Crowe, S., Currie, K., Dai, M., Deflandre, B., … Yasuhara, M. (2021). A Global Ocean Oxygen Database and Atlas for Assessing and Predicting Deoxygenation and Ocean Health in the Open and Coastal Ocean. *Frontiers in Marine Science*, *8*.

Gruber, N. (2011). Warming up, turning sour, losing breath: Ocean biogeochemistry under global change. *Philosophical Transactions of the Royal Society A: Mathematical, Physical and Engineering Sciences*, *369*(1943), 1980–1996. https://doi.org/10.1098/rsta.2011.0003

Gruber, N., Boyd, P. W., Frölicher, T. L., & Vogt, M. (2021). Biogeochemical extremes and compound events in the ocean. *Nature*, *600*(7889), 395–407. https://doi.org/10.1038/s41586-021-03981-7

Gruber, N., & Galloway, J. N. (2008). An Earth-system perspective of the global nitrogen cycle. *Nature*, *451*(7176), 293–296. https://doi.org/10.1038/nature06592

Gruber, N., Lachkar, Z., Frenzel, H., Marchesiello, P., Münnich, M., McWilliams, J. C., Nagai, T., & Plattner, G.-K. (2011). Eddy-induced reduction of biological production in eastern boundary upwelling systems. *Nature Geoscience*, *4*(11), 787–792. https://doi.org/10.1038/ngeo1273

Grundle, D. S., Löscher, C. R., Krahmann, G., Altabet, M. A., Bange, H. W., Karstensen, J., Körtzinger, A., & Fiedler, B. (2017). Low oxygen eddies in the eastern tropical North Atlantic: Implications for N2O cycling. *Scientific Reports*, *7*(1), 4806. https://doi.org/10.1038/s41598-017-04745-y

Gula, J. (2020). Mesoscale and submesoscale turbulence in the presence of topography.

Gula, J., Blacic, T. M., & Todd, R. E. (2019). Submesoscale Coherent Vortices in the Gulf Stream. *Geophysical Research Letters*, *46*(5), 2704–2714. https://doi.org/10.1029/2019GL081919

Gula, J., Molemaker, M. J., & McWilliams, J. C. (2015). Gulf Stream Dynamics along the Southeastern U.S. Seaboard. *Journal of Physical Oceanography*, *45*(3), 690–715. https://doi.org/10.1175/JPO-D-14-0154.1

Gula, J., Molemaker, M. J., & McWilliams, J. C. (2016). Topographic generation of submesoscale centrifugal instability and energy dissipation. *Nature Communications*, *7*, 1–7. https://doi.org/10.1038/ncomms12811

Hahn, J., Brandt, P., Greatbatch, R. J., Krahmann, G., & Körtzinger, A. (2014). Oxygen variance and meridional oxygen supply in the Tropical North East Atlantic oxygen minimum zone. *Climate Dynamics*, *43*(11), 2999–3024. https://doi.org/10.1007/s00382-014-2065-0

Hahn, J., Brandt, P., Schmidtko, S., & Krahmann, G. (2017). Decadal oxygen change in the eastern tropical North Atlantic. *Ocean Science*, *13*(4), 551–576. https://doi.org/10.5194/os-13-551-2017

Hailegeorgis, D., Lachkar, Z., Rieper, C., & Gruber, N. (2020). A Lagrangian study of the contribution of the Canary coastal upwelling to the open North Atlantic nitrogen budget. *Biogeosciences Discussions*, 1–40. https://doi.org/10.5194/bg-2020-25

Haller, G., Hadjighasem, A., Farazmand, M., & Huhn, F. (2016). Defining coherent vortices objectively from the vorticity. *Journal of Fluid Mechanics*, *795*, 136–173. https://doi.org/10.1017/jfm.2016.151

Haney, R. L. (1991). On the Pressure Gradient Force over Steep Topography in Sigma Coordinate Ocean Models.

Hasegawa, D., Lewis, M. R., & Gangopadhyay, A. (2009). How islands cause phytoplankton to bloom in their wakes. *Geophysical Research Letters*, *36*(20), 2–5. https://doi.org/10.1029/2009GL039743

Hauri, C., Gruber, N., McDonnell, A. M. P., & Vogt, M. (2013). The intensity, duration, and severity of low aragonite saturation state events on the California continental shelf. *Geophysical Research Letters*, *40*(13), 3424–3428. https://doi.org/10.1002/grl.50618

Hauss, H., Christiansen, S., Schütte, F., Kiko, R., Edvam Lima, M., Rodrigues, E., Karstensen, J., Löscher, C. R., Körtzinger, A., & Fiedler, B. (2016). Dead zone or oasis in the open ocean? Zooplankton distribution and migration in low-oxygen modewater eddies. *Biogeosciences*, *13*(6), 1977–1989. https://doi.org/10.5194/bg-13-1977-2016

Hays, G. C. (2003). A review of the adaptive significance and ecosystem consequences of zooplankton diel vertical migrations. In M. B. Jones, A. Ingólfsson, E. Ólafsson, G. V. Helgason, K. Gunnarsson, & J. Svavarsson (Eds.), *Migrations and Dispersal of Marine Organisms* (pp. 163–170). Springer Netherlands. https://doi.org/10.1007/978-94-017-2276-6_18

He, J., & Mahadevan, A. (2021). How the Source Depth of Coastal Upwelling Relates to Stratification and Wind. *Journal of Geophysical Research: Oceans*, *126*(12), e2021JC017621. https://doi.org/10.1029/2021JC017621

Helm, K. P., Bindoff, N. L., & Church, J. A. (2011). Observed decreases in oxygen content of the global ocean. *Geophysical Research Letters*, *38*(23). https://doi.org/10.1029/2011GL049513

Helmke, P., Romero, O., & Fischer, G. (2005). Northwest African upwelling and its effect on offshore organic carbon export to the deep sea. *Global Biogeochemical Cycles*, *19*(4), n/a–n/a. https://doi.org/10.1029/2004GB002265

Henson, S. A., Beaulieu, C., Ilyina, T., John, J. G., Long, M., Séférian, R., Tjiputra, J., & Sarmiento, J. L. (2017). Rapid emergence of climate change in environmental drivers of marine ecosystems. *Nature Communications*, *8*(1), 14682. https://doi.org/10.1038/ncomms14682

Henson, S. A., Laufkötter, C., Leung, S., Giering, S. L. C., Palevsky, H. I., & Cavan, E. L. (2022). Uncertain response of ocean biological carbon export in a changing world. *Nature Geoscience*, *15*(4), 248–254. https://doi.org/10.1038/s41561-022-00927-0

Hernández-Miranda, E., Quiñones, R. A., Aedo, G., Valenzuela, A., Mermoud, N., Román, C., & Yañez, F. (2010). A major fish stranding caused by a natural hypoxic event in a shallow bay of the eastern South Pacific Ocean. *Journal of Fish Biology*, *76*(7), 1543–1564. https://doi.org/10.1111/j.1095-8649.2010.02580.x

Heywood, K. J., Barton, E. D., & Simpson, J. H. (1990). The effects of flow disturbance by an oceanic island. *Journal of Marine Research*, *48*(1), 55–73. https://doi.org/10.1357/002224090784984623

Hilt, M., Auclair, F., Benshila, R., Bordois, L., Capet, X., Debreu, L., Dumas, F., Jullien, S., Lemarié, F., Marchesiello, P., Nguyen, C., & Roblou, L. (2020). Numerical modelling of hydraulic control, solitary waves and primary instabilities in the Strait of Gibraltar. *Ocean Modelling*.

Hobday, A., Oliver, E., Sen Gupta, A., Benthuysen, J., Burrows, M., Donat, M., Holbrook, N., Moore, P., Thomsen, M., Wernberg, T., & Smale, D. (2018). Categorizing and Naming Marine Heatwaves. *Oceanography*, *31*(2). https://doi.org/10.5670/oceanog.2018.205

Hofmann, A. F., Peltzer, E. T., Walz, P. M., & Brewer, P. G. (2011). Hypoxia by degrees: Establishing definitions for a changing ocean. *Deep Sea Research Part I: Oceanographic Research Papers*, *58*(12), 1212–1226. https://doi.org/10.1016/j.dsr.2011.09.004

Hogan, P. J., & Hurlburt, H. E. (2015). Why do Intrathermocline Eddies Form in the Japan/East Sea? A Modeling Perspective. *Oceanography*, *19*(3), 134–143. https://doi.org/10.5670/oceanog.2006.50

Holland, C. L., & Mitchum, G. T. (2001). Propagation of Big Island eddies. *Journal of Geophysical Research: Oceans*, *106*(C1), 935–944. https://doi.org/10.1029/2000JC000231

Holloway, G., Brink, K., & Haidvogel, D. (1989). Topographic stress in coastal circulation dynamics. In S. J. Neshyba, C. N. K. Mooers, R. L. Smith, & R. T. Barber (Eds.), *Poleward flows along eastern ocean boundaries* (pp. 315–330). Springer New York. https://doi.org/10.1007/978-1-4613-8963-7_20

Hood, R. R., Beckley, L. E., & Wiggert, J. D. (2017). Biogeochemical and ecological impacts of boundary currents in the Indian Ocean. *Progress in Oceanography*, *156*, 290–325. https://doi.org/10.1016/j.pocean.2017.04.011

Hoskins, B. J. (1974). The role of potential vorticity in symmetric stability and instability. *Quarterly Journal of the Royal Meteorological Society*, *100*(425), 480–482. https://doi.org/10.1002/qj.49710042520

Huthnance, J. M. (1984). Slope Currents and "JEBAR". *Journal of Physical Oceanography*, *14*(4), 795–810. https://doi.org/10.1175/1520-0485(1984)014<0795:SCA>2.0.CO;2

Huthnance, J. M., Inall, M. E., & Fraser, N. J. (2020). Oceanic Density/Pressure Gradients and Slope Currents. *Journal of Physical Oceanography*. https://doi.org/10.1175/JPO-D-19-0134.1

Huyer, A. (1983). Coastal upwelling in the California current system. *Progress in Oceanography*, *12*(3), 259–284. https://doi.org/10.1016/0079-6611(83)90010-1

Ioannou, A., Speich, S., & Laxenaire, R. (2022). Characterizing Mesoscale Eddies of Eastern Upwelling Origins in the Atlantic Ocean and Their Role in Offshore Transport. *9*(June), 1–20. https://doi.org/10.3389/fmars.2022.835260

Ioannou, A., Stegner, A., Dubos, T., Le Vu, B., & Speich, S. (2020). Generation and Intensification of Mesoscale Anticyclones by Orographic Wind Jets: The Case of Ierapetra Eddies Forced by the Etesians. *Journal of Geophysical Research: Oceans*, *125*(8), 1–23. https://doi.org/10.1029/2019JC015810

Ioannou, A., Stegner, A., Dumas, F., & Le Vu, B. (2020). Three-Dimensional Evolution of Mesoscale Anticyclones in the Lee of Crete. *Frontiers in Marine Science*, *7*(November), 1–15. https://doi.org/10.3389/fmars.2020.609156

Ioannou, A., Stegner, A., Le Vu, B., Taupier-Letage, I., & Speich, S. (2017). Dynamical Evolution of Intense Ierapetra Eddies on a 22 Year Long Period. *Journal of Geophysical Research: Oceans*, *122*(11), 9276–9298. https://doi.org/10.1002/2017JC013158

Iversen, M. H., Swoboda, S., Marchant, H., Ahmerkamp, S., Schwalfenberg, K., Hehemann, J., Buck-Wiese, H., Stock, L., Bolte, A., & Bäger, J. (2019). Benthic-pelagic coupling in sandy sediment regions and its interactions with the biological carbon in the open ocean - poseidon-bericht cruise no. pos531, 18.01.2019 - 01.02.2019, las palmas (canary islands) - mindelo (kap verden). https://doi.org/10.3289/cr_pos531

Iversen, M. H., Nowald, N., Ploug, H., Jackson, G. A., & Fischer, G. (2010). High resolution profiles of vertical particulate organic matter export off Cape Blanc, Mauritania: Degradation processes and ballasting effects. *Deep Sea Research Part I: Oceanographic Research Papers*, *57*(6), 771–784. https://doi.org/10.1016/j.dsr.2010.03.007

Izumo, T., Montégut, C. B., Luo, J.-J., Behera, S. K., Masson, S., & Yamagata, T. (2008). The Role of the Western Arabian Sea Upwelling in Indian Monsoon Rainfall Variability. https://doi.org/10.1175/2008JCLI2158.1

Jahnke, R. A. (1996). The global ocean flux of particulate organic carbon: Areal distribution and magnitude. *Global Biogeochemical Cycles*, *10*(1), 71–88. https://doi.org/10.1029/95GB03525

Johns, W. E., Baringer, M. O., Beal, L. M., Cunningham, S. A., Kanzow, T., Bryden, H. L., Hirschi, J. J. M., Marotzke, J., Meinen, C. S., Shaw, B., & Curry, R. (2011). Continuous, Array-Based Estimates of Atlantic Ocean Heat Transport at 26.5°N. https://doi.org/10.1175/2010JCLI3997.1

Johns, W. E., Zantopp, R. J., & Goni, G. J. (2003). Cross-gyre transport by North Brazil Current rings. *Elsevier Oceanography Series*, *68*(100), 411–441. https://doi.org/10.1016/S0422-9894(03)80156-3

Johnson, G. C., & McTaggart, K. E. (2010). Equatorial Pacific 13°C Water Eddies in the Eastern Subtropical South Pacific Ocean. https://doi.org/10.1175/2009JPO4287.1

Jones-Kellett, A. E., & Follows, M. J. (2024). A Lagrangian coherent eddy atlas for biogeochemical applications in the North Pacific Subtropical Gyre. *Earth System Science Data*, *16*(3), 1475–1501. https://doi.org/10.5194/essd-16-1475-2024

Kalvelage, T., Jensen, M. M., Contreras, S., Revsbech, N. P., Lam, P., Günter, M., LaRoche, J., Lavik, G., & Kuypers, M. M. M. (2011). Oxygen Sensitivity of Anammox and Coupled N-Cycle Processes in Oxygen Minimum Zones. *PLOS ONE*, *6*(12), e29299. https://doi.org/10.1371/journal.pone.0029299

Karstensen, J., Fiedler, B., Schütte, F., Brandt, P., Körtzinger, A., Fischer, G., Zantopp, R., Hahn, J., Visbeck, M., & Wallace, D. (2015). Open ocean dead zones in the tropical North Atlantic Ocean. *Biogeosciences*, *12*(8), 2597–2605. https://doi.org/10.5194/bg-12-2597-2015

Karstensen, J., Schütte, F., Pietri, A., Krahmann, G., Fiedler, B., Grundle, D., Hauss, H., Körtzinger, A., Löscher, C. R., Testor, P., Vieira, N., & Visbeck, M. (2017). Upwelling and isolation in oxygen-depleted anticyclonic modewater eddies and implications for nitrate cycling. *Biogeosciences*, *14*(8), 2167–2181. https://doi.org/10.5194/bg-14-2167-2017

Karstensen, J., Stramma, L., & Visbeck, M. (2008). Oxygen minimum zones in the eastern tropical Atlantic and Pacific oceans. *Progress in Oceanography*, *77*(4), 331–350. https://doi.org/10.1016/j.pocean.2007.05.009

Karstensen, J., & Tomczak, M. (1998). Age determination of mixed water masses using CFC and oxygen data. *Journal of Geophysical Research: Oceans*, *103*(C9), 18599–18609. https://doi.org/10.1029/98JC00889

Katzenmeier, S. N., Nothof, M., Breiner, H.-W., Fischer, T., & Stoeck, T. (2024). Mesoscale cyclonic eddies born in an Eastern Boundary Upwelling System enhance microbial eukaryote diversity in oligotrophic offshore waters. *Deep Sea Research Part II: Topical Studies in Oceanography*, 105425. https://doi.org/10.1016/j.dsr2.2024.105425

Kaufman, Y. J., Koren, I., Remer, L. A., Tanré, D., Ginoux, P., & Fan, S. (2005). Dust transport and deposition observed from the Terra-Moderate Resolution Imaging Spectroradiome-

ter (MODIS) spacecraft over the Atlantic Ocean. *Journal of Geophysical Research: Atmospheres*, *110*(D10). https://doi.org/10.1029/2003JD004436

Keates, T. R., Hazen, E. L., Holser, R. R., Fiechter, J., Bograd, S. J., Robinson, P. W., Gallo-Reynoso, J. P., & Costa, D. P. (2022). Foraging behavior of a mesopelagic predator, the northern elephant seal, in northeastern Pacific eddies. *Deep Sea Research Part I: Oceanographic Research Papers*, *189*, 103866. https://doi.org/10.1016/j.dsr.2022.103866

Keeling, R. F., Körtzinger, A., & Gruber, N. (2010). Ocean Deoxygenation in a Warming World. *Annual Review of Marine Science*, *2*(Volume 2, 2010), 199–229. https://doi.org/10.1146/annurev.marine.010908.163855

Kekuewa, S. A. H., Courtney, T. A., Cyronak, T., & Andersson, A. J. (2022). Seasonal nearshore ocean acidification and deoxygenation in the Southern California Bight. *Scientific Reports*, *12*(1), 17969. https://doi.org/10.1038/s41598-022-21831-y

Kiørboe, T. (2011). How zooplankton feed: Mechanisms, traits and trade-offs. *Biological Reviews*, *86*(2), 311–339. https://doi.org/10.1111/j.1469-185X.2010.00148.x

Kirchner, K., Rhein, M., Hüttl-Kabus, S., & Böning, C. W. (2009). On the spreading of South Atlantic Water into the Northern Hemisphere. *Journal of Geophysical Research: Oceans*, *114*(C5). https://doi.org/10.1029/2008JC005165

Kirichek, A. (1971). Water circulation in the north-eastern part of the tropical atlantic. *Internat. Counc. Explor. Sea. CM*, *100*(7).

Kjellsson, J., & Döös, K. (2012). Lagrangian decomposition of the Hadley and Ferrel cells. *Geophysical Research Letters*, *39*(15). https://doi.org/10.1029/2012GL052420

Klenz, T., Dengler, M., & Brandt, P. (2018). Seasonal Variability of the Mauritania Current and Hydrography at 18°N. *Journal of Geophysical Research: Oceans*, (November). https://doi.org/10.1029/2018JC014264

Klevjer, T. A., Melle, W., Knutsen, T., & Aksnes, D. L. (2020). Vertical distribution and migration of mesopelagic scatterers in four north Atlantic basins. *Deep Sea Research Part II: Topical Studies in Oceanography*, *180*, 104811. https://doi.org/10.1016/j.dsr2.2020.104811

Klymak, J. M., & Moum, J. N. (2003). Internal solitary waves of elevation advancing on a shoaling shelf. *Geophysical Research Letters*, *30*(20). https://doi.org/10.1029/2003GL017706

Köhn, E. E., Münnich, M., Vogt, M., Desmet, F., & Gruber, N. (2022). Strong Habitat Compression by Extreme Shoaling Events of Hypoxic Waters in the Eastern Pacific. *Journal of Geophysical Research: Oceans*, *127*(6), e2022JC018429. https://doi.org/10.1029/2022JC018429

Köhn, E. E., Vogt, M., Münnich, M., & Gruber, N. (2024). On the Vertical Structure and Propagation of Marine Heatwaves in the Eastern Pacific. *Journal of Geophysical Research: Oceans*, *129*(1), e2023JC020063. https://doi.org/10.1029/2023JC020063

Köhn, E. E. (2023). *Water column perspectives on marine heatwaves and low oxygen extreme events in the Eastern Pacific* [Doctoral Thesis]. ETH Zurich. https://doi.org/10.3929/ethz-b-000611971

Accepted: 2023-05-15T09:10:10Z.

Kolodziejczyk, N., Testor, P., Lazar, A., Echevin, V., Krahmann, G., Chaigneau, A., Gourcuff, C., Wade, M., Faye, S., Estrade, P., Capet, X., Mortier, L., Brehmer, P., Schütte, F., & Karstensen, J. (2018). Subsurface Fine-Scale Patterns in an Anticyclonic Eddy Off Cap-Vert Peninsula Observed From Glider Measurements. *Journal of Geophysical Research: Oceans*, *123*(9), 6312–6329. https://doi.org/10.1029/2018JC014135

Koračin, D., Dorman, C. E., & Dever, E. P. (2004). Coastal Perturbations of Marine-Layer Winds, Wind Stress, and Wind Stress Curl along California and Baja California in June 1999.

Körtzinger, A. (2012). Short cruise report r/v l'atalante cruise ifm-geomar, leg 3 from dakar, senegal to mindelo, cape verde february 3 to 20, 2008. https://doi.org/10.3289/SCR_ATA_3

Koschinsky, A., Brandt, P., & Körtzinger, A. (2009). *Tropical atlantic 2006 meteor cruise no. 68 april 26 - august 7, 2006 bridgetown - recife - mindelo - las palmas* (S.-B. Löffler, Ed.; Cruise Report). Hamburg, Germany, ARRAY(0x55870c7318f8). https://oceanrep.geomar.de/id/eprint/13683/

Kostianoy, A., & Belkin, I. (1989). A Survey of Observations on Intrathermocline Eddies in the World Ocean. In *Mesoscale/Synoptic Coherent Structures in Geophysical Turbulence* (pp. 821–841, Vol. 50). https://doi.org/10.1016/S0422-9894(08)70223-X

Kostianoy, A., & Zatsepin, A. (1996). The West African coastal upwelling filaments and cross-frontal water exchange conditioned by them. *Journal of Marine Systems*, *7*(2-4), 349–359. https://doi.org/10.1016/0924-7963(95)00029-1

Kounta, L., Capet, X., Jouanno, J., Kolodziejczyk, N., Sow, B., & Thierno Gaye, A. (2018). A model perspective on the dynamics of the shadow zone of the eastern tropical North Atlantic-Part 1: The poleward slope currents along West Africa. *Ocean Science*, *14*(5), 971–997. https://doi.org/10.5194/os-14-971-2018

Krahmann, G. (2022). Temperature, salinity and oxygen measured on CTD water bottle samples during METEOR cruise M156. https://doi.org/10.1594/PANGAEA.950356

Krahmann, G., Arévalo-Martínez, D. L., Dale, A. W., Dengler, M., Engel, A., Glock, N., Grasse, P., Hahn, J., Hauss, H., Hopwood, M. J., Kiko, R., Loginova, A. N., Löscher, C. R., Maßmig, M., Roy, A.-S., Salvatteci, R., Sommer, S., Tanhua, T., & Mehrtens, H. (2021). Climate-Biogeochemistry Interactions in the Tropical Ocean: Data Collection and Legacy. *Frontiers in Marine Science*, *8*. https://doi.org/10.3389/fmars.2021.723304

Krahmann, G., Dengler, M., Thomsen, S., & Kanzow, T. (2017). Physical oceanography from glider mission IFM02_depl22. https://doi.org/10.1594/PANGAEA.877392

Kurczyn, J. A., Beier, E., Lavín, M. F., & Chaigneau, A. (2012). Mesoscale eddies in the northeastern Pacific tropical-subtropical transition zone: Statistical characterization from satellite altimetry. *Journal of Geophysical Research: Oceans*, *117*(C10). https://doi.org/10.1029/2012JC007970

Kurian, J., Colas, F., Capet, X., McWilliams, J. C., & Chelton, D. B. (2011). Eddy properties in the California Current System. *Journal of Geophysical Research: Oceans*, *116*(8), 1–18. https://doi.org/10.1029/2010JC006895

Lachkar, Z., & Gruber, N. (2012). A comparative study of biological production in eastern boundary upwelling systems using an artificial neural network. *Biogeosciences*, *9*(1), 293–308. https://doi.org/10.5194/bg-9-293-2012

Lange, C. B., Romero, O. E., Wefer, G., & Gabric, A. J. (1998). Offshore influence of coastal upwelling off Mauritania, NW Africa, as recorded by diatoms in sediment traps at 2195 m water depth. *Deep-Sea Research Part I: Oceanographic Research Papers*, *45*(6), 985–1013. https://doi.org/10.1016/S0967-0637(97)00103-9

Large, W. G., McWilliams, J. C., & Doney, S. C. (1994). Oceanic vertical mixing: A review and a model with a nonlocal boundary layer parameterization. *Reviews of Geophysics*, *32*(4), 363–403. https://doi.org/10.1029/94RG01872

Lathuilière, C., Echevin, V., & Lévy, M. (2008). Seasonal and intraseasonal surface chlorophyll-a variability along the northwest African coast. *Journal of Geophysical Research*, *113*(C5), C05007. https://doi.org/10.1029/2007JC004433

Laufkötter, C., John, J. G., Stock, C. A., & Dunne, J. P. (2017). Temperature and oxygen dependence of the remineralization of organic matter. *Global Biogeochemical Cycles*, *31*(7), 1038–1050. https://doi.org/10.1002/2017GB005643

Laurindo, L. C., Mariano, A. J., & Lumpkin, R. (2017). An improved near-surface velocity climatology for the global ocean from drifter observations. *Deep Sea Research Part I: Oceanographic Research Papers*, *124*, 73–92. https://doi.org/10.1016/j.dsr.2017.04.009

Lauton, G., Pattiaratchi, C. B., & Lentini, C. A. D. (2021). Observations of Breaking Internal Tides on the Australian North West Shelf Edge. *Frontiers in Marine Science*, *8*. https://doi.org/10.3389/fmars.2021.629372

Lauvset, S. K., Lange, N., Tanhua, T., Bittig, H. C., Olsen, A., Kozyr, A., Alin, S., Álvarez, M., Azetsu-Scott, K., Barbero, L., Becker, S., Brown, P. J., Carter, B. R., da Cunha, L. C., Feely, R. A., Hoppema, M., Humphreys, M. P., Ishii, M., Jeansson, E., … Key, R. M. (2022). GLODAPv2.2022: The latest version of the global interior ocean biogeochemical data product. *Earth System Science Data*, *14*(12), 5543–5572. https://doi.org/10.5194/essd-14-5543-2022

Laxenaire, R., Speich, S., Blanke, B., Chaigneau, A., Pegliasco, C., & Stegner, A. (2018). Anticyclonic eddies connecting the western boundaries of Indian and Atlantic oceans. *Journal of Geophysical Research: Oceans*. https://doi.org/10.1029/2018JC014270

Lázaro, C., Fernandes, M. J., Santos, A. M. P., & Oliveira, P. (2005). Seasonal and interannual variability of surface circulation in the Cape Verde region from 8 years of merged T/P and ERS-2 altimeter data. *Remote Sensing of Environment*, *98*(1), 45–62. https://doi.org/10.1016/j.rse.2005.06.005

Le Boeuf, B. J., Crocker, D. E., Costa, D. P., Blackwell, S. B., Webb, P. M., & Houser, D. S. (2000). Foraging Ecology of Northern Elephant Seals. *Ecological Monographs*, *70*(3), 353–382. https://doi.org/10.1890/0012-9615(2000)070[0353:FEONES]2.0.CO;2

Le Vu, B., Stegner, A., & Arsouze, T. (2018). Angular Momentum Eddy Detection and Tracking Algorithm (AMEDA) and Its Application to Coastal Eddy Formation. *Journal of Atmo-*

spheric and Oceanic Technology, *35*(4), 739–762. https://doi.org/10.1175/JTECH-D-17-0010.1

Leth, O., & Shaffer, G. (2001). A numerical study of the seasonal variability in the circulation off central Chile. *Journal of Geophysical Research: Oceans*, *106*(C10), 22229–22248. https://doi.org/10.1029/2000JC000627

Levin, L. A., Ekau, W., Gooday, A. J., Jorissen, F., Middelburg, J. J., Naqvi, S. W. A., Neira, C., Rabalais, N. N., & Zhang, J. (2009). Effects of natural and human-induced hypoxia on coastal benthos. *Biogeosciences*, *6*(10), 2063–2098. https://doi.org/10.5194/bg-6-2063-2009

Levin, L. A. (2018). Manifestation, Drivers, and Emergence of Open Ocean Deoxygenation. *Annual Review of Marine Science*, *10*(1), 229–260. https://doi.org/10.1146/annurev-marine-121916-063359

Lévy, M., Iovino, D., Resplandy, L., Klein, P., Madec, G., Tréguier, A. M., Masson, S., & Takahashi, K. (2012). Large-scale impacts of submesoscale dynamics on phytoplankton: Local and remote effects. *Ocean Modelling*, *43–44*, 77–93. https://doi.org/10.1016/j.ocemod.2011.12.003

Lévy, M., Couespel, D., Haëck, C., Keerthi, M., Mangolte, I., & Prend, C. J. (2024). The Impact of Fine-Scale Currents on Biogeochemical Cycles in a Changing Ocean. *Annual Review of Marine Science*, *16*(1), null. https://doi.org/10.1146/annurev-marine-020723-020531

Lévy, M., Franks, P. J. S., & Smith, K. S. (2018). The role of submesoscale currents in structuring marine ecosystems. *Nature Communications*, *9*(1), 4758. https://doi.org/10.1038/s41467-018-07059-3

Lévy, M., Resplandy, L., Palter, J. B., Couespel, D., & Lachkar, Z. (2022). The crucial contribution of mixing to present and future ocean oxygen distribution. In *Ocean Mixing* (pp. 329–344). Elsevier. https://doi.org/10.1016/B978-0-12-821512-8.00020-7

Li, C., Zhang, Z., Zhao, W., & Tian, J. (2017). A statistical study on the subthermocline submesoscale eddies in the northwestern Pacific Ocean based on Argo data. *Journal of Geophysical Research: Oceans*, *122*(5), 3586–3598. https://doi.org/10.1002/2016JC012561

Li, J., & Roughan, M. (2023). Energetics of Eddy–Mean Flow Interactions in the East Australian Current System. https://doi.org/10.1175/JPO-D-22-0128.1

Liang, J.-H., McWilliams, J. C., Kurian, J., Colas, F., Wang, P., & Uchiyama, Y. (2012). Mesoscale variability in the northeastern tropical Pacific: Forcing mechanisms and eddy properties. *Journal of Geophysical Research: Oceans*, *117*(C7). https://doi.org/10.1029/2012JC008008

Liu, M., & Tanhua, T. (2021). Water masses in the Atlantic Ocean: Characteristics and distributions. *Ocean Science*, *17*(2), 463–486. https://doi.org/10.5194/os-17-463-2021

Löscher, C. R., Fischer, M. A., Neulinger, S. C., Fiedler, B., Philippi, M., Schütte, F., Singh, A., Hauss, H., Karstensen, J., Körtzinger, A., Künzel, S., & Schmitz, R. A. (2015). Hidden biosphere in an oxygen-deficient Atlantic open-ocean eddy: Future implications

of ocean deoxygenation on primary production in the eastern tropical North Atlantic. *Biogeosciences*, *12*(24), 7467–7482. https://doi.org/10.5194/bg-12-7467-2015

Lovecchio, E., Gruber, N., & Münnich, M. (2018). Mesoscale contribution to the long-range offshore transport of organic carbon from the Canary Upwelling System to the open North Atlantic. *Biogeosciences*, *15*(16), 5061–5091. https://doi.org/10.5194/bg-15-5061-2018

Lovecchio, E., Gruber, N., Münnich, M., & Frenger, I. (2022). On the processes sustaining biological production in the offshore propagating eddies of the northern Canary Upwelling System. *Journal of Geophysical Research: Oceans*, 1–39. https://doi.org/10.1029/2021JC017691

Lovecchio, E., Gruber, N., Münnich, M., & Lachkar, Z. (2017). On the long-range offshore transport of organic carbon from the Canary Upwelling System to the open North Atlantic. *Biogeosciences*, *14*(13), 3337–3369. https://doi.org/10.5194/bg-14-3337-2017

Low, N. H. N., Micheli, F., Aguilar, J. D., Arce, D. R., Boch, C. A., Bonilla, J. C., Bracamontes, M. Á., De Leo, G., Diaz, E., Enríquez, E., Hernandez, A., Martinez, R., Mendoza, R., Miranda, C., Monismith, S., Ramade, M., Rogers-Bennett, L., Romero, A., Salinas, C., … Woodson, C. B. (2021). Variable coastal hypoxia exposure and drivers across the southern California Current. *Scientific Reports*, *11*(1), 10929. https://doi.org/10.1038/s41598-021-89928-4

Lozier, M. S. (2010). Deconstructing the Conveyor Belt. *Science*, *328*(5985), 1507–1511. https://doi.org/10.1126/science.1189250

Lozier, M. S., Owens, W. B., & Curry, R. G. (1995). The climatology of the North Atlantic. *Progress in Oceanography*, *36*(1), 1–44. https://doi.org/10.1016/0079-6611(95)00013-5

Lukas, R., & Santiago-Mandujano, F. (2001). Extreme water mass anomaly observed in the Hawaii ocean time-series. *Geophysical Research Letters*, *28*(15), 2931–2934. https://doi.org/10.1029/2001GL013099

Lumpkin, R., & Johnson, G. C. (2013). Global ocean surface velocities from drifters: Mean, variance, El Niño–Southern Oscillation response, and seasonal cycle. *Journal of Geophysical Research: Oceans*, *118*(6), 2992–3006. https://doi.org/10.1002/jgrc.20210

Luyten, J. R., Pedlosky, J., & Stommel, H. (1983). The Ventilated Thermocline. *Journal of Physical Oceanography*, *13*(2), 292–309. https://doi.org/10.1175/1520-0485(1983)013<0292:TVT>2.0.CO;2

Machu, E., Capet, X., Estrade, P. A., Ndoye, S., Brajard, J., Baurand, F., Auger, P. A., Lazar, A., & Brehmer, P. (2019). First Evidence of Anoxia and Nitrogen Loss in the Southern Canary Upwelling System. *Geophysical Research Letters*, *46*(5), 2619–2627. https://doi.org/10.1029/2018GL079622

Mackas, D. L., Denman, K. L., & Bennett, A. F. (1987). Least squares multiple tracer analysis of water mass composition. *Journal of Geophysical Research: Oceans*, *92*(C3), 2907–2918. https://doi.org/10.1029/JC092iC03p02907

Mahadevan, A., Thomas, L. N., & Tandon, A. (2008). Comment on ”Eddy/Wind Interactions Stimulate Extraordinary Mid-Ocean Plankton Blooms”. *Science*, *320*(5875), 448b–448b. https://doi.org/10.1126/science.1152111

Malan, N., Archer, M., Roughan, M., Cetina-Heredia, P., Hemming, M., Rocha, C., Schaeffer, A., Suthers, I., & Queiroz, E. (2020). Eddy-Driven Cross-Shelf Transport in the East Australian Current Separation Zone. *Journal of Geophysical Research: Oceans*, *125*(2), e2019JC015613. https://doi.org/10.1029/2019JC015613

Malan, N., Roughan, M., Hemming, M., & Schaeffer, A. (2023). Mesoscale Circulation Controls Chlorophyll Concentrations in the East Australian Current Separation Zone. *Journal of Geophysical Research: Oceans*, *128*(4), e2022JC019361. https://doi.org/10.1029/2022JC019361

Malan, N., Roughan, M., Stanley, G. J., Holmes, R., & Li, J. (2022). Quantifying Cross-Shelf Transport in the East Australian Current System: A Budget-Based Approach. *Journal of Physical Oceanography*, *52*(10), 2555–2572. https://doi.org/10.1175/JPO-D-21-0193.1

Mancini, A. M., Lozar, F., Gennari, R., Capozzi, R., Morigi, C., & Negri, A. (2024). The past to unravel the future: Deoxygenation events in the geological archive and the anthropocene oxygen crisis. *Earth-Science Reviews*, *249*, 104664. https://doi.org/10.1016/j.earscirev.2023.104664

Mansfield, K. L., Mendilaharsu, M. L., Putman, N. F., dei Marcovaldi, M. A. G., Sacco, A. E., Lopez, G., Pires, T., & Swimmer, Y. (2017). First satellite tracks of South Atlantic sea turtle ‘lost years’: Seasonal variation in trans-equatorial movement. *Proceedings of the Royal Society B: Biological Sciences*, *284*(1868), 20171730. https://doi.org/10.1098/rspb.2017.1730

Marchesiello, P., & Estrade, P. (2009). Eddy activity and mixing in upwelling systems: A comparative study of Northwest Africa and California regions. *International Journal of Earth Sciences*, *98*(2), 299–308. https://doi.org/10.1007/s00531-007-0235-6

Marchesiello, P., Debreu, L., & Couvelard, X. (2009). Spurious diapycnal mixing in terrain-following coordinate models: The problem and a solution. *Ocean Modelling*, *26*(3), 156–169. https://doi.org/10.1016/j.ocemod.2008.09.004

Marchesiello, P., McWilliams, J. C., & Shchepetkin, A. (2003). Equilibrium Structure and Dynamics of the California Current System.

Martin, A. P., & Richards, K. J. (2001). Mechanisms for vertical nutrient transport within a North Atlantic mesoscale eddy. *Deep Sea Research Part II: Topical Studies in Oceanography*, *48*(4-5), 757–773. https://doi.org/10.1016/S0967-0645(00)00096-5

Martínez-Marrero, A., Rodríguez-Santana, A., Hernández-Guerra, A., Fraile-Nuez, E., López-Laatzen, F., Vélez-Belchí, P., & Parrilla, G. (2008). Distribution of water masses and diapycnal mixing in the Cape Verde Frontal Zone. *Geophysical Research Letters*, *35*(7), 1–5. https://doi.org/10.1029/2008GL033229

Martinez-Rey, J., Bopp, L., Gehlen, M., Tagliabue, A., & Gruber, N. (2015). Projections of oceanic N_2O emissions in the 21st century using the IPSL Earth system model. *Biogeosciences*, *12*(13), 4133–4148. https://doi.org/10.5194/bg-12-4133-2015

Masuda, Y., Yamanaka, Y., Smith, S. L., Hirata, T., Nakano, H., Oka, A., & Sumata, H. (2021). Photoacclimation by phytoplankton determines the distribution of global subsurface chlorophyll maxima in the ocean. *Communications Earth & Environment*, *2*(1), 1–8. https://doi.org/10.1038/s43247-021-00201-y

Matear, R. J., & Hirst, A. C. (2003). Long-term changes in dissolved oxygen concentrations in the ocean caused by protracted global warming. *Global Biogeochemical Cycles*, *17*(4). https://doi.org/10.1029/2002GB001997

Maximenko, N. A., Bang, B., & Sasaki, H. (2005). Observational evidence of alternating zonal jets in the world ocean. *Geophysical Research Letters*, *32*(12), 1–4. https://doi.org/10.1029/2005GL022728

McCarthy, G. D., Haigh, I. D., Hirschi, J. J.-M., Grist, J. P., & Smeed, D. A. (2015). Ocean impact on decadal Atlantic climate variability revealed by sea-level observations. *Nature*, *521*(7553), 508–510. https://doi.org/10.1038/nature14491

McDowell, S. E., & Rossby, H. T. (1978). Mediterranean Water: An Intense Mesoscale Eddy off the Bahamas. *Science*, *202*(4372), 1085–1087. https://doi.org/10.1126/science.202.4372.1085

McGillicuddy, D. J., & Robinson, A. R. (1997). Eddy-induced nutrient supply and new production in the Sargasso Sea. *Deep Sea Research Part I: Oceanographic Research Papers*, *44*(8), 1427–1450. https://doi.org/10.1016/S0967-0637(97)00024-1

McGillicuddy, D. J. (2015). Formation of Intrathermocline Lenses by Eddy–Wind Interaction. *Journal of Physical Oceanography*, *45*(2), 606–612. https://doi.org/10.1175/JPO-D-14-0221.1

McGillicuddy, D. J. (2016). Mechanisms of Physical-Biological-Biogeochemical Interaction at the Oceanic Mesoscale. *Annual Review of Marine Science*, *8*(1), 125–159. https://doi.org/10.1146/annurev-marine-010814-015606

McGillicuddy, D. J., Anderson, L. A., Bates, N. R., Bibby, T., Buesseler, K. O., Carlson, C. A., Davis, C. S., Ewart, C., Falkowski, P. G., Goldthwait, S. A., Hansell, D. A., Jenkins, W. J., Johnson, R., Kosnyrev, V. K., Ledwell, J. R., Li, Q. P., Siegel, D. A., & Steinberg, D. K. (2007). Eddy/Wind Interactions Stimulate Extraordinary Mid-Ocean Plankton Blooms. *Science*, *316*(5827), 1021–1026. https://doi.org/10.1126/science.1136256

McWilliams, J. C. (1985). Submesoscale, coherent vortices in the ocean. *Reviews of Geophysics*, *23*(2), 165–182. https://doi.org/10.1029/RG023i002p00165

Messié, M., & Chavez, F. P. (2015). Seasonal regulation of primary production in eastern boundary upwelling systems. *Progress in Oceanography*, *134*, 1–18. https://doi.org/10.1016/j.pocean.2014.10.011

Messié, M., Ledesma, J., Kolber, D. D., Michisaki, R. P., Foley, D. G., & Chavez, F. P. (2009). Potential new production estimates in four eastern boundary upwelling ecosystems.

Progress in Oceanography, *83*(1-4), 151–158. https://doi.org/10.1016/j.pocean.2009.07.018

Meunier, T., Barton, E. D., Barreiro, B., & Torres, R. (2012). Upwelling filaments off Cap Blanc: Interaction of the NW African upwelling current and the Cape Verde frontal zone eddy field? *Journal of Geophysical Research: Oceans*, *117*(C8), n/a–n/a. https://doi.org/10.1029/2012JC007905

Middelburg, J. J., Soetaert, K., Herman, P. M. J., & Heip, C. H. R. (1996). Denitrification in marine sediments: A model study. *Global Biogeochemical Cycles*, *10*(4), 661–673. https://doi.org/10.1029/96GB02562

Mittelstaedt, E. (1976). On the currents along the Northwest African coast South of 22° North. *Deutsche Hydrografische Zeitschrift*, *29*(3), 97–117. https://doi.org/10.1007/BF02227058

Mittelstaedt, E. (1983). The upwelling area off Northwest Africa—A description of phenomena related to coastal upwelling. *Progress in Oceanography*, *12*(3), 307–331. https://doi.org/10.1016/0079-6611(83)90012-5

Mittelstaedt, E. (1991). The ocean boundary along the northwest African coast: Circulation and oceanographic properties at the sea surface. *Progress in Oceanography*, *26*(4), 307–355. https://doi.org/10.1016/0079-6611(91)90011-A

Miyake, Y., Tellier, M.-A., Takeshige, A., Itakura, H., Yoshida, A., & Kimura, S. (2020). Past and lost influence of the Kuroshio on estuarine recruitment of Anguilla japonica glass eels. *Journal of Oceanography*, *76*(4), 259–270. https://doi.org/10.1007/s10872-020-00543-9

Mkhinini, N., Coimbra, A. L. S., Stegner, A., Arsouze, T., Taupier-Letage, I., & Béranger, K. (2014). Long-lived mesoscale eddies in the eastern Mediterranean Sea: Analysis of 20 years of AVISO geostrophic velocities. *Journal of Geophysical Research: Oceans*, *119*(12), 8603–8626. https://doi.org/10.1002/2014JC010176

Mohrholz, V., Eggert, A., Junker, T., Nausch, G., Ohde, T., & Schmidt, M. (2014). Cross shelf hydrographic and hydrochemical conditions and their short term variability at the northern Benguela during a normal upwelling season. *Journal of Marine Systems*, *140*, 92–110. https://doi.org/10.1016/j.jmarsys.2014.04.019

Molemaker, M. J., Mcwilliams, J. C., & Dewar, W. K. (2015). Submesoscale instability and generation of mesoscale anticyclones near a separation of the California undercurrent. *Journal of Physical Oceanography*, *45*(3), 613–629. https://doi.org/10.1175/JPO-D-13-0225.1

Monod, J. (1942). Diauxie et respiration au cours de la croissance des cultures de b. coli. *Annales de L'Institut Pasteur*, *68*, 548–550.

Monteiro, P. M. S., Dewitte, B., Scranton, M. I., Paulmier, A., & van der Plas, A. K. (2011). The role of open ocean boundary forcing on seasonal to decadal-scale variability and long-term change of natural shelf hypoxia. *Environmental Research Letters*, *6*(2), 025002. https://doi.org/10.1088/1748-9326/6/2/025002

Monteiro, P. M. S., van der Plas, A., Mohrholz, V., Mabille, E., Pascall, A., & Joubert, W. (2006). Variability of natural hypoxia and methane in a coastal upwelling system: Oceanic

physics or shelf biology? *Geophysical Research Letters*, *33*(16). https://doi.org/10.1029/2006GL026234

Monteiro, P. M. S., Van Der Plas, A., Mélice, J.-L., & Florenchie, P. (2008). Interannual hypoxia variability in a coastal upwelling system: Ocean–shelf exchange, climate and ecosystem-state implications. *Deep Sea Research Part I: Oceanographic Research Papers*, *55*(4), 435–450. https://doi.org/10.1016/j.dsr.2007.12.010

Moore, T. S., Matear, R. J., Marra, J., & Clementson, L. (2007). Phytoplankton variability off the Western Australian Coast: Mesoscale eddies and their role in cross-shelf exchange. *Deep Sea Research Part II: Topical Studies in Oceanography*, *54*(8), 943–960. https://doi.org/10.1016/j.dsr2.2007.02.006

Morales, C. E., Hormazabal, S., Correa-Ramirez, M., Pizarro, O., Silva, N., Fernandez, C., Anabalón, V., & Torreblanca, M. L. (2012). Mesoscale variability and nutrient–phytoplankton distributions off central-southern Chile during the upwelling season: The influence of mesoscale eddies. *Progress in Oceanography*, *104*, 17–29. https://doi.org/10.1016/j.pocean.2012.04.015

Morel, A. (1988). Optical modeling of the upper ocean in relation to its biogenous matter content (case I waters). *Journal of Geophysical Research: Oceans*, *93*(C9), 10749–10768. https://doi.org/10.1029/JC093iC09p10749

Moriarty, J. M., Harris, C. K., Friedrichs, M. A. M., Fennel, K., & Xu, K. (2018). Impact of Seabed Resuspension on Oxygen and Nitrogen Dynamics in the Northern Gulf of Mexico: A Numerical Modeling Study. *Journal of Geophysical Research: Oceans*, *123*(10), 7237–7263. https://doi.org/10.1029/2018JC013950

Morrow, R. (2004). Divergent pathways of cyclonic and anti-cyclonic ocean eddies. *Geophysical Research Letters*, *31*(24), L24311. https://doi.org/10.1029/2004GL020974

Morrow, R., & Le Traon, P. Y. (2012). Recent advances in observing mesoscale ocean dynamics with satellite altimetry. *Advances in Space Research*, *50*(8), 1062–1076. https://doi.org/10.1016/j.asr.2011.09.033

Moschos, E., Barboni, A., & Stegner, A. (2021). Why do inverse eddy surface temperature anomalies emerge ? The case of the Mediterranean Sea, 1–32. https://doi.org/10.1002/essoar.10509053.1

Mouriño-Carballido, B., & McGillicuddy, D. J. (2006). Mesoscale variability in the metabolic balance of the Sargasso Sea. *Limnology and Oceanography*, *51*(6), 2675–2689. https://doi.org/10.4319/lo.2006.51.6.2675

Nagai, T., Gruber, N., Frenzel, H., Lachkar, Z., McWilliams, J. C., & Plattner, G.-K. (2015a). Dominant role of eddies and filaments in the offshore transport of carbon and nutrients in the California Current System. *Journal of Geophysical Research: Oceans*, *120*(8), 5318–5341. https://doi.org/10.1002/2015JC010889

Nagai, T., Gruber, N., Frenzel, H., Lachkar, Z., McWilliams, J. C., & Plattner, G.-K. (2015b). Dominant role of eddies and filaments in the offshore transport of carbon and nutrients

in the California Current System. *Journal of Geophysical Research: Oceans*, *120*(8), 5318–5341. https://doi.org/10.1002/2015JC010889

Nakano, H., Matsunaga, H., Okamoto, H., & Okazaki, M. (2003). Acoustic tracking of bigeye thresher shark Alopias superciliosus in the eastern Pacific Ocean. *Marine Ecology Progress Series*, *265*, 255–261. https://doi.org/10.3354/meps265255

Napolitano, D. C., da Silveira, I. C. A., Tandon, A., & Calil, P. H. R. (2021). Submesoscale Phenomena Due to the Brazil Current Crossing of the Vitória-Trindade Ridge. *Journal of Geophysical Research: Oceans*, *126*(1), e2020JC016731. https://doi.org/10.1029/2020JC016731

Ndoye, S., Capet, X., Estrade, P., Sow, B., Dagorne, D., Lazar, A., Gaye, A., & Brehmer, P. (2014). SST patterns and dynamics of the southern Senegal-Gambia upwelling center. *Journal of Geophysical Research: Oceans*, *119*(12), 8315–8335. https://doi.org/10.1002/2014JC010242

Ndoye, S., Capet, X., Estrade, P., Sow, B., Machu, E., Brochier, T., Döring, J., & Brehmer, P. (2017). Dynamics of a "low-enrichment high-retention" upwelling center over the southern Senegal shelf. *Geophysical Research Letters*, *44*(10), 5034–5043. https://doi.org/10.1002/2017GL072789

Nykjær, L., & Van Camp, L. (1994). Seasonal and interannual variability of coastal upwelling along northwest Africa and Portugal from 1981 to 1991. *Journal of Geophysical Research*, *99*(C7), 14197. https://doi.org/10.1029/94JC00814

Ohde, T., & Siegel, H. (2010). Biological response to coastal upwelling and dust deposition in the area off Northwest Africa. *Continental Shelf Research*, *30*(9), 1108–1119. https://doi.org/10.1016/j.csr.2010.02.016

Ohde, T., Fiedler, B., & Körtzinger, A. (2015). Spatio-temporal distribution and transport of particulate matter in the eastern tropical North Atlantic observed by Argo floats. *Deep Sea Research Part I: Oceanographic Research Papers*, *102*, 26–42. https://doi.org/10.1016/j.dsr.2015.04.007

Oke, P. R., Roughan, M., Cetina-Heredia, P., Pilo, G. S., Ridgway, K. R., Rykova, T., Archer, M. R., Coleman, R. C., Kerry, C. G., Rocha, C., Schaeffer, A., & Vitarelli, E. (2019). Revisiting the circulation of the East Australian Current: Its path, separation, and eddy field. *Progress in Oceanography*, *176*, 102139. https://doi.org/10.1016/j.pocean.2019.102139

Okubo, A. (1970). Horizontal dispersion of floatable particles in the vicnity of velocity singularies such as convergences. *Deep-sea Res.*, *17*(445-454), 445–454. https://doi.org/10.1016/0011-7471(70)90059-8

Oliver, K. I. C., Eldevik, T., Stevens, D. P., & Watson, A. J. (2008). A Greenland Sea Perspective on the Dynamics of Postconvective Eddies. https://doi.org/10.1175/2008JPO3844.1

Ollitrault, M., Lankhorst, M., Fratantoni, D., Richardson, P., & Zenk, W. (2006). Zonal intermediate currents in the equatorial Atlantic Ocean. *Geophysical Research Letters*, *33*(5). https://doi.org/10.1029/2005GL025368

Oschlies, A., Brandt, P., Stramma, L., & Schmidtko, S. (2018). Drivers and mechanisms of ocean deoxygenation. *Nature Geoscience*, *11*(7), 467–473. https://doi.org/10.1038/s41561-018-0152-2

Oschlies, A., Schulz, K. G., Riebesell, U., & Schmittner, A. (2008). Simulated 21st century's increase in oceanic suboxia by CO2-enhanced biotic carbon export. *Global Biogeochemical Cycles*, *22*(4). https://doi.org/10.1029/2007GB003147

Ould-Dedah, S., Wiseman, W. J., & Shaw, R. F. (1999). Spatial and temporal trends of sea surface temperature in the northwest African region. *Oceanologica Acta*, *22*(3), 265–279. https://doi.org/10.1016/S0399-1784(99)80051-6

Paillet, J., Cann, B. L., Carton, X., Morel, Y., & Serpette, A. (2002). Dynamics and Evolution of a Northern Meddy.

Pantoja, D. A., Marinone, S. G., Parés-Sierra, A., & Gómez-Valdivia, F. (2012). Numerical modeling of seasonal and mesoscale hydrography and circulation in the Mexican Central Pacific. *Ciencias Marinas*, *38*(2), 363–379. https://doi.org/10.7773/cm.v38i2.2007

Pares-Sierra, A., White, W. B., & Tai, C.-K. (1993). Wind-driven Coastal Generation of Annual Mesoscale Eddy Activity in the California Current.

Pastor, M. V., Palter, J. B., Pelegrí, J. L., & Dunne, J. P. (2013). Physical drivers of interannual chlorophyll variability in the eastern subtropical North Atlantic. *Journal of Geophysical Research: Oceans*, *118*(8), 3871–3886. https://doi.org/10.1002/jgrc.20254

Pastor, M. V., Peña-Izquierdo, J., Pelegrí, J., & Marrero-Díaz, Á. (2011). Meridional changes in water mass distributions off NW Africa during November 2007/2008. *Ciencias Marinas*, *38*(1B), 223–244. https://doi.org/10.7773/cm.v38i1B.1831

Pastor, M. V., Pelegrí, J. L., Hernández-Guerra, A., Font, J., Salat, J., & Emelianov, M. (2008). Water and nutrient fluxes off Northwest Africa. *Continental Shelf Research*, *28*(7), 915–936. https://doi.org/10.1016/j.csr.2008.01.011

Pattiaratchi, C., James, A., & Collins, M. (1987). Island wakes and headland eddies: A comparison between remotely sensed data and laboratory experiments. *Journal of Geophysical Research*, *92*(C1), 783. https://doi.org/10.1029/JC092iC01p00783

Paulmier, A., & Ruiz-Pino, D. (2009). Oxygen minimum zones (OMZs) in the modern ocean. *Progress in Oceanography*, *80*(3), 113–128. https://doi.org/10.1016/j.pocean.2008.08.001

Pegliasco, C., Chaigneau, A., & Morrow, R. (2015). Main eddy vertical structures observed in the four major Eastern Boundary Upwelling Systems. *Journal of Geophysical Research: Oceans*, *120*(9), 6008–6033. https://doi.org/10.1002/2015JC010950

Pelegrí, J. L., Marrero-Díaz, A., & Ratsimandresey, A. (2006). Nutrient irrigation of the North Atlantic. *Progress in Oceanography*, *70*(2-4), 366–406. https://doi.org/10.1016/j.pocean.2006.03.018

Pelegrí, J. L., & Peña-Izquierdo, J. (2015). Inorganic nutrients and dissolved oxygen in the Canary Current Large Marine Ecosystem. In L. Valdés & I. Déniz-González (Eds.), *Oceanographic and biological features in the Canary Current Large Marine Ecosystem* (pp. 133–142, Vol. 115). IOC-UNESCO, Paris.

Peliz, Á., Dubert, J., Haidvogel, D. B., & Le Cann, B. (2003). Generation and unstable evolution of a density-driven Eastern Poleward Current: The Iberian Poleward Current. *Journal of Geophysical Research*, *108*(C8), 3268. https://doi.org/10.1029/2002JC001443

Peliz, Á., Dubert, J., & Haidvogel, D. B. (2003). Subinertial Response of a Density-Driven Eastern Boundary Poleward Current to Wind Forcing. https://doi.org/10.1175/2415.1

Peña-Izquierdo, J., Pelegrí, J. L., Pastor, M. V., Castellanos, P., Emelianov, M., Gasser, M., Salvador, J., & Vázquez-Domínguez, E. (2012). The continental slope current system between Cape Verde and the Canary Islands. *Scientia Marina*, *76*(S1), 65–78. https://doi.org/10.3989/scimar.03607.18C

Peña-Izquierdo, J., van Sebille, E., Pelegrí, J. L., Sprintall, J., Mason, E., Llanillo, P. J., & Machín, F. (2015). Water mass pathways to the North Atlantic oxygen minimum zone. *Journal of Geophysical Research: Oceans*, *120*(5), 3350–3372. https://doi.org/10.1002/2014JC010557

Peterson, J. O., Morgan, C. A., Peterson, W. T., & Lorenzo, E. D. (2013). Seasonal and interannual variation in the extent of hypoxia in the northern California Current from 1998–2012. *Limnology and Oceanography*, *58*(6), 2279–2292. https://doi.org/10.4319/lo.2013.58.6.2279

Peterson, R. G., & Stramma, L. (1991). Upper-level circulation in the South Atlantic Ocean. *Progress in Oceanography*, *26*(1), 1–73. https://doi.org/10.1016/0079-6611(91)90006-8

Pfannkuche, O. (2014). Climate-biogeochemistry interactions in the tropical ocean of the nw-african oxygen minimum zone $SFB754$ - cruise no. msm17/4 - march 10 - april 11, 2011 - dakar $Senegal$ - las palmas $Spain$, maria s. merian-berichte. https://doi.org/10.2312/cr_msm17_4

Pickett, M. H., & Paduan, J. D. (2003). Ekman transport and pumping in the California Current based on the U.S. Navy's high-resolution atmospheric model (COAMPS). *Journal of Geophysical Research: Oceans*, *108*(C10). https://doi.org/10.1029/2003JC001902

Pietri, A., & Karstensen, J. (2018). Dynamical Characterization of a Low Oxygen Submesoscale Coherent Vortex in the Eastern North Atlantic Ocean. *Journal of Geophysical Research: Oceans*, *123*(3), 2049–2065. https://doi.org/10.1002/2017JC013177

Pingree, R., & Le Cann, B. (1992). Three anticyclonic slope water oceanic eDDIES (SWODDIES) in the Southern Bay of Biscay in 1990. *Deep Sea Research Part A. Oceanographic Research Papers*, *39*(7-8), 1147–1175. https://doi.org/10.1016/0198-0149(92)90062-X

Pitcher, G. C., Aguirre-Velarde, A., Breitburg, D., Cardich, J., Carstensen, J., Conley, D. J., Dewitte, B., Engel, A., Espinoza-Morriberón, D., Flores, G., Garçon, V., Graco, M., Grégoire, M., Gutiérrez, D., Hernandez-Ayon, J. M., Huang, H. H. M., Isensee, K., Jacinto, M. E., Levin, L., … Zhu, Z. Y. (2021). System controls of coastal and open ocean oxygen depletion. *Progress in Oceanography*, *197*(May 2020). https://doi.org/10.1016/j.pocean.2021.102613

Polo, I., Lazar, A., Rodriguez-Fonseca, B., & Arnault, S. (2008). Oceanic Kelvin waves and tropical Atlantic intraseasonal variability: 1. Kelvin wave characterization. *Journal of Geophysical Research: Oceans*, *113*(C7). https://doi.org/10.1029/2007JC004495

Poole, R., & Tomczak, M. (1999). Optimum multiparameter analysis of the water mass structure in the Atlantic Ocean thermocline. *Deep Sea Research Part I: Oceanographic Research Papers*, *46*(11), 1895–1921. https://doi.org/10.1016/S0967-0637(99)00025-4

Pörtner, H.-O., Karl, D. M., Boyd, P. W., Cheung, W., Lluch-Cota, S. E., Nojiri, Y., Schmidt, D. N., Zavialov, P. O., Alheit, J., Aristegui, J., et al. (2014). Ocean systems. In *Climate change 2014: Impacts, adaptation, and vulnerability. part a: Global and sectoral aspects. contribution of working group ii to the fifth assessment report of the intergovernmental panel on climate change* (pp. 411–484). Cambridge University Press.

Pradhan, Y., Lavender, S. J., Hardman-Mountford, N. J., & Aiken, J. (2006). Seasonal and inter-annual variability of chlorophyll-a concentration in the Mauritanian upwelling: Observation of an anomalous event during 1998–1999. *Deep Sea Research Part II: Topical Studies in Oceanography*, *53*(14-16), 1548–1559. https://doi.org/10.1016/j.dsr2.2006.05.016

Qiu, B., Rudnick, D. L., Chen, S., & Kashino, Y. (2013). Quasi-stationary North Equatorial Undercurrent jets across the tropical North Pacific Ocean. *Geophysical Research Letters*, *40*(10), 2183–2187. https://doi.org/10.1002/grl.50394

Rabalais, N. N., Turner, R. E., & Jr, W. J. W. (2002). Gulf of Mexico Hypoxia, A.K.A. "The Dead Zone". *Annual Review of Ecology, Evolution, and Systematics*, *33*(Volume 33, 2002), 235–263. https://doi.org/10.1146/annurev.ecolsys.33.010802.150513

Reagan, J. R., Boyer, T. P., García, H. E., Locarnini, R. A., Baranova, O. K., Bouchard, C., Cross, S. L., Mishonov, A. V., Paver, C. R., Seidov, D., Wang, Z., & Dukhovskoy, D. (2023). *World ocean atlas 2023 (ncei accession 0270533)* [Accessed on 29 Nov 2024]. NOAA National Centers for Environmental Information. https://doi.org/10.25921/va26-hv25

Redfield, A. C. (1942). *The processes determining the concentration of oxygen, phosphate and other organic derivatives within the depths of the Atlantic Ocean*. Massachusetts Institute of Technology and Woods Hole Oceanographic Institution. https://doi.org/10.1575/1912/1053

Relvas, P., Barton, E. D., Dubert, J., Oliveira, P. B., Peliz, Á., da Silva, J. C. B., & Santos, A. M. P. (2007). Physical oceanography of the western Iberia ecosystem: Latest views and challenges. *Progress in Oceanography*, *74*(2-3), 149–173. https://doi.org/10.1016/j.pocean.2007.04.021

Renault, L., Marchesiello, P., Masson, S., & McWilliams, J. C. (2019). Remarkable Control of Western Boundary Currents by *Eddy Killing* , a Mechanical Air-Sea Coupling Process. *Geophysical Research Letters*, *46*(5), 2743–2751. https://doi.org/10.1029/2018GL081211

Resplandy, L., Lévy, M., Bopp, L., Echevin, V., Pous, S., Sarma, V. V. S. S., & Kumar, D. (2012). Controlling factors of the oxygen balance in the Arabian Sea's OMZ. *Biogeosciences*, *9*(12), 5095–5109. https://doi.org/10.5194/bg-9-5095-2012

Richardson, P. L., Price, J. F., Walsh, D., Armi, L., & Schröder, M. (1989). Tracking Three Meddies with SOFAR Floats.

Richardson, P. L. (1983). Eddy kinetic energy in the North Atlantic from surface drifters. *Journal of Geophysical Research*, *88*(C7), 4355. https://doi.org/10.1029/JC088iC07p04355

Richardson, P., McCartney, M., & Maillard, C. (1991). A search for meddies in historical data. *Dynamics of Atmospheres and Oceans*, *15*(3-5), 241–265. https://doi.org/10.1016/0377-0265(91)90022-8

Ridder, N. N., & England, M. H. (2014). Sensitivity of ocean oxygenation to variations in tropical zonal wind stress magnitude. *Global Biogeochemical Cycles*, *28*(9), 909–926. https://doi.org/10.1002/2013GB004708

Ridgway, K. R., Dunn, J. R., & Wilkin, J. L. (2002). Ocean interpolation by four-dimensional weighted least squares - Application to the waters around Australasia. *Journal of Atmospheric and Oceanic Technology*, *19*(9), 1357–1375. https://doi.org/10.1175/1520-0426(2002)019<1357:OIBFDW>2.0.CO;2

Robison, B. H. (2009). Conservation of Deep Pelagic Biodiversity. *Conservation Biology*, *23*(4), 847–858. https://doi.org/10.1111/j.1523-1739.2009.01219.x

Roemmich, D., & Gilson, J. (2009). The 2004–2008 mean and annual cycle of temperature, salinity, and steric height in the global ocean from the Argo Program. *Progress in Oceanography*, *82*(2), 81–100. https://doi.org/10.1016/j.pocean.2009.03.004

Romero, O. E., Fischer, G., Karstensen, J., & Cermeño, P. (2016). Eddies as trigger for diatom productivity in the open-ocean Northeast Atlantic. *Progress in Oceanography*, *147*, 38–48. https://doi.org/10.1016/j.pocean.2016.07.011

Rosell-Fieschi, M., Pelegrí, J. L., & Gourrion, J. (2015). Zonal jets in the equatorial Atlantic Ocean. *Progress in Oceanography*, *130*, 1–18. https://doi.org/10.1016/j.pocean.2014.08.008

Ruhland, G. (2005). *Report and preliminary results of poseidon cruise 320 (pos320), las palmas (spain) - las palmas (spain), march 08th - march 18th, 2005* (Cruise Report) (PANGAEA reference ID: 27624). Bremen, Germany. http://publications.marum.de/46/

Sale, J. W., & Skinner, W. W. (1917). The vertical distribution of dissolved oxygen and the precipitation by salt water in certain tidal areas. *Journal of the Franklin Institute*, *184*(6), 837–848. https://doi.org/10.1016/S0016-0032(17)90519-8

Samuel, C.-L., Norma Yolanda, H.-S., Salvador Emilio, L.-C., Pedro, C.-H., Felipe De Jesús, A.-V., & María Teresa, S. (2019). Survival and respiration of green abalone (*Haliotis fulgens*) facing very short-term marine environmental extremes. *Marine and Freshwater Behaviour and Physiology*, *52*(1), 1–15. https://doi.org/10.1080/10236244.2019.1607734

Sangrà, P., Pascual, A., Rodríguez-Santana, Á., Machín, F., Mason, E., McWilliams, J. C., Pelegrí, J. L., Dong, C., Rubio, A., Arístegui, J., Marrero-Díaz, Á., Hernández-Guerra, A., Martínez-Marrero, A., & Auladell, M. (2009). The Canary Eddy Corridor: A major pathway for long-lived eddies in the subtropical North Atlantic. *Deep Sea Research Part I: Oceanographic Research Papers*, *56*(12), 2100–2114. https://doi.org/10.1016/j.dsr.2009.08.008

Sarmiento, J. L., Hughes, T. M. C., Stouffer, R. J., & Manabe, S. (1998). Simulated response of the ocean carbon cycle to anthropogenic climate warming. *Nature*, *393*(6682), 245–249. https://doi.org/10.1038/30455

Sasaki, H., Klein, P., Qiu, B., & Sasai, Y. (2014). Impact of oceanic-scale interactions on the seasonal modulation of ocean dynamics by the atmosphere. *Nature Communications*, *5*(1), 5636. https://doi.org/10.1038/ncomms6636

Schafstall, J., Dengler, M., Brandt, P., & Bange, H. (2010). Tidal-induced mixing and diapycnal nutrient fluxes in the Mauritanian upwelling region. *Journal of Geophysical Research: Oceans*, *115*(C10). https://doi.org/10.1029/2009JC005940

Schmidt, M., & Eggert, A. (2016). Oxygen cycling in the northern Benguela Upwelling System: Modelling oxygen sources and sinks. *Progress in Oceanography*, *149*, 145–173. https://doi.org/10.1016/j.pocean.2016.09.004

Schmidtko, S., Stramma, L., & Visbeck, M. (2017). Decline in global oceanic oxygen content during the past five decades. *Nature*, *542*(7641), 335–339. https://doi.org/10.1038/nature21399

Schmitz Jr., W. J. (1995). On the interbasin-scale thermohaline circulation. *Reviews of Geophysics*, *33*(2), 151–173. https://doi.org/10.1029/95RG00879

Schroller-Lomnitz, U., Hensen, C., Dale, A., Scholz, F., Clemens, D., Sommer, S., Noffke, A., & Wallmann, K. (2019). Dissolved benthic phosphate, iron and carbon fluxes in the Mauritanian upwelling system and implications for ongoing deoxygenation. *Deep Sea Research Part I: Oceanographic Research Papers*, *143*, 70–84. https://doi.org/10.1016/j.dsr.2018.11.008

Schulz, H. N., & Schulz, H. D. (2005). Large Sulfur Bacteria and the Formation of Phosphorite. *Science*, *307*(5708), 416–418. https://doi.org/10.1126/science.1103096

Schütte, F., Brandt, P., & Karstensen, J. (2016). Occurrence and characteristics of mesoscale eddies in the tropical northeastern Atlantic Ocean. *Ocean Science*, *12*(3), 663–685. https://doi.org/10.5194/os-12-663-2016

Schütte, F., Karstensen, J., Krahmann, G., Hauss, H., Fiedler, B., Brandt, P., Visbeck, M., & Körtzinger, A. (2016). Characterization of "dead-zone" eddies in the eastern tropical North Atlantic. *Biogeosciences*, *13*(20), 5865–5881. https://doi.org/10.5194/bg-13-5865-2016

Seibel, B. A. (2011). Critical oxygen levels and metabolic suppression in oceanic oxygen minimum zones. *Journal of Experimental Biology*, *214*(2), 326–336. https://doi.org/10.1242/jeb.049171

Send, U., & Nam, S. (2012). Relaxation from upwelling: The effect on dissolved oxygen on the continental shelf. *Journal of Geophysical Research: Oceans*, *117*(C4). https://doi.org/10.1029/2011JC007517

Senjyu, T., Ishimaru, T., Matsuyama, M., & Koike, Y. (1998). High salinity lens from the strait of hormuz. *Offshore environment of the ROPME Sea area after the war-related oil spill*, 35–48.

Sharp, J. D., Fassbender, A. J., Carter, B. R., Johnson, G. C., Schultz, C., & Dunne, J. P. (2023). GOBAI-O_2: Temporally and spatially resolved fields of ocean interior dissolved oxygen over nearly 2 decades. *Earth System Science Data*, *15*(10), 4481–4518. https://doi.org/10.5194/essd-15-4481-2023

Shchepetkin, A. F., & McWilliams, J. C. (2003). A method for computing horizontal pressure-gradient force in an oceanic model with a nonaligned vertical coordinate. *Journal of Geophysical Research: Oceans*, *108*(C3), 2001JC001047. https://doi.org/10.1029/2001JC001047

Shchepetkin, A. F., & McWilliams, J. C. (2005). The regional oceanic modeling system (ROMS): A split-explicit, free-surface, topography-following-coordinate oceanic model. *Ocean Modelling*, *9*(4), 347–404. https://doi.org/10.1016/j.ocemod.2004.08.002

Shchepetkin, A. F., & McWilliams, J. C. (2009, January). Computational Kernel Algorithms for Fine-Scale, Multiprocess, Longtime Oceanic Simulations. In R. M. Temam & J. J. Tribbia (Eds.), *Handbook of Numerical Analysis* (pp. 121–183, Vol. 14). Elsevier. https://doi.org/10.1016/S1570-8659(08)01202-0

Siedlecki, S. A., Banas, N. S., Davis, K. A., Giddings, S., Hickey, B. M., MacCready, P., Connolly, T., & Geier, S. (2015). Seasonal and interannual oxygen variability on the Washington and Oregon continental shelves. *Journal of Geophysical Research: Oceans*, *120*(2), 608–633. https://doi.org/10.1002/2014JC010254

Siedler, G., Zangenberg, N., Onken, R., & Morlière, A. (1992). Seasonal changes in the tropical Atlantic circulation: Observation and simulation of the Guinea Dome. *Journal of Geophysical Research*, *97*(C1), 703. https://doi.org/10.1029/91JC02501

Siegel, D. A., McGillicuddy Jr., D. J., & Fields, E. A. (1999). Mesoscale eddies, satellite altimetry, and new production in the Sargasso Sea. *Journal of Geophysical Research: Oceans*, *104*(C6), 13359–13379. https://doi.org/10.1029/1999JC900051

Silva-Fernandes, S. M., & Peliz, A. J. (2020). The Turbulent Structure of the Azores Current System: A Statistical Analysis. *Journal of Geophysical Research: Oceans*, *125*(11), 1–19. https://doi.org/10.1029/2020JC016327

Soares, P. M. M., Lima, D. C. A., Semedo, Á., Cardoso, R. M., Cabos, W., & Sein, D. (2019). The North African coastal low level wind jet: A high resolution view. *Climate Dynamics*, *53*(1), 1211–1230. https://doi.org/10.1007/s00382-018-4441-7

Sokoll, S., Lavik, G., Sommer, S., Goldhammer, T., Kuypers, M. M. M., & Holtappels, M. (2016). Extensive nitrogen loss from permeable sediments off North-West Africa. *Journal of Geophysical Research: Biogeosciences*, *121*(4), 1144–1157. https://doi.org/10.1002/2015JG003298

Sommer, S., & Dale, A. W. (Eds.). (2021). Benthic work during METEOR cruise M107. https://doi.org/10.1594/PANGAEA.928206

Sommer, S., Dengler, M., & Treude, T. (2015). Benthic element cycling, fluxes and transport of solutes across the benthic boundary layer in the mauritanian oxygen minimum zone,

(sfb754) - cruise no. m107, may 30 - july 03, 2014, fortaleza (brazil) - las palmas (spain). https://doi.org/doi:10.2312/cr_m107

Sommer, S., Türk, M., Kriwanek, S., & Pfannkuche, O. (2008). Gas exchange system for extended in situ benthic chamber flux measurements under controlled oxygen conditions: First application—Sea bed methane emission measurements at Captain Arutyunov mud volcano. *Limnology and Oceanography: Methods*, *6*(1), 23–33. https://doi.org/10.4319/lom.2008.6.23

Song, Y., & Haidvogel, D. (1994). A Semi-implicit Ocean Circulation Model Using a Generalized Topography-Following Coordinate System. *Journal of Computational Physics*, *115*(1), 228–244. https://doi.org/10.1006/jcph.1994.1189

Sprintall, J., & Tomczak, M. (1993). On the formation of central water and thermocline ventilation in the southern hemisphere. *Deep Sea Research Part I: Oceanographic Research Papers*, *40*(4), 827–848. https://doi.org/10.1016/0967-0637(93)90074-D

Stammer, D., & Wunsch, C. (1999). Temporal changes in eddy energy of the oceans. *Deep Sea Research Part II: Topical Studies in Oceanography*, *46*(1-2), 77–108. https://doi.org/10.1016/S0967-0645(98)00106-4

Stegner, A., Le Vu, B., Dumas, F., Ghannami, M. A., Nicolle, A., Durand, C., & Faugere, Y. (2021). Cyclone-Anticyclone Asymmetry of Eddy Detection on Gridded Altimetry Product in the Mediterranean Sea. *Journal of Geophysical Research: Oceans*, *126*(9). https://doi.org/10.1029/2021jc017475

Stewart, A. L., Wang, Y., Solodoch, A., Chen, R., & McWilliams, J. C. (2024). Formation of Eastern Boundary Undercurrents via Mesoscale Eddy Rectification. https://doi.org/10.1175/JPO-D-23-0196.1

Stoer, A. C., Takeshita, Y., Maurer, T. L., Begouen Demeaux, C., Bittig, H. C., Boss, E., Claustre, H., Dall'Olmo, G., Gordon, C., Greenan, B. J. W., Johnson, K. S., Organelli, E., Sauzède, R., Schmechtig, C. M., & Fennel, K. (2023). A census of quality-controlled Biogeochemical-Argo float measurements. *Frontiers in Marine Science*, *10*. https://doi.org/10.3389/fmars.2023.1233289

Stramma, L., Czeschel, R., Tanhua, T., Brandt, P., Visbeck, M., & Giese, B. S. (2016). The flow field of the upper hypoxic eastern tropical North Atlantic oxygen minimum zone. *Ocean Science*, *12*(1), 153–167. https://doi.org/10.5194/os-12-153-2016

Stramma, L., Oschlies, A., & Schmidtko, S. (2012). Mismatch between observed and modeled trends in dissolved upper-ocean oxygen over the last 50 yr. *Biogeosciences*, *9*(10), 4045–4057. https://doi.org/10.5194/bg-9-4045-2012

Stramma, L., Brandt, P., Schafstall, J., Schott, F., Fischer, J., & Körtzinger, A. (2008). Oxygen minimum zone in the North Atlantic south and east of the Cape Verde Islands. *Journal of Geophysical Research: Oceans*, *113*(C4). https://doi.org/10.1029/2007JC004369

Stramma, L., Hüttl, S., & Schafstall, J. (2005). Water masses and currents in the upper tropical northeast Atlantic off northwest Africa. *Journal of Geophysical Research*, *110*(C12), C12006. https://doi.org/10.1029/2005JC002939

Stramma, L., Johnson, G. C., Sprintall, J., & Mohrholz, V. (2008). Expanding Oxygen-Minimum Zones in the Tropical Oceans. *Science*, *320*(5876), 655–658. https://doi.org/10.1126/science.1153847

Stramma, L., Prince, E. D., Schmidtko, S., Luo, J., Hoolihan, J. P., Visbeck, M., Wallace, D. W. R., Brandt, P., & Körtzinger, A. (2012). Expansion of oxygen minimum zones may reduce available habitat for tropical pelagic fishes. *Nature Climate Change*, *2*(1), 33–37. https://doi.org/10.1038/nclimate1304

Stramma, L., & Schmidtko, S. (2021). Spatial and Temporal Variability of Oceanic Oxygen Changes and Underlying Trends. *Atmosphere-Ocean*, *59*(2), 122–132. https://doi.org/10.1080/07055900.2021.1905601

Stramma, L., Schmidtko, S., Levin, L. A., & Johnson, G. C. (2010). Ocean oxygen minima expansions and their biological impacts. *Deep-Sea Research Part I: Oceanographic Research Papers*, *57*(4), 587–595. https://doi.org/10.1016/j.dsr.2010.01.005

Stramma, L., & Schott, F. (1999). The mean flow field of the tropical Atlantic Ocean. *Deep Sea Research Part II: Topical Studies in Oceanography*, *46*(1-2), 279–303. https://doi.org/10.1016/S0967-0645(98)00109-X

Stramma, L., & Siedler, G. (1988). Seasonal changes in the North Atlantic subtropical gyre. *Journal of Geophysical Research*, *93*(C7), 8111. https://doi.org/10.1029/JC093iC07p08111

Stramma, L., Weller, R. A., Czeschel, R., & Bigorre, S. (2014). Eddies and an extreme water mass anomaly observed in the eastern south Pacific at the Stratus mooring. *Journal of Geophysical Research: Oceans*, *119*(2), 1068–1083. https://doi.org/10.1002/2013JC009470

Strub, P. T., Combes, V., Shillington, F. A., & Pizarro, O. (2013). *Currents and processes along the eastern boundaries* (Vol. 103). Elsevier Ltd. https://doi.org/10.1016/B978-0-12-391851-2.00014-3

Strub, P. T., Kosro, P. M., & Huyer, A. (1991). The nature of the cold filaments in the California Current system. *Journal of Geophysical Research*, *96*(C8), 14743. https://doi.org/10.1029/91JC01024

Sunda, W. G., & Huntsman, S. A. (1997). Interrelated influence of iron, light and cell size on marine phytoplankton growth. *Nature*, *390*(6658), 389–392. https://doi.org/10.1038/37093

Sverdrup, H. U., Johnson, M. W., Fleming, R. H., et al. (1942). *The oceans: Their physics, chemistry, and general biology* (Vol. 1087). Prentice-Hall New York.

Sweeney, E. N., McGillicuddy, D. J., & Buesseler, K. O. (2003). Biogeochemical impacts due to mesoscale eddy activity in the Sargasso Sea as measured at the Bermuda Atlantic Time-series Study (BATS). *Deep Sea Research Part II: Topical Studies in Oceanography*, *50*(22-26), 3017–3039. https://doi.org/10.1016/j.dsr2.2003.07.008

Sylla, A., Mignot, J., Capet, X., & Gaye, A. T. (2019). Weakening of the Senegalo–Mauritanian upwelling system under climate change. *Climate Dynamics*, *53*(7), 4447–4473. https://doi.org/10.1007/s00382-019-04797-y

Tagliabue, A., Bopp, L., & Aumont, O. (2009). Evaluating the importance of atmospheric and sedimentary iron sources to Southern Ocean biogeochemistry. *Geophysical Research Letters*, *36*(13). https://doi.org/10.1029/2009GL038914

Tall, A. W., Machu, E., Echevin, V., Capet, X., Pietri, A., Corréa, K., Sall, S. M., & Lazar, A. (2021). Variability of Dissolved Oxygen in the Bottom Layer of the Southern Senegalese Shelf. *Journal of Geophysical Research: Oceans*, *126*(5), 1–27. https://doi.org/10.1029/2020JC016854

Tall, A. W., Echevin, V., Capet, X., & Machu, E. (2025). Variability of bottom dissolved oxygen on the southern Senegalese shelf at intraseasonal to interannual time scales using a modelling approach. *Deep Sea Research Part II: Topical Studies in Oceanography*, *221*, 105464. https://doi.org/10.1016/j.dsr2.2025.105464

Talley, L. D., Pickard, G. L., & Emery, W. J. (Eds.). (2011). *Descriptive physical oceanography: An introduction* (6th ed). Academic Press.

Tanhua, T. (2014). Oxygen supply tracer release experiment (ostre) cruise no. m97. https://doi.org/10.2312/cr_m97

Tanhua, T., & Liu, M. (2015). Upwelling velocity and ventilation in the Mauritanian upwelling system estimated by CFC-12 and SF6 observations. *Journal of Marine Systems*, *151*, 57–70. https://doi.org/10.1016/j.jmarsys.2015.07.002

Tegen, I., & Fung, I. (1995). Contribution to the atmospheric mineral aerosol load from land surface modification. *Journal of Geophysical Research: Atmospheres*, *100*(D9), 18707–18726. https://doi.org/10.1029/95JD02051

Teles-Machado, A., Peliz, Á., McWilliams, J. C., Couvelard, X., & Ambar, I. (2016). Circulation on the Northwestern Iberian Margin: Vertical structure and seasonality of the alongshore flows. *Progress in Oceanography*, *140*, 134–153. https://doi.org/10.1016/j.pocean.2015.05.021

Teles-Machado, A., Peliz, Á., McWilliams, J. C., Dubert, J., & Cann, B. L. (2016). Circulation on the Northwestern Iberian Margin: Swoddies. *Progress in Oceanography*, *140*, 116–133. https://doi.org/10.1016/j.pocean.2015.09.011

Thomas, L. N. (2005). Destruction of potential vorticity by winds. *Journal of Physical Oceanography*, *35*(12), 2457–2466. https://doi.org/10.1175/JPO2830.1

Thomas, L. N. (2008). Formation of intrathermocline eddies at ocean fronts by wind-driven destruction of potential vorticity. *Dynamics of Atmospheres and Oceans*, *45*(3-4), 252–273. https://doi.org/10.1016/j.dynatmoce.2008.02.002

Thomas, L. N., Taylor, J. R., Ferrari, R., & Joyce, T. M. (2013). Symmetric instability in the Gulf Stream. *Deep Sea Research Part II: Topical Studies in Oceanography*, *91*, 96–110. https://doi.org/10.1016/j.dsr2.2013.02.025

Thomsen, S., Capet, X., & Echevin, V. (2021). Competition between baroclinic instability and Ekman transport under varying buoyancy forcings in upwelling systems: An idealized analog to the Southern Ocean. *Journal of Physical Oceanography*, 3347–3364. https://doi.org/10.1175/jpo-d-20-0294.1

Thomsen, S., Kanzow, T., Krahmann, G., Greatbatch, R. J., Dengler, M., & Lavik, G. (2016). The formation of a subsurface anticyclonic eddy in the Peru-Chile Undercurrent and its impact on the near-coastal salinity, oxygen, and nutrient distributions. *Journal of Geophysical Research: Oceans*, *121*(1), 476–501. https://doi.org/10.1002/2015JC010878

Thomsen, S., Karstensen, J., Kiko, R., Krahmann, G., Dengler, M., & Engel, A. (2019). Remote and local drivers of oxygen and nitrate variability in the shallow oxygen minimum zone off Mauritania in June 2014. *Biogeosciences*, *16*(5), 979–998. https://doi.org/10.5194/bg-16-979-2019

Thouvenin-Masson, C., Boutin, J., Échevin, V., Lazar, A., & Vergely, J.-L. (2024). Influence of river runoff and precipitation on the seasonal and interannual variability of sea surface salinity in the eastern North Tropical Atlantic. *Ocean Science*, *20*(6), 1547–1566. https://doi.org/10.5194/os-20-1547-2024

Tilstone, G. H., Angel-Benavides, I. M., Pradhan, Y., Shutler, J. D., Groom, S., & Sathyendranath, S. (2011). An assessment of chlorophyll-a algorithms available for SeaWiFS in coastal and open areas of the Bay of Bengal and Arabian Sea. *Remote Sensing of Environment*, *115*(9), 2277–2291. https://doi.org/10.1016/j.rse.2011.04.028

Todd, R. E., Chavez, F. P., Clayton, S., Cravatte, S., Goes, M., Graco, M., Lin, X., Sprintall, J., Zilberman, N. V., Archer, M., Arístegui, J., Balmaseda, M., Bane, J. M., Baringer, M. O., Barth, J. A., Beal, L. M., Brandt, P., Calil, P. H. R., Campos, E., … Zhang, L. (2019). Global Perspectives on Observing Ocean Boundary Current Systems. *Frontiers in Marine Science*, *6*. https://doi.org/10.3389/fmars.2019.00423

Todd, R. E., Owens, W. B., & Rudnick, D. L. (2016). Potential Vorticity Structure in the North Atlantic Western Boundary Current from Underwater Glider Observations. https://doi.org/10.1175/JPO-D-15-0112.1

Tomczak, M., & Godfrey, J. S. (1994). *Regional oceanography: An introduction* (1st ed). Pergamon.

Tomczak, M. (1981). An analysis of mixing in the frontal zone of South and North Atlantic Central Water off North-West Africa. *Progress in Oceanography*, *10*(3), 173–192. https://doi.org/10.1016/0079-6611(81)90011-2

Tomczak, M., & Large, D. G. B. (1989). Optimum multiparameter analysis of mixing in the thermocline of the eastern Indian Ocean. *Journal of Geophysical Research*, *94*(C11), 16141. https://doi.org/10.1029/JC094iC11p16141

Torres, R., Turner, D., Rutllant, J., Sobarzo, M., Antezana, T., & Gonzalez, H. E. (2002). CO2 outgassing off central Chile (31–30°S) and northern Chile (24–23°S) during austral summer 1997: The effect of wind intensity on the upwelling and ventilation of CO2-rich waters. *Deep Sea Research Part I: Oceanographic Research Papers*, *49*(8), 1413–1429. https://doi.org/10.1016/S0967-0637(02)00034-1

Tsuchiya, M. (1986). Thermostads and circulation in the upper layer of the Atlantic Ocean. *Progress in Oceanography*, *16*(4), 235–267. https://doi.org/10.1016/0079-6611(86)90040-6

Váldes, L., & Déniz-González, I. (2015). Introduction. In L. Váldes & I. Déniz-González (Eds.), *Oceanographic and biological features in the canary current large marine ecosystem* (pp. 115–383, Vol. 115). IOC-UNESCO.

Valiente, S., Fernández-Castro, B., Campanero, R., Marrero-Díaz, A., Rodríguez-Santana, A., Gelado-Cabellero, M., Nieto-Cid, M., Delgado-Huertas, A., Arístegui, J., & Álvarez-Salgado, X. (2021). Dissolved and suspended organic matter dynamics in the Cape Verde Frontal Zone (NW Africa). *Progress in Oceanography*, *201*(April 2021), 102727. https://doi.org/10.1016/j.pocean.2021.102727

Van Camp, L., Nykjaer, L., Mittelstaedt, E., & Schlittenhardt, P. (1991). Upwelling and boundary circulation off Northwest Africa as depicted by infrared and visible satellite observations. *Progress in Oceanography*, *26*(4), 357–402. https://doi.org/10.1016/0079-6611(91)90012-B

Vaquer-Sunyer, R., & Duarte, C. M. (2008). Thresholds of hypoxia for marine biodiversity. *Proceedings of the National Academy of Sciences*, *105*(40), 15452–15457. https://doi.org/10.1073/pnas.0803833105

Vázquez, R., Parras-Berrocal, I. M., Koseki, S., Cabos, W., Sein, D. V., & Izquierdo, A. (2023). Seasonality of coastal upwelling trends in the Mauritania-Senegalese region under RCP8.5 climate change scenario. *Science of The Total Environment*, *898*, 166391. https://doi.org/10.1016/j.scitotenv.2023.166391

Vedor, M., Queiroz, N., Mucientes, G., Couto, A., da Costa, I., Dos Santos, A., Vandeperre, F., Fontes, J., Afonso, P., Rosa, R., Humphries, N. E., & Sims, D. W. (2021). Climate-driven deoxygenation elevates fishing vulnerability for the ocean's widest ranging shark. *eLife*, *10*, 1–29. https://doi.org/10.7554/eLife.62508

Vélez□Belchí, P., González□Carballo, M., Pérez□Hernández, M. D., & Hernández□Guerra, A. (2015). Open ocean temperature and salinity trends in the canary current large marine ecosystem. In L. Valdés & I. Déniz□González (Eds.), *Oceanographic and biological features in the canary current large marine ecosystem* (pp. 299–308). IOC□UNESCO.

Visbeck, M. (2013). Tracer survey in the cape verde region cruise no. m83/1. https://doi.org/10.2312/cr_m83_1

Voituriez, B., & Chuchla, R. (1978). Influence of the Southern Atlantic Central Water on the distribution of salinity and oxygen in the northeast tropical Atlantic Ocean. *Deep Sea Research*, *25*(1), 107–117. https://doi.org/10.1016/S0146-6291(21)00009-6

Waite, A. M., Stemmann, L., Guidi, L., Calil, P. H. R., Hogg, A. M. C., Feng, M., Thompson, P. A., Picheral, M., & Gorsky, G. (2016). The wineglass effect shapes particle export to the deep ocean in mesoscale eddies. *Geophysical Research Letters*, *43*(18), 9791–9800. https://doi.org/10.1002/2015GL066463

Wang, X., Du, Y., Zhang, Y., Wang, T., Wang, M., & Jing, Z. (2023). Subsurface Anticyclonic Eddy Transited from Kuroshio Shedding Eddy in the Northern South China Sea. https://doi.org/10.1175/JPO-D-22-0106.1

Wang, Y., Chen, X., Han, G., Jin, P., & Yang, J. (2022). From 1/4° to 1/8°: Influence of Spatial Resolution on Eddy Detection Using Altimeter Data. *Remote Sensing*, *14*(1), 149. https://doi.org/10.3390/rs14010149

Wattenberg, H. (1938). Die verteilung des sauerstoffs im atlantischen ozean, wissenschaftliche ergebnisse der deutschen atlantischen expedition auf dem forschungs-und vermessungsschiff meteor 1925–1927, 9.1, edited by: Defant, a.

Westphal, H. (Ed.). (2007). Report and preliminary results of poseidon cruise 346 [pos346], macuma. las palmas (spain) - las palmas (spain), 28.12.2006 - 15.01.2007 [Printausgabe in der GEOMAR Bibliothek vorhanden - PANGAEA reference ID: 27921]. http://publications.marum.de/68/

Westphal, H., Beuck, L., Braun, S., Freiwald, A., Hanebuth, T., Hetzinger, S., Klicpera, A., Kudrass, H., Lantzsch, H., Lundälv, T., Vicens, G. M., Preto, N., von Reumont, J., Schilling, S., Taviani, M., & Wienberg, C. (2014). Phaeton - paleoceanographic and paleoclimatic record on the mauritanian shelf - cruise no. msm16/3 - october 13 - november 20, 2010 - bremerhaven $Germany$ - mindelo $CapVerde$, maria s. merian-berichte. https://doi.org/10.2312/cr_msm16_3

Whitney, F. A., Freeland, H. J., & Robert, M. (2007). Persistently declining oxygen levels in the interior waters of the eastern subarctic Pacific. *Progress in Oceanography*, *75*(2), 179–199. https://doi.org/10.1016/j.pocean.2007.08.007

Wilding, J. L. (1939). The Oxygen Threshold for Three Species of Fish. *Ecology*, *20*(2), 253–263. https://doi.org/10.2307/1930744

Wilson, C. (2016). Does the wind systematically energize or damp ocean eddies? *Geophysical Research Letters*, *43*(24), 12, 538–12, 542. https://doi.org/10.1002/2016GL072215

Wong, J., Münnich, M., & Gruber, N. (2024). Column-Compound Extremes in the Global Ocean. *AGU Advances*, *5*(3), e2023AV001059. https://doi.org/10.1029/2023AV001059

Wooster, W. S., Bakun, A., & McLain, D. R. (1976). The seasonal upwelling cycle along the eastern boundary of the North Atlantic. *Journal of Marine Research*, *34*(2).

Worley, S. J., Woodruff, S. D., Reynolds, R. W., Lubker, S. J., & Lott, N. (2005). ICOADS release 2.1 data and products. *International Journal of Climatology*, *25*(7), 823–842. https://doi.org/10.1002/joc.1166

Wright, J. J., Konwar, K. M., & Hallam, S. J. (2012). Microbial ecology of expanding oxygen minimum zones. *Nature Reviews Microbiology*, *10*(6), 381–394. https://doi.org/10.1038/nrmicro2778

Wyrtki, K. (1962). The oxygen minima in relation to ocean circulation. *Deep Sea Research and Oceanographic Abstracts*, *9*(1-2), 11–23. https://doi.org/10.1016/0011-7471(62)90243-7

Xu, C., Zhai, X., & Shang, X.-d. (2016). Work done by atmospheric winds on mesoscale ocean eddies. *Geophysical Research Letters*, *43*(23), 12, 174–12, 180. https://doi.org/10.1002/2016GL071275

Yücel, M., Beaton, A. D., Dengler, M., Mowlem, M. C., Sohl, F., & Sommer, S. (2015). Nitrate and Nitrite Variability at the Seafloor of an Oxygen Minimum Zone Revealed by a Novel

Microfluidic In-Situ Chemical Sensor. *PLOS ONE*, *10*(7), e0132785. https://doi.org/10.1371/journal.pone.0132785

Zamudio, L., Hurlburt, H. E., Metzger, E. J., & Tilburg, C. E. (2007). Tropical wave-induced oceanic eddies at Cabo Corrientes and the María Islands, Mexico. *Journal of Geophysical Research: Oceans*, *112*(C5). https://doi.org/10.1029/2006JC004018

Zenk, W., Klein, B., & Schroder, M. (1991). Cape Verde Frontal Zone. *Deep Sea Research Part A. Oceanographic Research Papers*, *38*, S505–S530. https://doi.org/10.1016/S0198-0149(12)80022-7

Zhang, D., McPhaden, M. J., & Johns, W. E. (2003). Observational Evidence for Flow between the Subtropical and Tropical Atlantic: The Atlantic Subtropical Cells*. *Journal of Physical Oceanography*, *33*(8), 1783–1797. https://doi.org/10.1175/2408.1

Zhang, Z., Miao, M., Qiu, B., Tian, J., Jing, Z., Chen, G., Chen, Z., & Zhao, W. (2024). Submesoscale Eddies Detected by SWOT and Moored Observations in the Northwestern Pacific. *Geophysical Research Letters*, *51*(15), e2024GL110000. https://doi.org/10.1029/2024GL110000

Zhu, R., Yang, H., Chen, Z., Jing, Z., Zhang, Z., Sun, B., & Wu, L. (2024). Topography-Generated Submesoscale Coherent Vortices in the Kuroshio–Oyashio Extension Region from High-Resolution Simulations. https://doi.org/10.1175/JPO-D-23-0072.1

Zhu, Z.-Y., Wu, H., Liu, S.-M., Wu, Y., Huang, D.-J., Zhang, J., & Zhang, G.-S. (2017). Hypoxia off the Changjiang (Yangtze River) estuary and in the adjacent East China Sea: Quantitative approaches to estimating the tidal impact and nutrient regeneration. *Marine Pollution Bulletin*, *125*(1), 103–114. https://doi.org/10.1016/j.marpolbul.2017.07.029

Zonneveld, K. A. F., Akeerath Mundanatt, A., Bolte, A., Eldering, D., de Visser, J.-D., Gottwald, J., Grotheer, H., Klann, M., Knoke, M., Koster, B., Kotzem, K., Pfeil, L., Roza, S. E. V., Ruhland, G., Seidel, M., Stuut, J.-B. W., Versteegh, G. J. M., & Alves, E. Q. (2021). Sinking particles, their production, transfer and preservation, cruise no. msm104, 18.11.2021 - 15.12.2021, emden *Germany* - las palmas *Spain*, maria s. merian-berichte. https://doi.org/10.48433/cr_msm104

Appendix A

Supplementary material

A.1 Supplement to Chapter 3

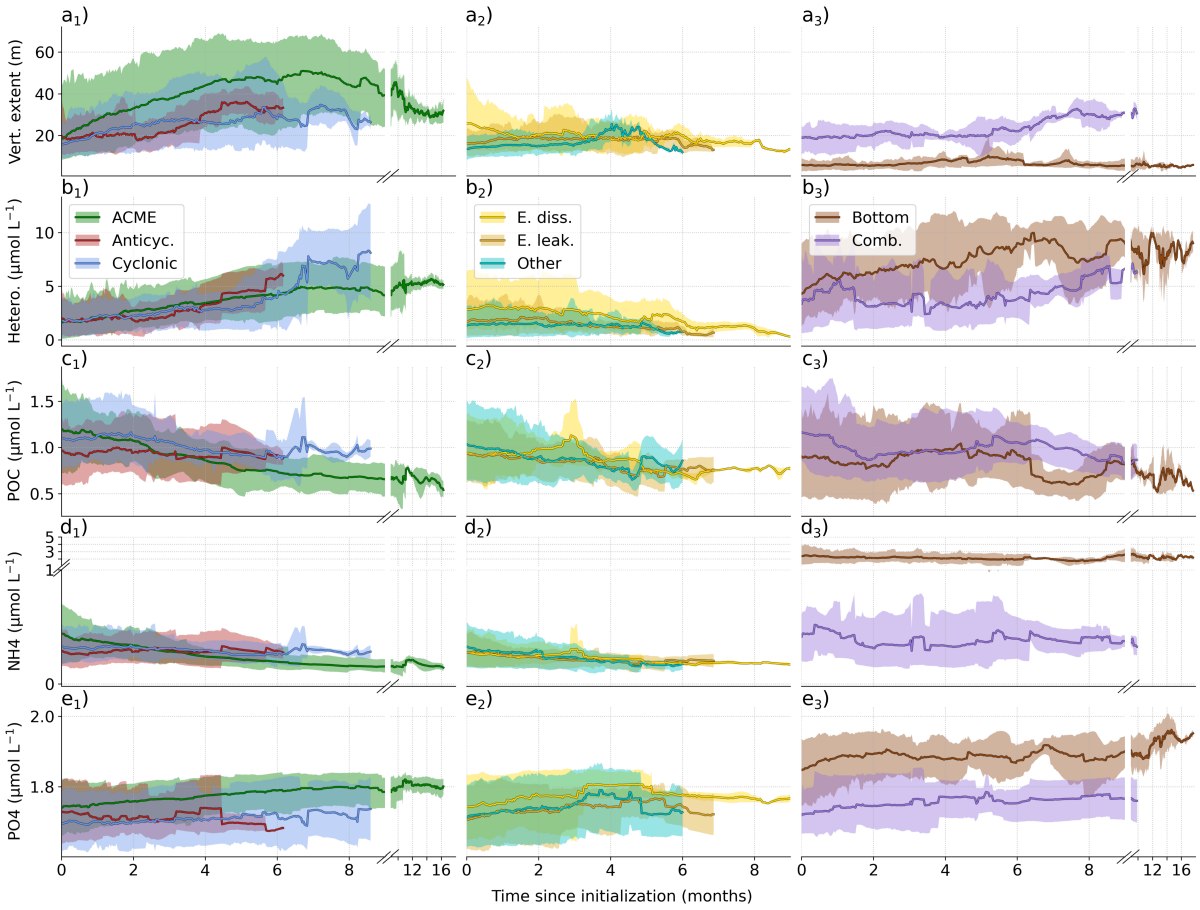


Figure A.1: Temporal evolution of complementary metrics per LHE category. Evolution is computed relative to the initiation date of each LHE. Solid lines and shaded areas represent the mean and the interquartile range between the 10th and 90th percentiles, respectively. Panels (c_{1-3}-e_{1-3}) refer to volume-weighted daily means. The horizontal axis is divided into two segments, with greater emphasis on the initial 9 months. Vertical axis is also split into two sections in (d_{1-3}) to enhance clarity.

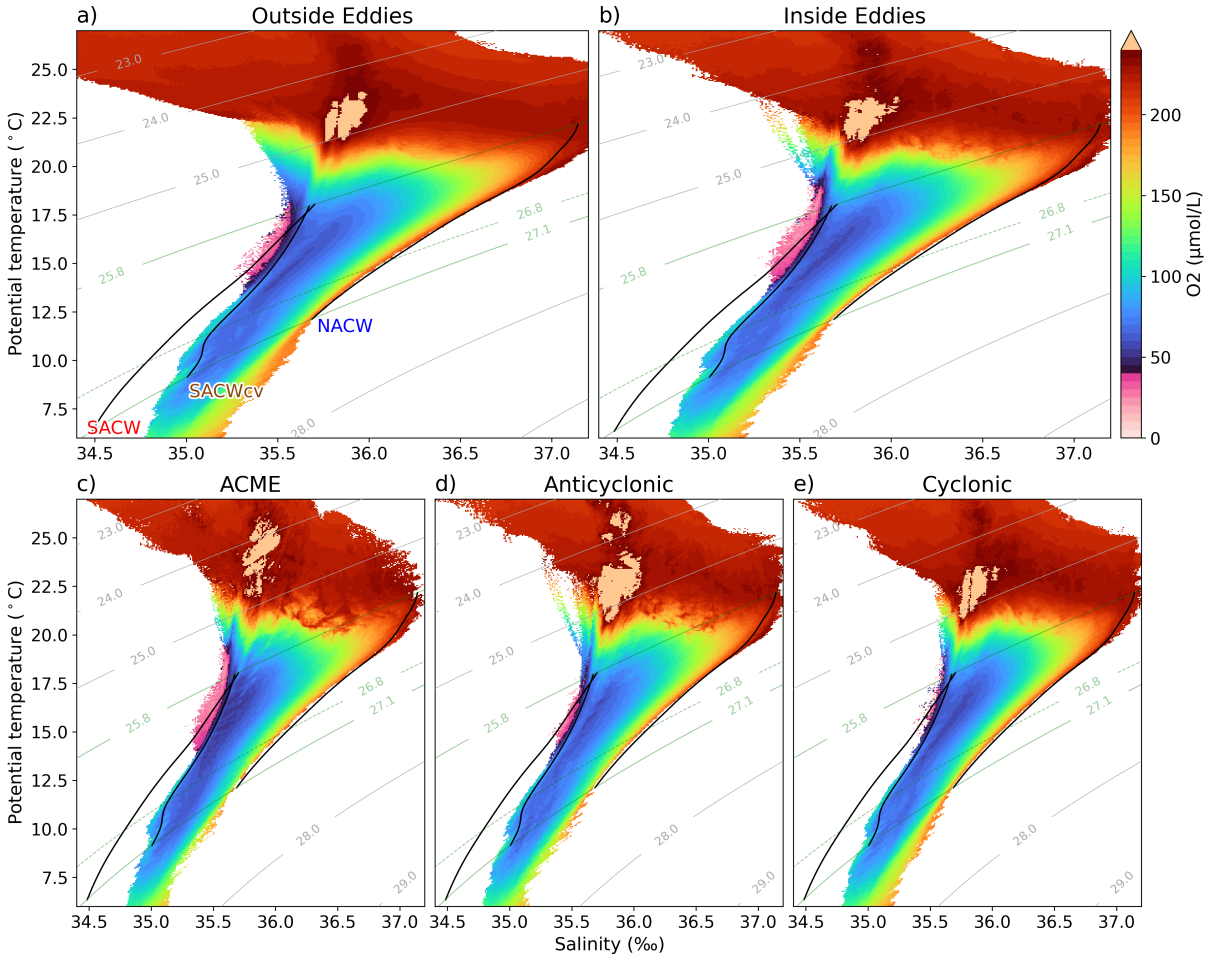


Figure A.2: θ-S histograms color-coded with volume-weighted average O_2 concentrations. Vertical profiles were taken in the region between 27° to 15°W and 10° to 22°N, with 2-day temporal resolution and 2× the original model horizontal resolution (≈6 km). Separate panels account for the profiles taken: (a) outside and (b) inside the perimeter of eddies; (c) ACME, (d) anticyclonic and (e) cyclonic eddies. Histograms have a resolution of 0.01 psu in the salinity field, and 0.1°C in the temperature field. Green contours at σ_θ 25.8 and 27.1 kg m^{-3} represent the upper and lower boundaries of the central water masses. Dashed red contour at σ_θ 26.8 kg m^{-3} represents the delimitation of the upper and lower central water masses.

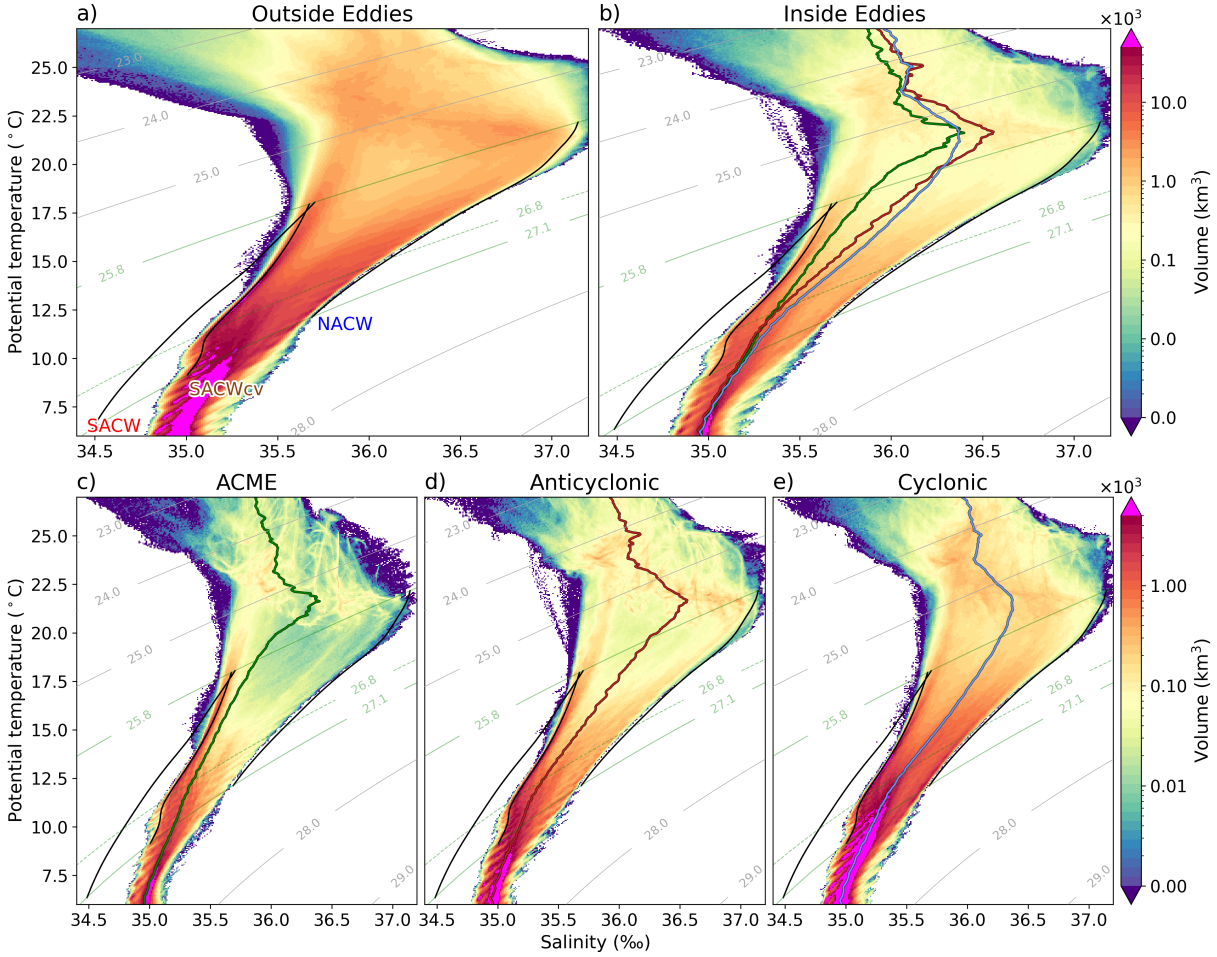


Figure A.3: θ-S histograms color-coded with the total volume. Vertical profiles were taken in the region between 27° to 15°W and 10° to 22°N, with 2-day temporal resolution and 2× the original model horizontal resolution (≈6 km). Separate panels account for the profiles taken: (a) outside and (b) inside the perimeter of eddies; (c) ACME, (d) anticyclonic and (e) cyclonic eddies. Green, red and blue θ-S in (b–e) represent the mean θ-S profiles of ACMEs, anticyclonic and cyclonic eddies, respectively. Histograms have a resolution of 0.01 psu in the salinity field, and 0.1°C in the temperature field. Green contours at σ_θ 25.8 and 27.1 kg m^{-3} represent the upper and lower boundaries of the central water masses. Dashed red contour at σ_θ 26.8 kg m^{-3} represents the delimitation of the upper and lower central water masses.

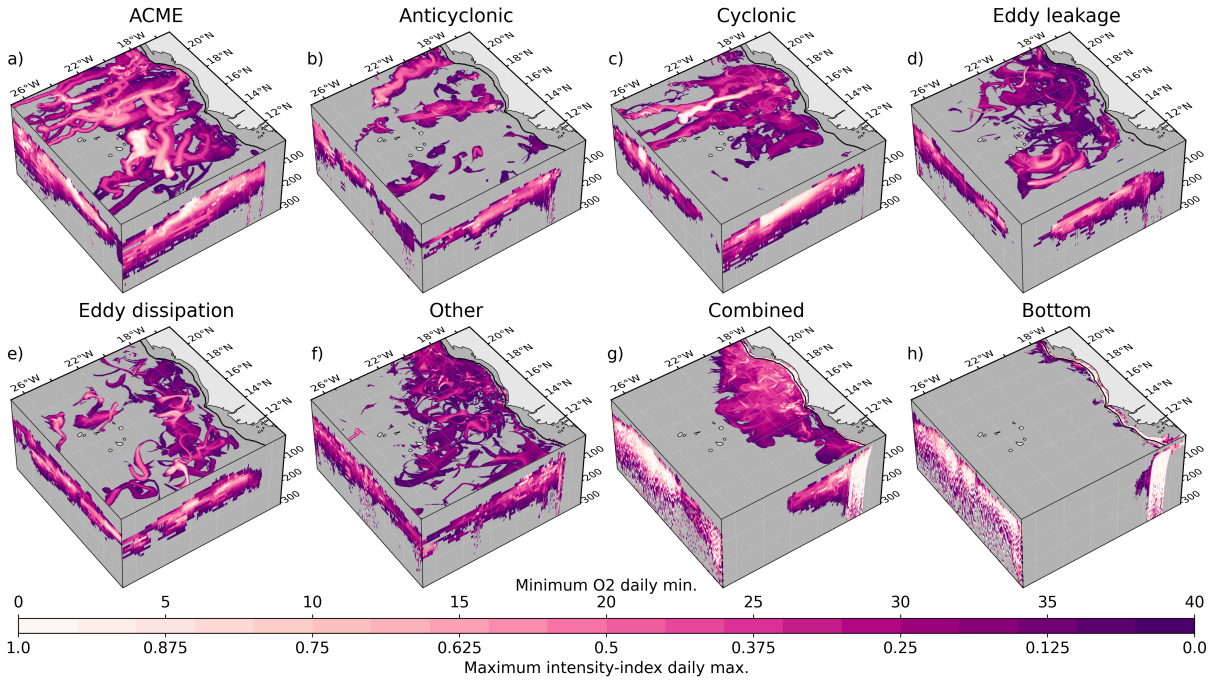


Figure A.4: Spatial distribution of minimum daily oxygen minimum per LHE category. Computation is made along depth (horizontal plane), zonal (meridional plane) and meridional (zonal plane) dimensions. Black think line parallel to the coastline represents the shelf break. Different color scales are used to illustrate relation between O_2 concentrations and intensity-index values.

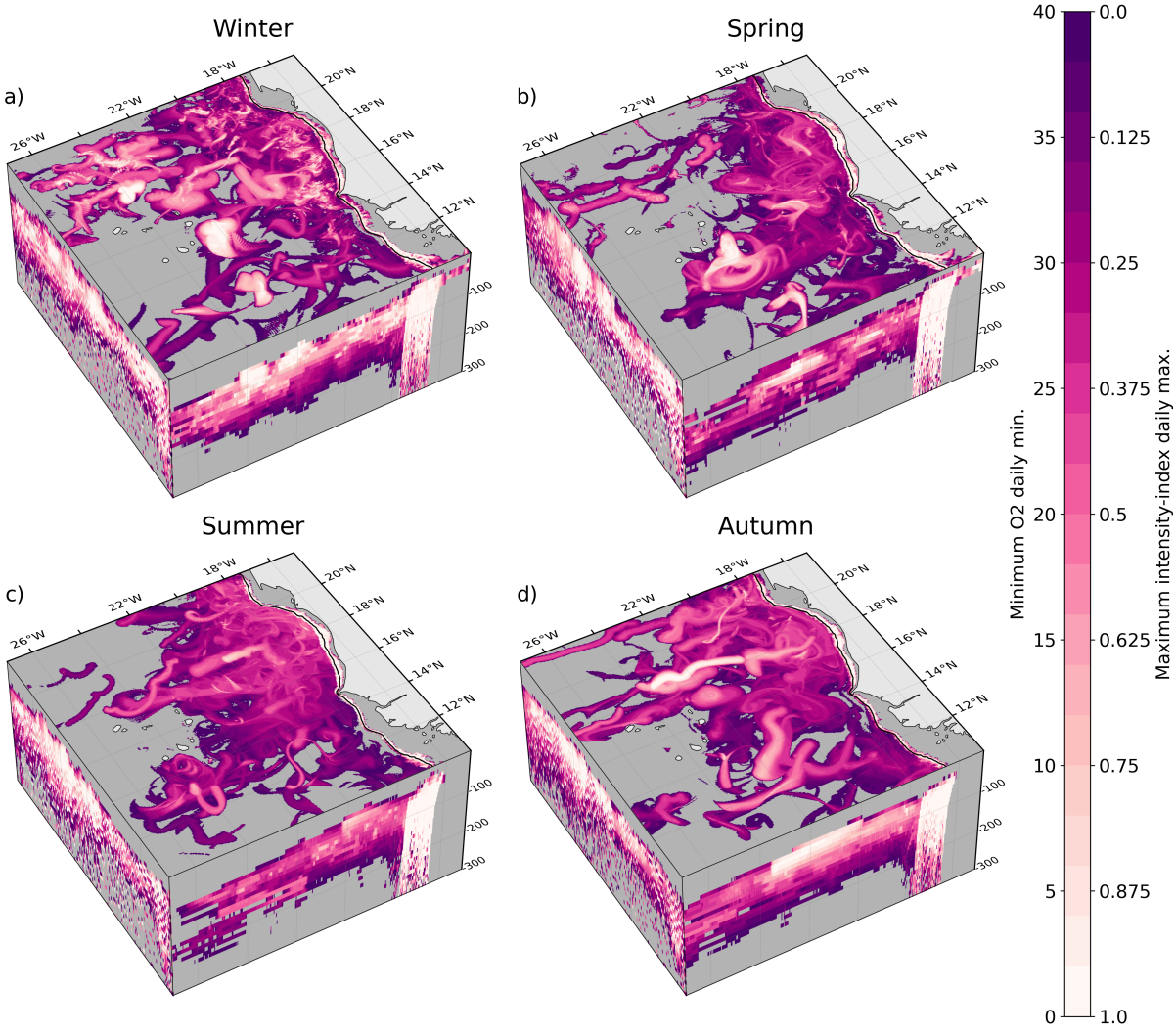


Figure A.5: Seasonal variability of minimum daily oxygen minimum within hypoxic events. Computation is made along depth (horizontal plane), zonal (meridional plane) and meridional (zonal plane) dimensions. Black think line parallel to the coastline represents the shelf break. Different scales in color bars are used to illustrate relation between O_2 concentrations and intensity-index.

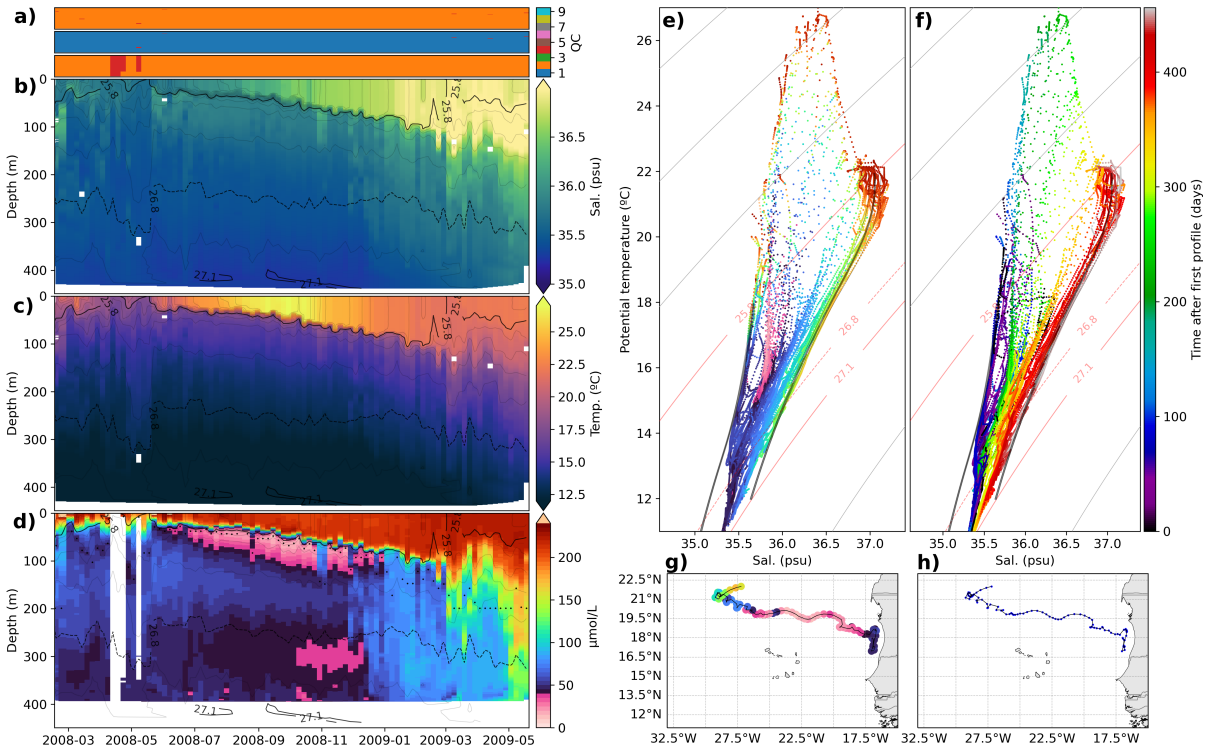


Figure A.6: Evolution of an Argo float trapped inside a cyclonic low-oxygen eddy. Argo float with id. 6900632 was used by Karstensen et al. (2015) to examine the evolution of oxygen concentrations and water mass characteristics within a low-oxygen cyclonic eddy. (a) Quality control (QC) flags for (b) temperature, (c) salinity, and (d) dissolved oxygen measurements. Isopycnals are shown as thick and thin contours in panels (a–d). Circular markers in (d) indicate the depth of minimum O_2 concentration in each profile. Only data with QC < 3 ("good" and "probably good") are shown. (e,f) θ-S diagrams colored by oxygen concentration and time since the first profile, respectively. (g,h) Maps showing the float trajectory and profile locations, with minimum O_2 concentrations indicated in panel (g).

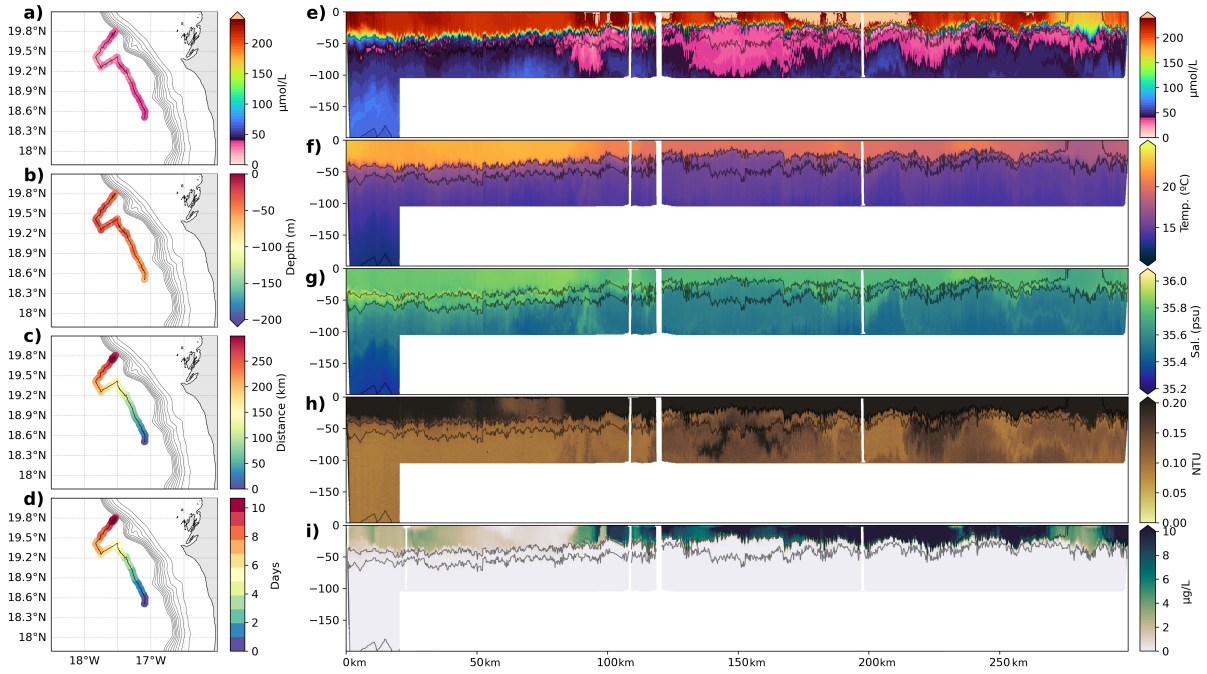


Figure A.7: Glider observations from the M107 campaign off the Mauritanian coast. Panels (a–d) show maps of the glider trajectory: (a) minimum O_2 concentration at each profile; (b) corresponding depth of the O_2 minimum; (c) cumulative distance from the first profile; and (d) time elapsed (in days) since the first profile. Panels (e–i) display vertical sections of key variables measured along depth and distance: (e) O_2 concentration; (f) temperature; (g) salinity; (h) turbidity (in Nephelometric Turbidity Units, NTU); and (i) Chl*a* concentrations. Black contours denote the 25.8 and 26.3 kg m^{-3} isopycnals. Data from Krahmann et al. (2017).

Table A.1: Summary statistics of LHEs for each category. Summary of temporal, structural, intensity, propagation, and biogeochemical characteristics of ACMEs, Anticyclones, Cyclones, "eddy leakage", "eddy dissipation", "other", "combined", and "bottom" LHEs. Metrics represent medians unless stated otherwise. Temporal metrics include event duration (median and maximum); structural metrics describe volume, area, and vertical extent; intensity metrics include daily and event-scale hypoxia indices; propagation metrics cover horizontal/vertical displacement and speed; and biogeochemical metrics include volume-weighted water mass composition, oxygen, nutrients, POC, PV, and mixed-layer (indicated with "@ML") POC and phytoplankton biomass. Daily and event-based metrics are denoted by superscripts ^{a} and ^{b}, respectively; "–" indicates missing values.

	ACME	Anticyclonic	Cyclonic	E. Leakage	E. Dissipation	Other	Combined	Bottom
a) Temporal metrics^{b} [median max.]								
Duration (days)	57 494	32.5 201	30 265	16 237	41.5 345	12 219	103.5 814	15 658
Local duration (days)	19 109	15 52	13 62	5.5 64	18 42	5 57	44.5 235	12.5 349
b) Structural metrics^{a}								
Daily volume (km^3)	64.44	14.38	25.58	9.52	18.16	3.73	274.51	6.68
Area (km^2)	1782.26	783.51	1286.34	606.74	906.63	291.06	12175.40	1247.22
Vertical extent (m)	35.55	18.54	18.29	16.16	19.05	13.67	24.00	5.48
Top depth (m)	-87.56	-91.74	-84.14	-96.37	-92.41	-98.24	-98.11	-132.79
Bottom depth (m)	-123.42	-115.90	-105.16	-114.38	-115.84	-113.27	-121.36	-138.83
Average depth (m)	-105.34	-104.60	-94.61	-106.00	-105.67	-105.76	-110.27	-148.09
c) Intensity metrics								
Daily intensity index^{a}	0.10	0.06	0.07	0.04	0.07	0.03	0.09	0.17
Event intensity index^{b}	0.30	0.30	0.30	0.30	0.30	0.30	0.31	0.37
Daily heterogeneity^{a}	0.07	0.04	0.05	0.03	0.04	0.02	0.09	0.15
Event heterogeneity^{b}	0.01	0.01	0.01	0.01	0.01	0.01	0.03	0.04
d) Propagation metrics^{b}								
Horizontal propagation	298.53	130.29	143.54	80.29	214.51	58.10	–	–
Vertical prop. (m)	-4.83	-0.55	0.41	-2.34	-2.34	-0.56	–	–
Horizontal speed (km d^{-1})	4.48	4.39	4.35	5.28	4.57	4.42	–	–
e) Biogeochemical characteristics^{a}								
%SACW	93.96	92.18	82.67	85.09	91.15	86.64	86.90	85.11
O_2 (µmol L^{-1})	35.92	37.47	37.32	38.22	37.22	38.62	36.36	33.01
NH_4 (µmol L^{-1})	0.24	0.25	0.28	0.23	0.22	0.24	0.34	2.05
NO_3 (µmol L^{-1})	28.23	28.01	27.93	28.07	28.35	28.04	27.93	25.30
PO_4 (µmol L^{-1})	1.78	1.68	1.68	1.74	1.78	1.73	1.72	1.89
POC (µmol L^{-1})	0.88	0.91	1.01	0.86	0.86	0.91	0.94	0.74
PV ($s^{-3} \times 10^{-9}$)	2.68	3.85	5.06	3.98	3.13	4.01	4.11	1.69
POC@ML (µmol C L^{-1})	0.69	1.26	0.50	0.48	0.33	1.00	1.36	1.38
Phytoplankton@ML (µmol C L^{-1})	1.91	2.56	1.68	1.44	0.92	2.74	3.91	4.47

A.2 Supplement to Chapter 4

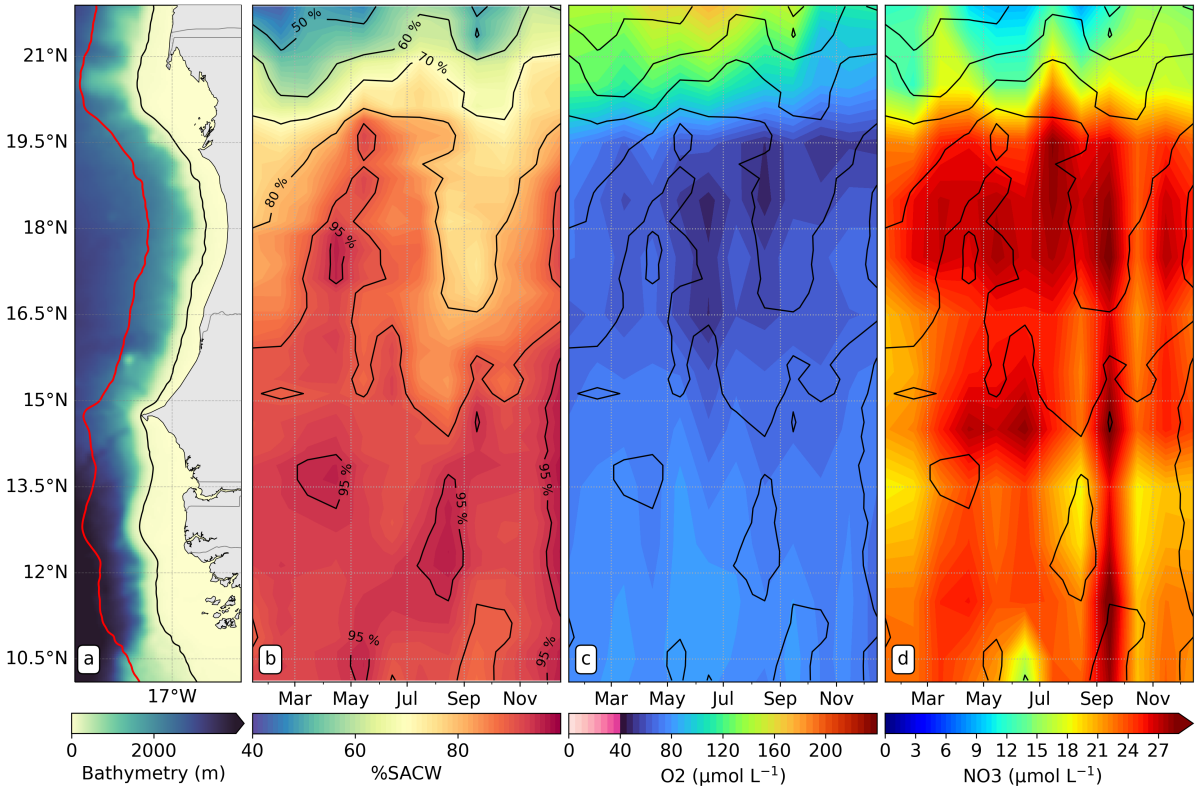


Figure A.8: Hovmöller diagrams for the meridional and temporal variability of physical and biogeochemical tracers along the coast (WOA23 data). Same as Figure 4.5, but for data from the WOA23 climatology. (b) Average proportion (%) of SACW relative to NACW between σ_θ 25.8 and 26.3 kg m^{-3} and longitude. (c,d) Average O_2 and NO_3 concentrations between 80 and 200 m depth and across longitude. Here we take into account data within a distance of 1° from the continental shelf due to coarser horizontal resolution.

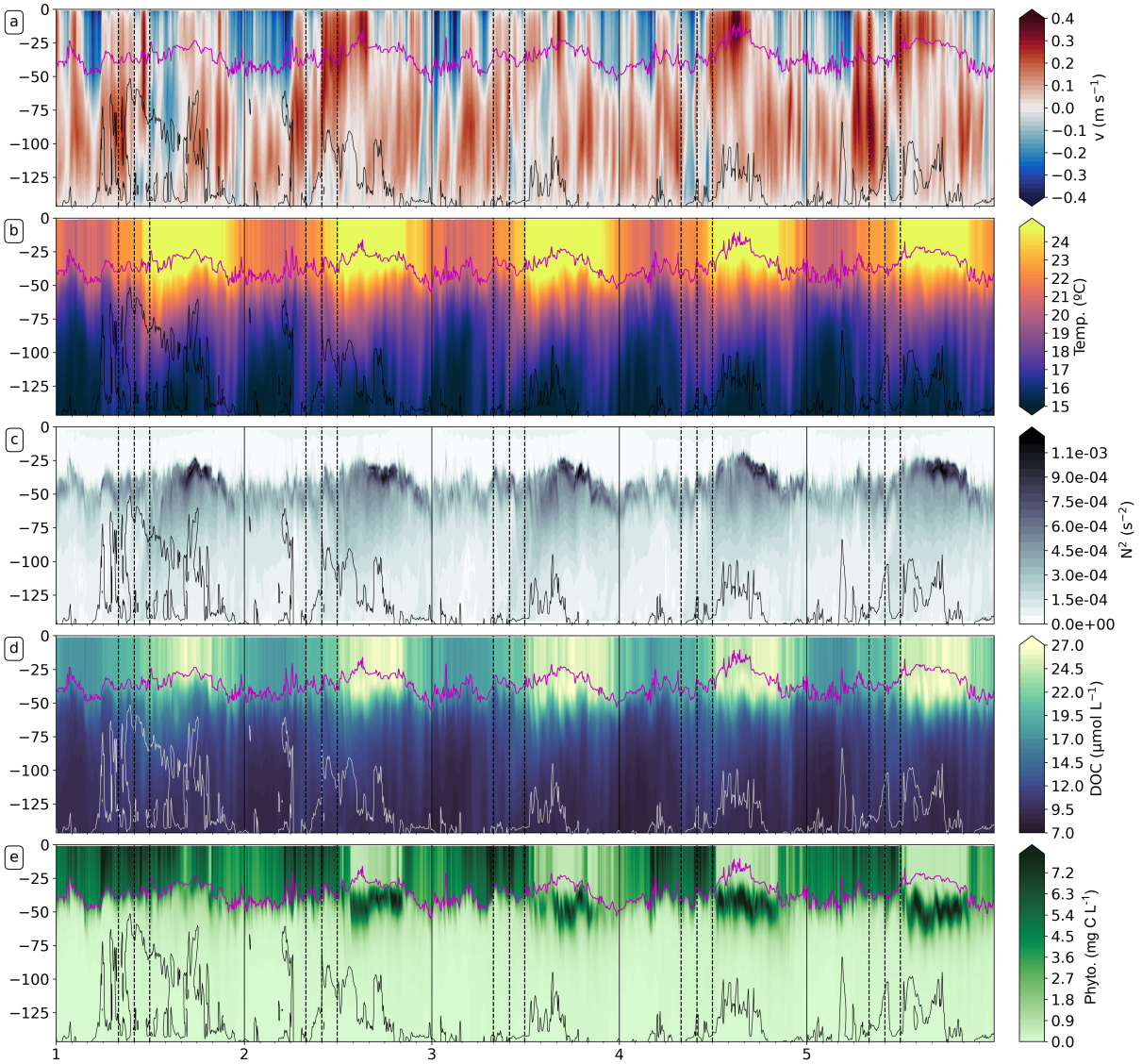


Figure A.9: Daily hovmöller diagram of a point extraction at 18°N and ≈160 m depth for complementary parameters. (a) Meridional current velocities (*V*), (b) temperature, (c) buoyancy frequency (N^2), (d) Dissolved Organic Carbon (DOC), and (e) phytoplankton biomass. Mixed layer depth is represented purple line in (a,b,d,e). O_2 = 40 µmol kg^{-1} is represented by black (a–c,e) and white (d) contours. Months of May, June and July are identified by black dashed vertical lines. Location of point extraction is represented by blue star in Figure 4.5a.

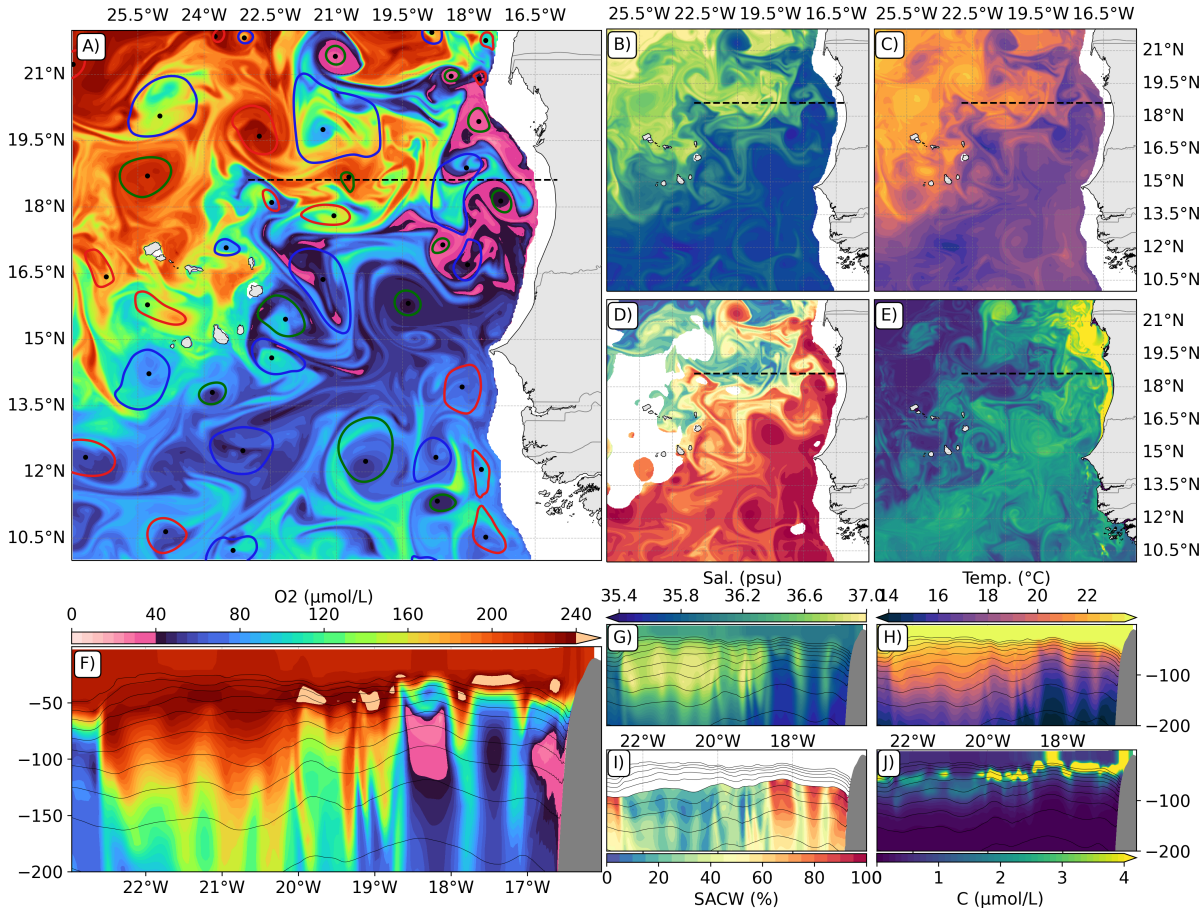


Figure A.10: Snapshot of key parameters, taken on the 24th of July of year 2. (A–E) Horizontal slice at 100 m depth and (F–J) vertical slices at zonal section identified by dashed lines on panels (A–E): (A,F) Oxygen concentrations; (B,G) salinity; (C,H) temperature; (D,I) %SACW; and (E) phytoplankton biomass (in carbon) integrated from the surface down to 80 m depth, with corresponding vertical slice in (J). Red, blue and green ellipsoids in panel (A) represent the perimeter of anticyclonic, cyclonic and ACMEs, respectively. Contours in lower panels (F–J) represent isopycnals from 25 to 27.2 kg m^{-3} at 0.2 kg m^{-3} interval.

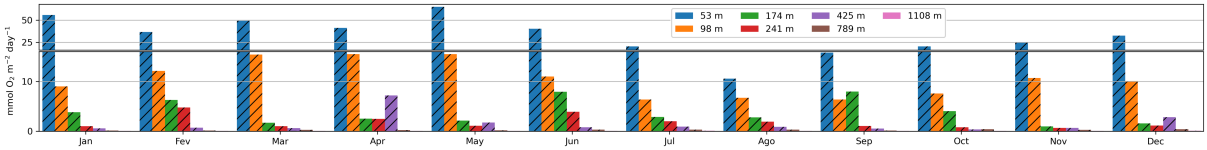


Figure A.11: Oxygen supply to the bottom via vertical mixing. Depths correspond to the locations of *in-situ* stations sampled during the M107 and MSM17/4 cruises off the Mauritanian coast. Only data from the 4th and 5th years of the simulation are shown.

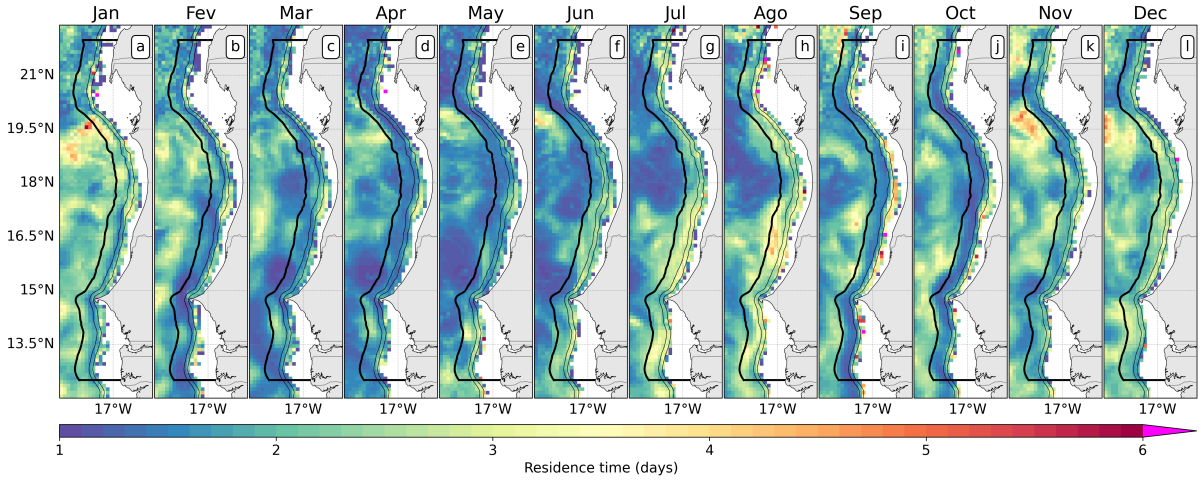


Figure A.12: Monthly average particle residence time. Spatial histogram with an horizontal resolution of 0.1°. Thick black contour represents the delimitation of the coastal region, while thin black contours indicate the 100 m and 300 m isobaths.

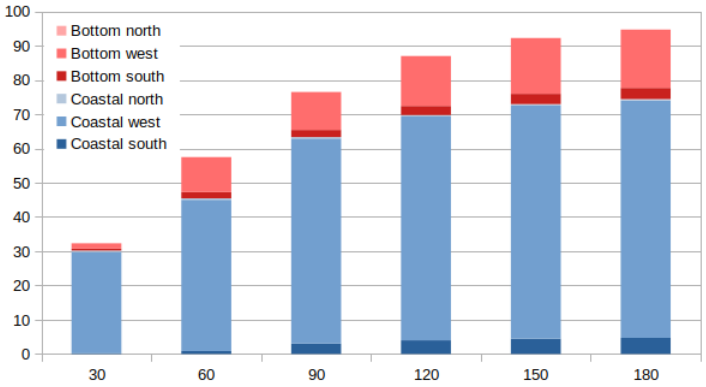


Figure A.13: Histogram indicating the proportion of coastal particles intersecting the coastal region boundaries per lifetime threshold. Only particles released within coastal area are accounted for. Six different particle lifetime thresholds (horizontal axis, in days) are considered. Particles released within the two bottom model layers (bottom particles; red) are distinguished from those released in the remaining layers (water column particles; blue).

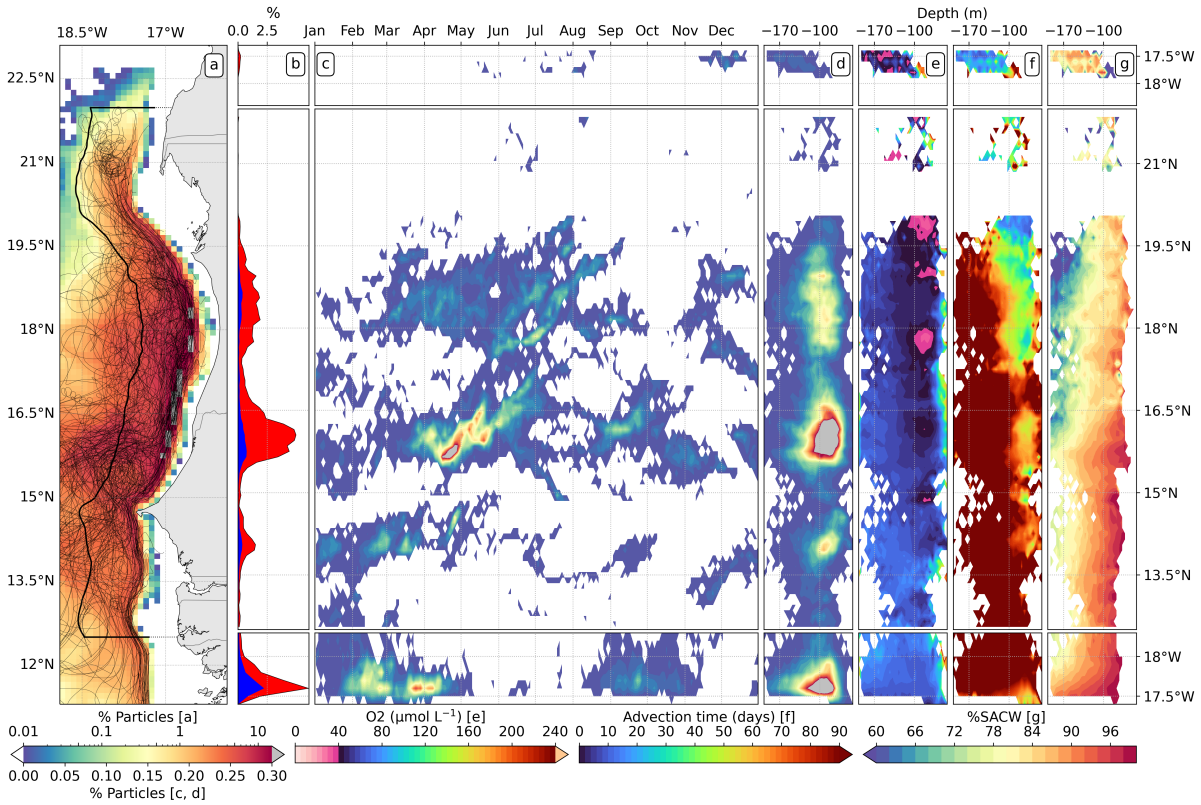


Figure A.14: Import of lagrangian particles released within the coastal region and crossing the respective boundary, set at 1° distance from the shelf break. Only particles intersecting the boundaries within 180 days after being released are accounted for. (a) Proportion of particles crossing each 0.1° bin. Thin black lines represent a subset of randomly selected trajectories of particles released in each 0.2° bin. Solid thick black line represents coastal boundary. (b) Total proportion of particles intersecting the coastal boundary along latitude and longitude. Following the same procedure as in Figure 4.13, blue and red areas represent the proportion of bottom and water column particles, respectively. (c) Hovmöller diagram with the proportion of particles intersecting the boundaries, with latitude and day of the year represented in the vertical and horizontal axis, respectively. (d–g) Vertical sections (with depth in the horizontal axis) for the proportion of intersecting particles, and average particle O_2 concentrations, advection time (from release to intersection with the boundary) and %SACW, respectively. Note the separation between upper, central and lower sub-panels from (b–g), representative of the northern, western and southern boundaries, respectively.

A.3 Supplement to Chapter 5

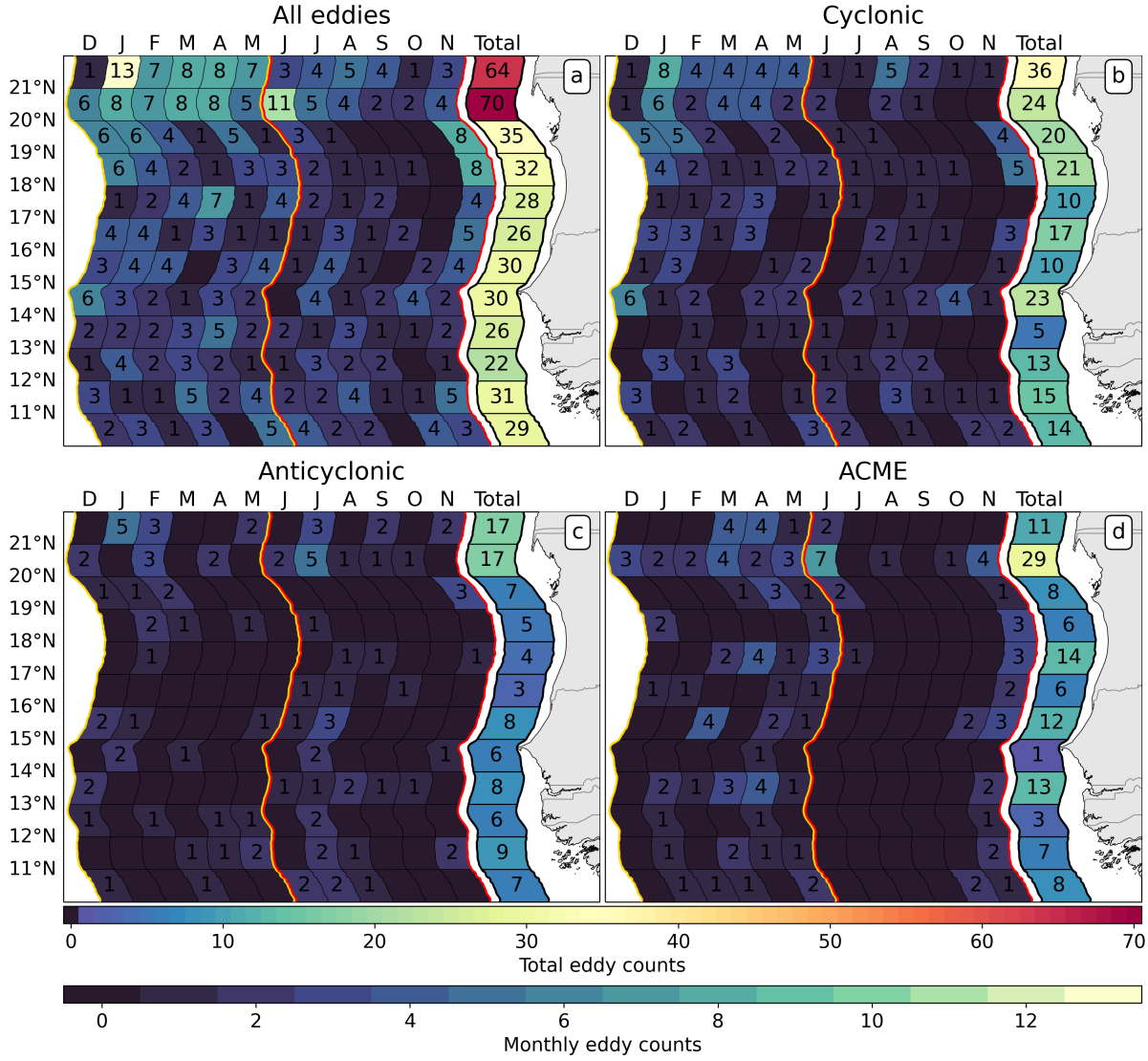


Figure A.15: Monthly genesis of coastal-generated eddies (lifetime > 10 days) along latitude. Only eddies formed within a 1.5° distance from the shelf break are accounted for. Latitudinal sections are spaced at a 1° interval. (a) Total number of eddies, with distinction between (b) cyclones, (c) anticyclones and (d) ACMEs. The yellow and red lines indicate the boundaries of the upwelling and relaxation seasons, respectively.

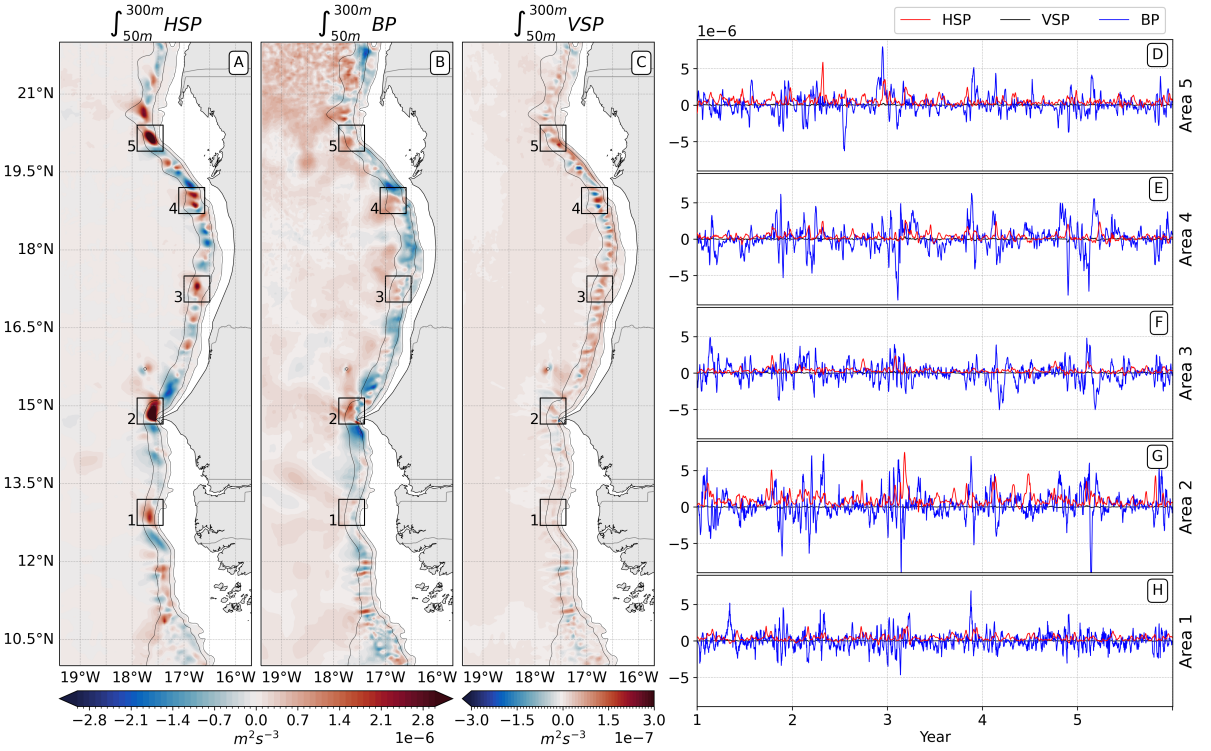


Figure A.16: Spatial and temporal variability of energy conversion terms to EKE. Terms are integrated from 50 to 300 m depth. (A) HSP, (B) BP and (C) VSP. Note that the scale of VSP (C) is one order of magnitude lower than the scale for HSP and BP (A–B). Topography is shown in black contours at 50, 100 and 1000 m isobaths. (D–H) Box-averaged time series of depth-integrated (50–300 m) HSP (red), BP (black), VSP (blue) within each box represented in (A–C).

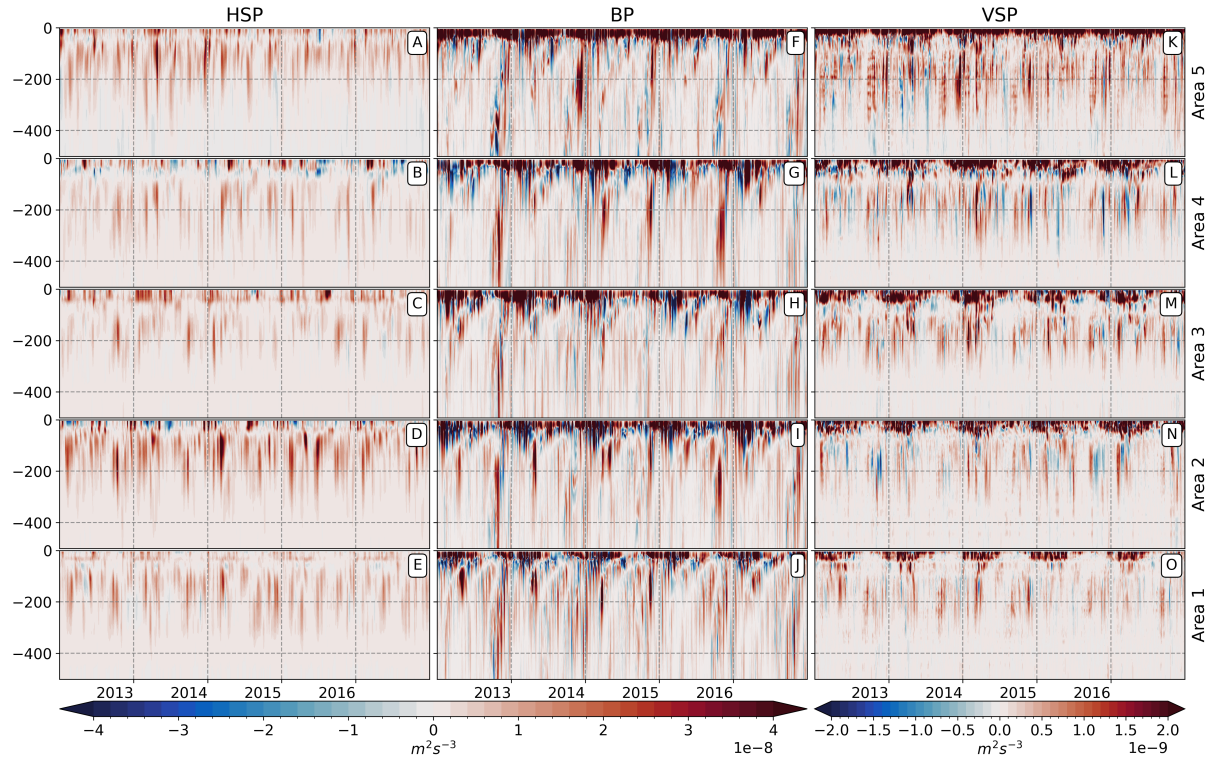


Figure A.17: Vertical and temporal variability of energy conversion terms to EKE. Terms are averaged within boxes identified in Figure A.16A–C. (A–E) HSP, (F–J) BP and (K–O) VSP. Note that the scale for VSP is one order of magnitude lower than the scale for HSP and BP.

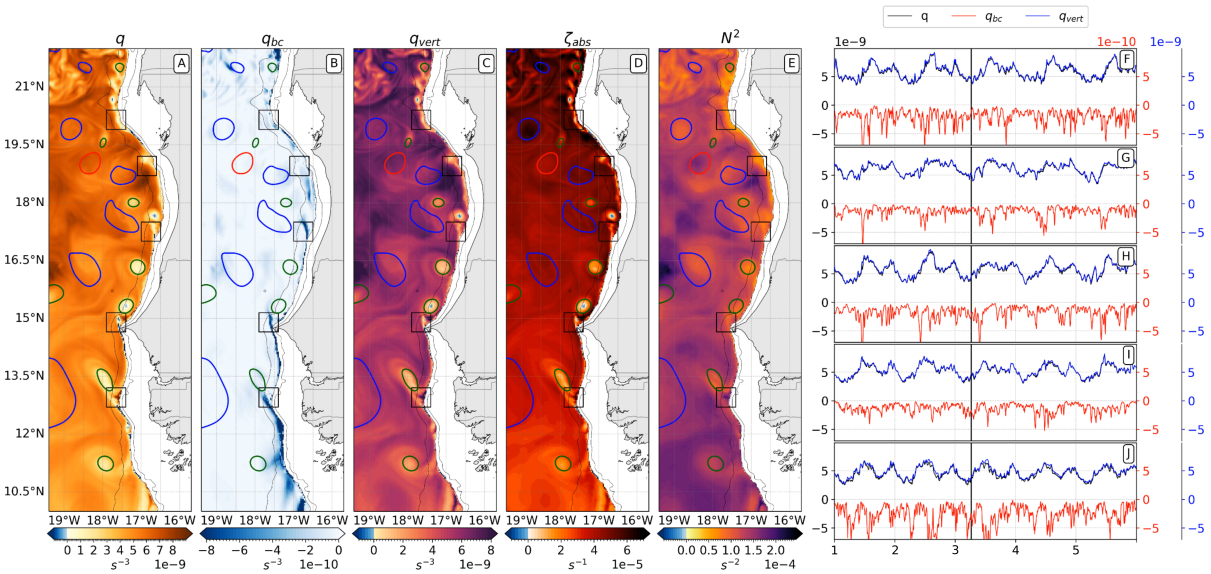


Figure A.18: Example of a snapshot with decomposition of Ertel PV terms at 100 m depth. Maps for (A) PV (q); (B) horizontal components of vorticity and buoyancy gradient (q_{bc}); (C) vertical component of the absolute vorticity and stratification q_{vert}; (D) absolute vorticity; and (E) buoyancy frequency squared. Topography is shown in black contours at 50-, 100- and 1000-m isobaths. (F–J) Box-average timeseries of q, q_{bc} and q_{vert} within respective boxes represented in (A–E), sorted along latitude.

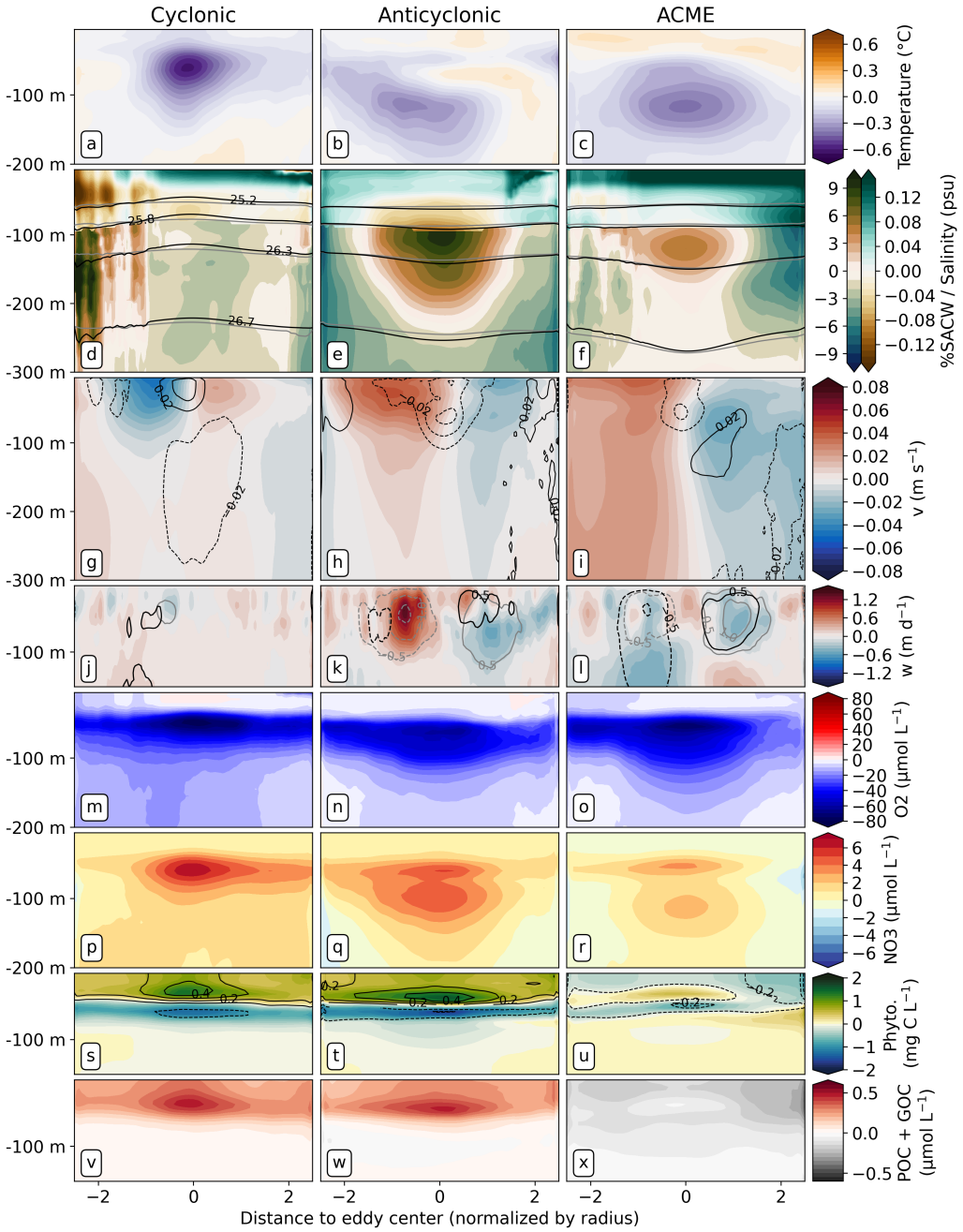


Figure A.19: Differences between vertical composites of hypoxic and non-hypoxic coastal-generated eddies, with no lifetime limit. Each eddy type is represented separately. Only eddies with lifetime exceeding 30 days are considered. (a–c) Temperature anomaly (with respect to the monthly climatology); (d–f) %SACW, with salinity differences for σ_θ < 25.8 kg m^{-3}. Black and gray contours represent average σ_θ isopycnal surfaces of hypoxic and non-hypoxic eddies, respectively. Differences in (g–i) meridional current velocities (v), with differences in ζ/f represented by dashed (negative) and solid (positive) contours; (j–l) vertical velocities (w), with average w for hypoxic and non-hypoxic eddies represented by black and gray contours respectively (upward and downward velocities are represented by solid and dashed lines, respectively); (m–o) O_2 concentrations; (p–r) NO_3 concentrations; (s–u) phytoplankton biomass, with differences in zooplankton biomass represented by solid (positive) and dashed (negative) contours; and (v–x) POC concentrations. Black contours in (m–p) and (v–x) represent isopycnals of hypoxic eddies at σ_θ 25.2, 25.8 and 26.3 kg m^{-3}.

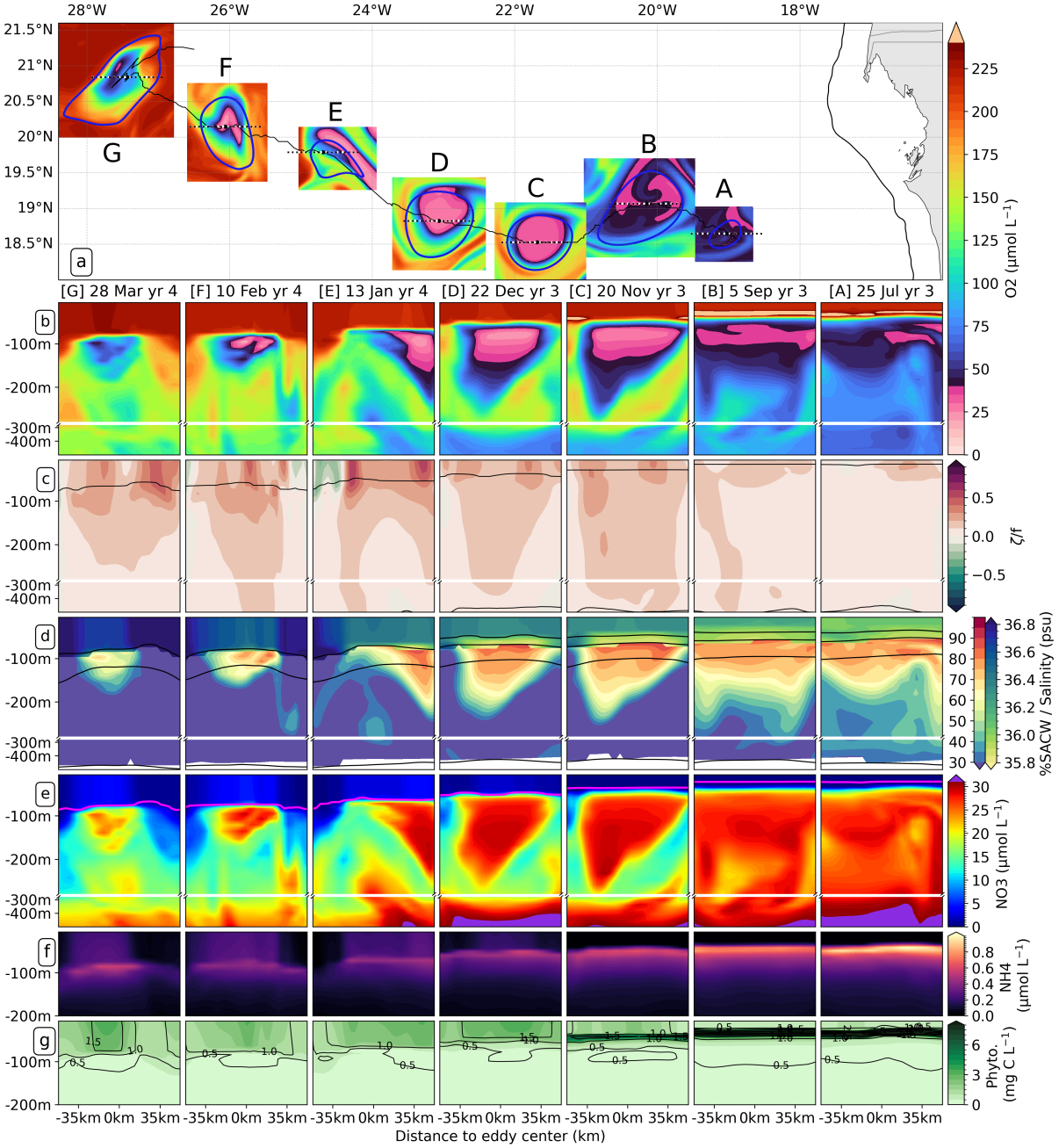


Figure A.20: Evolution of a second hypoxic cyclonic eddy (a) Selected timesteps of O_2 concentrations at 100 m depth around the perimeter of the eddy. The blue contours outline the eddy perimeter, the black dot marks the eddy center, the black thin line represents the eddy trajectory, and the dashed black/white line indicates the location of the vertical cross-sections shown in below panels. Vertical cross-sections taken at timesteps A–G of (b) O_2 concentrations; (c) relative vorticity (ζ/f), with black contours representing the 0.5×10^{-9} PV values; (d) water mass composition, showing %SACW at $\sigma_\theta > 25.8$ kg m^{-3}, and salinity at $\sigma_\theta < 25.8$ kg m^{-3}, with isopycnal surfaces at σ_θ 25.2, 25.8, 26.3 and 26.7 kg m^{-3} represented by contour lines; (e) NO_3 concentrations, with magenta line representing the base of the mixed layer; (f) NH_4 concentrations; and (g) Phytoplankton biomass, with contours representing zooplankton biomass (in mg C L^{-1}). Vertical sections are ordered from left to right to reflect the eddy's westward propagation.

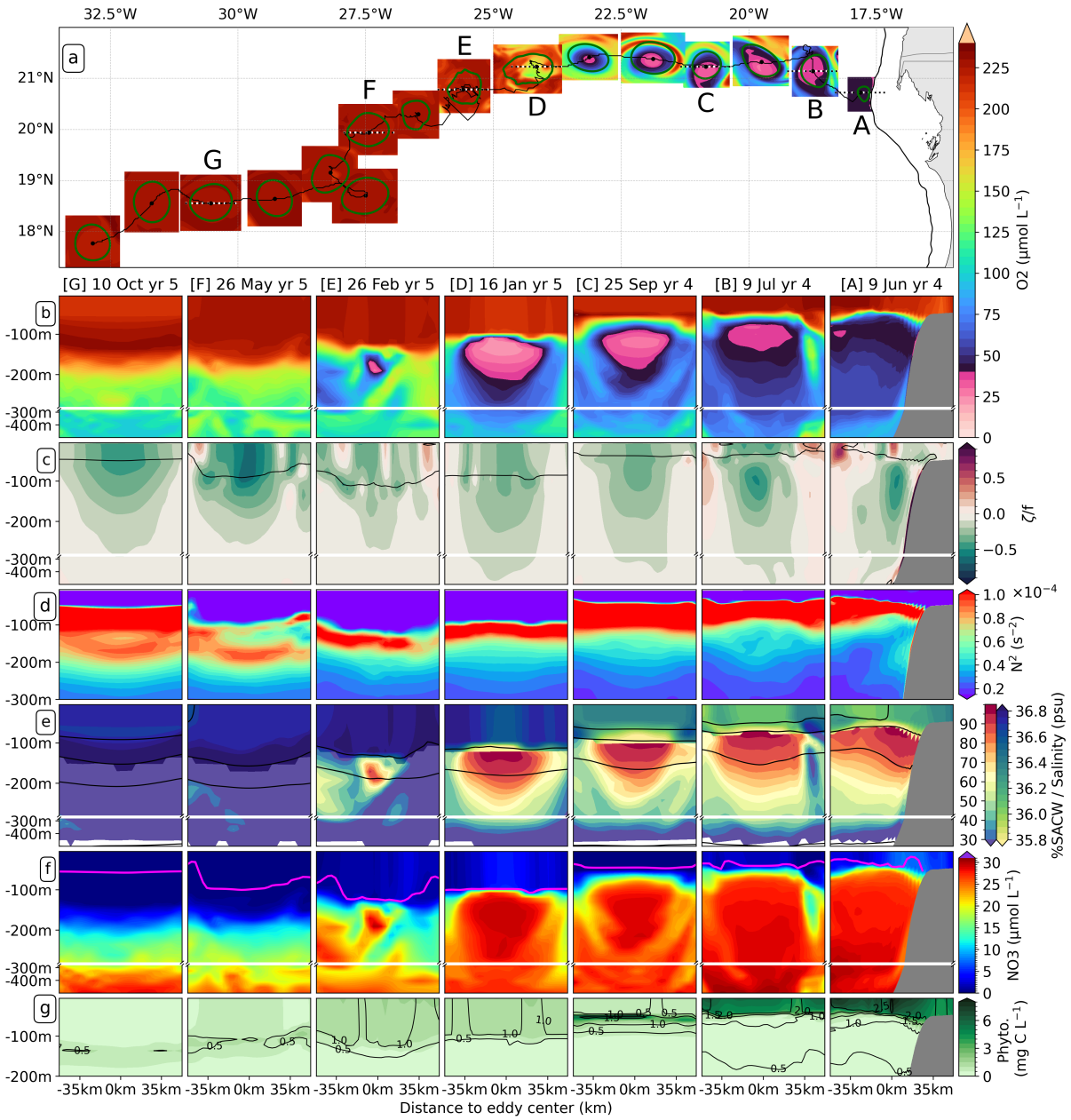


Figure A.21: Evolution of a second hypoxic ACME. (a) Selected timesteps of O_2 concentrations at 100 m depth around the perimeter of the eddy. The green contours outline the eddy perimeter, the black dot marks the eddy center, the black thin line represents the eddy trajectory, and the dashed black/white line indicates the location of the vertical cross-sections shown in below panels. Vertical cross-sections taken at timesteps A–G of (b) O_2 concentrations; (c) relative vorticity (ζ/f), with black contours representing the 0.5×10^{-9} PV values; (d) N^2; (e) water mass composition, showing %SACW at $\sigma_\theta > 25.8$ kg m^{-3}, and salinity at $\sigma_\theta < 25.8$ kg m^{-3}, with isopycnal surfaces at 25.2, 25.8, 26.3 and 26.7 kg m^{-3} represented by contour lines; (f) NO_3 concentrations; and (g) Phytoplankton biomass, with contours representing zooplankton biomass (in mg C L^{-1}). Vertical sections are ordered from left to right to reflect the eddy's westward propagation.

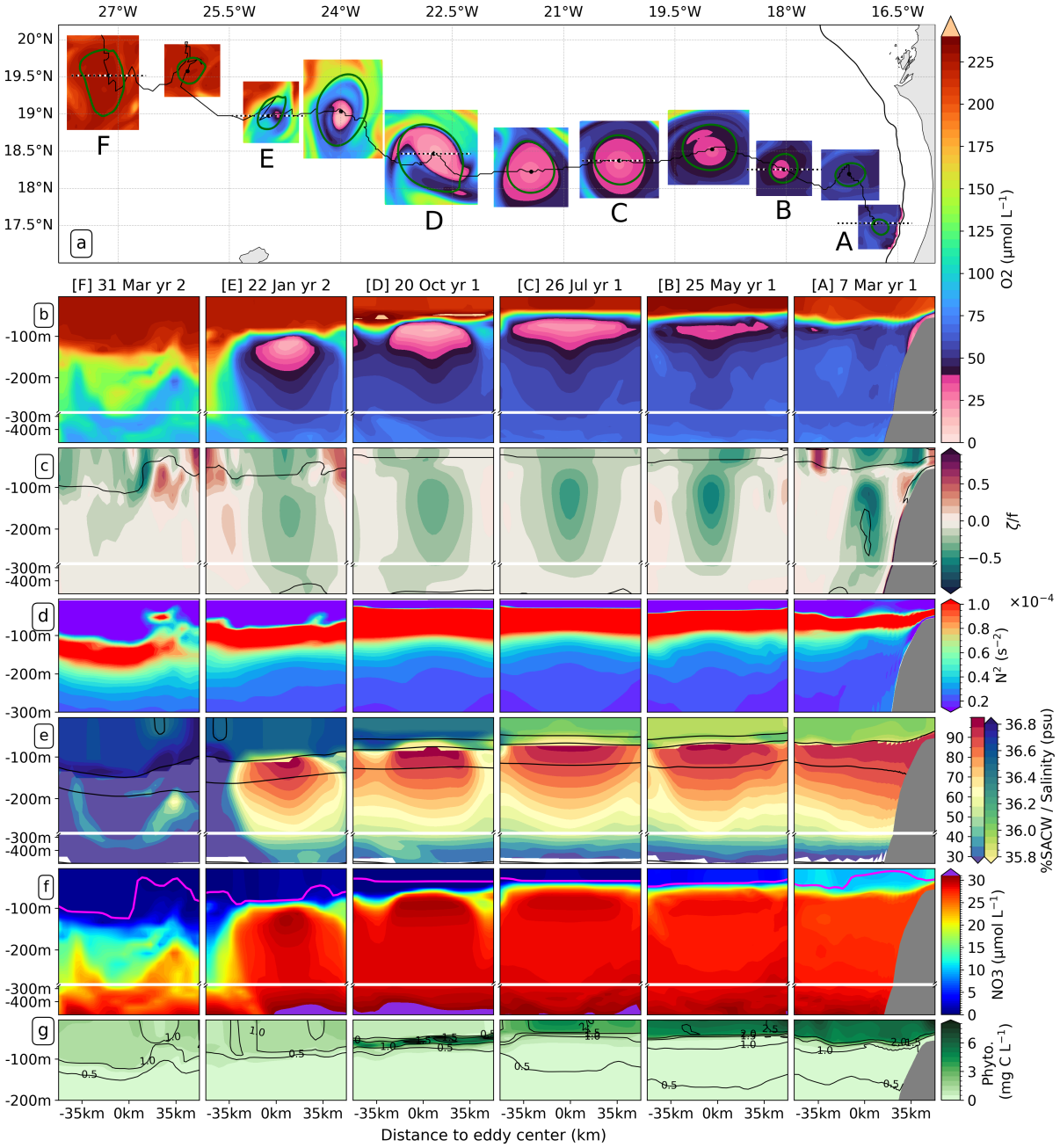


Figure A.22: Evolution of a third hypoxic ACME. (a) Selected timesteps of O_2 concentrations at 100 m depth around the perimeter of the eddy. The green contours outline the eddy perimeter, the black dot marks the eddy center, the black thin line represents the eddy trajectory, and the dashed black/white line indicates the location of the vertical cross-sections shown in below panels. Vertical cross-sections taken at timesteps A–F of (b) O_2 concentrations; (c) relative vorticity (ζ/f), with black contours representing the 0.5×10^{-9} PV values; (d) N^2; (e) water mass composition, showing %SACW at $\sigma_\theta > 25.8$ kg m^{-3}, and salinity at $\sigma_\theta < 25.8$ kg m^{-3}, with isopycnal surfaces at 25.2, 25.8, 26.3 and 26.7 kg m^{-3} represented by contour lines; (f) NO_3 concentrations; and (g) Phytoplankton biomass, with contours representing zooplankton biomass (in mg C L^{-1}). Vertical sections are ordered from left to right to reflect the eddy's westward propagation.

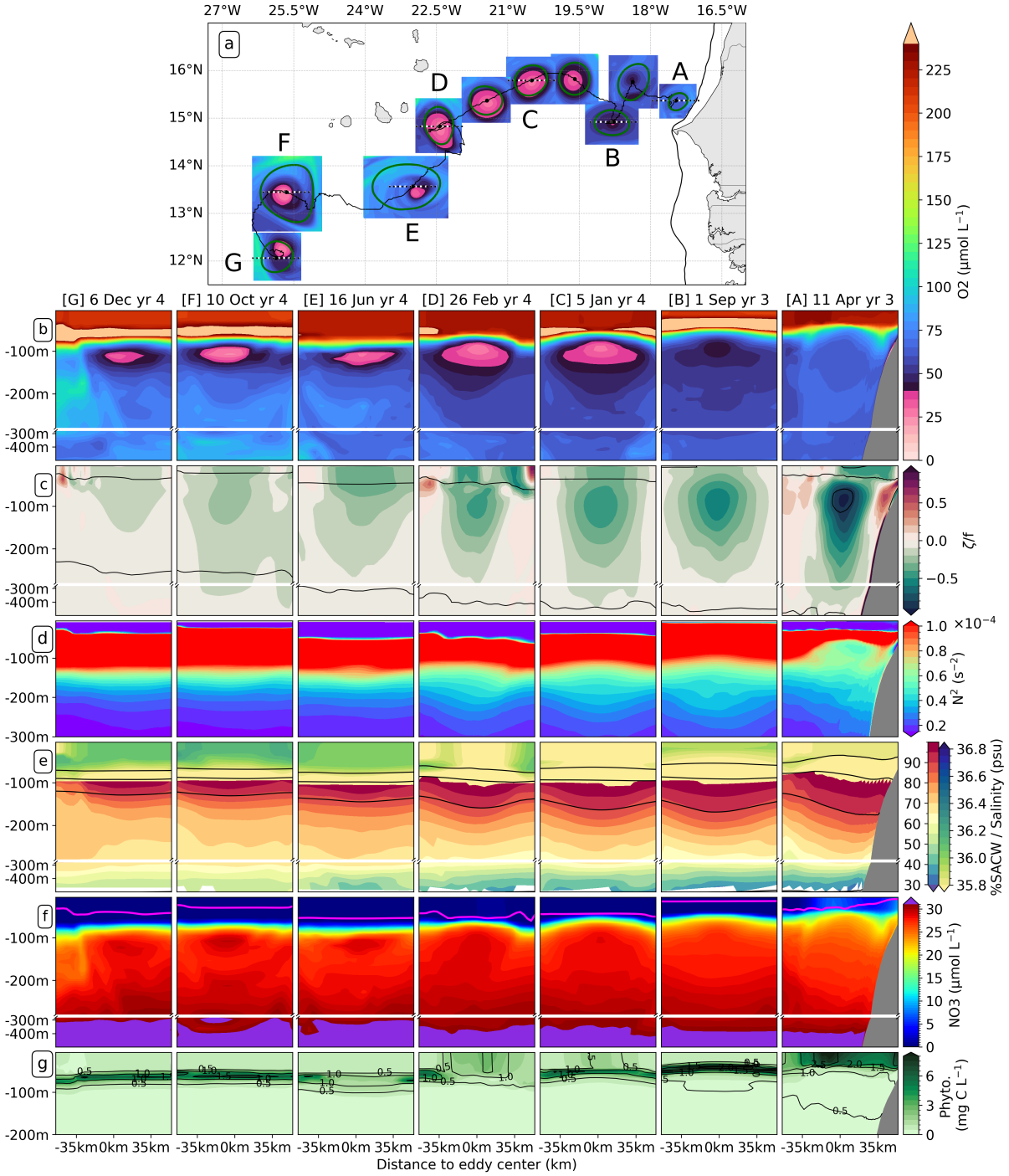


Figure A.23: Evolution of a forth hypoxic ACME. (a) Selected timesteps of O_2 concentrations at 100 m depth around the perimeter of the eddy. The green contours outline the eddy perimeter, the black dot marks the eddy center, the black thin line represents the eddy trajectory, and the dashed black/white line indicates the location of the vertical cross-sections shown in below panels. Vertical cross-sections taken at timesteps A–G of (b) O_2 concentrations; (c) relative vorticity (ζ/f), with black contours representing the 0.5×10^{-9} PV values; (d) N^2; (e) water mass composition, showing %SACW at $\sigma_\theta > 25.8$ kg m^{-3}, and salinity at $\sigma_\theta < 25.8$ kg m^{-3}, with isopycnal surfaces at 25.2, 25.8, 26.3 and 26.7 kg m^{-3} represented by contour lines; (f) NO_3 concentrations; and (g) Phytoplankton biomass, with contours representing zooplankton biomass (in mg C L^{-1}). Vertical sections are ordered from left to right to reflect the eddy's westward propagation.

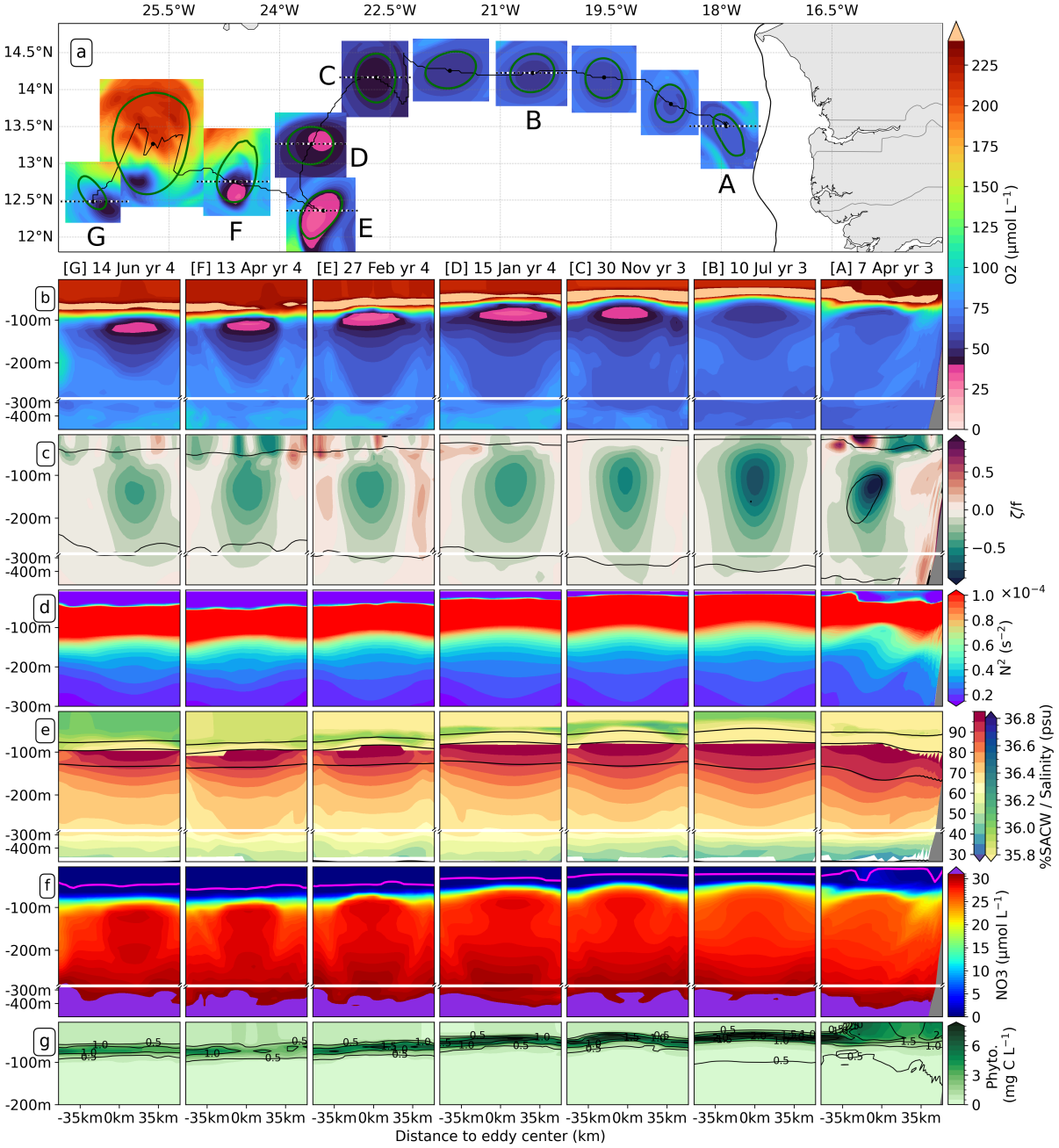


Figure A.24: Evolution of a fifth hypoxic ACME. (a) Selected timesteps of O_2 concentrations at 100 m depth around the perimeter of the eddy. The green contours outline the eddy perimeter, the black dot marks the eddy center, the black thin line represents the eddy trajectory, and the dashed black/white line indicates the location of the vertical cross-sections shown in below panels. Vertical cross-sections taken at timesteps A–G of (b) O_2 concentrations; (c) relative vorticity (ζ/f), with black contours representing the 0.5×10^{-9} PV values; (d) N^2; (e) water mass composition, showing %SACW at $\sigma_\theta > 25.8$ kg m^{-3}, and salinity at $\sigma_\theta < 25.8$ kg m^{-3}, with isopycnal surfaces at 25.2, 25.8, 26.3 and 26.7 kg m^{-3} represented by contour lines; (f) NO_3 concentrations; and (g) Phytoplankton biomass, with contours representing zooplankton biomass (in mg C L^{-1}). Vertical sections are ordered from left to right to reflect the eddy's westward propagation.

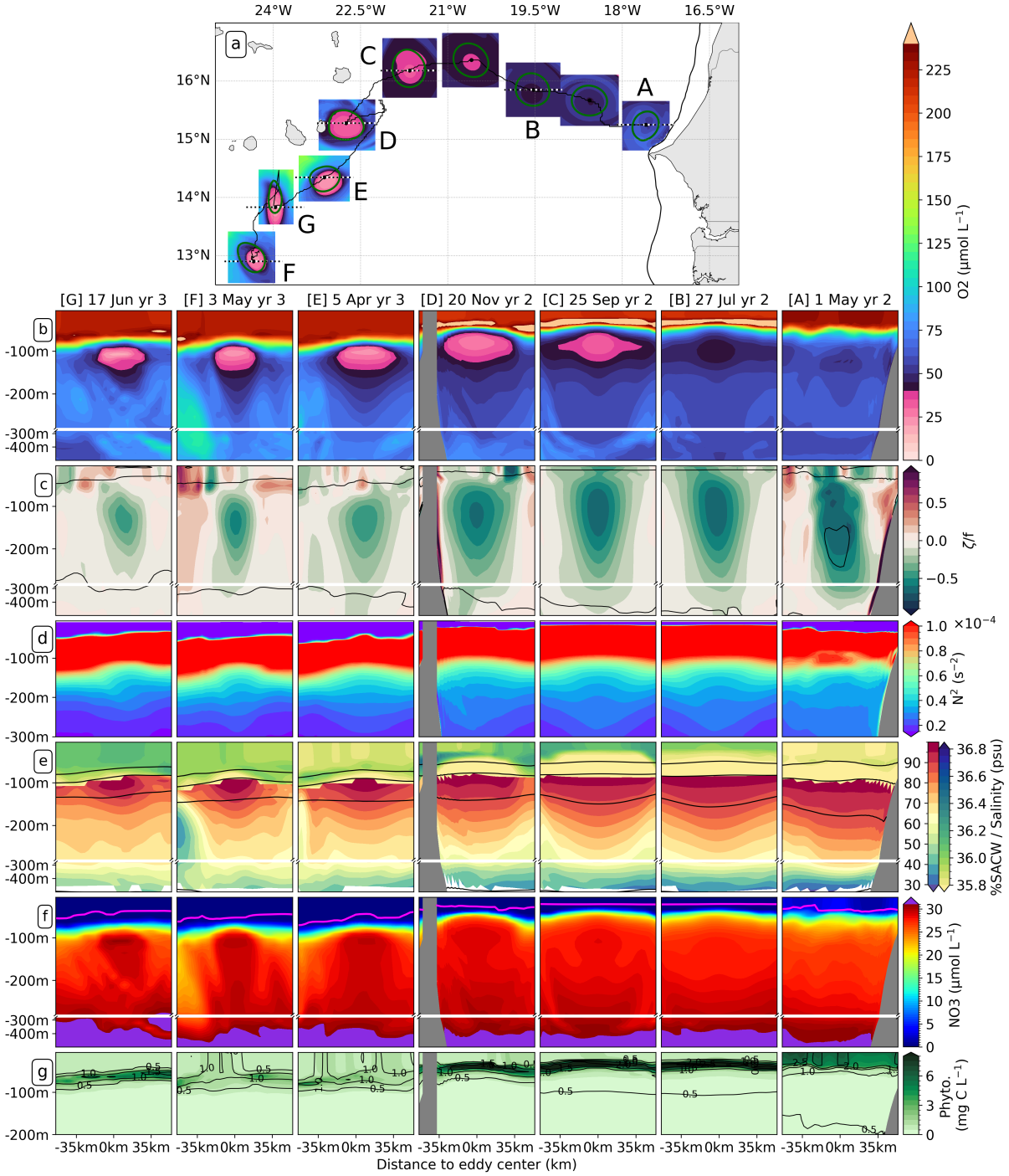


Figure A.25: Evolution of a sixth hypoxic ACME. (a) Selected timesteps of O_2 concentrations at 100 m depth around the perimeter of the eddy. The green contours outline the eddy perimeter, the black dot marks the eddy center, the black thin line represents the eddy trajectory, and the dashed black/white line indicates the location of the vertical cross-sections shown in below panels. Vertical cross-sections taken at timesteps A–G of (b) O_2 concentrations; (c) relative vorticity (ζ/f), with black contours representing the 0.5×10^{-9} PV values; (d) N^2; (e) water mass composition, showing %SACW at $\sigma_\theta > 25.8$ kg m^{-3}, and salinity at $\sigma_\theta < 25.8$ kg m^{-3}, with isopycnal surfaces at 25.2, 25.8, 26.3 and 26.7 kg m^{-3} represented by contour lines; (f) NO_3 concentrations; and (g) Phytoplankton biomass, with contours representing zooplankton biomass (in mg C L^{-1}). Vertical sections are ordered from left to right to reflect the eddy's westward propagation.